Vladimir Anisimov
Yuri Izyumov

SPRINGER SERIES IN SOLID-STATE SCIENCES 163

Electronic Structure of Strongly Correlated Materials

Springer

Springer Series in
SOLID-STATE SCIENCES 163

Springer Series in

SOLID-STATE SCIENCES

The Springer Series in Solid-State Sciences consists of fundamental scientific books prepared by leading researchers in the field. They strive to communicate, in a systematic and comprehensive way, the basic principles as well as new developments in theoretical and experimental solid-state physics.

Vladimir Anisimov
Yuri Izyumov

Electronic Structure of Strongly Correlated Materials

With 156 Figures

Springer

Professor Vladimir Anisimov
Professor Yuri Izyumov
Russian Academy of Sciences, Institute of Metal Physics
S. Kovalevskoy St. 18, 620041 Ekaterinburg, GSP-170, Russia
E-mail: via@imp.uran.ru, yuri.izyumov@uran.ru

Springer Series in Solid-State Sciences ISSN 0171-1873
ISBN 978-3-642-04825-8 e-ISBN 978-3-642-04826-5
DOI 10.1007/978-3-642-04826-5
Springer Heidelberg Dordrecht London New York

Library of Congress Control Number: 2010923616

Cover design: eStudio Calamar Steinen

Printed on acid-free paper

Springer is part of Springer Science+Business Media (www.springer.com)

To our wifes and life-long friends Marina and Tamara

Preface

This book, to our knowledge, is the first presentation, in form of a monograph, about the new approach in strongly correlated electrons systems called "Dynamical Mean-Field Theory" (*DMFT*). In nearly two decades, *DMFT* has become a universal tool to study strong electron correlations in solids. It was applied not only to all basic models of systems with partially filled electronic shells of transition, rare-earth and actinide elements, but also to real materials such as pure elements and various classes of chemical compounds.

DMFT was derived using only one characteristic of Coulomb interaction between d- or f-electrons of atoms in solids, that is, its spatial localization, and so this method can be applied to systems with any ratio value for Coulomb interaction strength and average kinetic energy defined as band width. *DMFT* does not use perturbation theory and hence is a perfect instrument for description of systems where Coulomb interaction strength and average kinetic energy are of comparable values and so there is no small parameter. The essential approximation of the method is the supposed local character of Coulomb correlations (electrons movements are correlated only when they are on the same lattice site). In other words, *DMFT* neglects spatial correlations but takes into account dynamical correlations in time variables for electrons on the same site fully. The influence of correlations on other lattice sites is combined in time (or energy) dependent mean-field. The method is named after this dynamical mean-field.

In this book, the *DMFT* method applications to two basic models, Hubbard and periodic Anderson models with computational procedures needed to calculate spectral function and various electronic properties, such as optical conductivity, magnetic susceptibility and superconductivity are described in detail. Various extensions of the method including combining *DMFT* with standard ab-initio band structure calculations approaches and *DMFT* generalizations to account for inter-site correlations and disorder are also given.

The growing number of studies using *DMFT* that appeared in the last few years and the most important among them are described in the book. The

authors worked many years on various issues of strongly correlated systems theory using model approaches as well as ab-initio band structure calculations and hope that the present book will be useful not only to researchers specializing on these problems but also can serve as a handbook for those who want to specialize in the field.

Yekaterinburg, Russia,
April 2010

Vladimir Anisimov
Yuri Izyumov

Contents

List of Acrnomys

DFT	Density Functional Theory
LDA	Local Density Approximation
$LSDA$	Local Spin Density Approximation
$LDA + U$	Combination of LDA and static mean-field approximation for Coulomb interaction
$LMTO$	Linearized "Muffin-Tin" Orbitals Method
$LAPW$	Linearized Augmented Plane Wave Method
$DMFT$	Dynamical Mean-Field Theory
$EDMFT$	Extended $DMFT$
$CDMFT$	Cluster $DMFT$
$LDA + DMFT$	Combination of LDA and $DMFT$
QMC	Quantum Monte Carlo Method
$PQMC$	Projective QMC
$CT - QMC$	Continuous time QMC
NRG	Numerical Renorm-Group Method
IPT	Iterative Perturbation Theory
ED	Exact diagonalization Method
RPA	Random Phase Approximation
SCF	Single-site Spin Fluctuation Theory
CPA	Coherent Potential Approximation
$din.CPA$	Dynamical CPA
$MB - CPA$	Many-body CPA
$PM - CPA$	Projection operator CPA
$SCPM$	Self-consistent $PM - CPA$
PAM	Periodic Anderson Model
$SIAM$	Single Impurity Anderson Model
KL	Kondo Lattice
GF	Green Function
WF	Wannier Function
SCS	Strongly Correlated Systems
MI	Metal–insulator phase transition
HF	Heavy Fermions
OP	Order Parameter

1

Introduction

1.1 Strongly Correlated Materials

In last decades main attention of experimental and theoretical studies for metallic systems has shifted to the field of transition and rare-earth elements with partially filled $3d$-, $4f$-, and $5f$-electronic shells and based on them chemical compounds. At the beginning of this process in 1960s, the most intriguing phenomenon in this field was metal–insulator phase transition (MI) observed for many transition metal oxides with variations in pressure, temperature, or doping. A decade later a new class of rare-earth compounds was discovered where charge carriers have effective mass value tens and hundreds time larger than free electron mass – so called "heavy fermion" (HF) systems. In such systems a great variety of interesting phenomena were found: phase transitions between magnetic order and superconductivity, appearance and disappearance of local magnetic moments, transport properties anomalies.

Such interplay of electric and magnetic properties is typical manifestation of strong coupling for electronic and magnetic degrees of freedom in many $3d$- and $4f$-elements compounds. Good example of such coupling are manganites with colossal magneto-resistive effect, where moderate magnetic filed can drastically change electronic state of the system from insulating to metallic. However, the most significant and totally unexpected was the discovery of high-temperature superconductivity ($high\text{-}T_{\mathrm{c}}$) in transition metal oxides. This discovery brought researchers attention to synthesis and physical properties study of new materials and in next 20 years there were found a lot of new compounds with anomalous properties.

It is clear that physical phenomena richness for these compounds is due to the presence of partially filled $3d$-, $4f$-, or $5f$-electronic shells with local magnetic moments preserved in solid. Strong interaction of d, f electrons with each other and with itinerant electronic states of the material is responsible for its anomalous properties. Such materials with strong electron–electron interaction are called strongly correlated systems (SCS). All the above mentioned

chemical compounds and many others discussed later belong to *SCS* (see e.g.[1]).

Anomalous physical properties of new materials are determined by their electronic structure. Classical band theory works very well for simple metals and semiconductors where interelectron interaction is weak but it is unable to describe *SCS*. In *SCS* a strength of Coulomb interaction among electrons is of the same order as band width for $3d$-, $4f$-, or $5f$-shells or even larger. In this case completely new approach is needed that is beyond perturbation theory. In last 40 years starting from pioneering Hubbard works [2,3] there were proposed many methods to treat *SCS* electronic structure problem. Those methods were based on simple models: Hubbard model, *sd*-model, and periodic Anderson model. Some of the proposed approaches were successful for certain *SCS* classes but they were far from being universal and failed for more complicated models describing real materials.

It seemed that *SCS* theory was doomed to be adequate only for certain limited cases and able to produce not more than semiquantitative results. The breakthrough was achieved when Metzner and Vollhardt [4] in 1989 proposed to study strongly interacting electrons systems in large dimensional d space (or equivalently lattices with large number of nearest neighbors z). It was shown that in the limit $d \to \infty$ (or $z \to \infty$) equations of motion for electrons on lattice are significantly simplified and can be exactly solved for any value of Coulomb interaction strength.

Theory simplification in $d \to \infty$ limit is because of the fact that in this case one can neglect spatial fluctuation in the system leaving in consideration only dynamical on-site fluctuations. This discovery led to development of Dynamical Mean-Field Theory (*DMFT*) where lattice problem was mapped to effective impurity problem with correlated electrons feeling time or energy dependent mean-field (hence the name *dynamical* mean-field) but the field dependence on wave vector responsible for spatial correlations is ignored. Solution of the impurity problem is used to build self-energy for lattice Green function that in its turn gives new approximation for dynamical mean-field. So this field is self-consistently determined in *DMFT* calculation scheme. First application of this method was done by Georges and Kotliar [5] and Jarrell [6] for Hubbard model in 1992. There was obtained so called three-peak spectral structure with central quasiparticle peak on Fermi energy and two broad side peaks corresponding to lower and upper Hubbard bands (see also [7]). Such three-peak structure was later found in experimental spectra. Metal–insulator transition with increasing Coulomb interaction strength U was described in this picture as spectral weight transferring from quasiparticle band to Hubbard bands with disappearance of quasiparticle peak and energy gap creation for critical U value.

Later *DMFT* was applied to basic *SCS* models and results were described in review [8]. In last years *DMFT* developments allowed to treat successfully not only simple systems but also complicated real compounds [8–11]. Some extensions of *DMFT* were proposed to take into account spatial

correlations. Successes of *DMFT* were recognized when its founders Georges, Kotliar, Metzner, and Vollhardt were awarded in 2006 Agilent Technologies Europhysics Prize [12].

It is necessary to note that long before *DMFT* development the importance of taking into account local on-site correlations was recognized. Local correlations has allowed Hubbard [13,14] to describe splitting of noninteracting band on two "Hubbard" sub-bands due to strong Coulomb interaction. The next important step was to use representation of partition function as a functional integral over fluctuating fields that has allowed to Hubbard and Hasegawa to develop "Single-site Spin Fluctuation" theory (*SSF*) [13,15–17].

Further progress in this direction was based on using "Coherent Potential Approximation" (*CPA*) developed originally to treat disordered alloys electronic structure. Later, it was shown that *CPA* is exact in the limit of infinite dimensions $d \to \infty$. Kakehashi and Fulde [18–25] have developed a number of approaches where *CPA* calculation scheme was generalized for taking into account dynamical fluctuations. It was done via introduction of frequency dependence in coherent potential corresponding to combined action of all electrons on distinguished lattice site. These approaches resulted in the development of "Dynamical *CPA*" (*din.CPA*) [19], "many-body *CPA*" (*MB-CPA*) [26], and "projection operator *CPA*" method (*PM-CPA*) [22].

As it was shown in [21,27] that *MB-CPA* and *PM-CPA* methods are equivalent to *DMFT*. All of them ignore spatial correlations in *SCS* but take into account local on-site dynamical fluctuations. Extension of those approaches to include spatial correlations was realized in "self-consistent *PM-CPA*" method (*SCPM*) [23,24]. Application of *SCPM* method to Hubbard model has allowed to reproduce all main effects of strong correlations near half-filling including three-peak structure of spectral function that was obtained in *DMFT*.

There is an important technical detail worth mentioning. In contrast to *DMFT* based on temperature (Matsubara) Green function formalism, in *PM–CPA* method and its extension *SCPM* retarded Green functions are used. In the result in those methods one does not need to perform analytical continuation procedure from imaginary frequencies to real energy values as it is the case in *DMFT* calculation scheme. That could be a significant advantage of *SCPM* method compared to *DMFT* because such analytical continuation can be an "ill defined problem".

Dynamical *CPA* approaches were developed in parallel to *DMFT* and the former could be regarded as a supplemental method to the latter. A detailed comparison of those two approaches is presented in Kakehashi review [27]. Later we will consider only *DMFT* method results for *SCS* theory.

1.2 Basic Models in Strongly Correlated Systems Theory

Quantum mechanical study of strongly correlated systems is done by two approaches: ab-initio electronic structure calculations and model investigations. In the first case real materials can be described with specifics of their chemical composition and crystal structure fully taken into account. In model approaches such specifics are neglected but more rigorous solution of the problem can be obtained with physical properties dependence on temperature and applied external fields. Sometimes, it is possible to get analytical description of the results with formulas but in general numerical calculations to find equations solutions are unavoidable.

For material with partially filled d- or f-shells three basic models are used: Hubbard model [2], sd-model [28, 29], and periodic Anderson model [30]. In Hubbard model only one group of nondegenerate electrons is considered with repulsive Coulomb interactions for electrons on the same site. Model Hamiltonian describing electrons motion on the lattice and their local Coulomb interaction is:

$$\mathcal{H} = \sum_{ij\sigma} t_{ij} \hat{c}^{+}_{i\sigma} \hat{c}_{j\sigma} + U \sum_{i} \hat{n}_{i\uparrow} \hat{n}_{i\downarrow}. \tag{1.2.1}$$

As electrons are not degenerate then two electrons can meet on the same site only when their spin directions are opposite to each other. Here $\hat{c}_{i\sigma}$ and $\hat{c}^{+}_{i\sigma}$ are creation and annihilation operators for electron on site i with spin index σ that can have two values: $\uparrow$ and $\downarrow$, $\hat{n}_{i\sigma} = \hat{c}^{+}_{i\sigma}\hat{c}_{i\sigma}$ is electrons number operator with spin σ on site i, t_{ij} is hopping matrix element. Usually, it is supposed that hopping is not zero only for nearest neighbors (number of those is z). Second term in (1.2.1) describes local Coulomb interaction among electrons with Coulomb parameter U defined as an energy needed to put two electrons on the same atomic site ($U \equiv E(2) + E(0) - 2E(1)$). This term was proposed by Anderson to describe a problem of local magnetic moment on impurity in metal [30]. Such simplified expression for Coulomb interaction was found very convenient for magnetism in metals study. Fundamental investigations performed by Hubbard on the basis of Hamiltonian (1.2.1) gave his name to the model [31].

In Hamiltonian (1.2.1) there are two parameters: zt and U (t is hopping matrix element value for nearest neighbors t_{ij}). For various values of their ratio two cases can be distinguished: weak coupling when $U \ll zt$ and strong coupling when $U \geq zt$. First case corresponds to standard itinerant magnetism model (see for example [32]) whereas second one to strongly correlated systems where Hubbard model is usually used. In the limit $U \gg zt$ Hamiltonian (1.2.1) can be reduced to effective tJ-model Hamiltonian [31]:

$$\mathcal{H} = t \sum_{ij\sigma} \tilde{c}^{+}_{i\sigma} \tilde{c}_{j\sigma} + J \sum_{ij} (\mathbf{S}^{\mathrm{e}}_{i} \mathbf{S}^{\mathrm{e}}_{j}). \tag{1.2.2}$$

Hamiltonian (1.2.2) describes correlated motion for electrons on the lattice (correlated means that electrons can hop to the neighboring site only when there is no other electron on this atom); operator $\tilde{c}^{+}_{i\sigma} = \hat{c}^{+}_{i\sigma}(1 - \hat{n}_{i-\sigma})$ correspond to creation for correlated electrons, electron number operator $\tilde{n}_{i\sigma}$ on the site i with spin σ assumes that only one electron can occupy the site. Second term in (1.2.2) describes exchange interaction among electrons on neighboring sites. Its parameter value $J = 4t^2/U$ is determined by Anderson kinetic exchange effect [33]. Exchange interaction in (1.2.2) describes the tendency to antiferromagnetic ordering in the system. Spin operators in (1.2.2) can be expressed via Fermi operators in a standard way [34]:

$$\mathbf{S}^{\mathrm{e}}_i = \sum_{\sigma\sigma'} c^{+}_{i\sigma}\mathbf{s}_{\sigma\sigma'}c_{i\sigma'}, \tag{1.2.3}$$

where $\mathbf{s}$ is a vector build from Pauli matrices:

$$s^x = \frac{1}{2}\begin{pmatrix} 0 & 1 \\ 1 & 0 \end{pmatrix}, \quad s^y = \frac{1}{2}\begin{pmatrix} 0 & -i \\ i & 0 \end{pmatrix}, \quad s^z = \frac{1}{2}\begin{pmatrix} 1 & 0 \\ 0 & -1 \end{pmatrix}. \tag{1.2.4}$$

It means that tJ-model Hamiltonian has purely electron nature and does not include local spin operators as in Heisenberg model.

Let us consider now hybrid models that include two types of electrons. One of them is *sd*-exchange model where electrons interact not with each other but with localized magnetic moments. Those moments are formed by atoms with partially filled electronic shells called *d*-electrons while itinerant electrons are named *s*-electrons. In reality, *sd*-model describes rare-earth elements compounds where $4f$ electrons are indeed very well localized. *sd*-model Hamiltonian is expressed via Fermi operators for itinerant electrons and local spin operators:

$$\mathcal{H} = \sum_{ij\sigma} t_{ij}\hat{c}^{+}_{i\sigma}\hat{c}_{j\sigma} - J\sum_{i\sigma\sigma'}(\mathbf{S}_i\mathbf{s}_{\sigma\sigma'})\hat{c}^{+}_{i\sigma}\hat{c}_{i\sigma'}. \tag{1.2.5}$$

Here J is so called *sd*-exchange integral defining strength of exchange interaction $J\mathbf{S}_i\mathbf{S}^{\mathrm{e}}_i$ of local spin $\mathbf{S}_i$ on site i and electron spin $\mathbf{S}^{\mathrm{e}}_i$ on the same site that is determined by (1.2.3). *sd* model Hamiltonian is quadratic for Fermi operators with off-diagonal exchange terms.

sd-model contains two parameters zt and J. Depending on their ratio value two cases can be distinguished. For $J \ll zt$ one has weak coupling and *sd*-exchange term can be treated in perturbation theory. In this approximation many interesting physical results were obtained: itinerant electrons magnetization in ferromagnetic metals, electron-band splitting in antiferromagnetic metal, exchange interaction between local spins via itinerant electrons, Kondo effect, connection between magnetic and electron properties in rare-earth metals, and superconductivity destruction by paramagnetic impurities. In strong coupling case $J \gg zt$ the problem can be reduced to effective double-exchange Hamiltonian [35–37] that describes ferromagnetism in manganites.

Second hybrid model is Periodic Anderson Model (PAM) that includes two type of electrons: itinerant (s-electrons) and localized (d-electrons). Coulomb interactions is taken into account only for localized electrons on the atomic site. In contrast to sd-model s- and d-electrons are coupled not via exchange interaction by through hybridization term. In general case Periodic Anderson Model Hamiltonian is:

$$\mathcal{H} = \sum_{ij\sigma} t_{ij}\hat{c}^{+}_{i\sigma}\hat{c}_{j\sigma} + \varepsilon_d \sum_{i\sigma} \hat{n}^{d}_{i\sigma} + U \sum_{i} \hat{n}^{d}_{i\uparrow}\hat{n}^{d}_{i\downarrow} + \sum_{ij\sigma}(V_{ij}\hat{c}^{+}_{i\sigma}\hat{d}_{j\sigma} + V^{*}_{ij}\hat{d}^{+}_{j\sigma}\hat{c}_{i\sigma}), \tag{1.2.6}$$

where $\hat{c}_{i\sigma}(\hat{c}^{+}_{i\sigma})$ and $\hat{d}_{i\sigma}(\hat{d}^{+}_{i\sigma})$ are Fermi operators for s- and d-electrons, respectively, and $\hat{n}^{d}_{i\sigma} = \hat{d}^{+}_{i\sigma}\hat{d}_{i\sigma}$ the electron number operators for d-electrons with spin σ on the site i. In Hamiltonian (1.2.6) ε_d is d-electron energy and V_{ij} the hybridization parameter. This model describes appearance of local magnetic moments, Kondo insulators, heavy fermions, and intermediate valence effect.

Models defined by Hamiltonians (1.2.1) and (1.2.6) are basis of strongly correlated systems theory where magnetic and transport properties are studied. Investigation results for those models help to understand metal–insulator phase transition, high-Tc superconductivity, heavy fermion effects in rare-earth and actinides compounds.

1.3 Methods for Models Investigation

We will exclude from our consideration one-dimensional Hubbard model where exact analytical solutions can be found. Our main interest will be $d = 3$ (sometimes $d = 2$) systems (d is space dimension) that are directly related to real materials with strong correlations effects.

Initially, models were investigated by simplest methods such as mean-filed theory and perturbation theory when small parameter can be found like $U \ll zt$ for Hubbard and Anderson models or $J \ll zt$ for sd model. In the cases where there is no small parameter ($zt \sim U$ or $zt \sim J$) serious difficulties appear in attempts to obtain analytical solution for the problem. In such cases sometimes another small parameter could be found such as number of electrons, $1/N$ expansion (N is a number of degenerate states), or $1/z$ expansion (z is nearest neighbors number). The last case in the limit of $d \to \infty$ (or $z \to \infty$) led to development of $DMFT$.

There were also approaches developed not based on perturbation theory for interaction parameter. Among them we mention decoupling method for double-time Green functions starting from pioneering Hubbard works and used in various models. Closely related to it is composite operators method [38] that was successfully applied to strong correlations problem. Rather apart stands variation Gutzwiller method [39] widely used for study strongly correlated systems.

Important development was also auxiliary particle approach: slave boson and auxiliary fermions methods. The idea on the basis of those methods is

to replace general operators (such as Hubbard X-operators) by the product of Fermi and Bose operators with additional procedure to exclude unphysical states. Good choice of auxiliary particles can lead to correct low-energy physics of the model in mean-filed approximation. Unfortunately, there is no universal recipe to construct such representation and often it is not clear which of the possible representations is the best one. There are many version of auxiliary particle methods.

In the physical literature there were proposed and used many different theoretical approaches to strong correlations problem. Reader can find their description in reviews [40–43] and monograph [44].

As we will show in this book the most universal method to study basic models is *DMFT* that allows to calculate electronic spectra and physical properties of strongly correlated systems with arbitrary value of interelectron interaction strength.

1.4 Ab-initio Electronic Structure Calculation Methods

Approach based on basic model study allows to understand electronic states in strongly correlated systems and to plot phase diagrams as a function of model parameters. However, in order to use these results for interpretation of real compounds experimental data one needs to know parameter values characteristic for particular material. For this purpose there are two approaches: empirical and first principles.

The first of them, empirical, is based on using experimental data to determine model parameters. Usually that is spectral data (optical, photoemission, and X-Ray spectra) that can give information about band width. In the case of strongly correlated systems on the edge of the metal–insulator transition (or already in Mott insulator state) it is possible to estimate also value for Coulomb interaction parameter U determined from the energy separation of the spectral peaks interpreted as Hubbard bands.

More often the approach is used where model parameters (such as Coulomb interaction parameter U and band width W) are varied to achieve the best agreement between experimental data for some characteristic (resistivity, susceptibility, etc.) and the corresponding value calculated in model solution. In such approach model parameters are considered to be adjustable parameters.

However, the most justified way to determine model parameters is using results of electronic structure calculations from *first principles* methods (or in other words ab-initio methods). The name *first principles* is used as opposite to empirical approach. *First principles* methods are not formally exact ones, because a lot of various approximations were done in their derivation. The key issue is the fact that in these methods construction only the most basic (*first*) Quantum Mechanics principles were used such as many-electron Schroedinger equation. For atoms and small molecules many-electron methods could be used where wave function is represented as linear combination of

Slater determinants. However for solids the most practical approach is Density Functional Theory (DFT) [45,46] that reduces many-particle problem to one-electron one. In Sect. 2.1.1 the basics of DFT are presented and in Sect. 2.1.2 the main calculation methods based on DFT are described.

In DFT one solves differential equations for one-electron wave functions with effective potential that is in its turn determined by the equation solutions. That results in very effective and practically realized iterative calculation scheme. However that means explicit neglect of correlation effects (all electrons feel the same time and energy independent potential). In the result for Mott insulators (for example transition metal oxides) DFT methods gave wrong metallic ground state (see Sect. 2.1.3).

There were proposed many corrections to DFT overcoming this defect and resulting in correct ground state for Mott insulators (see Sect. 2.1.4). However those correction were not derived from general enough equations and have rather restricted area of applicability.

Better perspectives has approach where electronic structure calculation results by DFT methods are used to calculate parameters for general Hamiltonian and then the problem defined by this Hamiltonian is solved by one of the methods developed in basic models theory (see Sect. 1.2). In Sect. 2.2 we describe how it is possible using Wannier functions formalism to calculate Hamiltonian parameters from eigenfunctions and eigenvalues obtained in DFT. Using constrain DFT (see Sect. 2.2.5) one can calculate also the value of Coulomb interaction parameter U.

The problem defined by this Hamiltonian can be solved in the simplest static mean-filed approximation (unrestricted Hartree-Fock). The resulting calculation scheme is called $LDA + U$ method and is described in Sect. 2.3. This method was found to be very successful when applied to systems with long-range spin and orbital order.

However, more general problems of paramagnetic insulator and strongly correlated metal can be solved only by $DMFT$ method that is described in details in Chaps. 3–5. Approach based on solving in $DMFT$ the problem defined by the Hamiltonian with parameters calculated in DFT calculations is called $LDA + DMFT$ method and is described in Chap. 6.

2

Electronic Structure Calculations in One-Electron Approximation

2.1 Density Functional Theory and Electronic Structure Calculations Methods

2.1.1 Density Functional Theory

The fundamental task of condensed matter physics is solution of many-electron problem that can be done only by using various approximations. At now there are two main approaches in solid state theory to solve this problem. One is based on taking into account restricted number of electronic states in small energy window around Fermi energy when the system is described by model Hamiltonian with a set of adjustable parameters (see Sect. 1.2).

Second approach is electronic structure calculations from *first principles* when the only input parameters are atomic number (nuclear charge) and number of electrons in the system. Positions of the atoms in the crystal (crystal structure parameters) is another information needed for calculation but in many cases those parameters can be obtained in *first principles* calculations via total energy minimization. The most widely used *first principles* methods are based on *DFT* [45, 46] that reduces many-electron problem to one-electron one.

According to Hohenberg-Kohn theorem [45, 46] that is a basis of *DFT*, all ground state properties of inhomogeneous interacting electron gas can be described by minimization of the total energy as a functional of electron density $\rho(\mathbf{r})$:

$$E[\rho] = T[\rho] + \int \mathrm{d}\mathbf{r}\rho(\mathbf{r})V_{\mathrm{ext}}(\mathbf{r}) + \int \mathrm{d}\mathbf{r}\rho(\mathbf{r}) \int \frac{\rho(\mathbf{r}')}{\mid \mathbf{r} - \mathbf{r}' \mid}\mathrm{d}\mathbf{r}' + E_{xc}[\rho], \quad (2.1.1)$$

where $T[\rho]$ is kinetic energy, $V_{\mathrm{ext}}(\mathbf{r})$ is the external potential acting on electrons (usually that is attractive nuclear potential), third term in (2.1.1) describes Coulomb interaction energy (Hartree energy) corresponding to charge distribution $\rho(\mathbf{r})$ and E_{xc} is so called exchange-correlation energy.

This term describes decreasing of Coulomb interaction between electrons in the same spin state due to the Pauli principle (so called exchange interaction that includes also self-interaction correction) and also purely correlation effects arising from the fact that electrons do not move independently from each other.

This method would be exact if the term E_{xc} in (2.1.1) could be rigorously defined. However for that one needs to solve exactly many-electron problem that is impossible in general case. Hence using approximations for exchange-correlation energy is unavoidable and they play a key role in *DFT*. Hohenberg-Kohn theorem states that system properties are defined by its charge density only and hence particular representation of wave functions building this density is undetermined. For practical applications $\rho(\mathbf{r})$ can be expressed via one-electron wave functions $\phi_i(\mathbf{r})$:

$$\rho(\mathbf{r}) = \sum_{i=1}^{N} \mid \phi_i(\mathbf{r}) \mid^2, \tag{2.1.2}$$

where N is total number of electrons.

To minimize functional (2.1.1) one need to vary it over new variables $\phi_i(\mathbf{r})$ with additional condition that wave functions are normalized. That leads to the system of Kohn-Sham differential equations (in the following we use atomic units system with Rydberg as energy unit that results in appearance of factor of 2 in Coulomb potential expression)

$$\left[-\nabla^2 - \sum_I \frac{2Z_I}{\mid \mathbf{r} - \mathbf{R}_I \mid} + 2\int \frac{\rho(\mathbf{r}')}{\mid \mathbf{r} - \mathbf{r}' \mid} \mathrm{d}\mathbf{r}' + V_{xc}(\mathbf{r})\right] \phi_i(\mathbf{r}) = \varepsilon_i \phi_i(\mathbf{r}). \tag{2.1.3}$$

Here $\mathbf{R}_I$ is position vector for nucleus with charge Z_I; ε_i are Lagrange multipliers having the meaning of one-electron eigenenergies and exchange-correlation potential V_{xc} is a functional derivative of exchange-correlation energy E_{xc}:

$$V_{xc}(\mathbf{r}) = \frac{\delta E_{xc}[\rho]}{\delta \rho(\mathbf{r})}. \tag{2.1.4}$$

Equations (2.1.3) allow to calculate electronic charge density $\rho(\mathbf{r})$ and total energy for ground state of the system.

Lagrange multipliers ε_i are usually interpreted as one-electron energies (eigenvalues) for the state corresponding to one-electron wave functions $\phi_i(\mathbf{r})$. There is an useful analog of (2.1.4) for ε_i. Eigenvalue ε_i is derivative of the total energy is respect to the occupancy of the corresponding one-electron state n_i:

$$\varepsilon_i = \frac{\partial E_{\mathrm{tot}}}{\partial n_i}. \tag{2.1.5}$$

DFT applications are based predominantly on so called Local Density Approximation (*LDA*) where exchange-correlation energy is defined as an

integral over space variables $\mathbf{r}$ with an expression under integral depending only on *local* value of electron density $\rho(\mathbf{r})$:

$$E_{xc}[\rho] = \int \rho(\mathbf{r})\varepsilon_{xc}(\rho(\mathbf{r}))\mathrm{d}\mathbf{r}. \tag{2.1.6}$$

Here $\varepsilon_{xc}(\rho)$ is contribution of exchange and correlation effects in total energy (per one electron) of homogeneous interacting electron gas with density $\rho(\mathbf{r})$.

For spin-polarized systems one can use Local *Spin* Density Approximation (*LSDA*) [47]:

$$E_{xc}[\rho^{\uparrow}, \rho^{\downarrow}] = \int \rho(\mathbf{r})\varepsilon_{xc}(\rho^{\uparrow}(\mathbf{r}), \rho^{\downarrow}(\mathbf{r}))\mathrm{d}\mathbf{r}, \tag{2.1.7}$$

where $\varepsilon_{xc}(\rho^{\uparrow}(\mathbf{r}), \rho^{\downarrow}(\mathbf{r}))$ is exchange-correlation energy per one electron in homogeneous spin-polarized electron gas with densities $\rho^{\uparrow}(\mathbf{r})$ and $\rho^{\downarrow}(\mathbf{r})$ for spin projections "up" and "down". Exchange-correlation potential (2.1.4) in this approximation become spin-dependent

$$V_{xc}^{\sigma}(\mathbf{r}) = \frac{\delta E_{xc}[\rho^{\uparrow}, \rho^{\downarrow}]}{\delta \rho^{\sigma}(\mathbf{r})}. \tag{2.1.8}$$

LDA approximation can be illustrated by introducing effective exchange-correlation hole surrounding every electron that produces attractive potential decreasing repulsive Coulomb interaction potential from all other electrons. As *LDA* is based on exchange-correlation energy expression for homogeneous electron gas it is expected to be justified if electron density variation in space is slow enough.

There are various approximation for exchange-correlation energy and potential [46, 48]. *L(S)DA* was used with great success to describe electronic properties for atoms, molecules and solids (see review [49]) where correlation effects were not too strong. In 1998 for "DFT development" Walter Kohn and John Pople were awarded Nobel prise (see Kohn's Nobel lecture [50].

2.1.2 Electronic Structure Calculations Methods Based on DFT

Calculation scheme for methods based on *DFT* consists in self-consistent solution of Kohn-Sham equations (2.1.3) to obtain a set of one-electron eigenfunctions $\phi_i(\mathbf{r})$ and corresponding eigenvalues ε_i. From those eigenfunctions new electron density $\rho(\mathbf{r})$ is calculated via (2.1.2). New $\rho(\mathbf{r})$ is used in its turn to get Coulomb $2\int \frac{\rho(\mathbf{r}')}{|\mathbf{r}-\mathbf{r}'|}\mathrm{d}\mathbf{r}'$ and exchange-correlation V_{xc} (2.1.4) potentials. Kohn-Sham equations are solved iteratively till self-consistency will be achieved with output electron density $\rho(\mathbf{r})$ (2.1.2) coinciding with the input value used to construct potential in (2.1.3).

Kohn-Sham equations (2.1.3) are homogeneous differential equation of the second order in three-dimensional space. Direct numerical solution for such problem with three-dimensional mesh would require prohibitively huge

computational expenses. The source of difficulties is strong spatial inhomogeneity of potential in (2.1.3). Near atomic center dominates attractive Coulomb potential $\frac{2Z_I}{|\mathbf{r}-\mathbf{R}_I|}$ from positive nuclear charge Z_I that diverges at $|\mathbf{r}-\mathbf{R}_I| \to 0$. That means that space mesh should be very fine at this area with huge number of mesh points. However in the area between atoms potential varies much more smoothly and space mesh could be made coarse.

Practically realized calculations schemes for Kohn-Sham equation solution are based on variational approach. Wave functions $\phi_i(\mathbf{r}) = |\phi_i\rangle$ are expressed as series in complete set of basis functions $|\varphi_n\rangle$:

$$|\phi_i\rangle = \sum_n a_n^i |\varphi_n\rangle \tag{2.1.9}$$

with unknown coefficients a_n^i. Let us write Kohn-Sham equation in the form:

$$\hat{H}|\phi_i\rangle = \varepsilon_i |\phi_i\rangle, \tag{2.1.10}$$

where we introduce one-electron Hamiltonian:

$$\hat{H} = -\nabla^2 - \sum_I \frac{2Z_I}{|\,\mathbf{r}-\mathbf{R}_I\,|} + 2\int \frac{\rho(\mathbf{r}')}{|\,\mathbf{r}-\mathbf{r}'\,|}\mathrm{d}\mathbf{r}' + V_{xc}(\mathbf{r}). \tag{2.1.11}$$

Let us substitute expansion (2.1.9) into (2.1.10) and multiply it from the left on basis function $\langle\varphi_{n'}|$. In the result we will get linear algebraic equations system for coefficients a_n^i:

$$\sum_n H_{n'n} a_n^i = \varepsilon_i \sum_n O_{n'n} a_n^i, \tag{2.1.12}$$

where $H_{n'n} = \langle\varphi_{n'}|\hat{H}|\varphi_n\rangle$ is Hamiltonian (2.1.11) matrix element in the $|\varphi_n\rangle$ function basis and $O_{n'n} = \langle\varphi_{n'}|\varphi_n\rangle$ - overlapping matrix in the same basis.

Then Kohn-Sham differential equations reduce to linear algebraic equations system (2.1.12) or to general problem of finding eigenvalues and eigenvectors of Hamiltonian matrix. Specific realization of the method is defined by the choice of basis functions set $|\varphi_n\rangle$.

Existing *DFT* methods could be divided in two major groups. One of them uses as a basis set atomic-like orbitals centered at atoms and decaying with increasing a distance from the center while another one uses delocalized plane waves:

$$|\mathbf{k}-\mathbf{g}\rangle = \mathrm{e}^{(\mathbf{k}-\mathbf{g})\mathbf{r}}, \tag{2.1.13}$$

where $\mathbf{k}$ is wave vector and $\mathbf{g}$ is the reciprocal lattice vector.

Among the first group the most popular is Linearized Muffin-Tin Orbitals (*LMTO*) method [51]. In this method basis function is so called Muffin-tin orbital (*MTO*) $\varphi_{lm}(\mathbf{r}) = \phi_l(|\mathbf{r}|)Y_{lm}(\hat{\mathbf{r}})$ ($\hat{\mathbf{r}}$ is angle variables for vector $\mathbf{r}$). It has atomic orbital symmetry corresponding to orbital moment value l and its projection m. Angular $\hat{\mathbf{r}}$ and radial $|\mathbf{r}|$ variables dependence are separated

with spherical harmonic $Y_{lm}(\hat{\mathbf{r}})$ depending on angle variables $\hat{\mathbf{r}}$ and radial function $\phi_l(|\mathbf{r}|)$ depending on distance to atomic nucleus $|\mathbf{r}|$:

$$\phi_l(|\mathbf{r}|) = \begin{cases} R_l(|\mathbf{r}|, E) & |\mathbf{r}| < S, \\ C|\mathbf{r}|^{-l-1} & |\mathbf{r}| > S, \end{cases} \tag{2.1.14}$$

where S is atomic sphere radius (equal to half of interatomic distance in the crystal). $R_l(|\mathbf{r}|, E)$ is radial variable dependent part of Kohn-Sham equation (2.1.10) solution for spherically symmetric potential inside atomic sphere. Muffin-tin orbital (2.1.14) is exact solution of (2.1.10) inside the atomic sphere and decaying "tail" $|\mathbf{r}|^{-l-1}$ outside of the sphere.

Such choice of atomic-like functions does not represent "hard" basis as it would be for fixed basis function set. On every iteration radial functions $R_l(|\mathbf{r}|, E)$ are recalculated for new potential and hence basis defined by (2.1.14) is an optimal one for Kohn-Sham equations (2.1.10). *LMTO* method is very efficient because number of functions in the basis needed for satisfactory description of crystal wave function is relatively small (10–15 orbitals per atom). This is also very convenient for calculation results analysis because it allows to naturally determine contribution of various atomic states to crystal wave function (2.1.9). However its accuracy is not enough to describe electron density changes due to atomic displacements from equilibrium positions that are needed to calculate lattice properties (ground state crystal structure, phonon spectra, etc.).

The choice of plane waves $|\mathbf{k} - \mathbf{g}\rangle$ (2.1.13) as basis set allows with good accuracy to reproduce fine details of charge density distribution in crystal. However a price for this advantage is a huge number of terms in expansion (2.1.9) ($\approx 10^5$) and correspondingly enormous Hamiltonian matrix dimension in the set of algebraic equations (2.1.12). Direct complete numerical diagonalization of matrices dimensions $\approx 10^5$ could be prohibitively expensive in computer resources. However it is not necessary to seek all $\approx 10^5$ eigenvalues and eigenfunctions but only few tens of lowest energy solutions corresponding to the occupied states. That fact significantly reduces the needed computational expenses making plane wave basis methods practical tool for electronic structure calculations.

Plane waves basis is a good approximation for wave function in interatomic area where electronic potential in (2.1.11) varies smoothly. However inside the atoms, especially approaching nucleus where potential diverges, plane wave become rather bad choice. In this region atomic-like orbitals would be much better basis set. There are two way to solve this problem: *LAPW* method [52] and pseudopotential method [53]. Later we briefly describe both of them.

The most rigorous of them is Linearized Augmented Plane Waves (*LAPW*) method [52]. Basis function here is not simple plane wave (2.1.13) but so called "augmented plane wave" $|\mathbf{k} - \mathbf{g}\rangle_{\text{LAPW}}$ defined by the following expression:

$$|\mathbf{k} - \mathbf{g}\rangle_{\text{LAPW}} = \begin{cases} \sum_{lm} b_{lm} R_l(|\mathbf{r}|, E) Y_{lm}(\hat{\mathbf{r}}) & \text{if } |\mathbf{r}| < S, \\ C\mathrm{e}^{(\mathbf{k}-\mathbf{g})\mathbf{r}} & \text{if } |\mathbf{r}| > S. \end{cases} \tag{2.1.15}$$

This function has optimal form for potential distribution in (2.1.11): inside atomic sphere it is a linear combination of exact solutions of (2.1.10) for spherically symmetric potential $R_l(|\mathbf{r}|, E)Y_{lm}(\hat{\mathbf{r}})$ and in interatomic area it is a plane wave $e^{(\mathbf{k}-\mathbf{g})\mathbf{r}}$.

Pseudopotential method solves the earlier mentioned problem for plane waves basis inside atom where potential diverges in a rather ingenious way. Preserving the basis in a form of simple plane waves (2.1.13) potential in (2.1.11) is replaced by "pseudopotential" that varies smoothly inside the atom. Correspondingly eigenfunction obtained in solution of equation with this "pseudopotential" is called "pseudowave" function. The key issue in this approximation is requirement to "pseudopotential" construction that for the distance from atomic center larger than some "cut-off" radius "pseudowave" function coincides with true wave function and its eigenvalues are the same as for true potential. As all physical properties of the material are defined by valence electrons whose wave functions are extended far from the atomic core area then pseudopotential method is a good approximation.

2.1.3 Breakdown of Local Density Approximation for Strongly Correlated Systems

In spite of the great success of *DFT* in application to electronic structure calculation and ground state properties study for many materials exchange-correlation energy approximation (2.1.6) based on homogeneous electron gas theory is not adequate for systems with narrow bands. For such materials where electrons preserve in significant degree their atomic orbital nature *DFT* can give qualitatively wrong results. Classical example of this failure are Mott insulators (such as transition metal oxides) [54] with partially filled electronic *d*-shells. *DFT* gave metallic ground state for these materials in contrast to experiment showing them to be wide gap insulators. The reason for insulator state appearance in partially filled *d*-bands is strong Coulomb repulsion [55]. Electron localization happens when kinetic energy gain due to electrons hopping from site to site is smaller than energy loss due to Coulomb repulsion between two electrons on the site. The system with strong Coulomb interaction can become metallic with doping or band width increase but resulting metallic state demonstrate anomalous many-electron (*correlation*) effects that could not be described in one-electron approach (see [8, 56–58]).

In $L(S)DA$ electron moves in mean-field created by all particle in the system including itself. This "self-interaction" is partially taken care of by exchange-correlation potential (2.1.4) but not in explicit and complete way like in Hartree-Fock approximation. In the result of this "residual self-interaction" effect $L(S)DA$ systematically underestimate energy gap value in insulators and semiconductors [59, 60].

For some materials (for example MnO, CuO, and NiO) *LSDA* calculations can result in insulating ground state due to magnetic ordering. However in this case localization is driven not by Coulomb interaction characterized by

parameter U but by exchange interaction with Stoner parameter I. In *LSDA* total energy is [61]:

$$E^{\mathrm{LSDA}} = E^{\mathrm{LDA}}\{\rho(\mathbf{r})\} + E_{xc}\{\rho_{\uparrow}(\mathbf{r}), \rho_{\downarrow}(\mathbf{r})\} - E_{xc}^{\mathrm{LDA}}\{\rho(\mathbf{r})\}, \tag{2.1.16}$$

where E^{LDA} is nonmagnetic state energy that is a functional of total electron density $\rho\{(\mathbf{r})\}$ and E_{xc} is exchange-correlation energy that depends on spin-polarized electron density. In this case one can express exchange splitting of the potential as a function of magnetization $m(\mathbf{r})$:

$$V_{\uparrow} - V_{\downarrow} = \frac{\delta E^{\mathrm{LSDA}}}{\delta \rho_{\uparrow}(\mathbf{r})} - \frac{\delta E^{\mathrm{LSDA}}}{\delta \rho_{\downarrow}(\mathbf{r})} = f(\mathbf{r}) m(\mathbf{r}). \tag{2.1.17}$$

In matrix element form:

$$\langle \psi^k | f(\mathbf{r}) m(\mathbf{r}) | \psi^k \rangle \sim -mI, \tag{2.1.18}$$

where ψ^k is Bloch function for d-band and I is Stoner parameter. If insulating electronic structure in the material is formed by occupied states with spin direction "up" and empty states with spin direction "down" then energy gap value in *LSDA* is determined by Stoner parameter I and not by Coulomb interaction parameter U as should be in Mott theory.

In transition metal compounds Stoner parameter I weakly depends on the material specifics and is completely defined by intraatomic properties and so can be identified with Hund exchange interaction parameter J. Its value is usually $\approx$1 eV while Coulomb parameter U is of the order of 10 eV. This fact can explain why energy gap values for insulating solution of *LSDA* calculations are strongly underestimated, for example for NiO calculated gap value is $\approx$0.4 eV while experimental value is $\approx$4 eV [62]. For cuprates the discrepancy between *LSDA* results and experiment could be even qualitative: for $LaCu_2O_4$ calculations gave nonmagnetic metal as a ground state while experimentally it is antiferromagnetic insulator [63].

"Residual self-interaction" effect is a reason for *LSDA* inability to treat charge ordering effects. Inhomogeneous charge distribution corresponding to charge ordered state is unstable in *LSDA* because on the atoms with larger electron occupation charge density will increases and potential will become more repulsive with the opposite effect on the atoms with smaller occupation value. This effect is unphysical because potential for the specific electron state should not depend on its occupancy. For magnetite Fe_3O_4 *LSDA* calculations results in metallic state without charge ordering [64, 65] in contrast to experimental charge ordered insulating ground state and only taking into account correlation correction in $LDA + U$ method (see Sect. 2.3) gave correct ground state [66].

2.1.4 Corrections for Electron–Electron Correlations

Later the most popular corrections to *LDA* are presented that were proposed to treat Coulomb interaction effects in real materials.

The natural correction to exchange-correlation potential in local density approximation (2.1.7) is to take into account inhomogeneity of electron gas in atoms and solids. That was done in Generalized Gradient Correction Approximation (*GGA*) [67–69] where exchange-correlation energy depends not only on the local electron density value but also on its local gradient value $E_{xc}^{\mathrm{GGA}}[\rho_\uparrow, \rho_\downarrow, \nabla\rho_\uparrow, \nabla\rho_\downarrow]$. *GGA* method improves ground state properties obtained in calculations such as total energy, equilibrium crystal structure, bulk modulus, cohesion energy. However quasiparticle energies forming one-electron spectra are practically unchanged [70].

For Mott insulators Hartree-Fock method is preferable [71] as it contains explicit self-interaction correction term that ensures reproducing an energy gap between occupied and empty states. However a serious problem is absence of Coulomb interaction screening effects in Hartree-Fock that leads to strong overestimation of effective Coulomb parameter U in this method ($\sim 18-20\,\mathrm{eV}$ in contrast to $\sim 8 \div 6\,\mathrm{eV}$ for screened value [61, 72]). As a result energy gap values obtained in Hartree-Fock calculations are overestimated 2–3 times comparing with experiment [71].

In Self-Interaction Correction *SIC* method [73–75] "residual self-interaction" present in *LDA* is explicitly canceled for all occupied states. For that from *LDA* functional (2.1.16) contribution is subtracted from charge density $\rho_i = |\psi_i(\mathbf{r})|^2$ corresponding to electron occupying state i. The resulting *SIC*-potential becomes orbital-dependent:

$$V_i(\mathbf{r}) = V_{\mathrm{ext}}(\mathbf{r}) + V_H[\rho](\mathbf{r}) + V_{xc}[\rho](\mathbf{r}) - V_H[\rho_i](\mathbf{r}) - V_{xc}[\rho_i](\mathbf{r}), \qquad (2.1.19)$$

where V_{ext}, V_H and V_{xc} are external, Coulomb and exchange-correlation potentials, $\rho_i = |\psi_i(\mathbf{r})|^2$ charge density for state i and $\rho = \sum \rho_i$ – total charge density. In *SIC* method repulsive interelectron potential acting on electron in occupied state is reduced while for empty states remains unchanged. That results in energy splitting between occupied and empty bands.

This method was applied to transition metal oxides [73] and calculated values for magnetic moments and energy gaps were found to be in much better agreement with experimental data that *LDA* results [76]. However *SIC* has the same disadvantage as Hartree-Fock method: effects of Coulomb interaction screening are not taken into account and effective U value estimated as energy separation between occupied and empty d-states is strongly overestimated.

Another approach to correlation effects problem is *GW* method [77,78] (see also review [79]). In this method one-electron spectrum is modified by self-energy that is defined by Green function G and screened energy dependent Coulomb interaction potential W. This approach is based on many-electron theory with perturbation series preserving first order term in W. Calculation by *GW* method gave good results for many real materials including simple metals, semiconductors and insulators [79–82]. With certain additional approximations good results were obtained also for Mott insulators such as NiO [79]. However as this method takes into account only first order term of

series in W expansion, it cannot describe properly strongly correlated metals where it is known that higher order terms are needed. It also requires significant computer time expenses.

In $LDA++$ method [83] three regimes can be treated defined by the ratio of Coulomb interaction parameter U to band width W: weak correlations ($U/W \ll 1$), strong correlations ($U/W \gg 1$) and intermediate correlations ($U/W \sim 1$) with different calculation schemes for each regime. This scheme was realized for intermediate valence system TmSe, classical Mott insulator NiO [83] and transition metals Fe and Ni [84–86].

A simple and practically effective comparing with GW and $LDA++$ is $LDA+U$ method [61] (see Sect. 2.3). In this approach electron states are divided into localized (d-orbitals) and delocalized (s, p states) subspaces with $d-d$ Coulomb interaction described by an expression:

$$\tfrac{1}{2}U \sum_{\substack{m\sigma, m'\sigma' \\ m\sigma \neq m'\sigma'}} n_{m\sigma} n_{m'\sigma'}, \tag{2.1.20}$$

where $n_{m\sigma}$ is occupancy of d-orbital with orbital projection and spin indexes $m\sigma$. This method corresponds to static mean-field approximation. $LDA+U$ method allows to get rid of "self-interaction" as in SIC method but using Coulomb parameter U taking into account screening effect in its determination gives better agreement with experimental data.

Generalized Transition State (GTS) method was proposed in [87]. In this method one-electron LDA energies are modified in such a way that they describe excitation energies calculated via Slater transition state approximation [88]. Slater has shown that ionization energy can be calculated using one-electron energies in so called "transition state" with half-integer occupancy value $n_i = 1/2$ equal to average between initial and final state: $\Delta_i = E[n_i = 1] - E[n_i = 0] \approx \epsilon_i(n_i = 1/2)$. Here $E[n_i]$ is total energy of the system with occupancy n_i of orbital i, and ϵ_i is one-electron energy for corresponding orbital. Excitation energy Δ_{ij} (energy cost for transition of electron from orbital i to orbital j) can be calculated as:

$$\Delta_{ij} = E[n_i = 1, n_j = 0] - E[n_i = 0, n_j = 1] = \epsilon_j(1/2) - \epsilon_i(1/2). \tag{2.1.21}$$

In GTS method Slater approximation is generalized to infinite periodic systems. It is assumed that excitations in crystal happens from and to localized states determined by Wannier functions [89]. Auxiliary GTS functional is defined in the following way [87]:

$$E_{\mathrm{GTS}}[\rho, \{\tilde{n}_i\}] = E_{\mathrm{LDA}}[\rho] - \frac{1}{2}\sum_{i=1}^{N}(1/2 - \tilde{n}_i)^2 \frac{\partial \tilde{\epsilon}_i}{\partial \tilde{n}_i}\Big|_{\tilde{n}_i = 1/2}. \tag{2.1.22}$$

Here $\tilde{\epsilon}_i$ and $\tilde{n}_i$ are energies and occupancies for i-th Wannier function, N is total number of Wanier functions in consideration. One-electron energies are calculated as (see (2.1.5)):

$$\tilde{\epsilon}_i = \frac{\partial E_{\mathrm{GTS}}}{\partial \tilde{n}_i} = \tilde{\epsilon}_i^{\mathrm{LDA}} + (1/2 - \tilde{n}_i)\frac{\partial \tilde{\epsilon}_i}{\partial \tilde{n}_i}\Big|_{\tilde{n}_i = 1/2}. \tag{2.1.23}$$

As one can see from (2.1.23) *GTS*-correction is equal to $(1/2 - \tilde{n}_i)\partial\tilde{\epsilon}_i/\partial\tilde{n}_i$ that decreases energy for occupied Wannier states and increases it for empty states. The correction value $\partial\tilde{\epsilon}_i/\partial\tilde{n}_i$ is calculated self-consistently for every Wannier function. *GTS* method is analogous to $LDA + U$ method but has wider area of applicability: it can be used not only for materials with *d*- and *f*-orbitals but also for band insulators and semiconductors.

With this method significant improvement was achieved for agreement of calculated energy gap and magnetic moment values with experimental data [87]. In [90] it was shown that *GTS* functional can be derived from more general requirement of restoring discontinuous properties of exact Density Functional.

2.2 Determining Problem Hamiltonian from Density Functional Theory

2.2.1 Problem Definition

Coulomb correlation problem was intensively studied with Hubbard and Anderson models. There were developed many methods to solve model Hamiltonian equations using analytical as well as numerical approaches. In order to use this rich set of tools for real materials it is necessary to define optimal Hamiltonian for the system under investigation and determine its parameters. *DFT* methods can give all information needed to fulfill this task.

Hilbert space of crystal electronic states can be divided into "weakly correlated" and "strongly correlated" subspaces. In the first of them kinetic energy ratio to Coulomb interaction energy is large enough for *DFT* one-electron equations (and corresponding to them one-electron Hamiltonian) to be a good approximation. For "strongly correlated" subspace Coulomb interaction term of Hamiltonian should be written in the full form through creation–annihilation operators (see Sect. 2.2.2) but all other terms could be described by one-electron *DFT* equations.

However in this recipe for defining Hamiltonian using *DFT* results inter-electron Coulomb interaction could be counted twice. If we add to one-electron *DFT* Hamiltonian Coulomb interaction term in the full form through creation–annihilation operators then we should subtract Coulomb energy that was already taken into account in *DFT*. Coulomb interaction energy in model Hamiltonians is expressed through occupancies of atomic-like orbitals while in *DFT* equations only total charge density distribution enters. That means that "double counting" problem has no rigorous solution and various approximations were proposed to treat it (see Sect. 2.2.3).

Another important problem is definition of atomic-like orbitals occupied by interacting electrons. Most justified choice for such orbitals are Wannier

functions forming complete basis of electronic states Hilbert space but resembling atomic orbitals being centered on atoms and decaying with increasing the distance from nucleus (see Sect. 2.2.4).

For Wannier functions as orbital basis set one needs to determine parameters for Coulomb U and exchange J interactions between electrons on the orbitals. This can be done by DFT methods with fixed values of orbital occupancies (so called "constrain DFT" calculations, see Sect. 2.2.5) .

2.2.2 Coulomb Interaction Hamiltonian

In order to treat Coulomb correlation problem one needs to define Hamiltonian where Coulomb interaction will be written in the full form through creation–annihilation operators. d or f electrons of partially filled electron shells occupy atomic-like orbitals forming orthonormalized basis set $|inlm\sigma\rangle$ (i is atomic site index, n the principal quantum number, l and m are orbital moment and its projection values and σ is spin index). Usually, there is only one partially filled electronic shell $n_d l_d$ for atom i_d.

In general form Coulomb interaction Hamiltonian can be written in the following form:

$$\hat{H}_{\text{Coulomb}} = \frac{1}{2} \sum_{i=i_d, l=l_d} \sum_{m,m',m'',m''',\sigma,\sigma'} \langle m, m'|V_{\text{ee}}|m'', m'''\rangle \times \hat{c}^{+}_{ilm\sigma} \hat{c}^{+}_{ilm'\sigma'} \hat{c}_{ilm''\sigma} \hat{c}_{ilm'''\sigma'}, \quad (2.2.24)$$

where V_{ee} is screened Coulomb interaction between electrons in $i_d n_d l_d$ shell. Matrix elements of operator V_{ee} can be expressed via complex spherical harmonics and effective Slater integral parameters F^k [91]:

$$\langle m, m'|V_{\text{ee}}|m'', m'''\rangle = \sum_k a_k(m, m'', m', m''')F^k, \quad (2.2.25)$$

where $k = 0, 2, \ldots, 2l$ and

$$a_k(m, m'', m', m''') = \frac{4\pi}{2k+1} \sum_{q=-k}^{k} \langle lm|Y_{kq}|lm''\rangle \langle lm'|Y^*_{kq}|lm'''\rangle, \quad (2.2.26)$$

where Y_{kq} are complex spherical harmonics.

Hamiltonian (2.2.24) assumes possibility of mixing for orbitals with different m values (or in other words possibility for electrons occupy arbitrary linear combinations of $|inlm\sigma\rangle$ orbitals). However in many cases, it is possible to choose "natural" orbital basis where mixing is forbidden by crystal symmetry. In this case terms $\hat{c}^{+}_{ilm\sigma}\hat{c}_{ilm'\sigma}$ with $m \neq m'$ are absent and Hamiltonian (2.2.24) can be written as [10]:

$$\hat{H}_{\text{Coulomb}} = \frac{1}{2}\sum_{i=i_d,l=l_d}\sum_{m,m',\sigma}\{U_{mm'}\hat{n}_{ilm\sigma}\hat{n}_{ilm'\bar{\sigma}} + (U_{mm'}-J_{mm'})\hat{n}_{ilm\sigma}\hat{n}_{ilm'\sigma}\}$$
$$- \frac{1}{2}\sum_{i=i_d,l=l_d}\sum_{m\neq m',\sigma} J_{mm'}\{\hat{c}^{+}_{ilm\sigma}\hat{c}_{ilm\bar{\sigma}}\hat{c}^{+}_{ilm'\bar{\sigma}}\hat{c}_{ilm'\sigma}\hat{c}^{+}_{ilm\sigma}\hat{c}^{+}_{ilm\bar{\sigma}}\hat{c}_{ilm'\sigma}\hat{c}_{ilm'\bar{\sigma}}\}. \tag{2.2.27}$$

($\hat{n}_{ilm\sigma} = \hat{c}^{+}_{ilm\sigma}\hat{c}_{ilm\sigma}$ is particle number operator for electrons on orbital $|inlm\sigma\rangle$, $\bar{\sigma} = \downarrow (\uparrow)$ for $\sigma = \uparrow (\downarrow)$). Here we have introduced matrices of direct $U_{mm'}$ and exchange $J_{mm'}$ Coulomb interaction:

$$U_{mm'} \equiv \langle m, m'|V_{\text{ee}}|m, m'\rangle,\ J_{mm'} \equiv \langle m, m'|V_{\text{ee}}|m', m\rangle. \tag{2.2.28}$$

Last two terms in Hamiltonian (2.2.27) describe interactions that cannot be expressed in density–density form ($\hat{n}_{ilm\sigma}\hat{n}_{ilm'\bar{\sigma}}$ and $\hat{n}_{ilm\sigma}\hat{n}_{ilm'\sigma}$) as in the first two terms. Third term corresponds to spin flip for electron on m orbital with simultaneous reverse spin flip on orbital m' that allows to describe x and y spin components whereas the fourth term describes pair transition of two electrons with opposite spin values from one orbital to another. Taking into account such spin-flip terms can significantly complicate the problem solution and, usually, they are neglected in calculations. In the result only density–density terms are left and Hamiltonian has the form:

$$\hat{H}_{\text{Coulomb}} = \frac{1}{2}\sum_{i=i_d,l=l_d}\sum_{m,m',\sigma}\{U_{mm'}\hat{n}_{ilm\sigma}\hat{n}_{ilm'\bar{\sigma}} + (U_{mm'} - J_{mm'})\hat{n}_{ilm\sigma}\hat{n}_{ilm'\sigma}\}. \tag{2.2.29}$$

Historically, instead of Coulomb matrix (2.2.28) so called Kanamori parametrization is used where for the same orbitals ($m = m'$) direct Coulomb interaction $U_{mm} \equiv U$, for different orbitals ($m \neq m'$) $U_{mm'} \equiv U'$ with $U' \equiv U - 2J$ and exchange interaction parameter does not depend on orbital index $J_{mm'} \equiv J$. In this approximation Hamiltonian is:

$$\hat{H}_{\text{Coulomb}} = \frac{1}{2}\sum_{i=i_d,l=l_d}\sum_{m,m',\sigma}\{[U\delta_{mm'} + U'(1-\delta_{mm'})]\hat{n}_{ilm\sigma}\hat{n}_{ilm'\bar{\sigma}} + (U'-J)\hat{n}_{ilm\sigma}\hat{n}_{ilm'\sigma}\}. \tag{2.2.30}$$

2.2.3 Double-Counting Problem for Coulomb Interaction

"Double counting" problem appears because of basically different approaches for Coulomb interaction energy description in *DFT* and Hubbard or Anderson models. When Coulomb interaction Hamiltonian in general form (2.2.24) is added to one-electron *DFT* Hamiltonian then it is necessary to cancel Coulomb energy that was already taken into account in *DFT*. Unfortunately, it is not possible to realize this cancellation in a rigorous way because Coulomb interaction energy in *DFT* equations is calculated as functional of charge density distribution while in model approach this energy is expressed as a sum of pair interactions for electrons on atomic orbitals.

Full Hamiltonian is defined as:

$$\hat{H} = \hat{H}_{\mathrm{LDA}} - \hat{H}_{\mathrm{DC}} + H_{\mathrm{Coulomb}}, \tag{2.2.31}$$

where $\hat{H}_{\mathrm{LDA}}$ is one-electron Hamiltonian corresponding to Kohn-Sham *DFT* equations (2.1.3), H_{Coulomb} the Coulomb interaction Hamiltonian (2.2.27) and $\hat{H}_{\mathrm{DC}}$ is a correction term to avoid "double counting" for Coulomb interaction energy.

To define $\hat{H}_{\mathrm{DC}}$ one need to express Coulomb interaction energy taken into account in *DFT* in the language of model Hamiltonian H_{Coulomb}. In *DFT* this energy is a functional of electron density that is defined by the total number of interacting electrons n_d. Hence it is reasonable to assume that Coulomb interaction energy in *DFT* is simply a function of n_d:

$$E_{\mathrm{DFT}} = \frac{1}{2}\bar{U} n_d (n_d - 1), \tag{2.2.32}$$

where n_d is number of electrons in shell $n_d l_d$, $\bar{U}$ the average value of Coulomb matrices $U_{mm'}$ and $(U_{mm'} - J_{mm'})$ is the over all orbital pairs $m\sigma, m'\sigma'$.

To obtain correction to atomic orbital energies ϵ_d in this approximation one needs to recall that in *DFT* one-electron eigenvalues are derivatives of the total energy over corresponding state occupancy n_d (see (2.1.5)):

$$\epsilon_d = \frac{\partial E_{\mathrm{DFT}}}{\partial n_d}, \tag{2.2.33}$$

and hence correction to atomic orbital energy ϵ_{DC} can be determined as:

$$\epsilon_{\mathrm{DC}} = \bar{U}\left(n_d - \frac{1}{2}\right), \tag{2.2.34}$$

and the term in Hamiltonian responsible for "double counting" correction $\hat{H}_{\mathrm{DC}}$ is:

$$\widehat{H}_{\mathrm{DC}} = \sum_{inlm\sigma} \epsilon_{\mathrm{DC}} \hat{n}_{inlm\sigma} \tag{2.2.35}$$

(sum in (2.2.35) is only over orbital indices corresponding to interacting electronic shell $i_d n_d l_d$).

2.2.4 Wannier Functions as Coulomb Interaction Hamiltonian Basis

In Hamiltonian (2.2.24) interacting electrons are in quantum states defined by "atomic orbitals" $|inlm\sigma\rangle$. The simplest choice of free atom orbitals for such states is a bad approximation because in crystal atomic states are significantly modified comparing with free atoms. The problem of definition for atomic-like orbitals in crystal does not have unambiguous rigorous solution but the most

mathematically justified choice for them are Wannier functions [89]. Those function form complete basis set of crystal electronic states Hilbert space while resembling atomic orbitals being centered on atomic sites and exponentially decaying with increasing the distance from atomic center.

Wannier functions (WF) $|W_n^{\mathbf{T}}\rangle$ are defined as Fourier transformed Bloch functions $|\Psi_{n\mathbf{k}}\rangle$ [89]:

$$|W_n^{\mathbf{T}}\rangle = \frac{1}{\sqrt{N}} \sum_{\mathbf{k}} \mathrm{e}^{-\mathrm{i}\mathbf{k}\mathbf{T}} |\Psi_{n\mathbf{k}}\rangle, \tag{2.2.36}$$

where $\mathbf{T}$ is translation vector, n the band number, and N is the number of discrete $\mathbf{k}$ points in the first Brillouin zone.

Wannier functions are not unambiguously defined because in multiband case any orthonormal linear combination of Bloch functions $|\Psi_{n\mathbf{k}}\rangle$ can be used in (2.2.36). In general it means that the freedom of choice of Wannier functions corresponds to freedom of choice of a unitary transformation matrix $U_{\nu n}^{(\mathbf{k})}$:

$$|\Psi_{n\mathbf{k}}\rangle \rightarrow \sum_{\nu} U_{\nu n}^{(\mathbf{k})} |\Psi_{\nu\mathbf{k}}\rangle. \tag{2.2.37}$$

In last years method proposed by Marzari and Vanderbilt [92] is widely used for Wannier functions construction. They imposed condition of maximum localization for WFs, resulting in a variational procedure to calculate $U_{\nu n}^{(\mathbf{k})}$. As an initial guess to start iterative solution of the variational procedure the authors of [92] proposed choosing a set of localized trial orbitals and projecting them onto Bloch functions. It was found that Wannier functions obtained in this projection are already so well localized that later authors of [93] proposed to abandon variation procedure and use projected orbitals as a definition of unitary transformation matrix $U_{\nu n}^{(\mathbf{k})}$.

Bloch function are presented as expansion series in some basis functions with specific form depending on the particular *DFT* calculation method (see Sect. 2.1.2). Examples are atomic-like "linearized muffin-tin orbitals" of *LMTO* method or plane waves $|\mathbf{k}-\mathbf{g}\rangle = \mathrm{e}^{\mathrm{i}(\mathbf{k}-\mathbf{g})\mathbf{r}}$ as in pseudopotential and *LAPW* methods. Later we present Wannier function formalism for pseudopotential method in plane wave basis with pseudoatomic wave functions ϕ_n as localized trial orbitals. Formulas for other methods could be obtained by replacing matrix elements $\langle\phi_n|\mathbf{k}-\mathbf{g}\rangle$ on integrals between corresponding basis function and trial orbitals.

Nonorthogonalized approximation for *WF* in real space $|\widetilde{W}_n^{\mathbf{T}}\rangle$ and in reciprocal space $|\widetilde{W}_{n\mathbf{k}}\rangle$ is calculated as projection of atomic orbital on Hilbert subspace defined by Bloch functions in energy interval $E_1 \leq \varepsilon_\nu(\mathbf{k}) \leq E_2$ or in band number interval $N_1 \leq \nu \leq N_2$:

$$|\widetilde{W}_n^{\mathbf{T}}\rangle = \sum_{\mathbf{k}} |\widetilde{W}_{n\mathbf{k}}\rangle \mathrm{e}^{-\mathrm{i}\mathbf{k}\mathbf{T}}, \tag{2.2.38}$$

$$|\widetilde{W}_{n\mathbf{k}}\rangle \equiv \sum_{\nu=N_1}^{N_2} |\Psi_{\nu\mathbf{k}}\rangle\langle\Psi_{\nu\mathbf{k}}|\phi_{n\mathbf{k}}\rangle = \sum_{E_1\le\varepsilon_\nu(\mathbf{k})\le E_2} |\Psi_{\nu\mathbf{k}}\rangle\langle\Psi_{\nu\mathbf{k}}|\phi_{n\mathbf{k}}\rangle. \tag{2.2.39}$$

In plane wave basis Bloch functions and pseudoatomic orbital Bloch sums $|\phi_{n\mathbf{k}}\rangle = \sum_{\mathbf{T}} \mathrm{e}^{\mathrm{i}\mathbf{k}\mathbf{T}}|\phi_n^{\mathbf{T}}\rangle$ are presented as expansion in plane waves:

$$|\Psi_{\nu\mathbf{k}}\rangle = \sum_{\mathbf{g}} c_{\nu,\mathbf{g}}(\mathbf{k})|\mathbf{k}-\mathbf{g}\rangle, \tag{2.2.40}$$

$$|\phi_{n\mathbf{k}}\rangle = \sum_{\mathbf{g}'} a_{n,\mathbf{g}'}(\mathbf{k})|\mathbf{k}-\mathbf{g}'\rangle, \tag{2.2.41}$$

where n is combined index $jlm\sigma$ (j is atomic number, lm the orbital moment and its projection, σ is the spin projection).

In plane wave basis nonorthogonalized approximation for *WF* (2.2.39) is:

$$\begin{aligned}
|\widetilde{W}_{n\mathbf{k}}\rangle &\equiv \sum_{\nu=N_1}^{N_2} |\Psi_{\nu\mathbf{k}}\rangle\langle\Psi_{\nu\mathbf{k}}|\phi_{n\mathbf{k}}\rangle \\
&= \sum_{\nu=N_1}^{N_2} |\Psi_{\nu\mathbf{k}}\rangle \sum_{\mathbf{g},\mathbf{g}'} c^*_{\nu,\mathbf{g}}(\mathbf{k}) a_{n,\mathbf{g}'}(\mathbf{k})\langle\mathbf{k}-\mathbf{g}|\mathbf{k}-\mathbf{g}'\rangle \\
&= \sum_{\nu=N_1}^{N_2} |\Psi_{\nu\mathbf{k}}\rangle \sum_{\mathbf{g}'} c^*_{\nu,\mathbf{g}'}(\mathbf{k}) a_{n,\mathbf{g}'}(\mathbf{k}) \sum_{\nu=N_1}^{N_2} \tilde{b}_{\nu,n}(\mathbf{k})|\Psi_{\nu\mathbf{k}}\rangle \\
&= \sum_{\mathbf{g}} \tilde{\omega}_{n,\mathbf{g}}(\mathbf{k})|\mathbf{k}-\mathbf{g}\rangle,
\end{aligned} \tag{2.2.42}$$

$$\tilde{b}_{\nu,n}(\mathbf{k}) \equiv \sum_{\mathbf{g}'} c^*_{\nu,\mathbf{g}'}(\mathbf{k}) a_{n,\mathbf{g}'}(\mathbf{k}), \qquad \tilde{\omega}_{n,\mathbf{g}}(\mathbf{k}) \equiv \sum_{\nu=N_1}^{N_2} \tilde{b}_{\nu,n}(\mathbf{k}) c_{\nu,\mathbf{g}}(\mathbf{k}). \tag{2.2.43}$$

In order to produce orthonormal set of *WF*s one needs to define overlapping matrix:

$$O_{nn'}(\mathbf{k}) \equiv \langle\widetilde{W}_{n\mathbf{k}}|\widetilde{W}_{n'\mathbf{k}}\rangle = \sum_{\nu=N_1}^{N_2} \tilde{b}^*_{\nu,n}(\mathbf{k})\tilde{b}_{\nu,n'}(\mathbf{k}), \tag{2.2.44}$$

then orthonormal *WF* is:

$$|W_n^{\mathbf{T}}\rangle = \sum_{\mathbf{k}} |W_{n\mathbf{k}}\rangle \mathrm{e}^{\mathrm{i}\mathbf{k}\mathbf{T}}, \tag{2.2.45}$$

where

$$\begin{aligned}
&|W_{n\mathbf{k}}\rangle = \sum_{n'} (O_{nn'}(\mathbf{k}))^{-\frac{1}{2}} |\widetilde{W}_{n'\mathbf{k}}\rangle = \sum_{\nu=N_1}^{N_2} b_{\nu,n}(\mathbf{k})|\Psi_{\nu\mathbf{k}}\rangle = \sum_{\mathbf{g}} \omega_{n,\mathbf{g}}(\mathbf{k})|\mathbf{k}-\mathbf{g}\rangle \\
&b_{\nu,n}(\mathbf{k}) \equiv \sum_{n'} (O_{nn'}(\mathbf{k}))^{-\frac{1}{2}} \tilde{b}_{\nu,n'}(\mathbf{k}) \qquad \omega_{n,\mathbf{g}}(\mathbf{k}) \equiv \sum_{n'} (O_{nn'}(\mathbf{k}))^{-\frac{1}{2}} \tilde{\omega}_{n',\mathbf{g}}(\mathbf{k}).
\end{aligned} \tag{2.2.46}$$

For practical applications (for example to define kinetic energy term in Hamiltonian in *WF* basis or to run constrain *DFT* calculations to determine Coulomb interaction parameter value U (see Sect. 2.2.5)) it is necessary to calculate matrix elements for various operators in *WF* basis. One-electron Hamiltonian in reciprocal space representation in *WF* basis is:

$$\begin{aligned} H_{nm}^{\mathrm{WF}}(\mathbf{k}) &= \langle W_{n\mathbf{k}}| \left(\sum_{\nu=N_1}^{N_2} |\Psi_{\nu\mathbf{k}}\rangle \varepsilon_\nu(\mathbf{k}) \langle \Psi_{\nu\mathbf{k}}| \right) |W_{m\mathbf{k}}\rangle \\ &= \sum_{\nu=N_1}^{N_2} b_{\nu,n}^*(\mathbf{k}) b_{\nu,m}(\mathbf{k}) \varepsilon_\nu(\mathbf{k}), \end{aligned} \tag{2.2.47}$$

where $\varepsilon_\nu(\mathbf{k})$ is band ν energy.

In real space representation Hamiltonian matrix in *WF* basis is:

$$\begin{aligned} H_{nm}^{\mathrm{WF}}(\mathbf{T}' - \mathbf{T}) &= \langle W_n^{\mathbf{T}}| \left(\sum_{\mathbf{k}} \sum_{\nu=N_1}^{N_2} |\Psi_{\nu\mathbf{k}}\rangle \varepsilon_\nu(\mathbf{k}) \langle \Psi_{\nu\mathbf{k}}| \right) |W_m^{\mathbf{T}'}\rangle \\ &= \sum_{\mathbf{k}} \sum_{\nu=N_1}^{N_2} b_{\nu,n}^*(\mathbf{k}) b_{\nu,m}(\mathbf{k}) \varepsilon_\nu(\mathbf{k}) \mathrm{e}^{\mathrm{i}\mathbf{k}(\mathbf{T}'-\mathbf{T})}. \end{aligned} \tag{2.2.48}$$

Occupation matrix for in *WF* basis Q_{nm}^{WF} is:

$$\begin{aligned} Q_{nm}^{\mathrm{WF}} &= \langle W_n^0| \left(\sum_{\mathbf{k}} \sum_{\nu=N_1}^{N_2} |\Psi_{\nu\mathbf{k}}\rangle \theta(\varepsilon_\nu(\mathbf{k}) - E_F) \langle \Psi_{\nu\mathbf{k}}| \right) |W_m^0\rangle \\ &= \sum_{\mathbf{k}} \sum_{\nu=N_1}^{N_2} b_{\nu,n}^*(\mathbf{k}) b_{\nu,m}(\mathbf{k}) \theta(\varepsilon_\nu(\mathbf{k}) - E_F), \end{aligned} \tag{2.2.49}$$

where θ is step function and E_F is the Fermi energy.

Transformation from plane waves to Wannier functions basis is defined by 2.2.42–2.2.46 and for matrix elements by (2.2.48) and (2.2.49). One can define inverse transformation from *WF* to plane wave basis. This transformation is needed for example in constrain *DFT* calculations of Coulomb parameter U (see Sect. 2.2.5) where auxiliary potential is used with operator diagonal in *WF* representation $H_{nn'} = \delta V_n \delta_{nn'}$. In plane wave basis this operator is:

$$\begin{aligned} \widehat{H}_{\mathrm{constr}}(\mathbf{k}) &= \sum_n |W_{n\mathbf{k}}\rangle \delta V_n \langle W_{n\mathbf{k}}|, \\ H_{\mathbf{g}\mathbf{g}'}^{\mathrm{constr}}(\mathbf{k}) &= \langle \mathbf{k}-\mathbf{g}| \widehat{H}_{\mathrm{constr}}(\mathbf{k}) |\mathbf{k}-\mathbf{g}'\rangle \\ &= \sum_n \langle \mathbf{k}-\mathbf{g}|W_{n\mathbf{k}}\rangle \delta V_n \langle W_{n\mathbf{k}}|\mathbf{k}-\mathbf{g}'\rangle \\ &= \sum_n \omega_{n,\mathbf{g}}^*(\mathbf{k}) \delta V_n \omega_{n,\mathbf{g}'}(\mathbf{k}). \end{aligned} \tag{2.2.50}$$

Equations (2.2.46)–(2.2.50) give practical realization for transforming Wannier functions representation of Hamiltonian (2.2.24) used for correlation effects study to plane waves representation that is optimal for *DFT* electronic structure calculations. This allows to define calculation scheme for $LDA + U$ (Sect. 2.3) and $LDA + DMFT$ (Sect. 6) methods that combine approaches based on model Hamiltonians (Chap. 3 and 5) with Density Functional Theory (Sect. 2.1).

As an example of Wannier functions formalism we present results for nickel oxide NiO [94]. In upper part of Fig. 2.1 band structure for NiO calculated by pseudopotential method [95] is plotted. Three lowest bands from -8 eV to -3 eV are formed predominantly by oxygen p-states and upper five bands by $3d$ nickel states.

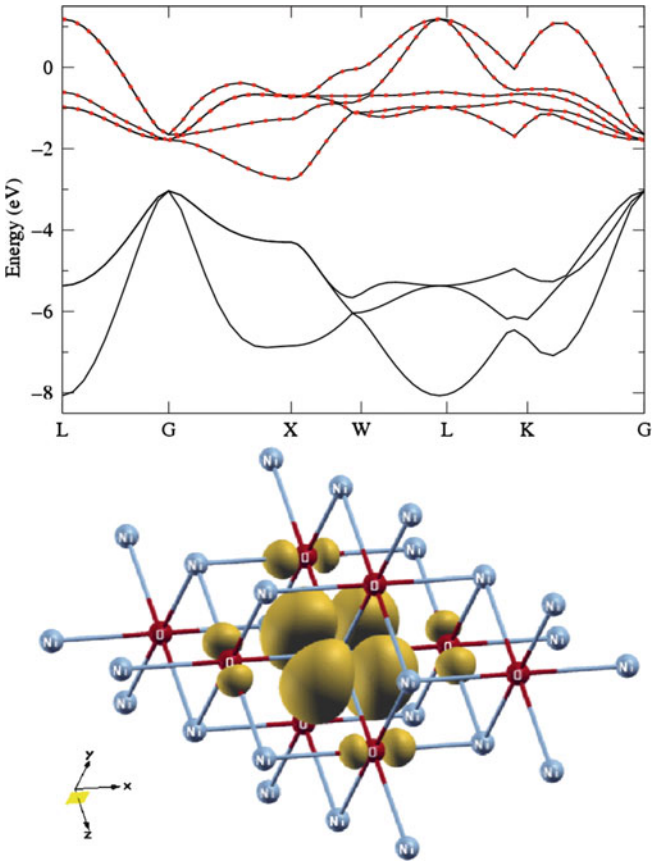

Fig. 2.1. *Upper part:* Full set of bands calculated in *DFT* (*solid line*) and bands corresponding to five d-symmetry Wannier functions (points). Energy interval used for Wannier functions calculations was defined as $[-2.5, +1.5]$ eV relative to Fermi energy. *Lower part: Modulus square* of Wannier function corresponding to d_{xz}-orbital [94]

As it was explained earlier Wannier functions are not unambiguously defined and in projection procedure for their determination by (2.2.39) it is necessary to give a set of trial atomic orbitals and a set of Bloch functions defined by energy interval $E_1 \leq \varepsilon_\nu(\mathbf{k}) \leq E_2$ or by bands numbers $N_1 \leq \nu \leq N_2$. In order to demonstrate how resulting Wannier function depends on projection procedure parameters we present results of two calculations. In a first of them Bloch functions Hilbert space was defined by only five bands formed predominantly by d states (energy interval $[-2.5, +1.5]$ eV relative to Fermi energy) and in the second one all five d-bands and three p-bands (energy interval $[-8.5, +1.5]$ eV) were included.

Results are presented in Figs. 2.1 and 2.2. Please note that in both cases d-bands calculated by diagonalization of Hamiltonian matrix in Wannier function basis (2.2.47) (points) are identical with bands obtained in full *DFT* calculations (solid lines). However Wannier functions themselves obtained in two calculations are significantly different. In lower parts of Figs. 2.1 and 2.2 spatial distribution for modulus square of Wannier function corresponding to d_{xz}-orbital is presented. While in Fig. 2.2 *WF* is nearly pure d-orbital in Fig. 2.1 one can see significant contribution from neighboring oxygen atoms p-orbitals.

d-bands Bloch functions are build by antibonding combinations of nickel d-orbitals and oxygen p-orbitals. Hence Wannier function calculated as wave vector summation over Bloch functions also contains mixture of d- and p-orbitals (Fig. 2.1). However, if summation in (2.2.39) includes also p bands that corresponds to bonding combinations of nickel d-orbitals and oxygen p-orbitals then p bands contributions will be canceled and resulting *WF* is nearly pure d-orbital (Fig. 2.2). In calculation corresponding to case of Fig. 2.2 *WF* Hamiltonian (2.2.47) has basis functions of both d and p symmetry and hence $d-p$ hybridization can be explicitly reproduced. However in the case of Fig. 2.1 there is no explicit p states in the *WF* basis and $d-p$ hybridization pronounce itself in the form of Wannier function.

2.2.5 Coulomb Parameter *U* Value from Constrain *DFT* Calculation

The matrix elements values for direct $U_{mm'}$ and exchange $J_{mm'}$ Coulomb interaction (2.2.28) can be calculated using the following expressions [91]:

$$\begin{aligned} U_{mm'} &\equiv \langle m, m' | V_{\mathrm{ee}} | m, m' \rangle \\ &= \int \mathrm{d}\mathbf{r}\mathrm{d}\mathbf{r}' |\varphi_d(|\mathbf{r}|) Y_{lm}(\hat{\mathbf{r}})|^2 \frac{1}{|\mathbf{r} - \mathbf{r}'|} |\varphi_d(|\mathbf{r}'|) Y_{lm'}(\hat{\mathbf{r}}')|^2. \end{aligned} \tag{2.2.51}$$

Integration over angle variables $\hat{\mathbf{r}}, \hat{\mathbf{r}}'$ in (2.2.51) for spherical harmonics $Y_{lm}(\hat{\mathbf{r}})$ and over radial variables $|\mathbf{r}| \equiv r, |\mathbf{r}'| \equiv r'$ for radial wave functions $\varphi_d(r)$ can be separated and in the result we have:

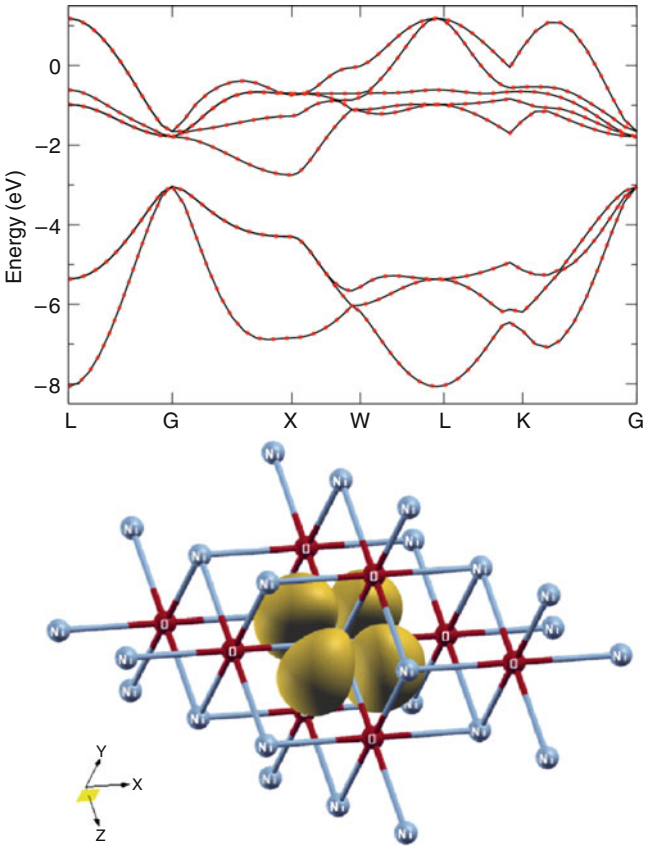

Fig. 2.2. *Upper part:* Full set of bands calculated in *DFT* (*solid line*) and bands corresponding to eight *d*- and *p*-symmetry Wannier functions (points). Energy interval used for Wannier functions calculations was defined as $[-8.5, +1.5]$ eV relative to Fermi energy. *Lower part: Modulus square* of Wannier function corresponding to d_{xz}-orbital [94]

$$
\begin{aligned}
U_{mm'} &= \sum_k a_k F^k, \qquad J_{mm'} = \sum_k b_k F^k, \\
F^k &= e^2 \int_0^\infty r^2 \mathrm{d}r [\varphi_d(r)]^2 \int_0^\infty (r')^2 \mathrm{d}r' [\varphi_d(r')]^2 \frac{r_<^k}{r_>^{k+1}}, \\
a_k &= \frac{4\pi}{2k+1} \sum_{q=-k}^{k} \langle lm|Y_{kq}|lm\rangle \langle lm'|Y_{kq}^*|lm'\rangle, \\
b_k &= \frac{4\pi}{2k+1} \sum_{q=-k}^{k} |\langle lm|Y_{kq}|lm'\rangle|^2,
\end{aligned}
\tag{2.2.52}
$$

($r_< = r, r_> = r'$ if $r' > r$ and vice versa).

In expressions (2.2.52) F^k are Slater integrals with $k = 0, 2, 4$ for d states and $k = 0, 2, 4, 6$ for f states, $\varphi_d(r)$ are radial wave functions for d or f orbitals, a_k and b_k are Klebsch-Gordan coefficients expressed via integrals over product of three spherical harmonics:

$$\langle lm|Y_{kq}|lm'\rangle \equiv \int \mathrm{d}\hat{\mathbf{r}} Y_{lm}(\hat{\mathbf{r}})^* Y_{kq}(\hat{\mathbf{r}}) Y_{lm'}(\hat{\mathbf{r}}), \tag{2.2.53}$$

that could be calculated analytically.

Using Klebsch-Gordan coefficients properties the following relation could be found between Slater integrals F^k and Coulomb parameters U and J [91]:

$$\begin{aligned} U &= \frac{1}{(2l+1)^2}\sum_{mm'} U_{mm'} = F^0, \\ U - J &= \frac{1}{2l(2l+1)}\sum_{mm'}(U_{mm'} - J_{mm'}) = F^0 - (F^2 + F^4)/14, \\ l = 2: &\qquad J = (F^2 + F^4)/14, \\ l = 3: &\qquad J = (286F^2 + 195F^4 + 250F^6)/6{,}435. \end{aligned} \tag{2.2.54}$$

Slater integrals F^k are usually calculated not by wave functions integration as in (2.2.52) but by using formulas (2.2.54) from Coulomb parameters U and J that are obtained in constrain DFT method [96]. The simplest case is integral $F^0 = U$. Slater integrals F^k for $k \neq 0$ are calculated via exchange parameter J. For d ions ratio F^4/F^2 is with a good accuracy constant [97] and equal 0.625. For f ions ratios F^4/F^2 and F^6/F^2 could be estimated from hydrogen-like $4f$ radial wave functions as 451/675 and 1,001/2,025, correspondingly [98]. Then

$$\begin{aligned} l = 2: &\quad F^2 = \frac{14}{1 + 0.625}J, && F^4 = 0.625F^2; \\ l = 3: &\quad F^2 = \frac{6435}{286 + \frac{195\cdot 451}{675} + \frac{250\cdot 1001}{2025}}J, && F^4 = \frac{451}{675}F^2, \quad F^6 = \frac{1001}{2025}F^2. \end{aligned} \tag{2.2.55}$$

The direct way to calculate Coulomb parameter U value for Wannier function $W_n(\mathbf{r})$ is to compute integral:

$$U = \int \mathrm{d}\mathbf{r}\mathrm{d}\mathbf{r}' |W_n(\mathbf{r})|^2 U(\mathbf{r}, \mathbf{r}') |W_n(\mathbf{r}')|^{\mathbf{2}}, \tag{2.2.56}$$

where screened Coulomb potential $U(\mathbf{r}, \mathbf{r}')$ is defined by operator equation:

$$U = [1 - vP]^{-1} v \tag{2.2.57}$$

with unscreened Coulomb potential $v(\mathbf{r}, \mathbf{r}') = 1/(\mathbf{r} - \mathbf{r}')$ and polarization operator P:

$$P(\mathbf{r},\mathbf{r}') = \sum_{i}^{\text{occ}} \sum_{j}^{\text{unocc}} \psi_i(\mathbf{r})\psi_i^*(\mathbf{r}')\psi_j^*(\mathbf{r})\psi_j(\mathbf{r}') \left\{ \frac{1}{\epsilon_i - \epsilon_j + i0^+} - \frac{1}{\epsilon_j - \epsilon_i - i0^+} \right\}. \tag{2.2.58}$$

However various attempts [99–101] to use (2.2.56–2.2.58) to calculate Coulomb parameter U gave wide dispersion of resulting values due to uncertainty in choosing screening channels defined by a set of occupied and empty states in (2.2.58). If transitions anong d-states are included in (2.2.58) (which is clearly unphysical because localized d-electrons cannot screen each other) the screening is too effective and resulting U value is strongly underestimated. Without $d-d$ transitions opposite effect of strong U value overestimation is observed when transitions to very high energy empty states and low energy core states are neglected in (2.2.58).

Alternative way to obtain Coulomb parameter U value is constrain *DFT* calculations with fixed occupancy values [96, 102, 103]. In this case screening and relaxation effects are taken into account not via perturbation theory as in (2.2.57–2.2.58) but directly in self-consistent solution of Kohn-Sham equations. If Coulomb interaction energy contribution to *DFT* as a function of d electrons number n_d obeys (2.2.32) then U can be calculated as a second derivative of total energy:

$$U = \frac{\partial^2 E_{\text{DFT}}}{\partial^2 n_d}. \tag{2.2.59}$$

Using (2.2.33) U can be expressed via first derivative of one-electron energy ϵ_d:

$$U = \frac{\partial \epsilon_d}{\partial n_d}. \tag{2.2.60}$$

In order to use (2.2.60) one needs to perform constrain *DFT* calculations with various values of fixed orbital occupancies n_d. Practically, it is done using auxiliary potentials in the form of projection operator acting on d-symmetry Wannier functions $|W_n\rangle$:

$$\widehat{H}_{\text{constr}} = \sum_n |W_n\rangle \delta V_n \langle W_n| \tag{2.2.61}$$

[in reciprocal space this equation has form (2.2.50)]. One-electron energies can be calculated as diagonal elements of Hamiltonian matrix (2.2.48) and corresponding occupancies as diagonal matrix elements of occupancy matrix (2.2.49):

$$\begin{aligned} \epsilon_d &= H_{nn}^{\text{WF}}(0), \\ n_d &= Q_{nn}^{\text{WF}}, \end{aligned} \tag{2.2.62}$$

and then derivative value $\partial\epsilon_d/\partial n_d$ (2.2.60) is calculated numerically.

For exchange parameter J one can use expressions similar to (2.2.60–2.2.62) but replacing one-electron energies ϵ_d on spin polarization energy $\epsilon_{d\downarrow} - \epsilon_{d\uparrow}$ and occupancy n_d on local magnetization $n_{d\uparrow} - n_{d\downarrow}$ [96].

2.3 Static Mean-Field Approximation: *LDA* + *U* Method

The next step after defining Hamiltonian appropriate for material under investigation and determining its parameters from *DFT* methods is to choose an approach for the problem solution among rich set of tools developed for Hubbard and Anderson models. In this book two most popular methods based on mean field approximation are described. One of them using the simplest *static* mean-filed approximation or unrestricted Hartree-Fock is called *LDA* + *U* method proposed by Anisimov, Andersen, and Zaanen in [61] and will be described in this section. Another one is more sophisticated in use but much more powerful in its abilities *LDA* + *DMFT* method based on *Dynamical* mean-field theory that will be described in Chap. 6.

Static mean-filed approximation or unrestricted Hartree-Fock method is based on decoupling of four-operator term in Coulomb interaction Hamiltonian (2.2.24) in such a way that a product of two creation–annihilation operators is replaced by its average value:

$$\begin{aligned}&\hat{c}^{+}_{ilm\sigma}\hat{c}^{+}_{ilm'\sigma'}\hat{c}_{ilm''\sigma}\hat{c}_{ilm'''\sigma'}\\ &\quad\Rightarrow\ -\hat{c}^{+}_{ilm\sigma}\hat{c}_{ilm''\sigma}\langle\hat{c}^{+}_{ilm'\sigma'}\hat{c}_{ilm'''\sigma'}\rangle-\langle\hat{c}^{+}_{ilm\sigma}\hat{c}_{ilm''\sigma}\rangle\hat{c}^{+}_{ilm'\sigma'}\hat{c}_{ilm'''\sigma'}\\ &\qquad+\ \hat{c}^{+}_{ilm\sigma}\hat{c}_{ilm'''\sigma'}\langle\hat{c}^{+}_{ilm'\sigma'}\hat{c}_{ilm''\sigma}\rangle+\langle\hat{c}^{+}_{ilm\sigma}\hat{c}_{ilm'''\sigma'}\rangle\hat{c}^{+}_{ilm'\sigma'}\hat{c}_{ilm''\sigma}.\end{aligned}\tag{2.3.63}$$

Expectation value for two Fermi operators with the opposite spins is equal to zero and hence:

$$\langle\hat{c}^{+}_{ilm'\sigma'}\hat{c}_{ilm''\sigma}\rangle=\delta_{\sigma\sigma'}n^{\sigma}_{m'm''}.\tag{2.3.64}$$

Approximation (2.3.63) leads to one-electron Hamiltonian:

$$\widehat{H}_{\mathrm{LDA+U}}=\widehat{H}_{\mathrm{LDA}}+V^{\sigma}_{mm'}\hat{c}^{+}_{ilm\sigma}\hat{c}_{ilm'\sigma}=\widehat{H}_{\mathrm{LDA}}+\sum_{mm'}|ilm\sigma\rangle V^{\sigma}_{mm'}\langle ilm'\sigma|,\tag{2.3.65}$$

where one-electron potential $V^{\sigma}_{mm'}$ is defined by expression:

$$\begin{aligned}V^{\sigma}_{mm'}=\sum_{\{m\}}\{&\langle m,m''|V_{\mathrm{ee}}|m',m'''\rangle n^{-\sigma}_{m''m'''}+(\langle m,m''|V_{\mathrm{ee}}|m',m'''\rangle\\ &-\langle m,m''|V_{\mathrm{ee}}|m''',m'\rangle)n^{\sigma}_{m''m'''}\}-\bar{U}\left(n_d-\frac{1}{2}\right)\end{aligned}\tag{2.3.66}$$

(term $-\bar{U}(n_d-1/2)$ appears from "double counting" correction term (Hamiltonian (2.2.35))). Density (occupancy) matrix $n^{\sigma}_{mm'}\equiv\langle\hat{c}^{+}_{ilm\sigma}\hat{c}_{ilm'\sigma}\rangle$ is calculated as:

$$n^{\sigma}_{mm'}=-\frac{1}{\pi}\int_{-\infty}^{E_F}\mathrm{Im}G^{\sigma}_{ilm,ilm'}(E)\mathrm{d}E,\tag{2.3.67}$$

where $G^{\sigma}_{ilm,ilm'}(E)=\langle ilm\sigma|(E+i\delta-\widehat{H}_{\mathrm{LDA+U}})^{-1}|ilm'\sigma\rangle$ are matrix elements of Green function for Hamiltonian (2.3.65).

$LDA+U$ method equations (2.3.65–2.3.66) can be derived also in variational way (as it was originally proposed by authors in [61,104]) from $LDA+U$ functional:

$$E^{\mathrm{LDA+U}}[\rho(\mathbf{r}),\{n\}] = E^{\mathrm{LDA}}[\rho(\mathbf{r})] + E^{U}[\{n\}] - E_{dc}[\{n\}]. \tag{2.3.68}$$

Here $\rho(\mathbf{r})$ is electron density, $E^{\mathrm{LDA}}[\rho(\mathbf{r})]$ the standard LDA total energy functional (2.1.1) with exchange-correlation energy in the form of (2.1.7) and term responsible for Coulomb interaction E^{U} is a functional of orbital occupancy matrix $\{n\}$ postulated as:

$$\begin{aligned} E^{U}[\{n\}] = \frac{1}{2}\sum_{\{m\},\sigma} \{&\langle m,m''|V_{\mathrm{ee}}|m',m'''\rangle n^{\sigma}_{mm'} n^{-\sigma}_{m''m'''} \\ &+ (\langle m,m''|V_{\mathrm{ee}}|m',m'''\rangle - \langle m,m''|V_{\mathrm{ee}}|m''',m'\rangle) n^{\sigma}_{mm'} n^{\sigma}_{m''m'''}\}, \end{aligned} \tag{2.3.69}$$

where V_{ee} is screened Coulomb interaction between electrons in nl shell. The last term in (2.3.68) corresponds to "double counting" correction (see (2.2.32)):

$$E_{dc}[\{n\}] = \frac{1}{2} U n_d (n_d - 1). \tag{2.3.70}$$

$LDA+U$ method equations (2.3.65–2.3.66) can be derived by variation of (2.3.68) functional.

Equations (2.3.65–2.3.66) are written in a most general form invariant with respect to orbital basis transformation. That means that for any unitary matrix $A_{mm'}$ transition to new orbitals basis set $|ilm\sigma\rangle \to \sum_{m'} A_{mm'}|ilm'\sigma\rangle$ does not change the value of (2.3.69) functional. In majority of real systems there is a "natural" orbital basis determined by symmetry with forbidden orbital mixing. In this basis occupancy matrix (2.3.67) becomes diagonal $n^{\sigma}_{mm'} = \delta_{mm'} n_{m\sigma}$ and Coulomb interaction energy can be expressed in the form (2.2.27). Then one-electron potential matrix (2.3.66) will also become diagonal $V^{\sigma}_{mm'} = \delta_{mm'} V_{m\sigma}$:

$$V_{m\sigma} = \sum_{m'} U_{mm'} n_{m'\bar{\sigma}} + \sum_{m'\neq m} (U_{mm'} - J_{mm'}) n_{m'\sigma} - \bar{U}\left(n_d - \frac{1}{2}\right). \tag{2.3.71}$$

Keeping in mind that d-electrons number is a sum over all orbital occupancies $n_d = \sum_{m\sigma} n_{m\sigma}$ expression (2.3.71) can be rewritten as:

$$V_{m\sigma} = \sum_{m'} (U_{mm'} - \bar{U}) n_{m'\bar{\sigma}} + \sum_{m'\neq m} (U_{mm'} - J_{mm'} - \bar{U}) n_{m'\sigma} + \bar{U}\left(\frac{1}{2} - n_{m\sigma}\right). \tag{2.3.72}$$

$\bar{U}$ is defined as an average over Coulomb interaction matrix elements $U_{mm'}$, $(U_{mm'} - J_{mm'})$ over all possible spin-orbital pairs $m\sigma, m'\sigma'$:

$$\bar{U} = \left(\frac{\sum_{mm'} U_{mm'} + \sum_{m,m' \neq m} (U_{mm'} - J_{mm'})}{(2N_d(2N_d - 1))} \right) \tag{2.3.73}$$

(N_d is orbital degeneracy). First two terms in (2.3.72) containing deviations from the average $U_{mm'} - \bar{U}$ are relatively small and the main contribution is given by last term $\bar{U}(\frac{1}{2} - n_{m\sigma})$. For fully occupied or empty orbitals this term has a simple form:

$$V_{m\sigma} \approx \bar{U} \left(\frac{1}{2} - n_{m\sigma} \right) = \begin{cases} -U/2 & \text{if } \ n_{m\sigma} = 1 \\ +U/2 & \text{if } \ n_{m\sigma} = 0. \end{cases} \tag{2.3.74}$$

That means that main effect of $LDA+U$ correction (2.3.65) to LDA potential is increasing empty states energy on $U/2$ and decreasing on the same value occupied states energy.

Expression (2.3.74) demonstrates that $LDA + U$ method leads to splitting of empty and occupied states energies that were degenerate in LDA on average Coulomb interaction $\bar{U}$. In the result partially filled d-band that in standard LDA calculation would give metallic state in $LDA + U$ method could result in insulator. This effect will be illustrated later for compounds NiO, $CaCuO_2$, and CoO.

Eigenvalues $\epsilon_{n\mathbf{k}}$ and eigenfunctions $\psi_{n\mathbf{k}}$ obtained in $LDA + U$ method could be used to calculate exchange interaction parameters J_{ij} for Heisenberg model:

$$\mathcal{H} = \sum_{ij} J_{ij} (\mathbf{S}_i^{\mathrm{e}} \mathbf{S}_j^{\mathrm{e}}), \tag{2.3.75}$$

where $\mathbf{S}_i^{\mathrm{e}}$ are electron spin operators (1.2.3).

Equations for J_{ij} were derived by Lichtenstein et al. in [104, 105] using analitic second derivative of total energy as a function of magnetic moment rotation angles ϕ_i, ϕ_j on lattice sites i, j:

$$J_{ij} = \sum_{\{m\}} I^i_{mm'} \chi^{ij}_{mm'm''m'''} I^j_{m''m'''}, \tag{2.3.76}$$

Potentials I^i are expressed via spin-dependent $LDA + U$ potentials (2.3.66) for i-th atom in crystal unit cell:

$$I^i_{mm'} = V^{i\uparrow}_{mm'} - V^{i\downarrow}_{mm'}, \tag{2.3.77}$$

and static susceptibility χ^{ij} is expressed via eigenfunctions $\psi_{n\mathbf{k}\sigma}$ and eigenvalues $\epsilon_{n\mathbf{k}\sigma}$:

$$\chi^{ij}_{mm'm''m'''} = \sum_{\mathbf{k}nn'} \frac{n_{n\mathbf{k}\downarrow} - n_{n'\mathbf{k}\uparrow}}{\epsilon_{n\mathbf{k}\uparrow} - \epsilon_{n'\mathbf{k}\downarrow}} \psi^{ilm^*}_{n\mathbf{k}\uparrow} \psi^{jlm''^*}_{n\mathbf{k}\uparrow} \psi^{ilm'}_{n'\mathbf{k}\downarrow} \psi^{jlm'''}_{n'\mathbf{k}\downarrow}.$$

($n_{n\mathbf{k}\downarrow}$ is occupation of $n\mathbf{k}\downarrow$ state).

Hamiltonian (2.3.65) contains orbital-dependent potential (2.3.66) in the form of projecting wave functions on orbitals $|ilm\sigma\rangle$ that allows to realize $LDA + U$ calculation scheme in the frame of any DFT calculation methods for example $LMTO$ [51].

While $LDA+U$ approach overcomes some major deficiencies of LDA such as metallic solution for Mott insulators it is still one-electron method because it is based on static mean-filed approximation. It completely fails for strongly correlated metals where electrons reveal simultaneously localized and itinerant properties. It cannot also describe paramagnetic insulator because in $LDA+U$ equations nontrivial results can be obtained only when orbitals occupancies $n_{m\sigma}$ are essentially different for different orbitals that corresponds to long-range spin and orbital order. However for magnetically ordered insulators $LDA + U$ gave significant qualitative improvement for calculation results agreement with experimental data comparing with standard DFT methods. In the next section we describe $LDA + U$ results for various physical effects and real materials.

2.4 $LDA + U$ Method Applications

2.4.1 Mott Insulators: NiO, CoO, and $CaCuO_2$

Late transition metal oxides NiO, CoO, and $CaCuO_2$ are antiferromagnetic insulators with energy gap value about few eV. However, DFT methods give electronic and magnetic structure with strongly underestimated energy gap and magnetic moment values or even qualitatively wrong metallic ground state.

Nickel and cobalt monoxides have cubic crystal structure of NaCl type where transition metal atom is surrounded by six oxygen atoms forming perfect octahedron. d-level is split by cubic crystal field on lower energy states transforming according to triply degenerate irreducible representation t_{2g} (xy, xz, yz orbitals) and higher energy states corresponding to doubly degenerate representation e_g ($3z^2 - r^2, x^2 - y^2$ orbitals). Transition metal ions have 2+ valence in these compounds that gives configurations d^8 for NiO and d^7 for CoO.

For NiO and CoO $LSDA$ calculations gave spin-polarized antiferromagnetic ground state [62]. However while experimentally these compounds are wide gap insulators calculated band structure for NiO (see Fig. 2.3, left side) shows very small energy gap value (0.4 eV comparing with experimental value 4.0 eV) while for CoO $LSDA$ results in metal with Fermi level inside partially filled d band (see Fig. 2.3, right side).

The source of this discrepancy is the fact that in DFT the same one-electron potential (2.1.4) acts on occupied and empty orbitals. In the result partially filled t_{2g} band with spin projection "down" for CoO is metallic. In $LSDA$ spin-polarization leads to one-electron potential dependence on spin

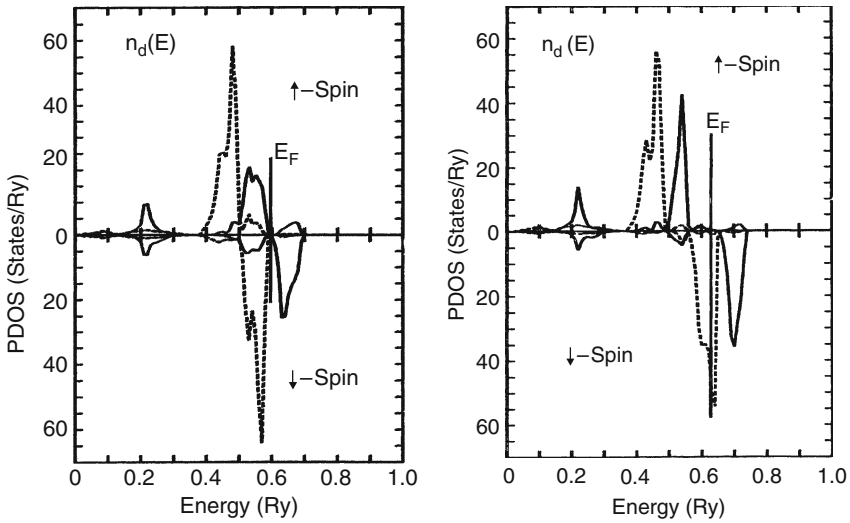

Fig. 2.3. Partial 3*d* densities of states (*dashed line* corresponds to t_{2g} states and *solid line* to e_g orbitals) obtained in *LSDA* calculations for NiO (*left side*) and CoO (*right side*) [62]

direction (2.1.8). For NiO half-filled e_g shell is split by spin polarization and small energy gap appears in the *LSDA* spectra.

Using $LDA + U$ correction drastically changes calculations result [61] (see Figs. 2.4 and 2.5). Orbitally dependent potential (2.3.66) gives splitting for empty and occupied *d*-states approximately on average Coulomb interaction parameter $\bar{U}$ (2.3.74). Empty $e_g \downarrow$ states are shifted up in energy while occupied states energies go down and for NiO large energy gap appears $\approx 4\,\text{eV}$. In CoO *d*-electrons number is less than in NiO on 1 electron and in addition to energy shift of e_g states as in NiO partially filled $t_{2g} \downarrow$ states are split on empty $t_{2g} - 1 \downarrow$ states with increased energy and occupied $t_{2g} - 2 \downarrow$ states with energy shifted down. In the result instead of metallic *LSDA* solution (Fig. 2.3, right side) $LDA + U$ gives wide gap insulator for CoO (Fig. 2.5).

$CaCuO_2$ has tetragonal crystal structure with CuO_2 layers and calcium ions in between. Copper atom is surrounded by four oxygen atoms forming square. Copper valence in this compound is equal +2 that gives configuration d^9 with one hole in *d*-shell. From five Cu *d*-orbitals the highest energy because of the crystal filed splitting has $x^2 - y^2$ orbital with lobes directed to oxygen ions. In Fig. 2.6 total and partial densities of states are presented obtained from *LDA* calculation [106]. All bands are occupied except half-filled band formed by Cu $x^2 - y^2$ orbital.

In contrast to nickel and cobalt oxides in $CaCuO_2$ *LSDA* method did not result in stable spin-polarized solution and the calculated ground state is nonmagnetic metal instead of experimentally observed antiferromagnetic insulator. The reason for this discrepancy is large width of $x^2 - y^2$ band

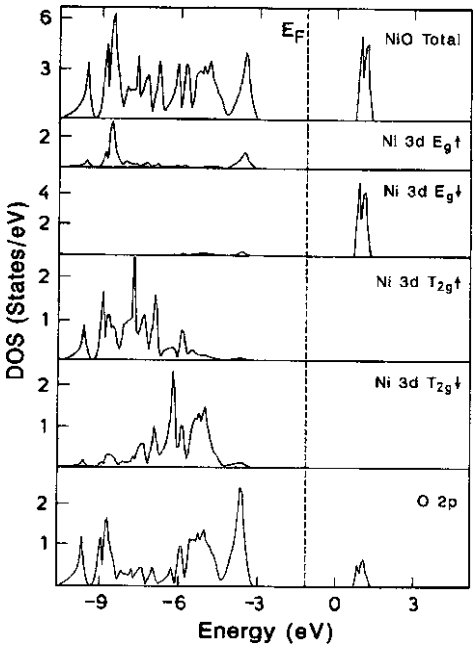

Fig. 2.4. Full and partial densities of states from $LDA + U$ calculation for NiO [61]

($\approx$4 eV) comparing with intraatomic exchange interaction parameter $J \approx 1$ eV driving spin-polarization. $LDA + U$ method applied to this material led to significant increase of energy splitting between occupied $x^2 - y^2 \uparrow$ and empty $x^2 - y^2 \downarrow$ states that is determined by large Coulomb parameter $U \approx 8$ (2.3.74) instead of small exchange parameter $J \approx 1$ eV. In the result spin-polarized solution becomes stable and $LDA + U$ calculation gives antiferromagnetic wide-gap insulator as a ground state (see Fig. 2.7).

2.4.2 Charge Ordering: Fe_3O_4

Magnetite Fe_3O_4 crystallizes in spinel structure (Fig. 2.8, left side) with iron ions in two different crystallographic positions. A position has tetrahedral coordination of four oxygen ions and is occupied by iron ions with valence +3 (configuration d^5). Iron ions in position B (whose number is two times larger than number of atoms in A position) are surrounded by six oxygen ions forming octahedron and they formally have noninteger valence +2.5 that corresponds to mixture of d^5 and d^6 configurations with equal weights. Spin ordering is ferrimagnetic with antiparallel spin directions for iron ions in positions A and B.

With lowering temperature below 120 K transition happens with increasing of resistivity on two orders of magnitude and lowering crystal structure

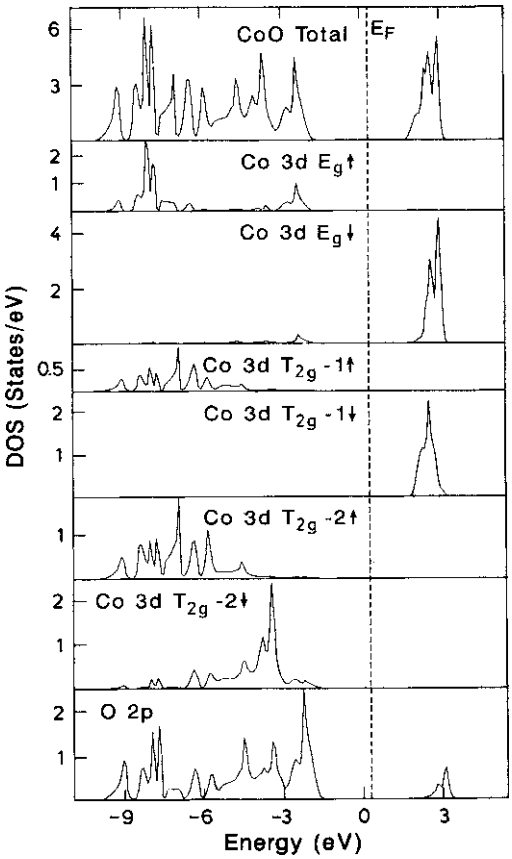

Fig. 2.5. Full and partial densities of states from $LDA+U$ calculation for CoO [61]

symmetry from cubic to monoclinic. Verwey proposed [107,108] that this transition is caused by charge ordering of iron ions with valence +2 and +3 in sublattice B (see Fig. 2.8, right side).

LSDA calculation [66] (see Fig. 2.9, left side) gave metallic electronic structure with Fermi level crossing partially filled band formed by spin-down t_{2g}-states of iron ions in crystallographic positions B. Charge ordered state was found to be unstable in *LSDA* and ground state is homogeneous in charge distribution with equivalent electronic state for iron ions in B positions. For those ions spin-up d states are completely filled and additional 0.5 electrons per B atom are in spin-down t_{2g}-states.

The source of charge ordered state instability is residual "self-interaction" error in *LSDA* (see Sect. 2.1.3). Charge ordering corresponds to increase of d-shell occupancy for one of B type iron atoms in unit cell ($B1$) on δn_d and decrease on the same value occupancy for the second iron atom ($B2$). Redistribution of electronic density between $B1$ and $B2$ leads to changes of

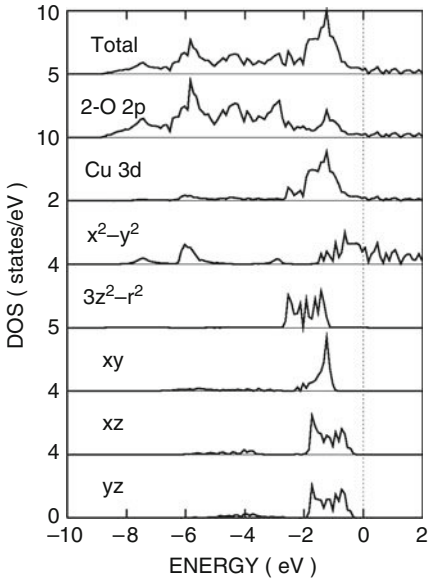

Fig. 2.6. Full and partial densities of states from LDA calculation for $CaCuO_2$ [106]

$LSDA$ one-electron potentials and corresponding eigenvalues. In the result d-orbital energy ϵ_d for atom $B1$ increases on $\frac{\partial \epsilon_d}{\partial n_d}\delta n_d$ and ϵ_d for atom $B2$ decreases on the same value. In self-consistency iterations this potential change leads to reverse flow of charge density from $B1$ atoms to $B2$ atoms and δn_d will decreases till charge homogeneity is restored. This effect is unphysical because energy of some orbital should not depend on its occupancy and is a result of residual "self-interaction" error in $LSDA$.

In $LDA + U$ method main part of potential correction $V_{m\sigma}$ (2.3.71) is $\bar{U}(\frac{1}{2} - n_{m\sigma})$ (2.3.74). With occupancy decrease on δn_d for one of spin-down t_{2g} orbitals on $B1$ iron atom $LDA + U$ potential correction $V_{m\sigma}$ will increases on $\bar{U}\delta n_d$ with opposite effect on $B2$ atoms. Average Coulomb interaction parameter $\bar{U}$ is determined in constrain DFT calculations (2.2.60) as derivative $\frac{\partial \epsilon_d}{\partial n_d}$ and the change of $LDA + U$ potential correction $V_{m\sigma} \approx -\bar{U}\delta n_d$ is equal in absolute value but opposite in sign for the change of $LSDA$ potential $\frac{\partial \epsilon_d}{\partial n_d}\delta n_d$. This means that $LDA + U$ potential correction cancels the change of $LSDA$ potential and thus removes residual "self-interaction" error present in $LSDA$.

Figure 2.9 (right side) presents the densities of states obtained in $LDA+U$ calculation for Fe_3O_4 [66]. $LDA + U$ potential correction (2.3.71) results in insulator solution with a small energy gap. $Bt_{2g} \downarrow$ band that was partially filled in $LSDA$ solution is split on occupied $B2t_{2g} \downarrow$ and empty $B1t_{2g} \downarrow$ subbands with a gap between them. This result shows that $LDA + U$ method

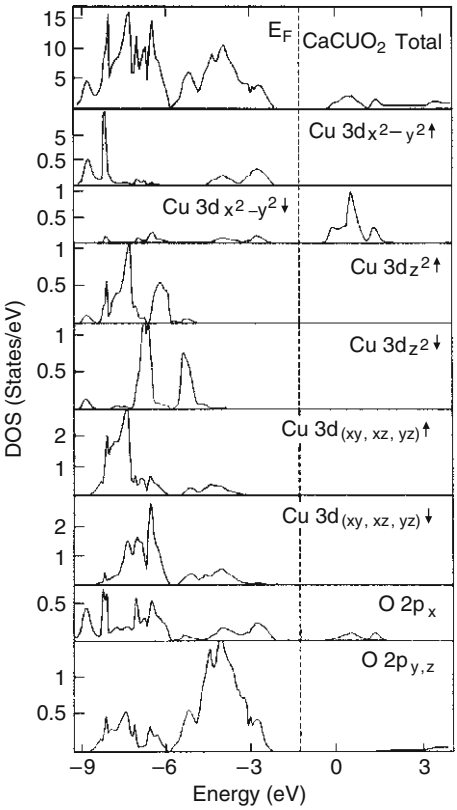

Fig. 2.7. Full and partial densities of states from $LDA+U$ calculation for $CaCuO_2$ [61]

developed for treating Coulomb correlation effects can also serve to cure "self-interaction" error of *LSDA* and so makes possible stable charge ordered solution.

Real charge ordering pattern is much more complicated than simple picture proposed by Verwey (Fig. 2.8 right). $LDA+U$ calculation [109] with experimentally observed low-temperature monoclinic crystal structure for Fe_3O_4 gave charge and orbital ordering shown in Fig. 2.10.

2.4.3 Orbital Ordering: $KCuF_3$

Compound $KCuF_3$ has perovskite crystal structure (Fig. 2.11, left side). Copper atoms are surrounded by six oxygen ions forming octahedron. Copper in $KCuF_3$ has valence +2 that corresponds to configuration d^9 with fully occupied t_{2g} shell and one hole in e_g states. Cu^{+2} is Jahn-Teller ion because partially filled e_g shell is unstable to Jahn-Teller distortion lowering crystal symmetry with splitting of partially filled energy level on occupied and empty

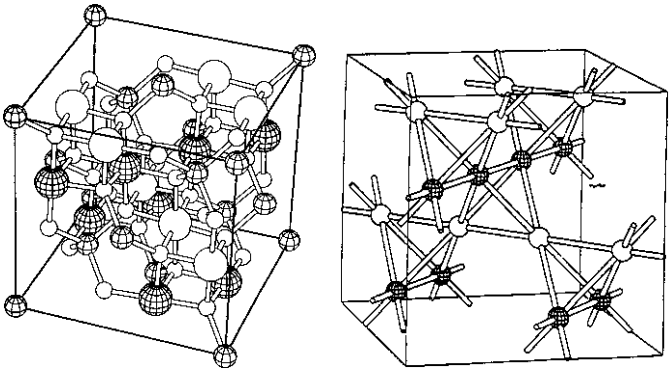

Fig. 2.8. Magnetite Fe_3O_4 crystal structure (*left side* with large *spheres* corresponding to iron ions and *small ones* to oxygen ions) and charge ordering scheme for electrons on iron ions in octahedral positions proposed by Verwey [107,108] (*right side* with only iron ions in octahedral positions shown, *shaded spheres* correspond to Fe^{+2} and *open ones* to Fe^{+3})

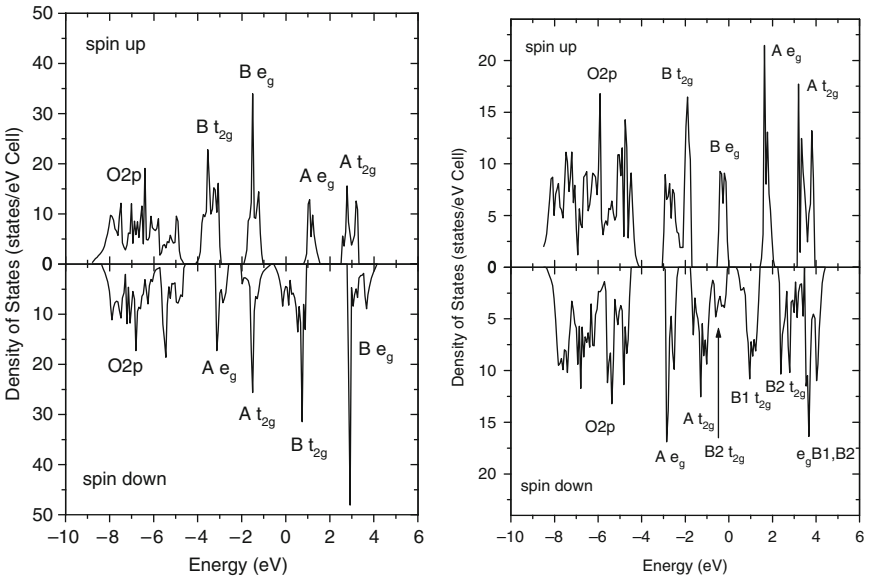

Fig. 2.9. Densities of states obtained in calculations for magnetite Fe_3O_4 by *LSDA* method (*left side*) and by $LDA + U$ method (*right side*) [66]

states. Such distortion is indeed observed in $KCuF_3$ where CuF_6 octahedra are elongated in direction perpendicular to c axis (see Fig. 2.11, right side) with long Cu–F bond alternatively directed along x and y axes. Such distortion increases energy for orbital with lobes directed along short Cu–F bonds (in this case that are y, z for the first case and x, z for the second case). Then

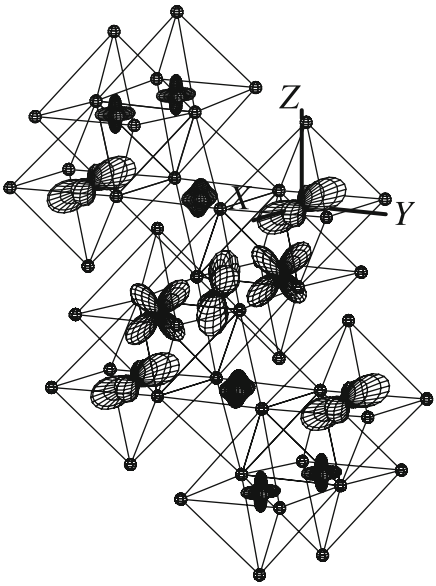

Fig. 2.10. Charge and orbital ordering from $LDA + U$ calculation for Fe_3O_4 in monoclinic crystal structure corresponding to low-temperature phase [109] (*small spheres* correspond to oxygen ions forming octahedra with iron ions in the center)

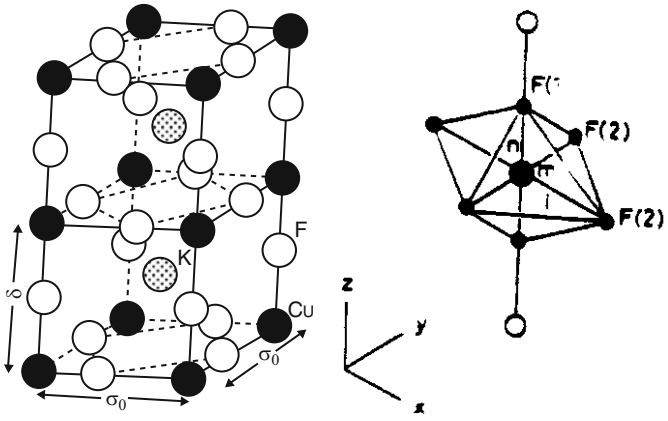

Fig. 2.11. Perovskite crystal structure for $KCuF_3$ (*left side*) and distorted octahedron CuF_6 (*right side*)

the only hole on copper d shell will be occupied by orbitals $y^2 - z^2$ and $x^2 - z^2$ as is shown in Fig. 2.12 (left side).

In Jahn-Teller theory the cause of the effect is electron–lattice interaction. However Kugel and Khomskii [110, 111] proposed different explanation. They have shown that orbital ordering for electrons (or holes) in degenerate partially

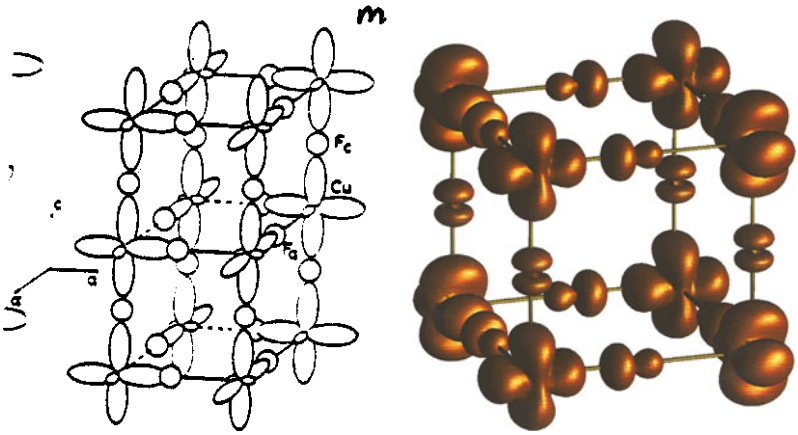

Fig. 2.12. Orbital ordering scheme in $KCuF_3$ [110, 111] (*left side*) and spin density distribution from $LDA + U$ calculation [104] (*right side*)

filled states can be obtained taking into account only electronic degrees of freedom as for example in degenerate Hubbard model (4.2.71). $LDA + U$ calculations [104] for $KCuF_3$ in crystal structure without Jahn-Teller distortion (in perovskite crystal structure with equal Cu–F bond lengths along x and y axes) indeed gave solution with orbital order in agreement with experimentally observed (Fig. 2.12, right side).

It is interesting to note that in *LSDA* calculation total energy has minimum for undistorted perovskite crystal structure and only with orbital dependent $LDA + U$ potential Jahn-Teller distortion for CuF_6 octahedra can be reproduced in calculations (Fig. 2.13).

2.4.4 Orbital and Charge Ordering: $Pr_{0.5}Ca_{0.5}MnO_3$

Manganite $PrMnO_3$ also belongs to Jahn-Teller systems. Its crystal structure (Fig. 2.14 left) is based on perovskite with MnO_6 octahedra rotated and tilted from ideal directions. Manganese has valence +3 in this compound with configuration d^4. High-spin state d^4 ion in octahedral crystal field corresponds to three electrons in $t_{2g} \uparrow$ states and one electron in partially filled e_g shell. $LDA + U$ calculations [112] for crystal structure where MnO_6 octahedra were undistorted gave solution with orbital ordering for e_g shown at Fig. 2.14 (right side). This ordering pattern agrees well with experimentally observed Jahn-Teller distortion of MnO_6 octahedra with long Mn–O bonds alternatively directed along axes perpendicular to each other.

In $Pr_{0.5}Ca_{0.5}MnO_3$ compound obtained by replacing in $PrMnO_3$ half of three-valence praseodymium on two-valence calcium, manganese valence is

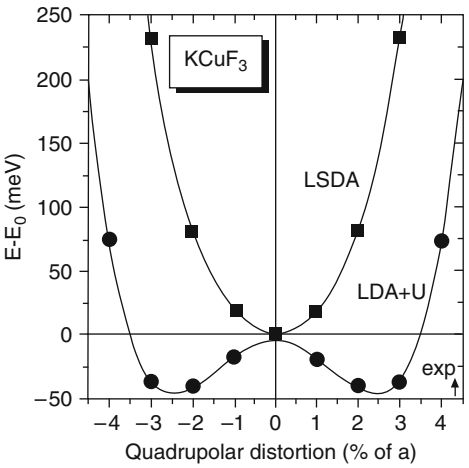

Fig. 2.13. Total energy dependence on octahedron CuF_6 distortion in perovskite crystal structure for $KCuF_3$ from $LDA + U$ and $LSDA$ calculations [104]

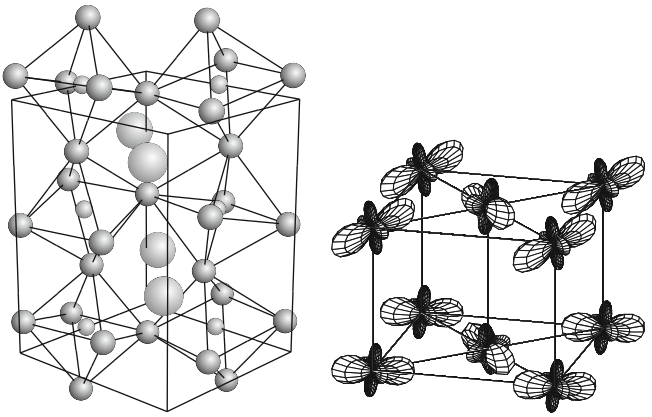

Fig. 2.14. $PrMnO_3$ crystal structure (*left side*, *large spheres* are Pr ions, medium size spheres – oxygen ions forming octahedra with manganese ions (*small spheres*) in the center) and angle dependence for occupied e_g orbitals from $LDA+U$ calculations (*right side*) [112]

formally +2.5 and one electron in e_g shell is now for two Mn ions. That leads to experimentally observed very complicated spin, charge, and orbital ordering (see Fig. 2.15, left side). $LDA + U$ calculations for this compound [112] resulted in successful reproducing of this ordering (see Fig. 2.15, right side). It is interesting to note that total number of d-electrons on two types of manganese ions with formal configurations d^4 and d^3 is nearly equal (difference

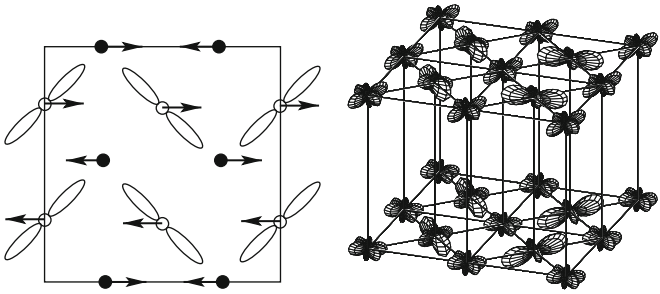

Fig. 2.15. Spin,orbital and charge ordering scheme for Mn3d electrons in $Pr_{0.5}Ca_{0.5}MnO_3$ from neutron diffraction data analysis [113] (*left side*) and angle dependence for occupied e_g orbitals from $LDA + U$ calculations (*right side*) [112]

is <0.1). In other words ordering in $Pr_{0.5}Ca_{0.5}MnO_3$ is better described as having orbital nature than a charge one.

2.4.5 Spin Ordering: CaV_nO_{2n+1}

Compounds series CaV_nO_{2n+1} have attracted attention due to unusual magnetic properties with so called "spin gap" effect. Long-range magnetic ordering is not observed till the lowest temperatures but neutron diffraction experiments show a gap in spin excitation spectrum. In other words there is a final energy needed to move a system from magnetic ground state to excited one. On the curve for magnetic susceptibility temperature dependence (Fig. 2.18) this effect reveals itself in small susceptibility value at low temperatures with fast increase at higher T.

Crystal structure for these compounds is formed by layers of VO_5 pyramids (Fig. 2.16) with calcium ions in between. Vanadium valence is +4 with configuration d^1. Crystal field splitting for d states is very strong in this crystal structure and orbital degeneracy is completely lifted. One electron in d shell occupies xy orbital as it is shown in Fig. 2.16.

The layers are formed by connecting VO_5 pyramids via vertex and edges in various combinations for compounds CaV_2O_5, CaV_3O_7, and CaV_4O_9. That gives various types of V–V bonds with different exchange coupling parameters J_{ij} (2.3.75) between magnetic moments on vanadium ions (see Fig. 2.17).

$LDA + U$ calculations [114] gave eigenvalues and eigenfunctions that were used to determine exchange coupling parameters J_{ij} via equations (2.3.76). The results are presented on Table 2.1. As one can see the values of J_{ij} could differ for various V–V bonds and compounds by an order of magnitude and even have a different sign. Unexpected was strong difference (in ≈6 times) of parameter $J2$ for compounds CaV_2O_5 and MgV_2O_5 that have the same

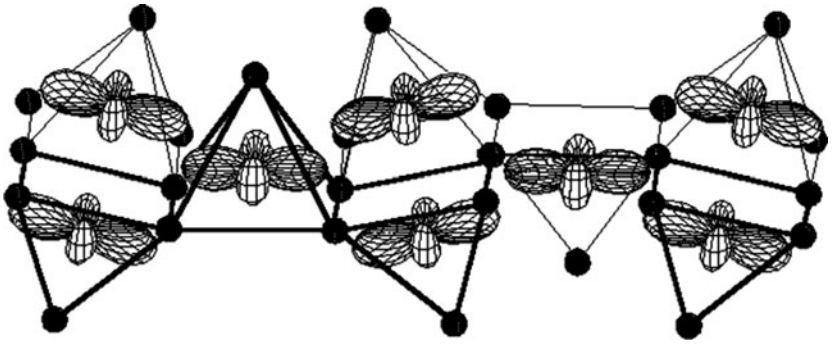

Fig. 2.16. CaV_3O_7 crystal structure and angle dependence for occupied vanadium d-orbital from $LDA + U$ calculation [114] (*dark spheres* are oxygen ions forming pyramids with vanadium ions in the center)

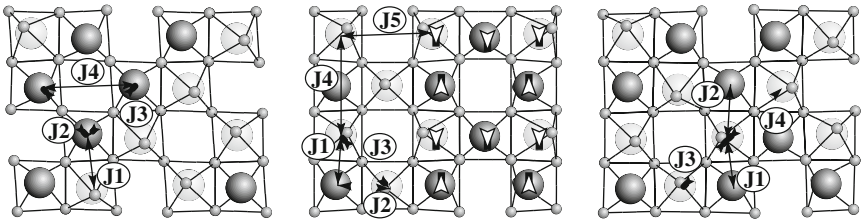

Fig. 2.17. Crystal structure and various exchange couplings between magnetic moments on vanadium ions for CaV_2O_5 MgV_2O_5 (*left*), CaV_3O_7 (*center*) CaV_4O_9 (*right*) [114]. *Small spheres* are oxygen ions, *dark and light* spheres corresponds to vanadium ions position above and below the plane

Table 2.1. Calculated values for parameters of interatomic exchange couplings (in Kelvin units) [114]. Minus sign means ferromagnetic interaction

	CaV_2O_5	MgV_2O_5	CaV_3O_7	CaV_4O_9
$J1$	−28	60	46	62
$J2$	608	92	−14	89
$J3$	122	144	75	148
$J4$	20	19	18	91
$J5$			5	

type of crystal structure but with slightly different values of tilting angle for pyramids axes with respect to layer plane.

Exchange coupling parameters J_{ij} obtained in $LDA+U$ calculations were used in [114] to calculate magnetic susceptibility temperature dependence by Quantum Monte Carlo method for Heisenberg model (2.3.75). Comparison of

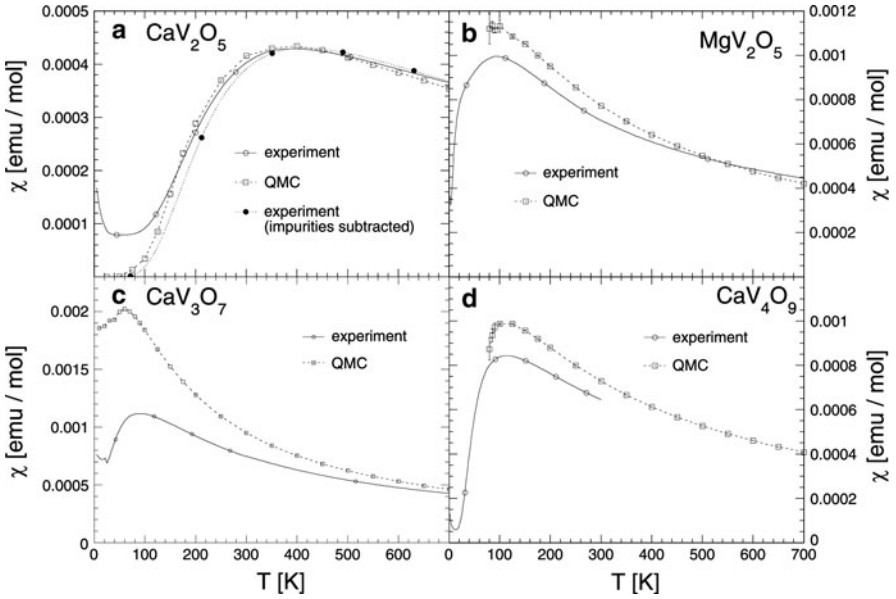

Fig. 2.18. Comparison between experimental and calculated temperature dependence of magnetic susceptibility for CaV_nO_{2n+1}. Calculations were done by Quantum Monte Carlo method for Heisenberg model with exchange coupling parameters from $LDA + U$ calculations [114]

calculations results with experimental curves is presented in Fig. 2.18. A good agreement between theoretical and experimental curves could be seen especially for CaV_2O_5 where experimentally was found a large "spin gap" value $\approx$500 K.

3

Hubbard Model in Dynamical Mean-Field Theory

3.1 Reducing Lattice Model to Effective Single Impurity Anderson Model

3.1.1 Electronic Green Function

Let us consider standard Hubbard model for nondegenerate electrons. Model Hamiltonian in second quantization representation is:

$$\hat{H} = \sum_{ij\sigma} t_{ij} \hat{c}^{+}_{i\sigma} \hat{c}_{j\sigma} + \sum_{i} U \hat{n}_{i\uparrow} \hat{n}_{i\downarrow}, \tag{3.1.1}$$

where $\hat{c}^{+}_{i\sigma}(\hat{c}_{i\sigma})$ are creation (annihilation) operators for electron on site i with spin $\sigma = \uparrow, \downarrow$; $\hat{n}_{i\sigma} = \hat{c}^{+}_{i\sigma}\hat{c}_{i\sigma}$ the number of electrons operator in state $i\sigma$, t_{ij} is the matrix element for electron hopping from site j to site i, U is Coulomb interaction energy for two electrons on the same site.

Fermi operators $\hat{c}^{+}_{i\sigma}$ and $\hat{c}_{i\sigma}$ satisfy anticommutation relations:

$$\left[\hat{c}_{i\sigma}, \hat{c}^{+}_{i\prime\sigma\prime}\right]_{+} = \delta_{ii\prime}\delta_{\sigma\sigma\prime}, \ \left[\hat{c}_{i\sigma}, \hat{c}_{i\prime\sigma\prime}\right]_{+} = 0. \tag{3.1.2}$$

Let us introduce one-particle Green function (GF) in a standard form (see Appendix B):

$$g^{\sigma}(i_1\tau_1, i_2\tau_2) = -\left\langle T_\tau \hat{c}_{i_1\sigma}(\tau_1)\hat{c}^{+}_{i_2\sigma}(\tau_2)\right\rangle, \tag{3.1.3}$$

where $\langle \ldots \rangle$ means statistical averaging

$$\langle \ldots \rangle = \frac{\mathrm{Tr}(\mathrm{e}^{-\beta\hat{H}} \ldots)}{\mathrm{Tr}(\mathrm{e}^{-\beta\hat{H}})}, \tag{3.1.4}$$

and $\hat{c}^{+}_{i\sigma}(\tau)$, $\hat{c}_{i\sigma}(\tau)$ are operators in Heisenberg representation:

$$\hat{c}^{+}_{i\sigma}(\tau) = \mathrm{e}^{\tau\hat{H}}\hat{c}^{+}_{i\sigma}\mathrm{e}^{-\tau\hat{H}}, \ \hat{c}_{i\sigma}(\tau) = \mathrm{e}^{\tau\hat{H}}\hat{c}_{i\sigma}\mathrm{e}^{-\tau\hat{H}} \tag{3.1.5}$$

with thermodynamic "time" τ in the interval $0 \leq \tau \leq \beta = 1/T$ (T is temperature and Bolzman constant k is set to 1). Symbol T_τ in GF definition (3.1.3) is time τ ordering operator.

Using Fourier transformation with respect to variables $\tau_1 - \tau_2$ and $i_1 - i_2$ GF (3.1.3) can be presented in the following form (later we skip spin index σ assuming paramagnetic phase):

$$g(\mathbf{k}, i\omega_n) = (i\omega_n + \mu - \epsilon_{\mathbf{k}} - \Sigma(\mathbf{k}, i\omega_n))^{-1}, \tag{3.1.6}$$

where $\omega_n = (2n+1)\pi T$, $n = 0, \pm 1, \pm 2, \ldots$ are odd Matsubara frequencies,

$$\epsilon_{\mathbf{k}} = 2t \sum_{\alpha=1}^{d} \cos k_\alpha \tag{3.1.7}$$

is noninteracting electron energy for hypercubic lattice with space dimension d in nearest neighbors approximation for hopping matrix elements, μ is chemical potential and $\Sigma(\mathbf{k}, i\omega_n)$ is self-energy corresponding to interelectron Coulomb interaction. To determine $\Sigma(\mathbf{k}, i\omega_n)$ as series in U expansion there was developed diagrammatic technique [115] that should be valid for $U \ll W$ where W is noninteracting electrons band.

For strongly correlated systems where $U \geq W$ standard perturbation theory [115] is not valid and one should use Dynamical Mean-Field Theory ($DMFT$) based on Metzner and Vollhardt [4] discovery that for large space dimension ($d \to \infty$) electron self-energy does not depend on momentum (wave vector) $\mathbf{k}$ but only on frequency $i\omega_n$:

$$\Sigma(\mathbf{k}, i\omega_n) = \Sigma(i\omega_n). \tag{3.1.8}$$

$\mathbf{k}$-independence of self-energy in real space representation means that only local matrix elements $\Sigma_{ij}(i\omega_n)$ with $i = j$ are nonzero and all nonlocal terms with $i \neq j$ vanish. That allows to reduce the problem of electron on the lattice in Hubbard model to single impurity Anderson model [30] that can be solved much easier by various numerical methods. This "mapping" of lattice problem to single impurity one is an essence of $DMFT$ method.

To show that we start with single-site GF obtained by summation of (3.1.6) over wave vector $\mathbf{k}$:

$$g_{ii}(i\omega_n) \equiv G(i\omega_n) = \sum_{\mathbf{k}} (i\omega_n + \mu - \epsilon_{\mathbf{k}} - \Sigma(i\omega_n))^{-1}, \tag{3.1.9}$$

where we use (3.1.8) and the fact that for homogeneous systems diagonal in site indexes matrix element g_{ii} does not depend on site index. The $DMFT$ mapping idea is to identify single-site GF (3.1.9) with GF of some effective single impurity model having the same on-site Coulomb interaction as in Hubbard model. Hybridization of the site orbitals with the rest of the crystal in effective single impurity model is described by effective hybridization function $\Delta(i\omega_n)$ or effective noninteracting *bath* Green function $\mathcal{G}_0(i\omega_n)$:

$$\mathcal{G}_0(i\omega_n) = (i\omega_n + \mu - \Delta(i\omega_n))^{-1}. \tag{3.1.10}$$

Let us denote *GF* and self-energy for this impurity model as $G_{\text{imp}}(i\omega_n)$ and $\Sigma_{\text{imp}}(i\omega_n)$. The mapping means:

$$\begin{aligned} G(i\omega_n) &= G_{\text{imp}}(i\omega_n), \\ \Sigma(i\omega_n) &= \Sigma_{\text{imp}}(i\omega_n). \end{aligned} \tag{3.1.11}$$

The effective noninteracting *bath* Green function $\mathcal{G}_0(i\omega_n)$ can be obtained from Dyson equation:

$$G^{-1}_{\text{imp}}(i\omega_n) = \mathcal{G}_0^{-1}(i\omega_n) - \Sigma_{\text{imp}}(i\omega_n). \tag{3.1.12}$$

Dyson equation is used twice in *DMFT*. At first when self-energy $\Sigma(i\omega_n)$ and lattice *GF* (3.1.9) are known the *bath* Green function $\mathcal{G}_0(i\omega_n)$ is calculated

$$\mathcal{G}_0^{-1}(i\omega_n) = G^{-1}(i\omega_n) + \Sigma(i\omega_n). \tag{3.1.13}$$

Then impurity model defined by this *bath GF* is solved by taking into account all *local* Coulomb correlation with resulting impurity *GF* $G_{\text{imp}}(i\omega_n)$. Using new $G_{\text{imp}}(i\omega_n)$ new approximation for self-energy can be defined:

$$\Sigma_{\text{imp}}(i\omega_n) = \mathcal{G}_0^{-1}(i\omega_n) - G^{-1}_{\text{imp}}(i\omega_n). \tag{3.1.14}$$

New self-energy is used to determine new lattice *GF*:

$$G(i\omega_n) = \sum_{\mathbf{k}} (i\omega_n + \mu - \epsilon_{\mathbf{k}} - \Sigma_{\text{imp}}(i\omega_n))^{-1}. \tag{3.1.15}$$

Equations (3.1.9)–(3.1.15) can be regarded as equation system for unknown functions $\mathcal{G}_0(i\omega_n)$ and $\Sigma_{\text{imp}}(i\omega_n)$. The system is solved iteratively till self-consistency will be achieved assuming that we know how to solve single-impurity Anderson model with *bath GF* $\mathcal{G}_0(i\omega_n)$. Later we show how one can calculate Green function of single-impurity Anderson model.

3.1.2 Single Impurity Anderson Model

Anderson model Hamiltonian is:

$$\begin{aligned} \hat{H} = &\sum_{ij\sigma} t_{ij} \hat{c}^+_{i\sigma} \hat{c}_{j\sigma} + \sum_{i\sigma} \left[V_i \hat{c}^+_{i\sigma} \hat{d}_\sigma + V_i^* \hat{d}^+_\sigma \hat{c}_{i\sigma} \right] \\ &+ \epsilon_d \sum_\sigma \hat{d}^+_\sigma \hat{d}_\sigma + U \hat{n}_\uparrow \hat{n}_\downarrow, \end{aligned} \tag{3.1.16}$$

where $\hat{n}_{d\sigma} = \hat{d}^+_\sigma \hat{d}_\sigma$ is operator for number of localized electrons on impurity site.

The model describes localized on impurity center *d*-electrons embedded in noninteracting electrons system (called *s*-electrons). Coulomb interaction

between d-electrons is described by term $U\hat{n}_\uparrow\hat{n}_\downarrow$ and there is also hybridization between d and s electrons determined by parameter V_i.

To study the model (3.1.16) let us introduce localized electrons Green function:

$$g^\sigma_{dd}(\tau-\tau') = -\left\langle T_\tau \hat{d}_\sigma(\tau)\hat{d}^+_\sigma(\tau')\right\rangle. \tag{3.1.17}$$

As we will see later it is coupled via hybridization with another GF:

$$g^\sigma_{sd}(\tau-\tau') = -\left\langle T_\tau \hat{c}_\sigma(\tau)\hat{d}^+_\sigma(\tau')\right\rangle. \tag{3.1.18}$$

Both GF (and two other GFs g^σ_{ds} and g^σ_{ss}) have the same structure:

$$g_{12}(\tau-\tau') = -\left\langle T_\tau \hat{f}_1(\tau)\hat{f}^+_2(\tau')\right\rangle, \tag{3.1.19}$$

where $\hat{f}_1$ and $\hat{f}_2$ are Fermi operators.

In order to derive equations of motion for these GFs we use definition of time-ordered product with θ-function:

$$\theta(\tau-\tau') = \begin{cases} 1 & \text{if } \tau > \tau', \\ 0 & \text{if } \tau < \tau'. \end{cases} \tag{3.1.20}$$

We have:

$$\begin{aligned} g_{12}(\tau-\tau') = &-\theta(\tau-\tau')\left\langle \hat{f}_1(\tau)\hat{f}^+_2(\tau')\right\rangle \\ &+\theta(\tau'-\tau)\left\langle \hat{f}^+_2(\tau')\hat{f}_1(\tau)\right\rangle. \end{aligned} \tag{3.1.21}$$

If we differentiate both sides of this equation with respect to time τ and take into account that: $\frac{\partial}{\partial\tau}\theta(\tau-\tau') = \delta(\tau-\tau')$, then we will get equation

$$\begin{aligned} \frac{\partial}{\partial\tau}g_{12}(\tau-\tau') = &-\theta(\tau-\tau')\left\langle \frac{\partial}{\partial\tau}\hat{f}_1(\tau)\hat{f}^+_2(\tau')\right\rangle \\ &+\theta(\tau'-\tau)\left\langle \hat{f}^+_2(\tau')\frac{\partial}{\partial\tau}\hat{f}_1(\tau)\right\rangle - \delta_{12}\delta(\tau-\tau'), \end{aligned} \tag{3.1.22}$$

which we rewrite in a form:

$$-\frac{\partial}{\partial\tau}g_{12}(\tau-\tau') + \left\langle T_\tau \frac{\partial}{\partial\tau}\hat{f}_1(\tau)\hat{f}^+_2(\tau')\right\rangle = \delta_{12}\delta(\tau-\tau'). \tag{3.1.23}$$

Derivative of operator $\hat{f}_1(\tau)$ can be obtained from Heisenberg equation

$$\frac{\partial}{\partial\tau}\hat{f}_1(\tau) = \left[\hat{H}, \hat{f}_1(\tau)\right]. \tag{3.1.24}$$

For operators $\hat{c}_{i\sigma}(\tau)$ and $\hat{d}_{\sigma}(\tau)$ these equations have a following form:

$$\frac{\partial}{\partial\tau}\hat{d}_{\sigma}(\tau) = \epsilon_d\hat{d}_{\sigma} + \sum_i V_i\hat{c}_{i\sigma} + U\hat{n}_{\bar{\sigma}}\hat{d}_{\sigma}, \tag{3.1.25}$$

$$\frac{\partial}{\partial\tau}\hat{c}_{i\sigma}(\tau) = \sum_{ij\sigma} t_{ij}\hat{c}_{j\sigma} + V_i\hat{d}_{\sigma}.$$

Substituting these expressions in (3.1.23) we obtain GF equations for g^{σ}_{dd} and g^{σ}_{sd}:

$$\begin{aligned}
&\left(-\frac{\partial}{\partial\tau} - \epsilon_d + \mu\right) g^{\sigma}_{dd} - \sum_i V_i g^{\sigma}_{sd,i} \\
&\quad + U\left\langle T_{\tau}\hat{n}_{\bar{\sigma}}(\tau)\hat{d}_{\sigma}(\tau)\hat{d}^{+}_{\sigma}(\tau')\right\rangle = \delta(\tau-\tau'), \\
&\quad -\frac{\partial}{\partial\tau}g^{\sigma}_{sd,i} - \sum_{j\sigma} t_{ij}g^{\sigma}_{sd,j} - V_i g^{\sigma}_{dd} = 0.,
\end{aligned} \tag{3.1.26}$$

In these derivation we have taken into account that total number of electrons is fixed via replacing in (3.1.24) $\hat{H} \to \hat{H} - \mu\hat{N}$ where $\hat{N}$ is total electrons number operator and μ is chemical potential.

Coulomb term in (3.1.26) for GF g^{σ}_{dd} can be written formally as:

$$U\left\langle T_{\tau}\hat{n}_{\bar{\sigma}}(\tau)\hat{d}_{\sigma}(\tau)\hat{d}^{+}_{\sigma}(\tau')\right\rangle = \int \mathrm{d}\tau_1 \Sigma^{\sigma}_{dd}(\tau-\tau_1)g^{\sigma}_{dd}(\tau_1-\tau'), \tag{3.1.27}$$

where $\Sigma^{\sigma}_{dd}(\tau-\tau_1)$ is called self-energy for GF g^{σ}_{dd}. Then after Fourier transformation in variable $(\tau-\tau')$

$$g^{\sigma}_{dd}(\tau-\tau') = T\sum_n \mathrm{e}^{-\mathrm{i}\omega_n(\tau-\tau')}g^{\sigma}_{dd}(i\omega_n), \tag{3.1.28}$$

and also for all other functions in (3.1.26) we have:

$$\begin{aligned}
&(i\omega_n - \epsilon_d + \mu)g^{\sigma}_{dd}(i\omega_n) - \sum_i V_i g^{\sigma}_{sd,i}(i\omega_n) - \Sigma^{\sigma}_{dd}(i\omega_n)g^{\sigma}_{dd}(i\omega_n) = 1, \\
&(i\omega_n + \mu)g^{\sigma}_{sd,i}(i\omega_n) - \sum_{j\sigma} t_{ij}g^{\sigma}_{sd,j}(i\omega_n) - V_i g^{\sigma}_{dd}(i\omega_n) = 0.
\end{aligned} \tag{3.1.29}$$

Equations system (3.1.29) can be solved with Fourier transformation in site variables and resulting GF is (we skip in the following spin index σ):

$$g_{dd}(i\omega_n) = \left[i\omega_n - \epsilon_d + \mu - \sum_{\mathbf{k}} \frac{|V(\mathbf{k})|^2}{i\omega_n - \epsilon_{\mathbf{k}} + \mu} - \Sigma^{\sigma}_{dd}(i\omega_n)\right]^{-1}, \tag{3.1.30}$$

$$g_{sd}(\mathbf{k}, i\omega_n) = \frac{V(\mathbf{k})}{i\omega_n - \epsilon_{\mathbf{k}} + \mu} g_{dd}(i\omega_n). \tag{3.1.31}$$

Two last terms in the denominator in expression (3.1.30) are contributions to self-energy for GF $g_{dd}(i\omega_n)$ from hybridization and Coulomb interaction. Let

us define hybridization function $\Delta(i\omega_n)$ as:

$$\Delta(i\omega_n) = \sum_{\mathbf{k}} \frac{|V(\mathbf{k})|^2}{i\omega_n - \epsilon_{\mathbf{k}} + \mu} \tag{3.1.32}$$

and introduce noninteracting *GF* $\mathcal{G}_0$ (defined as *GF* (3.1.30) with Coulomb interaction switched off):

$$\mathcal{G}_0(i\omega_n) = (i\omega_n + \mu - \epsilon_d - \Delta(i\omega_n))^{-1}. \tag{3.1.33}$$

In *GF* for *d*-electrons hybridization is fully taken into account but Coulomb interaction part of self-energy $\Sigma^{\sigma}_{dd}(i\omega_n)$ is not explicitly determined and its calculation is a main difficulty in solving Anderson impurity model.

It is convenient to use path integral representation of *GF*. In Appendix A such representation is described for electronic *GF* with very general electron–electron interaction form. For Hubbard model with Hamiltonian (3.1.1) the *GF* in path integral form is:

$$g^{\sigma}(i_1\tau_1, i_2\tau_2) = -\frac{\int \mathcal{D}\left[c^+\right]\mathcal{D}\left[c\right]\mathrm{e}^{-S\left[c^+,c\right]}\left\{c_{i_1\sigma}(\tau_1)c^+_{i_2\sigma}(\tau_2)\right\}}{\int \mathcal{D}\left[c^+\right]\mathcal{D}\left[c\right]\mathrm{e}^{-S[c^+,c]}}, \tag{3.1.34}$$

where

$$S\left[c^+, c\right] = -\sum_{\sigma}\sum_{ii'}\int \mathrm{d}\tau \int \mathrm{d}\tau' c^+_{i\sigma}(\tau)\mathcal{G}_0(i\tau, i'\tau')^{-1}c_{i'\sigma}(\tau') \tag{3.1.35}$$

$$+\sum_{i} U \int \mathrm{d}\tau n_{i\uparrow}(\tau)n_{i\downarrow}(\tau)$$

is an action. In contrast to notations $\beta^*_{i\sigma}$ and $\beta_{i\sigma}$ for Grassmann variables used in Appendix A later we will use for Grassmann variables the same symbols as for Fermi operators but without cap above.

Let us use now general formulas (3.1.34) and (3.1.35) to calculate *GF* for single impurity Anderson model. In this model Coulomb interaction is taken into account only for *d*-electrons whereas *s*-electrons are considered to be noninteracting and kinetic energy term together with hybridization term have quadratic form in operators $\hat{c}_{i\sigma}$ and $\hat{d}_{\sigma}$. In order to apply general expression (3.1.34) to one-band Hubbard model transformation of variables $\hat{c}_{i\sigma} \rightarrow \left\{\hat{c}_{i\sigma}, \hat{d}_{\sigma}\right\}$ should be performed where index i marks all lattice sites except the central one with localized *d*-electrons. As Coulomb interaction in (3.1.35) is present only for *d*-electrons then integration over Grassmann variables can be done and in the result *GF* for *d*-electrons is expressed via integral:

$$g^{\sigma}(i_1\tau_1, i_2\tau_2) = -\frac{\int \mathcal{D}\left[d^+\right]\mathcal{D}\left[d\right]\mathrm{e}^{-S\left[d^+,d\right]}\left\{d_{\sigma}(\tau_1)d^+_{\sigma}(\tau_2)\right\}}{\int \mathcal{D}\left[d^+\right]\mathcal{D}\left[d\right]\mathrm{e}^{-S[d^+,d]}} \tag{3.1.36}$$

with action

$$S\left[d^{+},d\right]=-\sum_{\sigma}\int \mathrm{d}\tau\int \mathrm{d}\tau' d^{+}_{i\sigma}(\tau)\mathcal{G}_0(\tau-\tau')^{-1}d_{i'\sigma}(\tau')$$
$$+U\int \mathrm{d}\tau n_{\uparrow}(\tau)n_{\downarrow}(\tau). \tag{3.1.37}$$

Here $\mathcal{G}_0(\tau-\tau')$ is noninteracting d-electrons GF where hybridization is taken into account given by expression (3.1.33).

Formula (3.1.36) with (3.1.37) gives exact expression for d-electrons GF in Anderson model. It is the starting point for GF calculation in Quantum Monte Carlo method (QMC).

3.1.3 Basic *DMFT* Equations

QMC method allows to calculate d-electrons GF for Anderson model with parameters $U, V(\mathbf{k})$ or $U, \Delta(i\omega_n)$. In *DMFT* method Anderson model solution is an auxiliary problem for Hubbard model where hybridization function $\Delta(i\omega_n)$ is determined from self-consistency equations (3.1.9)–(3.1.15). Let us rewrite those equations in the following form:

$$G(i\omega_n)=\sum_{\mathbf{k}}\frac{1}{i\omega_n+\mu-\epsilon_{\mathbf{k}}-\Sigma(i\omega_n)}=G_{\mathrm{imp}}(i\omega_n), \tag{3.1.38}$$

$$\mathcal{G}_0^{-1}(i\omega_n)=G_{\mathrm{imp}}^{-1}(i\omega_n)+\Sigma(i\omega_n). \tag{3.1.39}$$

These equations allow to determine two unknown functions $\Sigma(i\omega_n)$ and $\mathcal{G}_0(i\omega_n)$, if GF for single impurity Anderson model $G_{\mathrm{imp}}(i\omega_n)$ was calculated by one of the numerical methods, for example *QMC*. The equations solution is found by self-consistency iterations. On every iteration the following steps are performed:

1. An input value for self-energy $\Sigma(i\omega_n)$ is set (it could be zero in the beginning for example) and lattice GF $G(i\omega_n)$ is calculated with (3.1.38).
2. Using Dyson equation (3.1.39) *bath* GF $\mathcal{G}_0(i\omega_n)$ is calculated.
3. Single impurity Anderson model with this $\mathcal{G}_0(i\omega_n)$ is solved and interacting impurity GF $G_{\mathrm{imp}}(i\omega_n)$ is found.
4. From Dyson equation (3.1.39) new approximation for self-energy $\Sigma(i\omega_n)=\mathcal{G}_0^{-1}(i\omega_n)-G_{\mathrm{imp}}^{-1}(i\omega_n)$ is obtained that is used to calculate new lattice GF in (3.1.38) that closes self-consistency iteration loop. Iterations continue till input values of self-energy $\Sigma(i\omega_n)$ for step 1 will become equal to output values from step 4 with some given accuracy.

Those steps define *DMFT* calculation scheme for Hubbard model. Electron *GF* is defined by expression (3.1.6) and local *GF* (diagonal matrix element is site representation) by expression (3.1.9). Instead of noninteracting spectrum $\epsilon_{\mathbf{k}}$ in (3.1.38) one can use corresponding density of states $\rho_0(\epsilon)$ to calculate lattice *GF* using integral over energy variable:

$$G(i\omega_n) = \int \mathrm{d}\epsilon \frac{\rho_0(\epsilon)}{i\omega_n + \mu - \epsilon - \Sigma(i\omega_n)}, \tag{3.1.40}$$

where

$$\rho_0(\epsilon) = \sum_{\mathbf{k}} \delta(\epsilon - \epsilon_{\mathbf{k}}). \tag{3.1.41}$$

As resulting *GF* is defined on Matsubara frequencies one needs to perform analytical continuation from discrete imaginary energies to real energy. Transformation $i\omega_n \to \omega + i\delta$ gives retarded *GF*:

$$G(i\omega_n \to \omega + i\delta) \equiv G(\omega) = \mathrm{Re}G(\omega) + i\mathrm{Im}G(\omega), \tag{3.1.42}$$

Imaginary part of this local *GF* defines density of states with Coulomb interaction taken into account:

$$\rho(\omega) = -\frac{1}{\pi}\mathrm{Im}G(\omega). \tag{3.1.43}$$

Analytical continuation procedure is described in the next section.

As it was mentioned earlier the basis of *DMFT* is an observation that in a space of large dimensions d (or a lattice with large number of nearest neighbors z) self-energy for electronic *GF* does not depend on wave vector and is local in-site representation:

$$\Sigma_{ij} = \delta_{ij}\Sigma_i. \tag{3.1.44}$$

When we use locality condition (3.1.44) for system with final space dimension ($d = 2, 3$) that means neglect of intersite (spatial) correlations. However realistic final space dimension is fully taken into account as one can see from (3.1.38) or (3.1.40). It is interesting to note that *DMFT* equations have two exact limits: $U \to 0$ and $U \to \infty$. For final value of Coulomb interaction parameter U *DMFT* method is in approximation with an error determined by the strength of neglected intersite correlations.

However *local* dynamical on-site correlations are fully taken into account with frequency dependent functions $\mathcal{G}_0(i\omega_n)$ and $\Sigma(i\omega_n)$. Noninteracting *bath GF* $\mathcal{G}_0(i\omega_n)$ (or corresponding hybridization function $\Delta(i\omega_n)$ in (3.1.33)) in effective single impurity model can be interpreted as a mean field that takes into account fluctuations on all other lattice sites. This mean-filed is dynamic because $\Delta(i\omega_n)$ depends on frequency $i\omega_n$ (or "time" τ). Conceptual problems of *DMFT* and its relations to mean-field approach in statistical physics are discussed in detail by Georges, Kotliar, Krauth, and Rozenberg review [8].

As it was discussed earlier *DMFT* is exact in limit $d \to \infty$. That means that spatial correlation neglected in *DMFT* could be taken into account as perturbation in $1/d$ parameter. Various realizations for such correction are described later.

3.1.4 *DMFT* Equations for Bethe Lattice

Let us consider a special case of semielliptical density of states in noninteracting spectrum:

$$\rho(\varepsilon) = \frac{1}{2\pi t^2}\sqrt{4t^2 - \varepsilon^2},\ |\varepsilon| \le 2t. \tag{3.1.45}$$

This model density of states corresponds to Bethe lattice in the limit of infinite number of nearest neighbors $z \to \infty$ [8]. *DMFT* equations are significantly simplified in this case while physical picture described by their solution is still very general and does not essentially depends on the noninteracting density of states specific form.

Let us rewrite interacting *GF* (3.1.40) in the following form:

$$G_{\mathrm{loc}}(\zeta) = \int \mathrm{d}\varepsilon \frac{\rho_0(\varepsilon)}{\zeta(i\omega_n) - \varepsilon}, \tag{3.1.46}$$

where

$$\zeta(i\omega_n) = i\omega_n + \mu - \Sigma(i\omega_n). \tag{3.1.47}$$

Integral (3.1.46) is known as Hilbert transformation for function $\rho_0(\varepsilon)$. One can define inverse Hilbert transformation for ζ as a function of G_{loc}. Let us note it as $\zeta = R[G]$. With density of states defined by (3.1.45) integration in (3.1.46) can be done analytically and the resulting *GF* is [8]:

$$G_{\mathrm{loc}}(\zeta) = \frac{1}{2t^2}\left(\zeta - s\sqrt{\zeta^2 - 4t^2}\right), \tag{3.1.48}$$

where $s = \mathrm{sgn}[\mathrm{Im}\zeta]$. This equation can be solved for variable ζ as a function of G_{loc}:

$$\zeta(i\omega_n) = R[G] = G^{-1}_{\mathrm{loc}}(i\omega_n) + t^2 G_{\mathrm{loc}}(i\omega_n). \tag{3.1.49}$$

Using this equation together with Dyson equation relating self-energy $\Sigma(i\omega_n)$ and effective *bath GF* $\mathcal{G}_0$ with local *GF* G_{loc}:

$$\Sigma(i\omega_n) = \mathcal{G}_0^{-1}(i\omega_n) - G^{-1}_{\mathrm{loc}}(i\omega_n), \tag{3.1.50}$$

we obtain a simple equation between $\mathcal{G}_0$ and $G_{\mathrm{loc}}(i\omega_n)$:

$$\mathcal{G}_0^{-1}(i\omega_n) = i\omega_n + \mu - t^2 G_{\mathrm{loc}}(i\omega_n). \tag{3.1.51}$$

Thus in this special case *DMFT* equations system (3.1.9)–(3.1.15) reduces to a single equation (3.1.51) that is very convenient for qualitative analysis of *DMFT* [8].

3.1.5 Methods for Solution of Single Impurity Anderson Model

In *DMFT* method electron on a lattice problem is reduced to equivalent single impurity problem solution. In a case of nondegenerate Hubbard model that

is Single Impurity Anderson Model (*SIAM*). This model is throughly investigated by various methods and its physics is well understood. When *SIAM* is considered as a step in *DMFT* calculation scheme the main issue is efficiency and accuracy of the method used for *SIAM* solution. In this subsection we will list main methods used to solve *SIAM* and the most important of them will be presented in the next sections and chapters.

Quantum Monte Carlo Method

The main idea of *QMC* is to write Anderson model electronic *GF* as an integral over fluctuating fields. For that thermodynamic time interval $0 \leq \tau \leq \beta$ is divided on L segments. This discretization allows to approximate infinite dimensions path integral by finite dimensions integral. There are several versions of *QMC* method and the most widely used is Hirsh-Fye method (see Sect. 3.2.1) using discrete Hubbard–Stratonovich transformation for linearization of Coulomb interaction term $U\hat{n}_{\uparrow}\hat{n}_{\downarrow}$. In the result interacting electrons problem is converted to the problem of noninteracting particles moving in fluctuating in time field defined by a set of pseudo-Ising spins for every of L segments in τ interval. A *GF* is determined as a sum over all possible pseudo-Ising spins configurations. This approximation will be exact if a number of discrete segments $L \to \infty$. As the number of configurations is 2^L and grows exponentially with L a direct summation over all configurations is not possible and is replaced by stochastic Markov process for Monte Carlo method of many dimensional integral evaluation.

Hirsh-Fye version of *QMC* gives practically realized and computer resources effective calculation scheme to solve *SIAM* problem. However it can be used only for high-enough temperature values. With decreasing temperature a length of thermodynamic time interval $0 \leq \tau \leq \beta = 1/T$ increases together with a number of segments L. That results in exponential increase in computation expenses that make low-temperature area practically unaccessible for this method.

There are other versions of *QMC* algorithm. One of them is so called *Projective QMC* method (*PQMC*) (see Sect. 3.2.4). In this method a limit of parameter $\beta = 1/T \to \infty (T \to 0)$ is taken analytically that allows to investigate ground state of the system.

The most promising now is *Continuous Time Quantum Monte Carlo* ($CT - QMC$) method (see Sect. 3.2.5). In this method *GF* is used in the form of functional integral with expansion series over Coulomb interaction parameter U or over hybridization parameter V. The last case is the most efficient one. Local Coulomb interaction U together with intrasite exchange J are included in zero-th order and the method works for arbitrary strong interaction. Instead of regular discretization of thermodynamic time interval $0 \leq \tau \leq \beta$ a set of segments $\{\tau_i, \tau_j\}$ with stochastic choice of τ_i, τ_j is used that continuously fill the interval (hence the name of the method). An absence of the fixed set of L segments allows to treat the problem for arbitrary large β value and so to investigate low-temperatures region.

In $CT-QMC$ GF is expressed as infinite series over hybridization V with all possible diagrams contributions. For a certain k-th order term a sum over all diagrams is calculated as $k \times k$ determinant containing GFs for time segments $G(\tau_i - \tau_j)$. Markov process corresponds to adding one segment thus increasing order $k \to k+1$ or removing a segment $(k \to k-1)$. It is interesting that the process converges for any value of parameters U and V and resulting GF is calculated from general series expansion without any approximations.

All the above mentioned versions of QMC method are described later in Sect. 3.2.

Numerical Renormalization Group

Numerical renormalization group (NRG) method was developed by Willson [116] and is actively used in $DMFT$ study of strongly correlated systems. The method is based on nonlinear (logarithmic) discretization of real energy ϵ dependence for hybridization function $\Delta(\epsilon)$ in such a way that energy mesh is very dense near the Fermi level but becomes coarse far from it. This discrete model is mapped on a semi-infinite chain form for a set of noninteracting electron states with impurity coupling only to a single fermionic degree of freedom $\hat{c}^+_{0\sigma}$, with a hybridization V:

$$\hat{H} = \sum_{\sigma,n=0}^{\infty} t_n(\hat{c}^+_{n\sigma}\hat{c}_{n+1\sigma} + \hat{c}^+_{n+1\sigma}\hat{c}_{n\sigma}) + \sum_{\sigma}\left[V\hat{c}^+_{0\sigma}\hat{d}_\sigma + V^*\hat{d}^+_\sigma\hat{c}_{0\sigma}\right] + \epsilon_d\sum_{\sigma}\hat{d}^+_\sigma\hat{d}_\sigma + U\hat{n}_\uparrow\hat{n}_\downarrow. \tag{3.1.52}$$

One starts with the solution of the isolated impurity, i.e., with the knowledge of all eigenstates, eigenenergies, and matrix elements. The first step of the renormalization-group transformation is to add the first conduction electron site, set up the Hamiltonian matrices for the enlarged Hilbert space, and obtain the new eigenstates, eigenenergies, and matrix elements by diagonalizing these matrices. This procedure is then iterated. An obvious problem occurs only after a few steps of the iteration. The Hilbert space grows as 4^N (with N the size of the cluster), which makes it impossible to keep all the states in the calculation. Wilson, therefore, devised a very simple truncation procedure in which only those states with the lowest energies (typically a few hundred) are kept.

In the result the fine details of the quasiparticle peak near the the Fermi level are well described while preserving Hubbard bands in the picture too. NRG method is widely used in $DMFT$ studies especially when low-temperature properties are important [117]. Unfortunately, this method works satisfactorily only for nondegenerate localized states. For degenerate case Hilbert space involved in calculations grows exponentially and NRG becomes unpractical for degeneracy larger than 2. In a chapter 5 we will describe applications of NRG method.

Exact Diagonalization Method

Exact diagonalization method (*ED*) is similar to *NRG* because in both cases continuous energy dependence hybridization function $\Delta(\epsilon)$ is replaced by a set of discrete energy states. The difference is that logarithmic energy mesh and semi-infinite chain representation are not used. In the result finite size Hamiltonian problem is solved by *exact diagonalization*. In contrast to *NRG* method it is not possible to describe fine details of quasiparticle peak near the Fermi level but integral properties of the solution could be sometimes satisfactorily described. The disadvantage of the method is small number of discrete states in hybridization function approximation that can be practically treated. The *ED* method description could be found in [8, 118, 119].

Iterative Perturbation Theory

Iterative Perturbation Theory (*IPT*) method formally can be used only for weakly correlated systems where $U < W/2$ because it is based on perturbation theory in Coulomb interaction parameter U. However, it was found that *IPT* is valid for much broader parameters range. For Anderson model second-order perturbation in U term for self-energy has a form [7, 120]:

$$\Sigma(\tau) = -U^2 \mathcal{G}_0^3(\tau), \tag{3.1.53}$$

where $\mathcal{G}_0(\tau)$ is effective impurity *bath GF* (3.1.39) after Fourier transformation (3.1.28). Using spectral representation (3.1.46) for $\mathcal{G}_0$ expression (3.1.53) can give self-energy as a function of real energy ω:

$$\begin{aligned}\Sigma(\omega) = U^2 \int_{-\infty}^{0} \mathrm{d}\varepsilon_1 \int_{0}^{\infty} \mathrm{d}\varepsilon_2 \int_{0}^{\infty} \mathrm{d}\varepsilon_3 \frac{\rho_0(\varepsilon_1)\rho_0(\varepsilon_2)\rho_0(\varepsilon_3)}{\omega + \varepsilon_1 - \varepsilon_2 - \varepsilon_3 - i\eta} \\ + U^2 \int_{0}^{\infty} \mathrm{d}\varepsilon_1 \int_{-\infty}^{0} \mathrm{d}\varepsilon_2 \int_{-\infty}^{0} \mathrm{d}\varepsilon_3 \frac{\rho_0(\varepsilon_1)\rho_0(\varepsilon_2)\rho_0(\varepsilon_3)}{\omega + \varepsilon_1 - \varepsilon_2 - \varepsilon_3 - i\eta},\end{aligned} \tag{3.1.54}$$

where η is small imaginary part. In this integral $\rho_0(\omega) = -\frac{1}{\pi}\mathrm{Im}\mathcal{G}_0(\omega)$.

For special case of half filling expression (3.1.54) has correct atomic limit $W/U \to 0$:

$$\begin{aligned}\mathcal{G}_0(\omega) &= 1/\omega, \\ G(\omega) &= \frac{1}{2}\left(\frac{1}{\omega + U/2} + \frac{1}{\omega - U/2}\right) = \frac{1}{\omega - \Sigma(\omega)}, \\ \Sigma(\omega) &= \frac{(U/2)^2}{\omega}.\end{aligned} \tag{3.1.55}$$

For weak coupling limit $U \to 0$ expression (3.1.53) is correct because it is a perturbation theory in U/W. With two correct limits (3.1.53) can be regarded as interpolation formula with reasonable results for intermediate values of U/W.

For deviations from half filing an extension of *IPT* was proposed [121, 122]. It becomes exact in various limits: (a) the atomic limit, (b) in an expansion in powers of U up to second order in U, (c) at very high frequencies, and (d) at zero frequency. It was shown that *generalized IPT* can give good results for various range of model parameters [121]. It is very efficient in computer time expenses method without stochastic errors unavoidable in *QMC* with low-temperature region easily accessible. However, *IPT* is not reliable enough because it was not rigorously derived but proposed as a simple interpolation formula.

Another method based on perturbation theory is Noncrossing Approximation (*NCA*) [123] where atomic limit is used with first terms in perturbation expansion in hybridization. Closely related to *NCA* is Self-consistent Born Approximation (*SCBA*) method [124]. We can mention also the method for solving *SIAM* problem based on decoupling of equations of motion [125, 126].

The existence of many different approaches to *SIAM* as a crucial step in *DMFT* calculation scheme shows that there is no universal solution to this problem. Every of the earlier mentioned methods (so called "impurity solvers") has its advantages and shortcomings. Later, we will discuss the most popular of them.

3.2 Quantum Monte Carlo Method as Single Impurity Anderson Model Solver

3.2.1 Hirsch–Fye Algorithm

Partition function Z representation in a form of functional integral over Grassmann variables (see Appendix A) is a convenient starting point to develop Quantum Monte Carlo method for models where electron–electron interaction is local such as Hubbard and Anderson models. Coulomb interaction in those models is described by a term:

$$H_{\text{int}} = U n_{\uparrow} n_{\downarrow}. \tag{3.2.56}$$

Product $n_{\uparrow} n_{\downarrow}$ can be rewritten as a sum of quadratic and linear terms:

$$n_{\uparrow} n_{\downarrow} = -\frac{1}{2}(n_{\uparrow} - n_{\downarrow})^2 + \frac{1}{2}(n_{\uparrow} + n_{\downarrow}). \tag{3.2.57}$$

Hubbard–Stratonovich method allows to replace quadratic term in Hamiltonian for partition function calculation on linear term via integral over auxiliary variable. Hirsch proposed [127] discrete analog of Hubbard–Stratonovich method based on identity:

$$\mathrm{e}^{\frac{x}{2}(n_{\uparrow} - n_{\downarrow})^2} = \frac{1}{2} \sum_{s=\pm 1} \mathrm{e}^{\lambda s (n_{\uparrow} - n_{\downarrow})}, \tag{3.2.58}$$

where parameter λ is defined by equation

$$\cosh\lambda = \mathrm{e}^{\frac{x}{2}}. \tag{3.2.59}$$

The sum over $s = \pm 1$ in expression (3.2.58) is a discrete analog of auxiliary variable integration in original Hubbard–Stratonovich method.

Using identity (3.2.58) it is possible to present partition function Z for Hamiltonian $H_0 + H_{\mathrm{int}}$ as a sum over set of discrete variables $\{s_l\}$ where l is time segment index (interval $0 \le \tau \le \beta = 1/T$ is divided on L segments). Numerical calculation of this sum is an essence of Hirsch–Fye *QMC* algorithm [128, 129]. Such representation of Z is closely connected with functional integral over Grassmann variables described in Appendix A and below we give derivation of basic formulas of Hirsch–Fye *QMC* method (see also [8, 10, 130, 131]). Analogous to (A.23) partition function Z is:

$$Z = \mathrm{Tr}\mathrm{e}^{-\beta\hat{H}} = \mathrm{Tr}\prod_{l=1}^{L}\mathrm{e}^{-\Delta\tau(\hat{H}_0+\hat{H}_1)}, \tag{3.2.60}$$

where $\Delta\tau = \beta/L$ is a length of time segment and operator terms of product in right side (3.2.60) correspond to l-th segment $\tau_l = l\Delta\tau$. Assuming that $\Delta\tau$ is small (that means L is sufficiently large) (3.2.60) can be approximated as:

$$Z = \mathrm{Tr}\prod_{l=1}^{L}\mathrm{e}^{-\Delta\tau\hat{H}_0}\mathrm{e}^{-\Delta\tau\hat{H}_1}, \tag{3.2.61}$$

[here so called Trotter decomposition $\mathrm{e}^{-\Delta\tau(\hat{H}_0+\hat{H}_1)} \approx \mathrm{e}^{-\Delta\tau\hat{H}_0}\mathrm{e}^{-\Delta\tau\hat{H}_1}$ was used with an error of this approximation of the order of $(\Delta\tau)^2[\hat{H}_0, \hat{H}_1]$ as it was shown in Appendix A (see (A.7))].

Factor $\mathrm{e}^{-\Delta\tau\hat{H}_1}$ can be transformed in a sum according to Hirsch identity (3.2.58) and then (3.2.61) is:

$$Z = \frac{1}{2^L}\sum_{s_1,\ldots,s_L=\pm 1} Z_{s_1,\ldots,s_L}, \tag{3.2.62}$$

where

$$Z_{s_1,\ldots,s_L} = \prod_{\sigma=\uparrow\downarrow}\mathrm{Tr}\{\mathrm{e}^{-\Delta\tau H_0}\mathrm{e}^{V^\sigma(s_1)}\mathrm{e}^{-\Delta\tau H_0}\mathrm{e}^{V^\sigma(s_2)}\cdots\mathrm{e}^{-\Delta\tau H_0}\mathrm{e}^{V^\sigma(s_L)}\}. \tag{3.2.63}$$

In the last expression $V^\sigma(s_l)$ is diagonal matrix in lattice site space of the size $N \times N$ with element $\mathrm{e}^{\lambda\sigma s_l}$ for impurity site and 1 for all other sites:

$$\mathrm{e}^{V^\sigma(s_l)} = \begin{pmatrix} \mathrm{e}^{\sigma s_l\lambda} & 0 & 0 & \cdots \\ 0 & 1 & 0 & \cdots \\ 0 & 0 & 1 & \cdots \\ \cdots & \cdots & \cdots & \cdots \end{pmatrix}.$$

Matrix trace in (3.2.63) is a product of exponents for every time interval $\tau_l = l\Delta\tau$ and can be calculated as in Appendix A. That gives result expressed via functional integral over Grassmann variables:

$$Z_{s_1,\ldots,s_L} = \int \mathcal{D}[c^+]\mathcal{D}[c]\exp\{-(\Delta\tau)^2 \sum_{ll'ii'\sigma} c_i^+(\tau_l) g^{-1\sigma}_{s_1,\ldots,s_L}(\tau_l,\tau_{l'}) c_{i'}(\tau_{l'})\}, \tag{3.2.64}$$

where g^{-1} is a matrix with elements

$$B(s_l) = \mathrm{e}^{-\Delta\tau h}\mathrm{e}^{V^\sigma(s_l)}, \tag{3.2.65}$$

where h and $V^\sigma(s_l)$ are themselves matrix in lattice site index space. Matrix h defines noninteracting Hamiltonian $\hat{H}_0$:

$$\hat{H}_0 = \sum_{ij\sigma} c^+_{i\sigma} h_{ij} c_{i\sigma}. \tag{3.2.66}$$

In time variables $\tau_l, \tau_{l'}$ indexes $L \times L$ matrix $g^{-1}(\tau_l, \tau_{l'})$ has a form:

$$g^{-1} = \begin{pmatrix} 1 & \cdots & 0 & B(s_L) \\ -B(s_1) & \cdots & \cdots & 0 \\ \cdots & \cdots & 1 & 0 \\ 0 & \cdots & -B(s_{L-1}) & 1 \end{pmatrix}. \tag{3.2.67}$$

Matrix elements structure corresponds to expression for Fermi system partition function derived in Appendix A (A.52). Appearance of the element $B(s_L)$ in the end of first line (3.2.67) with the opposite sign is due to antiperiodicity of Grassmann variables (A.56).

Please note that matrix g^{-1} has size $NL \times NL$ and every element in (3.2.67) is a matrix size $N \times N$ in lattice site space including diagonal matrix elements of (3.2.67) equal to 1.

Grassmann variables integration of Gauss integral (3.2.64) gives (compare with (A.61)):

$$Z_{s_1,\ldots,s_L} = \mathrm{det} g^{-1\sigma}_{s_1,\ldots,s_L} \cdot \mathrm{det} g^{-1\bar{\sigma}}_{s_1,\ldots,s_L}. \tag{3.2.68}$$

Then final expression for partition function is:

$$Z = \frac{1}{2^L} \sum_{s_1,\ldots,s_L} [\mathrm{det} g^{-1\sigma}_{s_1,\ldots,s_L} \cdot \mathrm{det} g^{-1\bar{\sigma}}_{s_1,\ldots,s_L}]. \tag{3.2.69}$$

Matrix g defined as inverse to matrix (3.2.67) corresponds to fermionic GF in fluctuating field of quasi-Ising spins $s_1, \ldots, s_L$. Analogous to expression (3.2.63) for $Z_{s_1,\ldots,s_L}$ this GF is:

$$g_{s_1,\ldots,s_L}(\tau_l,\tau_{l'}) = \frac{1}{Z_{s_1,\ldots,s_L}} \mathrm{Tr}\{[-c_{i\sigma}(\tau_l)c^+_{i\sigma}(\tau_{l'})] \prod_{\sigma'=\uparrow\downarrow} \mathrm{e}^{-\Delta\tau H_0}\mathrm{e}^{V^{\sigma'}(s_1)}\mathrm{e}^{-\Delta\tau H_0}\mathrm{e}^{V^{\sigma'}(s_2)}\cdots\mathrm{e}^{-\Delta\tau H_0}\mathrm{e}^{V^{\sigma'}(s_L)}\}, \tag{3.2.70}$$

To prove that one should calculate matrix trace for two conditions $\tau_l > \tau_{l'}$ and $\tau_l < \tau_{l'}$ that gives matrix equation (3.2.67). Detailed derivation can be found in [130].

Electronic *GF* defined by standard expression

$$G^{\sigma}_{ii'}(\tau_l, \tau_{l'}) = -\langle T_\tau \hat{c}_{i\sigma}(\tau_l)\hat{c}^{+}_{i\sigma}(\tau_{l'})\rangle, \tag{3.2.71}$$

is obtained by summation of fermionic *GF* $g_{s_1,\ldots,s_L}(\tau_l, \tau_{l'})$ over all Ising spin configuration:

$$G^{\sigma}(\tau_l, \tau_{l'}) = \frac{\sum_{s_1,\ldots,s_L} Z_{s_1,\ldots,s_L} g^{\sigma}_{s_1,\ldots,s_L}(\tau_l, \tau_{l'})}{\sum_{s_1,\ldots,s_L} Z_{s_1,\ldots,s_L}}, \tag{3.2.72}$$

(lattice site indexes are omitted). Taking into account expression (3.2.68) for $Z_{s_1,\ldots,s_L}$ finally we have:

$$G^{\sigma}(\tau_l, \tau_{l'}) = \frac{\sum_{s_1,\ldots,s_L} [\det g^{-1\uparrow}_{s_1,\ldots,s_L} \cdot \det g^{-1\downarrow}_{s_1,\ldots,s_L}] g^{\sigma}_{s_1,\ldots,s_L}(\tau_l, \tau_{l'})}{\sum_{s_1,\ldots,s_L} [\det g^{-1\uparrow}_{s_1,\ldots,s_L} \cdot \det g^{-1\downarrow}_{s_1,\ldots,s_L}]}. \tag{3.2.73}$$

Noninteracting *GF* can be obtained from (3.2.73) with all spins $s_1, \ldots, s_L$ set to zero. In Hirsch-Hubbard–Stratonovich identity (3.2.58) $s = 0$ is equivalent to $U = 0$ case.

So due to discrete Hirsch–Hubbard–Stratonovich transformation we replace the problem of single impurity Anderson model with Coulomb interaction between on-site electrons to the noninteracting electrons problem in the field of time $\tau_l = l\Delta\tau$ dependent Ising spins. The price for this is summation over all Ising spins configurations. For $L \to \infty$ expressions (3.2.69) and (3.2.73) for partition function are exact but in practical calculations the accuracy is determined by final L value and the completeness of summation over Ising spins configurations.

Inversion of g^{-1} matrix of large size for every set $s_1, \ldots, s_L$ of Ising spins is a very expensive in computer resources task. Hirsch and Fye proposed very effective procedure where g matrix is calculated once for a certain $s_1, \ldots, s_L$ set and then g is recalculated for a set where only one Ising spin component is changed. Two *GF*s for the sets differing only by one "spin flip" are connected by a simple equation which we will derive now.

Let us define diagonal matrix

$$\mathrm{e}^{-V} = \begin{pmatrix} \mathrm{e}^{-V(s_1)} & 0 & 0 & \cdots \\ 0 & \mathrm{e}^{-V(s_2)} & 0 & \cdots \\ 0 & 0 & \mathrm{e}^{-V(s_3)} & \cdots \\ \cdots & \cdots & \cdots & \mathrm{e}^{-V(s_L)} \end{pmatrix} \tag{3.2.74}$$

and write a product of two matrices

$$g^{-1}\mathrm{e}^{-V} = \begin{pmatrix} \mathrm{e}^{-V(s_1)} & 0 & 0 & \cdots \\ -\mathrm{e}^{-\Delta\tau h} & \mathrm{e}^{-V(s_2)} & 0 & \cdots \\ 0 & -\mathrm{e}^{-\Delta\tau h} & \mathrm{e}^{-V(s_3)} & \cdots \\ \cdots & \cdots & \cdots & \cdots \\ \cdots & \cdots & -\mathrm{e}^{-\Delta\tau h} & \mathrm{e}^{-V(s_L)} \end{pmatrix}. \tag{3.2.75}$$

Let us introduce also auxiliary matrix $\tilde{g} = e^V g$. Using relation $\tilde{g} = (g^{-1}\mathrm{e}^{-V})^{-1}$ and matrix form (3.2.75) one can see that two matrices $\tilde{g}(V)$ and $\tilde{g}(V')$ for two sets $V(s_1), \ldots, V(s_L)$ and $V(s'_1), \ldots, V(s'_L)$ noted as V and V' are connected with each other by the following relation

$$\tilde{g}^{-1}(V') = \tilde{g}^{-1}(V) + \mathrm{e}^{-V'} - \mathrm{e}^{-V}. \tag{3.2.76}$$

From this immediately follows expression for fermionic GF:

$$g' = g + (g-1)(\mathrm{e}^{V'-V} - 1)g', \tag{3.2.77}$$

(we have simplified notations $g = g(V), g' = g(V')$). That is the most important for Hirsch–Fye algorithm relation allowing to calculate GF for a set V' if it is known for a set V:

$$g' = A^{-1}g, \ A = 1 + (1-g)(\mathrm{e}^{V'-V} - 1). \tag{3.2.78}$$

In a special case of a single-spin flip when V and V' differ only for one spin p with $s_p = -s_p$ matrix A has a s form [10,130]:

$$A = \begin{pmatrix} 1 & 0 & \cdots & A_{1p} & 0 & \cdots \\ 0 & 1 & \cdots & A_{2p} & 0 & \cdots \\ & & & \vdots & & \\ 0 & \ldots & & A_{pp} & 0 & \cdots \\ & & & \vdots & \ddots & \\ \cdots\cdots & & & \cdots & 1 & 0 \\ 0 & \ldots & & A_{Lp} & \cdots\ 0 & 1 \end{pmatrix}. \tag{3.2.79}$$

In this case

$$\det A = A_{pp} = 1 + (1-g_{pp})a, \ a = (\mathrm{e}^{\lambda\sigma(s'_p - s_p)} - 1). \tag{3.2.80}$$

It is easy to prove that $(A)^{-1}_{lk} = 0$ for $k \neq l$ and from (3.2.78) one can find explicit expression for matrix elements g' resulting from spin flip $s_p = -s_p$:

$$g'_{l_1 l_2} = g_{l_1 l_2} + \frac{a}{1 + a(1-g_{pp})}(g_{l_1 p} - \delta_{l_1 p})g_{p l_2}. \tag{3.2.81}$$

Corresponding expression for determinants of matrices g' and g:

$$\frac{\det(g')^{-1}}{\det g^{-1}} = \frac{\det g}{\det g'} = \det tA. \tag{3.2.82}$$

Hirsch–Fye algorithm starts from calculation of GF g for some initial spin configuration s_l (from noninteracting GF $g_0 = \mathcal{G}$ using (3.2.78) with $V = 0$) and then step by step recalculating it for spin configurations differing from the previous one by a single-spin flip $s_p = -s_p$ via (3.2.78). Summation of these GF with corresponding statistical weights (3.2.69) and (3.2.73) gives partition function and fermionic Green function.

Matrix g^{-1} (3.2.67) has size $NL \times NL$ but its inversion reduces to inversion of $L \times L$ size matrix because we need only one element of matrix g in site space corresponding to impurity site. Let us denote this element as $G(\tau)$. In this way we define a function $G(\tau) \equiv g_{00}(\tau_l - \tau_{l'})$, where $\tau = \tau_l - \tau_{l'}$ is a segment of time interval $-\beta \le \tau_l - \tau_{l'} \le \beta$. Then relations (3.2.74)–(3.2.81) can be rewritten by replacing $g \to G$ with $V(s_l) = \lambda \sigma s_l$ (previously $V(s_l)$ contained a site index factor $\delta_{i0}\delta_{j0}$ that for our case $i = j = 0$ is equal to 1).

In practical QMC calculations L value should be chosen large enough so that discretization interval ("time slice") $\Delta\tau = \beta/L$ was sufficiently small (usually $L \approx 10^2$). Such size matrix inversion is not a serious problem for modern computers but the total number of all possible spin configurations $\{s_l\} = s_1, \ldots, s_L$ for which one should calculate $G(\tau)$ is equal to 2^L ($\approx 2^{100} \approx 10^{30}$). Such huge number of configurations cannot be evaluated exactly and some approximated evaluation procedure is needed here.

The same problem appears in many-dimensional integrals calculation that can be solved by statistical Monte Carlo method. In this method an expression under integral should be presented as a product of two functions $F(\mathbf{x})$ and $P(\mathbf{x})$ with a condition that one of them ($P(\mathbf{x})$) is positive definite. Then the integral could be interpreted as an average value of $F(\mathbf{x})$ with statistical weight $P(\mathbf{x})$:

$$\int \mathrm{d}\mathbf{x} F(\mathbf{x}) P(\mathbf{x}) = \langle F \rangle \approx \frac{\sum_{\mathbf{x}_i} F(\mathbf{x}_i) P(\mathbf{x}_i)}{\sum_{\mathbf{x}_i} P(\mathbf{x}_i)} \tag{3.2.83}$$

(it is supposed that $\int \mathrm{d}\mathbf{x} P(\mathbf{x}) = 1$). The sum in (3.2.83) is calculated by stochastic Monte Carlo sampling. Stochastically, generated points in many-dimensional space $\mathbf{x}_i$ are accepted to be included in summation with probability proportional to $P(\mathbf{x}_i)$ and $\langle F \rangle = \sum_{\mathbf{x}_i} F(\mathbf{x}_i)/N_i$. The efficient algorithm of points generation is so called Markov process where point $\mathbf{x}_{i+1}$ is obtained from the point $\mathbf{x}_i$ by small stochastic deviation in many-dimensional space and is accepted with probability proportional to $P(\mathbf{x}_i)$. In such a way Markov chain of points always runs in an area of space where statistical weight $P(\mathbf{x})$ has largest value.

In Hirsch–Fye algorithm analog of integral (3.2.83) is expression (3.2.72). In a Monte Carlo simulation, Ising spin configurations are generated with a probability proportional to $[\det g^{-1\uparrow}_{s_1,\ldots,s_L} \cdot \det g^{-1\downarrow}_{s_1,\ldots,s_L}]$ and the physical Greens

function (3.2.72) is then given as an average of $g^{\sigma}_{s_1,\ldots,s_L}(\tau_l,\tau_{l'})$ with this measure. The Markov process is realized by going from configuration s to configuration s' by a single spin flip $s_p = -s_p$ for all p. Probability of acceptance $P_{\{s\}\to\{s'\}}$ for new configuration $\{s'\}$ obtained from $\{s\}$ is calculated according to Metropolis formula using determinant ratio from (3.2.82):

$$P_{\{s\}\to\{s'\}} = \begin{cases} 1 & \text{if } \frac{\det(g')^{-1}}{\det g^{-1}} > 1, \\ \frac{\det(g')^{-1}}{\det g^{-1}} & \text{in other case.} \end{cases} \tag{3.2.84}$$

Markov chain is given by every accepted configuration:

$$\{s\} \to \{s'\} \to \{s''\} \to \{s'''\} \to \ldots,$$

and summation in (3.2.72) is done only for those accepted configurations. Practically, instead of summation with weights $Z_{s_1,\ldots,s_L}$ an averaging of $g^{\sigma}_{s_1,\ldots,s_L}(\tau_l,\tau_{l'})$ over all accepted configuration is performed because probability of acceptance is proportional to $Z_{s_1,\ldots,s_L}$. It is important to note that this algorithm is a very efficient one. Calculation expenses needed to estimate probability of acceptance (3.2.84) are defined by evaluation of determinant ratio from (3.2.82) calculated by a simple formula (3.2.80) that does not scales with a number of time slices L. *GF* for accepted configuration is updated using (3.2.81) that scales as L^2 instead of L^3 as it would be for completely new configuration where formula (3.2.78) should be used.

Calculation scheme is the following. Random number generator gives initial configuration $\{s_l\}$. Then for every $l = 1,\ldots,L$ spin flip is attempted that is accepted or not with probability (3.2.84). This consequence of attempted spin flips is called a "sweep." After every sweep new configuration is obtained that is considered as a starting point for the next sweep. A number of sweeps is usually $\approx 10^6$ that is practically manageable comparing with total configuration number (for $L = 100$ it is $2^L \approx 10^{30}$). However, the pay for this is stochastic error appearing in *QMC* calculations.

QMC method to solve single impurity Anderson model requires an input noninteracting *bath GF* in imaginary time domain $g_0 = \mathcal{G}_0(\tau)$ and results in interacting impurity *GF* also as a function of time $G_{\mathrm{imp}}(\tau)$. *DMFT* calculation scheme (Sect. 3.1.3) assumes that both *GF*s are frequency dependent because *bath GF* $\mathcal{G}_0(i\omega_n)$ is calculated in Dyson equation (3.1.39) and from the same Dyson equation new approximation for self-energy $\Sigma(i\omega_n) = \mathcal{G}_0^{-1}(i\omega_n) - G^{-1}_{\mathrm{imp}}(i\omega_n)$ is obtained for lattice *GF* $G(i\omega_n)$ calculation in (3.1.38).

That means that Fourier transformation from frequency to time domain for *GF* should be done in *DMFT* calculation scheme before *QMC* step

$$G(\tau) = T\sum_{i\omega_n} \mathrm{e}^{-\mathrm{i}\omega_n\tau} G(i\omega_n), \tag{3.2.85}$$

and inverse one from time to frequency after *QMC*

$$G(i\omega_n) = \int_0^{\beta} \mathrm{e}^{\mathrm{i}\omega_n\tau} G(\tau). \tag{3.2.86}$$

3.2.2 Maximum Entropy Method for Spectral Function Calculation

Hirsch–Fye calculation procedure results in Matsubara *GF* $G(\tau)$ for discrete imaginary time points $\tau_l - \tau_{l'}$. Next necessary step is to calculate density of states on real energies $A(\omega)$ that is expressed via retarded *GF* $G^R(\omega)$:

$$A(\omega) = -\frac{1}{\pi}\mathrm{Im}G^R(\omega), \tag{3.2.87}$$

where

$$G^R(\omega) = \int \frac{\mathrm{d}t}{2\pi}\mathrm{e}^{\mathrm{i}\omega t}G^R(t) \tag{3.2.88}$$

is Fourier transformation of $G^R(t)$. Retarded *GF* is defined by expression

$$G^R(t) = -i\theta(t)\langle[c_{j\sigma}(t), c^+_{j\sigma}(0)]_+\rangle \tag{3.2.89}$$

(we consider homogeneous paramagnetic phase where *GF* does not depend on spin and site indexes).

Dynamical mean-field theory described in previous section uses Matsubara *GF* defined by:

$$G(\tau) = -\langle T_\tau \hat{c}_{j\sigma}(\tau)\hat{c}^+_{j\sigma}(0)\rangle. \tag{3.2.90}$$

Spectral representation for this function is given [115] by the equation:

$$G(i\omega_n) = \int_{-\infty}^{\infty} \mathrm{d}\omega' \frac{A(\omega')}{i\omega_n - \omega'}, \tag{3.2.91}$$

that connects Matsubara and retarded *GF*s. In (3.2.91) $G(i\omega_n)$ is Fourier component of function $G(\tau)$ in thermodynamic time τ space with periodicity β:

$$G(i\omega_n) = \int_0^\beta \mathrm{d}\tau \mathrm{e}^{-\mathrm{i}\omega_n\tau}G(\tau). \tag{3.2.92}$$

Inverse Fourier transformation is

$$G(\tau) = \frac{1}{\beta}\sum_n \mathrm{e}^{\mathrm{i}\omega_n\tau}G(i\omega_n). \tag{3.2.93}$$

Substituting here expression (3.2.91) for $G(i\omega_n)$ and integrating over τ we arrive to the following equation[1]:

$$G(\tau) = -\int_{-\infty}^{\infty} \mathrm{d}\omega \frac{\mathrm{e}^{-\tau\omega}}{1+\mathrm{e}^{-\beta\omega}}A(\omega), \tag{3.2.94}$$

that connects spectral density with Matsubara *GF* as a function of thermodynamic time τ.

[1] In *QMC* literature definition of $G(\tau)$ without minus sign in (3.2.90) is used and hence in (3.2.94) there is no minus sign.

Spectral representation for retarded GF is [115]:

$$G(\omega) = \int_{-\infty}^{\infty} \mathrm{d}\omega' \frac{A(\omega')}{\omega - \omega' + i\delta}, \delta > 0. \tag{3.2.95}$$

Comparing expressions (3.2.91) and (3.2.95) we can see that retarded GF can be obtained from Matsubara GF by analytical continuation from discrete imaginary frequencies to real axis $i\omega_n \to \omega + i\delta$. Equation (3.2.94) can serve as a tool for such analytical continuation that gives integral equation with a kernel:

$$K(\tau, \omega) = -\frac{\mathrm{e}^{-\tau\omega}}{1 + \mathrm{e}^{-\beta\omega}}. \tag{3.2.96}$$

The kernel decays exponentially with ω increase and hence $G(\tau)$ determined by (3.2.94) is weakly sensitive to spectral function $A(\omega)$ features on large frequencies $|\omega| > 1/\beta$. As $G(\tau)$ from QMC is determined with stochastic error and in relatively small number of time points L that makes $A(\omega)$ calculation using (3.2.94) not well defined problem. For this task Maximum Entropy ($MaxEnt$) method was developed [132–134] that is described in details in reviews by Jarrell and Gubernatis [135] and by Jarrel [136]. Later we will follow this review.

As $A(\omega)$ is fermionic system spectral function the following two relations are valid:

$$A(\omega) > 0, \int_{-\infty}^{\infty} \mathrm{d}\omega A(\omega) < \infty, \tag{3.2.97}$$

and $A(\omega)$ (normalized to 1) can be interpreted as some probability distribution function. Then solution of (3.2.94) with statistical set of many calculated in QMC $G(\tau)$ values can be considered as the most probable $A(\omega)$ function. Criteria for choosing such $A(\omega)$ is determined in $MaxEnt$ method.

The method is based on Bayesian Statistics. If we have two events a and b, then according to Bayes theorem, the joint probability of these two events is

$$\mathrm{Pr}[a, b] = \mathrm{Pr}[a|b]\mathrm{Pr}[b] = \mathrm{Pr}[b|a]\mathrm{Pr}[a], \tag{3.2.98}$$

where $\mathrm{Pr}[a]$ is event a probability, $\mathrm{Pr}[a|b]$ is the conditional probability of a given b. The probabilities are normalized so that

$$\mathrm{Pr}[a] = \int \mathrm{d}b\mathrm{Pr}[a, b], \tag{3.2.99}$$

$$\int \mathrm{d}a\mathrm{Pr}[a|b] = 1, \int \mathrm{d}a\mathrm{Pr}[a] = 1. \tag{3.2.100}$$

Let event a be values of $G(\tau)$ obtained in QMC and b the $A(\omega)$ values. The determination of the spectrum is an ill-posed problem, since an infinite number of solutions exists which are consistent with the QMC data and associated error bars. $MaxEnt$ selects from these solutions the most probable

one. According to Bayes theorem (3.2.98) given the data G, the conditional probability of the spectrum A, $P[A|G]$, is given by

$$\Pr[A|G] = \frac{\Pr[G|A]\Pr[A]}{\Pr[G]}. \tag{3.2.101}$$

Here $\Pr[G|A]$ is the likelihood function which represents the conditional probability of the data G with given A, $\Pr[A]$ is the prior probability which contains prior information about A and $P[G]$ is called the evidence and can be considered a normalization constant.

We should maximize conditional probability $P[A|G]$ and for that need to maximize $\Pr[G|A]$ and $\Pr[A]$. For prior probability $\Pr[A]$ we use its representation in terms of information entropy:

$$\Pr[A] = \mathrm{e}^{\alpha S}, \tag{3.2.102}$$

with a real positive constant α and the entropy function S defined by

$$S = \int \mathrm{d}\omega \left\{ A(\omega) - m(\omega) - A(\omega) \ln \frac{A(\omega)}{m(\omega)} \right\}, \tag{3.2.103}$$

$m(\omega)$ is a function called "default model," The specific form of the entropy function is a result of some general and reasonable assumption imposed on the spectrum, like subset independence, coordinate invariance, system independence, and scaling. By defining the entropy relative to a default model, the prior probability is also used to incorporate prior knowledge about the spectrum, such as the high-frequency behavior and certain sum-rules. In the absence of data the resultant spectrum will be identical to the model.

The main focus of *MaxEnt* method is the calculation of the likelihood function, $P[G|A]$. The central limit theorem says that for some random variable χ, if each of its measurements is completely independent of the others, then probability distribution is always Gaussian:

$$P(\chi) = \frac{1}{2\pi\sigma} \mathrm{e}^{-\chi^2/2}, \tag{3.2.104}$$

where σ is dispersion.

In our case in *QMC* calculations we have $G(\tau)$ obtained in *GF* averaging $g_{s_1,\ldots,s_L}(\tau_l, \tau_{l'})$ (see (3.2.73)) over large number of "accepted" Ising spin configurations $\{s_l\}$ (*GF* calculation for every "accepted" configuration is called "measurement" so that $G(\tau)$ is an average over all "measurements"). If we will divide whole set of these configurations on N_d subsets called bins and make averaging separately in every bin, then we will get a set of $\{G_l^i\}$ where l is an imaginary time τ index and i is bin index. For every i value G_l^i has an error ΔG_l^i defined as a deviation of G_l^i from average over all configurations value $\bar{G}_l$. ΔG_l^i values are "random" and are assumed to be independent so their distribution function should be according (3.2.104)) with the following

expressions for χ^2 and σ^2:

$$\chi_j^2 = \frac{1}{\sigma^2}\left(\frac{1}{N_d}\sum_{i=1}^{N_d} G_l^i - G_l^j\right)^2 \equiv \frac{1}{\sigma^2}(\bar{G}_l - G_l^j)^2, \tag{3.2.105}$$

$$\sigma^2 = \frac{1}{N_d(N_d-1)}\sum_{i=1}^{N_d}(\bar{G}_l - G_l^i)^2. \tag{3.2.106}$$

In *QMC* procedure G_l^i values obtained in various bins are not completely independent and distribution $P(G)$ can deviate from the normal one. If random data are correlated then instead of (3.2.105)) for χ^2 we have [136]:

$$\chi_j^2 = \sum_{ll'}(\bar{G}_l - G_l^j)[C^{-1}]_{ll'}(\bar{G}_{l'} - G_{l'}^j), \tag{3.2.107}$$

where

$$C_{ll'} = \frac{1}{N_d(N_d-1)}\sum_{i=1}^{N_d}(\bar{G}_l - G_l^i)(\bar{G}_{l'} - G_{l'}^i) \tag{3.2.108}$$

is covariation matrix.

In this case C matrix should be diagonalized by unitary transformation $C \to U^{-1}CU$ with vector $G \equiv \{G_l^i\}$ transforming to vector $G' = U^{-1}G$. In the result quadratic form (3.2.105) will become normal:

$$\chi_j^2 = \sum_l (\frac{\bar{G}_l - G_l^j}{\sigma_l})^2, \tag{3.2.109}$$

where σ_l are eigenvalues of C matrix. Then analytical continuation problem reduces to solution of integral equation (3.2.94) with $G'(\tau)$ in the left side instead of $G(\tau)$.

There is another procedure for normalizing distribution of $\{G_l^i\}$ values. If distribution $P(G_l)$ for *QMC* results deviates significantly from Gauss function then additional averaging of G_l^i over several bins can be performed. This is done by defining more coarse mesh in bins space $1, 2, \ldots, N_d$ combining bin in blocks with n_b bins and to average G_l^i for all data in the block. The instead of G_l^i set we will have a set G_l^b, where $b = 1, 2, \ldots, N_b$ is block index for N_b blocks. This procedure is called *rebinning* and usually allows to suppress correlations and make distribution function for G_l^i closer to Gauss distribution.

So we assume for likelihood function $\Pr[G|A]$ Gauss distribution of G values:

$$\Pr[G|A] \approx \mathrm{e}^{-\chi^2/2}. \tag{3.2.110}$$

Combining representations (3.2.110) and (3.2.102) in (3.2.101) we obtain expression for conditional probability of the spectrum A, $P[A|G]$:

$$\Pr[A|G] \approx \mathrm{e}^{Q_\alpha[A]},\ Q_\alpha[A] = \alpha S[A] - \frac{1}{2}\chi^2[A], \tag{3.2.111}$$

Entropy S is a functional (3.2.103) of function $A(\omega)$. χ^2 is expressed via discrete function $G(\tau)$. Main equation (3.2.94) connects it with $A(\omega)$ and right side of (3.2.111) becomes explicit functional of $A(\omega)$ and depends on parameter α. Maximization of this functional is done by solution of equations:

$$\frac{\delta Q_\alpha[A]}{\delta A(\omega)} = 0, \quad \frac{\partial Q_\alpha[A]}{\partial \alpha} = 0. \tag{3.2.112}$$

These equations define the most probable function $A(\omega)$ corresponding to calculated in *QMC* set $\{G_l^i\}$. We do not present explicit equations for (3.2.112) maximization. In reviews [135,136] various calculations schemes are described.

MaxEnt method is illustrated later for the case of periodic Anderson model with parameters $U = 2$, $V = 0.6$, and $\beta = 20$ (in t units) [136]. Time interval $0 \le \tau \le \beta$ discretization was done for slices number L from 40 to 160 for various β values. In Fig. 3.1 $G(\tau)$ values from *QMC* calculations are presented as a function of "measurement" number.

From these 1,000 "measurement" values one can see that $G(\tau)$ is a random variable fluctuating around some average value. Fluctuation distribution asymmetry (see Fig. 3.2) shows deviation from Gauss distribution.

This deviation from Gauss distribution indicates correlations among various *QMC* "measurements." The correlations can be suppressed after

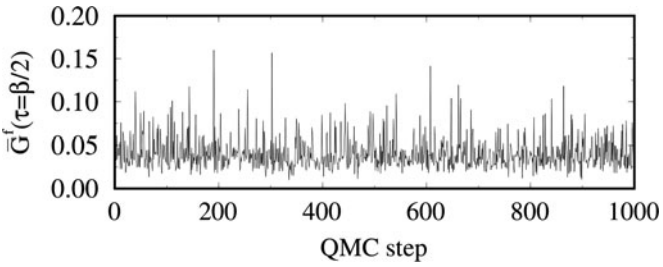

Fig. 3.1. Symmetric *PAM* f-electron local Green's function $G(\tau)$ ($\tau = \beta/2$) plotted as a function of the *QMC* step for $U = 2$, $V = 0.6$, and $\beta = 20$ [136]

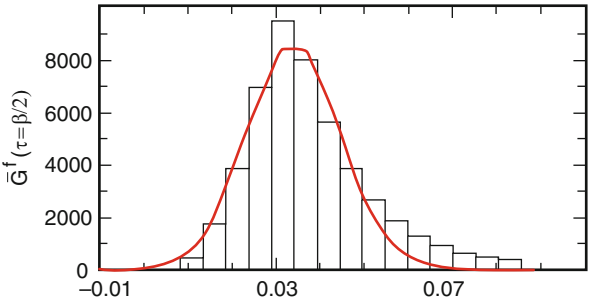

Fig. 3.2. Distribution of the data shown in Fig. 3.1. The *solid line* is a Gaussian fit [136]

"rebinning" where separate measurements were combined in bins with averaging in every bin. The result of such rebinning is presented in Fig. 3.3. One can see that fluctuation distribution become more Gaussian and that means more probable values for $G(\tau)$ function.

In Fig. 3.4 the average values for $G(\tau)$ function are compared with the result of single "measurement." It is interesting to note that if the result from a single measurement at a certain point differs from the essentially exact result obtained by averaging over many bins, then the results at adjacent points also deviate from the exact results.

As we note earlier further approaching to Gauss distribution for $G(\tau)$ fluctuations can be done by covariance matrix diagonalization (3.2.108) that suppress correlations among various time values. Both rebinning and covariance matrix diagonalization should be performed till $G(\tau)$ fluctuations distribution will become as close to Gaussian as possible.

After preparing the $\bar{G}(\tau)$ values one should run analytic continuation on $MaxEnt$ procedure. It is important to show how calculated spectral function $A(\omega)$ depends on the choice of default model $m(\omega)$. These dependence are shown in Fig. 3.5.

One can see that for every choice of $m(\omega)$ results for $A(\omega)$ are practically the same. However, the best result is obtained for $m(\omega)$ from perturbation theory and the worst one for $m(\omega) = \text{const}$. It means that the choice of

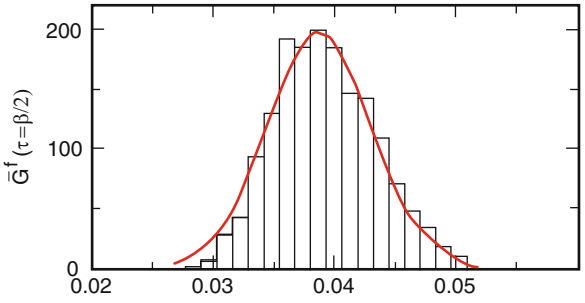

Fig. 3.3. Distribution of the data shown in Fig. 3.1 after rebinning. The data was processed by packing it sequentially into bins of 30 measurements each [136]

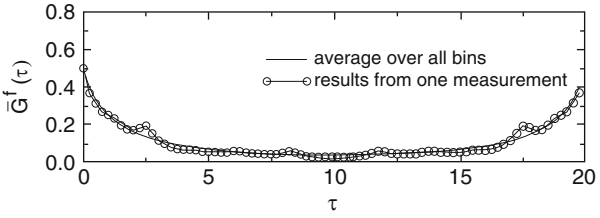

Fig. 3.4. $G(\tau)$ from one measurement compared to $G(\tau)$ obtained from the average over 800 bins of data, each containing 1,520 measurements [136]

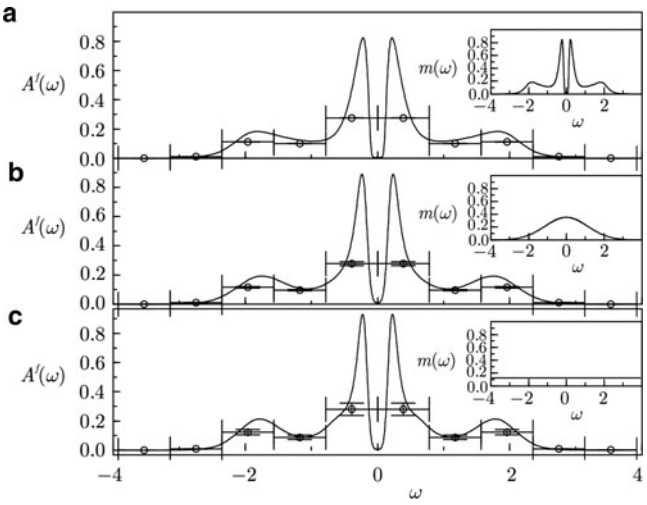

Fig. 3.5. The f-electron density of states $A(\omega)$ generated using (**a**) a perturbation theory, (**b**) a Gaussian, and (**c**) a flat default model. These models are shown as insets to each graph. The data points indicate the integrated spectral weight within 10 nonoverlapping regions of width indicated by the horizontal error bar. The vertical error bar indicates the uncertainty of the integrated weight within each region [136]

default model is not so important and *MaxEnt* method is reliable tool for analytical continuation procedure.

3.2.3 *QMC* for Single Impurity Anderson Model with Orbital Degrees of Freedom

Hirsch–Fye algorithm can be easily generalized to the case with several orbitals on impurity site [130]. Let us write model Hamiltonian as:

$$\hat{H} = \sum_q \epsilon_{q0} \hat{c}^+_{0q} \hat{c}_{0q} + \frac{1}{2} \sum_{q \neq q'} U \hat{n}_{0q} \hat{n}_{0q'} + \sum_{p>0,q} \left[V_{0p} \hat{c}^+_{0q} \hat{c}_{pq} + V^*_{0p} \hat{c}^+_{pq} \hat{c}_{0q} \right] + \sum_{p>0,q} \epsilon_p \hat{c}^+_{pq} \hat{c}_{pq}. \tag{3.2.113}$$

Here q is electronic state index for impurity site including orbital moment projection m and spin σ.

As an example, we will consider the doubly degenerate case where q index have values $1, 2, 3, 4$. Coulomb interaction term can be transformed with

identity:

$$\frac{1}{2}\sum_{q\neq q'} U\hat{n}_{0q}\hat{n}_{0q'} = \left[n_1n_2 - \frac{1}{2}(n_1+n_2)\right] + \left[n_1n_3 - \frac{1}{2}(n_1+n_3)\right] + \left[n_1n_4 - \frac{1}{2}(n_1+n_4)\right] + \left[n_2n_3 - \frac{1}{2}(n_2+n_3)\right] + \left[n_2n_4 - \frac{1}{2}(n_2+n_4)\right] + \left[n_3n_4 - \frac{1}{2}(n_3+n_4)\right] + \frac{3}{2}(n_1+n_2+n_3+n_4).$$

Every one of six terms in square brackets can be written in the form of (3.2.57) and then Hirsch formula (3.2.58) is applied. In partition function for Hamiltonian (3.2.113) Coulomb term will generate a factor:

$$\begin{aligned}\mathrm{e}^{-\Delta\tau\frac{1}{2}\sum_{q\neq q'} U\hat{n}_{0q}\hat{n}_{0q'}} &= \frac{1}{2^6}\sum_{s_1,\ldots,s_6} \exp\lambda\{s_1(n_1-n_2) + s_2(n_1-n_3) \\ &\quad + s_3(n_1-n_4) + s_4(n_2-n_3) + s_5(n_2-n_4) + s_6(n_3-n_4)\} \\ &= \frac{1}{2^6}\sum_{s_1,\ldots,s_6} \mathrm{e}^{\sum_{k=1}^{6}\sum_{\nu=1}^{4}\lambda s_k f_{k\nu}\hat{n}_\nu}, \end{aligned} \tag{3.2.114}$$

here λ is defined by

$$2\cosh\lambda = \mathrm{e}^{-\Delta\tau U},$$

analogous to (3.2.59) and $f_{k\nu}$ is a rectangular matrix

$$f = \begin{vmatrix} 1 & -1 & 0 & 0 \\ 1 & 0 & -1 & 0 \\ 1 & 0 & 0 & -1 \\ 0 & 1 & -1 & 0 \\ 0 & 1 & 0 & -1 \\ 0 & 0 & 1 & -1 \end{vmatrix}. \tag{3.2.115}$$

The generalization for degenerate case is done by using Hirsch formula for every index pair qq' with the same Hirsch–Fye algorithm as in nondegenerate Anderson model described earlier with matrices size increased from $L \times L$ to $N_f L \times N_f L$, where N_f is a number of different orbital pairs (in our example $N_f = 6$). More detailed description of multiorbital *QMC* is presented in Sect. 4.2.5.

3.2.4 Projective Quantum Monte Carlo Method

Hirsch–Fye algorithm is practical only for high enough temperatures T because time discretization parameter $\Delta\tau = \beta/L$ should be small because of Trotter decomposition error [see (3.2.61)] and hence number of time slices L

is large for large $\beta = 1/T$. Low temperatures are unaccessible in this method because computational expenses grow exponentially with L. In the same time the most interesting physics for strongly correlated systems is observed at low temperatures, for example superconductivity, magnetic ordering, and anomalies of transport properties.

To study low temperature and ground-state properties Numerical renormalization group (*NRG*) method developed by Willson [116] is often used (see Sect. 3.1.5). For nondegenerate Anderson model *NRG* is very effective but computational expenses grow exponentially with increasing of interacting orbitals number M so it practically works only for $M \leq 2$. However for realistic materials $M > 2$ and *NRG* cannot be used.

Recently, Projective Quantum Monte Carlo method (*PQMC*) was developed [137–139] that is based on Hirsch–Fye algorithm but allows to treat low-temperature and ground state properties. This method uses idea of wave function projection on ground-state proposed by the authors of [140] to study Hubbard model.

The basic idea of *PQMC* is to take some trial wave function Ψ_0 and project it on ground state wave function Ψ_{GS} using the limit:

$$|\Psi_{\mathrm{GS}}\rangle = \lim_{\theta\to\infty} \frac{\mathrm{e}^{-(\theta/2)\hat{H}}|\Psi_0\rangle}{\sqrt{\langle\Psi_0|\mathrm{e}^{-\theta\hat{H}}|\Psi_0\rangle}}, \tag{3.2.116}$$

where $\hat{H}$ is the system Hamiltonian. The right side of (3.2.116) is nonzero only if in $|\Psi_0\rangle$ expansion there is a component corresponding to $|\Psi_{\mathrm{GS}}\rangle$. After applying operator $\mathrm{e}^{-(\theta/2)\hat{H}}$ to function $|\Psi_0\rangle$ in the limit of $\theta \to \infty$ only the term $\mathrm{e}^{-(\theta/2)\hat{H}}|\Psi_{\mathrm{GS}}\rangle = \mathrm{e}^{-(\theta/2)E_0}|\Psi_{\mathrm{GS}}\rangle$ with minimal energy E_0 will survive that proves validity of (3.2.116).

Ground state average value for any operator $\hat{O}$ can be written as:

$$\langle\hat{O}\rangle = \langle\Psi_{\mathrm{GS}}|\hat{O}|\Psi_{\mathrm{GS}}\rangle = \lim_{\theta\to\infty} \frac{\langle\Psi_0|\mathrm{e}^{-\theta/2\hat{H}}\hat{O}\mathrm{e}^{-\theta/2\hat{H}}|\Psi_0\rangle}{\langle\Psi_0|\mathrm{e}^{-\theta\hat{H}}|\Psi_0\rangle}. \tag{3.2.117}$$

The same average value can be expressed in another way introducing a second limit in variable β (inverse temperature):

$$\langle\hat{O}\rangle = \lim_{\theta\to\infty}\lim_{\beta\to\infty} \frac{\mathrm{Tr}\{\mathrm{e}^{-\beta\hat{H}_0}\mathrm{e}^{-\theta/2\hat{H}}\hat{O}\mathrm{e}^{-\theta/2\hat{H}}\}}{\mathrm{Tr}\{\mathrm{e}^{-\beta\hat{H}_0}\mathrm{e}^{-\theta\hat{H}}\}}, \tag{3.2.118}$$

due to relation

$$\lim_{\beta\to\infty} \mathrm{Tr}\{\mathrm{e}^{-\beta\hat{H}_0}\hat{O}\} = \mathrm{e}^{-\beta E_0}\langle\Psi_0|\hat{O}|\Psi_0\rangle. \tag{3.2.119}$$

In the last two equations $\hat{H}_0$ is an auxiliary Hamiltonian with ground state function $|\Psi_0\rangle$ and its energy E_0.

The idea of (3.2.118) is to represent ground state average as a trace of operator with a factor $e^{-\beta\hat{H}_0}$ that has a form of statistical operator for fictitious inverse temperature β. Using identity (3.2.118) expression for electronic GF can be derived:

$$G_{ij}^{\sigma}(\tau,\tau') = -\langle T_\tau \hat{c}_{i\sigma}(\tau)\hat{c}_{j\sigma}^{+}(\tau')\rangle = \lim_{\theta\to\infty}\lim_{\beta\to\infty}\frac{\mathrm{Tr}\{e^{-\beta\hat{H}_0}e^{-\theta/2\hat{H}}\hat{c}_{i\sigma}(\tau)\hat{c}_{j\sigma}^{+}(\tau')e^{-\theta/2\hat{H}}\}}{\mathrm{Tr}\{e^{-\beta\hat{H}_0}e^{-\theta\hat{H}}\}}. \quad (3.2.120)$$

A natural choice for the trial wave function $|\Psi_0\rangle$ is the ground state of a noninteracting Anderson impurity model ($U = 0$ in Hamiltonian (3.1.16)). Hamiltonian $\hat{H}_0$ can be identified with noninteraction impurity Hamiltonian with corresponding Green function equal to *bath* Green function $\mathcal{G}_0$. An expression in denominator of (3.2.120) $\mathrm{Tr}\{e^{-\beta\hat{H}_0}e^{-\theta\hat{H}}\}$ can be compared with partition function representation in Hirsch–Fye algorithm (3.2.60)–(3.2.63) $Z = \mathrm{Tr}e^{-\beta\hat{H}} = \mathrm{Tr}\prod_{l=1}^{L} e^{-\Delta\tau(\hat{H}_0+\hat{H}_1)}$. If we will divide interval $[0,\theta]$ on L time slices and the interval $[0,\beta]$ on another L' slices then Hirsch–Fye analog will be

$$\mathrm{Tr}\{e^{-\beta\hat{H}_0}e^{-\theta\hat{H}}\} = \prod_{l=L+1}^{L+L'} e^{-\Delta\tau\hat{H}_0}\mathrm{Tr}\prod_{l=1}^{L} e^{-\Delta\tau(\hat{H}_0+\hat{H}_1)}. \quad (3.2.121)$$

Then Hirsch-Hubbard–Stratonovich transformation (3.2.58) will be necessary only for the first L time slices corresponding to the interval $[0,\theta]$ and for time slices τ_l with $L < l < L + L'$ (corresponding to the interval $[\theta,\theta+\beta]$) Ising spins s_l could be set to zero.

The limit $\beta\to\infty$ can now be taken analytically, leaving a problem on the imaginary time interval $[0,\theta]$ discretized into $L = \theta/\Delta\tau$ steps. As was shown by Feldbacher et al. [137], one then arrives at the same algorithm as the Hirsch–Fye finite-temperature algorithm. The only difference is that instead of the finite temperature noninteracting GF $\mathcal{G}_0$ a zero-temperature $\mathcal{G}_0$ enters defined for finite values of imaginary time $-\theta < \tau < \theta$.

For practical realization of $PQMC$ method standard Hirsch–Fye algorithm is used with final fictitious inverse temperature θ. Formally, real inverse temperature is infinite but Ising spins s_l are used only for time slices for interval $[0,\theta]$ and are assumed to be zero for time values from $[\theta,\infty]$ interval. In QMC formalism time is considered to be homogeneous so that calculated GF $G(\tau_i,\tau_j)$ depends only on time difference and if $\tau_i \in [0,\theta]$ then the resulting GF will be obtained for $\tau\in[-\theta,\theta]$. To minimize "border" effects QMC measurements are performed only for time values $\tau_i\in[0,\beta_1]$, where $\beta_1 < \theta$.

To close $DMFT$ self-consistency loop one need to calculate frequency dependent $G(i\omega_n)$ from $G(\tau)$. Usually it is done by Fourier transformation (3.2.86). However in $PQMC$ algorithm $G(\tau)$ is determined only for $\tau\in[-\beta_1,\beta_1]$ and full integration over τ in (3.2.86) is not possible. Feldbacher

et al. [137] proposed to use for that Maximum Entropy method $MaxEnt$ (see Sect. 3.2.2). This method can give spectral function $A(\omega)$ using as an input $G(\tau)$ and it is not necessary for $G(\tau)$ to be determined for every $\tau \in [0, \beta]$. $A(\omega)$ can be calculated by $MaxEnt$ using $G(\tau)$ with $\tau \in [-\beta_1, \beta_1]$. Knowing spectral function $A(\omega)$ $G(i\omega_n)$ can be calculated for all $i\omega_n$ values using Hilbert transformation (3.2.92).

3.2.5 Continuous-Time *QMC*

While Hirsch–Fye algorithm is very popular it has one essential drawback: time discretization. The thermodynamic time interval $0 \leq \tau \leq \beta$ is divided on L time slices and for every $\Delta\tau$ discrete Hirsch-Hubbard–Stratonovich transformation (3.2.58) is applied allowing to linearize Coulomb interaction contribution to partition function Z (3.2.60)–(3.2.63). Typical number of time slices $L \approx 0.5U\beta$ that become very large with temperature lowering. As number of possible configuration of Ising spins s_l is 2^L, the variational space grows exponentially with L.

Recently new QMC method for single impurity Anderson model was developed that does not use time discretization and hence it was called "Continuous-Time QMC" – $CT-QMC$. Originally, it was used for bosonic fields [141] and later was applied to fermionic fields [142, 143]. In the last case the formalism starts from standard perturbation theory expansion. There are two versions of $CT-QMC$: with expansion series in Coulomb interaction U [142] and another one where as a perturbation hybridization V is assumed [143]. Later we will describe hybridization expansion version of $CT-QMC$ developed in [130, 144–146].

Single impurity Anderson model Hamiltonian is:

$$\hat{H} = \sum_{\sigma} \epsilon_0 \hat{c}^+_{0\sigma} \hat{c}_{0\sigma} + U \hat{n}_{0\uparrow} \hat{n}_{0\downarrow} + \sum_{p\sigma} \epsilon_p \hat{c}^+_{p\sigma} \hat{c}_{p\sigma} + \sum_{p\sigma} \left[V_{0p} \hat{c}^+_{0\sigma} \hat{c}_{p\sigma} + V^*_{0p} \hat{c}_{p\sigma} \hat{c}^+_{0\sigma} \right], \tag{3.2.122}$$

where 0 is impurity site and index p corresponds to electronic states on other lattice site. Partition function is expressed via functional integral over Grassmann variables $c_{0\sigma}$ and $c_{p\sigma}$ (we denote them by the same symbols as Fermi operators in (3.2.122)):

$$Z = \int \mathcal{D}[c^+_0] \mathcal{D}[c_0] \mathcal{D}[c^+_p] \mathcal{D}[c_p] \mathrm{e}^{-S_a - \Delta S}, \tag{3.2.123}$$

with atomic action:

$$S_a = \int_0^\beta \mathrm{d}\tau \left[\sum_{\sigma} c^+_{0\sigma}(\tau) \left(\frac{\partial}{\partial \tau} - \mu + \epsilon_0 \right) c_{0\sigma}(\tau) + U c^+_{0\uparrow}(\tau) c_{0\uparrow}(\tau) c^+_{0\downarrow}(\tau) c_{0\downarrow}(\tau) \right], \tag{3.2.124}$$

and action for hybridization of atomic states with the rest of the system (reservoir):

$$\Delta S = \int_0^\beta \mathrm{d}\tau \sum_{p\sigma} \left[c_{p\sigma}^+(\tau) \left(\frac{\partial}{\partial \tau} - \mu + \epsilon_p \right) c_{p\sigma}(\tau) + V_{0p} c_{0\sigma}^+(\tau) c_{p\sigma}(\tau) + V_{0p}^* c_{p\sigma}^+(\tau) c_{0\sigma}(\tau) \right]. \tag{3.2.125}$$

In expression for ΔS it is possible to integrate out reservoir variables $c_{p\sigma}$. Then ΔS is:

$$\Delta S = \int_0^\beta \mathrm{d}\tau \int_0^\beta \mathrm{d}\tau' \sum_\sigma c_{0\sigma}^+(\tau) \Delta(\tau - \tau') c_{0\sigma}(\tau'), \tag{3.2.126}$$

where $\Delta(\tau - \tau')$ is hybridization function. Its Fourier transformation to Matsubara frequences is:

$$\Delta(i\omega) = \sum_p \frac{V_{0p}^* V_{0p}}{i\omega + \mu - \epsilon_p}. \tag{3.2.127}$$

Now partition function can be written as integral over impurity center Grassmann variables only:

$$Z = \int \mathcal{D}[c^+]\mathcal{D}[c] \exp\{-S_a - \int_0^\beta \mathrm{d}\tau \int_0^\beta \mathrm{d}\tau' \sum_{\alpha\alpha'} c_\alpha^+(\tau) \Delta_{\alpha\alpha'}(\tau - \tau') c_{\alpha'}(\tau')\}, \tag{3.2.128}$$

(we will use later the combined index $(0\sigma \equiv \alpha)$; in general nondegenerate model case index α can be spin-orbital index $m\sigma$ or even local cluster variable).

Let us present exponent in (3.2.128) as an expansion series in hybridization

$$Z = \int \mathcal{D}[c^+]\mathcal{D}[c] \mathrm{e}^{-S_a} \sum_k \frac{1}{k!} \int_0^\beta \prod_{i=1}^k \mathrm{d}\tau_i \int_0^\beta \prod_{i=1}^k \mathrm{d}\tau_i' \sum_{\{\alpha\}\{\alpha'\}} \prod_{i=1}^k [c_{\alpha_i'}(\tau_i') c_{\alpha_i}^+(\tau_i)] \prod_{i=1}^k \Delta_{\alpha_i \alpha_i'}(\tau_i - \tau_i'). \tag{3.2.129}$$

Every k-th order contribution to Z is a product of two factors. The first one is an average over impurity degrees of freedom and corresponding pairs of Grassmann variables and the second one is a product of hybridization functions. Full product of those factors is integrated over all time variables.

S_a has quadratic form in Fermi operators and hence expression (3.2.129) contains Gaussian integrals in Grassmann variables. These integrals generate Feinman diagrams with fermionic GFs $g_{\alpha\alpha'}(\tau - \tau')$ and hybridization functions $\Delta_{\alpha\alpha'}(\tau - \tau')$.

Expression (3.2.129) can be presented in following form:

$$Z = Z_a \sum_k \frac{1}{k!} \int_0^\beta \mathrm{d}\tau_1 \int_0^\beta \mathrm{d}\tau_1' \ldots \int_0^\beta \mathrm{d}\tau_k \int_0^\beta \mathrm{d}\tau_k' \sum_{\alpha_1\alpha_1',\ldots,\alpha_k\alpha_k'} \langle T\{c_{\alpha_1'}(\tau_1')c_{\alpha_1}^+(\tau_1),\ldots,c_{\alpha_k'}(\tau_k')c_{\alpha_k}^+(\tau_k)\}\rangle_{\mathrm{loc}} \cdot \frac{1}{k!} \det \begin{vmatrix} \Delta_{\alpha_1\alpha_1'}(\tau_1-\tau_1') & \Delta_{\alpha_1\alpha_2'}(\tau_2-\tau_2') & \ldots & \ldots \\ \ldots & \ldots & \ldots & \ldots \\ \ldots & \ldots & \ldots & \ldots \\ \Delta_{\alpha_k\alpha_1'}(\tau_k-\tau_1') & \ldots & \ldots & \Delta_{\alpha_k\alpha_k'}(\tau_k-\tau_k') \end{vmatrix}. \tag{3.2.130}$$

Here we introduce partition function of free atom

$$Z_a = \int \mathcal{D}[c^+]\mathcal{D}[c]\mathrm{e}^{-S_a}, \tag{3.2.131}$$

and average value of some operator $\hat{O}$ over impurity states

$$\langle \hat{O} \rangle_{\mathrm{loc}} = \int \mathcal{D}[c^+]\mathcal{D}[c]\mathrm{e}^{-S_a}\hat{O}, \tag{3.2.132}$$

Equation (3.2.130) was obtained from (3.2.129) by summing $k!$ terms with possible permutation of $\tau_1, \tau_2, \ldots, \tau_k$ variables. Taking into account sign change with commutation of c_α and c_α^+ operators in $\langle T\{\ldots\}\rangle_{\mathrm{loc}}$ one can see that the sum of $k!$ products of k functions $\Delta_{\alpha\alpha'}(\tau - \tau')$ is a determinant written in (3.2.130).

Expression (3.2.130) for partition function of single impurity Anderson model is a basis of $CT{-}QMC$ method. Let us rewrite (3.2.130) in the following form:

$$Z = \sum_{k=0}^\infty \int_0^\beta \mathrm{d}\tau_1 \int_0^\beta \mathrm{d}\tau_1' \ldots \int_0^\beta \mathrm{d}\tau_k \int_0^\beta \mathrm{d}\tau_k' \sum_{\alpha_1\alpha_1',\ldots,\alpha_k\alpha_k'} P_{\alpha_1\alpha_1',\ldots,\alpha_k\alpha_k'}(\tau_1\tau_1',\ldots,\tau_k\tau_k'), \tag{3.2.133}$$

Function $P_{\{\alpha\},\{\alpha'\}}(\{\tau\},\{\tau'\})$ can be considered (if it has positive value) as a probability for time distribution $\{\tau\},\{\tau'\}$ in k-th order term in Z. Many-dimensional integral (3.2.133) over time variables can be calculated by stochastic Monte Carlo sampling (3.2.83). $CT-QMC$ calculation scheme consists of the following steps:

- For some k-th order term k stochastic values of time $\tau_1, \ldots, \tau_k$ and the same number of $\tau_1', \ldots, \tau_k'$ times from the interval $\{0, \beta\}$ are generated.
- Probability function $P_{\alpha_1\alpha_1',\ldots,\alpha_k\alpha_k'}(\tau_1\tau_1', \ldots, \tau_k\tau_k')$ is calculated.
- By adding or removing one of τ values in a set $\{\tau\},\{\tau'\}$ a new time set is obtained that corresponds to $(k+1)$-th or $(k-1)$-th order term and corresponding change of probability functions is calculated.

- Comparing new probability function values with an old one new time configuration is accepted or not.
- Summation is performed over all accepted time configurations giving partition function Z.

GF in $CT-QMC$ calculation scheme is defined in a standard way via T-ordered product of Fermi operators $\hat{c}_{0\sigma}$ and $\hat{c}^{+}_{0\sigma}$:

$$G(\tau-\tau') = -\langle T\hat{c}_{0\sigma}(\tau)\hat{c}^{+}_{0\sigma}(\tau')\rangle, \tag{3.2.134}$$

This GF is expressed as a functional integral over Grassmann variables that gives analog of expression (3.2.133) for partition function Z:

$$G(i\omega_n) = \frac{1}{Z}\sum_{k=0}^{\infty}\int_0^\beta \mathrm{d}\tau_1\int_0^\beta \mathrm{d}\tau_1'\ldots\int_0^\beta \mathrm{d}\tau_k\int_0^\beta \mathrm{d}\tau_k' \\ P(\{\tau\},\{\tau'\})G(i\omega_n;\{\tau\},\{\tau'\}), \tag{3.2.135}$$

(we omit α index assuming that electronic GF on impurity site depends only on spin index σ). Contribution to GF is defined by the matrix M that is inverse to matrix Δ:

$$M = \Delta^{-1} = \begin{vmatrix} \Delta(\tau_1-\tau_1') & \Delta(\tau_1-\tau_2') & \ldots & \ldots \\ \ldots & \ldots & \ldots & \ldots \\ \ldots & \ldots & \ldots & \ldots \\ \Delta(\tau_k-\tau_1') & \ldots & \ldots & \Delta(\tau_k-\tau_k') \end{vmatrix}^{-1}, \tag{3.2.136}$$

so that GF is:

$$G(i\omega_n;\{\tau\},\{\tau'\}) = \frac{1}{\beta}\sum_{ij}\mathrm{e}^{\mathrm{i}\omega_n\tau_i}M_{ij}(\{\tau\},\{\tau'\})\mathrm{e}^{-\mathrm{i}\omega_n\tau_j}. \tag{3.2.137}$$

Please note that expressions (3.2.133) and (3.2.135) for partition function and GF have the same structure as expressions (3.2.69) and (3.2.73) in Hirsch–Fye algorithm. In the last case GF is calculated in a stochastic Ising spin field and the result is obtained by summation over all spin configurations. In $CT-QMC$ summation is performed over stochastic time distributions $\{\tau\},\{\tau'\}$.

Stochastic Monte Carlo process gives time set $\{\tau\},\{\tau'\}$ for contribution to k-th order term. For this time set probability function $P(\{\tau\},\{\tau'\})$ and GF $G(i\omega_n;\{\tau\},\{\tau'\})$ are calculated. On the next step time set is changed by adding new pair of times (by this going to $(k+1)$-th order term) or removing a pair of times for going to $(k-1)$-th order. This adding or removing time pair corresponds to adding or removing a row and column in a matrix M^{-1} (3.2.136).

As in Hirsch–Fye algorithm new contribution to GF $G(i\omega_n;\{\tau\},\{\tau'\})$ can be calculated from the previous one by "update" procedure. If a new column

i and row i' are added to matrix M^{-1} then new and old contributions to GF are connected by the following relation [143,144]:

$$G^{\text{new}} = G^{\text{old}} - \frac{p}{\beta}\left(\sum_{j=1}^{k} \mathrm{e}^{\mathrm{i}\omega_n \tau_j} L_j\right)\left(\sum_{j'=1}^{k} \mathrm{e}^{-\mathrm{i}\omega_n \tau'_{j'}} R_{j'}\right). \tag{3.2.138}$$

L_j and $R_{j'}$ are defined as

$$L = (\tilde{L}_1, \ldots, \tilde{L}_{i-1}, -1, \ldots, \tilde{L}_k),$$
$$R = (\tilde{R}_1, \ldots, \tilde{R}_{i'-1}, -1, \ldots, \tilde{R}_k),$$

where

$$\tilde{L}_j = \sum_i M^{\text{old}}_{ij} \Delta(\tau_i - \tau'), \;\; \tilde{R}_i = \sum_j \Delta(\tau - \tau_j) M^{\text{old}}_{ji},$$

and p is equal to

$$\frac{1}{p} = \Delta(\tau - \tau') - \sum_{ij} \Delta(\tau - \tau_j) M^{\text{old}}_{ji} \Delta(\tau_i - \tau').$$

When column i and row i' are removed the following relation is valid:

$$G^{\text{new}} = G^{\text{old}} + \frac{1}{\beta M_{ii'}}\left(\sum_{j=1}^{k} \mathrm{e}^{\mathrm{i}\omega_n \tau_j} M_{ji}\right)\left(\sum_{j'=1}^{k} M_{i'j'} \mathrm{e}^{-\mathrm{i}\omega_n \tau'_{j'}}\right). \tag{3.2.139}$$

To estimate every-step probability in Monte Carlo process one need to calculate ratio for matrix M determinants. If matrix M has initially dimensions $(n-1) \times (n-1)$ and one column and one row were added to matrix M^{-1} then

$$\frac{\det M}{\det M_{\text{new}}} = \frac{1}{p}. \tag{3.2.140}$$

If k-th column and row were removed from matrix M^{-1} then determinant ratio is:

$$\frac{\det M}{\det M_{\text{new}}} = M_{kk}. \tag{3.2.141}$$

Formulas (3.2.138)–(3.2.141) define Monte Carlo process allowing determining to accept new time configuration or not and to calculate new contribution to GF for accepted configuration.

$CT-QMC$ method has advantages comparing with Hirsch–Fye method because it can be used for lower temperatures where Hirsch–Fye algorithm fails. $CT-QMC$ version with series expansion in Coulomb interaction U [142] allows to work with general four-operator form of Coulomb interaction Hamiltonian (2.2.24).

In $CT-QMC$ formalism contribution from all orders of expansion series in hybridization are summed. It is interesting to note that this series summation

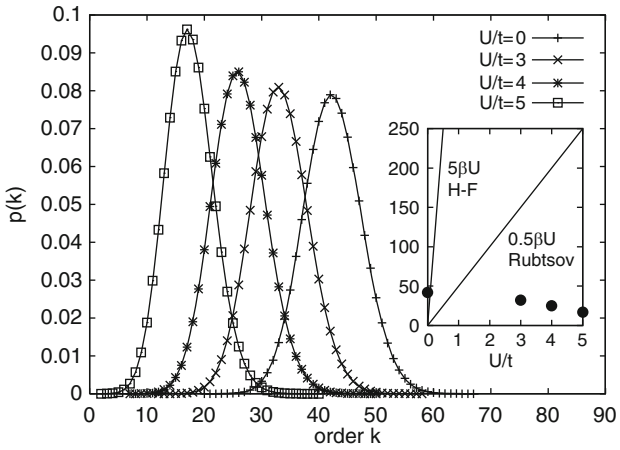

Fig. 3.6. Probability $P(k)$ for k-order contributions in $CT-QMC$ calculations for Hubbard model as a function of Coulomb interaction parameter U [143]

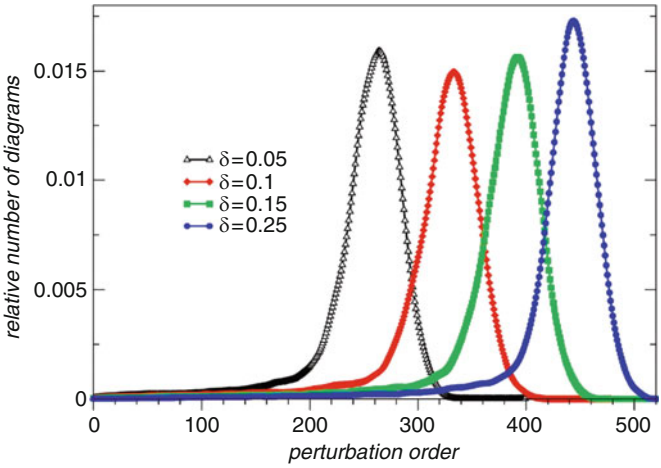

Fig. 3.7. Probability $P(k)$ for k-order contributions in $CT-QMC$ calculations for Hubbard model as a function of doping value δ [144]

converges for any hybridization values. This convergence is demonstrated in Figs. 3.6 and 3.7 where probability $P(k)$ of k-th order contributions is plotted.

In both cases presented in Figs. 3.6 and 3.7 results show rather narrow probability distributions for various order contributions with center positions depending on model parameter values (U for Fig. 3.6 and δ for Fig. 3.7). With U increase actual k are shifted for lower values (as it is expected for hybridization expansion series) while with deviation from half-filling higher orders are needed.

3.3 Hubbard Model Spectral Function in *DMFT* Approximation

3.3.1 Three Peak Spectral Structure for Half-Filling

It was shown in the Sect. 3.1 how *DMFT* maps a problem of electron on a lattice to effective single impurity problem and in this way dramatically reduces needed computational expenses. Lattice information is in the right side of (3.1.38) where it is possible to go from wave vector $\mathbf{k}$ integration to integration over energy variable ϵ of the noninteracting density of states (3.1.40). In this way one always treats finite dimensions ($d = 3, 2$) lattice problem and the $d \to \infty$ limit reveal itself only in using local self-energy independent of wave vector $\mathbf{k}$. Comparison of *DMFT* results with exact numerical lattice calculations shows that $d = 3$ and even $d = 2$ are "large" enough for *DMFT* to be a good approximation. It is important to note that *DMFT* does not assumes any small parameter in the problem Hamiltonian. Formally the only small parameter is $1/d$.

Georges, Kotliar, Krauth, and Jarrell [5,6,147] were the first to apply general *DMFT* idea to Hubbard model with Hamiltonian (3.1.1). They have shown that the problem of electrons moving on the lattice with strong Coulomb interelectron interaction can be reduced to the problem of impurity center embedded in noninteracting electrons system that creates effective dynamical mean field acting on impurity electrons, i.e., to well known Anderson impurity model. The basis of *DMFT* equations is calculation of effective parameters for this auxiliary impurity model. The widely used method to solve single impurity problem is *QMC* but other nonperturbative approaches such as Numerical Renormalization Group method are often used too (see Sect. 3.1.5).

The main effect of using *DMFT* for Hubbard model with Hamiltonian (3.1.1) can be illustrated in Fig. 3.8 where local spectral function

$$A(\omega) = \sum_{\mathbf{k}} A(\mathbf{k}, \omega) \tag{3.3.142}$$

obtained in *DMFT* calculations is presented.

This figure is used in all *DMFT* reviews because it is a classical illustration of electronic structure evolution for strongly correlated systems. With Coulomb interaction parameter U increase the system goes from weakly correlated to strongly correlated regime so that for half-filled case metal–insulator transition happens at large U values. For intermediate U values three-peak structure is observed with central quasiparticle peak and two broad side maximums. These maximums corresponds to two Hubbard bands obtained more than 40 year ago by Hubbard [2, 3] using heuristic approach for electronic Green function decoupling. They describe noncoherent electron states with electron removal from single occupied atomic level (lower Hubbard band) or second electron addition to atom (upper Hubbard band).

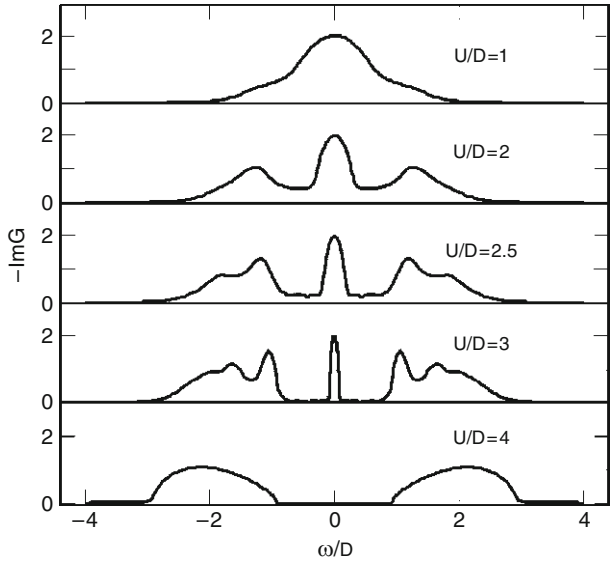

Fig. 3.8. Local spectral function for half-filled ($n = 1$) Hubbard model for various values of Coulomb interaction parameter U obtained in *DMFT* calculations. D the half-width of noninteracting band [7]

The Hubbard bands origin can be understood from Hamiltonian (3.1.1). Kinetic energy term becomes diagonal in momentum representation whereas Coulomb interaction term is diagonal in atomic site representation. In the result for weak interaction case $U \ll W$ momentum representation is more appropriate and spectral function is slightly modified noninteracting density of states. From other side for $U \gg W$ case atomic site representation better describes the system and spectral function is close to free atom solution:

$$A(\omega) = -\frac{1}{\pi}\mathrm{Im}\left(\frac{1/2}{\omega + U/2 + i\eta} + \frac{1/2}{\omega - U/2 + i\eta}\right). \tag{3.3.143}$$

with two peaks at $\pm U/2$.

In the intermediate $U \approx W$ case spectral function should have features typical for both limits and hence three peak structure appears in Fig. 3.8.

Single particle spectrum for Hubbard model is characterized by two energy scales. One is quasiparticle band width ϵ_f^* and another one is energy separation between noncoherent Hubbard bands $\approx U$. Low-energy scale ϵ_f^* is determined by expression $\epsilon_f^* = ZD$ where Z is quasiparticle weight and D is half-width of noninteracting band that is equal to Fermi energy for half filling. For strongly correlated systems $Z \ll 1$ and hence ϵ_f^* is much smaller than D. Integral intensity for high-energy Hubbard bands corresponding to noncoherent states is determined by a factor $1 - Z$. As we will show later such three peak structure

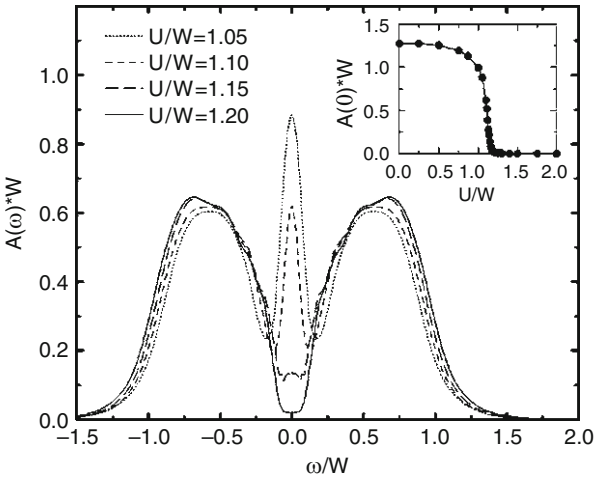

Fig. 3.9. Spectral function evolution with U increase for Hubbard model at temperature $T = 0.0276W$ (W is a width of noninteracting band). On the inset the dependence of quasiparticle peak height on U value is presented [117]

of spectral function is very general for strongly correlated systems and is experimentally observed in real material spectra.

The quasiparticle peak in Fig. 3.8 can be identified with Abrikosov-Suhl resonance that was at first predicted for Kondo effect problem appearing in a metal with paramagnetic impurities. Another name is Kondo peak that has its origin due to multiple scattering of conduction electrons near Fermi level on impurity with spin flips. In Hubbard model there is no explicit localized spins but there are local spin fluctuations and scattering of electrons on these fluctuations gives a resonance on the Fermi surface.

In Fig. 3.9 spectral function for Hubbard model is presented obtained in *DMFT* calculations with impurity problem solved by Numerical renormalization group method [117]. Again for intermediate U values three-peak structure is realized.

In Fig. 3.10 real and imaginary parts of self-energy $\Sigma(\omega)$ are shown calculated for the same U values and the same temperature as for Fig. 3.9. With U increase imaginary part $\Sigma(\omega)$ for small ω is deformed in such a way that a dip appears instead of the parabolic behavior typical for Fermi liquid regime. The dip depth is enhanced for larger U values. Such behavior of $\mathrm{Im}\Sigma(\omega)$ corresponds to transition from three peak structure of spectral function to two-peak structure as shown in Fig. 3.9. To quasiparticle peak disappearance corresponds slope sign change for $\mathrm{Re}\Sigma(\omega)$ function at $\omega = 0$. Self-energy pattern presented in Fig. 3.10 is typical for half-filled Hubbard model. Please note that imaginary part of $\Sigma(\omega)$ is even function of energy while real part is odd function as it is required by *DMFT* equations for particle–hole symmetric case. Also analytical properties for retarded Green function requires condition $\mathrm{Im}\Sigma(\omega) < 0$ that is satisfied in Fig. 3.10.

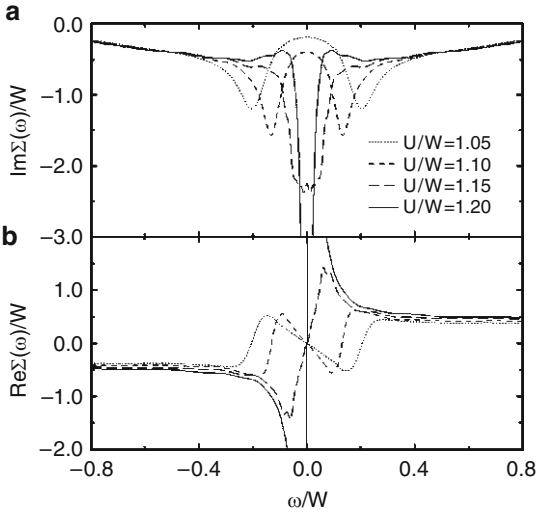

Fig. 3.10. Imaginary part (**a**) and real part (**b**) of self-energy $\Sigma(\omega)$ for the same temperature ($T = 0.0276W$) and the same U values as in Fig. 3.9 [117]

As *QMC* method is unpractical for low temperatures special interest deserve calculations for Hubbard model spectral function at $T = 0$ by *NRG* method. In work [148] such calculations were performed for two lattices: Bethe and hypercubic in a limit $d \to \infty$. For those lattices noninteracting density of states is given by formulas:

$$\rho(\epsilon) = \frac{1}{2\pi}\sqrt{4 - \epsilon^2}, \ -2 \leq \epsilon \leq 2, \tag{3.3.144}$$

and

$$\rho(\epsilon) = \frac{1}{2\pi} e^{\epsilon^2/2}, \tag{3.3.145}$$

correspondingly. In the last case spectral function decays infinitely for large frequencies and it is convenient to introduce effective band width $W = 4\sqrt{\int d\epsilon \rho(\epsilon)\epsilon^2}$ that is equal $W = 4$, that is the same value as for Bethe lattice. That allows to compare *DMFT* results for both lattices. The results are presented in Figs. 3.11 and 3.12.

In Fig. 3.11 calculation results for quasiparticle weight Z are presented that is defined by expression:

$$Z = \frac{1}{1 - \frac{\partial \mathrm{Re}\Sigma(\omega)}{\partial \omega}|_{\omega=0}}. \tag{3.3.146}$$

One can see that a particular form of noninteracting density of states has negligible influence on interacting spectral function in the limit of $Z \to 0$.

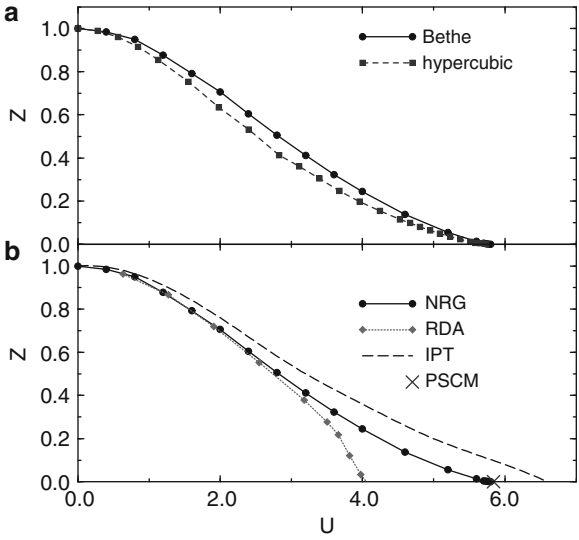

Fig. 3.11. U-dependence of quasiparticle weight Z calculated by *NRG* for Bethe lattice and hypercubic lattice (**a**) and also comparison of the results for Bethe lattice calculated by various methods (**b**) [148]

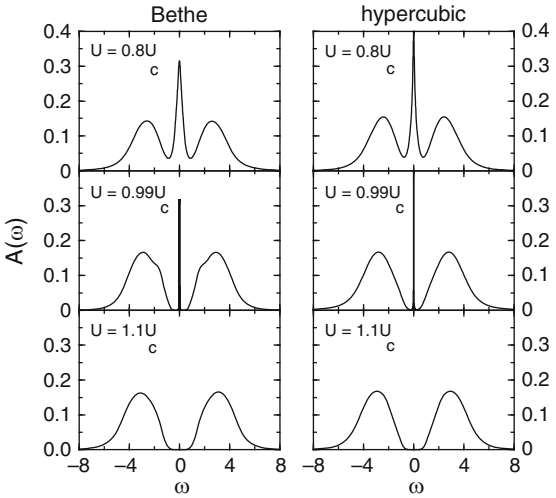

Fig. 3.12. Spectral functions comparison for Bethe and hypercubic lattices for various U values [148]

Near critical values of Coulomb parameter U_c spectrum evolves from three-peak to two-peak structure with gradual spectral weight transfer from quasiparticle peak to Hubbard bands till complete disappearance of the central peak. The general scenario for spectral function evolution is the same for high temperatures used in *QMC* calculations and for $T = 0$ in *NRG* calculations.

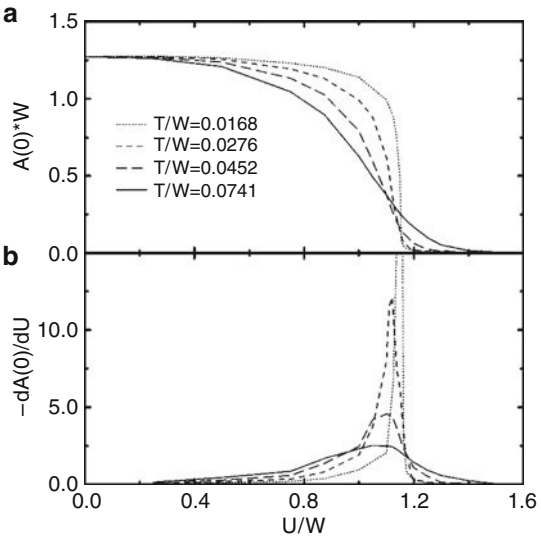

Fig. 3.13. Temperature dependence of quasiparticle peak height (**a**) as a function of U [117]

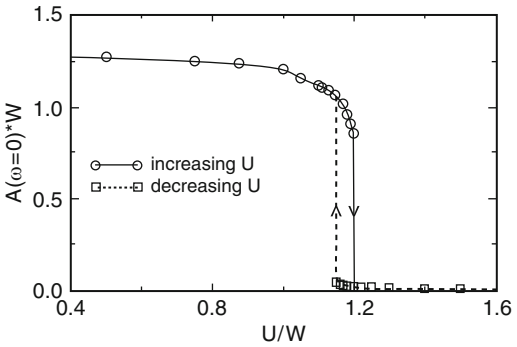

Fig. 3.14. Quasiparticle peak height at $T = 0.0103W$ and hysteresis for increasing and decreasing of U [117]

3.3.2 Metal–Insulator Phase Transition

Let us look again in Fig. 3.9 with *DMFT* results for finite temperature. One can see that quasiparticle peak strengths drops sharply with U increase but does not becomes zero at some critical point but the curve has a tail decaying for large U. The corresponding temperature dependence is shown in Fig. 3.13.

Hysteresis found at increasing and decreasing of U value signals the first-order phase transition (Fig. 3.14). Critical values U_{c1} and U_{c2} where metallic and insulating phases become unstable are starting points for the boundary curves crossing at critical temperature T_c where phase transition becomes of

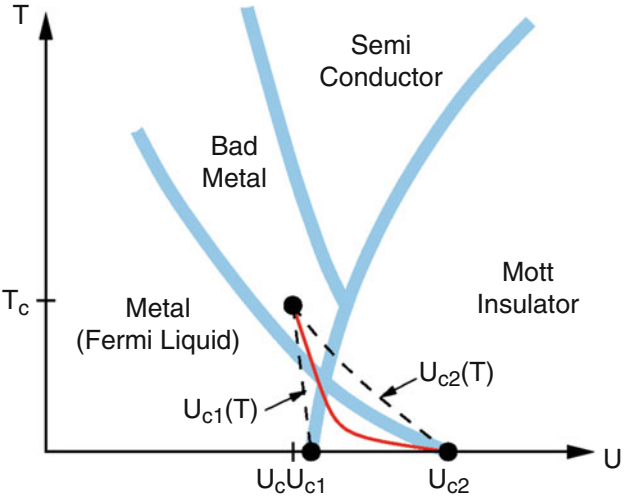

Fig. 3.15. Schematic phase diagram for Hubbard model at half filling

the second order. For $T < T_c$ one has first-order phase transition while for $T > T_c$ there is no phase transition between metallic and insulating phases but only a gradual crossover (Fig. 3.15).

Coexistence of two metastable phases – metallic and insulating – was confirmed also in another Hubbard model study using Projective *QMC* method [137] as impurity solver in *DMFT*. In this work projective parameter was chosen to be $\theta = 20, 30, 40$ (see (3.2.118) in Sect. 3.2.4) and energy was in the units where noninteracting band width $W = 4$. Calculation were performed for Bethe lattice with fixed imaginary time slice value $\Delta\tau = 0.2$, number of *QMC* sweeps was equal to 10^6 .

It was found that in the interval $5.0 = U_{c1} < U < U_{c2} = 6.0$ *DMFT* equations have two solutions corresponding to metallic and insulating phases. In Fig. 3.16 calculated values of probability for double occupancy D as a function of Coulomb parameter U is shown.

$$D = \langle \hat{n}_\uparrow \hat{n}_\downarrow \rangle. \tag{3.3.147}$$

Shaded part on the plane (D, U) corresponds to two phases coexistence area. With accuracy 0.1–0.2 coexistence interval $U_{c1} < U < U_{c2}$ agrees with the results of *NRG* calculations [117, 148] where it was found that $U_{c1} = 4.78$, $U_{c2} = 5.88$.

All this results confirm that *DMFT* equations allow to describe metal–insulator transition for half-filled Hubbard model with Coulomb interaction parameter U variation and this phase transition is of the first order.

Temperature dependence of resistivity in metallic phase of Hubbard model near metal–insulator phase transition is shown in Fig. 3.17. This result was obtained in *DMFT* equations solution where effective Anderson impurity

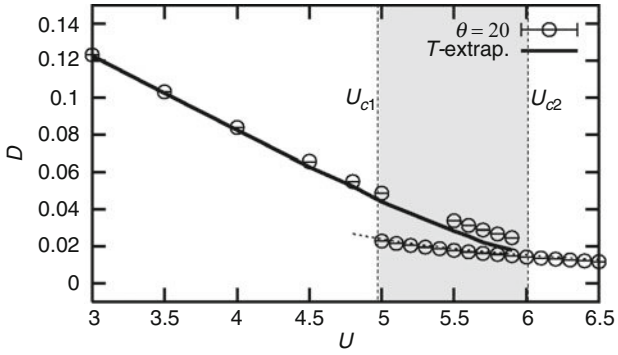

Fig. 3.16. Probability for double occupancy D as a function of Coulomb parameter U obtained in *DMFT* calculation using *PQMC* method [137]

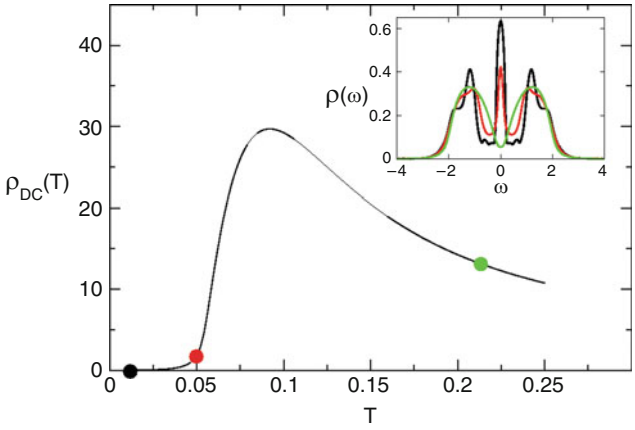

Fig. 3.17. Metallic phase resistivity near metal–insulator transition ($U = 2.4W$) as a function of U from *DMFT* calculations for Hubbard model [149]. T values are in the units of nearest neighbors hopping t. In the inset spectral function is shown for three points on the curve $\rho(T)$

problem was solved by Iterative Perturbation Theory (*IPT*), an approximate method that was often used in earlier *DMFT* applications (see Sect. 3.1.5). At low temperatures $\rho \propto T^2$. For $T \ll \epsilon_f^*$ resistivity is described by the expression:

$$\rho \propto \rho_{\mathrm{M}}(T/\epsilon_f^*)^2, \ \rho_{\mathrm{M}} \approx ha/e^2. \tag{3.3.148}$$

where ρ_{M} is Mott limit of ρ corresponding to mean free path of electron value of the order of interatomic distance a. Sharp ρ increase for $T \propto \epsilon_f^*$ corresponds to bad (fover "incoherent") metal where quasiparticle peak is strongly suppressed.

3.4 Hubbard Model with Deviation from Half-Filling

3.4.1 Quasiparticle Peak Evolution

The study of electronic spectra structure for Hubbard model with noninteger occupancy is directly related to experimental data for materials obtained from stoichiometric compounds by doping with nonisovalency elements. Of the special interest is spectral function evolution for Hubbard model close to metal–insulator transition at occupancy values deviating from half-filing: $\delta = 1 - n \neq 0$.

Let us consider Hubbard model for $U > U_c$ where with $n = 1$ Fermi level is in the energy gap Δ_g between Hubbard bands. What happens with small doping of the hole $\delta > 0$ or electron $\delta < 0$ type? Chemical potential should experience a jump $\mu(\delta = 0^+) - \mu(\delta = 0^-)$ going from hole to electron doping and important problem is a value of this jump: is it equal to Δ_g or smaller? This problem was investigated in earlier *DMFT* works [118, 121, 123, 150] using various impurity solvers: *QMC* [123], exact diagonalization [118] and generalized *IPT* method [121, 150]. Systematic investigation of this problem was done in [121].

In Fig. 3.18 we present one of *IPT* method results for hole doping at $T = 0$. One can see that at small doping resonance peak on the Fermi level appears that is well separated from the Hubbard band edge. With doping value increase spectral weight is transfered from both Hubbard bands to developing quasiparticle band with gradual merging of it with lower Hubbard band. At large doping values there is only quasiparticle band with a shoulder at former lower Hubbard band position and weak intensity upper Hubbard band. So for small doping quasiparticle states (so called "midgap states") appears inside the gap of the insulating case at $n = 1$. This result is very general and was confirmed in [121] by exact diagonalization for small clusters.

In Fig. 3.18 one can see that with doping value increase the originally insulating system becomes more and more metallic with standard Fermi liquid regime. At small δ quasiparticle peak is very narrow with large effective electron mass. With δ increase spectral weigh is transfered from Hubbard bands to quasiparticle band but Hubbard bands positions are unchanged with energy separation between them $\approx U$.

In [121] phase diagram on the plane $\mu - U$ was produced (Fig. 3.19). Near metal–insulator transition at $n = 1$ there is an interval $U_{c1} < U < U_{c2}$ where *DMFT* equations have two solutions: metallic one with final density of states value at $\omega = 0$ and insulating one with zero value. It is important to know how the boundaries of this coexistence area change with doping δ.

3.4.2 Phase Diagram for $T = 0$

DMFT results at $T = 0$ calculated with exact diagonalization and *IPT* methods for impurity solvers are presented in Fig. 3.19. By black color is marked

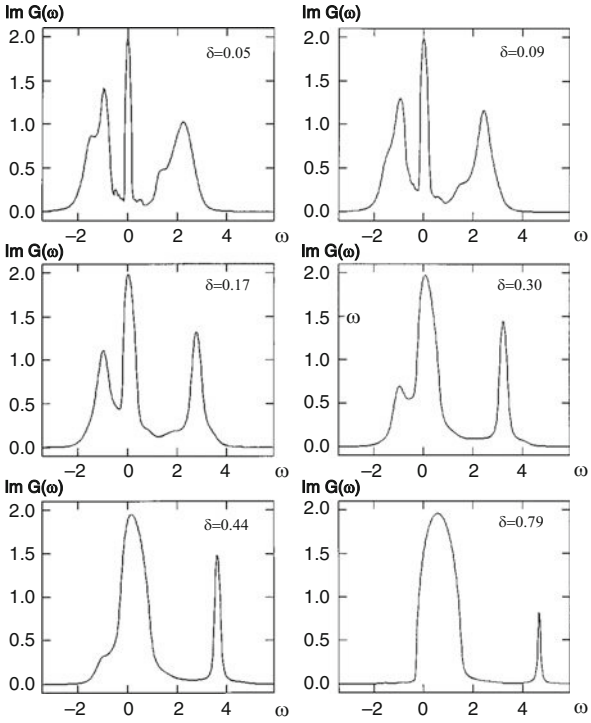

Fig. 3.18. Spectral function evolution for various doping values for $U = 3$ (in the units of half-width D of semielliptical band) [121]

the coexistence area for metallic M and insulating I solutions of $DMFT$ equations. Boundaries for this area are obtained from position of the top of lower Hubbard band for I-phase and from the position of quasiparticle peak at very small doping for M-phase. Comparison of energies for both solutions shows that in whole coexistence area metallic phase has lower energy than insulating one [121].

In Fig. 3.20 a similar phase diagram on the plane (μ, U) for $T = 0$ calculated by $DMFT(DMRG)$ method is presented [152]. $DMRG$ method for effective impurity problem has certain advantages comparing with NRG method that is aimed on spectra reproducing for small frequency values in quasiparticle peak area. In contrast to this $DMRG$ can reproduce also noncoherent Hubbard bands too. This method was tested earlier for half-filled Hubbard model [153]. It was found also to be very effective for one-dimensional strongly correlated systems [154, 155].

Figure 3.20 shows that metallic phase exists for $\mu > \mu_{c1}(U)$ and insulating one for $\mu < \mu_{c2}(U)$. Between $\mu_{c1}(U)$ and $\mu_{c2}(U)$ both phases coexist. This diagram agrees with obtained earlier in [121, 150]. One should note that both phases were supposed to be in paramagnetic state. It is known that in Hubbard model insulating ground state is antiferromagnetic so those diagrams should be correspondingly modified.

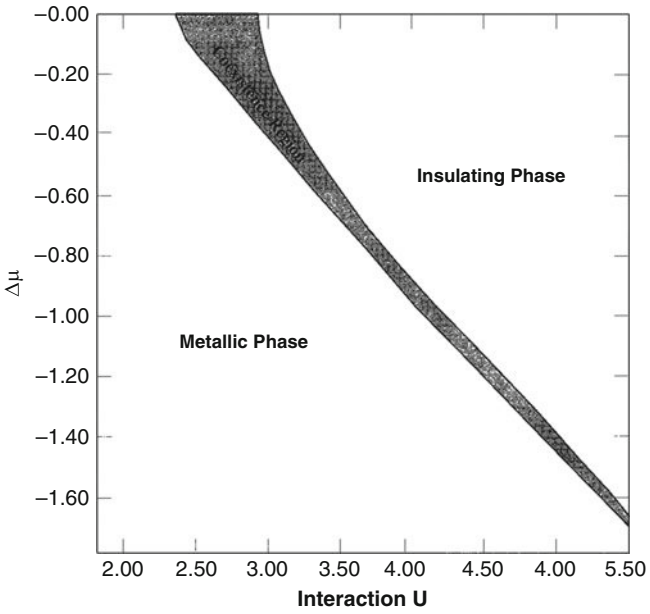

Fig. 3.19. Phase diagram of Hubbard model at $T = 0$ on the plane (μ, U) [121]. $\Delta\mu = \mu - U/2$

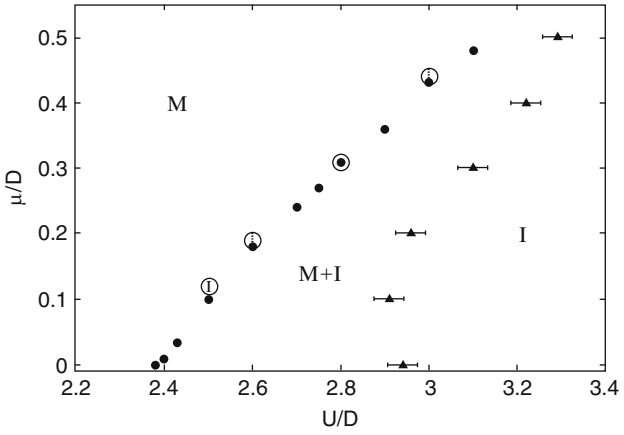

Fig. 3.20. Phase diagram of Hubbard model at $T = 0$ on the plane (μ, U) [151]. The *circles* and *triangles* define the boundaries for intervals $U_{c1}(\mu) \leq U \leq U_{c2}(\mu)$ where *DMFT* equations have two solutions

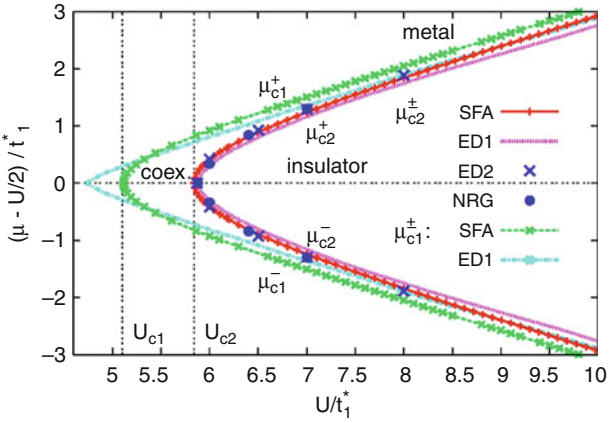

Fig. 3.21. Paramagnetic phase diagram of Hubbard model for $T = 0$ on the plane (μ, U) [157]

DMRG results agree with recent Hubbard model calculations by *SFA* method [156] (Fig. 3.21). The calculations were performed for semielliptical noninteracting density of states corresponding to Bethe lattice in $d = \infty$ limit.

At $T = 0$ and half-filling when $\mu = U/2$ the system is insulating at $U > U_{c2}$ where $U_{c2} \approx 5.84t_1^*$ (compare with Fig. 3.15). At deviation from half-filling chemical potential jumps from $\mu = \mu_{c2}^-$ to μ_{c2}^+ when number of electrons n approaches 1 from below or from above. Hence at $\mu_{c2}^- < \mu < \mu_{c2}^+$ the system is insulating, for $\mu_{c1}^- < \mu < \mu_{c2}^-$ and $\mu_{c1}^+ < \mu < \mu_{c2}^+$ metallic and insulating phases coexist and outside of this intervals metallic phase is stable. Appearance of metallic phase at $\mu = \mu_{c2}^{\pm}$ is due to "midgap states" development and disappearance of insulating phase at $\mu = \mu_{c1}^{\pm}$ happens because chemical potential μ approaches energy gap boundaries.

At final temperature phase separation area appears close to $n = 1$ (Fig. 3.22). This area extends significantly with T increase if next-nearest neighbors hoppings are taken into account. This hoppings lead to frustration and break electron-hole symmetry resulting in phase diagram asymmetric relative to $n = 1$ point that is typical for real strongly correlated material based on d-elements compounds.

DMFT is approximate theory when applied to real systems with a final space dimension however this method has significant advantages in describing strongly correlated materials comparing with other approaches. Its equations have two exact limits: at $U = 0$ (free electrons limit) and $t = 0$ (atomic limit). For final U values it can be considered as an interpolation approach taking into account both itinerant and localized character of electronic states in strongly correlated systems. Important fact is that all sum rules and analytical properties for electronic Green functions are satisfied in *DMFT*. The most significant result of *DMFT* is half-filled Hubbard model spectral evolution with

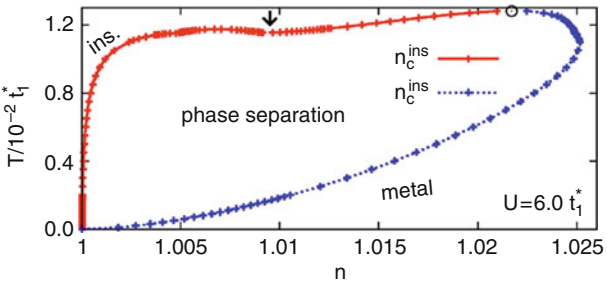

Fig. 3.22. (T, n) phase diagram for $U = 6t_1^*$. Phase separation area is explicitly shown [157]

U variation from insulating state with an energy gap between Hubbard bands to metallic state with quasiparticle peak on Fermi level. In earlier theories those two regimes were described by completely different approaches: decoupling of Green functions (so called Hubbard III approximation) for insulator and Gutzwiller method for quasiparticle states. *DMFT* can describe both regimes in the same formalism and reproduces gradual transition between them. Neglect of spatial correlations in *DMFT* seems to be not very high price for such ability. Moreover there are few versions of taking into account spatial correlations in *DMFT* and we will discuss them later.

3.4.3 Spin-Polarized Case

In this section we will consider spin-polarized state in Hubbard model. Such state can appear with external magnetic field or due to spontaneous magnetization leading to ferromagnetism or antiferromagnetism. In *DMFT* spin-polarized state is described by equations for spin dependent Green functions and self-energy:

$$G_\sigma(\mathbf{k}, i\omega_n) = \frac{1}{i\omega_n + \mu + \sigma h - \Sigma_\sigma(i\omega_n) - \varepsilon_\mathbf{k}}, \tag{3.4.149}$$

$$G_\sigma^{\mathrm{loc}}(i\omega_\mathbf{k}) = \sum_\mathbf{k} \frac{1}{i\omega_n + \mu + \sigma h - \Sigma_\sigma(i\omega_n) - \varepsilon_\mathbf{k}}. \tag{3.4.150}$$

Local Green function $G_\sigma^{\mathrm{loc}}(i\omega_n)$ is identified with effective Anderson impurity *GF*:

$$G_\sigma^{\mathrm{loc}}(i\omega_n) = \frac{1}{\mathcal{G}_{0\sigma}^{-1}(i\omega_n) - \Sigma_\sigma(i\omega_n)}, \tag{3.4.151}$$

where noninteracting auxiliary impurity model *GF* $\mathcal{G}_{0\sigma}(i\omega_n)$ is expressed via spin dependent hybridization function $\Delta_\sigma(i\omega_n)$:

$$\mathcal{G}_{0\sigma}^{-1}(i\omega_n) = i\omega_n + \mu + \sigma h - \Delta_\sigma(i\omega_n), \tag{3.4.152}$$

with effective action defined by expression:

$$S_{\text{eff}} = S_{\text{atom}} + \int_0^\beta \mathrm{d}\tau \int_0^\beta \mathrm{d}\tau' \sum_\sigma c_\sigma^+(\tau)\Delta_\sigma(\tau - \tau')c_\sigma(\tau'), \qquad (3.4.153)$$

where S_{eff} is action for impurity variables only with Coulomb interaction taken into account. Equations (3.4.149)–(3.4.153) are the same as original *DMFT* equations described in Sect. 3.1 but with explicit spin direction dependence.

Using these equations the role of magnetic field for strongly correlated electrons was investigated in [158] with impurity problem solved by *NRG*. Later we will describe results showing magnetic field influence on electronic density of states and effective electron mass. In Fig. 3.23 calculated spectral function in magnetic field is presented for both spin directions. For all cases sharp

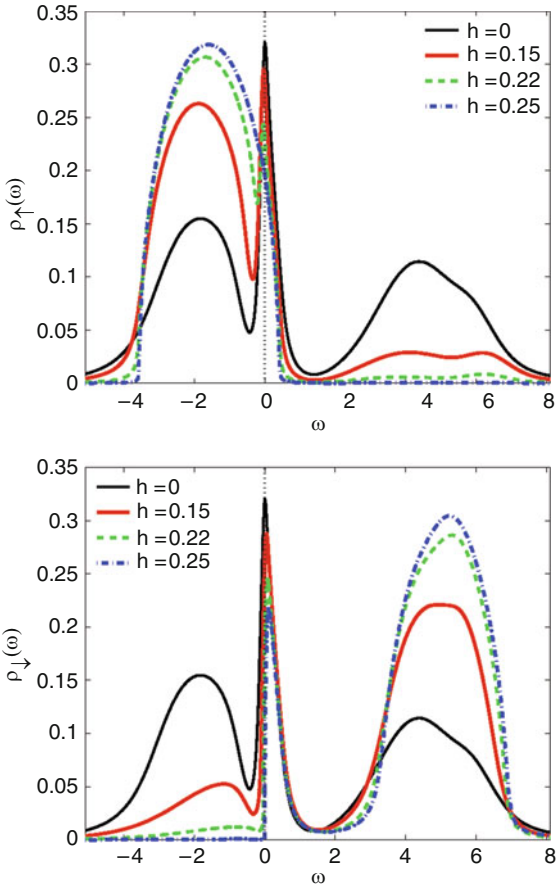

Fig. 3.23. Density of states for spin ↑ (*upper panel*) and spin ↓ (*lower panel*) in Hubbard model for $U = 6t$ and $n = 0.95$ at various magnetic field h values. All energies are in the units of t [158]

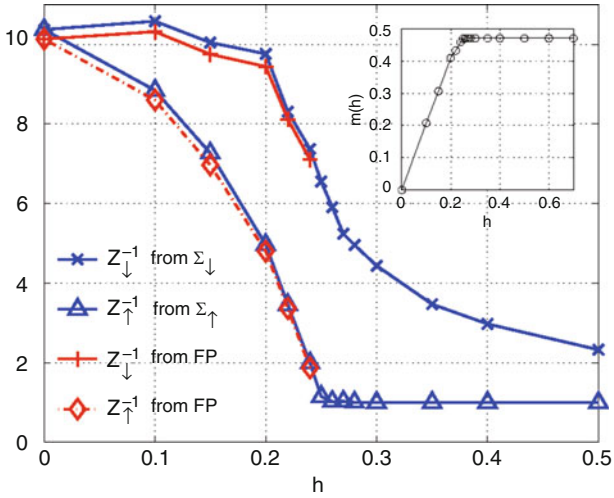

Fig. 3.24. Effective electron mass for both spin projections as a function of magnetic filed h for the same parameters as for Fig. 3.23 [158]. At the inset polarization as a function of the field is shown

quasiparticle peak and two Hubbard bands are observed. Magnetic field redistribute electronic states increasing occupancy for electrons with spin along the field and decreasing it for opposite spin direction. Spectral density lost in lower Hubbard band are transfered to upper Hubbard band. With field strength increase a tendency to full spin-polarization is developing but central quasiparticle peak does not disappear while its width is decreasing.

Using (3.3.146) one can calculate central peak intensity Z_σ for both spin projections and estimate quasiparticle effective mass m_σ^*:

$$m_\sigma^* = Z_\sigma^{-1}, \tag{3.4.154}$$

as a function of magnetic field that is shown in Fig. 3.24. For both spin projections effective mass decreases with field increase and $m_\downarrow > m_\uparrow$. As one can see in Fig. 3.24 inset for field values $h > 0.2$ magnetization is close to saturation because such very high field value corresponds to $0.2t$ that is an order of 1 eV. In [158] there were also investigated longitudinal and transverse susceptibilities and comparison was done with earlier polarized *DMFT* problem study. Those works were stimulated by experimental studies for "heavy fermion" materials where the influence of magnetic field on carriers effective mass was measured.

Let us consider now spontaneous magnetization (ferromagnetism). In *DMFT* this problem was studied intensively (see [159]) and we will discuss results of the most recent study [159]. In this work the case $U \to \infty$ near half filling was considered where according to Nagaoka theorem [160] saturated ferromagnetism should be realized. *DMFT* equations (3.4.149)–(3.4.153) were

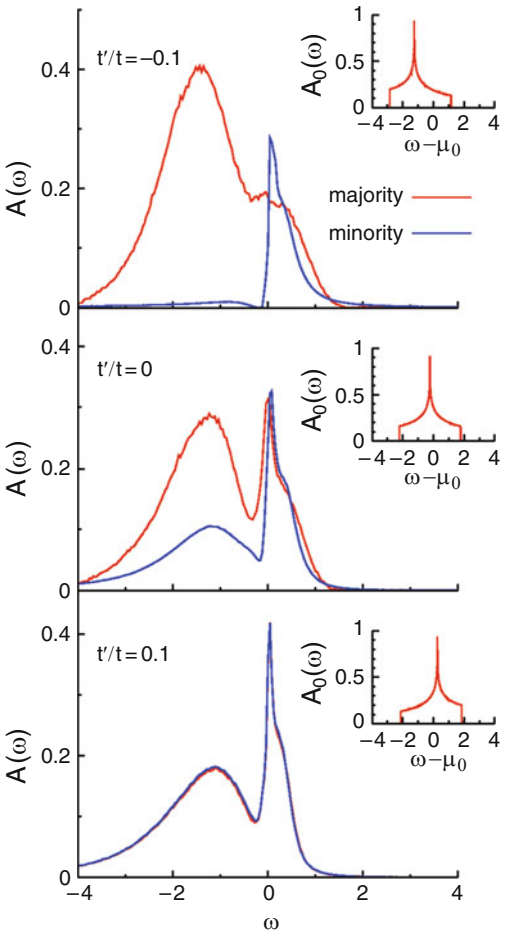

Fig. 3.25. Spectral function $A(\omega)$ for three values of t'/t and fixed occupancy value $n = 0.85$ for Hubbard model at $U = \infty$ [159]. Calculations were performed for $T = 0.01t$. In the insets noninteracting densities of states for two-dimensional Hubbard model used in calculations are shown

used here and effective Anderson impurity problem was solved by $CT-QMC$ method that allowed to treat very low temperatures ($T = 0.001t$). It was found that next-nearest neighbors hoppings t' should be taken into account in this case in addition to nearest neighbors hoppings t. In Fig. 3.25 calculation results are presented for positive and negative t'/t values in comparison with $t' = 0$ case. In all cases quasiparticle peak on the Fermi level is present with lower Hubbard bands. Upper Hubbard band is absent because of $U \to \infty$ condition.

One can see that for $t' = 0$ there is nonsaturated ferromagnetism while for negative t'/t ferromagnetism is nearly saturated. However for positive t'/t

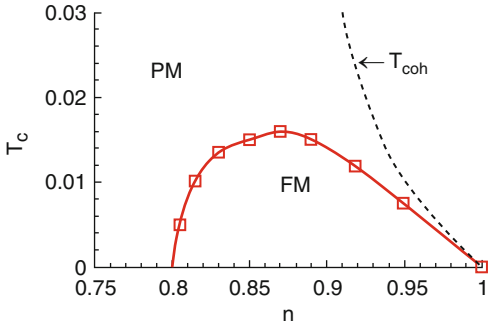

Fig. 3.26. Phase diagram of Hubbard model on the plane (T, n) for $U = \infty$ from $DMFT(CT-QMC)$ calculations [159]

ferromagnetism is absent. So asymmetric DOS for $t'/t \neq 0$ case strongly influence ferromagnetism formation.

In Fig. 3.26 phase diagram on (T, n) plane is shown. Calculations were performed for two-dimensional Hubbard model where according to Mermine-Ashcroft theorem there is no long-range order for final temperatures so the boundary between paramagnetic PM and ferromagnetic FM phases is a crossover to the phase with large ferromagnetic correlations length. For three-dimensional model this boundary would become real phase transition line.

3.5 Antiferromagnetism

3.5.1 *DMFT* Equations with Antiferromagnetic Order Parameter

In Sect. 3.1 $DMFT$ equations were formulated for Hubbard model assuming the absence of long-range order. In this section we describe $DMFT$ extensions to the cases with antiferromagnetic AFM order, superconducting order SC (Sect. 3.6), or both AFM and SC simultaneously. There are two ways to define the boundary between paramagnetic and magnetically ordered phases. The first one is to calculate paramagnetic susceptibility $\chi(\mathbf{q}, T)$ and from its divergence at some reciprocal space point $\mathbf{q} = \mathbf{Q}$ to determine system instability to Spin Density Wave (SDW) formation with $\mathbf{Q}$ vector. Another way is to break paramagnetic symmetry by introducing order parameter and to investigate system stability with respect to this order parameter. Practically, it is done by looking for $DMFT$ equations solutions with broken symmetry. We will consider bellow the last way that is described in review [8] for AFM and SC phases in $DMFT$.

In this section AFM order parameter problem is described following Bauer and Heuston [158]. Let us consider bipartite crystal lattice with two sublattices A and B, so that for the sites of sublattice A nearest neighbors

belong to sublattice B and vice versa. Alternated staggered magnetic field h_i is defined as:

$$H_i = \begin{cases} h, & i \in A \\ -h, & i \in B. \end{cases} \tag{3.5.155}$$

Hubbard model Hamiltonian with alternated field is:

$$\hat{H} = \sum_{ij\sigma} t_{ij}(\hat{c}^+_{Ai\sigma}\hat{c}_{Bj\sigma} + \hat{c}^+_{Bj\sigma}\hat{c}_{Ai\sigma}) + \sum_{i\alpha} U\hat{n}_{\alpha i\uparrow}\hat{n}_{\alpha i\downarrow} - \sum_{i\sigma}(\mu_\sigma \hat{c}^+_{Ai\sigma}\hat{c}_{Ai\sigma} + \mu_{-\sigma}\hat{c}^+_{Bi\sigma}\hat{c}_{Bi\sigma}), \tag{3.5.156}$$

Here summation is over sublattice sites i, j, $\mu_\sigma = \mu + \sigma h$ where μ is chemical potential and $\pm\sigma h$ is magnetic energy for electron with spin σ.

Hamiltonian (3.5.155) assumes matrix form of equations and Green functions. Let us introduce spinor $\hat{c}^+_{\mathbf{k}\sigma} = (\hat{c}^+_{A\mathbf{k}\sigma}, \hat{c}^+_{B\mathbf{k}\sigma})$ and matrix GF:

$$G^\sigma(\mathbf{k}, \tau - \tau') = -\langle T_\tau \hat{c}_{\mathbf{k}\sigma}(\tau)\hat{c}^+_{\mathbf{k}\sigma}(\tau')\rangle = \begin{pmatrix} G^\sigma_{AA} & G^\sigma_{AB} \\ G^\sigma_{BA} & G^\sigma_{BB} \end{pmatrix}. \tag{3.5.157}$$

Equations of motion could be derived for four GF components in a standard way. After Fourier transformation over $\tau - \tau'$ variables matrix equations for GF are:

$$\begin{pmatrix} i\omega_n + \mu_\sigma - \Sigma_{A\sigma}(\mathbf{k}, i\omega_n) & \epsilon_{\mathbf{k}} \\ \epsilon_{\mathbf{k}} & i\omega_n + \mu_{-\sigma} - \Sigma_{B\sigma}(\mathbf{k}, i\omega_n) \end{pmatrix} \begin{pmatrix} G^\sigma_{AA} & G^\sigma_{AB} \\ G^\sigma_{BA} & G^\sigma_{BB} \end{pmatrix} = \begin{pmatrix} 1 & 0 \\ 0 & 1 \end{pmatrix}. \tag{3.5.158}$$

Here we have introduced self-energy $\Sigma_{\alpha\sigma}(\mathbf{k}, i\omega_n)$ that is diagonal in spin indexes.

Matrix equation (3.5.158) is easily solved. Let us write solution for matrix element G^σ_{AA}=G^σ:

$$G^\sigma(\mathbf{k}, i\omega_n) = \frac{1}{\xi^\sigma_A(\mathbf{k}, i\omega_n)\xi^\sigma_A(\mathbf{k}, i\omega_n) - \epsilon^2_{\mathbf{k}}} \begin{pmatrix} \xi^\sigma_B(\mathbf{k}, i\omega_n) & -\epsilon_{\mathbf{k}} \\ -\epsilon_{\mathbf{k}} & \xi^\sigma_A(\mathbf{k}, i\omega_n) \end{pmatrix}, \tag{3.5.159}$$

where $\xi^\sigma_\alpha(\mathbf{k}, i\omega_n) = i\omega_n + \mu_\sigma - \Sigma_{\alpha\sigma}(\mathbf{k}, i\omega_n)$. According to basic $DMFT$ idea we ignore self-energy dependence on wave vector $\mathbf{k}$. Bipartite lattice symmetry means that $\Sigma_{A\sigma}(i\omega_n) = \Sigma_{B-\sigma}(i\omega_n) \equiv \Sigma_\sigma(i\omega_n)$ and hence:

$$\xi^\sigma_A(i\omega_n) = \xi^{-\sigma}_B(i\omega_n) \equiv \xi^\sigma(i\omega_n). \tag{3.5.160}$$

So lattice GF depends on one function $\Sigma_\sigma(i\omega_n)$ (or $\xi^\sigma(i\omega_n)$).

Let us introduce local GF by summation (3.5.158) over wave vector $\mathbf{k}$. For integral matrix element $\sum_{\mathbf{k}} G^\sigma_{AA}(\mathbf{k}, i\omega_n) \equiv G^\sigma_{\mathrm{loc}}(i\omega_n)$ expression is:

$$G^\sigma_{\mathrm{loc}}(i\omega_n) = \frac{\xi^{-\sigma}(i\omega_n)}{\sqrt{\xi^{-\sigma}(i\omega_n)\xi^\sigma(i\omega_n)}} = \int \mathrm{d}\epsilon \frac{\rho_0(\epsilon)}{\sqrt{\xi^{-\sigma}(i\omega_n)\xi^\sigma(i\omega_n)} - \epsilon}, \tag{3.5.161}$$

where summation over $\mathbf{k}$ is replaced by integration over ϵ with noninteracting density of states $\rho_0(\epsilon)$.

It is assumed in *DMFT* that local *GF* $G^{\sigma}_{\mathrm{loc}}(i\omega_n)$ and self-energy $\Sigma^{\sigma}(i\omega_n)$ are identical with corresponding values for effective impurity model that is in this particular case Anderson model in magnetic field with Hamiltonian:

$$\hat{H}_{\mathrm{SIAM}} = \sum_{\mathbf{k}\sigma} \epsilon_{\mathbf{k}\sigma} \hat{c}^{+}_{\mathbf{k}\sigma} \hat{c}_{\mathbf{k}\sigma} + \sum_{\mathbf{k}\sigma} \left[V_{\mathbf{k}\sigma} \hat{c}^{+}_{\mathbf{k}\sigma} \hat{d}_{\sigma} + V^{*}_{\mathbf{k}\sigma} \hat{d}^{+}_{\sigma} \hat{c}_{\mathbf{k}\sigma} \right] + \sum_{\sigma} \epsilon_{d\sigma} \hat{d}^{+}_{\sigma} \hat{d}_{\sigma} + U \hat{n}_{\uparrow} \hat{n}_{\downarrow}, \tag{3.5.162}$$

where $\epsilon_{d\sigma} = \epsilon_d - \sigma h, \epsilon_{\mathbf{k}\sigma} = \epsilon_{\mathbf{k}} - \sigma h$.

One-electron *GF* for this model is:

$$G^{\sigma}_{\mathrm{imp}}(i\omega_n) = \frac{1}{i\omega_n - \epsilon_{d\sigma} - \Delta^{\sigma}(i\omega_n) - \Sigma^{\sigma}(i\omega_n)}, \tag{3.5.163}$$

where

$$\Delta^{\sigma}(i\omega_n) = \sum_{\mathbf{k}} \frac{|V_{\mathbf{k}\sigma}|^2}{i\omega_n - \epsilon_{\mathbf{k}\sigma}} \tag{3.5.164}$$

is hybridization function depending on spin σ.

According to general *DMFT* idea we introduce noninteracting impurity *GF* with spin dependence $\mathcal{G}^{\sigma}_0(i\omega_n)$. Self-consistency conditions for lattice and effective impurity models are defined by two equations:

$$G^{\sigma}_{\mathrm{imp}}(i\omega_n) = G^{\sigma}_{\mathrm{loc}}(i\omega_n), \tag{3.5.165}$$

$$(\mathcal{G}^{\sigma}_0(i\omega_n))^{-1} = (G^{\sigma}_{\mathrm{loc}}(i\omega_n))^{-1} + \Sigma^{\sigma}(i\omega_n). \tag{3.5.166}$$

These equations define two functions: $\Sigma^{\sigma}(i\omega_n)$ and $\mathcal{G}^{\sigma}_0(i\omega_n)$. Using (3.5.163) and (3.5.166) we can derive relation between $\mathcal{G}^{\sigma}_0$ and Δ^{σ}:

$$\Delta^{\sigma}(i\omega_n) = i\omega_n + \mu_{\sigma} - (\mathcal{G}^{\sigma}_0(i\omega_n))^{-1}. \tag{3.5.167}$$

With this relation *DMFT* equations (3.5.165) and (3.5.166) could be considered as equations system for two variables $\Delta^{\sigma}(i\omega_n)$ $\Sigma^{\sigma}(i\omega_n)$.

Impurity model can be solved by *QMC*, *NRG*, or some other method. Using *NRG* one works with retarded *GF* obtained by analitical continuation $i\omega \to \omega + i\delta$ and in this case one solves the equations for two variables $\Delta^{\sigma}(\omega)$ and $\Sigma^{\sigma}(\omega)$. For some starting $\Delta^{\sigma}(\omega)$ value self-energy $\Sigma^{\sigma}(\omega)$ is calculated from impurity model solution, then new $G^{\sigma}_{\mathrm{loc}}(\omega)$ is found and using (3.5.166) and (3.5.167) new value for $\Delta^{\sigma}(\omega)$ is calculated. Iterations continue till stable solution is found. For *AFM* case one should start from small alternated magnetic field h value and then to switch off magnetic field in self-consistency iterations to reproduce spontaneous magnetization.

3.5.2 *NRG* Method Results for *AFM* Phase

Detailed *DMFT* investigation of *AFM* phase was done in [158] using effective impurity model solution by *NRG* method. Calculation were performed for Gaussian noninteracting density of states corresponding to hypercubic lattice in $d = \infty$ limit. Band width value was $W = 4$ assuming normalized hopping $t^* = 1$.

In Fig. 3.27 calculated spectral functions for spins $\uparrow$ and $\downarrow$ are shown. One can see that with decreasing magnetic field h value the curves are converging to $h = 0$ values. Spectral function are different for spins $\uparrow$ and $\downarrow$ because spontaneous magnetization on site A m_A:

$$m_A = \frac{1}{2}(n_{A\uparrow} - n_{A\downarrow}), \tag{3.5.168}$$

was found in calculations that does not disappear at $h = 0$.

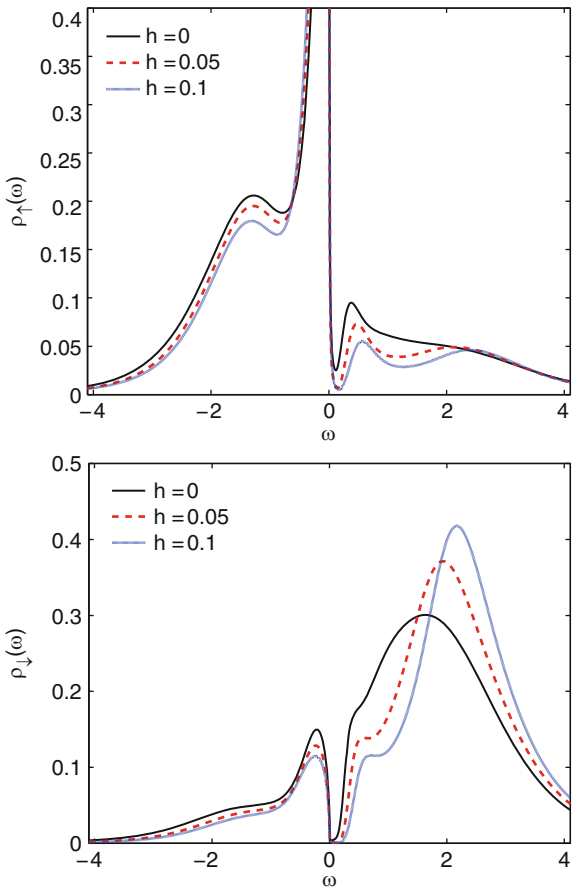

Fig. 3.27. Spectral function for electrons with spins $\uparrow$ and $\downarrow$ on the sublattice A for various values of applied alternating magnetic field h and parameter values $U = 3$ and $\delta = 0.05$ [158]

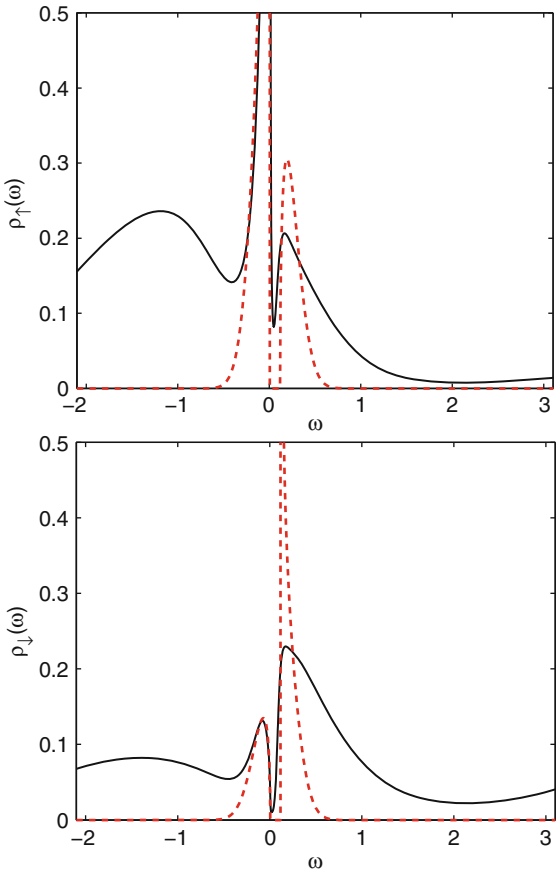

Fig. 3.28. Spectral function for electrons with spins ↑ and ↓ for $U = 6$ and $n = 0.9$ (*solid lines*) and free quasiparticles at $U = 0$ and $\delta = 0.1$ (*dashed lines*) [158]

With increasing U value quasiparticle peak at Fermi level becomes more pronounced (Fig. 3.28). On this figure the curves for free quasiparticles in alternated magnetic field corresponding to spontaneous magnetization are shown by dashed lines. Comparing two curves one can separate the influence of magnetic field and Coulomb interaction on the spectra. The alternated magnetic field results in energy bands splitting and opening a gap while Coulomb interaction results in Hubbard bands formation similar to paramagnetic case.

Quasiparticle spectrum is defined by lattice *GF* (3.5.159). Let us calculate matrix element of this *GF* for *A*-sublattice site. Using (3.5.160) we have:

$$G^{\sigma}_{AA}(\mathbf{k},\omega) = \frac{\xi^{-\sigma}(\omega)}{\xi^{-\sigma}(\omega)\xi^{\sigma}(\omega) - \varepsilon^2_{\mathbf{k}}}. \tag{3.5.169}$$

Fermi surface is defined by equation

$$\varepsilon_{\mathbf{k}}^2 = \xi^{\sigma}(0)\xi^{-\sigma}(0). \tag{3.5.170}$$

According to Luttinger theorem the volume inside Fermi surface is the same for interacting and noninteracting particles. As self-energy $\Sigma^{\sigma}(\omega)$ does not depend on wave vector $\mathbf{k}$ Fermi surface does not change with interaction and (3.5.170) can be rewritten:

$$(\mu_{\uparrow} - \Sigma_{\uparrow}(0))(\mu_{\downarrow} - \Sigma_{\downarrow}(0)) = \mu_0^2. \tag{3.5.171}$$

where μ_0 is noninteracting particles chemical potential $\mu_0^2 = \varepsilon_{\mathbf{k}_F}^2$ determined by the particles number condition

$$n = 2\int_{-\infty}^{\mu_0} \rho_0(\omega)\mathrm{d}\omega. \tag{3.5.172}$$

In order to obtain dispersion for quasipaticles near Fermi level let us expand in (3.5.169) function $\xi^{\sigma}(\omega)$ in series over ω:

$$\xi^{\sigma}(\omega) = \omega(1 - \Sigma'_{\sigma}(0)) + \mu_{\sigma} - \Sigma_{\sigma}(0) \equiv Z_{\sigma}^{-1}(\omega + \tilde{\mu}_{0\sigma}), \tag{3.5.173}$$

where $\tilde{\mu}_{0\sigma} = Z_{\sigma}(\mu - \Sigma_{\sigma}(0))$, $Z_{\sigma}^{-1} = 1 - \Sigma'_{\sigma}(0)$. Then poles condition for GF (3.5.169)

$$\xi^{\sigma}(\omega)\xi^{-\sigma}(\omega) - \varepsilon_{\mathbf{k}}^2 = 0 \tag{3.5.174}$$

defines quasiparticle spectrum (dispersion law)

$$E_{\mathbf{k}}^{\pm} = -\tilde{\mu} \pm \sqrt{\tilde{\varepsilon}_{\mathbf{k}} + (\Delta\tilde{\mu})^2} \tag{3.5.175}$$

where

$$\tilde{\varepsilon}_{\mathbf{k}} = \sqrt{Z_{\uparrow}Z_{\downarrow}}\varepsilon_{\mathbf{k}},\ \Delta\tilde{\mu} = \frac{1}{2}(\tilde{\mu}_{0\uparrow} - \tilde{\mu}_{0\downarrow}),\ \tilde{\mu} = \frac{1}{2}(\tilde{\mu}_{0\uparrow} + \tilde{\mu}_{0\downarrow}), \tag{3.5.176}$$

here $\tilde{\mu}$ is quasiparticles chemical potential.

Deriving (3.5.174) we have neglected $\mathrm{Im}\Sigma(\omega)$ that defines quasiparticles decay because it should be small near the Fermi energy ($\mathrm{Im}\Sigma(\omega) = 0$ exactly on Fermi level). Using dispersion (3.5.175) one can calculate quasiparticle effective mass by differentiating $E_{\mathbf{k}}^{\pm}$ over $\varepsilon_{\mathbf{k}}$. From derivatives ratio $\mathrm{d}E_{\mathbf{k}}^{\pm}/\mathrm{d}\varepsilon_{\mathbf{k}}$ for interacting and noninteracting particles on Fermi level we obtain effective mass ratio:

$$\frac{m^*}{m} = \frac{1}{\sqrt{Z_{\uparrow}Z_{\downarrow}}}\frac{|\tilde{\mu}|}{\sqrt{\tilde{\mu}_{0\uparrow}\tilde{\mu}_{0\downarrow}}}. \tag{3.5.177}$$

In contrast to paramagnetic case effective mass is defined not only renormalization parameter Z but also by renormalized chemical potentials $\tilde{\mu}_{0\sigma}$.

In Fig. 3.29 dispersion curves are, presented, calculated from peaks positions in $\varepsilon_{\mathbf{k}}$ as a function of $\varepsilon_{\mathbf{k}}$ (solid lines) together with noninteracting particle

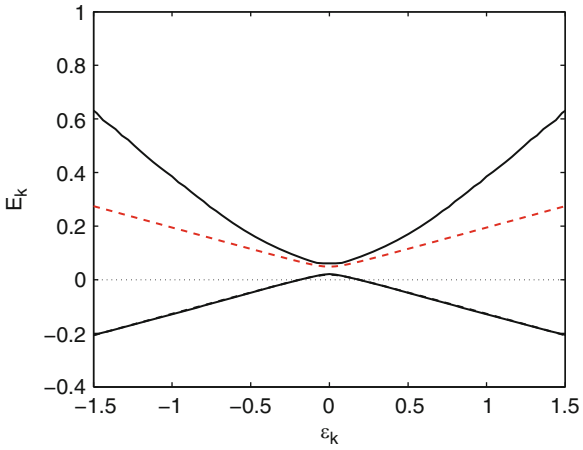

Fig. 3.29. Peak position $E^{\pm}_{\mathbf{k}}$ in spectral function $\rho_{\mathbf{k}\sigma}(\omega)$ (*solid line*) for $U = 6$ and $\delta = 0.125$ in comparison with free particles dispersion curves (*dashed lines*) [158]

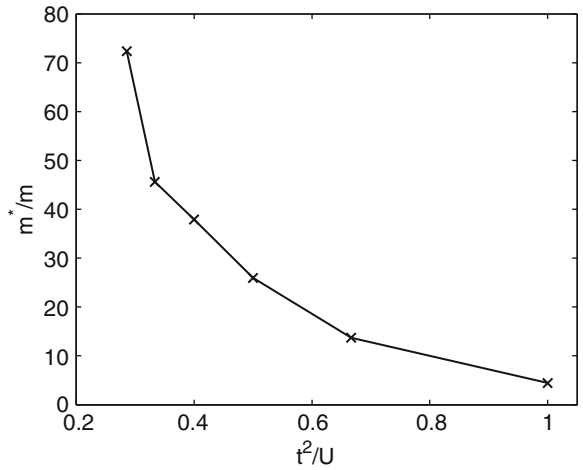

Fig. 3.30. Quasiparticles effective mass as a function of effective exchange parameter t^2/U for $\delta = 0.075$ [158]

curves ($\Sigma(\omega) = 0$) in alternated magnetic field corresponding to spontaneous magnetization (dashed lines). Second dashed line conside with lower spectrum branch. In [158] quasiparticle peak width was calculated and was shown that its value is small near $\varepsilon_{\mathbf{k}} = 0$ but strongly increases with $|\varepsilon_{\mathbf{k}}|$ increase.

Comparing solid and dashed lines slopes in Fig. 3.29 one can see that effective mass m^*/m increase with U. That is also follows from Fig. 3.30 where m^*/m is presented as a function of effective exchange parameter t^2/U. With doping value increase m^*/m decreases for fixed U. Authors of [158] have found that Luttinger theorem for total particle number is obeyed with calculations accuracy. Boundary line on the plane (U, δ) separating antiferromagnetic and

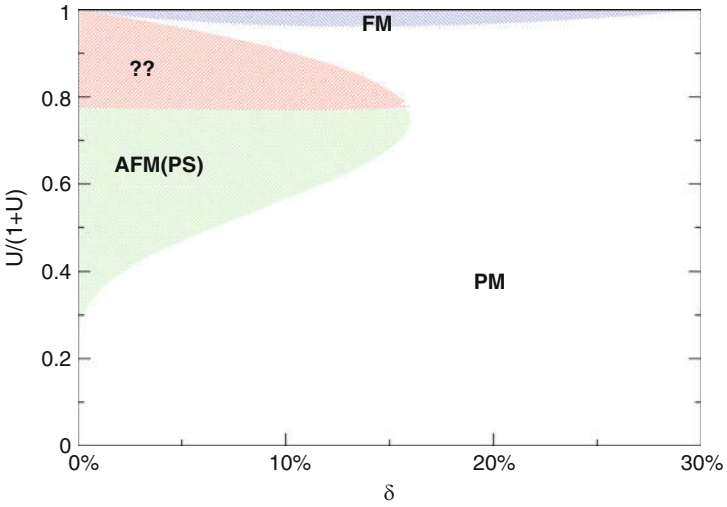

Fig. 3.31. Schematic phase diagram at $T = 0$ calculated by $DMFT(NRG)$ in [161]. Energy unit is t^*. At y-coordinate $U/(1 + U)$ is shown to present whole interval $0 < U < \infty$

paramagnetic phases calculated for $0 < U < 1.5W$ and doping $0 < \delta < 0.2$ agrees with earlier results of [161].

In Fig. 3.31 phase diagram is presented for magnetic ordering in Hubbard model with Gaussian noninteracting density of states corresponding to hypercubic lattice in $d = \infty$ limit obtained in [161] by $DMFT - NRG$ calculations for $T = 0$. For small but final doping antiferromagnetic state preserves till $U < 4$. Sublattice magnetization in this case falls with δ in the same way as for mean-field theory and vanishes for $\delta = 0.06$ at $U = 1$ and $\delta = 0.16$ for $U = 3$.

For $U > 4$ system has a tendency to magnetic instability but it is not clear to what particular type of magnetic ordering. Ferromagnetic state does not appear yet but for this intermediate U values noncommensurate magnetic structures and phase separation can happen.

For very large values $U > 25$ ferromagnetic ordering appears for doping $0 < \delta < 0.3$. For fixed U magnetization shows a tendency to saturation for small δ however with indetermined critical occupation value. In ferromagnetic phase an essential redistribution for spectral function with spins $\uparrow$ and $\downarrow$ is observed and ferromagnetic ordering does not means simple bands shift as in mean-filed Stoner theory.

$DMFT(NRG)$ results gave only qualitative pattern of magnetic phase diagram for Hubbard model. There are still many unanswered questions: the character of phase transition between AFM and FM phases, magnetic state for intermediate values $U \approx W$, where on the plane (U, δ) there are areas with phase separation and so on.

3.6 Superconductivity in Two-Dimensional Hubbard Model

3.6.1 *DMFT* Equations for Superconducting State

Discovery of high-temperature superconductivity in cuprates inspired many works investigating possibility of superconducting state in two-dimensional Hubbard model with pairing mechanism due to Coulomb interaction. As it was established in the experiment (see reviews [42,162,163]) superconducting state in cuprates has order parameter with d-symmetry (later denoted as $d-SC$ state). Superconductivity in cuprates appears close to antiferromagnetic state and even partially overlaps with it. Typical phase diagram for hole doped cuprates is shown in the inset (b) in Fig. 3.32.

At weak Coulomb interaction ($U \ll W$) calculations by functional renorm-group method showed that two-dimensional Hubbard model has instabilities toward AFM and $d-SC$ states but this method cannot describe competition of those states and the possibility of mixed state at $T=0$. Coexistence possibility for AFM and $d-SC$ phases at deviation from half filling was investigated by various methods [164–166] for strong and intermediate Coulomb interaction ($U \approx W$). Those investigations will be discussed later and now we will describe in details $DMFT$ scheme for $d=2$ Hubbard model taking into

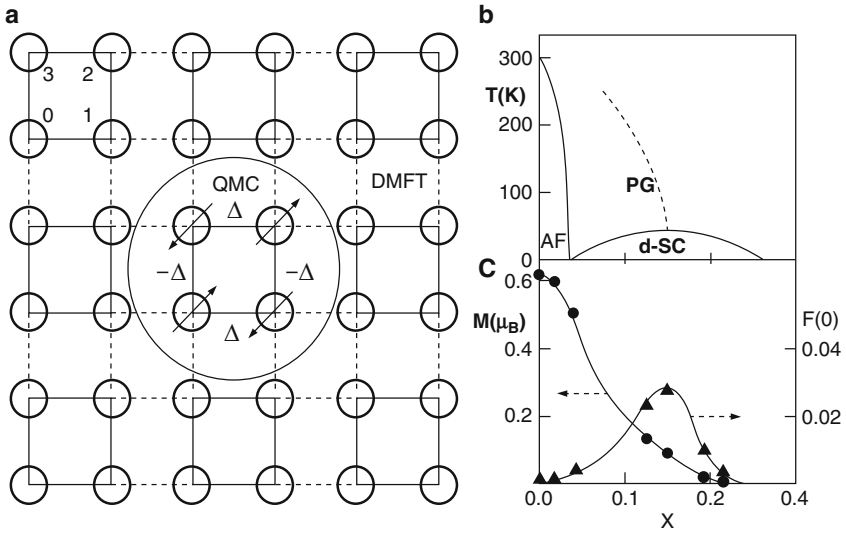

Fig. 3.32. Square lattice with four atom cluster. Denoted by a *circle cluster* is used as a local object (supersite) for model solution by $DMFT(QMC)$ method [167]. *Arrows* show spin directions in AFM state, Δ is $d-SC$ order parameter. Sites numeration 0, 1, 2, 3 shown in left-upper corner is used in a text. In the inset (**b**) a typical phase diagram for cuprates is shown and in inset (**c**) doping dependence for magnetic and superconducting order parameters

account AFM and $d-SC$ order parameters developed by Lichtenstein and Katsnelson [167].

In Fig. 3.32 in a circle is shown 2×2 plaquet (cluster) with four atoms that was chosen as a local object in the $DMFT$ scheme. In standard $DMFT$ such an object is a single impurity site. It is natural to introduce superspinor $c_i^+ = \{c_{i\alpha}^+\}$ where $\alpha = 0, 1, 2, 3$ (spin indexes are not shown). If spin degrees of freedom are taken into account then such spinor has eight components corresponding to electron creation operators on cluster sites.

Electronic GF for Hubbard model in matrix form is

$$G(\mathbf{k}, i\omega_n) = (i\omega_n + \mu - h(\mathbf{k}, i\omega_n))^{-1}, \tag{3.6.178}$$

where $h(\mathbf{k}, i\omega_n)$ is hopping matrix for electrons on the lattice. In nearest-neighbors approximation this matrix is

$$h(\mathbf{k}, i\omega_n) = \begin{pmatrix} \Sigma_0 & t_x K_x^+ & 0 & t_y K_y^+ \\ t_x^* K_x^- & \Sigma_0 & t_y K_y^+ & 0 \\ 0 & t_y^* K_x^- & \Sigma_0 & t_x^* K_x^- \\ t_y^* K_y^- & 0 & t_x K_x^+ & \Sigma_0 \end{pmatrix}, \tag{3.6.179}$$

where

$$K_{x(y)}^{\pm} = 1 + \mathrm{e}^{\pm k_{x(y)} a}, \tag{3.6.180}$$

a is lattice constant. In cluster $DMFT$ in addition to on-site self-energy Σ_0 intersite components Σ_x and Σ_y are introduced. They do not depend on wave vector $\mathbf{k}$ but only on frequency. Then self-energy is a matrix corresponding to plaquet cluster:

$$\Sigma(i\omega_n) = \begin{pmatrix} \Sigma_0 & \Sigma_x & 0 & \Sigma_y \\ \Sigma_x^* & \Sigma_0 & \Sigma_y & 0 \\ 0 & \Sigma_y^* & \Sigma_0 & \Sigma_x^* \\ \Sigma_y^* & 0 & \Sigma_x & \Sigma_0 \end{pmatrix}, \tag{3.6.181}$$

With respect to spin variables every element of this matrix and also (3.6.179) matrix is itself a matrix of 2×2 size. Off-diagonal self-energy elements will result in renormalization of effective hopping matrix (3.6.179):

$$t_x = t + \Sigma_x, \; t_y = t + \Sigma_y. \tag{3.6.182}$$

In cluster $DMFT$ or in Dynamical Cluster Approximation (DCA) [168] matrix "bath" GF $\mathcal{G}$ is introduced that describes effective interaction of cluster with a lattice:

$$\mathcal{G}^{-1}(i\omega_n) = G^{-1}(i\omega_n) + \Sigma(i\omega_n). \tag{3.6.183}$$

Here local matrix GF is used obtained by lattice GF summation over wave vector:

$$G_{\alpha\beta}(i\omega_n) = \sum_{\mathbf{k}} G_{\alpha\beta}(\mathbf{k}, i\omega_n). \tag{3.6.184}$$

Equations (3.6.183) and (3.6.184) are cluster generalization of standard *DMFT* equations defined in Sect. 3.1. These matrix equations allow to study Hubbard model with *AFM* and $d-SC$ order parameters because those parameters can be calculated from cluster atomic states (see Fig. 3.32).

We use generalized Nambu technique [169,170] and introduce superspinor:

$$\Psi_i^+ = (c_{i\uparrow}^+, c_{i\downarrow}^+, c_{i\uparrow}, c_{i\downarrow}) \tag{3.6.185}$$

and electronic *GF* on spinors Ψ_i and Ψ_j^+:

$$\hat{G}_{ij}(\tau,\tau') = -\langle T_\tau \Psi_i(\tau)\Psi_j^+(\tau')\rangle. \tag{3.6.186}$$

Let us separate normal and anomalous parts of *GF*. After Fourier transformation in site indexes one can write:

$$\hat{G}(\mathbf{k},\tau,\tau') = \begin{pmatrix} G(\mathbf{k},\tau,\tau') & F(\mathbf{k},\tau,\tau') \\ F^+(\mathbf{k},\tau,\tau') & -G(-\mathbf{k},\tau',\tau) \end{pmatrix}, \tag{3.6.187}$$

where

$$\begin{aligned} G(\mathbf{k},\tau,\tau') &= -\langle T_\tau c_{\mathbf{k}}(\tau)c_{\mathbf{k}}^+(\tau')\rangle \\ F(\mathbf{k},\tau,\tau') &= -\langle T_\tau c_{\mathbf{k}}(\tau)c_{\mathbf{k}}(\tau')\rangle \end{aligned} \tag{3.6.188}$$

are matrices in spin and "orbital" space (by "orbitals" here we call cluster sites indexes). Then Green functions G and F are 8×8 matrices. By summing expression (3.6.187) over $\mathbf{k}$ we define local *GF*:

$$\hat{G}(\tau,\tau') = \begin{pmatrix} G(\tau,\tau') & F(\tau,\tau') \\ F^+(\tau,\tau') & -G(\tau',\tau) \end{pmatrix}. \tag{3.6.189}$$

Let us define now order parameters (*OP*). Antiferromagnetic *OP* is an average $\langle c_{i\uparrow}^+ c_{j\downarrow}\rangle$ and superconducting *OP* is $\Delta_{ij} = \langle c_{i\downarrow}c_{j\uparrow}\rangle$. For singlet d-symmetry *OP* nonzero elements are:

$$\Delta = \Delta_{01} = -\Delta_{12} = \Delta_{23} = -\Delta_{30}. \tag{3.6.190}$$

Hence matrix (3.6.189) of general *GF* can be reduced to 2×2 matrix:

$$G(\tau,\tau') = \begin{pmatrix} G_\uparrow(\tau,\tau') & F(\tau,\tau') \\ F^+(\tau,\tau') & -G_\downarrow(\tau',\tau) \end{pmatrix}, \tag{3.6.191}$$

and after Fourier transformation over $\tau-\tau'$ variables

$$G(i\omega_n) = \begin{pmatrix} G_\uparrow(i\omega_n) & F(i\omega_n) \\ F^+(i\omega_n) & -G_\downarrow^*(i\omega_n) \end{pmatrix}. \tag{3.6.192}$$

Let us formulate *DMFT* equations for superconducting phase. Generalization of matrix equation (3.6.183) for normal phase is super-matrix equation

including anomalous self-energy part $S(i\omega_n)$:

$$\hat{\mathcal{G}}^{-1}(i\omega_n) - \hat{G}^{-1}(i\omega_n) = \begin{pmatrix} \Sigma_\uparrow(i\omega_n) & S(i\omega_n) \\ S(i\omega_n) & -\Sigma_\downarrow^*(i\omega_n) \end{pmatrix}, \tag{3.6.193}$$

where $\Sigma_\sigma(i\omega_n)$ is defined by (3.6.181) matrix for one spin σ. Generalization of (3.6.178) for lattice *GF* is matrix equation

$$\hat{G}^{-1}(\mathbf{k}, i\omega_n) = \begin{pmatrix} i\omega_n + \mu - h(\mathbf{k}, i\omega_n) & S(\mathbf{k}, i\omega_n) \\ S(\mathbf{k}, i\omega_n) & i\omega_n + \mu + h^*(\mathbf{k}, i\omega_n) \end{pmatrix}, \tag{3.6.194}$$

where $S(\mathbf{k}, i\omega_n)$ is anomalous self-energy of lattice *GF* $\hat{G}(\mathbf{k}, i\omega_n)$ analogous to matrix equation (3.6.179).

As in standard *DMFT* lattice problem is mapped on numerical solution of a problem for cluster embedded in superconducting "bath." It can be solved by one of the methods developed for single impurity model described earlier.

Please note that cluster is embedded in effective "bath" defined by "non-interacting" electrons that should feel the order parameter. For our case with *AFM* and *d-SC OP* that is defined by two terms in "single-impurity" model Hamiltonian:

$$H_M = M \sum_\alpha (-1)^\alpha (n_{\alpha\uparrow} - n_{\alpha\downarrow}), \tag{3.6.195}$$

$$H_\Delta = \Delta \sum_{\alpha\beta} \zeta_{\alpha\beta} (c_{\alpha\uparrow} c_{\beta\downarrow} + c_{\beta\downarrow}^+ c_{\alpha\uparrow}^+), \tag{3.6.196}$$

where $\zeta_{\alpha\beta} = 1$ when sites α and β are nearest neighbors in direction x and $\zeta_{\alpha\beta} = -1$ when they are in direction y (see Fig. 3.32). M and Δ defined in expressions (3.6.195) and (3.6.196) are antiferromagnetic and superconducting order parameters.

3.6.2 Coexistence Problem for Superconducting and Antiferromagnetic Order Parameters

Lichtenstein and Katsnelson [167] calculated matrix *GF* using Hirsch–Fye *QMC* algorithm for impurity cluster embedded in the lattice with noninteracting electrons feeling superconducting fluctuations field. Imaginary time interval $0 \le \tau \le \beta$ was discretized on $L = 64$ time slices for $T = 1/\beta = 190$K. They obtained *DMFT* equations solutions with *AFM* or $d - SC$ order parameters. Phase diagram was calculated on the plane order parameter – deviation from half-filling δ, i.e., the curves $M(\delta)$ and $\Delta(\delta)$ where M is sublattice magnetization and Δ – superconducting gap value. There is an interval of δ where these curves overlap and so there is a possibility for both order parameters to coexist. Superconducting gap value Δ can serve as an estimation for superconducting transition temperature T_c and magnetization M – for Neel temperature T_N and so calculated phase digram with curves $M(\delta)$ and $\Delta(\delta)$ resembles experimental phase diagram with overlapping $T_N(\delta)$ and

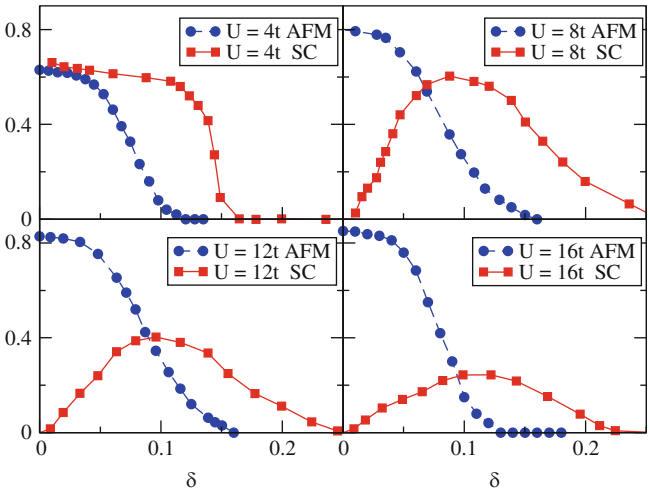

Fig. 3.33. *AFM* and $d-SC$ order parameters for two-dimensional Hubbard model for various values of Coulomb parameter $U/t = 4, 8, 12, 16$ calculated by *DMFT*(*ED*) method at $T = 0$ [166]. $d-SC$ order parameter values are enhanced 10 times

$T_c(\delta)$ curves. However direct comparison of the calculation results with experimental phase diagram for cuprates is not justified because *QMC* calculation temperature $T = 190\,\mathrm{K}$ is too large and to lower T is impossible because of "sign problem." To clarify coexistence problem for two phases there are needed calculations at $T = 0$.

Capone and Kotliar [166] have used the cluster Exact Diagonalization *ED* method and have solved *DMFT* equations for Hubbard model with two order parameters at $T = 0$. Their results are presented in Fig. 3.33.

A half-filling ($\delta = 0$) sublattice magnetization increases with U/t increase while with doping magnetization is suppressed and vanishes for $\delta \approx 0.14-0.16$ practically independent of U/t.

Superconducting OP Δ for small $U/t = 4$ decays with doping analogous with M. However situation changes drastically for large U/t where metal–insulator transition can happen even without magnetic ordering. For large U/t values Δ vanishes when the system is close to metal–insulator transition at $\delta \to 0$. With δ increase Δ shows a maximum. At $U/t = 8, 12, 16\Delta(\delta)$ curve has bell-shaped form and resembles experimental curve for cuprates.

In Fig. 3.33 pure OP are shown where in the system there is either *AFM* or $d-SC$ state. In [166] there were also obtained *DMFT* equations solutions with both OP and conditions for their coexistence were clarified. Stability of mixed $AFM + d-SC$ state essentially depends on Coulomb interaction U/t value with small U/t favorable for coexistence. For $U/t = 4$ mixed solutions were obtained and mixed phase energy where $d-SC$ dominates is lower than

for pure $d-SC$ state. In the same time admixture of superconducting order parameter to AFM state is very small.

This analysis shows that for $U/t = 12, 16$ pure phases have lower energy than mixed states and in overlapping area AFM and $d-SC$ states are competing and do not mix. Phase transition between them for small δ should be of the first order with phase separation. For small $U/t \leq 8$ two OP can coexist and system gradually evolves with δ from AFM to $d-SC$ state.

3.7 Transport Properties and Susceptibility

3.7.1 Optical Conductivity

In $d = \infty$ limit description is simplified not only for one-particle excitations (because self-energy of electronic GF does not depends on wave vector) but also for transport properties and dynamical susceptibilities. This simplification is because of the fact that two-particle vertexes are local functions in this limit [5,171,172]. Following [5] we will give derivation for optical conductivity and magnetic susceptibility with local vertex.

Conductivity tensor $\sigma_{\alpha\beta}$ is defined via susceptibility (retarded GF) of the type current–current according to [123]:

$$\sigma_{\alpha\beta}(\omega) = \frac{1}{N}\mathrm{Re}\left\{\frac{1}{i\omega} \ll j_\alpha | j_\beta \gg_{\omega+i\delta}\right\} \equiv \mathrm{Re}\tilde{\sigma}_{\alpha\beta}(\omega + i\delta). \tag{3.7.197}$$

General definition of retarded $GF \ll \ldots | \ldots \gg_{\omega+i\delta}$ is given in Appendix B. Current operator can be written as:

$$\mathbf{j} = \sum_{\mathbf{k},\sigma} \mathbf{v}_\mathbf{k} \hat{n}_{\mathbf{k},\sigma}, \tag{3.7.198}$$

where $\hat{n}_{\mathbf{k},\sigma}$ is particle number operator and $\mathbf{v}_\mathbf{k}$ is Fermi velocity that for Hubbard model is $\mathbf{v}_\mathbf{k} = \nabla t_\mathbf{k}$ ($t_\mathbf{k}$ is Fourier component of hopping matrix element t_{ij}). We are using unit system where $e = \hbar = 1$.

For simplicity let us consider hypercubic lattice with dimension d where second rank tensor is diagonal and expression for it is:

$$\mathrm{d}\tilde{\sigma}(z) = \frac{1}{N}\frac{1}{iz}\sum_\alpha \ll j_\alpha | j_\alpha \gg_z . \tag{3.7.199}$$

Here we have introduced complex frequency z. Then using expression (3.7.198) for current we express conductivity via GF "density–density":

$$\mathrm{d}\tilde{\sigma}(z) = \frac{1}{N}\frac{1}{iz}\sum_{\mathbf{k},\mathbf{k}'\sigma}\sum_\alpha v_{k_\alpha} v_{k'_\alpha} \ll n_{\mathbf{k}\sigma} | n_{\mathbf{k}'\sigma} \gg_z . \tag{3.7.200}$$

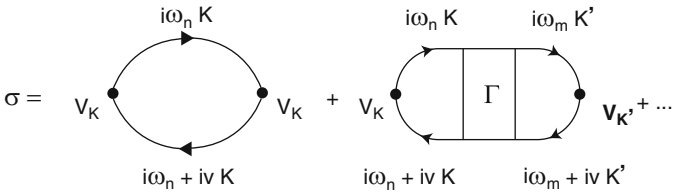

Fig. 3.34. Diagrammatic expansion for conductivity. Two first terms are shown. *Lines with arrows* correspond to electronic *GF* $G(\mathbf{k}, i\omega_n)$, points – $\mathbf{v_k}$ and Γ – irreducible vertex part [123]

This expression has diagrammatic expansion shown in Fig. 3.34. Four-point Γ is irreducible vertex part in particle–hole channel (with antiparallel Green lines) that cannot be cut over one Green line. Dots in right side means multiple repetition of vertex part in this channel. In $d = \infty$ limit vertex part $\Gamma(i\omega_n, i\omega_m, i\nu)$ does not depend on wave vectors but only on frequencies. Due to frequency preservation law Γ depends not on four but only three frequencies and $i\nu$ is external frequency that defines conductivity $\sigma(i\nu)$.

Hence a fragment in second graph:

$$\sum_{\mathbf{k},\sigma,\omega_n} \mathbf{v_k} G_\sigma(\mathbf{k}, i\omega_n) G_\sigma(\mathbf{k}, i\omega_n + i\nu) \tag{3.7.201}$$

is equal to zero because *GF* $G(\mathbf{k}, \omega_n)$ depends only on $\mathbf{k}$ only via even function $\varepsilon_\mathbf{k}$ and function $\mathbf{v_k}$ is odd. So in the limit $d = \infty$ conductivity is defined by a simple loop and then

$$\begin{aligned} \mathrm{d}\tilde{\sigma}(i\nu) = \frac{1}{N\beta}\frac{1}{\nu} \sum_{\mathbf{k},\sigma,\omega_n} \sum_\alpha v_{k_\alpha}^2 G_\sigma(\mathbf{k}, i\omega_n) G_\sigma(\mathbf{k}, i\omega_n + i\nu) \\ \frac{1}{\nu\beta} \sum_{\sigma,\omega_n} \int_{-\infty}^{\infty} \mathrm{d}\varepsilon R(\varepsilon) G_\sigma(\varepsilon, i\omega_n) G_\sigma(\varepsilon, i\omega_n + i\nu), \end{aligned} \tag{3.7.202}$$

where

$$R(\varepsilon) = \frac{1}{N} \sum_\mathbf{k} \sum_\alpha \sin^2 k_\alpha \delta(\varepsilon - \varepsilon_\mathbf{k}), \tag{3.7.203}$$

here we have used nearest neighbors approximation for hopping matrix element t_{ij}.

Expression (3.7.203) is calculated using representation for function $\delta(\varepsilon - \varepsilon_\mathbf{k})$ as an integral over exponent and then integrals over k_α can be expressed via Bessel functions of various orders and sum over $\alpha = 1, 2, \ldots, \infty$ results in [123]:

$$R(\varepsilon) = \frac{d}{2} A_0(\varepsilon) \tag{3.7.204}$$

where $A_0(\varepsilon) = -\frac{1}{\pi}\mathrm{Im}G_0(\varepsilon)$ is noninteracting density of states.

Sum over frequencies ω_n in expression (3.7.203) can be calculated in spectral representation for electronic GF (see Appendix B):

$$G(\varepsilon, i\omega_n) = \int \mathrm{d}\omega' \frac{A(\varepsilon, \omega')}{i\omega_n - \omega'}, \tag{3.7.205}$$

where $A(\varepsilon, \omega) = -\frac{1}{\pi}\mathrm{Im}G_0(\varepsilon, \omega)$ is spectral function for interacting lattice GF. Using spectral representation (3.7.205) for both GFs in formula (3.7.203) and summing over frequencies ω_n we arrive to expression

$$\mathrm{d}\tilde{\sigma}(i\nu) = \frac{1}{\nu}\int \mathrm{d}\varepsilon \mathrm{d}\omega' \mathrm{d}\omega'' A_0(\varepsilon) A(\varepsilon, \omega') A(\varepsilon, \omega'') \frac{f(\omega') - f(\omega'')}{\omega' - \omega'' + i\nu}. \tag{3.7.206}$$

Now one should perform analytical continuation $i\nu \to \omega + i\delta$ and after separating real part we arrive to final formula for optical conductivity [123]:

$$d\sigma(\omega) = \sigma_0 \int \mathrm{d}\varepsilon \mathrm{d}\omega' A_0(\varepsilon) A(\varepsilon, \omega') A(\varepsilon, \omega' + \omega) \frac{f(\omega') - f(\omega' + \omega)}{\omega}, \tag{3.7.207}$$

here $f(\omega)$ is Fermi function obtained in frequencies ω_n summation and

$$\sigma_0 = \frac{\pi e^2 a^2 t^2}{2\hbar} \frac{N}{V} \tag{3.7.208}$$

is parameter appearing after restoring e and $\hbar$ constants; V is a system volume. So in order to calculate optical conductivity one needs to get lattice GF (or equivalently to find self-energy $\Sigma(\omega)$) and to perform integration in (3.7.207).

Calculation for optical conductivity and other transport properties for Hubbard model in $DMFT(QMC)$ were done originally in [123, 173, 174]. We will describe below main physical results of these investigations. In Figs. 3.35 and 3.36 optical conductivity frequency dependence is shown calculated for various temperatures at fixed doping $\delta = 0.068$ (Fig. 3.35) and for various dopings at fixed temperature $\beta = 43.2$ (Fig. 3.36). Analysis of these results was done in review [8].

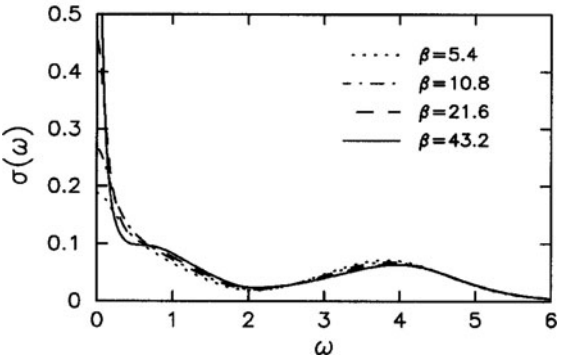

Fig. 3.35. Optical conductivity at $U = 4$, $\delta = 0.068$, and various temperatures [174]

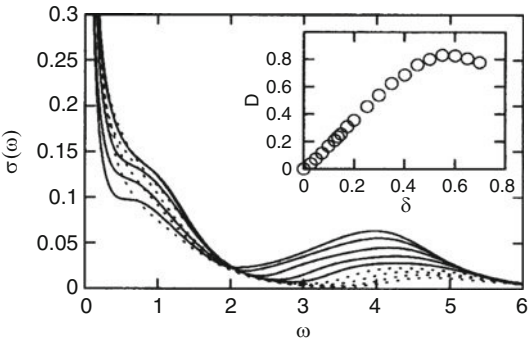

Fig. 3.36. Optical conductivity at $U = 4$, $\beta = 43.2$, and various dopings [174]

One can clearly see three different frequency regions. At small ω there is a narrow peak due to electrons excitations by electromagnetic field inside quasiparticle band. In the limit $T = 0$ this peak is δ-function and corresponds to Drude peak for metallic systems. In intermediate frequencies there is a broad peak determined by electrons transitions from lower Hubbard band to unoccupied quasiparticle states with a width of the order of quasiparticle band. For high frequencies one can observe broad peak due to electrons transition between Hubbard bands and its position is of the order of U.

This picture agrees well with three-peak structure of spectral function $A(\omega)$ for Hubbard model near half filling (Fig. 3.37). For small doping on the edge of lower Hubbard band narrow quasiparticle peak appears whose intensity increases with lowering temperature. That is correlated with Drude peak enhancement with T decreasing (Fig. 3.35). This correspondence of spectral functions $\sigma(\omega)$ and $A(\omega)$ is due to the expression (3.7.207) where optical conductivity is presented as a convolution of spectral functions.

In Fig. 3.35 and 3.36 optical conductivity is presented for Hubbard model with deviation from half filling. With δ increase Drude peak contribution increases because the system becomes more metallic. With temperature increase Drude peak intensity is suppressed similar to half-filled case (Fig. 3.38).

3.7.2 Magnetic Susceptibility

Magnetic susceptibility formula is also simplified in $d \to \infty$ limit. To derive it one should use general expression for two-particle GF:

$$\chi^{\alpha\beta}(\mathbf{q}, i\omega_n) = \int_0^\beta \mathrm{d}\tau \mathrm{e}^{\mathrm{i}\omega_n \tau} \sum_j \mathrm{e}^{\mathrm{i}\mathbf{q}\mathbf{R}_j} \langle T S_j^\alpha(\tau) S_0^\beta(0) \rangle \tag{3.7.209}$$

that defines spin susceptibility tensor via analytical continuation $i\omega_n \to \omega + i\delta$. Here spin operator S_j^α is expressed via Fermi operators in a standard form:

$$S_j^\alpha = \frac{1}{2} \sum_{\sigma\sigma'} \hat{c}_{j\sigma}^+ \sigma_{\sigma\sigma'}^\alpha \hat{c}_{j\sigma'}. \tag{3.7.210}$$

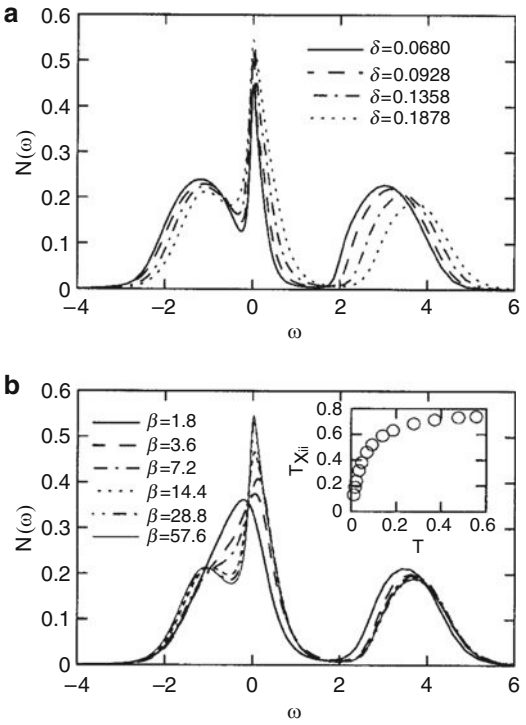

Fig. 3.37. Spectral density for Hubbard model calculated by *DMFT*(*QMC*) method for $U = 4$ (in t units): (**a**) at $\beta = 43.2$ and various dopings; (**b**) at $\delta = 0.188$ and various temperatures [174]

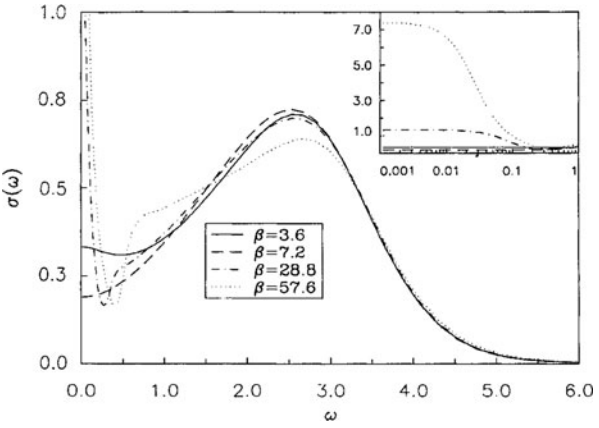

Fig. 3.38. Optical conductivity for Hubbard model at half-filing for $U = 3$ and various temperatures calculated by *DMFT*(*QMC*) method [123]

For S_j^z spin component this expression is

$$S_j^z = \frac{1}{2}\sum_{\sigma} \mathrm{sgn}(\sigma)\hat{c}_{j\sigma}^{+}\hat{c}_{j\sigma}. \tag{3.7.211}$$

Let us derive expression for longitudinal susceptibility χ^{zz} (for transverse susceptibility derivation is analogous). In particle–hole channel graphic expansion for χ^{zz} has the same structure as in Fig. 3.34. In analytical form it is expressed as series:

$$\begin{aligned}\chi(\mathbf{q}, i\nu) = &-\sum_{\mathbf{k},\omega_n} G(\mathbf{k}, i\omega_n)G(\mathbf{k}+\mathbf{q}, i\omega_n + i\nu) \\ &+\sum_{\mathbf{k},\omega_n\sigma}\sum_{\mathbf{k}',\omega_m\sigma'} \mathrm{sgn}(\sigma)G(\mathbf{k}, i\omega_n)G(\mathbf{k}+\mathbf{q}, i\omega_n + i\nu)\Gamma^{\sigma\sigma'}_{\mathbf{k}\mathbf{k}'\mathbf{q}}(i\omega_n, i\omega_m, i\nu) \\ &G(\mathbf{k}', i\omega_m)G(\mathbf{k}'+\mathbf{q}, i\omega_m + i\nu)\mathrm{sgn}(\sigma') + \cdots .\end{aligned} \tag{3.7.212}$$

Spin indexes of electronic GFs are omitted because we consider paramagnetic case. Later spin indexes for vertex part are also omitted.

In $d \to \infty$ limit as it was said earlier vertex part does not depend on wave vectors and so expansion (3.7.212) can be reduced to equation for three frequencies dependent function $\tilde{\chi}$ that is defined by:

$$\chi(\mathbf{q}, i\nu) = \sum_{\omega_n,\omega_m} \tilde{\chi}_{\mathbf{q}}(i\omega_n, i\omega_m, i\nu).$$

From series (3.7.212) for $\chi(\mathbf{q}, i\nu)$ one can obtain series for $\tilde{\chi}_{\mathbf{q}}$ and reduce it to the following equation

$$\begin{aligned}\tilde{\chi}_{\mathbf{q}}(i\omega_n, i\omega_m, i\nu) = &\tilde{\chi}^0_{\mathbf{q}}(i\omega_n, i\nu)\delta_{nm} \\ &+\tilde{\chi}^0_{\mathbf{q}}(i\omega_n, i\nu)\frac{1}{\beta}\sum_{\omega_l} \Gamma(i\omega_n, i\omega_l, i\nu)\tilde{\chi}_{\mathbf{q}}(i\omega_l, i\omega_m, i\nu),\end{aligned} \tag{3.7.213}$$

where

$$\tilde{\chi}^0_{\mathbf{q}}(i\omega_n, i\nu) = -\sum_{\mathbf{k}} G(\mathbf{k}, i\omega_n)G(\mathbf{k}+\mathbf{q}, i\omega_n + i\nu) \tag{3.7.214}$$

is a loop of two Green lines without summation over intermediate frequency.

Let us write equation (3.7.214) in matrix form

$$\tilde{\chi}_{\mathbf{q}} = \tilde{\chi}^0_{\mathbf{q}} + \tilde{\chi}^0_{\mathbf{q}}\Gamma\tilde{\chi}_{\mathbf{q}}, \tag{3.7.215}$$

or equivalent form

$$\tilde{\chi}^{-1}_{\mathbf{q}} = (\tilde{\chi}^0_{\mathbf{q}})^{-1} - \Gamma. \tag{3.7.216}$$

Now equation for $\tilde{\chi}_{\mathbf{q}}$ is ready for analysis.

In $d \to \infty$ limit for hypercubic lattice $\tilde{\chi}^0_{\mathbf{q}}$ depends on $\mathbf{q}$ via

$$X(\mathbf{q}) = \frac{1}{d}\sum_{\alpha=1}^{d} \cos q_\alpha, \tag{3.7.217}$$

that can be proved by presenting expression (3.7.214) in a form

$$\tilde{\chi}^0_{\mathbf{q}}(i\omega_n, i\omega_m, i\nu) = -\int_{-\infty}^{\infty} \mathrm{d}\varepsilon_1 \rho_0(\varepsilon_1) \int_{-\infty}^{\infty} \mathrm{d}\varepsilon_2 \rho_0(\varepsilon_2) \frac{\Delta_{\mathbf{q}}(\varepsilon_1, \varepsilon_2)}{(\zeta_\nu - \varepsilon_1)(\zeta_{\nu+\omega} - \varepsilon_2)}, \tag{3.7.218}$$

where

$$\Delta_{\mathbf{q}}(\varepsilon_1, \varepsilon_2) = \sum_{\mathbf{k}} \delta(\varepsilon_{\mathbf{k}} - \varepsilon_1)\delta(\varepsilon_{\mathbf{k}+\mathbf{q}} - \varepsilon_2). \tag{3.7.219}$$

Expression (3.7.218) can be checked by substituting in it $\Delta_{\mathbf{q}}(\varepsilon_1, \varepsilon_2)$ and using condition $\int \mathrm{d}\varepsilon \rho_0(\varepsilon) = 1$. Here $\zeta_n = i\omega_n + \mu - \Sigma(i\omega_n)$.

Sum over wave vectors in expression (3.7.219) is computed using δ-function representation as an integral of exponent and gives

$$\Delta_{\mathbf{q}}(\varepsilon_1, \varepsilon_2) = \frac{1}{2\pi t^2 \sqrt{1 - X^2(\mathbf{q})}} \exp\left\{ -\frac{\varepsilon_1^2 + \varepsilon_2^2 - 2\varepsilon_1\varepsilon_2 X(\mathbf{q})}{2t^2(1 - X^2(\mathbf{q}))} \right\}, \tag{3.7.220}$$

where one can see that $\tilde{\chi}^0_{\mathbf{q}}$ depends on $\mathbf{q}$ only via $X(\mathbf{q})$.

These properties of $\tilde{\chi}^0_{\mathbf{q}}$ allow to solve basic equation (3.7.215) for $\tilde{\chi}_{\mathbf{q}}$. Please note that $X(\mathbf{q})$ strongly depends in $d \to \infty$ limit on the type of vector $\mathbf{q}$. If $\mathbf{q}$ is a general type ("generic") point in Brillouin zone then $X(\mathbf{q}) = 0$ because in a sum (3.7.217) contributions with opposite sign will cancel each other. For such a vector

$$\chi(\mathbf{q}, i\omega_n) = \frac{1}{N}\sum_{\mathbf{q}} \chi(\mathbf{q}, i\omega_n) \equiv \chi_{\mathrm{loc}}(i\omega_n), \tag{3.7.221}$$

i.e., susceptibility with this $\mathbf{q}$ coincide with local susceptibility (diagonal matrix element in site representation).

However $X(\mathbf{q})$ can have values $-1 \le X \le 1$ for special $\mathbf{q}$ points. For example for $\mathbf{q} = \mathbf{0}$ or $\mathbf{q} = \mathbf{Q} = (\pm\pi, \pm\pi, \ldots, \pm\pi)$ its values are:

$$X(0) = 1;\ X(\mathbf{Q}) = -1. \tag{3.7.222}$$

For "generic" point $\mathbf{q}$ equation (3.7.216) can be rewritten as:

$$\Gamma = (\tilde{\chi}^0_{\mathrm{loc}})^{-1} - \tilde{\chi}^{-1}_{\mathrm{loc}}. \tag{3.7.223}$$

Substituting this expression for irreducible vertex part in general equation (3.7.216) it can be rewritten in a form:

$$\tilde{\chi}^{-1}_{\mathbf{q}} = \tilde{\chi}^{-1}_{\mathrm{loc}} + (\tilde{\chi}^0_{\mathbf{q}})^{-1} - (\tilde{\chi}^0_{\mathrm{loc}})^{-1}. \tag{3.7.224}$$

In the right side of this equation are variables defined by single-impurity model only. Indeed to calculate $\tilde{\chi}^0_{\mathbf{q}}$ one need to know only self-energy whereas

$\tilde{\chi}_{\text{loc}}$ and $\tilde{\chi}^0_{\text{loc}}$ can be expressed via single-impurity action S_{eff}. For spin susceptibility χ^{zz} there is an explicit expression:

$$\tilde{\chi}_{\text{loc}}(i\omega_n, i\omega_m, i\nu) = \frac{1}{4}\int_0^\beta \mathrm{d}\tau_1\mathrm{d}\tau_2\mathrm{d}\tau_3\mathrm{d}\tau_4 \mathrm{e}^{\mathrm{i}\omega_n(\tau_1-\tau_2)}\mathrm{e}^{\mathrm{i}\omega_m(\tau_4-\tau_3)}\mathrm{e}^{\mathrm{i}\nu(\tau_4-\tau_2)} \sum_{\sigma\sigma'}(-1)^{\sigma}(-1)^{\sigma'}\langle T\hat{c}^+_{\sigma}(\tau_1)\hat{c}_{\sigma}(\tau_2)\hat{c}^+_{\sigma'}(\tau_3)\hat{c}_{\sigma'}(\tau_4)\rangle_{S_{\text{eff}}}, \tag{3.7.225}$$

where symbol $\langle\ldots\rangle_{S_{\text{eff}}}$ means averaging with effective single-impurity action S_{eff}. Local correlator $\langle\ldots\rangle_{S_{\text{eff}}}$ can be calculated numerically using exact diagonalization or *QMC* methods.

In Hirsch–Fye algorithm action S_{eff} is linearized via discrete Hirsch-Hubbard–Stratonovich transformation and average value of T-product of Fermi operators can be expressed via pair average through Wick theorem and hence

$$\begin{aligned}&\langle T\hat{c}^+_{\sigma}(\tau_1)\hat{c}_{\sigma}(\tau_2)\hat{c}^+_{\sigma'}(\tau_3)\hat{c}_{\sigma'}(\tau_4)\rangle_{S_{\text{eff}}} \\ &= \overline{g^{\sigma}_{s_1\ldots s_L}(\tau_2,\tau_1)g^{\sigma'}_{s_1\ldots s_L}(\tau_4,\tau_3)} - \delta_{\sigma\sigma'}\overline{g^{\sigma}_{s_1\ldots s_L}(\tau_2,\tau_3)g^{\sigma'}_{s_1\ldots s_L}(\tau_4,\tau_1)}.\end{aligned} \tag{3.7.226}$$

By line above we define averaging over Ising pseudospins appearing in time interval $0 \le \tau \le \beta$ discretization as it was described in Sect. 3.2.

It was left only to show how $\tilde{\chi}^0_{\mathbf{q}}$ is calculated. From formula (3.7.218) taking into account that for "generic" point $\mathbf{q}$ $\tilde{\chi}^0_{\mathbf{q}} = \tilde{\chi}^0_{\text{loc}}$ one can obtain using (3.7.218) and (3.7.219):

$$\tilde{\chi}^0_{\mathbf{q}}(i\omega_n, i\nu) = -\tilde{\mathcal{D}}[\zeta(i\omega_n)]\tilde{\mathcal{D}}[\zeta(i\omega_n + i\nu)], \tag{3.7.227}$$

where we have used Hilbert transformation for noninteracting density of states:

$$\tilde{\mathcal{D}}[\zeta] = \int \mathrm{d}\varepsilon \frac{\rho_0(\varepsilon)}{\zeta - \varepsilon}. \tag{3.7.228}$$

For vector $\mathbf{q} = \mathbf{0}$ using (3.7.218) we have

$$\tilde{\chi}^0_{\mathbf{q}=0}(i\omega_n, i\nu) = -\frac{\tilde{\mathcal{D}}[\zeta(i\omega_n)] - \tilde{\mathcal{D}}[\zeta(i\omega_n + i\nu)]}{\zeta(i\omega_n + i\nu) - \zeta(i\omega_n)}. \tag{3.7.229}$$

Let us discuss magnetic susceptibility investigation results in Hubbard model obtained by $DMFT-QMC$ method in [6,174,175]. In pioneering work of Jarrell [6] magnetic susceptibility for antiferromagnetic wave vector $\mathbf{Q}$ was calculated in paramagnetic phase (Fig. 3.39).

With temperature lowering to $T_N = 0.0866$ (in band width units) susceptibility diverges that corresponds to antiferromagnetic state formation. In the inset the same data are shown in logarithmic scale and from them critical index ν can be found for susceptibility $\chi_{\text{AFM}} \propto |T - T_N|^{\nu}$ with value $\nu = -0.99 \pm 0.05$.

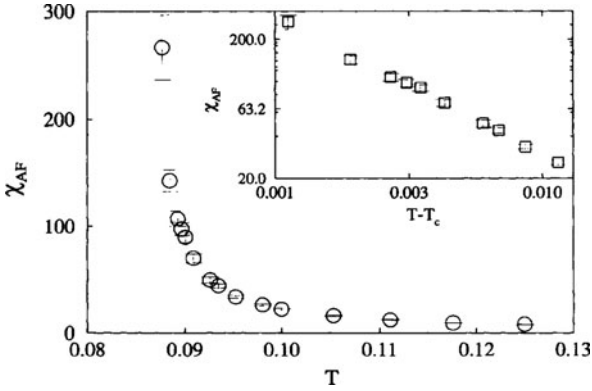

Fig. 3.39. Antiferromagnetic susceptibility of Hubbard model for $n = 1$ calculated by *DMFT*(*QMC*) method at $U = 1.5$ (in the band width units). In the inset the same data are shown in logarithmic scale [6]

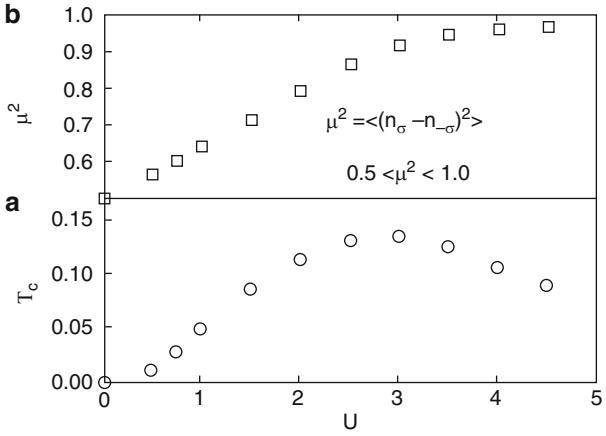

Fig. 3.40. (**a**) Neel temperature and (**b**) average quadratic value of local moment μ^2 in Hubbard model for $n = 1$ and $T = T_N$ as a function of U [6]

Analogous calculation results with different U values are presented in Fig. 3.40. Neel temperature as a function of U has a maximum near $U \approx 3$. Such $T_N(U)$ dependence agrees with earlier predictions obtained by various methods. For example for large $U \gg W$ $T_N \propto W^2/U$. In Fig. 3.40b U dependence is shown for average value of the square of electron magnetic moment on the atomic site $\mu^2 = < (n_\uparrow) - n_\downarrow >)^2$ that gives a measure of local magnetic moment. With U increase μ^2 varies from 0.5 at $U = 0$ till 1 for $U \gg W$. That means that local magnetic moment value increases with U increase saturating for strongly correlated case. One can see that $T_N(U)$ curve maximum is in the area where μ^2 approaches saturation.

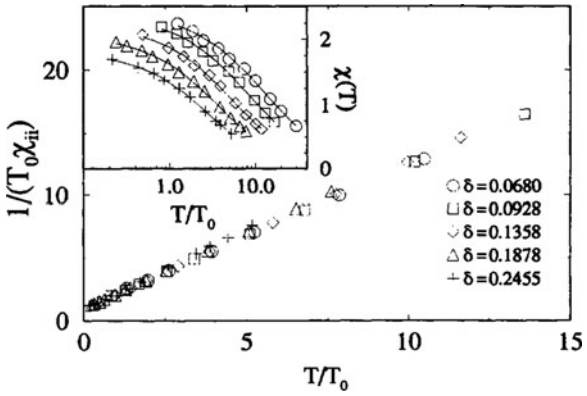

Fig. 3.41. Local static susceptibility χ_{ii} in equivalent Anderson model as a function of temperature for various doping values. In the inset: uniform static susceptibility $\chi(T)$ is calculated by $DMFT(QMC)$ method [175]

In Fig. 3.41 result from earlier susceptibility investigation [175] is presented. Here inverse local static susceptibility is shown as a function of temperature for various doping values near half-filling. One can see scaling behavior of $(T_0\chi_{ii})^{-1}$ as a function of T/T_0 where T_0 is defined as in Anderson model via $\chi_{ii}(T = 0) = 1/T_0$. In the inset static antiferromagnetic susceptibility $\chi(T)$ as a function of temperature is shown. This function does not show this scaling behavior. A difference between local and uniform susceptibilities is discussed in details in review [8].

4

DMFT Extensions

4.1 $t-J$ Model as a Hubbard Model Limit

4.1.1 Hamiltonian and Green Function

One of the fundamental models in strongly correlated system theories is tJ model defined by the Hamiltonian

$$H = \sum_{ij\sigma} t_{ij} \tilde{c}^{\dagger}_{i\sigma} \tilde{c}_{j\sigma} + \frac{1}{2} \sum_{ij} J_{ij} \mathbf{S}_i \mathbf{S}_j. \tag{4.1.1}$$

Here $\tilde{c}^{\dagger}_{i\sigma}(\tilde{c}_{i\sigma})$ are creation (annihilation) operators for correlated electrons on site i. Correlated electrons means that a particle can be created on site i only if there is no already another electron on this site. This requirement is satisfied in definition of $\tilde{c}^{\dagger}_{i\sigma}$ and $\tilde{c}_{i\sigma}$ operator via standard Fermi operators $\hat{c}^{\dagger}_{i\sigma}$ and $\hat{c}_{i\sigma}$:

$$\tilde{c}^{\dagger}_{i\sigma} = \hat{c}^{\dagger}_{i\sigma}(1 - \hat{n}_{i\overline{\sigma}}), \quad \tilde{c}_{i\sigma} = \hat{c}_{i\sigma}(1 - \hat{n}_{i\overline{\sigma}}), \tag{4.1.2}$$

where $\hat{n}_{i\sigma} = \hat{c}^{\dagger}_{i\sigma}\hat{c}_{i\sigma}$.

Such requirement is valid when there is very strong Coulomb repulsion and so tJ model can be considered as a Hubbard model limit at $U \to \infty$.

When Hubbard model Hamiltonian is projected on the space where two electrons presence on the same site is forbidden effective exchange interaction appears between nearest neighbors with exchange integral $J \sim \frac{t^2}{U} \ll W$ [33]. It is also assumed that the system is close to half filling (doping $\delta = 1-n \ll 1$). Local on-site spin operator is expressed via $\tilde{c}^{\dagger}_{i\sigma}$ and $\tilde{c}_{i\sigma}$ operators with standard relation:

$$\mathbf{S}_i = \frac{1}{2} \sum_{\sigma\sigma'} \tilde{c}^{\dagger}_{i\sigma} \boldsymbol{\sigma}_{\sigma\sigma'} \tilde{c}_{i\sigma}. \tag{4.1.3}$$

It is generally accepted that tJ model for two-dimensional lattice is a basic model for high-T_c materials and was very popular in last two decades. For

tJ model investigation various approaches were proposed among them non-perturbative ones (see e.g., review [41]). It is interesting to apply *DMFT* for Hamiltonian (4.1.1). In contrast to Hubbard model where Coulomb interaction is local in *tJ* model Hamiltonian exchange term is nonlocal so one should use extended *DMFT* (*EDMFT*). One of the possible extensions is two-atoms local center similar to two sublattice antiferromagnetic state in Hubbard model (Sect. 3.5). Another approach [176, 177] uses single-atomic center embedded in effective medium and interacting not only with fermionic degrees of freedom as in standard *DMFT* but also with bosonic variables imitating interaction of local spins on neighboring sites. In this approach one should consider simultaneously electronic and spin *GF*s. Let us write their definition in wave vectors representation:

$$\begin{aligned} G_{\mathbf{k}\sigma}(i\omega_{\mathrm{n}}) &= -\int\limits_0^\beta \mathrm{d}\tau \mathrm{e}^{\mathrm{i}\omega_{\mathrm{n}}\tau} \left\langle T_\tau \tilde{c}_{\mathbf{k}\sigma}(\tau) c^\dagger_{\mathbf{k}\sigma}(0) \right\rangle \\ &= \left[i\omega_{\mathrm{n}} + \mu - \varepsilon_{\mathbf{k}} - \Sigma_{\mathbf{k}\sigma}(i\omega_{\mathrm{n}}) \right]^{-1}, \end{aligned} \tag{4.1.4}$$

and

$$\begin{aligned} \chi^\alpha_{\mathbf{q}}(i\Omega_{\mathrm{n}}) &= \int\limits_0^\beta \mathrm{d}\tau \mathrm{e}^{\mathrm{i}\Omega_{\mathrm{n}}\tau} \left\langle T_\tau S^\alpha_{-\mathbf{q}}(\tau) S^\alpha_{\mathbf{q}}(0) \right\rangle \\ &= \left[J_{\mathbf{q}} + M^\alpha_{\mathbf{q}}(i\Omega_{\mathrm{n}}) \right]^{-1}. \end{aligned} \tag{4.1.5}$$

Here $i\omega_{\mathrm{n}}$ and $i\Omega_{\mathrm{n}}$ are Fermi and Bose frequencies.

In the following, we will investigate *tJ* model at the temperature values higher than ordering temperatures for any order parameter and so magnetic susceptibility tensor $\chi^{\alpha\beta}_{\mathbf{q}}$ is diagonal with $\chi^\alpha_{\mathbf{q}}$, $\alpha = x, y, z$ components. Relation (4.1.5) needs to be clarified. Using diagrammatic technique for spin operators [178] fundamental equation for spin *GF* was derived that can be written in the following form (Larkin equation [178]):

$$\chi^\alpha_{\mathbf{q}}(i\Omega_{\mathrm{n}}) = \Sigma^\alpha_{\mathbf{q}}(i\Omega_{\mathrm{n}}) + \Sigma^\alpha_{\mathbf{q}}(i\Omega_{\mathrm{n}}) J_{\mathbf{q}} \chi^\alpha_{\mathbf{q}}(i\Omega_{\mathrm{n}}). \tag{4.1.6}$$

$\Sigma^\alpha_{\mathbf{q}}(i\Omega_{\mathrm{n}})$ is called irreducible (in exchange interaction $J_{\mathbf{q}}$) part of spin *GF*. In general case (4.1.6) is a matrix one. If all its parts are scalars as it is in our case then its solution is:

$$\chi^\alpha_{\mathbf{q}}(i\Omega_{\mathrm{n}}) = \left[J_{\mathbf{q}} + \frac{1}{\Sigma^\alpha_{\mathbf{q}}(i\Omega_{\mathrm{n}})} \right]^{-1}. \tag{4.1.7}$$

Comparing expressions (4.1.5) and (4.1.7) one can get the relation $M^\alpha_{\mathbf{q}} = \frac{1}{\Sigma^\alpha_{\mathbf{q}}(i\Omega_{\mathrm{n}})}$ that proves spin *GF* representation in the form (4.1.5). $M^\alpha_{\mathbf{q}}(i\Omega_{\mathrm{n}})$ plays for spin *GF* the same role as irreducible part $\Sigma_{\mathbf{k}\sigma}(i\omega_{\mathrm{n}})$ for electronic *GF*. Our goal is to write equations for $\Sigma_{\mathbf{k}\sigma}(i\omega_{\mathrm{n}})$ and $M^\alpha_{\mathbf{q}}(i\Omega_{\mathrm{n}})$ in *DMFT* style, i.e., in $d = \infty$ limit. Later we will follow work [176].

4.1.2 *DMFT* Equations Derivation

Let us assume that both $\Sigma_{\mathbf{k}\sigma}(i\omega_\mathrm{n})$ and $M^{\alpha}_{\mathbf{q}}(i\Omega_\mathrm{n})$ do not depend on wave vector (we will omit spin and vector indexes assuming paramagnetic phase in hypercubic lattice) and then

$$\Sigma_{\mathbf{k}}(i\omega_\mathrm{n}) \approx \Sigma(i\omega_\mathrm{n}); \quad M_{\mathbf{q}}(i\omega_\mathrm{n}) \approx M(i\omega_\mathrm{n}). \tag{4.1.8}$$

Let us define local GFs

$$G_\mathrm{loc}(i\omega_\mathrm{n}) = \sum_{\mathbf{k}} G_{\mathbf{k}}(i\omega_\mathrm{n}), \tag{4.1.9}$$

$$\chi_\mathrm{loc}(i\Omega_\mathrm{n}) = \sum_{\mathbf{q}} G_{\mathbf{q}}(i\Omega_\mathrm{n}) \tag{4.1.10}$$

and identify them with single-site electronic and spin GFs determining them as usual with effective action S_eff.

It is convenient to work not with tJ model Hamiltonian (4.1.1) but with more general Hamiltonian

$$H_U = \sum_{ij\sigma} t_{ij}\hat{c}^{\dagger}_{i\sigma}\hat{c}_{j\sigma} + U\sum_{i}\hat{n}_{i\uparrow}\hat{n}_{i\downarrow} + \frac{1}{2}\sum_{ij} J_{ij}\hat{\mathbf{S}}_i\hat{\mathbf{S}}_j \tag{4.1.11}$$

that is expressed not via "correlated" operators $\tilde{c}^{\dagger}_{i\sigma}$ and $\tilde{c}_{i\sigma}$ but through usual Fermi operators. If in the end of calculations with Hamiltonian H_U use a limit $U\to\infty$ then the result will correspond to tJ model.

To Hamiltonian (4.1.11) corresponds an action for lattice model (4.1.11):

$$\begin{aligned} S = \int\limits_0^\beta \mathrm{d}\tau \Bigg\{ \sum_{ij\sigma} c^{\dagger}_{i\sigma}(\tau) \left[\left(\frac{\partial}{\partial\tau} - \mu \right) \delta_{ij} - t_{ij} \right] c_{j\sigma}(\tau) \\ + \frac{1}{2}\sum_{ij} J_{ij}\mathbf{S}_i(\tau)\mathbf{S}_j(\tau) + \sum_i U n_{i\uparrow}(\tau) n_{i\downarrow}(\tau) \Bigg\}. \end{aligned} \tag{4.1.12}$$

The action can be divided in three contribution: single-site part S_0

$$S_0 = \int\limits_0^\beta \mathrm{d}\tau \left[\sum_{\sigma} c^{\dagger}_{0\sigma}(\tau) \left(\frac{\partial}{\partial\tau} - \mu \right) c_{0\sigma}(\tau) + U n_{0\uparrow}(\tau) n_{0\downarrow}(\tau) \right], \tag{4.1.13}$$

ΔS part originating from interaction of site 0 with the rest of the system

$$\begin{aligned} \Delta S = \int\limits_0^\beta \mathrm{d}\tau \Bigg[\sum_{i\sigma} -t_{i0} c^{\dagger}_{i\sigma}(\tau) c_{0\sigma}(\tau) - t_{0i} c^{\dagger}_{0\sigma}(\tau) c_{i\sigma}(\tau) \\ + \frac{1}{2}(J_{i0} + J_{0i})\mathbf{S}_i(\tau)\mathbf{S}_0(\tau) \Bigg] \equiv \int\limits_0^\beta \mathrm{d}\tau \Delta\mathcal{L}(\tau), \end{aligned} \tag{4.1.14}$$

and action for whole lattice except 0 site $S^{(0)}$ that is equal to the expression (4.1.12) where site 0 is excluded from all sums over i and j.

Let us write now expression for partition function Z as a functional integral over Grassmann variables and expend it in powers of ΔS:

$$\begin{aligned} Z &= \int D[c^{\dagger}_{0\sigma}]D[c_{0\sigma}] \int \prod_{i\neq 0} D[c^{\dagger}_{i\sigma}]D[c_{i\sigma}] \mathrm{e}^{-S_0 - S^{(0)} - \int\limits_0^{\beta} \mathrm{d}\tau \Delta\mathcal{L}(\tau)} \\ &= \int D[c^{\dagger}_{0\sigma}]D[c_{0\sigma}] \mathrm{e}^{-S_0} Z^{(0)} \Big\{ 1 - \int\limits_0^{\beta} \langle \Delta\mathcal{L}(\tau) \rangle^{(0)} \, \mathrm{d}\tau \\ &\quad + \frac{1}{2!} \int\limits_0^{\beta} \mathrm{d}\tau_1 \int\limits_0^{\beta} \mathrm{d}\tau_2 \, \langle T_\tau \Delta\mathcal{L}(\tau_1) \Delta\mathcal{L}(\tau_2) \rangle^{(0)} + \cdots \Big\}. \end{aligned} \tag{4.1.15}$$

Various order terms analysis in parameter $1/d$ shows [177] that all terms higher than second order in $\Delta\mathcal{L}$ vanishes in $d = \infty$ limit. Second order term vanishes also because in paramagnetic phase $< S_i(\tau) >= 0$. The terms with correlation function $< c_{i\sigma}(\tau_1)\mathbf{S}(\tau_2) >^{(0)}$ vanish too and the rest of terms can be put in the exponent and the final result for effective on-site action is:

$$\begin{aligned} S_{\text{eff}} = \; & S_0 - \int\limits_0^{\beta} \int\limits_0^{\beta} \mathrm{d}\tau_1 \mathrm{d}\tau_2 \Big\{ c^{\dagger}_{0\sigma}(\tau_1) \sum_{ij} \Big\langle T_\tau c_{i\sigma}(\tau_1) c^{\dagger}_{j\sigma}(\tau_2) \Big\rangle^{(0)} c_{0\sigma}(\tau_2) \\ & \mathbf{S}_0(\tau_1) \frac{1}{2} \sum_{ij} J_{i0} J_{0j} \, \langle T_\tau \mathbf{S}_i(\tau_1) \mathbf{S}_j(\tau_2) \rangle^{(0)} \, \mathbf{S}_0(\tau_2) \Big\}. \end{aligned} \tag{4.1.16}$$

In this expression symbol $< \ldots >^{(0)}$ means averaging over $S^{(0)}$ contribution to whole action, i.e., integration over Grassmann variables for all lattice site except distinguished 0 site.

Expression (4.1.16) can be rewritten in a shortened form as:

$$\begin{aligned} S_{\text{eff}} = & \int\limits_0^{\beta} U n_{0\uparrow}(\tau) n_{0\downarrow}(\tau) \\ & - \int\limits_0^{\beta} \mathrm{d}\tau_1 \int\limits_0^{\beta} \mathrm{d}\tau_2 c^{\dagger}_{0\sigma}(\tau_1) \mathcal{G}_0^{-1}(\tau_1 - \tau_2) c_{0\sigma}(\tau_2) \\ & - \frac{1}{2} \int\limits_0^{\beta} \mathrm{d}\tau_1 \int\limits_0^{\beta} \mathrm{d}\tau_2 \mathbf{S}_0(\tau_1) \chi_0^{-1}(\tau_1 - \tau_2) \mathbf{S}_0(\tau_2), \end{aligned} \tag{4.1.17}$$

where two function are introduced $\mathcal{G}_0(\tau_1 - \tau_2)$ and $\boldsymbol{\chi}_0(\tau_1 - \tau_2)$ representing dynamical fields acting on distinguished site from the rest of the lattice. Let us write their explicit form in Fourier representation:

$$\mathcal{G}_0^{-1}(i\omega_n) = i\omega_n + \mu - \sum_{ij} t_{i0}t_{0j}G_{ij}^{(0)}(i\omega_n), \tag{4.1.18}$$

$$\chi_0^{-1}(i\Omega_n) = \sum_{ij} J_{i0}J_{0j}\chi_{ij}^{(0)}(i\Omega_n). \tag{4.1.19}$$

Dynamical fields depend on electronic $G_{ij}^{(0)}$ and spin $\chi_{ij}^{(0)}$ GFs for the lattice with the site 0 cut off. They can be expressed via full lattice GFs [177]:

$$G_{ij}^{(0)} = G_{ij} - G_{i0}G_{00}^{-1}G_{0j}, \tag{4.1.20}$$

$$\chi_{ij}^{(0)} = \chi_{ij} - \chi_{i0}\chi_{00}^{-1}\chi_{0j}. \tag{4.1.21}$$

Using general relations (4.1.4) and (4.1.5) it is possible to find lattice GFs for paramagnetic phase in approximation (4.1.8):

$$G_{\mathbf{k}}(i\omega_n) = \frac{1}{i\omega_n + \mu - \varepsilon_{\mathbf{k}} - \Sigma(i\omega_n)}, \tag{4.1.22}$$

$$\chi_{\mathbf{q}}(i\Omega_n) = \frac{1}{J_{\mathbf{q}} + M(i\Omega_n)}. \tag{4.1.23}$$

Let us substitute expressions (4.1.22) and (4.1.23) in (4.1.21) and then obtained result for $G_{ij}^{(0)}$ and $\chi_{ij}^{(0)}$ in expressions (4.1.18) and (4.1.19). That gives two equations connecting dynamical fields with self-energy parts of electronic and spin GFs and local GFs

$$\mathcal{G}_0^{-1} = \Sigma + G_{\text{loc}}^{-1}, \tag{4.1.24}$$

$$\chi_0^{-1} = M - \chi_{\text{loc}}^{-1}. \tag{4.1.25}$$

These equations together with (4.1.9) and (4.1.10) constitute self-contained equations system for $EDMFT$, keeping in mind that $G_{\text{loc}} = G_{\text{imp}}$ and $\chi_{\text{loc}} = \chi_{\text{imp}}$ whereas single-impurity GFs G_{imp} and χ_{imp} should be calculated using an action (4.1.17). This $EDMFT$ calculation scheme is not convenient because a limit $U \to \infty$ should be taken to arrive to tJ model. For practical calculations the equations should be reformulated.

The ideology of this method and $EDMFT$ equations derivation for the system with intersite interaction was developed earlier by Smith and Si [179] using diagrammatic perturbation theory. Practical realization for tJ model was developed in [176, 177].

4.1.3 Reformulation of *DMFT* Equations

The aim is to choose Hamiltonian for distinguished site 0 (where electrons interact with each other via Coulomb force U) embedded in a medium created by free fermions and bosons on the lattice in such a way so that this Hamiltonian results in action (4.1.17). In contrast to standard $DMFT$ scheme

here bosonic degrees of freedom should be taken into account. This problem has many solutions and one of them was proposed in [177]:

$$H_{\text{imp}} = \sum_{\mathbf{k}\sigma} E_{\mathbf{k}} \hat{c}^{\dagger}_{\mathbf{k}\sigma} \hat{c}_{\mathbf{k}\sigma} + V \sum_{\mathbf{k}\sigma} \left(\hat{c}^{\dagger}_{\mathbf{k}\sigma} \hat{c}_{0\sigma} + \hat{c}^{\dagger}_{0\sigma} \hat{c}_{\mathbf{k}\sigma} \right) - \sum_{\sigma} \mu \hat{c}^{\dagger}_{0\sigma} \hat{c}_{0\sigma} + U n_{0\uparrow} n_{0\downarrow} + \sum_{\mathbf{q}} \omega_{\mathbf{q}} \hat{\mathbf{h}}^{\dagger}_{\mathbf{q}} \hat{\mathbf{h}}_{\mathbf{q}} + I \sum_{\mathbf{q}} \hat{\mathbf{S}}_0 \left(\hat{\mathbf{h}}_{\mathbf{q}} + \hat{\mathbf{h}}^{\dagger}_{-\mathbf{q}} \right). \tag{4.1.26}$$

Here the first line corresponds to standard *DMFT* scheme for site 0 embedded in fermion medium and the second one describes bosonic medium. It corresponds to magnetic field acting on site 0 electronic spin. Quantities $\hat{h}^{\alpha}_{\mathbf{q}}$, $\alpha = x, y, z$ are Bose operators with general commutation relations

$$\left[\hat{h}^{\alpha}_{\mathbf{q}}, \hat{h}^{\beta}_{\mathbf{q}'} \right] = \delta_{\mathbf{q}\mathbf{q}'} \delta_{\alpha\beta}. \tag{4.1.27}$$

Dispersion relations $E_{\mathbf{k}}$ and $\omega_{\mathbf{q}}$ for fermions and bosons and coupling constants V and I should be chosen so that effective single-impurity model H_{imp} was equivalent to original lattice tJ model with Hamiltonian (4.1.1).

To model (4.1.26) corresponds an action

$$\begin{aligned} S = S_0 &+ \int_0^{\beta} \mathrm{d}\tau \sum_{\mathbf{k}\sigma} \left[c^{\dagger}_{\mathbf{k}\sigma}(\tau) \left(\frac{\partial}{\partial \tau} + E_{\mathbf{k}} \right) c_{\mathbf{k}\sigma}(\tau) + V c^{\dagger}_{\mathbf{k}\sigma}(\tau) c_{0\sigma}(\tau) + V c^{\dagger}_{0\sigma}(\tau) c_{\mathbf{k}\sigma}(\tau) \right] \\ &+ \int_0^{\beta} \mathrm{d}\tau \sum_{\mathbf{q}} \left[\mathbf{h}^{\dagger}_{\mathbf{q}}(\tau) \left(\frac{\partial}{\partial \tau} + \omega_{\mathbf{q}} \right) \mathbf{h}_{\mathbf{q}}(\tau) + I \mathbf{h}_{\mathbf{q}}(\tau) \mathbf{S}_0(\tau) + I \mathbf{S}_0(\tau) \mathbf{h}_{-\mathbf{q}}(\tau) \right]. \end{aligned} \tag{4.1.28}$$

Here $c^{\dagger}_{\mathbf{k}\sigma}$, $c_{\mathbf{k}\sigma}$ are Grassmann variables and $h^{*\alpha}_{\mathbf{q}}$, $h^{\alpha}_{\mathbf{q}}$ are complex quantities corresponding to Bose-fields (see Appendix A). In expression for partition function

$$Z = \int D[c^{\dagger}_{0\sigma}] D[c_{0\sigma}] \prod_{\mathbf{k}\sigma} D[c^{\dagger}_{\mathbf{k}\sigma}] D[c_{\mathbf{k}\sigma}] \prod_{\mathbf{q}\alpha} D[h^{*\alpha}_{\mathbf{q}}] D[h^{\alpha}_{\mathbf{q}}] \mathrm{e}^{-S} \tag{4.1.29}$$

integral over Bose-fields and fermionic medium can be easily calculated and remaining integral over Grassmann variables for electrons on site 0 defines an effective action:

$$Z = \int \prod_{\sigma} D[c^{\dagger}_{0\sigma}] D[c_{0\sigma}] \mathrm{e}^{-S_{\text{eff}}[c^{\dagger}_{0\sigma}, c_{0\sigma}]}, \tag{4.1.30}$$

where

$$S_{\text{eff}} = S_0 - \int_0^\beta \int_0^\beta \mathrm{d}\tau_1 \mathrm{d}\tau_2 \sum_\sigma c_{0\sigma}^\dagger(\tau_1) \left[\sum_{\mathbf{k}} V^2 \frac{\delta(\tau_1 - \tau_2)}{\frac{\partial}{\partial\tau} + E_{\mathbf{k}}} \right] c_{0\sigma}(\tau_2)$$
$$- \int_0^\beta \int_0^\beta \mathrm{d}\tau_1 \mathrm{d}\tau_2 \mathbf{S}_0(\tau_1) \left[\sum_{\mathbf{q}} I^2 \frac{\delta(\tau_1 - \tau_2)}{\frac{\partial}{\partial\tau} + \omega_{\mathbf{q}}} \right] \mathbf{S}_0(\tau_2). \tag{4.1.31}$$

This action is equivalent to (4.1.17) with condition that

$$\mathcal{G}_0^{-1}(\tau_1 - \tau_2) = -\left(\frac{\partial}{\partial\tau_1} - \mu \right) \delta(\tau_1 - \tau_2) + \sum_{\mathbf{k}} V^2 \frac{\delta(\tau_1 - \tau_2)}{\frac{\partial}{\partial\tau} + E_{\mathbf{k}}}, \tag{4.1.32}$$

$$\chi_0^{-1}(\tau_1 - \tau_2) = \sum_{\mathbf{q}} I^2 \left(\frac{\delta(\tau_1 - \tau_2)}{\frac{\partial}{\partial\tau} + \omega_{\mathbf{q}}} + \frac{\delta(\tau_1 - \tau_2)}{-\frac{\partial}{\partial\tau} - \omega_{\mathbf{q}}} \right). \tag{4.1.33}$$

In Fourier representation this relations have the form:

$$\mathcal{G}_0^{-1}(i\omega_{\mathrm{n}}) = i\omega_{\mathrm{n}} + \mu - V^2 G_{\mathrm{c}}(i\omega_{\mathrm{n}}), \tag{4.1.34}$$

$$\chi_0^{-1}(i\Omega_{\mathrm{n}}) = -I^2 G_h(i\Omega_{\mathrm{n}}). \tag{4.1.35}$$

where

$$G_{\mathrm{c}}(i\omega_{\mathrm{n}}) = \sum_{\mathbf{k}} \frac{1}{i\omega_{\mathrm{n}} - E_{\mathbf{k}}}, \tag{4.1.36}$$

$$G_h(i\Omega_{\mathrm{n}}) = \sum_{\mathbf{q}} \frac{2\omega_{\mathbf{q}}}{(i\Omega_{\mathrm{n}})^2 - \omega_{\mathbf{q}}^2}. \tag{4.1.37}$$

One can see that (4.1.34) has standard *DMFT* form keeping in mind that the term $V^2 G_{\mathrm{c}}(i\omega_{\mathrm{n}})$ corresponds to hybridization function $\Delta(i\omega_{\mathrm{n}})$. Equation (4.1.35) is a new one in *DMFT* and defines dynamical mean-field acting on electronic spin and formed by the lattice spins. In $d = \infty$ fermionic and bosonic fields are separated.

Let us write in conclusion self-consistency equations for lattice and single-impurity models:

$$G_{\mathrm{loc}}^{-1}(i\omega_{\mathrm{n}}) = i\omega_{\mathrm{n}} + \mu - \Sigma(i\omega_{\mathrm{n}}) - V^2 G_{\mathrm{c}}(i\omega_{\mathrm{n}}), \tag{4.1.38}$$

$$\chi_{\mathrm{loc}}^{-1}(i\Omega_{\mathrm{n}}) = M(i\Omega_{\mathrm{n}}) + I^2 G_k(i\Omega_{\mathrm{n}}) \tag{4.1.39}$$

that follow from Dyson equations for electron GF and Larkin equation for spin GF.

4.1.4 Numerical Calculation Results

Authors of [177] have used modified $EDMFT$ (4.1.38) and (4.1.39) where $\Sigma(i\omega_n)$ and $M(i\Omega_n)$ were calculated using perturbation theory in a spirit of NCA. We will present below main results of numerical calculations for electronic and spin spectral functions.

In Fig. 4.1 spectral function $A(\omega) = -\frac{1}{\pi}G_{\rm loc}(\omega)$ is shown for various doping δ values and fixed temperature $T = 0.6t$. This temperature is high enough to be above any magnetic ordering for high-T_c cuprates. On the band edge near chemical potential quasiparticle peak appears whose intensity grows fast with δ increase in the interval between 0.01 and 0.24. This peak has the same Kondo nature as in Anderson model. Its width increases with exchange interaction $\sim J$. So with doping the system becomes more metallic. In the inset in Fig. 4.1 the pseudo-gap value as a function of doping is shown.

Spin fluctuation spectrum is illustrated in Figs. 4.2–4.4. Their dynamical susceptibilities are shown: local $\chi_{\rm loc}(\omega)$, wave vector dependent $\chi_{\mathbf{q}}(\omega)$ and also spin fluctuation self-energy $M(\omega)$, with real and imaginary parts.

Local susceptibility (Fig. 4.2) is shown for various values of exchange parameter t/J. One can see that its linear part (the quantity $\frac{\chi''_{\rm loc}}{\omega}$) for small t/J has a sharp maximum that with increasing t/J becomes a broad peak with width $\Delta\omega \approx J$ without any trace of pseudo-gap T^*. From other side imaginary part of spin fluctuation self-energy $M''_{\rm loc}/\omega$ (Fig. 4.3 has clear pseudo-gap character for $\omega \lesssim J$.

Pseudo-gap reveals itself in susceptibility $\chi_{\mathbf{q}}(\omega)$ (Fig. 4.4) for wave vector direction $\mathbf{q} = (q, q)$. For small $\mathbf{q}$ $\frac{\chi''_{\mathbf{q}}}{\omega}$ has pseudo-gap that is gradually filled with approaching $\mathbf{q}$ to antiferromagnetic vector $\mathbf{Q} = (\pi, \pi)$ where $\frac{\chi''_{\mathbf{Q}}}{\omega}$ has maximum and real part a dip for $\omega \lesssim J$.

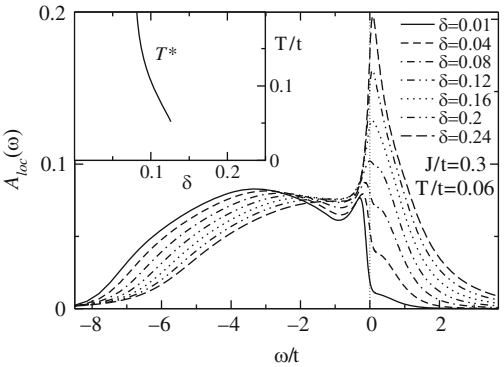

Fig. 4.1. tJ-model spectral function in $EDMFT$ for various doping values $\delta = 1-n$ and fixed $J = 0.3t$, $T = 0.06t$. [177] In the inset characteristic temperature for pseudogap opening T^* as a function of doping is shown

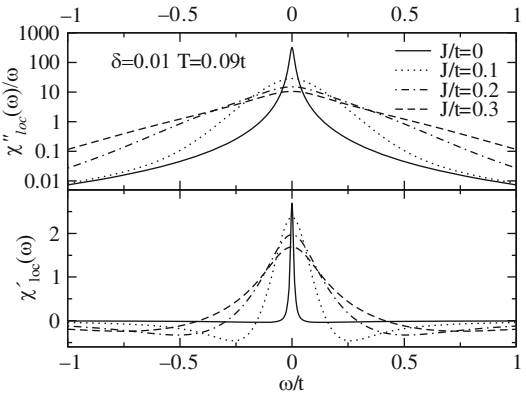

Fig. 4.2. Local dynamical susceptibility for various J/t at fixed doping $\delta = 0.01$ and temperature $T = 0.09t$ [177]

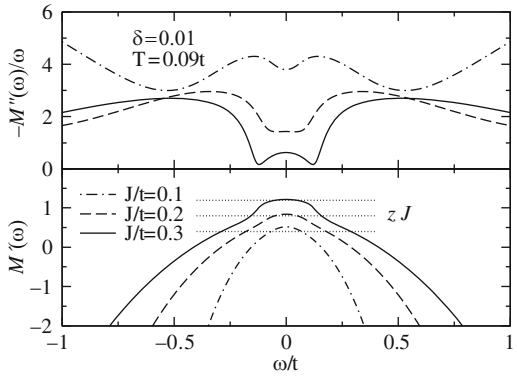

Fig. 4.3. Spin self-energy $M(\omega)$ at various J/t and δ, T values the same as in Fig. 4.1 [177]

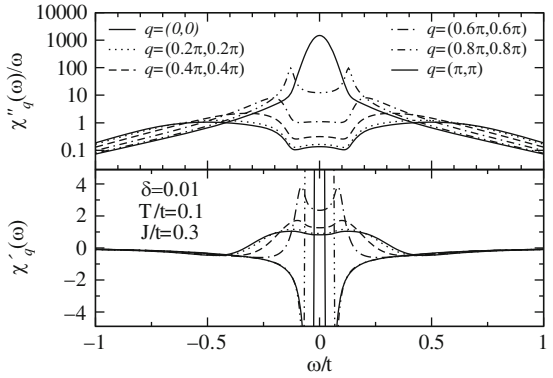

Fig. 4.4. Spin susceptibility $\chi_{\mathbf{q}}(\omega)$ along wave vector $\mathbf{q}$ $(0,0) - (\pi,\pi)$ at various J/t and parameters $\delta = 0.01$, $T = 0.1t$ [177]

Statical part $\chi_{\mathbf{q}}(0)$ varies on two orders of magnitude with $\mathbf{q}$ changing from 0 to $\mathbf{Q}$. Such behavior reflects large correlation length ξ existence that defines static spin susceptibility near vector $\mathbf{Q}$:

$$\chi_{\mathbf{q}}(0) = \frac{2}{zJ} \frac{1}{\xi^{-2} + (\mathbf{q} - \mathbf{Q})^2} \tag{4.1.40}$$

Here $z = 4$ and a length is measured in lattice constants a.

Let us recall the above described $EDMFT$ calculation scheme for tJ model was derived for two conditions: $T > T_c$ and $\delta \ll 1$ where T_c is ordering temperature. These conditions correspond to degenerate incoherent state that is described by small holes concentration in antiferromagnetic matrix (see review [41] and references there). With δ increasing and T lowering system will come to coherent state regime of Fermi liquid.

In work [177] there were also calculated many other thermodynamic and transport properties of the model that qualitatively are close to observed in high-T_c cuprates.

4.2 *DMFT* Extensions for Nonlocal Coulomb and Exchange Interaction Case

4.2.1 Hamiltonian and Green Function for Extended Model

Described earlier tJ model is not the only one where nonlocal interactions are present and $DMFT$ scheme needs to be extended by introducing interaction of impurity site with bosonic degrees of freedom for medium. Examples are U-V model where Coulomb interaction V between electrons on neighboring sites is included [180] and a model treating electrons interaction with lattice vibrations via introducing bosonic field [181, 182]. The most general model including local and nonlocal Coulomb interactions was developed by Sun and Kotliar [183] in the frame of $EDMFT$ and will be described later.

Let us introduce general Hamiltonian in the form [183]:

$$H = \sum_{ij\sigma} t_{ij} \hat{c}^{\dagger}_{i\sigma} \hat{c}_{j\sigma} - \sum_{i} \sum_{\alpha=0}^{3} h_{i\sigma} \hat{S}_{i\alpha} + U \sum_{i} \hat{n}_{i\uparrow} \hat{n}_{i\downarrow} + \frac{1}{2} \sum_{ij} \sum_{\alpha,\beta=0}^{3} \hat{S}_{i\alpha} V_{i\alpha,j\beta} \hat{S}_{j\beta}. \tag{4.2.41}$$

Here operator $\hat{S}_{i\alpha} = \hat{c}^{\dagger}_{i\sigma} \tau^{\alpha}_{\sigma\sigma'} c^{\dagger}_{i\sigma'}$ contains Pauli matrices τ^{α} for $\alpha = 1, 2, 3$ and unity matrix for $\alpha = 0$. So zero component S_{i0} is simply particles number and other components $\hat{S}_{i\alpha}$ are spin operators. Analogously h_{i0} is chemical potential and $h_{i\alpha}$ $(\alpha = 1, 2, 3)$ is external magnetic field.

The Hamiltonian (4.2.41) corresponds to Hubbard model with addition of intersite Coulomb interaction and in the following we will assume that matrix

elements t_{ij} and $V_{i\alpha,j\beta}$ are nonzero only for nearest neighbors. It is assumed also that fields $h_0, h_3 \neq 0$ while $h_1 = h_2 = 0$. In this case second term in H defines spin dependent chemical potential $\mu_\sigma \equiv h_{i0} + \sigma h_{i3}$ and this term can be written as $-\sum\limits_{i\sigma} \mu_\sigma \hat{n}_{i\sigma}$.

It is convenient to separate Hartree term in Hamiltonian (4.2.41) and write H in a form:

$$H = \sum_{ij\sigma} t_{ij} \hat{c}^\dagger_{i\sigma} \hat{c}_{j\sigma} - \sum_{i\sigma} \mu^{\text{eff}}_{i\sigma} \hat{n}_{i\sigma} + U \sum_i : \hat{n}_{i\uparrow} :: \hat{n}_{i\downarrow} : + \frac{1}{2} \sum_{ij} \sum_{\alpha,\beta} : \hat{S}_{i\alpha} : V_{i\alpha,j\beta} \hat{S}_{j\beta}. \quad (4.2.42)$$

Here we introduce symbol $: O :\equiv O - < O >$, where $< O >$ is an average of operator O over statistical ensemble. In the following we will assume that any operator O means a difference between O and its average value so that the second line in (4.2.42) describes fluctuations and Hartree terms are present in the first line in a term

$$\mu^{\text{eff}}_{i\sigma} = \mu_{i\sigma} - \sum_{j(\neq i)} V_{i0,j0} \left(\langle \hat{n}_{j\uparrow} \rangle + \langle \hat{n}_{j\downarrow} \rangle \right) - \sigma \sum_{j(\neq i)} V_{i3,j3} \left(\langle \hat{n}_{j\uparrow} \rangle - \langle \hat{n}_{j\downarrow} \rangle \right). \quad (4.2.43)$$

Let us express partition function Z as a functional integral over Grassmann variables and use Hubbard–Stratonovich transformation in order to linearize last (nonlinear) Hamiltonian term. Then

$$Z = \int D[c^\dagger_{i\sigma}(\tau), c_{i\sigma}(\tau); \Phi_{i\alpha}(\tau)] \mathrm{e}^{-S}, \quad (4.2.44)$$

where action S has a form

$$S = \int_0^\beta \mathrm{d}\tau \Big\{ \sum_{i\sigma} c^\dagger_{i\sigma} \left(\frac{\partial}{\partial \tau} - \mu^{\text{eff}}_{i\sigma} \right) c_{i\sigma} + \sum_{ij\sigma} t_{ij} c^\dagger_{i\sigma}(\tau) c_{j\sigma}(\tau) + U \sum_i n_{i\uparrow}(\tau) n_{i\downarrow}(\tau) + \frac{1}{2} \sum_{ij} \sum_{\alpha,\beta=0}^{3} \Phi_{i\alpha}(\tau) [\tilde{V}]^{-1}_{i\alpha,j\beta} \Phi_{j\beta}(\tau) - \sum_i \sum_{\alpha=0}^{3} \Phi_{i\alpha}(\tau) S_{i\alpha}(\tau) \Big\}. \quad (4.2.45)$$

Here $\Phi_{i\alpha}(\tau)$ are complex quantities conjugated to $S_{i\alpha}(\tau)$ that appear in Hubbard–Stratonovich integral identity. In expression (4.2.44) integration is assumed over Grassmann variables $[c^\dagger_{i\sigma}(\tau)]$ and $[c_{i\sigma}(\tau)]$ and also over complex field $[\Phi_{i\alpha}(\tau)]$.

In [183] a new quantity was introduced

$$\tilde{V}_{i\alpha,j\beta} = \lambda_{\alpha\beta} I_{ij} - V_{i\alpha,j\beta}, \quad (4.2.46)$$

where I_{ij} is nonzero if sites i and j are nearest neighbors. Quantities $\lambda_{\alpha\beta}$ are necessary to ensure interaction matrix to be positive definite. In [183] it was shown that physical properties do not depend on $\lambda_{\alpha\beta}$ choice.

In order to use representation (4.2.44) the following GF should be defined:

$$G_{i\sigma,j\sigma'}(\tau-\tau') = -\left\langle T_\tau \hat{c}_{i\sigma}(\tau)\hat{c}^\dagger_{j\sigma}(\tau')\right\rangle, \tag{4.2.47}$$

$$\chi_{i\alpha,j\beta}(\tau-\tau') = -\left\langle T_\tau \hat{S}_{i\alpha}(\tau)\hat{S}_{j\beta}(\tau')\right\rangle, \tag{4.2.48}$$

$$D_{i\alpha,j\beta}(\tau-\tau') = -\left\langle T_\tau \Phi_{i\alpha}(\tau)\Phi_{j\beta}(\tau')\right\rangle, \tag{4.2.49}$$

corresponding to electrons, charge-spin density, and auxiliary bosons ("phonons").

For density–density GF Larkin equation in Fourier representation is:

$$\chi^{-1}(\mathbf{k}, i\omega_\mathrm{n}) = \tilde{V}_\mathbf{k} + \Pi^{-1}(\mathbf{k}, i\omega_\mathrm{n}); \tag{4.2.50}$$

Here all quantities are matrices size 4×4 in indexes $\alpha,\beta = 0,1,2,3$. This equation is similar in structure with equation (4.1.7) for spin GF in tJ model.

Self-energy part $\Pi(\mathbf{k}, i\omega_\mathrm{n})$ for density–density GF is the same as for phonon GF. Dyson equation gives relation for Π and D^{-1} [183]:

$$\Pi(\mathbf{k}, i\omega_\mathrm{n}) = -\tilde{V}^{-1}_\mathbf{k} - \mathcal{D}^{-1}(\mathbf{k}, i\omega_\mathrm{n}), \tag{4.2.51}$$

here also all quantities are 4×4 matrices. For GFs χ and D Matsubara frequencies are even in contrast to odd frequencies for electron GF.

General representation (4.2.44) together with (4.2.45) is a starting point for extended $DMFT$ ($EDMFT$) scheme construction. For that as in Hubbard model one should integrate over all lattice sites except the distinguished impurity site. There are two possible ways of extending $DMFT$. One of them assumes homogeneous state so that integration over all sites except impurity one results in effective impurity model. Electrons on impurity site interact with fermionic and bosonic degrees of freedom of effective medium where impurity is embedded in. Another way is to assume long-range order in a system, for example, antiferromagnetism with two sublattices. In the last case two impurity sites belonging to two sublattices can be defined and after integration over all other lattice site one arrives to effective cluster (two atom) model with 2×2 matrices. Sun and Kotliar in [183] considered both those cases and bellow we will describe their results.

4.2.2 *EDMFT* for Homogeneous System

After integration over Grassmann variables in functional integral (4.2.44) for all lattice site except impurity one we obtain effective model with electron and boson degrees of freedom:

$$S_0^{\text{eff}} = -\int_0^\beta \mathrm{d}\tau \int_0^\beta \mathrm{d}\tau' \sum_\sigma c_{0\sigma}^\dagger(\tau)\mathcal{G}_\sigma^{-1}(\tau-\tau')c_{0\sigma}(\tau')$$
$$-\frac{1}{2}\int_0^\beta \mathrm{d}\tau \int_0^\beta \mathrm{d}\tau' \sum_{\alpha,\beta=0}^{3} \Phi_{0\alpha}(\tau)\mathcal{D}_{\alpha\beta}^{-1}(\tau-\tau')\Phi_{0\beta}(\tau-\tau')$$
$$+U\int_0^\beta \mathrm{d}\tau n_{0\uparrow}(\tau)n_{0\downarrow}(\tau) - \int_0^\beta \mathrm{d}\tau \sum_{\alpha=0}^{3} \Phi_{0\alpha}(\tau)S_{0\alpha}(\tau). \tag{4.2.52}$$

$\mathcal{G}_0^{-1}$ and $\mathcal{D}_{\alpha\beta}^{-1}$ have a meaning of dynamical mean-field acting on site 0 from the rest of the lattice. Those quantities can be connected with local *GF*s for electrons and bosons:

$$G_{\text{loc}}^\sigma(i\omega_\text{n}) = \sum_{\mathbf{k}} \left[i\omega_\text{n} - \varepsilon_{\mathbf{k}} + \mu_\sigma^{\text{eff}} - \Sigma_\sigma(i\omega_\text{n})\right]^{-1}, \tag{4.2.53}$$

$$\chi_{\text{loc}}^\sigma(i\omega_\text{n}) = \sum_{\mathbf{k}} \left[\tilde{V}_{\mathbf{k}} + \Pi^{-1}(i\omega_\text{n})\right]^{-1}, \tag{4.2.54}$$

$$D_{\text{loc}}^\sigma(i\omega_\text{n}) = -\sum_{\mathbf{k}} \left[\tilde{V}_{\mathbf{k}}^{-1} + \Pi(i\omega_\text{n})\right]^{-1}. \tag{4.2.55}$$

In deriving relations (4.2.53)–(4.2.55) we assumed a main *DMFT* approximation: electronic and bosonic self-energy parts (Σ_σ and Π) do not depend on wave vector $\mathbf{k}$.

Using Dyson equation for electron and boson *GF*s one can write expressions for Σ_σ and Π via local *GF*s (due to self-consistency conditions they coincide with effective impurity model *GF*s):

$$\Sigma_\sigma(i\omega_\text{n}) = \mathcal{G}_\sigma^{-1}(i\omega_\text{n}) - G_{\text{loc}}^{\sigma-1}(i\omega_\text{n}), \tag{4.2.56}$$

$$\Pi_\sigma(i\omega_\text{n}) = \mathcal{D}^{-1}(i\omega_\text{n}) - D_{\text{loc}}^{-1}(i\omega_\text{n}). \tag{4.2.57}$$

EDMFT calculation scheme is the same as for standard *DMFT*: for starting values of functions $\mathcal{G}_\sigma^{-1}(i\omega_\text{n})$ and $\mathcal{D}^{-1}(i\omega_\text{n})$ electron and phonon impurity *GF*s are calculated using action (4.2.52). Those functions are identified with local *GF*s $G_{\text{loc}}^{-1}(i\omega_\text{n})$ and $D_{\text{loc}}^{-1}(i\omega_\text{n})$. Self-energies $\Sigma_\sigma(i\omega_\text{n})$ and $\Pi(i\omega_\text{n})$ are calculated using equations (4.2.53)–(4.2.55). Then from Dyson equations (4.2.56)–(4.2.57) new values for $\mathcal{G}_\sigma^{-1}(i\omega_\text{n})$ and $\mathcal{D}^{-1}(i\omega_\text{n})$ are found and self-consistency loop is repeated till input values will be equal to output ones with a given accuracy.

In contrast to Hubbard model with local Coulomb interaction that is reduced in *DMFT* to effective Anderson impurity model when nonlocal interactions are included in the Hamiltonian-effective single impurity model is in dynamical field that is formed by effective medium with fermionic and bosonic degrees of freedom.

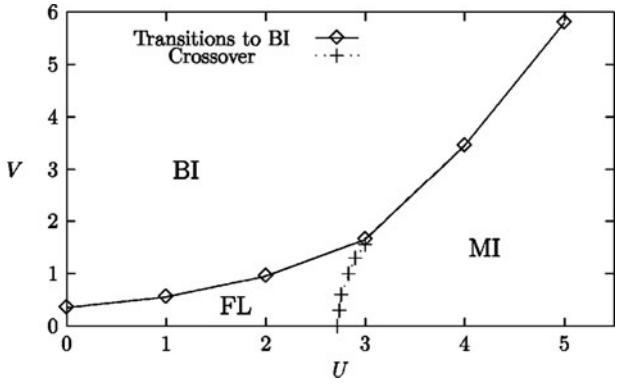

Fig. 4.5. Phase diagram for three-dimensional U-Vmodel at $\beta = 5.0$. Symbols show numerical results. Lines separate phases: Fermi liquid (FL), Mott insulator (MI) and exciton insulator (BI)

As an example, we will consider three-dimensional Hubbard model with Coulomb interaction on neighboring sites included (so called $U - V$ model):

$$H = \sum_{ij\sigma} t_{ij}\hat{c}^{\dagger}_{i\sigma}\hat{c}_{j\sigma} + U\sum_{i}\hat{n}_{i\uparrow}\hat{n}_{i\downarrow} + V\sum_{<ij>}(\hat{n}_{i\uparrow}+\hat{n}_{i\downarrow})(\hat{n}_{j\uparrow}+\hat{n}_{j\downarrow}). \tag{4.2.58}$$

Intersite interaction Fourier component is:

$$V_{\mathbf{k}} = V(\cos k_x + \cos k_y + \cos k_z). \tag{4.2.59}$$

This problem was solved by QMC method with generalized Hirsch-Fye algorithm. Semielliptical density of states was used with a width equal to $\sqrt{2}$. Imaginary time interval $\beta = 5.0$ was divided on 20 slices with $\Delta\tau = 1/4$ value. The calculation results are presented in Fig. 4.5 in a form of phase diagram on the plane (U, V) [183]. There are three phases: Fermi liquid (FL), Mott insulator (MI), and exciton insulator (BI). Phase transition line was found by approaching to instability in $EDMFT$ iterations with decreasing of V. Line between FL and MI phases is a crossover. It was defined from parameters U and V values where $\mathrm{Im}G_{\sigma}(i\omega_{\mathrm{n}}) = -0.5$. This method allows to treat a model with exchange interactions.

4.2.3 *EDMFT* for the System with Two Sublattices

Let us consider a system with two interpenetrating sublattices that is described by the Hamiltonian (4.2.58). For the state with a long-range order let us rewrite (4.2.58) as a sum over sites for sublattices A and B:

$$H = t \sum_{<Ai,Bj>\sigma} \hat{c}^{\dagger}_{Ai\sigma}\hat{c}_{Bj\sigma} - \sum_{Xi,\sigma} \mu_{Xi,\sigma}\hat{n}_{Xi,\sigma} + U\sum_{Xi} \hat{n}_{Xi\uparrow}\hat{n}_{Xi\downarrow} + \sum_{<Ai,Bj>} (\hat{n}_{Ai\uparrow} + \hat{n}_{Ai\downarrow})V_{Ai,Bj}(\hat{n}_{Bj\uparrow} + \hat{n}_{Bj\downarrow}). \quad (4.2.60)$$

We assumed that nearest neighbors belong to different sublattices. Indexes i and j run over one sublattice only. Indexes $X = A, B$ denote sublattices.

Chemical potential is homogeneous inside sublattice:

$$\mu_{Xi,\sigma} = \begin{cases} \mu_{A\sigma}, & X = A \\ \mu_{B\sigma}, & X = B \end{cases}. \quad (4.2.61)$$

Using Hubbard–Stratonovich transformation in expression (4.2.44) for Z one can write an action as:

$$S = \int_0^{\beta} \mathrm{d}\tau \Big\{ \sum_{Xi\sigma} c^{\dagger}_{Xi\sigma}(\tau)\frac{\partial}{\partial\tau}c_{Xi\sigma}(\tau) - \mu^{\mathrm{eff}}_{X\sigma}n_{Xi\sigma}(\tau) + t\sum_{<Ai,Bj>\sigma} c^{\dagger}_{Ai\sigma}(\tau)c_{Bj\sigma}(\tau) + U\sum_{Xi} n_{Xi\uparrow}n_{Xi\downarrow} + \frac{1}{2}\sum_{Xi,Yj} \Phi_{Xi}(\tau)\tilde{V}^{-1}_{Xi,Yj}\Phi_{Yj}(\tau) - \sum_{Xi}\Phi_{Xi}(\tau)(n_{Xi\uparrow}(\tau) + n_{Xi\downarrow}(\tau))\Big\}. \quad (4.2.62)$$

Here

$$\mu^{\mathrm{eff}}_{X\sigma} = \mu_{X\sigma} - \frac{1}{2}U - \sum_j V_{<Xi,\bar{X}j>}\big\langle \big[n_{\bar{X}i\uparrow}(\tau) + n_{\bar{X}j\downarrow}(\tau)\big]\big\rangle$$

is effective chemical potential for sublattice obtained by separating Hartree terms in original Hamiltonian.

In going from lattice model to effective local model we should use as a local object not one site but a cluster (A, B) containing two neighboring atoms A and B. Performing in (4.2.44) integration with action (4.2.62) over all lattice sites except cluster sites gives an effective action

$$S^{\mathrm{eff}} = -\int_0^{\beta}\mathrm{d}\tau\int_0^{\beta}\mathrm{d}\tau' \sum_{XY\sigma} c^{\dagger}_{X\sigma}(\tau)[\mathcal{G}^{-1}_{\sigma}]^{XY}(\tau-\tau')c_{Y\sigma}(\tau') - \frac{1}{2}\int_0^{\beta}\mathrm{d}\tau\int_0^{\beta}\mathrm{d}\tau' \sum_{XY}\Phi_X(\tau)[D^{-1}]^{XY}(\tau-\tau')\Phi_Y(\tau') + U\int_0^{\beta}\mathrm{d}\tau\sum_X n_{X\uparrow}n_{X\downarrow} - \int_0^{\beta}\mathrm{d}\tau\sum_X \Phi_X(\tau)[n_{X\uparrow} + n_{X\downarrow}], \quad (4.2.63)$$

where two new functions were introduced $[\mathcal{G}_\sigma^{-1}]^{XY}$ and $[D^{-1}]^{XY}$ having a meaning of fermionic and bosonic mean-fields that should be calculated using standard self-consistency conditions.

Let us define now GF corresponding to action S^{eff}:

$$G_\sigma^{XY}(i\tau, i'\tau') = \left\langle T_\tau \hat{c}_{Xi\sigma}(\tau)\hat{c}^\dagger_{Yi'\sigma}(\tau')\right\rangle, \tag{4.2.64}$$

$$\chi^{XY}(i\tau, i'\tau') = \left\langle T_\tau \left[\hat{n}_{Xi\uparrow}(\tau) + \hat{n}_{Xi\downarrow}(\tau)\right]\left[\hat{n}_{Yi'\uparrow}(\tau') + \hat{n}_{Yi'\downarrow}(\tau')\right]\right\rangle, \tag{4.2.65}$$

$$D^{XY}(i\tau, i'\tau') = \left\langle T_\tau \hat{\Phi}_{Xi}(\tau)\hat{\Phi}_{Yi'}(\tau')\right\rangle. \tag{4.2.66}$$

Here X and Y can have values A and B so GFs are matrices of 2×2 size in sublattices index. Equations for them in symbolic matrix form coincide with equations (4.2.53)–(4.2.55). In explicit form these equations are:

$$\begin{pmatrix} G_{\text{loc}}^{\sigma AA}(i\omega_{\text{n}}) & G_{\text{loc}}^{\sigma AB}(i\omega_{\text{n}}) \\ G_{\text{loc}}^{\sigma BA}(i\omega_{\text{n}}) & G_{\text{loc}}^{\sigma BB}(i\omega_{\text{n}}) \end{pmatrix} = \sum_{\mathbf{k}} \left[\begin{pmatrix} i\omega_{\text{n}} + \mu_{A\sigma} & -\varepsilon_{\mathbf{k}} \\ -\varepsilon_{\mathbf{k}} & i\omega_{\text{n}} + \mu_{B\sigma} \end{pmatrix} - \begin{pmatrix} \Sigma_\sigma^{AA}(i\omega_{\text{n}}) & \Sigma_\sigma^{AB}(i\omega_{\text{n}}) \\ \Sigma_\sigma^{BA}(i\omega_{\text{n}}) & \Sigma_\sigma^{BB}(i\omega_{\text{n}}) \end{pmatrix} \right]^{-1}, \tag{4.2.67}$$

$$\begin{pmatrix} D_{\text{loc}}^{AA}(i\omega_{\text{n}}) & D_{\text{loc}}^{AB}(i\omega_{\text{n}}) \\ D_{\text{loc}}^{BA}(i\omega_{\text{n}}) & D_{\text{loc}}^{BB}(i\omega_{\text{n}}) \end{pmatrix} [3pt] = -\sum_{\mathbf{k}} \left[\begin{pmatrix} \lambda & -2V_{\mathbf{k}} \\ -2V_{\mathbf{k}} & \lambda \end{pmatrix}^{-1} + \begin{pmatrix} \Pi^{AA}(i\omega_{\text{n}}) & \Pi^{AB}(i\omega_{\text{n}}) \\ \Pi^{BA}(i\omega_{\text{n}}) & \Pi^{BB}(i\omega_{\text{n}}) \end{pmatrix} \right]^{-1}, \tag{4.2.68}$$

$$\begin{pmatrix} \chi_{\text{loc}}^{AA}(i\omega_{\text{n}}) & \chi_{\text{loc}}^{AB}(i\omega_{\text{n}}) \\ \chi_{\text{loc}}^{BA}(i\omega_{\text{n}}) & \chi_{\text{loc}}^{BB}(i\omega_{\text{n}}) \end{pmatrix} = \sum_{\mathbf{k}} \left[\begin{pmatrix} \lambda & -2V_{\mathbf{k}} \\ -2V_{\mathbf{k}} & \lambda \end{pmatrix} + \begin{pmatrix} \Pi^{AA}(i\omega_{\text{n}}) & \Pi^{AB}(i\omega_{\text{n}}) \\ \Pi^{BA}(i\omega_{\text{n}}) & \Pi^{BB}(i\omega_{\text{n}}) \end{pmatrix} \right]^{-1}. \tag{4.2.69}$$

In equations (4.2.68) and (4.2.69) parameter λ is used that was defined earlier. We emphasize again that observable properties do not depend on λ [183].

Combining two last equations one can obtain relation for local density–density GF and phonon GF:

$$\begin{pmatrix} \chi_{\text{loc}}^{AA} & \chi_{\text{loc}}^{AB} \\ \chi_{\text{loc}}^{BA} & \chi_{\text{loc}}^{BB} \end{pmatrix} = \begin{pmatrix} \Pi^{AA} & \Pi^{AB} \\ \Pi^{BA} & \Pi^{BB} \end{pmatrix} \begin{pmatrix} 1 & 0 \\ 0 & 1 \end{pmatrix} + \begin{pmatrix} \Pi^{AA} & \Pi^{AB} \\ \Pi^{BA} & \Pi^{BB} \end{pmatrix} \begin{pmatrix} D_{\text{loc}}^{AA} & D_{\text{loc}}^{AB} \\ D_{\text{loc}}^{BA} & D_{\text{loc}}^{BB} \end{pmatrix}; \tag{4.2.70}$$

all quantities depend on one argument $i\omega_{\text{n}}$.

Self-consistency equations (4.2.67)–(4.2.69) together with the expressions for three *GF*s $G_\sigma^{XY}(\tau-\tau')$, $\chi^{XY}(\tau-\tau')$, and $D^{XY}(\tau-\tau')$ calculated with an action S^{eff} (4.2.63) create a closed equations system to determine $\Sigma_\sigma^{XY}(i\omega_\text{n})$, $\Pi^{XY}(i\omega_\text{n})$, $\mathcal{G}_\sigma^{XY}(i\omega_\text{n})$, and $D^{XY}(i\omega_\text{n})$. These equations can be easily generalized if a local cluster includes an arbitrary number of atoms. *QMC* method can be also generalized for effective cluster problem [183].

4.2.4 *DMFT* with Orbital Degeneracy

Going from models to real materials one should take into account orbital degeneracy of transition metal ions in the crystal. First of all full electrons state space must be separated in itinerant electrons subspace where Coulomb interaction is small enough to be treated in static mean-field approximation and localized electrons subspace with strong Coulomb interaction that should be treated in *DMFT*. Let us write full system Hamiltonian as:

$$\begin{aligned} H = H^0 &+ \frac{1}{2}\sum_{i=i_d,l=l_d}\sum_{m\sigma,m'\sigma'}{}' U_{mm'}^{\sigma\sigma'}\hat{n}_{ilm\sigma}\hat{n}_{ilm'\sigma'} \\ &-\frac{1}{2}\sum_{i=i_d,l=l_d}\sum_{mm'\sigma}{}' J_{mm'}\hat{c}_{ilm\sigma}^\dagger\hat{c}_{ilm'\bar{\sigma}}^\dagger\hat{c}_{ilm'\sigma}\hat{c}_{ilm\bar{\sigma}} \\ &-\sum_{i=i_d,l=l_d}\sum_{m\sigma}\Delta\varepsilon_d\hat{n}_{ilm\sigma}. \end{aligned} \tag{4.2.71}$$

here H^0 is Hamiltonian for electrons on the lattice without Coulomb interaction between them.

Three last terms describe local interaction for second subspace orbitals (site and orbital indexes for those orbitals are i_d and l_d). Coulomb interaction parameters $U_{mm'}^{\sigma\sigma'}$ in general depend on specific orbitals m, m' and σ, σ'. However, the following approximation is often used:

$$U_{mm}^{\uparrow\downarrow} \equiv U, \quad J_{mm'} \equiv J, \quad U_{mm'}^{\sigma\sigma'} = U - 2J - J\delta_{\sigma\sigma'} \quad (m \neq m'). \tag{4.2.72}$$

The last term in (4.2.71) corresponds to the the shift of one-electron potential for interacting orbitals.

H^0 has a quadratic form in Fermi operators:

$$\begin{aligned} H^0 = \sum_{ilm,jl'm'}\sum_\sigma \big(&\delta_{ilm,jl'm'}\varepsilon_{ilm}\hat{n}_{ilm\sigma} \\ &+t_{ilm,jl'm'}c_{ilm\sigma}^\dagger c_{jl'm'\sigma},\big). \end{aligned} \tag{4.2.73}$$

Later we apply to Hamiltonian (4.2.71) Dynamical Mean-Field Theory described in Chap. 3 for simple one-band Hubbard model. Green function now has more general form:

$$g_{qlm,q'l'm'}^\sigma(i\tau,i'\tau') = -\left\langle T\hat{c}_{iqlm\sigma(\tau)}\hat{c}_{i'q'l'm'\sigma}^\dagger(\tau)\right\rangle \tag{4.2.74}$$

Here i is crystal cell number, q is atom in a cell number, l and m are orbital moment and its projection. Fourier transformation of local GF in variables $j - j'$ $\tau - \tau'$ gives:

$$g^{\sigma}_{qlm,q'l'm'}(j,j;i\omega_{\rm n}) \equiv G^{\sigma}_{qlm,q'l'm'}(i\omega_{\rm n}) = \sum_{\mathbf{k}} \left(\left[i\omega_{\rm n}\hat{1} + \mu\hat{1} - \hat{H}^0(\mathbf{k}) - \hat{\Sigma}(i\omega_{\rm n}) \right]^{-1} \right)^{\sigma}_{qlm,q'l'm'} \tag{4.2.75}$$

In derivation of the above formula it was taken into account that in $d \to \infty$ limit self-energy does not depend on wave vector but only on frequency. In expression (4.2.75) $\hat{1}$ symbol means unit matrix in orbital space $n = \{qlm\}$ and $\hat{\Sigma}(i\omega_{\rm n})$ is a matrix with elements $\Sigma_{nn'}$. Nonzero elements of this matrix form a block with $n = \{q_d l_d m\}$ corresponding to interacting orbitals only.

Omitting indexes q_d and l_d GF will have a form $G_{mm'}(i\omega_{\rm n})$. Then simplified form of expression (4.2.75) is:

$$G^{\sigma}_{mm'}(i\omega_{\rm n}) = \sum_{\mathbf{k}} \left(\left[i\omega_{\rm n}\hat{1} + \mu\hat{1} - \hat{H}^0(\mathbf{k}) - \hat{\Sigma}(i\omega_{\rm n}) \right]^{-1} \right)^{\sigma}_{mm'}. \tag{4.2.76}$$

Basic *DMFT* idea is to identify local GF with effective single impurity model GF. Analogous to relation (3.1.34) this impurity GF can be written as a functional integral over Grassmann variables:

$$G_{m_1 m_2}(\tau_1 - \tau_2) = -\frac{1}{Z} \int D[c^{\dagger}]D[c] \left\{ c_{m_1\sigma}(\tau_1) c^{\dagger}_{m_2\sigma}(\tau_2) \right\} {\rm e}^{-S[c^{\dagger},c]}, \tag{4.2.77}$$

$$Z = \int D[c^{\dagger}]D[c] {\rm e}^{-S[c^{\dagger},c]}, \tag{4.2.78}$$

where

$$\begin{aligned} S[c^{\dagger},c] = &- \sum_{\sigma} \int {\rm d}\tau \int {\rm d}\tau' c^{\dagger}_{m\sigma}(\tau) \left(\mathcal{G}_0^{-1}(\tau - \tau') \right)^{\sigma}_{mm'} c_{m'\sigma}(\tau') \\ &+ \frac{1}{2} {\sum_{m\sigma,m'\sigma'}}' U^{\sigma\sigma'}_{mm'} \int {\rm d}\tau c^{\dagger}_{m\sigma}(\tau) c_{m\sigma}(\tau) c^{\dagger}_{m'\sigma'}(\tau) c_{m'\sigma'}(\tau) \\ &- \frac{1}{2} {\sum_{m\sigma m'}}' J_{mm'} \int {\rm d}\tau c^{\dagger}_{m\sigma}(\tau) c_{m\bar{\sigma}}(\tau) c^{\dagger}_{m'\sigma}(\tau) c_{m'\bar{\sigma}}(\tau) \end{aligned} \tag{4.2.79}$$

is effective action.

Here $\mathcal{G}_0(\tau - \tau')$ is noninteracting single impurity model GF having a meaning of dynamical mean-field acting on impurity orbitals from the rest of the lattice. It is expressed via hybridization function $\Delta(i\omega_{\rm n})$ using equation (see (3.1.33)):

$$\left(\mathcal{G}_0^{-1}(i\omega_{\rm n}) \right)_{mm'} = (i\omega_{\rm n} + \mu)\hat{1} - \Delta_{mm'}(i\omega_{\rm n}), \tag{4.2.80}$$

where GF and hybridization function are matrices. Green function $\mathcal{G}_0$ is determined by Dyson equation:

$$\mathcal{G}_0 = \left(G^{-1} - \Sigma\right)^{-1}. \tag{4.2.81}$$

DMFT calculation scheme for self-consistent solution of equations (4.2.76), (4.2.77) and (4.2.81) was described in Sect. 3.1.5. In this method the problem of electronic spectra for lattice is reduced to solution of effective Anderson impurity problem. This problem can be solved by one of the methods described in Chap. 3, for example by Quantum Monte Carlo method.

4.2.5 *QMC* Impurity Solver for the Problem with Orbital Degeneracy

In order to generalize Hirsch-Fye method formulas to multiorbital case one should (see Sect. 3.2) go from functional integral to integral over discretized imaginary time $0 \le \tau \le \beta = 1/T$. Dividing it on L time slices of the size $\Delta\tau = \beta/L$ integral (4.2.79) is approximated by a sum:

$$\begin{aligned} S[c^\dagger, c] = &-(\Delta\tau)^2 \sum_{m\sigma} \sum_{l,l'=1}^{L} c^\dagger_{m\sigma l} \mathcal{G}^{\sigma-1}_m(\tau_l - \tau_{l'}) c_{m\sigma l'} \\ &+ \frac{1}{2}\Delta\tau \sum_{m\sigma m'\sigma'}{}' U^{\sigma\sigma'}_{mm'} \sum_{l=0}^{L-1} c^\dagger_{m\sigma l} c_{m\sigma l} c^\dagger_{m'\sigma' l} c_{m'\sigma' l}. \end{aligned} \tag{4.2.82}$$

We omitted exchange term in action because it has more complicated form than direct Coulomb term.

The integral term in (4.2.82) is linearized using discrete Hubbard–Stratonovich transformation (see Sect. (3.2)). For multiorbital case instead of formulas ((3.2.58) and (3.2.59)) we have:

$$\begin{aligned} &\exp\left\{\frac{\Delta\tau}{2} U^{\sigma\sigma'}_{mm'} \left(c^\dagger_{m\sigma l} c_{m\sigma l} - c^\dagger_{m'\sigma' l} c_{m'\sigma' l}\right)^2\right\} \\ &= \frac{1}{2} \sum_{S_{lmm'}=\pm 1}^{\sigma\sigma'} \exp\left\{\Delta\tau \lambda^{\sigma\sigma'}_{lmm'} S^{\sigma\sigma'}_{lmm'} \left(c^\dagger_{m\sigma l} c_{m\sigma l} - c^\dagger_{m'\sigma' l} c_{m'\sigma' l}\right)\right\}, \end{aligned} \tag{4.2.83}$$

where parameter $\lambda^{\sigma\sigma'}_{lmm'}$ is found from equation

$$\cos h \lambda^{\sigma\sigma'}_{lmm'} = \exp\left(\frac{\Delta\tau U^{\sigma\sigma'}_{mm'}}{2}\right), \tag{4.2.84}$$

corresponding to equation (3.2.59).

In the result instead of formulas (3.2.69) and (3.2.73) we have now:

$$Z = \frac{1}{2^L} \sum_l \sum_{m'\sigma', m''\sigma''}{}' \sum_{S^{\sigma''\sigma'}_{lm''m'}=\pm 1} \prod_{m\sigma} \det M^{\sigma S}_m, \tag{4.2.85}$$

$$G^{\tilde{\sigma}}_{\tilde{m}l_1l_2} = \frac{1}{Z}\frac{1}{2^L}\sum_{l}\sum_{m'\sigma',m''\sigma''}{}' \sum_{S^{\sigma''\sigma'}_{lm''m'}=\pm 1} \left[(M^{\tilde{\sigma}S}_{\tilde{m}})^{-1}\right]_{l_1l_2} \prod_{m\sigma} \det M^{\sigma S}_{m}, \quad (4.2.86)$$

$$M^{\tilde{\sigma}S}_{\tilde{m}} = (\Delta\tau)^2\left[G^{\sigma -1}_{m} + \Sigma^{\sigma}_{m}\right]\mathrm{e}^{-\lambda^{\sigma S}_{m}} + 1 - \mathrm{e}^{-\tilde{\lambda}^{\sigma S}_{m}}. \quad (4.2.87)$$

Matrix elements $\tilde{\lambda}^{\sigma S}_{m}$

$$\tilde{\lambda}^{\sigma S}_{mll'} = -\delta_{ll'}\sum_{m'\sigma'} \lambda^{\sigma\sigma'}_{mm'}\xi^{\sigma\sigma'}_{mm'}S^{\sigma\sigma'}_{lmm'} \quad (4.2.88)$$

are linear combination of Ising variables $S^{\sigma\sigma'}_{lmm'}$ and summation over them is performed in expressions (4.2.85) and (4.2.86) for partition function and GF. Quantities $\xi^{\sigma\sigma'}_{mm'}$ are defined via θ function:

$$\theta(x) = \begin{cases} 1, & x > 0 \\ -1, & x < 0 \end{cases}; \quad (4.2.89)$$

$$\xi^{\sigma\sigma'}_{mm'} = 2\theta\left[\sigma' - \sigma + \delta_{\sigma\sigma'}(m' - m) - 1\right]. \quad (4.2.90)$$

Going from quantities $\hat{O}^{\sigma}$ in Hubbard model expressions to formulas (4.2.85)-(4.2.88) we have used relations (B.17) and (B.18). It is easy to see that formulas (4.2.85)–(4.2.88) can be reduced to corresponding expressions in Sect. 3.2 by omitting indexes m, m' that corresponds to a single correlated orbital.

Practical realization of Hirsch-Fye algorithm for the system with degenerate orbitals is the same as for nondegenerate Hubbard model. The essential difference is a number of Ising spins $S^{\sigma\sigma'}_{lmm'}$. If previously spin components S_l number was L, then now it is equal to $M(2M-1)L$ where M is number of orbitals on impurity site $(m, m' = 1, 2, \ldots, M)$. Correspondingly, a total number of spin configuration in a sum (4.2.85)–(4.2.88) is huge: $2^{M(2M-1)L}$. A number of configuration is growing exponentially with M and so for d- and f-orbitals where M is 5 and 7 calculations could become very expensive. However modern computers can treat such problems but the price for that is relatively high-temperature values where computations are possible: it is difficult to go significantly below room temperature.

4.2.6 Exchange Interactions in *QMC*

We have omitted earlier the exchange terms in Hamiltonian (4.2.71) for degenerate orbital case. There is also so called pair hopping term. Let us consider now both those contributions to Hamiltonian $H = H_0 + H_1 + H_2$ where

$$H_2 = J\sum_{\substack{i \\ m\neq m'}}\left(\hat{c}^{\dagger}_{im\uparrow}\hat{c}^{\dagger}_{im'\downarrow}\hat{c}_{im\downarrow}\hat{c}_{im'\uparrow} + \hat{c}^{\dagger}_{im\uparrow}\hat{c}^{\dagger}_{im\downarrow}\hat{c}_{im'\downarrow}\hat{c}_{im'\uparrow}\right). \quad (4.2.91)$$

H_0 is kinetic energy term and H_1 is Coulomb interaction.

In Hirsch-Fye method Coulomb term is linearized via Hubbard–Stratonovich transformation (4.2.83). However, H_2 term cannot be linearized in this way. Authors of [138] have proposed another transformation for double-degenerate case $m = 1, 2$:

$$\mathrm{e}^{-\Delta\tau H_2} = \frac{1}{2}\sum_{\nu=\pm1} \mathrm{e}^{\lambda\nu(f_\uparrow - f_\downarrow)}\mathrm{e}^{a(N_\uparrow+N_\downarrow)+bN_\uparrow N_\downarrow}, \tag{4.2.92}$$

where variables λ, a and b are defined by equations

$$\lambda = \frac{1}{2}\ln\bigl(\mathrm{e}^{2J\Delta\tau} + \sqrt{\mathrm{e}^{4J\Delta\tau} - 1}\bigr), \tag{4.2.93}$$

$$a = -\ln\cosh\lambda, \quad b = \ln\cosh(J\Delta\tau), \tag{4.2.94}$$

and f_σ, N_σ are Hermitian operators:

$$\begin{aligned} f_\sigma &= c^\dagger_{1\sigma}c_{2\sigma} + c^\dagger_{2\sigma}c_{1\sigma}, \\ N_\sigma &= n_{1\sigma} + n_{2\sigma} - 2n_{1\sigma}n_{2\sigma} \end{aligned} \tag{4.2.95}$$

All operators in equation (4.2.92) correspond to the same time value τ_l however index l was omitted.

The transformation (4.2.92) partially linearizes interaction H_2 but still leaves unchanged nonlinear term $N_\uparrow N_\downarrow$. However because of projective properties of the operator $N_\sigma^2 = N_\sigma$ the term $\mathrm{e}^{bN_\uparrow N_\downarrow}$ can be connected to the corresponding Coulomb term and linearized by standard Hirsch-Hubbard–Stratonovich transformation. In the result we have Hirsch-Fye algorithm but with summation over two sets of Ising spins $\{S_l\}$ and $\{\nu_l\}$. In this case "sign problem" appears, i.e., quantities $\det M_m^{\sigma S}$ can have negative values. However analysis in [138] have shown that probability of negative terms is relatively small and their influence is suppressed by overwhelming majority of positive determinants. So this *QMC* algorithm can give physically reasonable results for models in wide parameters range. Earlier approaches to this problem were discussed in [138, 184–186].

4.2.7 Continuous-Time *QMC* for Two-Orbital Model

An important generalization of nondegenerate Hubbard model investigated in Chap. 3 is two-orbitals on-site model with exchange interaction and pair hopping terms. The effective single impurity model Hamiltonian has three terms: $H = H_{\mathrm{loc}} + H_t + H_V$ where H_{loc} describes all on-site interactions, H_t describes electrons hopping on the lattice and H_V is the *sd*-hybridization.

Let us choose local term in the following form [145]

$$\begin{aligned} H_{\mathrm{loc}} = &\sum_{\alpha\sigma}\mu n_{\alpha\sigma} + \sum_{\alpha} U n_{\alpha\uparrow}n_{\alpha\downarrow} + \sum_{\sigma} U' n_{1\sigma}n_{2\bar{\sigma}} + \sum_{\sigma}(U' - J)n_{1\sigma}n_{2\sigma} \\ &-J\bigl(d^\dagger_{1\downarrow}d^\dagger_{2\uparrow}d_{2\downarrow}d_{1\uparrow} + d^\dagger_{2\uparrow}d^\dagger_{2\downarrow}d_{1\uparrow}d_{1\downarrow} + K.C.\bigr). \end{aligned} \tag{4.2.96}$$

Here index $\alpha = 1, 2$ denotes orbitals, $n_{\alpha\sigma} = d^{\dagger}_{\alpha\sigma} d_{\alpha\sigma}$ is d-electrons number operator for α orbital. Coulomb interaction parameters U, U' and exchange parameter J are connected via relation $U' = U - 2J$.

Hopping operator is written in nearest neighbors approximation:

$$H_t = t_1 \sum_{<ij>\sigma} c^{\dagger}_{i1\sigma} c_{j1\sigma} + t_2 \sum_{<ij>\sigma} c^{\dagger}_{i2\sigma} c_{j2\sigma} \tag{4.2.97}$$

with different matrix elements for different orbitals. We will assume that $t_2 = 2t_1$. That gives two bands: narrow ($\alpha = 1$) and broad ($\alpha = 2$). Hybridization term H_V has a standard form.

It is interesting to investigate Mott phase transition in this model. Is it possible, for example, that "Orbital Selective Mott Transition" [187] is realized when narrow band states correspond to insulator while broad band is still metallic? This probelm was investigated in many works [138, 145, 184–186, 188–191] but no unambiguous answer was found.

Using Exact Diagonalization method for impurity problem authors of [188] have found that narrow band becomes insulating for smaller U values that a broad band. For semielliptical density of states with $t_2/t_1 = 2$ critical values are $U_1^c/t_1 \simeq 5.4$ and $U_2^c/t_1 \simeq 7$. From other side earlier works using *QMC* gave simultaneous metal–insulator transition [190]. However, *QMC* method has "sign problem" for exchange and pair hopping terms and [190] results were reconsidered in other works. Arita and Held [138] using new discrete Hubbard–Stratonovich transformation [184] in projective *QMC* method have found possibility of "Orbital Selective Mott Transition" in two-orbital model and calculated by them critical value U_1^c agrees with [188] results. However projective *QMC* method does not allow to perform calculation for large enough U_2^c values.

All these difficulties can be overcome by using Continuous Time *QMC* method (see Sect. 3.2.5). Werner and Millis [145] have used $CT - QMC$ for two-orbital paramagnetic model with Hamiltonian (4.2.96) for half-filled band and relation $\frac{t_2}{t_1} = 2$ for hopping elements. For local Hamiltonian (4.2.96) there are 16 eigenstates and so one has to treat 16×16 size matrices but U and J values can be arbitrary. Hybridization H_V expansion *QMC* method does not have "sign problem" so this method results are reliable.

In Fig. 4.6 calculated *GF* $G(\tau)$ is presented for parameters $\beta t_1 = 50$, $J = U/4$ and $U/t_1 = 4$, 6, 8. Chemical potential corresponds to half filling. From Fig. 4.6 follows that at $U/t_1 = 4$ both band (narrow and broad) are metallic whereas for $U/t_1 = 8$ they are insulating. Phase transition should happen for intermediate U/t_1 value. For one of the intermediate values $U/t_1 = 6$ in Fig. 4.6 calculated values of $G(\tau)$ for both bands are shown. One can see that broad band is still metallic while a narrow one is insulating. So in this calculations "Orbital Selective Mott Transition" was found with an energy gap in only one of the bands.

Earlier, it was suggested [187] that insulating orbital can play a role of local magnetic moment that is connected with metallic orbital via exchange

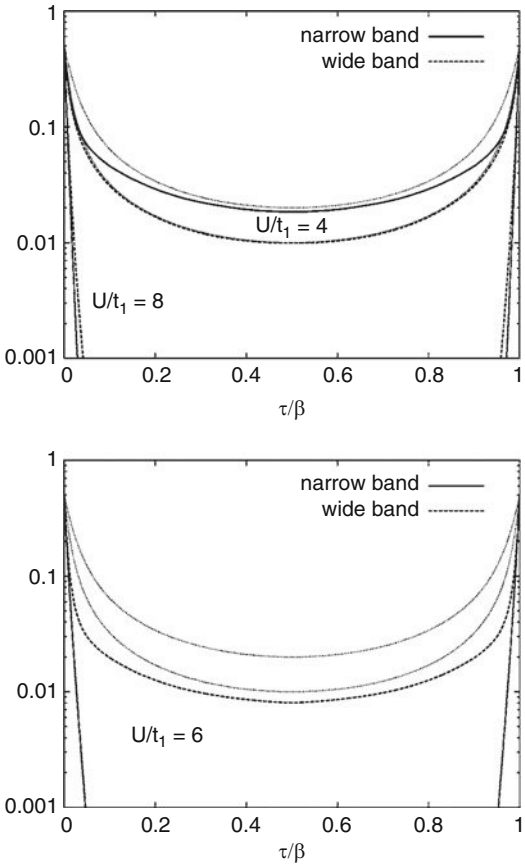

Fig. 4.6. Green function for two-orbital model calculated for semielliptical density of states and $n = 1$ for Coulomb interaction parameters values U/t_1 equal to (**a**) $U/t_1 = 4$ and 8; (**b**) $U/t_1 = 6$. Dots show for comparison GF for noninteracting system at $\beta t = 50$ $\beta t = 100$ [145]

interaction J (usually it is Hund exchange interaction of ferromagnetic sign $J > 0$). That means that two-orbital model with $J > 0$ is equivalent to ferromagnetic Kondo-Hubbard lattice. In work [145] spin correlation function $\langle S_z(0)S_z(\tau)\rangle$ was calculated for two-orbital model at $U/t_1 = 6$ and also for ferromagnetic Kondo lattice. Dependence of $\langle S_z(0)S_z(\tau)\rangle$ on τ for ferromagnetic Kondo lattice is very close to narrow band of two-orbital model results that confirms equivalence of those two models.

These calculations confirm high efficiency of $CT - QMC$ method that is free from "sign problem" and has no restrictions on U and J parameter values. As it will be discussed in Sect. 5.3 Werner and Millis [145] have investigated by this method Kondo lattice with exchange interaction of ferromagnetic and antiferromagnetic sign.

4.3 Taking into Account Spatial Fluctuations

4.3.1 Heuristic Approach to *DMFT* Extension for Spatial Fluctuations

High efficiency of *DMFT* is defined by its basic approximation: self-energy depends only on frequency but not on wave vector. In real space that means that self-energy matrix is diagonal in site indexes or in other words spatial correlations are neglected. That is a severe approximation because spatial fluctuations reveal itself in many physical phenomena. Examples are spin susceptibility behavior near phase transition in antiferromagnetic state, Fermi surface features in strongly correlated systems, and appearance of pseudogap state leading to Fermi surface destruction for specific areas. As *DMFT* corresponds to $d = \infty$ limit spatial fluctuations description requires corrections of the order of $\frac{1}{d}$. There are many approaches to this problem. We start from the simplest one where no $\frac{1}{d}$ theory analysis is performed but spatial fluctuations are explicitly introduced in *DMFT* equations. This scheme is an heuristic development for magnetic susceptibility calculations in the frame of *DMFT* described in Sect. 3.6. Kusunose [192] proposed to use Bethe-Solpeter equation for particle–hole channel where two-particle GF (dashed square in Fig. 4.7) allows to derive equations for charge and spin susceptibilities. The quantity Γ (open square) is uncutable in particle–hole lines vertex part. Two-particle GFs are correlators for charge and spin densities

$$\rho_{\mathrm{c}} = \hat{c}^{\dagger}_{\uparrow}\hat{c}_{\uparrow} + \hat{c}^{\dagger}_{\downarrow}\hat{c}_{\downarrow}, \quad \rho_{\mathrm{s}} = \hat{c}^{\dagger}_{\uparrow}\hat{c}_{\uparrow} - \hat{c}^{\dagger}_{\downarrow}\hat{c}_{\downarrow}. \tag{4.3.98}$$

and depend on three 4-momenta. Let us denote them as $\chi_{\mathrm{c}}(k, k'; q)$ and $\chi_{\mathrm{s}}(k, k'; q)$. To four-momenta k and k' correspond fermionic frequencies ω_n and $\omega_{n'}$ while to 4-momentum q the bosonic frequency ε_m.

To graphic Bethe-Solpeter equation (Fig. 4.7) correspond two analytic equations, one for charge and another for spin GF:

$$\chi_{\mathrm{c}}(k, k'; q) = \chi_0(k, q)\left[\delta_{kk'} - \sum_{k''} \Gamma_{\mathrm{c}}(k, k''; q)\chi_{\mathrm{c}}(k'', k'; q)\right], \tag{4.3.99}$$

$$\chi_{\mathrm{s}}(k, k'; q) = \chi_0(k, q)\left[\delta_{kk'} + \sum_{k''} \Gamma_{\mathrm{s}}(k, k''; q)\chi_{\mathrm{s}}(k'', k'; q)\right]. \tag{4.3.100}$$

Here

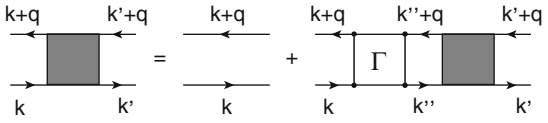

Fig. 4.7. Bethe-Solpeter equation for particle–hole channel

$$\chi_0(k;q) = -G(k)G(k+q) \tag{4.3.101}$$

is two-particle zero-order GF. Paramagnetic phase is assumed so spin indexes are omitted. Standard susceptibilities can be obtained by summation of two-particles GFs over fermionic 4-momenta:

$$\chi_\alpha(q) = \sum_{kk'} \chi_\alpha(k,k';q), \quad \alpha = c,s \tag{4.3.102}$$

Single particle electronic GF obeys to Dyson equation

$$G^{-1}(k) = i\omega_n + \tilde{\mu} - \varepsilon_{\mathbf{k}} - \Sigma(k), \tag{4.3.103}$$

where $\Sigma(k)$ is self-energy where Hartree part is subtracted and included in renormalized chemical potential $\tilde{\mu} = \mu - U\frac{n}{2}$, where $n = \sum_k G(k)\mathrm{e}^{\mathrm{i}\omega 0^+}$.

Self-energy $\Sigma(k)$ is expressed via charge and longitudinal spin GFs:

$$\Sigma(k) = \frac{U}{2}\sum_q \sum_{k'k''} \big[\Gamma_{\mathrm{c}}(k,k'';q)\chi_{\mathrm{c}}(k'',k';q) + \Gamma_{\mathrm{s}}(k,k'';q)\chi_{\mathrm{s}}(k'',k';q)\big]G(k+q). \tag{4.3.104}$$

In order to solve (4.3.99) and (4.3.100) two approximations are proposed. At first irreducible vertexes Γ_{c} and Γ_{s} are calculated in local approximation in agreement with basic idea of $DMFT$ with frequency dependence only including bosonic frequency ε_m. We assume that

$$\Gamma_\alpha(k,k';q) \approx \Gamma_\alpha(\varepsilon_m). \tag{4.3.105}$$

Then (4.3.99) and (4.3.100) can be formally solved in the following way:

$$\chi_{\mathrm{c}}^{-1}(q) = \chi_0^{-1}(q) + \Gamma_{\mathrm{c}}(\varepsilon_m), \tag{4.3.106}$$

$$\chi_{\mathrm{s}}^{-1}(q) = \chi_0^{-1}(q) - \Gamma_{\mathrm{s}}(\varepsilon_m). \tag{4.3.107}$$

In the result four-momentum dependence is included only via quantity $\chi_0(q)$.

Approximation (4.3.105) allows to present expression for self-energy (4.3.104) in the following form:

$$\Sigma(k) = \Sigma(\omega_n) + \frac{U}{2}\sum_q \big[\Gamma_{\mathrm{c}}(\varepsilon_m)\Delta\chi_{\mathrm{c}}(q) + \Gamma_{\mathrm{s}}(\varepsilon_m)\Delta\chi_{\mathrm{s}}(q)\big]G(k+q), \tag{4.3.108}$$

where $\Delta\chi_\alpha(q) = \chi_\alpha(q) - \chi_\alpha(\omega_n)$ describes nonlocal contribution. $\Sigma(\omega_n)$ gives a local contribution nondependent on wave vector $\mathbf{q}$:

$$\Sigma(\omega_n) = \frac{U}{2}T\sum_{\varepsilon_m} \big[\Gamma_{\mathrm{c}}(\varepsilon_m)\chi_{\mathrm{c}}(\varepsilon_m) + \Gamma_{\mathrm{s}}(\varepsilon_m)\chi_{\mathrm{s}}(\varepsilon_m)\big]G_{\mathrm{loc}}(\omega_n + \varepsilon_m), \tag{4.3.109}$$

here $G_{\mathrm{loc}}(\omega_n) = \sum_{\mathbf{k}} G(\mathbf{k})$ is local GF.

Second approximation is to replace quantities $\Sigma(\omega_n)$ and $\chi_0(\varepsilon_m)$ for $\Sigma_{\rm loc}(\omega_n)$ and $\chi_{0,{\rm loc}}(\varepsilon_m)$ calculated in standard *DMFT* scheme. Then from equations (4.3.99) and (4.3.100) we have equations for irreducible vertexes analogous to (4.3.106) and (4.3.107):

$$\Gamma_{\rm c}(\varepsilon_m) \approx \frac{1}{\chi_{c,{\rm loc}(\varepsilon_m)}} - \frac{1}{\chi_{0,{\rm loc}}(\varepsilon_m)}, \tag{4.3.110}$$

$$-\Gamma_{\rm s}(\varepsilon_m) \approx \frac{1}{\chi_{s,{\rm loc}}(\varepsilon_m)} - \frac{1}{\chi_{0,{\rm loc}}(\varepsilon_m)}. \tag{4.3.111}$$

Here local irreducible susceptibility is given by

$$\chi_{0,{\rm loc}}(\varepsilon_m) = -T\sum_{\omega_n} G_{\rm loc}(\omega_n)G_{\rm loc}(\omega_n+\varepsilon_m). \tag{4.3.112}$$

With these expression for irreducible vertexes formula (4.3.108) describes self-energy with spatial charge and spin correlations taken into account. Local vertexes and susceptibilities should be calculated in *DMFT*.

In [192] as an impurity solver Iterative Perturbation Theory (*IPT*) (see Sect. 3.1.5) was used. Two-dimensional Hubbard model was investigated with 2048 Matsubara frequencies used in *DMFT* equations solution. Analytical continuation from imaginary to real energies was done with Pade approximants.

In Fig. 4.8 calculated imaginary part of dynamical susceptibility at wave vector $\mathbf{Q} = (\pi, \pi)$ is shown. Low-energy peak increases sharply with temperature approaching Neel point. In Fig. 4.9 phase diagram is presented on the

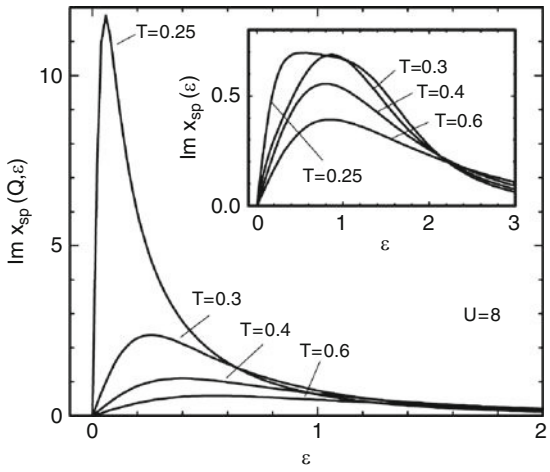

Fig. 4.8. Spectral intensity of spin susceptibility in two-dimensional Hubbard model for $n = 1$ and wave vector $\mathbf{Q} = (\pi, \pi)$ at $U = 8$ and various temperatures. In the inset local spin susceptibility is shown [192]

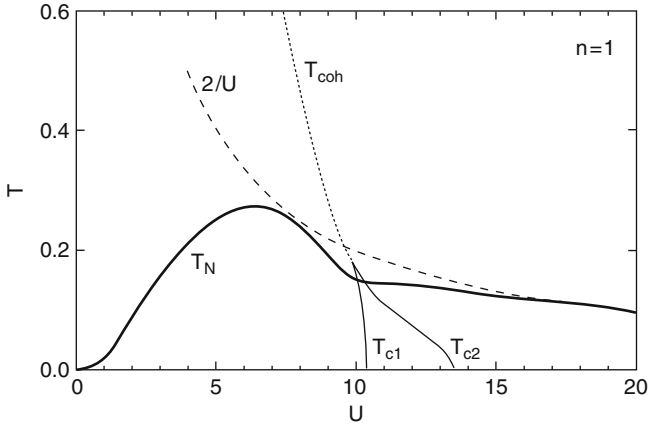

Fig. 4.9. Phase diagram of two-dimensional Hubbard model for $n = 1$ on the plane (T, U) calculated with spatial spin fluctuation taken into account [192]

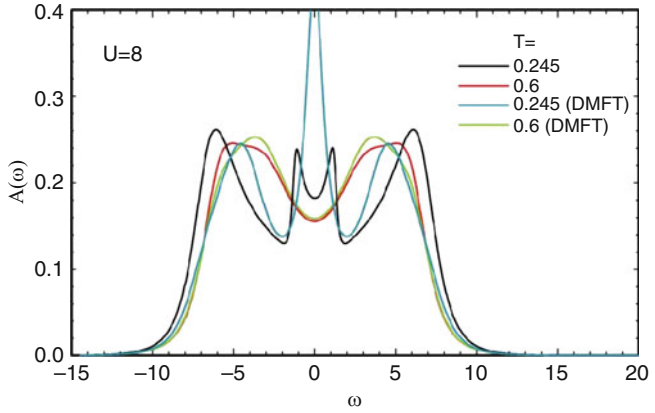

Fig. 4.10. Density of states $A(\omega)$ for $U = 8$ calculated in standard *DMFT* and with spatial correlations taken into account [192]

plane (T, U). Neel temperature was determined from condition $\chi_s^{-1}(\mathbf{Q}, 0) \approx 0$. Dependence of T_N on U is typical to other calculations with maximum T_N close to exchange parameter $J \sim t^2/U$ value. The curves T_{c1} and T_{c2} defines boundaries for metallic and insulating phases in metal–insulator neighborhood. In Fig. 4.9 coherence temperature T_{coh} is shown defined as temperature of central peak in *DMFT* spectral function $A(\omega)$ appearance. The curve $T_N(U)$ lies below the corresponding curve obtained in *DMFT* calculations without spatial correlations taken into account.

Spatial fluctuations produce interesting changes in spectral properties. In Fig. 4.10 spectral function $A(\omega)$ is shown calculated in standard *DMFT* and with spatial correlations taken into account for two temperatures: $T = 0.245$

slightly above $T_{\mathrm{N}} = 0.241$ and $T = 0.6$ that is much larger than T_{N} and where spin fluctuations are much weaker than near transition temperature. One can see that at high temperature taking into account spatial correlations does not change spectral function significantly while near T_{N} spectral functions with and without spatial correlations are very different. The central peak is strongly suppressed due to spatial correlations and at $\omega = 0$ pseudogap appears. Spectral weight is transfered from quasiparticle peak to Hubbard bands. Pseudogap appears not uniformly on the Fermi surface. Spectral function $A(\mathbf{k}, \omega)$ calculations show that pseudogap is most pronounced near Brillouin zone points $(\pi, 0)$ while in the direction on (π, π) quasiparticle peaks are preserved. Fermi surface has a form of "arcs". It is preserved in a sector with direction on (π, π) and destroyed in directions on $(\pi, 0)$ and $(0, \pi)$. This pseudogap effect was found in earlier works that we referenced earlier.

Spectral function $A(\mathbf{k}, \omega)$ calculation were performed on discrete wave vector mesh in first Brillouin zone size 64×64 for 2,048 Matsubara frequencies. Calculation were not self-consistent with respect to spatial correlations so self-energy did not feel effect of pseudogap appearance. In the calculations self-energy $\Sigma(\mathbf{k}) = \Sigma(\omega_n) + \Sigma_{\mathbf{k}}(\omega_n)$ consists of two contributions: purely local $\Sigma(\omega_n)$ from *DMFT* and $\Sigma_{\mathbf{k}}(\omega_n)$ corresponding to spatial spin fluctuations. In fully self-consistent solution interference between both contributions should appear but its role is still unclear.

4.3.2 Dynamical Vertex Approximation

More consistent approach to the problem based on standard diagrammatic technique was proposed by Toschi, Katanin, and Held [193]. Self-energy Σ can be expressed via vertex part Γ (see Fig. 4.11):

$$\Sigma(\mathbf{k}, \nu) = U\frac{n}{2} - T^2 U \sum_{\mathbf{k}'\nu'\mathbf{q}\omega} \Gamma^{\nu\nu'\omega\uparrow\downarrow}_{\mathbf{k}\mathbf{k}'\mathbf{q}} G(\mathbf{k}' + \mathbf{q}, \nu' + \omega) G(\mathbf{k}', \nu') G(\mathbf{k} + \mathbf{q}, \nu + \omega). \tag{4.3.113}$$

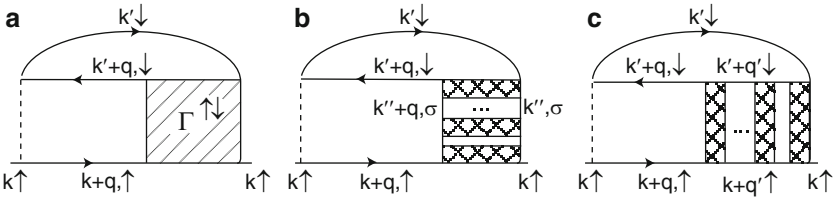

Fig. 4.11. Graphic representation of self-energy Σ for electrons in Hubbard model. Solid line with arrows denote GF $G_\sigma(\mathbf{k}, \nu)$, dots correspond to Coulomb potential U. (**a**) Exact representation for Σ via complete vertex part, (**b**) and (**c**) describe contribution to Σ due to two particle–hole channels in ladder approximation. Dashed rectangles denote irreducible vertex part

(we have preserved notations used in [193]). This expression is exact if Γ is a complete vertex part. Taking into account only ladder diagrams shown in Figs. 4.11b and c expression (4.3.113) will be an approximate one and correspond to charge and spin fluctuations taken into account. Dashed rectangles are irreducible vertexes in particle–hole channel.

Vertex Γ in (4.3.113) can be presented as a sum of vertexes in spin (s) and charge (c) channels depending only on wave vectors difference:

$$\Gamma^{\nu\nu'\omega\uparrow\downarrow}_{\mathbf{k}\mathbf{k}'\mathbf{q}} = \frac{1}{2}(\Gamma^{\nu\nu'\omega}_{s,\mathbf{q}} + \Gamma^{\nu\nu'\omega}_{c,\mathbf{q}}) + \Gamma^{\nu,\nu+\omega,\nu'-\nu}_{s,\mathbf{k}'-\mathbf{k}} - \frac{1}{2}(\Gamma^{\nu\nu'\omega}_{s,\mathrm{loc}} - \Gamma^{\nu\nu'\omega}_{c,\mathrm{loc}}) \quad (4.3.114)$$

Here first two terms describe longitudinal and transverse fluctuations (paramagnons) and the last term is needed to avoid local terms double-counting.

The quantities in the right part of (4.3.114) can be expressed via irreducible parts $\Gamma^{\nu\nu'\omega}_{s(c),ir}$ in the following way:

$$\Gamma^{\nu\nu'\omega}_{s(c),\mathbf{q}} = \left[(\Gamma^{\nu\nu'\omega}_{s(c),ir})^{-1} - \chi_0^{\nu'}(\mathbf{q},\omega)\delta_{\nu\nu'}\right]^{-1}, \quad (4.3.115)$$

where

$$\chi_0^{\nu'}(\mathbf{q},\omega) = -T\sum_{\mathbf{k}} G(\mathbf{k},\nu')G(\mathbf{k}+\mathbf{q},\nu'+\omega). \quad (4.3.116)$$

Expression (4.3.115) is solution of equations (4.3.99) and (4.3.100) for spin and charge two-particle GF.

Equation (4.3.115) is derived in ladder approximation for particle–hole channel where only one irreducible vertex $\Gamma^{\nu\nu'\omega}_{s(c),ir}$ is taken into account. The second approximation is the fact that electron GF is calculated in $DMFT$:

$$G(\mathbf{k},\nu) = \left[i\nu - \varepsilon_{\mathbf{k}} + \mu - \Sigma_{\mathrm{loc}}(\nu)\right]^{-1}. \quad (4.3.117)$$

Substituting (4.3.114) in (4.3.113) we obtain expression for self-energy:

$$\Sigma(\mathbf{k},\nu) = \frac{1}{2}U_n + \frac{1}{2}TU\sum_{\nu'\omega\mathbf{q}} \chi_0^{\nu'}(\mathbf{q},\omega)(3\Gamma^{\nu\nu'\omega}_{s,\mathbf{q}} - \Gamma^{\nu\nu'\omega}_{c,\mathbf{q}} + \Gamma^{\nu\nu'\omega}_{c,\mathrm{loc}} - \Gamma^{\nu\nu'\omega}_{s,\mathrm{loc}})G(\mathbf{k}+\mathbf{q},\nu+\omega). \quad (4.3.118)$$

This expression comes to $DMFT$ self-energy if nonlocal terms will be replaced by local ones. Expression (4.3.118) with (4.3.115) differs from $SCBA$ approximation by replacing Coulomb parameter U with dynamical local vertexes and so the authors of [193] called it Dynamical Vertex Approximation ($D\Gamma A$). Diagrammatic analysis in $1/d$ parameter shows [193] that this approximation correctly describes all corrections to $DMFT$ in the first order in $1/d$. Approximations proposed in [192, 193] are equivalent to each other but in [193] equations are written in more general form using parquet equations.

For practical calculations one needs to compute four-point local vertex $\Gamma^{\nu\nu'\omega}_{s(c),ir}$ for single impurity Anderson model:

$$\chi_{\text{loc}}^{\nu\nu'\omega\sigma\sigma'} = T^2 \int_0^\beta \mathrm{d}\tau_1 \mathrm{d}\tau_2 \mathrm{d}\tau_3 \mathrm{e}^{-i\tau_1\nu} \mathrm{e}^{i\tau_2(\nu+\omega)} \mathrm{e}^{-i\tau_3(\nu'+\omega)}$$
$$\left[\left\langle T_\tau \hat{c}_{i\sigma}^\dagger(\tau_1)\hat{c}_{i\sigma}(\tau_2)\hat{c}_{i\sigma'}^\dagger(\tau_3)\hat{c}_{i\sigma'}(0)\right\rangle \right.$$
$$\left. - \left\langle T_\tau \hat{c}_{i\sigma}^\dagger(\tau_1)\hat{c}_{i\sigma}(\tau_2)\right\rangle \left\langle T_\tau \hat{c}_{i\sigma'}^\dagger(\tau_3)\hat{c}_{i\sigma'}(0)\right\rangle\right],$$

where ν and ν' are fermionic and ω bosonic frequencies. Charge and spin susceptibilities for Anderson model are expressed via symmetrized vertexes combinations (4.3.119):

$$\chi_{s(c),\text{loc}}^{\nu\nu'\omega} = \chi_{\text{loc}}^{\nu\nu'\omega\uparrow\uparrow} \pm \chi_{\text{loc}}^{\nu\nu'\uparrow\downarrow}. \tag{4.3.119}$$

Local vertexes calculation is a most computer time consuming part. It is done using the formula (4.3.119) where two-particle and one-electron GFs are written in Lemann representation and Hamiltonian eigenvalues are computed in Exact Diagonalization (ED) method. Calculations for Anderson model were done for lowest $N_{\max} = 20$ Matsubara frequencies and then analytical continuation by Pade approximants was performed. Wave vectors summation in (4.3.118) was done using $N_{\mathbf{k}} = 96$ points in Brillouin zone.

$D\Gamma A$ calculations results are shown in comparison with $DMFT$ results in Fig. 4.12 for three values of Coulomb parameter $U = D; 1.5D$ and $2D$ in

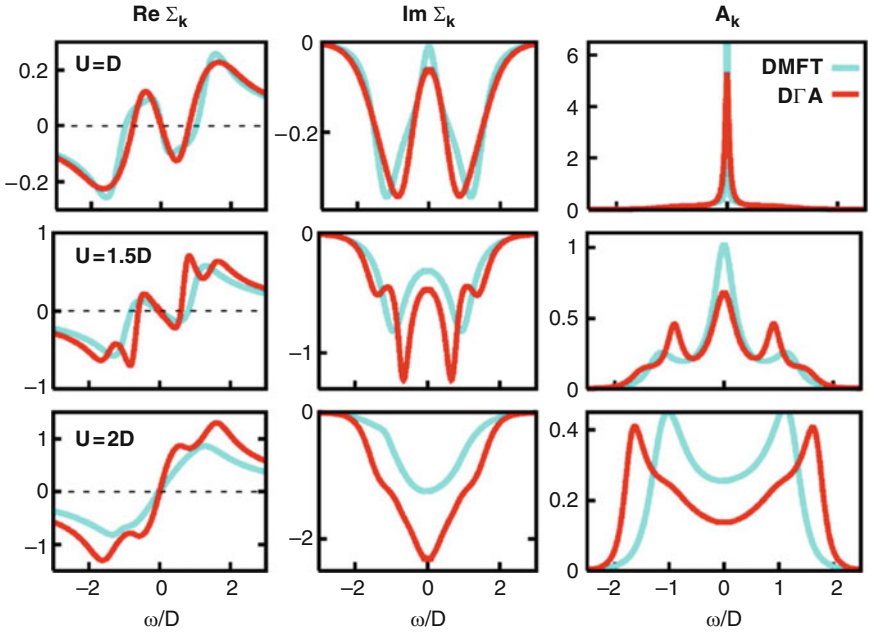

Fig. 4.12. Real and imaginary part of self-energy and density of states for Hubbard model calculated in $DMFT$ and $D\Gamma A$ [193] for $\mathbf{k} = (\pi/2, \pi/2, \pi/2)$ and $U = D$

metal–insulator transition neighborhood. For these U values four-point vertex part $\Gamma^{\nu\nu'\omega}_{\mathrm{s(c)},ir}$ depends strongly on frequencies and near antiferromagnetic ordering for small frequencies singularity can appear. This singularity leads to suppression of spectral density on Fermi surface comparing with *DMFT* results. So dynamical fluctuations reconstruct electronic spectra in strongly correlated systems. Local spin fluctuations enhance nonlocal fluctuations leading to electron scattering and dumping that essentially modify spectral functions. One of such systematic changes is pseudogap appearance that will be discussed in the next section.

4.3.3 Pseudogap

One of the most spectacular effects of spatial correlations is pseudogap formation. Pseudogap state appears in two-dimensional Hubbard model near half-filling and is experimentally observed in cuprates. On cuprates phase diagram (Fig. 4.13) dashed line marks pseudogap state in normal metallic phase for underdoped materials. T^* line is not phase transition line but only crossover corresponding to gradual transition between high-temperature phase for $T > T^*$ with normal Fermi liquid properties and low-temperature $T < T^*$ area where anomalies are observed in electronic properties. Pseudogap effect means suppression of the density of states on Fermi level. It reveals itself in decreasing of linear coefficient γ of electronic specific heat and Pauli

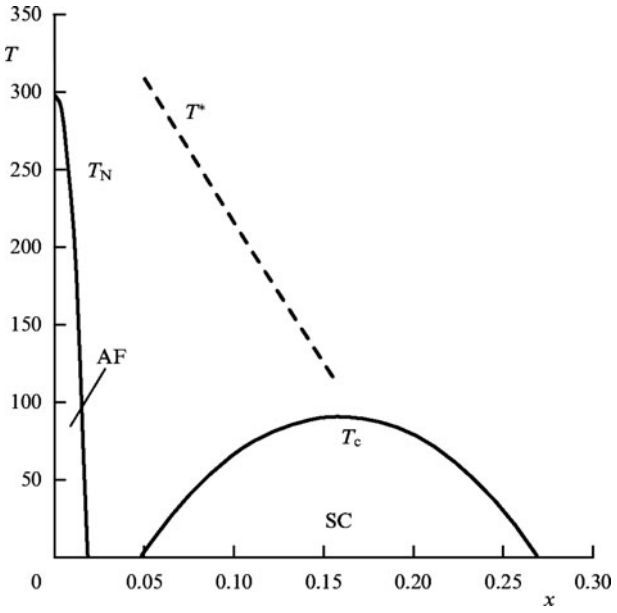

Fig. 4.13. Schematic phase diagram for cuprates. *Dashed line* T^* marks the pseudogap existence area at $T < T^*$

susceptibility χ_0 in crossing T^* line and especially in experiments in tunneling spectroscopy and angle-resolved photoemission spectroscopy (*ARPES*).

ARPES allows to measure directly quasiparticle spectral density near Fermi surface and reconstruct Fermi surface itself. It was found that in all cuprate materials the same phenomenon is observed: Fermi surface destruction in directions $(0, k_y)$ and $(0, k_x)$ while in diagonal Brillouin zone directions (k_x, k_y) Fermi surface is preserved. In this directions *ARPES* intensity drops sharply when wave vector crosses Fermi surface. In directions $(0, k_y)$ and $(0, k_x)$ evolution of $A(\mathbf{k}, \omega)$ is gradual and for fixed wave vector $\mathbf{k}$ spectral function has two-peak structure with a depression on the "former" Fermi surface that would exist without pseudogap effect. Detailed discussion of this phenomenon one can find in Sadovskii reviews [194,195]. Reviews of *ARPES* results are presented in [196] for $La_{2-x}Sr_xCuO_4$ and in [197] for *Bi*2212. So in cuprates Fermi surface has "arcs" form with well pronounced Fermi surface parts only on the arcs near diagonal directions in Brillouin zone.

It was suggested earlier that pseudogap state in cuprates appears due to electron scattering on spin fluctuations when the system is close to antiferromagnetic ordering. Dynamical magnetic susceptibility for two-dimensional square lattice near half filling can be represented by the following phenomenological expression [198]

$$\chi_s(\mathbf{q}, \omega) \approx \frac{\xi^2}{1 + \xi^2(\mathbf{q} - \mathbf{Q})^2 - i\omega/\omega_s}. \tag{4.3.120}$$

Here $\mathbf{Q} = (\pi, \pi)$ is antiferromagnetic wave vector, ξ is spin fluctuations correlation length and ω_s is their characteristic frequency. Expression (4.3.120) is valid only in the neighborhood of vector $\mathbf{Q}$ where spin fluctuations are strong and their dumping is weak. Electrons scatter on those fluctuations and this scattering can lead to pseudogap state formation. To describe this effect one needs to go beyond first order of perturbation theory.

For one-dimensional case Sadovskii [199] has summed perturbation theory series for self-energy of electron interacting with static spin fluctuation and obtained recurrent equation to calculate series sum. This method can be extended for two-dimensional lattice if static susceptibility is approximated by factorization:

$$\chi_s(\mathbf{q}, 0) \approx \frac{\xi^2}{[1 + \xi^2(\mathbf{q}_x - \mathbf{Q}_x)^2][1 + \xi^2(\mathbf{q}_y - \mathbf{Q}_y)^2]}. \tag{4.3.121}$$

Then infinite series summation for self-energy $\Sigma(\mathbf{k}, i\omega)$ comes to solution of recurrent equation

$$\Sigma_n(\mathbf{k}, i\omega) = \frac{\Delta^2 S(n)}{i\omega + \mu - \Sigma(i\omega) - \varepsilon_n(\mathbf{k}) + inv_n\varkappa - \Sigma_{n+1}(\mathbf{k}, i\omega_n)}, \tag{4.3.122}$$

where Δ characterizes energy scale of spin fluctuations, $\varkappa = \xi^{-1}$ is inverse correlation length, $\varepsilon_n(\mathbf{k}) = \varepsilon(\mathbf{k} + \mathbf{Q})$ and $v_n = |v^x_{\mathbf{k}+\mathbf{Q}}| + |v^y_{\mathbf{k}+\mathbf{Q}}|$ for even n.

Fermi velocities $v_{\mathbf{k}}^x$ and $v_{\mathbf{k}}^y$ are defined as dispersion law $\varepsilon(\mathbf{k})$ gradient. $S(n)$ is some factor that in the case of commensurate vector $\mathbf{Q}$ is $S(n) = n$. Electron self-energy determined by scattering on spin fluctuations is $\Sigma_n(\mathbf{k}, i\omega)$ for $n = 1$:

$$\Sigma_{n=1}(\mathbf{k}, i\omega) \equiv \Sigma_{\mathbf{k}}(i\omega). \tag{4.3.123}$$

In expression (4.3.122) $\Sigma(i\omega)$ is local self-energy in *DMFT* approximation determined by local Coulomb interaction without long-range spin fluctuations taken into account. Then total self-energy is sum of two contributions:

$$\Sigma(\mathbf{k}, i\omega) = \Sigma(i\omega) + \Sigma_{\mathbf{k}}(i\omega), \tag{4.3.124}$$

where the first one is purely local and can be calculated in *DMFT* scheme and the second one is defined by equations (4.3.122), (4.3.123). This calculation scheme was named by the authors DMFT + $\Sigma_{\mathbf{k}}$.

Electronic GF now can be written as

$$G(\mathbf{k}, i\omega) = \frac{1}{i\omega + \mu - \varepsilon(\mathbf{k}) - \Sigma(i\omega) - \Sigma_{\mathbf{k}}(i\omega)}. \tag{4.3.125}$$

Let us introduce local GF

$$G_{\text{loc}}(i\omega) = \sum_{\mathbf{k}} \frac{1}{i\omega + \mu - \varepsilon(\mathbf{k}) - \Sigma(i\omega) - \Sigma_{\mathbf{k}}(i\omega)}, \tag{4.3.126}$$

and define noninteracting GF for single impurity model in standard relation

$$\mathcal{G}_0^{-1}(i\omega) = \Sigma(i\omega) + G_{\text{loc}}^{-1}(i\omega). \tag{4.3.127}$$

As usual $\mathcal{G}(i\omega)$ defines an action for equivalent Anderson model that can be solved by *QMC* or *NRG* methods. Calculation scheme in DMFT + $\Sigma_{\mathbf{k}}$ is the same as in standard *DMFT*: for a given $\Sigma(i\omega)$ from recurrent equations (4.3.122) $\Sigma_{\mathbf{k}}(i\omega)$ is calculated and then $G_{\text{loc}}(i\omega)$. Relation (4.3.127) defines "Weiss field" $\mathcal{G}_0^{-1}(i\omega_n)$. From $\mathcal{G}_0^{-1}(i\omega_n)$ GF for Anderson impurity model is found and identified with $G_{\text{loc}}(i\omega_n)$. That gives new value of $\Sigma(i\omega)$ and the whole procedure is iteratively repeated till self-consistency is achieved.

This procedure is semiphenomenological one because one should use parameters Δ and ξ determining strength and spatial extension of spin fluctuations. Both parameters should be in general calculated from local Coulomb parameter U that is a single model Hamiltonian parameter. The quantity Δ can be derived from the model Hamiltonian solution [200]:

$$\Delta^2 = U^2 \frac{< n_{i\uparrow} n_{i\downarrow} >}{n^2} \frac{1}{3} < \mathbf{S}_i^2 >; \tag{4.3.128}$$

It is defined by average value for double occupancy probability and average square value of spin on the site. Unfortunately, correlation length cannot be calculated analytically.

Parameters Δ and ξ in expression (4.3.122) are better to be considered as phenomenological constants and then DMFT+$\Sigma_{\mathbf{k}}$ scheme allows to investigate electronic state of the system as a function of spin correlation strength and correlation length. DMFT+$\Sigma_{\mathbf{k}}$ method was realized in [201–204] for Hubbard model near half filling to describe pseudogap state in cuprates.

In Fig. 4.14 spectral function $A(\mathbf{k},\omega)$ is shown along symmetric lines in Brillouin zone of square lattice. Energies are measured from Fermi level. One can see sharp peaks in spectral functions corresponding to quasiparticle states. However in $\Gamma - X$ direction two-peak structure appears with a depression exactly on the Fermi level. That fact tells about Fermi surface destruction near $(\pi, 0)$ and $(0, \pi)$ points while in direction $(0, 0) - (\pi, \pi)$ quasiparticle states are well preserved in good agreement with experimental observations for cuprates.

Fermi surface destruction is illustrated in Fig. 4.15 where contour maps for spectral function are presented in $\mathbf{k}$ space at $\omega = 0$ that corresponds to Fermi surface. Solid lines correspond to solution of equation

$$\omega - \varepsilon(\mathbf{k}) + \mu - \mathrm{Re}\Sigma(\omega) - \mathrm{Re}\Sigma_{\mathbf{k}}(\omega) = 0, \tag{4.3.129}$$

defining real parts of poles for electron GF $G(\mathbf{k},\omega)$ (4.3.125). One can see that with Δ increase Fermi surface destruction happens near $(\pi, 0)$ and $(0, \pi)$ points.

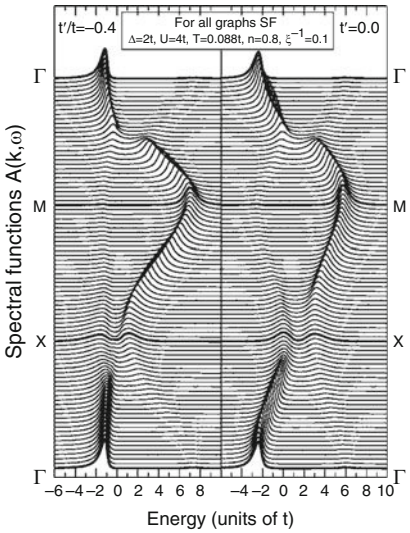

Fig. 4.14. Spectral function $A(\mathbf{k},\omega)$ for Hubbard model at parameters values: $U = 4t$, $n = 0.8$, $\Delta = 2t$, $T = 0.0088t$, $\xi^{-1} = 0.1a$ along symmetric lines in Brillouin zone $\Gamma(0,0) \to X(\pi,0) \to M(\pi,\pi) \to \Gamma(0,0)$, calculated by $DMFT + \Sigma_{\mathbf{k}}$ method [201]. Left panel is for $t'/t = 0.4$, the right one for $t'/t = 0$

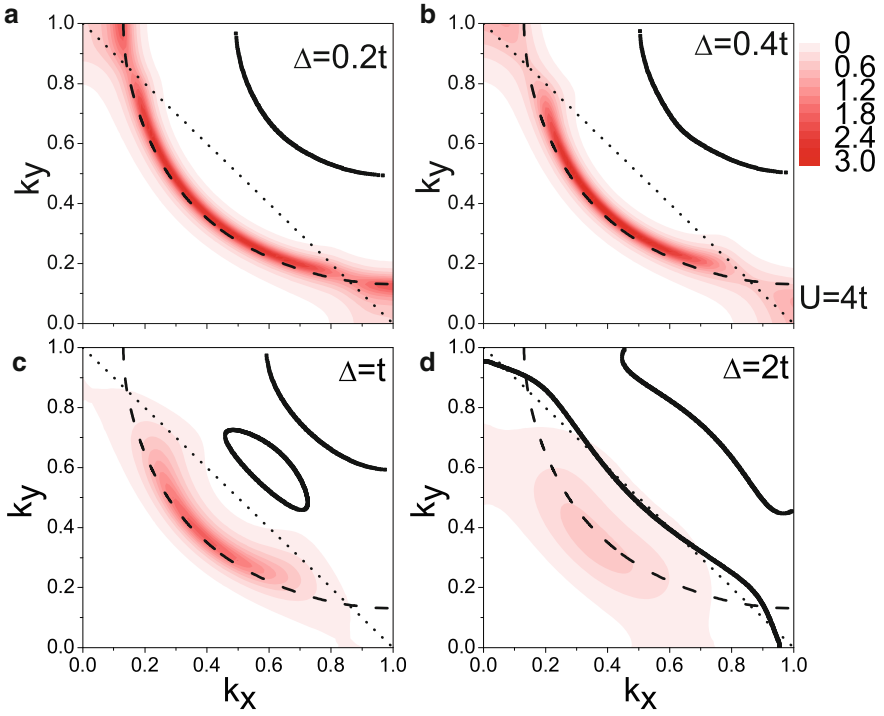

Fig. 4.15. Fermi surface calculated by $DMFT(NRG)+\Sigma_{\mathbf{k}}$ method [202] for $U = 4t$, $n = 0.8$, $\xi = 10a$ and various Δ values. *Dashed line* corresponds to noninteracting Fermi surface (without spin fluctuation). *Solid lines* correspond to (4.3.129) solution

In [203] a theory for optical conductivity in DMFT + $\Sigma_{\mathbf{k}}$ scheme was developed and real part of $\sigma(\omega)$ was calculated for few parameters sets to investigate spin fluctuations strength influence. Results are shown in Fig. 4.16. One can see that for nonzero Δ on the curve $\mathrm{Re}\sigma(\omega)$ in metallic phase a dip appears in low frequency region that gradually disappears with temperature increase. For large frequencies in addition to Drude peak broad maximum appears corresponding to electrons excitations in upper Hubbard band. In insulating phase $U \gg 4t$ Drude peak disappears and conductivity at $\omega = 0$ decays fast with correlation length ξ decrease. Such $\mathrm{Re}\sigma(\omega)$ behavior agrees with the pattern observed experimentally in cuprates.

DMFT + $\Sigma_{\mathbf{k}}$ method is not systematic expansion in $1/d$ parameter but is heuristic approach. Nevertheless, it has a certain attraction because allows to study spin fluctuations influence on electronic spectra.

Results described earlier and illustrated in Figs. 4.14–4.16 agree with the results obtained in different techniques [205–212]. One of them is called Dynamical Cluster Approximation (DCA) [205–207] and is described in details in review [205]. To take into account short-range fluctuations single impurity

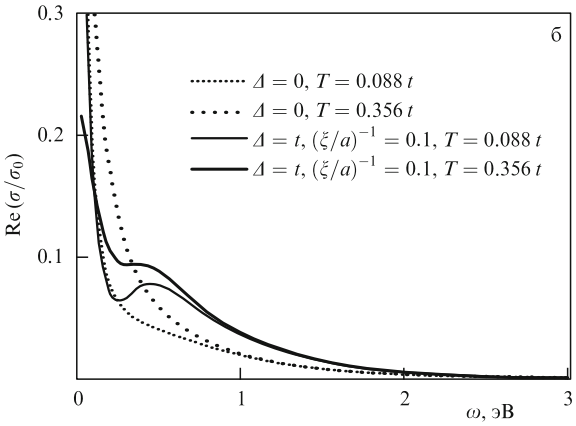

Fig. 4.16. Pseudogap state effect in optical conductivity for $U = 4t$, $t = 0.25$ and two temperature values. *Dashed lines* are for $\Delta = 0$ and *solid lines* for $\Delta = t$ and $\xi/a = 10$ [203]

problem is replaced on local cluster containing few atoms. Such approach was already described earlier (see Sect. 3.6) when we discussed superconductivity with d-symmetry order parameter. There as a cluster plaquet of four atoms was chosen. Cluster size can be increased but that need very significant computer resources. In [205–207] a scheme was developed where two clusters were considered. Small cluster is used to treat short-range fluctuations and a large one is for long-range fluctuations. For pseudogap state problem DMFT + $\Sigma_{\mathbf{k}}$ method is more convenient because one still has only single site cluster but this approach in not microscopic one.

There is another approach realized in [212] for Hubbard model and not using *DMFT* ideas. There self-energy $\Sigma(\mathbf{k}, \omega)$ is calculated in self-consistent Born approximation ($SCBA$). In this case $\Sigma(\mathbf{k}, \omega)$ is calculated as a convolution of spin and electron GFs that gives integral equation for $\Sigma(\mathbf{k}, \omega)$ that is solved numerically for both wave vector and frequency dependencies. For Hubbard model on square lattice $SCBA$ equations were solved for parameter values characteristic to real cuprates materials: $U = 8t$ and $4t$, $t = 0.4\,\text{eV}$, $t = -0.3t'$, $\omega_s = 0.4t$. Calculations were performed for two doping values $\delta = 0.05$ and 0.3 and two temperatures $T = 0.03t \approx 140\,\text{K}$ and $T = 0.3t$. Calculated quasiparticle spectra agree well with *DMFT* results for cuprates discussed earlier. In underdoped regime pseudogap state is observed in neighborhood of $(\pi, 0)$ and $(0, \pi)$ points while in diagonal direction quasiparticle states were preserved. This approach is not microscopic one because it uses phenomenological expression for dynamical susceptibility $\chi(\mathbf{q}, \omega)$ with adjustable parameters. From approximations described in this section only first two [192, 193] can be considered as microscopic ones however they are not completely rigorous with respect to $1/d$ expansion corrections.

We mention also works [213–215] where pseudogap state in two-dimensional Hubbard model near half filling was obtained in perturbation theory in parameter W/U. This theory uses diagrammatic technique where zero-order approximation is single-site Coulomb interaction term and as a perturbation intersite hopping is considered. This diagrammatic technique has its origin in [216,217] and contains various order cumulants connected by lines corresponding to hoppings t_{ij}. The whole combination of irreducible graphs gives Larkin equation. In [213, 214] as simplest approximation first two graphs were taken containing first- and second-order cumulants. The first of them comes to Hubbard-I approximation and a second one results in spectral function $A(\mathbf{k}, \omega)$ with pseudogap states in directions $(\pi, 0)$ and $(0, \pi)$. As all those approaches do not use *DMFT* ideas then pseudogap state is not connected with *DMFT* approximation but is a result of long-range spin fluctuations.

Significant result of diagrammatic approach [213, 214] is dynamical spin susceptibility calculation. For this spin *GF* that is two-particle *GF* in Fermi operators is calculated using expansion in W/U parameter with irreducible diagrams. Larkin equation with approximate irreducible part gives spin *GF* that resembles *GF* from *DMFT* calculations. Static *GF* for $\mathbf{q} = 0$ is final at $T = 0$ and for $\mathbf{q} = \mathbf{Q}$ it diverges. Dynamical susceptibility $\chi(\mathbf{q}, \omega)$ for $\mathbf{q} = \mathbf{Q}$ has maximum for frequencies $\omega \sim t^2/U$ and another maximum for $\omega \sim U$. First maximum increases with temperature lowering that is an evidence of antiferromagnetic ordering for certain values of U and electronic concentration n. Those results agree well with Monte Carlo calculations [218]. In approach [213–215] all specific features of strongly correlated systems appears from frequency dependence of local cumulants of the second order as it is the case in *DMFT* spin susceptibility calculations.

4.3.4 Dynamical Cluster Method

Standard *DMFT* method reduces electrons on the lattice problem to single impurity model and hence neglects intersite correlations in the system. However, a lot of important physical effects cannot be described without such correlations taken into account. Among them is superconductivity with d-symmetry order parameter. In Sect. 3.6 we have shown how *DMFT* scheme should be extended to solve this problem. For that impurity should be replaced by a cluster containing not one but several atoms. As such cluster for square lattice a plaquet was chosen formed by four atoms. Inside the plaquet all correlations can be taken into account but because of small cluster size that corresponds in reciprocal space to short wave length correlations only.

This approach can be considered as a general way to include short wave length correlations in *DMFT* and is called Cluster *DMFT* (*CDMFT*). *DMFT* equations are still the same as in single-impurity formalism but self-energy Σ and hybridization function Δ are now matrices. In the case of plaquet they are 4×4 matrices. There are two realizations of *CDMFT*. One of them uses real space representation where matrix indexes are atomic numbers inside the

cluster while in the second one reciprocal space representation is used. In this case Brillouin zone is divided by so called "coarse" mesh with a wave vectors $\mathbf{K}_\alpha$ (number of those vectors is equal to the number of atoms in the cluster) and α play the role of matrix indexes for Σ and Δ matrices [205].

As an example of the second *CDMFT* version we will consider work [219] where metal–insulator transition was investigated for two-dimensional Hubbard model in half-filling. Reciprocal space "coarse" mesh was chosen as four points $\mathbf{K}_\alpha$: (0,0), (0,π), (π,0) and (π,π). 4×4 matrix equations for Σ and Δ were solved by Continuous Time *QMC* method that allows low-temperature region to be investigated. Calculated phase digram on the plane (T, U) is presented in Fig. 4.17 where for comparison phase diagram obtained in single-impurity *DMFT* is also shown. The basic features of both diagrams are the same: there are metallic and insulating phases that overlaps with first

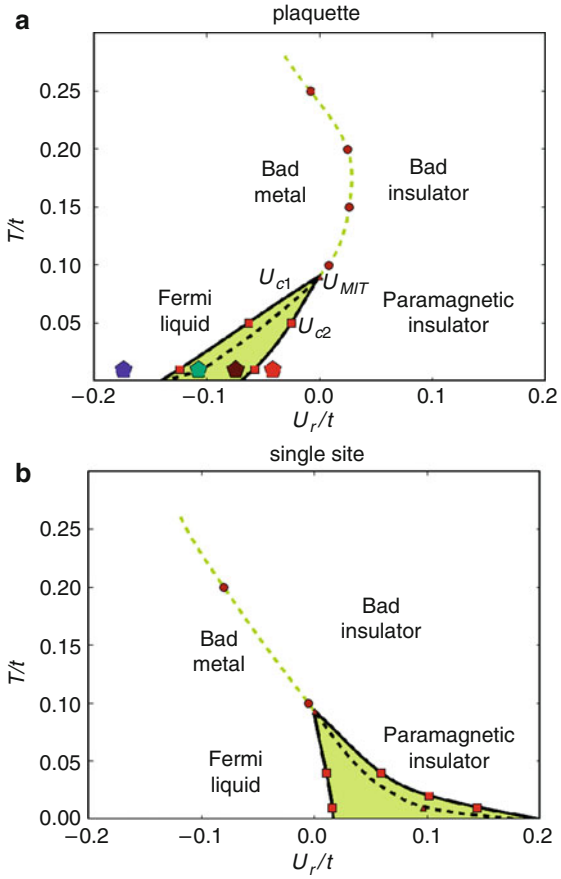

Fig. 4.17. Phase diagram of paramagnetic Hubbard model at half-filling calculated by (**a**) cluster *DMFT* and (**b**) single impurity *DMFT* [219]

order metal–insulator transition. However coexistence area for metallic and insulating phases (dashed areas in Fig. 4.17) are very different in two calculations. Phase transition lines have different slopes, critical value of Coulomb parameter U in the point where transition becomes of the second order (apex of the dashed triangle) is $U_{MIT} = 6.05t$ for cluster case and $U_{MIT} = 9.35t$ in single impurity calculation. At $T = 0$ phase transition in cluster case is close to U_{C1} while in single impurity to U_{C2}. That means that line U_{C1} plays more fundamental role than U_{C2} line.

So short wave length correlations that are taken into account in *CDMFT* but are absent in single impurity calculations do not change the nature of Mott transition in Hubbard model but modify a form of the phase diagram on (U, T) plane and the structure of coexistence area.

In work [220] *CDMFT* with cluster in **k**-space for used for detailed study of two-dimensional Hubbard model as a model approximating superconducting cuprates. Cluster problem was solved by $CT - QMC$ method for low-temperature values. From many interesting results obtained in this work we will present only two of them concerning pseudogap state and local density of states in superconducting gap energy scale.

In Fig. 4.18 spectral function $A(\mathbf{k}, \omega)$ at $\omega = 0$ is shown calculated for doping $\delta = 0.09$ below and above superconducting transition temperature T_c. For $T < T_c$ unstable normal metallic phase was considered. One can see that Fermi surface has "arcs" structure: quasiparticle states exist on directions to $(\pm\pi, \pm\pi)$ while on directions to $(\pm\pi, 0)$ and $(0, \pm\pi)$ they do not exist. That agrees with earlier results [221, 222] using approaches described in previous section. Advantage of $CT - QMC$ method is possibility to study temperature dependence of pseudogap state. From comparison of two figures in Fig. 4.18 one can see that with temperature lowering "arcs" are compressed. Calculations show that with doping increase quasiparticle states develop "banana" structure.

Another interesting result is presented in Fig. 4.19 where tunnel density of states (local density) in superconducting state is shown near Fermi energy as a function of doping. This picture agrees with experimental data for tunnel spectroscopy in cuprates.

Calculations shown in Fig. 4.19 were done at $T = 0.025t$. For optimally doped system superconducting gap estimated from the spectrum is $\Delta \sim 0.09t$. Calculated values of T_c depends significantly on calculations procedure and very in the limits limits from $0.026t$ to $0.036t$. The ratio $2\Delta/T_c$ values are in a broad interval between 5 and 18 and that means strong coupling superconductivity because weak coupling theory should give $2\Delta/T_c = 3.5$.

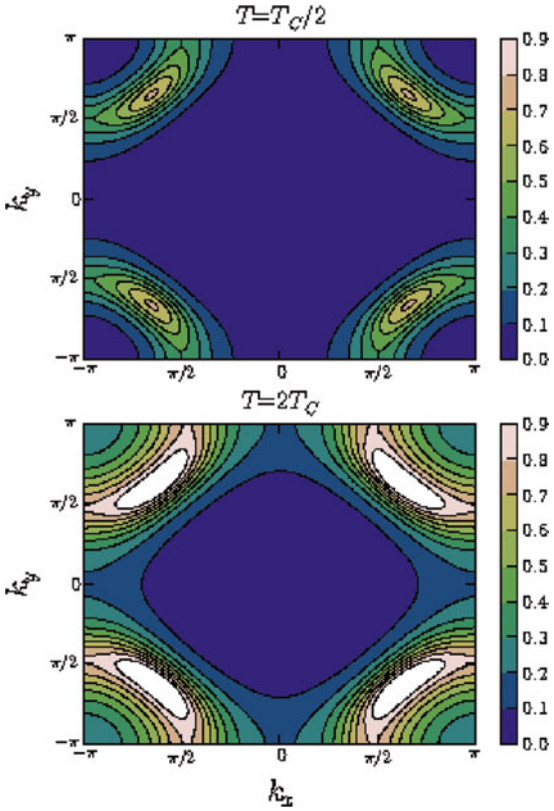

Fig. 4.18. Spectral function $A(\mathbf{k}, \omega)$ for $\omega = 0$ at doping value $\delta = 0.09$ for two-dimensional Hubbard model calculated in $CDMFT(CT - QMC)$ for temperatures (**a**) $T = T_c/2$ and (**b**) $T = 2T_c$, where T_c is superconducting transition temperature [220]

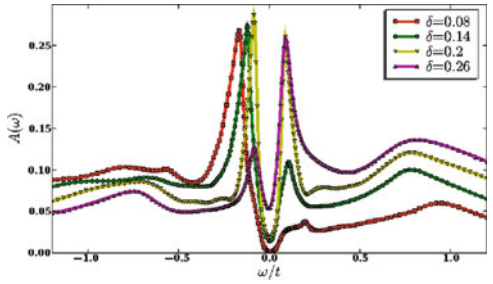

Fig. 4.19. Tunnel density of states for superconducting phase of two-dimensional Hubbard model at various doping values, $T = 0.025t$ [220]

4.4 Generating Functional for Green Functions

4.4.1 Baym-Kadanoff Functional

In the theory of interacting particles Baym-Kadanoff functional F_{BK} for one-electron GF is often used [223]. As there is no a rigorous way to construct this functional its approximated forms allow analyze self-consistently all approximations in calculation scheme. Another advantage of the functional is possibility to calculate free energy and so to investigate thermodynamic of the system. In application to strongly correlated model approaches based on Baym-Kadanoff functional were developed in [9, 210, 224–227]. Very detailed description of this approach is given in review [9]. In this section we will present basis ideas of generating functional method.

Let us consider functional $Z[J]$ for partition function with a source J:

$$Z[J] \equiv \mathrm{e}^{-F[J]} = \int \mathcal{D}\psi^{+}\mathcal{D}\psi \mathrm{e}^{-S-\int \mathrm{d}x\mathrm{d}x'\psi^{+}(x)J(x,x')\psi(x')}, \tag{4.4.130}$$

functional integral is taken over Grassmann variables $\psi^{+}(x)$ and $\psi(x)$ where x includes all characteristics of one-electrons state: coordinate, time (thermodynamic) and quantum numbers. Integration over x and x' mean summation over all those variables. S is an action for the system and $F[J]$ is free energy in the field of the source.

Variating functional (4.4.130) over the source we obtain expression for GF as a derivative of the functional $F(J)$:

$$\frac{\delta F[J]}{\delta J} = G. \tag{4.4.131}$$

In order to get equation for GF one need to define free energy functional $F[J]$.

Let us write functional (4.4.130) without interaction between particles

$$\begin{aligned} \mathrm{e}^{-F_0[J_0]} &= \int \mathcal{D}\psi^{+}\mathcal{D}\psi \, \exp\left[-\int \mathrm{d}x\mathrm{d}x'\psi^{+}(x)(\frac{\partial}{\partial\tau} - \mu + H_0 + J_0)\psi(x')\right] \\ &= \mathrm{Det}(\frac{\partial}{\partial t} - \mu + H_0 + J_0). \end{aligned} \tag{4.4.132}$$

We have used results of integration for Gauss functional integral (see Appendix A). That gives us explicit expression for free energy

$$F_0[J_0] = -\mathrm{Tr}\,\ln(G_0^{-1} - J_0), \tag{4.4.133}$$

where we drop constant term $\mathrm{Tr}\,\ln(-1)$ and used expression for noninteracting particles GF: $G_0 = (i\omega + \mu - H_0)^{-1}$. From functional stationarity condition (4.4.131) we can find expression for GF without the source:

$$G = (G_0^{-1} - J_0)^{-1}. \tag{4.4.134}$$

We will consider this relation as Dyson equation for GF of interacting system where J_0 is identified with self-energy of the GF G:

$$J_0 \equiv \Sigma_{\text{int}}[G] = G_0^{-1} - G^{-1}. \tag{4.4.135}$$

Using equations (4.4.133) and (4.4.135) let us write expression for Baym-Kadanoff functional:

$$F_{\text{BK}}[G] = -\text{Tr}\,\ln\left(G_0^{-1} - \Sigma_{\text{int}}[G]\right) - \text{Tr}\left(\Sigma_{\text{int}}[G]G\right) + \Phi_{\text{BK}}[G]. \tag{4.4.136}$$

Here first term comes from expression (4.4.133), the second realizes Legendre transformation and the third one corresponds to interaction between particles. $\Phi_{\text{BK}}(G)$ is defined as a sum of infinite series of irreducible skeleton diagrams for free energy [223].

In functional (4.4.136) quantities Σ_{int} and G can be considered as independent variables. Differentiation of (4.4.136) over G gives equation for self-energy:

$$\Sigma_{\text{int}} = \frac{\delta \Phi_{\text{BK}}}{\delta G}, \tag{4.4.137}$$

as a functional of GF G. Substituting this relation to (4.4.135) we obtain Dyson equation:

$$G_0^{-1} - G^{-1} = \frac{\delta \Phi_{\text{BK}}}{\delta G}, \tag{4.4.138}$$

defining GF that after substituting it in functional (4.4.136) gives system free energy. Hence, GF and free energy are determined by irreducible Baym-Kadanoff functional Φ_{BK}. The accuracy of Φ_{BK} calculation gives the accuracy of GF and free energy.

4.4.2 Total Energy

Let us express total energy $\langle H\rangle = \langle H_0\rangle + \langle H_{\text{int}}\rangle$ via one-electron GF that in our notation is:

$$G(x_1, x_2) = -\langle T_\tau \hat{\psi}(x_1)\hat{\psi}^+(x_2)\rangle, \tag{4.4.139}$$

together with expression for zero order Hamiltonian and interaction Hamiltonian

$$\beta H_0 = \int \mathrm{d}x_1 \mathrm{d}x_2 \hat{\psi}^+(x_1) H_0(x_1, x_2)\delta(\tau_1 - \tau_2)\hat{\psi}(x_2), \tag{4.4.140}$$

$$\beta H_{\text{int}} = \frac{1}{2}\int \mathrm{d}x_1 \mathrm{d}x_2 \hat{\psi}^+(x_1)\hat{\psi}^+(x_2) U_c(x_1 - x_2)\hat{\psi}(x_2)\hat{\psi}(x_1). \tag{4.4.141}$$

In review [9] an elegant derivation is given for $\langle H\rangle$. It is done by expressing $\langle H_0\rangle$ and $\langle H_{\text{int}}\rangle$ via one-particle GF (4.4.139). It is obvious that

$$\beta\langle H_0\rangle = \int \mathrm{d}x_1 \mathrm{d}x_2 H_0(x_1, x_2) G(x_2, x_1)\delta(\tau_2 - \tau_1 + O^+). \tag{4.4.142}$$

For $\langle H_{\rm int}\rangle$ one should use equation of motion for GF with equal space and time variables:

$$\left(\frac{\partial G(x_1,x_2)}{\partial\tau_1}\right)_{\substack{\tau_1\to\tau_2-O^+\\ \mathbf{r}_1\to\mathbf{r}_2}} = \langle\hat\psi^+(x_1)\left[H-\mu N,\hat\psi(x_1)\right]\rangle. \tag{4.4.143}$$

It is easy to check two identities following form definitions (4.4.140) and (4.4.141) for H_0 and $H_{\rm int}$:

$$\int \mathrm{d}x\hat\psi^+(x)\left[\hat\psi(x),H_0\right] = H_0, \tag{4.4.144}$$

$$\int \mathrm{d}x\hat\psi^+(x)\left[\hat\psi(x),H_{\rm int}\right] = 2H_{\rm int}, \tag{4.4.145}$$

Using Fourier expansions of GF in variables $(\tau_1-\tau_2)$

$$G(x_1,x_2) = T\sum_{\omega_n}\mathrm{e}^{-\omega_n(\tau_1-\tau_2)}G(\mathbf{r}_1,\mathbf{r}_2;i\omega_n), \tag{4.4.146}$$

we obtain two relations:

$$T\int \mathrm{d}\mathbf{r}_1\mathrm{d}\mathbf{r}_2H_0(\mathbf{r}_1,\mathbf{r}_2)\sum_{\omega_n}G(\mathbf{r}_2\mathbf{r}_1;i\omega_n)\mathrm{e}^{\mathrm{i}\omega_nO^+} = \langle H_0\rangle, \tag{4.4.147}$$

$$T\int \mathrm{d}\mathbf{r}_1\sum_{\omega_n}(i\omega_n)\mathrm{e}^{\mathrm{i}\omega_nO^+}G(\mathbf{r}_1\mathbf{r}_1;i\omega_n) = \langle H_0+2H_{\rm int}-\mu n\rangle. \tag{4.4.148}$$

The last relation can be derived with integration of equation (4.4.143) over x_1 variable and using expansion (4.4.141) of GF in series. Combining relations (4.4.147) and (4.4.148) we find:

$$\begin{aligned}\langle H_{\rm int}\rangle &= \frac{1}{2}T\int \mathrm{d}\mathbf{r}_1\mathrm{d}\mathbf{r}_2\sum_{\omega_n}\mathrm{e}^{\mathrm{i}\omega_nO^+}\left[(i\omega_n+\mu)\delta(\mathbf{r}_1-\mathbf{r}_1)-H_0(\mathbf{r}_1\mathbf{r}_2)\right]\\ G(\mathbf{r}_2\mathbf{r}_1;i\omega_n) &= \frac{1}{2}\mathrm{Tr}\left[\mathrm{e}^{\mathrm{i}\omega_nO^+}G_0^{-1}G\right] = \frac{1}{2}\mathrm{Tr}(\Sigma G)\end{aligned} \tag{4.4.149}$$

Finally total energy is given by a simple expression [9]

$$\langle H\rangle = \mathrm{Tr}\left(H_0G+\frac{1}{2}\Sigma G\right). \tag{4.4.150}$$

Free energy can be calculated by (4.4.136) that we rewrite as:

$$F_{\rm BK} = -\mathrm{Tr}\ln\left[(i\omega_n+\mu)\delta_{ij}-t_{ij}-\Sigma_{ij}(i\omega_n)\right]-\mathrm{Tr}[\Sigma G]+\Phi_{\rm BK}[G_{ij}]. \tag{4.4.151}$$

DMFT approximation is equivalent to presenting Φ_{BK} as a sum over independent atoms where every contribution is determined by local GF only:

$$\Phi_{\mathrm{BK}}^{\mathrm{DMFT}} = \sum_i \Phi[G_{ii}]. \tag{4.4.152}$$

Relation (4.4.137) immediately gives local self-energy:

$$\Sigma_{ij}(i\omega_n) = \delta_{ij}\Sigma(i\omega_n). \tag{4.4.153}$$

Substituting this expression in general formula (4.4.151) we come to expression for free energy functional in *DMFT* approximation:

$$\begin{aligned} F_{\mathrm{BK}}[G_{ii}] = &-\mathrm{Tr}\,\ln\left[\left(i\omega_n + \mu - \frac{\delta\Phi}{\delta G_{ii}})\right)\delta_{ij} - t_{ij}\right] \\ &- \mathrm{Tr}\left[\frac{\delta\Phi}{\delta G_{ii}}G_{ii}\right] + \sum_i \Phi[G_{ii}]. \end{aligned} \tag{4.4.154}$$

Free energy is defined by this functional if corresponding GF is obtained from stationarity condition:

$$\frac{\delta F_{\mathrm{BK}}}{\delta G_{ii}} = 0. \tag{4.4.155}$$

It is necessary that stationarity condition defines extremum (minimum or maximum) but not saddle point so that all second derivatives of F_{BK} were of the same sign (positive or negative). So Baym-Kadanoff functional should be constructed in a way to satisfy this condition. Such problem was investigated in works [9, 210, 225–227] and is discussed in details in reviews.

4.5 *DMFT* for Systems with Disorder

4.5.1 Anderson-Hubbard Model

Till now we have considered homogeneous systems with translational symmetry. The most interesting effect of strong Coulomb interaction is metal–insulator transition happening for large enough value of Coulomb interaction parameter U (Mott phase transition). There is known another physical mechanism for metal–insulator phase transition determined by disorder in the crystal: so called Anderson localization [228]. This phenomenon was predicted by Anderson for the system of noninteracting electrons moving in a stochastic static field that can be produced by random distribution of small concentration impurities in the crystal. Because of electrons scattering on inhomogeneous field mobility edge ε_{c} appears in continuous electron spectrum separating localized electrons area $\varepsilon < \varepsilon_{\mathrm{c}}$ from itinerant electrons $\varepsilon > \varepsilon_{\mathrm{c}}$. If Fermi level $\varepsilon_{\mathrm{F}} < \varepsilon_{\mathrm{c}}$ then the system is insulator and for $\varepsilon_{\mathrm{F}} > \varepsilon_{\mathrm{c}}$ it is metal.

The question what role Coulomb interaction plays in Anderson localization was investigated in many works [229–231] (see also references there) however no final answer was found. It is difficult to take into account in theoretical analysis both factors: strong disorder and large value of Coulomb interaction parameter $U \sim W$. Coherent potential method does not lead to Anderson localization [232]. Dobroslavljevic and Kotliar [233] investigated *DMFT* version [234] where stochastic *DMFT* equations were solved. Generalization of this method [235] resulted later in development *DMFT* method taking into account both disorder and strong Coulomb correlations. Phase diagram on the plane (Δ, U) was calculated where both localization mechanisms: Anderson and Mott are acting. Analogous phase diagram was obtained with another way of *DMFT* extension for disordered systems in [236].

In both works [234,236] a simplest model was used with Anderson-Hubbard Hamiltonian:

$$H = t \sum_{\langle ij \rangle \sigma} \hat{c}^{+}_{i\sigma} \hat{c}_{j\sigma} + \sum_{i\sigma} \varepsilon_i \hat{n}_{i\sigma} + U \sum_{i} \hat{n}_{i\downarrow} \hat{n}_{i\uparrow}, \tag{4.5.156}$$

Here second term accounts for stochastic value of atomic level energy on the lattice ε_i. Without this term Hamiltonian is a standard Hubbard model where hopping and local Coulomb interaction do not depend on site number. The Hamiltonian (4.5.156) is a minimal model that can describe both Anderson localization and Mott transition.

4.5.2 Phase Diagram for Nonmagnetic State

In work [234] the following model probability distribution for atomic level energy ε_i was used:

$$\mathcal{P}(\varepsilon_i) = \Theta \frac{(\Delta/2 - |\varepsilon_i|)}{\Delta}, \tag{4.5.157}$$

where Θ is step function and Δ is disorder measure. Then in (4.5.157) model probability of realization for ε_i values is the same in an interval $-\Delta/2 < \varepsilon_i < \Delta/2$ and is equal to $1/\Delta$. The probability is normalized to unit.

Model with Hamiltonian (4.5.156) comes to single impurity Anderson model ensemble with various values of ε_i:

$$\begin{aligned} H_{\mathrm{SIAM}} = & \sum_{\sigma} (\varepsilon_i - \mu) \hat{c}^{+}_{i\sigma} \hat{c}_{i\sigma} + U \hat{n}_{i\uparrow} \hat{n}_{i\downarrow} \\ & + \sum_{\mathbf{k}\sigma} \left(V_{\mathbf{k}} \hat{c}^{+}_{i\sigma} \hat{c}_{\mathbf{k}\sigma} + V^{*}_{\mathbf{k}} \hat{c}^{+}_{\mathbf{k}\sigma} \hat{c}_{i\sigma} \right) + \sum_{\mathbf{k}\sigma} \varepsilon_{\mathbf{k}} c^{+}_{\mathbf{k}\sigma} c_{\mathbf{k}\sigma}. \end{aligned} \tag{4.5.158}$$

As noninteracting spectrum $\varepsilon_{\mathbf{k}}$ semielliptical density of states was used.

$$N_0(\varepsilon) = \frac{2}{\pi \mathrm{d}^2} \sqrt{\mathrm{d}^2 - \varepsilon^2}, \tag{4.5.159}$$

where D is half band width ($W = 2D$).

For every ε_i value single impurity *GF* $G(\omega, \varepsilon_i)$ was calculated with density of states $\rho_i(\omega) = -\frac{1}{\pi}\mathrm{Im}G(\omega, \varepsilon_i)$ and then average density of states for the system described by Hamiltonian (4.5.156). This average density of states was chosen as:

$$\rho(\omega) = \left(\prod_{i=1}^{N} \rho_i\right)^{1/N} = \exp\left[\left(\sum_{i=1}^{N} \ln\rho_i\right)\frac{1}{N}\right] \equiv \exp\left[\langle \ln\rho_i(\omega)\rangle\right]. \quad (4.5.160)$$

So by multiple *SIAM* solution $\rho(\omega)$ and local *GF* are calculated

$$G(\omega) = \int \mathrm{d}\omega' \frac{\rho(\omega')}{\omega - \omega'}. \quad (4.5.161)$$

$G(\omega)$ can be expressed via self-energy

$$G(\omega) = \int \mathrm{d}\varepsilon \frac{N_0(\varepsilon)}{\omega - \varepsilon - \Sigma(\omega)}, \quad (4.5.162)$$

that for Anderson model is defined by hybridization function:

$$\Sigma(\omega) = \omega - \eta(\omega) - G^{-1}(\omega), \quad (4.5.163)$$

$$\eta(\omega) = \sum_{\mathbf{k}} \frac{|V_{\mathbf{k}}|^2}{\omega - \varepsilon_{\mathbf{k}}}. \quad (4.5.164)$$

For density of state (4.5.159) expression (4.5.164) comes to

$$\eta(\omega) = \frac{1}{4}\mathrm{d}^2 G(\omega). \quad (4.5.165)$$

Substituting expression (4.5.165) to (4.5.163) we find equation connecting $G(\omega)$ and $\Sigma(\omega)$. $G(\omega)$ can be calculated by relation (4.5.161) if $\rho(\omega)$ is known from *SIAM* solution for fixed atomic energy ε_i value. This problem was solved by *NRG* method for $T = 0$. Calculated phase diagram on the plane (U, Δ) is presented in Fig. 4.20. For small U values with increasing disorder parameter Δ Mott phase transition happens. Curves $\Delta_{C1}^{\mathrm{MH}}$ and $\Delta_{C2}^{\mathrm{MH}}$ define the the coexistence area for metallic and insulating phases similar to usual Hubbard model phase diagram on the plane (T, U). Dashed area in Fig. 4.20 marks transition between Mott and Anderson insulators. This transition is not a phase transition but a crossover. So nonmagnetic phases of Mott and Anderson insulator continuously transform to each other.

Basic features of this phase diagram were confirmed in work [236] where $DMFT + \Sigma_{\mathbf{k}}$ calculation scheme was used that was earlier applied to describe spatial fluctuations in *DMFT* (see Sect. 4.3.3). In this scheme local correlations were treated in *DMFT* with local self-energy $\Sigma(i\omega)$ determined by Coulomb interaction. Spatial fluctuations were introduced in phenomenological way and self-energy $\Sigma_{\mathbf{k}}(i\omega_n)$ defined bythese fluctuations was added to

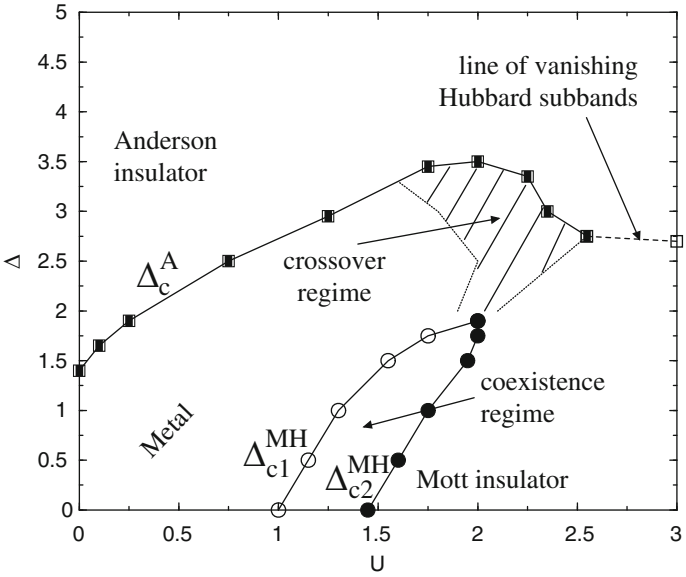

Fig. 4.20. Phase diagram for Anderson-Hubbard model at half-filling [234]

local $\Sigma(i\omega_n)$. For model (4.5.156) $\Sigma_{\mathbf{k}}(i\omega_n)$ is determined by a second term in the Hamiltonian and can be written as:

$$\Sigma_{\mathbf{k}}(i\omega_n) = \Delta^2 \sum_{\mathbf{k}} G(\mathbf{k}, i\omega_n). \tag{4.5.166}$$

Here $\sum_{\mathbf{k}} G(\mathbf{k}, i\omega_n)$ is average electron number n on the site and Δ^2 is a measure of random distribution for atomic energy level ε_i. Gaussian distribution of ε_i on the lattice was supposed [237]

$$\mathcal{P}(\varepsilon_i) = \frac{1}{\sqrt{2\pi}\Delta} \mathrm{e}^{-\frac{\varepsilon_i^2}{2\Delta^2}}, \tag{4.5.167}$$

and was normalized to unit as it was done for (4.5.157). Additivity of two contributions $\Sigma(i\omega_n)$ and $\Sigma_{\mathbf{k}}(i\omega_n)$ means neglecting of interference between electron scattering on local potential inhomogeneity and due to electron–electron Coulomb interaction. The term (4.5.166) presents self-consistent Born approximation for local inhomogeneity (second term in Hamiltonian (4.5.156)).

$DMFT + \Sigma_{\mathbf{k}}$ calculation scheme was described in previous section. In the present case it was applied to three-dimensional cubic lattice.

Phase diagram on the plane (Δ, U) calculated in $DMFT + \Sigma_{\mathbf{k}}$ method is presented in Fig. 4.21. One can see common features with phase diagram in Fig. 4.20 with three phases: correlated metal, Anderson insulator and Mott insulator. There are however two differences: at first coexistence area for

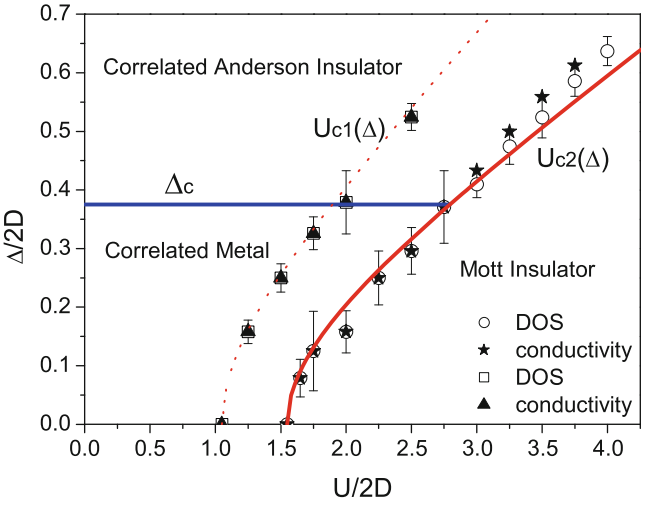

Fig. 4.21. Phase diagram of Anderson-Hubbard model at half-filing calculated by $DMFT + \Sigma_{\mathbf{k}}$ method [236]

metallic and Mott insulator phases is defined by two diverging U_{c1} and U_{c2} lines in contrast to converging lines in Fig. 4.20. At second separation line between correlated metal and Anderson insulator is parallel to abscissa axis when in Fig. 4.20 it is going up for small U and down for large U. These differences are due to simplified approach in [236] where interference between two contributions to Σ from Coulomb interaction and scattering on inhomogeneities is neglected. Please note that lines defining coexistence area are obtained by two methods: from density of states and from conductivity calculations. Comparing phase diagrams in Figs. 4.20 and 4.21 one can conclude that there are more similarity then difference between them that demonstrates that both approaches used in [234, 236] are adequate.

In order to illustrate physics behind phase diagram in Fig. 4.21 we show densities of states (Figs. 4.22 and 4.23) for two U values corresponding to metallic and insulating phases and their change with increasing of disorder parameter Δ. In Fig. 4.22 U value was chosen corresponding to metallic phase without disorder. One can see three-peak structure with high central peak and two Hubbard bands. With disorder increase central peak broadens and side maximums disappear. Broad and featureless spectra distribution for strong disorder corresponds to normal metal with effective mass close to unit.

While ordered metal with large U has a gap on Fermi level disorder leads to gap filling and central peak creation (Fig. 4.23). Numerical analysis of spectra evolution with Δ and U variation results in phase diagram shown in Fig. 4.21.

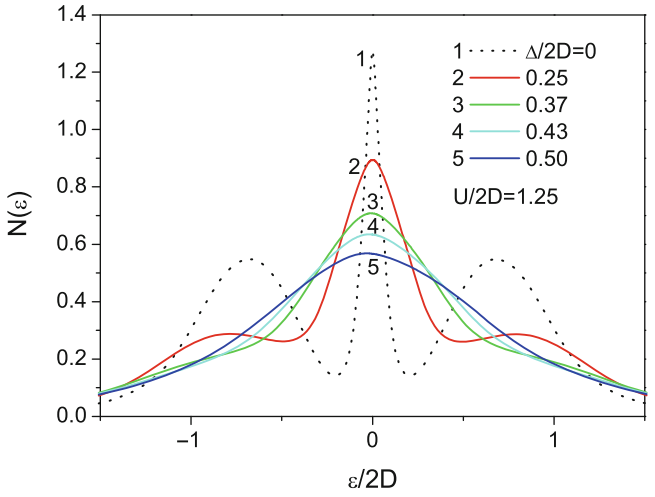

Fig. 4.22. Density of states for Anderson-Hubbard model at half-filling for various disorder parameter Δ and $U = 2.5$ typical for correlated metal [236]

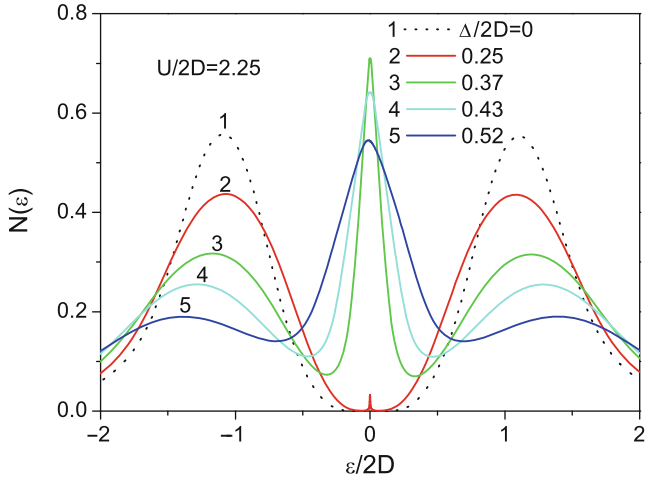

Fig. 4.23. The same as in Fig. 4.22 for $U = 4.5D$ typical for Mott insulator [236]

4.5.3 Optical Conductivity

In work [236] optical conductivity was calculated in self-consistent localization theory using equations for diffusion coefficients of electrons in disordered systems [237]. In Figs.4.24 and 4.25 we present two results from [236] for real part of optical conductivity. In Fig. 4.24 optical conductivity is given for five values of Δ (curves $1, 2, \ldots, 5$). Coulomb parameter $U = 2.5D$ is typical for correlated metal. With Δ increase curves change dramatically. Curves 1

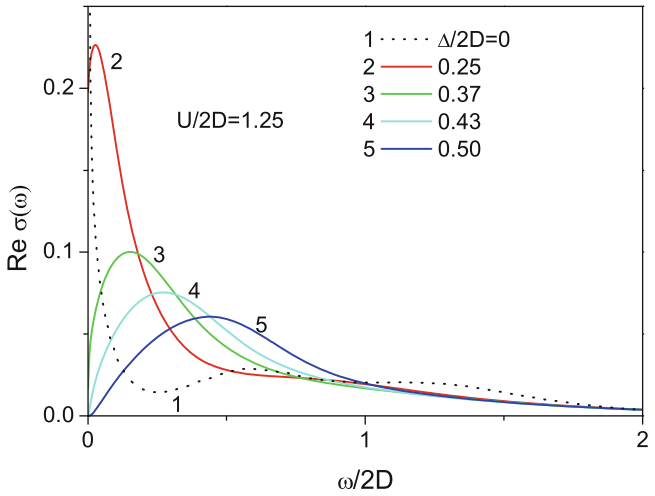

Fig. 4.24. Optical conductivity for Anderson-Hubbard model at half-filling calculated by $DMFT + \Sigma_{\mathbf{k}}$ method for various disorder parameter Δ and $U = 2.5D$ typical for correlated metal [236]

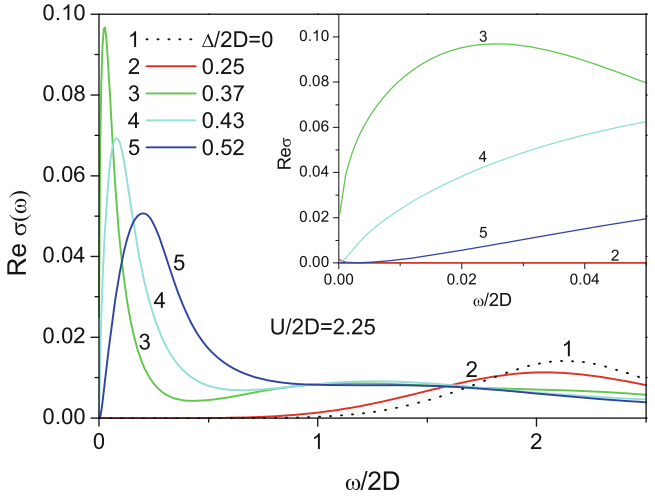

Fig. 4.25. The same as in Fig. 4.24 for $U = 4.5D$ typical for Mott insulator [236]

and 2 show metallic phase due to Drude peak presence. Curve 3 corresponds to mobility edge and curves 4 and 5 to correlated Anderson insulator.

Figure 4.25 was done for larger value $U = 4.5D$ typical for Mott insulator so lines 1 and 2 for small Δ values show Mott insulator. Line 3 corresponds to mobility edge and curves 4 and 5 to Anderson insulator. Such phase change with disorder parameter increase one can see on phase diagram Fig. 4.21.

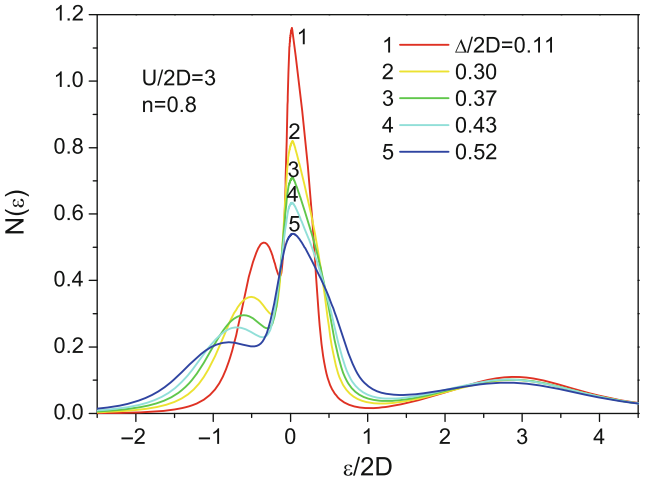

Fig. 4.26. Density of states for Anderson-Hubbard model with electron concentration $n = 0.8$ and $U = 6.0D$ typical for doped Mott insulator [236]

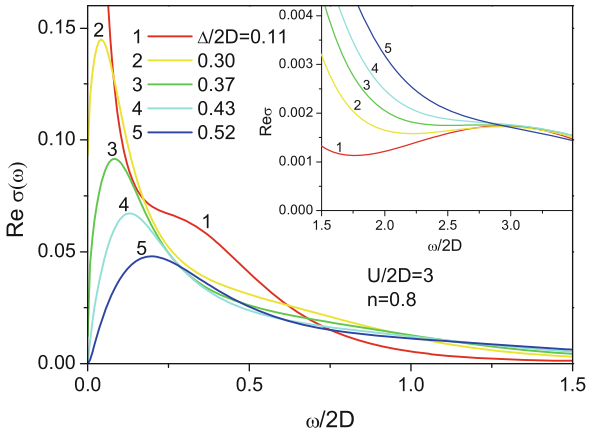

Fig. 4.27. Optical conductivity for Anderson-Hubbard model at $n = 0.8$ for various disorder parameters Δ and $U = 6.0D$ typical for doped Mott insulator [236]. In the inset: high frequency Re$\sigma(\omega)$ showing transitions to upper Hubbard band

Till now results of Anderson-Hubbard model for half-filling were discussed. In Fig. 4.26 density of states for electronic concentration $n = 0.8$ at $U = 6.0D$ is shown. For all disorder parameter Δ values three-peak structure is observed. Central peak intensity decreases with Δ enhancement and spectral weight is partially transfered to Hubbard bands. In Fig. 4.27 optical conductivity is presented calculated for the same parameters values as in previous figure. For Figs. 4.26 and 4.27 one can see that doped Mott insulator behaves with disorder increase similar to correlated metal considered earlier.

Two different approaches to Anderson-Hubbard model described earlier lead to qualitatively the same results. It is worth to note that calculation scheme of [236] is much simpler then full numerical calculations in [234].

In both works [234,236] nonmagnetic phases were considered. For low temperatures in strongly correlated materials spin ordering can happen: antiferromagnetic for insulator and ferromagnetic for metallic phases so it would be interesting to investigate Anderson-Hubbard model with magnetic ordering. Recently such investigations were done for periodic Anderson model (*PAM*). In [238] *DMFT* was used to study ferromagnetic state in *PAM* in the presence of alloy disorder. Such disorder can be created in a metal by substituting part of the atoms by isovalence elements. Alloy disorder can increase Curie temperature due to enhancement of local magnetic moment. In work [239] localization effects in *PAM* due to alloy disorder were investigated. In [240] by the same method transport properties were studied. Such studies should be continued because there are a lot of experimental data showing strong influence of disorder on electronic and magnetic properties for f-electron systems that can be described by *PAM* or Kondo-lattice models (see references in [238–240]).

5

Periodic Anderson Model (*PAM*)

5.1 Early Studies for *PAM*

5.1.1 *PAM* as a Basic Model for Heavy Fermion Systems

Among many f-electrons (rare-earth and actinides) compounds especially interesting are so called "heavy fermion" (*HF*) systems. Anomalously high values of electronic specific heat and low-temperature magnetic susceptibility evidence high effective mass m^* value for charge carriers that can be tens and hundreds time larger than electron mass m. Magnetic and transport properties of such compounds are strongly temperature dependent. For high T f-electrons seems to be weakly interacting with itinerant electrons forming localized magnetic moments. However for low temperatures the picture is drastically different: local magnetic moments are suppressed and transport properties correspond to approaching to insulating state with T decrease. At $T = 0$ they could become insulators due to gap appearance on Fermi surface. Such systems are called Kondo insulators.

Two main questions require theoretical explanation: what determines energy scale T^* separating low- and high-temperature behavior and what is the origin of heavy fermion phenomena? It is clear that the basis of this phenomena is hybridization between localized and itinerant electrons and also itinerant electrons scattering on localized electrons magnetic moments with spin flip resulting in Kondo resonance appearance on Fermi surface. In diluted magnetic systems Kondo resonance leads to localized spin screening due to polarized electrons cloud around local magnetic moment. Energy of this screening is determined by parameter T_K called Kondo temperature. This parameter separates two regimes: high-temperature $T \gg T_\mathrm{K}$ where local spins are not screened and low-temperature $T < T_\mathrm{K}$ where such screening is effective.

In concentrated systems where number of f-atoms with partially filled shells is comparable with a number of crystal cells a screening effect is also present and the problem of connection between parameters T^* and T_K

appears. In general T_{K} defines the temperature where local moments become to be screened by itinerant electrons and T^* is a temperature when coherent state for itinerant electrons is stabilized.

Fundamental answers to these questions were found before *DMFT* development and later we will give a short review of the earlier studies. Basic model for f-systems is periodic Anderson model (*PAM*) with Hamiltonian:

$$H = \varepsilon_{\mathrm{c}} \sum_{i\sigma} \hat{c}^{\dagger}_{i\sigma} \hat{c}_{i\sigma} + \sum_{ij\sigma} t_{ij} \hat{c}^{\dagger}_{i\sigma} \hat{c}_{j\sigma} + \varepsilon_f \sum_{i\sigma} \hat{n}^f_{i\sigma} + U \sum_i \hat{n}^f_{i\uparrow} \hat{n}^f_{i\downarrow} \sum_{ij\sigma} \left(V_{ij} \hat{c}^{\dagger}_{i\sigma} \hat{f}_{j\sigma} + V^*_{ij} \hat{f}^{\dagger}_{j\sigma} \hat{c}_{i\sigma} \right). \quad (5.1.1)$$

It describes localized f-electrons on all sites embedded in itinerant electrons bath with a term responsible for hybridization between localized and itinerant electrons.

PAM is described by one-electron matrix *GF*

$$G^{\sigma}(1,2) = \begin{pmatrix} -\left\langle T \hat{f}_{1\sigma} \hat{f}^{\dagger}_{2\sigma} \right\rangle & -\left\langle T \hat{f}_{1\sigma} \hat{c}^{\dagger}_{2\sigma} \right\rangle \\ -\left\langle T \hat{c}_{1\sigma} \hat{f}^{\dagger}_{2\sigma} \right\rangle & -\left\langle T \hat{c}_{1\sigma} \hat{c}^{\dagger}_{2\sigma} \right\rangle \end{pmatrix} \equiv \begin{pmatrix} G^{\sigma}_{ff}(1,2) G^{\sigma}_{fs}(1,2) \\ G^{\sigma}_{sf}(1,2) G^{\sigma}_{ss}(1,2) \end{pmatrix}. \quad (5.1.2)$$

Here numbers note combined indexes including site number and thermodynamic time. For example $1 = (i_1 \tau_1)$ and so on.

It is easy to write equation of motion for all four *GF* similar to what we did in Chap. 3 for single impurity Anderson model (*SIAM*). Their solution is:

$$G^{\sigma}_{ff}(k) = \frac{1}{i\omega_n + \mu - \varepsilon_f - \Sigma^{\sigma}(k) - \frac{|V_{\mathbf{k}}|^2}{i\omega_n + \mu - \varepsilon_{\mathbf{k}}}}, \quad (5.1.3)$$

$$G^{\sigma}_{fs}(k) = \frac{V^*_k}{(i\omega_n + \mu - \varepsilon_{\mathbf{k}}) \left[i\omega_n + \mu - \varepsilon_f - \Sigma^{\sigma}(k) \right] - |V_{\mathbf{k}}|^2}, \quad (5.1.4)$$

$$G^{\sigma}_{sf}(k) = \frac{V_k}{(i\omega_n + \mu - \varepsilon_{\mathbf{k}}) \left[i\omega_n + \mu - \varepsilon_f - \Sigma^{\sigma}(k) \right] - |V_{\mathbf{k}}|^2}, \quad (5.1.5)$$

$$G^{\sigma}_{ss}(k) = \frac{1}{i\omega_n + \mu - \varepsilon_{\mathbf{k}} - \Sigma^{\sigma}(k) - \frac{|V_{\mathbf{k}}|^2}{i\omega_n + \mu - \varepsilon_f - \Sigma^{\sigma}(\mathbf{k})}}. \quad (5.1.6)$$

Here $k = (\mathbf{k}, i\omega_n)$ is four-component momentum including wave vector and frequency.

Expressions (5.1.3)–(5.1.6) give formal solution without a way to calculate self-energy $\Sigma(\mathbf{k}, i\omega_n)$ determined by Coulomb interaction among f-electrons. In a case $U = 0$ relations (5.1.3)–(5.1.6) are fully defined and poles of any component of matrix *GF* can be found from

$$(i\omega_n + \mu - \varepsilon_{\mathbf{k}}) (i\omega_n + \mu - \varepsilon_f) - |V_{\mathbf{k}}|^2 = 0. \quad (5.1.7)$$

This equation defines two branches of spectra separated by hybridization gap $|V_{\mathbf{k}}|$. Self-energy $\Sigma^{\sigma}(\mathbf{k}, i\omega_n)$ modifies the spectrum and its calculation is a central problem. For strong Coulomb interaction ($U \geq W$) various nonperturbative methods are used for this purpose. At first we will give short review of *PAM* investigation before *DMFT* was developed.

5.1.2 Review of Early Analytical Studies for *PAM*

At the beginning we consider single impurity Anderson model (*SIAM*). It is defined by Hamiltonian following from (5.1.1) if summation over sites occupied by f atoms is omitted. After Fourier transformation we have:

$$H_{\mathrm{SIAM}} = \sum_{\mathbf{k}\sigma} \varepsilon_{\mathbf{k}} \hat{c}^{\dagger}_{\mathbf{k}\sigma} \hat{c}_{\mathbf{k}\sigma} + \varepsilon_f \sum_{\sigma} \hat{f}^{\dagger}_{\sigma} \hat{f}_{\sigma} + U \hat{n}_{f\uparrow} \hat{n}_{f\downarrow} + \sum_{\mathbf{k}\sigma} \left(V_{\mathbf{k}} \hat{c}^{\dagger}_{\mathbf{k}\sigma} \hat{f}_{\sigma} + V^{*}_{\mathbf{k}} \hat{f}^{\dagger}_{\sigma} \hat{c}_{\mathbf{k}\sigma} \right). \tag{5.1.8}$$

SIAM Hamiltonian contains many parameters (W, ε_f, U and electronic concentration) that means very complicated phase diagram. Two main regimes can be distinguished differing by position of f-level relatively to Fermi level of itinerant electrons band.

In Fig. 5.1 those two regimes are illustrated. At first case atomic level ε_f lies below conduction band and level $\varepsilon_f + U$ corresponding to double occupancy lies above the band (Kondo regime). At the second case f-level is very close to Fermi energy and as a result noninteger occupation of impurity state happens (intermediate valence regime).

There is special case: symmetric Anderson model where

$$\varepsilon_{\mathrm{F}} - \varepsilon_f = (\varepsilon_f + U) - \varepsilon_{\mathrm{F}}, \tag{5.1.9}$$

i.e., both levels ε_f and $\varepsilon_f + U$ have equal energy separation from Fermi energy. In this case hole and particle excitations in f-state need the same energy. If energy is measured relative to Fermi level ($\varepsilon_{\mathrm{F}} = 0$) then relation (5.1.9) can be rewritten as:

$$2\varepsilon_f + U = 0. \tag{5.1.10}$$

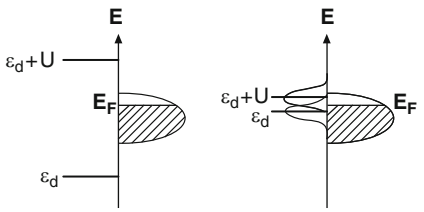

Fig. 5.1. Localized magnetic moment regime (Kondo regime, *left side*) and intermediate valence regime (*right side*) in single impurity Anderson model

Schrieffer and Wolf [241] have shown that in Kondo regime Anderson model is equivalent to single impurity sf-exchange model defined by Hamiltonian

$$H_{Sf} = \sum_{\mathbf{k}\sigma} \varepsilon_{\mathbf{k}} \hat{c}^{\dagger}_{\mathbf{k}\sigma} \hat{c}_{\mathbf{k}\sigma} - J\,(\mathbf{Ss})\,, \tag{5.1.11}$$

where $\mathbf{S}$ is local spin operator on impurity site, $\mathbf{s}$ the itinerant electron spin operator, J is exchange integral expressed via H_{SIAM} Hamiltonian parameters:

$$J = -2\,|V_{\mathbf{k}}|^2\,\frac{U}{|\varepsilon_f|\,|\varepsilon_f + U|} < 0 \tag{5.1.12}$$

Effective sf-exchange coupling is antiferromagnetic that results in formation of itinerant electrons cloud with spin polarization opposite to localized spin direction.

This state is called Kondo singlet and its coupling energy is Kondo temperature [242]:

$$T_{\mathrm{K}} \approx W \mathrm{e}^{-\frac{1}{|J|\rho_0}}\,. \tag{5.1.13}$$

Here and in the following we assume Boltsman constant equal to unit. In this expression ρ_0 is density of states on Fermi level and in expression (5.1.12) for effective exchange wave vector $\mathbf{k}$ lies on Fermi energy. Formula (5.1.13) was obtained in perturbation theory over parameter $|J|\rho_0 \ll 1$ and so T_{K} is very small quantity comparing with characteristic electron energy scale: band width W or Fermi energy ε_{F} for normal metal.

In perturbation theory T_{K} is a temperature where this theory fails. In more sophisticated approach (see Hewson book [243]) T_{K} defines a temperature when localized moment starts to be screened by conduction electrons cloud. Exact solution of Kondo model shows that at $T = 0$ local spin $S = 1/2$ is completely screened. T_{K} is not phase transition point but rather a crossover where gradual transition from weak coupling to strong coupling regimes happens.

In concentrated Kondo system that is equivalent to *PAM* simultaneously with local moment screening a sharp peak in the density of states on the Fermi level appears (Abrikosov-Suhl resonance [34,244]). Its origin is a hybridization of f-states with itinerant electrons.

Characteristic feature of *PAM* is existence of energy scale similar to Kondo temperature in *SIAM*. This was shown by Rice and Ueda [245, 246] in calculations using one of the nonperturbative approaches: variation Gutzwiller method [247]. In Kondo regime for nearly fully occupied f-level (i.e., at $n_f \simeq 1$) and large Coulomb interaction value they have derived effective Hamiltonian for low-energy properties of the model. This Hamiltonian has a form:

$$H_{\mathrm{eff}} = \sum_{\mathbf{k}\sigma} \varepsilon_{\mathbf{k}} \hat{c}^{\dagger}_{\mathbf{k}\sigma} \hat{c}_{\mathbf{k}\sigma} + \varepsilon_f \sum_{i\sigma} \hat{n}^{f}_{i\sigma} + \sum_{i\sigma} \widetilde{V}_{\sigma} \left(\hat{c}^{\dagger}_{i\sigma} \hat{f}_{i\sigma} + \hat{f}^{\dagger}_{i\sigma} \hat{c}_{i\sigma} \right). \tag{5.1.14}$$

Here explicit Coulomb interaction among f-electrons is absent and hybridization matrix element is renormalized via dependence on f-level occupancy:

$$\widetilde{V}_\sigma = \sqrt{q}_\sigma V. \tag{5.1.15}$$

Normalizing parameter q_σ in the limit $U \to \infty$ depends on f-states occupancy:

$$q_\sigma = \frac{1 - n_f}{1 - n_f^\sigma}. \tag{5.1.16}$$

For occupancy $n_f \approx 1$ quantity q_σ and hybridization $\widetilde{V}_\sigma$ have small value. This means appearance of narrow band of hybridized states. From Hamiltonian (5.1.14) one can see that in second-order perturbation theory in hybridization f-electrons can hop over the lattice sites that results in electronic band with effective width

$$W_{\text{eff}}^f \sim \left|\widetilde{V}_\sigma\right|^2 \sim q_\sigma \sim (1 - n_f) \tag{5.1.17}$$

that vanishes with n_f approaching to unit. With band narrowing effective mass strongly increases

$$\frac{m^*}{m} \sim (W_{\text{eff}}^f)^{-1} \sim \frac{1}{1 - n_f} \gg 1. \tag{5.1.18}$$

that means "heavy fermion" effect. This relation can be rewritten as

$$\frac{m^*}{m} \sim \frac{T_{\text{F}}}{T^*}, \tag{5.1.19}$$

where T_{F} is degeneracy temperature in noninteracting conduction band and T^* quasiparticle energy scale (band width for f-electrons). From Gutzwiller method calculations [247] follows that for Kondo regime ($n_f \approx 1$)

$$T^* \approx W \mathrm{e}^{-\frac{1}{2|J|\rho}}. \tag{5.1.20}$$

Comparing (5.1.20) with (5.1.13) one can see that $T^* \gg T_{\text{K}}$. Combining expressions (5.1.13), (5.1.18), (5.1.19), and (5.1.20) we find relations between effective masses in lattice and impurity models:

$$\frac{m^*_{\text{PAM}}}{m^*_{\text{SIAM}}} \sim \mathrm{e}^{-\frac{1}{2|J|\rho}}. \tag{5.1.21}$$

Please note that relations (5.1.18)–(5.1.21) are valid only for Kondo regime that is realized for $n_f \approx 1$.

In addition to this relations we will write another one for density of f-states on the Fermi level [248]:

$$\rho_f(\varepsilon_{\text{F}}) \approx \rho(\varepsilon_{\text{F}}) \frac{T_{\text{F}}}{T^*} \tag{5.1.22}$$

that is equivalent to (5.1.19). So it was shown using variational Gutzwiller method that in Kondo regime for *PAM* there is a sharp f-states peak on Fermi level. Energy scale of lattice model T^* is much larger that corresponding energy scale T_K for single impurity model. Those results were confirmed in further *PAM* investigations by other nonperturbative methods: "slave bosons" [249, 250], $1/N$ expansion method (N is f-orbital degeneracy) [124, 248].

Simplest explanation for narrow f-band and correspondingly large effective mass is that at $n_f \approx 1$ the number of holes (and doubles) is very small so that f-electron cannot move on the lattice without paying large Coulomb energy price.

5.1.3 *DMFT* for *PAM*

As for Hubbard model the most rigorous solution of periodic Anderson model can be obtained in *DMFT* method where lattice problem is reduced to equivalent single impurity problem. *DMFT* equations for *PAM* are formulated analogously to those for Hubbard model.

Let us consider *GF* for f-electrons defined by (5.1.3). In agreement with basic *DMFT* idea we assume that self-energy $\Sigma(\mathbf{k}, \omega)$ depends only on frequency (spin index is omitted because we consider only paramagnetic state). We write local *GF* (diagonal in site indexes matrix element G_{ff}) and note it as $G_{\mathrm{loc}}(i\omega_n)$:

$$G_{\mathrm{loc}}(i\omega_n) = \sum_{\mathbf{k}} \frac{1}{i\omega_n + \mu - \varepsilon_f - \Sigma(i\omega_n) - \frac{|V_{\mathbf{k}}|^2}{i\omega_n + \mu - \varepsilon_{\mathbf{k}}}}. \tag{5.1.23}$$

Here *GF* differs from corresponding local *GF* in Hubbard model by hybridization term in denominator. If we neglect $\mathbf{k}$-dependence of matrix element $V_{\mathbf{k}}$ and replace it by real constant V we can in (5.1.23) come from summation over $\mathbf{k}$ to integration over ε using density of states $\rho(\varepsilon)$ for noninteracting band.

Then we define f-electrons *GF* for effective single impurity Anderson model with the same self-energy as for lattice model:

$$G_{\mathrm{imp}}(i\omega_n) = \frac{1}{i\omega_n + \mu - \varepsilon_f - \Delta(i\omega_n) - \Sigma(i\omega_n)}. \tag{5.1.24}$$

Here $\Delta(i\omega_n)$ is hybridization function that implicitly depends on $\Sigma(i\omega_n)$ and that should be calculated together with $\Sigma(i\omega_n)$ from self-consistency condition

$$G_{\mathrm{loc}}(i\omega_n) = G_{\mathrm{imp}}(i\omega_n). \tag{5.1.25}$$

For that one should calculate $G_{\mathrm{imp}}(i\omega_n)$ of single impurity Anderson model in the same way as it was done for Hubbard model, for example by *QMC* method that was described in Chap. 3.

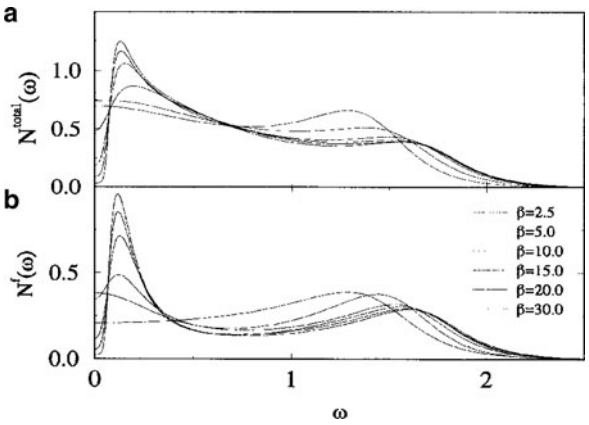

Fig. 5.2. Temperature dependence of (**a**) total density of states and (**b**) f-electrons partial density of states $\rho_f(\omega)$ calculated in *DMFT(QMC)* for parameter values $V = 0.5$, $U = 2$ [251]

By this method (in Hirsch-Fye algorithm) *DMFT* investigations for *PAM* were done in pioneering work of Jarrell [251] for symmetric model with condition:

$$\varepsilon_f = -\frac{U}{2}, \quad n_f = 1, \quad n_c = 1 \tag{5.1.26}$$

In this condition at $T = 0$ the gap should appear in quasiparticle spectrum on Fermi level and Kondo insulator state is realized.

In Fig. 5.2 spectral function is shown obtained in final temperature *QMC* calculations. At low T values pseudogap appears that should transform to real gap with temperature interpolation to zero.

At high temperatures higher than characteristic temperature T^* $\rho_f(\omega)$ is a smooth frequency function. At $T < T^*$ sharp maximum is formed. Peak appearance in $\rho_f(\omega)$ is determined by resonance Kondo scattering of conduction electrons on localized f-electron magnetic moments and its position is comparable with Kondo temperature for *PAM*. In Fig. 5.2 $T^* = 0.23$ (in band width W units) and energy gap value in electronic spectrum is $\Delta \approx 0.5T^*$. Calculations for dynamical magnetic χ_s and charge χ_c susceptibilities show that their corresponding gaps are twice as large as quasiparticle spectrum gap: $\Delta_s = \Delta_c \approx 2\Delta \approx T^*$. So *DMFT(QMC)* calculations demonstrate energy scale T^* existence.

In Jarrell work temperature dependence of magnetic susceptibility and electronic specific heat were calculated for various Hamiltonian parameter values satisfying condition (5.1.26). This quantities scale with T^* while for *SIAM* corresponding energy scale is Kondo temperature T_K (Figs. 5.3–5.4).

So numerical calculations for *PAM* using *DMFT(QMC)* method confirm results of earlier studies based on approximated nonperturbative methods. They demonstrate gap existence in quasiparticle spectrum at $T = 0$ and

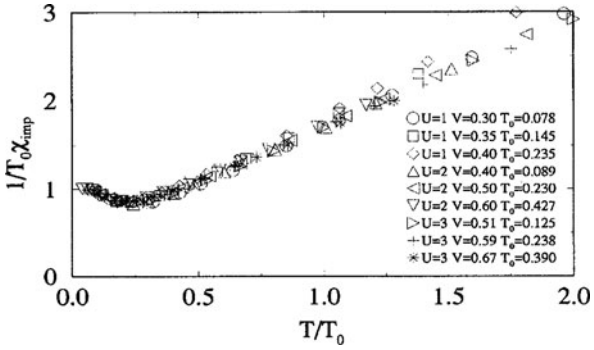

Fig. 5.3. Scaling behavior of magnetic susceptibility as a function of temperature from *DMFT(QMC)* calculations [251]

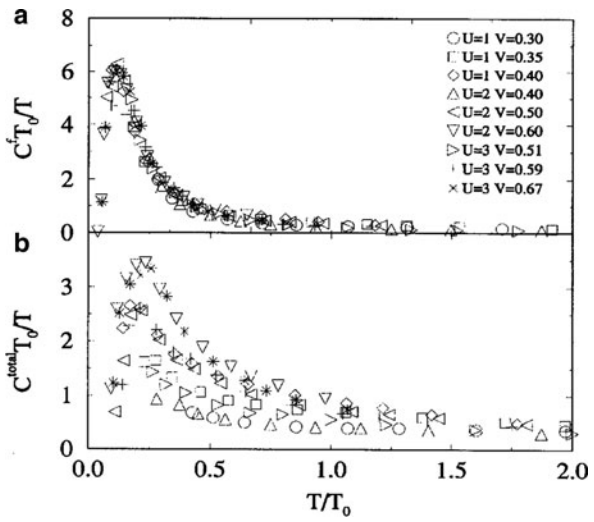

Fig. 5.4. Scaling behavior of f-electrons contribution to specific heat as a function of temperature from *DMFT(QMC)* calculations [251]

low-energy properties show energy scale T^* that is much larger than Kondo temperature T_K for *SIAM* at the same parameters ε_f, U, and V values.

5.2 *PAM* Studies by *DMFT* Method

5.2.1 *DMFT(NRG)* Results at $T = 0$

Detail study of *PAM* spectral properties at $T = 0$ was done in *DMFT* with auxiliary single impurity Anderson model solved by numerical renorm-group (see Sect. 3.1.5) in work of Pruschke, Bulla, and Jarrell [252]. In this section

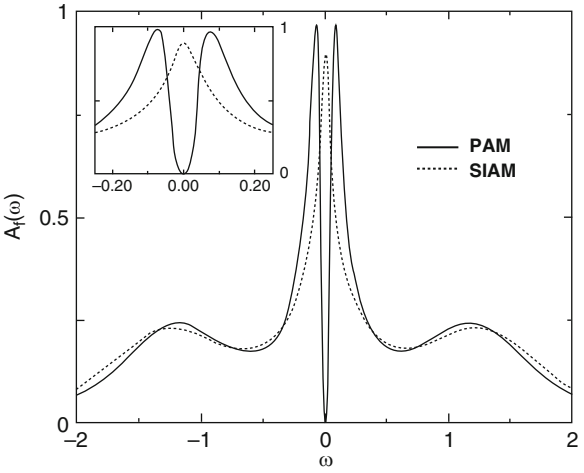

Fig. 5.5. Local density of f-states $A_f(\omega)$ for *SIAM* (*dashed line*) and *PAM* (*solid line*) for particle–hole symmetric case and parameters values $U = 2$, $V^2 = 0.2$. The inset shoes magnification for area near Fermi level [252]

we present results of this study. *NRG* technique will be described in the next section when we will discuss more simple model: Kondo lattice model (*KLM*).

At first we consider particle–hole symmetric case defined by condition (5.1.26). In Fig. 5.5 spectral function $A_f(\omega)$ is presented for *PAM* and *SIAM* for fixed values of model parameters U and V.

Results for *SIAM* show well known picture: two broad peaks at frequencies $\omega = \pm U/2$ (Hubbard bands) and Abrikosov-Suhl resonance at the Fermi level. In *PAM* case incoherent peaks at $\omega = \pm U/2$ are preserved but the central peak corresponding to coherent states is split because of hybridization between f and s electrons. The width of this peak in *PAM* is significantly larger than resonance peak width in *SIAM*. For *SIAM* the width of the peak defines characteristic energy scale – Kondo temperature T_{K}. In *PAM* case peak width defines lattice energy scale T^* and $T^* \gg T_{\mathrm{K}}$ as one can see in the inset in Fig. 5.5. This result agrees with predictions in Rice and Ueda work [246].

In Fig. 5.6 frequency dependence of imaginary and real parts of self-energy is presented for impurity and lattice models for the same parameter U and V values as in Fig. 5.5. One can see that imaginary part of $\Sigma_f(\omega)$ is negative for all frequencies as it is required by analytical properties of retarded *GF*. Difference between results for impurity and lattice models reveals itself mostly in area near Fermi level that can be seen in insets in Fig. 5.6.

Please note different slope of $\mathrm{Re}\Sigma_f(\omega)$ curves near $\omega = 0$. The derivative $\frac{\mathrm{d}}{\mathrm{d}\omega}\mathrm{Re}\Sigma_f(\omega)\big|_{\omega=0}$ defines according to (3.3.146) intensity of quasiparticle peak and also quasiparticle effective mass:

$$Z_f^{-1} = 1 - \frac{\mathrm{d}\mathrm{Re}\Sigma_f(\omega)}{\mathrm{d}\omega}\bigg|_{\omega=0} = \frac{m^*}{m}, \tag{5.2.27}$$

One can see that $m^*_{\mathrm{PAM}} \ll m^*_{\mathrm{SIAM}}$.

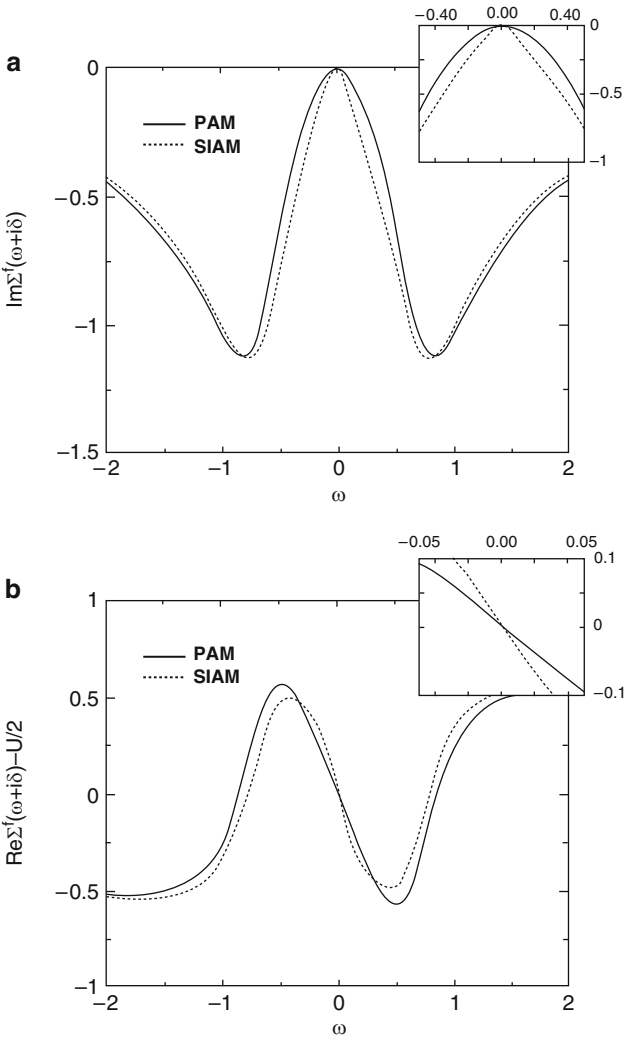

Fig. 5.6. Self-energy $\Sigma_f(\omega)$ for *SIAM* (*dashed line*) and *PAM* (*solid line*) for particle–hole symmetric case and parameters values the same as in Fig. 5.5. The inset shoes magnification for area near Fermi level [252]

Numerical calculations for various parameter U and V values (or different $J\rho$ values) show the following dependence:

$$\frac{m^*_{\mathrm{PAM}}}{m^*_{\mathrm{SIAM}}} \sim \mathrm{e}^{-\frac{1}{3J\rho}}. \tag{5.2.28}$$

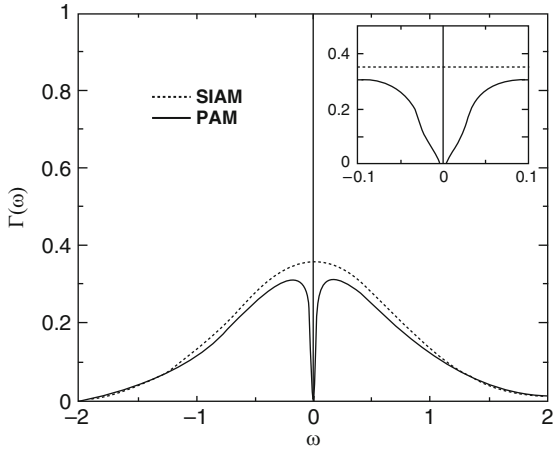

Fig. 5.7. Anderson width $\Gamma(\omega)$ of d-level for *SIAM* and *PAM* for the same conditions as in Fig. 5.5 [252]

So numerical calculations in *DMFT(NRG)* method results in exponentially small effective mass value for lattice model comparing with impurity one. That agrees well with Rice and Ueda results (5.1.21) however numerical coefficient in exponent is 1/3 instead of 1/2.

Important model characteristics in *DMFT* together with self-energy $\Sigma_f(\omega)$ are hybridization function $\Delta(\omega)$ and Anderson impurity level width $\Gamma(\omega) = -\mathrm{Im}\Delta(\omega)$. In impurity model $\Gamma(\omega)$ could be chosen as a constant but for lattcie model it is impossible because $\Gamma(\omega)$ has deep depression near $\omega = 0$ and on $\omega = 0$ δ-peak appears (Fig. 5.7).

Let us consider now state with broken particle–hole symmetry. It can be realized by two ways: by braking relation $2\varepsilon_d + U = 0$ preserving other conditions or by changing Fermi level position. Example of the first case is shown in Fig. 5.8.

For given values of Hamiltonian parameters $\langle n_c \rangle \approx 1$ and $\langle n_f \rangle \approx 0.92$ one can see as in symmetric case three peak structure with a quasiparticle peak split by hybridization gap. This gap is now above the Fermi level and its width is significantly larger than Kondo peak width in *SIAM* again demonstrating increase of energy scale for lattice model. This feature is also seen on Anderson width curve. In $\Gamma(\omega)$ narrow peak is observed slightly above Fermi level but in contrast to $n_f = 1$ case this peak has final width due to quasiparticle decays for $\omega > 0$.

Another case of particle–hole symmetry braking is in setting $\varepsilon_c > 0$. In contrast to considered earlier case $\varepsilon_c = 0$ where conduction electron number $n_c = 1$, for $\varepsilon_c > 0$ case conduction electrons number $n_c < 1$ and with increase of ε_c deviation of n_c from 1 can become significant. In this situation

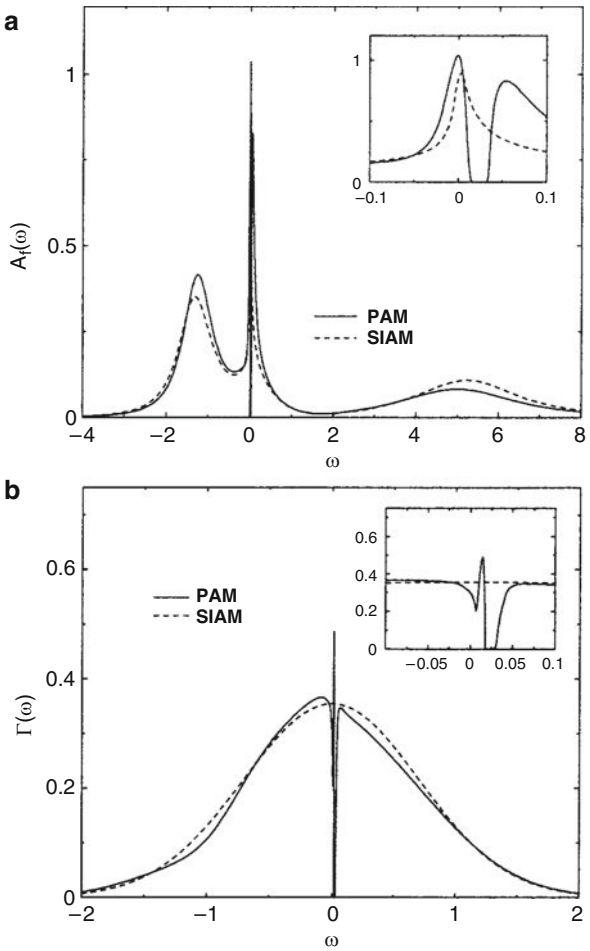

Fig. 5.8. Local density of states $A_f(\omega)$ and Anderson width $\Gamma(\omega)$ for *SIAM* and *PAM* in symmetric case for parameters values: $\varepsilon_c = 0$, $\varepsilon_f = -1$, $U = 6$, $V^2 = 0.2$. The inset shoes magnification for area near Fermi level [252]

hybridization gap in f-electrons spectral function $A_f(\omega)$ disappears. The same happens for conduction electrons density of states $\rho_c(\omega)$ (Fig. 5.9).

Hybridization gap disappearance at small n_c leads to exhaustion phenomenon predicted by Nozieres [253] from phenomenological considerations. The essence of this phenomenon is the fact that in order to screen local moments one needs one conduction electron on every lattice site occupied by f-atom. When conduction electrons number n_c becomes too small screening of all lattice site become impossible and hybridization gap become a pseudogap with a width decreasing with n_c decrease. That means that energy scale T^* decreases with n_c and T^* becomes smaller than T_K.

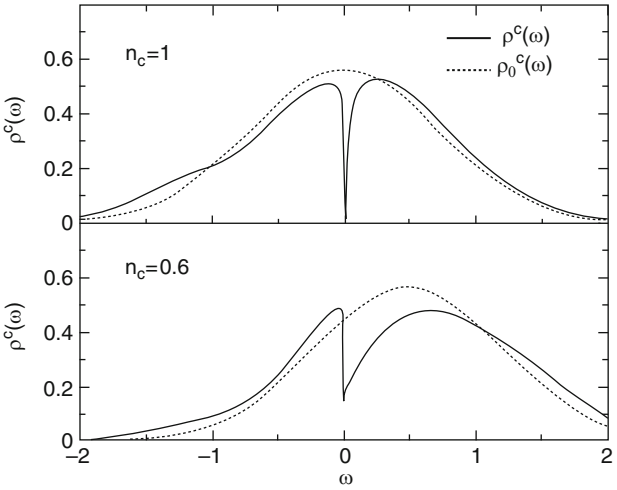

Fig. 5.9. Density of states $\rho^c(\omega)$ of itinerant electrons for *PAM* at parameters values: $\varepsilon_f = -1$, $V^2 = 0.2$, (a) $U = 6$, $\varepsilon_c = 0 (n_c \approx 1)$ and (b) $U = 2$, $\varepsilon_c = 0.5 (n_c \approx 0.6)$. *Dashed lines* are for noninteracting density of states $\rho_0^c(\omega)$ for corresponding values of ε_c [252]

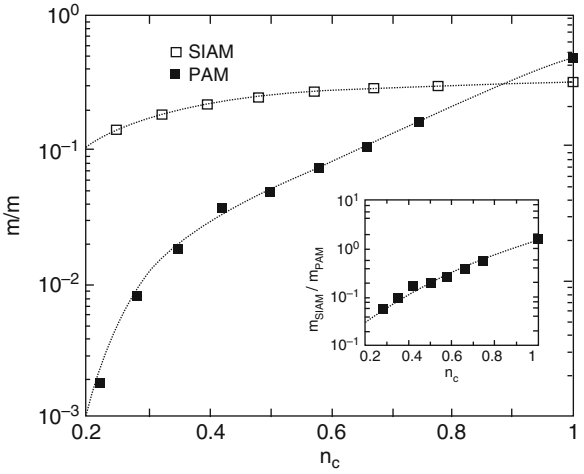

Fig. 5.10. Dependence of $\frac{m}{m^*}$ (m^* is effective mass for quasiparticle peak) on number of electrons in itinerant band n_c for $U = 2$, $V^2 = 0.25$, $n_f \approx 1$. In the inset: ratio $\frac{m^*_{\mathrm{SIAM}}}{m^*_{\mathrm{PAM}}} \equiv \frac{T_0}{T_K}$ as a function of n_c [252]

In Fig. 5.10 the change of effective mass with n_c decrease is shown calculated for lattice and impurity models. One can see that at $n_c \approx 1$ m_{SIAM} and m_{PAM} are of the same order but $m_{\mathrm{PAM}} < m_{\mathrm{SIAM}}$ and so $T^* > T_K$.

With n_c decreasing quantity $\frac{m}{m_{\mathrm{PAM}}} \sim T^*$ falls drastically that confirms Nozieres prediction that for the systems with small conduction band occupancy there are two energy scales: one of the order of T_K characterizes beginning of Kondo screening and another one corresponds to coherent states appearance or in other words Fermi liquid behavior. Detailed comparison of predicted by Nozieres exhaustion picture at small n_c with numerical calculations results by *DMFT(NRG)* method is given in [252].

5.3 Kondo Lattice

5.3.1 *DMFT* for Kondo Lattice

In the previous section we have shown that in Kondo regime Anderson model is equivalent to sf-model (5.1.11) with antiferromagnetic exchange interaction between localized spins and itinerant electrons that is called Kondo lattice model (*KLM*). That means that found in *DMFT* calculations features of *PAM* should be observed in *KLM* too. That includes existence of two energy scales T^* and T_0. We will show that it is indeed so from *KLM* analysis. *KLM* Hamiltonian is:

$$H = \sum_{\mathbf{k}\sigma} \varepsilon_{\mathbf{k}} \hat{c}^{\dagger}_{\mathbf{k}\sigma} \hat{c}_{\mathbf{k}\sigma} + J \sum_i \mathbf{S}_i \mathbf{s}_i. \tag{5.3.29}$$

Here $\mathbf{S}$ is local spin operator on impurity site and $\mathbf{s}$ is itinerant electron spin operator that can be expressed via Fermi operators:

$$\mathbf{s}_i = \sum_{\mu\nu} \hat{c}^{\dagger}_{i\mu} \boldsymbol{\sigma}_{\mu\nu} \hat{c}_{i\nu}, \tag{5.3.30}$$

where $\boldsymbol{\sigma}$ is a vector formed by Pauli matrices $\sigma^{\alpha}_{\mu\nu}$ and $\hat{c}_{i\sigma}$ ($\hat{c}^{\dagger}_{i\sigma}$) are Fermi operators of creation (annihilation) of conduction electron on cite i that are connected with $\hat{c}_{\mathbf{k}\sigma}$ ($\hat{c}^{\dagger}_{\mathbf{k}\sigma}$) operators by Fourier transformation:

$$\hat{c}_{i\sigma} = \frac{1}{\sqrt{N}} \sum_{\mathbf{k}} \hat{c}_{\mathbf{k}\sigma} \mathrm{e}^{\mathrm{i}\mathbf{k}\mathbf{R}_i}. \tag{5.3.31}$$

DMFT method can be applied to Hamiltonian (5.3.29). Such calculations were done in Costi and Manini works [254, 255] that will be described in this section.

Retarded *GF* for conduction electrons is:

$$G^{\sigma}_{ij}(t-t') \equiv \langle\langle \hat{c}_{i\sigma}(t) | \hat{c}^{\dagger}_{j\sigma}(t') \rangle\rangle \tag{5.3.32}$$

(definition is given in Appendix B). Its Fourier component in spatial and time variables $G^\sigma(\mathbf{k},\omega)$ is expressed by Dyson equation via self-energy $\Sigma^\sigma(\mathbf{k},\omega)$:

$$G^\sigma(\mathbf{k},\omega) = \frac{1}{\omega + \mu - \varepsilon_{\mathbf{k}} - \Sigma^\sigma(\mathbf{k},\omega)}. \tag{5.3.33}$$

Following basic *DMFT* idea we neglect wave vector dependence and introduce local *GF* (diagonal in site indexes matrix element):

$$G_L^\sigma(\omega) = \sum_{\mathbf{k}} \frac{1}{\omega + \mu - \varepsilon_{\mathbf{k}} - \Sigma^\sigma(\omega)}. \tag{5.3.34}$$

We define *GF* of auxiliary sf-model $G^\sigma_{\mathrm{imp}}(\omega)$ with the same self-energy $\Sigma^\sigma(\omega)$ and parameters satisfying self-consistency condition:

$$G_L^\sigma(\omega) = G^\sigma_{\mathrm{imp}}(\omega). \tag{5.3.35}$$

To two *DMFT* equations (5.3.34) and (5.3.35) we add equation for chemical potential that expresses conduction electron number n_c via electronic *GF*:

$$n_{\mathrm{c}} = \frac{1}{N}\sum_{j\sigma}\langle \hat{c}^\dagger_{j\sigma}\hat{c}_{j\sigma}\rangle = \sum_\sigma \int \mathrm{d}\omega f(\omega)\rho_c^\sigma(\omega), \tag{5.3.36}$$

$$\rho_c^\sigma(\omega) = -\frac{1}{\pi}\mathrm{Im}G_L^\sigma(\omega). \tag{5.3.37}$$

In the following we will consider paramagnetic phase and so spin index in *GF* and density of states will be omitted.

As usual in *DMFT* one need to calculated single-impurity problem *GF*. We have already described in Chap. 3 quantum Monte Carlo (*QMC*) method for this problem and now we will describe another popular method Numerical Renorm-Group (*NRG*). Applications of this method to *PAM* were described in previous section and now we will describe how this method can be applied to *KLM*.

5.3.2 Numerical Renorm-Group Method for Single Impurity Kondo Problem Solution

Single impurity Kondo problem Hamiltonian is:

$$H_{\mathrm{imp}} = \sum_{\mathbf{k}\sigma} \varepsilon_{\mathbf{k}} \hat{c}^\dagger_{\mathbf{k}\sigma}\hat{c}_{\mathbf{k}\sigma} + J\mathbf{S}\mathbf{s}. \tag{5.3.38}$$

NRG method was initially applied to this model by Wilson and later by other authors [116,148,252,256,257]. It includes logarithmic discretization of energy space and then consecutive taking into account contributions from high-energy

states to effective Hamiltonian. In the result we obtain Hamiltonian corresponding to low-energy physics of the system. That is very important for Kondo model where sharp Kondo resonance appears on the Fermi level.

We assume that Fermi level (chemical potential for final temperatures) lies inside conduction electron band of width $2D$ and its low edge is $-D_-$ and high edge is D_+. We will divide energy region on unequal energy slices $\pm D_\pm \Lambda^{-n}$, $n = 1, 2, \ldots$ and $\Lambda > 1$. Value $n = 0$ corresponds to initial energies $\pm D_\pm$ and with n increase chosen energy mesh become more dense. Let us assume that in the limits of one energy slice between points n and $n+1$ Hamiltonian parameters are constant. With some unitary transformation of discretized Hamiltonian we will come from Hamiltonian (5.3.38) with continuous states to discrete states Hamiltonian so that $\lambda_n \sim \Lambda^{-n/2}$.

$$H_{\text{imp}} = J \sum_{\mu\nu} \mathbf{S} \hat{b}^\dagger_{0\mu} \boldsymbol{\sigma}_{\mu\nu} \hat{b}_{0\nu} + \sum_{n=0,\nu}^{\infty} \varepsilon_n \hat{b}^\dagger_{n\nu} \hat{b}_{n\nu} + \sum_{n=0,\nu}^{\infty} \lambda_\nu (\hat{b}^\dagger_{n\nu} \hat{b}_{n+1,\nu} + \hat{b}^\dagger_{n+1,\nu} \hat{b}_{n,\nu}), \tag{5.3.39}$$

where we have new set of $\hat{b}_{n\sigma}$ such that $\hat{b}_{0\sigma} = \hat{c}_{0\sigma}$.

We distinguish in this Hamiltonian point with $n = 0$ and the rest with states $n = 1, 2, \ldots$ we diagonalize and come to new set of $\mathbf{k}$ states $\hat{a}_{\mathbf{k}\sigma}$ with dispersion $E_{\mathbf{k}\sigma}$. In the result effective Hamiltonian has a form:

$$H_{\text{imp}} = J \sum_{\mu\nu} \mathbf{S} \hat{b}^\dagger_{0\mu} \boldsymbol{\sigma}_{\mu\nu} \hat{b}_{0\nu} + \sum_{\mu} \varepsilon_0 \hat{b}^\dagger_{0\mu} \hat{b}_{0\nu} + \sum_{\mathbf{k}\nu} E_{\mathbf{k}\nu} \hat{a}^\dagger_{\mathbf{k}\nu} \hat{a}_{\mathbf{k}\nu} + \sum_{\mathbf{k}\nu} (V_{\mathbf{k}} \hat{a}^\dagger_{\mathbf{k}\nu} \hat{b}_{0\nu} + V^*_{\mathbf{k}} \hat{b}^\dagger_{0\nu} \hat{a}_{\mathbf{k}\nu}). \tag{5.3.40}$$

Hybridization parameter $V_{\mathbf{k}}$ is formally defined here via relation:

$$\lambda_0 \hat{b}_{1\sigma} = \sum_{\mathbf{k}} V_{\mathbf{k}} \hat{a}_{\mathbf{k}\sigma}. \tag{5.3.41}$$

So in the result of energy discretization we come to effective Hamiltonian (5.3.40) that is generalization of single-impurity Anderson Hamiltonian where "localized" state with energy ε_0 is embedded in continuum of states with energies $E_{\mathbf{k}0}$ and localized state has exchange interaction with localized spin.

Retarded *GF* for "localized" state is:

$$G^\sigma(\omega) = \langle\langle \hat{c}_{0\sigma} | \hat{c}^\dagger_{0\sigma} \rangle\rangle_\omega \equiv \langle\langle \hat{b}_{0\sigma} | \hat{b}^\dagger_{0\sigma} \rangle\rangle_\omega. \tag{5.3.42}$$

Equation of motion for it gives a pair of connected equations:

$$(\omega - \varepsilon_0) G^\sigma(\omega) = 1 + \sum_{\mathbf{k}} V_{\mathbf{k}} \langle\langle \hat{a}_{\mathbf{k}\sigma} | \hat{b}^\dagger_{0\sigma} \rangle\rangle_\omega + \Gamma^\sigma(\omega)$$
$$(\omega - E_{\mathbf{k}\sigma}) \langle\langle \hat{a}_{\mathbf{k}\sigma} | \hat{b}^\dagger_{0\sigma} \rangle\rangle_\omega = V_{\mathbf{k}} G^\sigma(\omega), \tag{5.3.43}$$

where

$$\Gamma^{\sigma}(\omega) = \langle\langle O_{\sigma} | \hat{b}^{\dagger}_{0\sigma} \rangle\rangle_{\omega}, \tag{5.3.44}$$

$$O_{\sigma} = \frac{J}{2}(\hat{b}_{0\bar{\sigma}} S^{-\sigma} + \sigma \hat{b}_{0\sigma} S^{z}). \tag{5.3.45}$$

Solution for system of (5.3.43) can be written as:

$$G^{\sigma}(\omega) = \frac{1}{\omega - \varepsilon_0 - \Delta^{\sigma}(\omega) - \Sigma^{\sigma}(\omega)}, \tag{5.3.46}$$

$$\Delta^{\sigma}(\omega) = \sum_{\mathbf{k}} \frac{|V_{\mathbf{k}}|^2}{\omega - E_{\mathbf{k}}}, \tag{5.3.47}$$

$$\Sigma^{\sigma}(\omega) = \frac{\Gamma^{\sigma}(\omega)}{G^{\sigma}(\omega)}. \tag{5.3.48}$$

5.3.3 Two Energy Scales

In works [254, 255] all expressions for Kondo lattice and spin $S = 1/2$ were derived at fixed value of parameter $J/D = 0.3$ and different values of n_c and T. In Fig. 5.11 density of states is presented for conduction electrons $\rho_s(\omega)$ and spectral function for localized electrons $A_f(\omega)$ for two values of n_c at zero temperature.

One can see that exchange interaction with localized spins leads to two effects: broadening of conduction electrons band (noninteracting band is restricted by $-D < \omega < D$ area) and pseudogap formation due to hybridization effects. Local density of states shows Kondo resonance on Fermi level

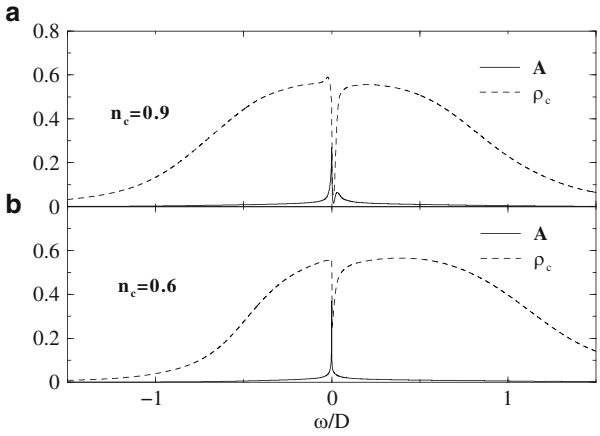

Fig. 5.11. Local spectral function $A_f(\omega)$ for Kondo lattice (*solid line*) and itinerant electrons $\rho_c(\omega)$ (*dashed line*) for two values of band filling n_c: (**a**) $n_c = 0.9$ and (**b**) $n_c = 0.6$; $T = 0$ [254, 255]

(sharp peak) that for $n_c = 1$ is split due hybridization in the same energy scale as a pseudogap. For $n_c = 0.6$ this splitting is not observed because second (right) peak intensity is strongly suppressed with n_c decrease but the splitting can still be seen at all values $0.2 \lesssim n_c \leq 0.96$. So in Fig. 5.11 two energy scales existence can be observed. One for pseudogap width and another low energy one for Kondo resonance width. For small conduction band occupancy only low energy scale is present in $A_f(\omega)$.

For half-filling ($n_c = 1$) pseudogap becomes true gap and Kondo insulator state is realized. We call characteristic high energy scale defined by pseudogap width as T^*. Numerical calculations analysis shows that T^* is of the order of Kondo temperature T_K for single impurity case. With occupancy n_c decrease T^* slowly decreases, however, for $n_c \gtrsim 0.6$ T^* is in the interval $T^*/D \approx 0.02 - 0.025$. So high energy scale is approximately the same for all electron concentrations.

Low energy scale T_0 reveals itself in temperature dependence. Let us consider imaginary part of self-energy $\Sigma(\omega)$ as a function of frequency at various temperatures (Fig. 5.12). $\mathrm{Im}\Sigma(\omega)$ defines quasiparticle decay and becomes zero at Fermi level as temperature approaches T_0 and so T_0 is called Fermi liquid coherence temperature. Deep minimum in $\mathrm{Im}\Sigma(\omega)$ evidence strong quasiparticle damping on the pseudogap edge above the Fermi level and corresponding frequency ω value has an order of high energy scale T^*. As one can see from the figure its values do not change in broad temperature interval values well beyond T_0.

As for the second scale T_0 its value strongly depends on electron concentration n_c. At $n_c \approx 1$ T_0 has an order of T^* values but for n_c decreasing T_0

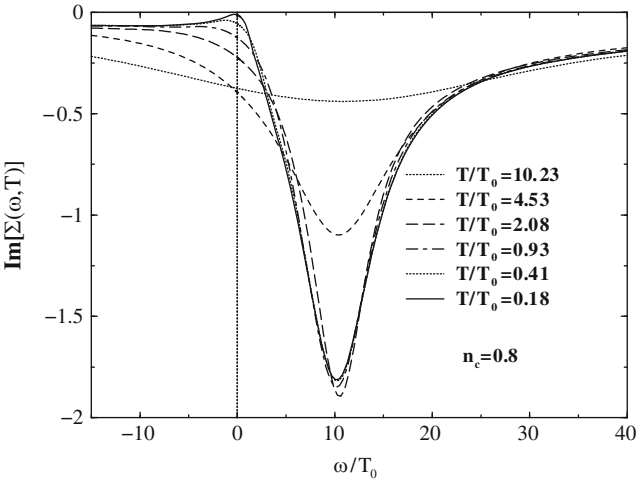

Fig. 5.12. Temperature dependence of imaginary part of self-energy $\Sigma(\omega)$ for $n_c = 0.8$ showing existence for scale T_0 [254, 255]

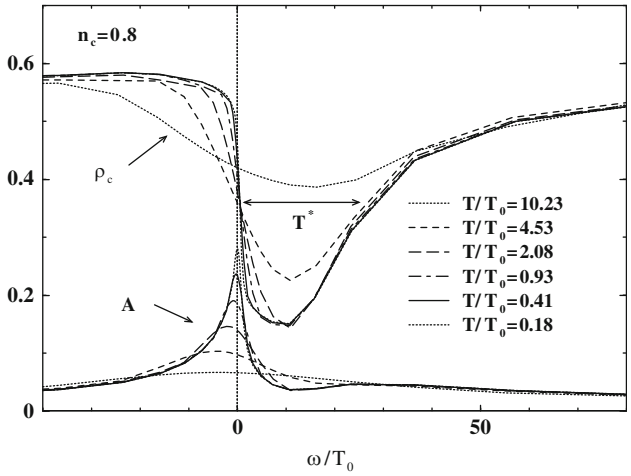

Fig. 5.13. Temperature dependence of $\rho_c(\omega)$ and $A_f(\omega)$ for $n_c = 0.8$ showing existence of high-energy scale T^* together with low-energy scale T_0 [254, 255]

drastically falls. Already for concentration $n_c = 0.8$ $\frac{T^*}{T_0} \simeq 17$ and for $n_c = 0.4$ $\frac{T^*}{T_0} \approx 300$. In the same time at fixed n_c T_0 and T^* vary with J change in the same way.

Two energy scales existence is well pronounced in Fig. 5.13 where temperature dependence of spectral functions $\rho_c(\omega)$ and $A_f(\omega)$ is presented. Behavior of this quantities is direct consequence of $\mathrm{Im}\Sigma(\omega)$ behavior as shown in Fig. 5.12. One can see that as for self-energy quantity T_0 describes temperature dependence of $\rho_c(\omega)$ and $A_f(\omega)$ near Fermi level. In contrast to that energy region corresponding to minimum in $\rho_c(\omega)$ (pseudogap area) starts changing with temperature at $T \gg T_0$. Two energy scales existence T_0 and T^* in Kondo lattice was also demonstrated in work [258] with slave boson technique.

5.3.4 Photoemission Spectra Calculations by *NRG* Method

Low-energy physics of Kondo lattice systems obtained in theoretical studies can be checked in photoelectron spectroscopy (*PES*) and inverse photoelectron spectroscopy (*IPES*) experiments. Spectral intensity can be calculated as:

$$I_-(\omega) = f(\omega)A_f(\omega), \tag{5.3.49}$$

$$I_+(\omega) = [1 - f(\omega)]\, A_f(\omega), \tag{5.3.50}$$

where $f(\omega)$ is Fermi distribution function. So $I_-(\omega)$ (*PES*) gives information about occupied states and $I_+(\omega)$ (*IPES*) about empty states.

In Fig. 5.14 calculated spectra for Kondo lattice are presented at $n_c = 0.8$. As *PES* and *IPES* intensities are proportional to local density of states

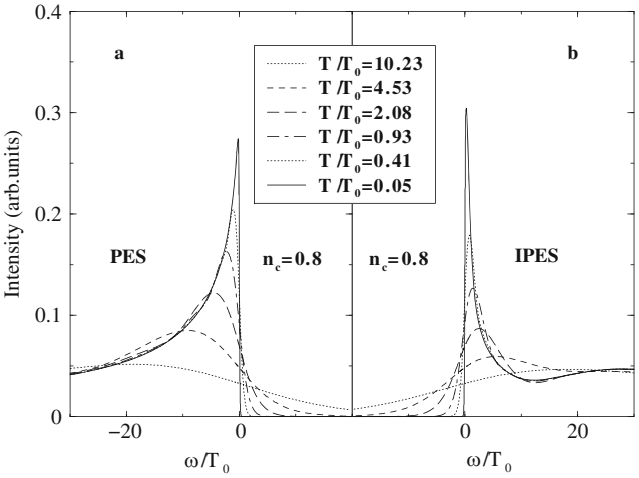

Fig. 5.14. Temperature dependence of *PES* (*left*) and *IPES* (*right*) for Kondo lattice at $n_c = 0.8$ [254, 255]

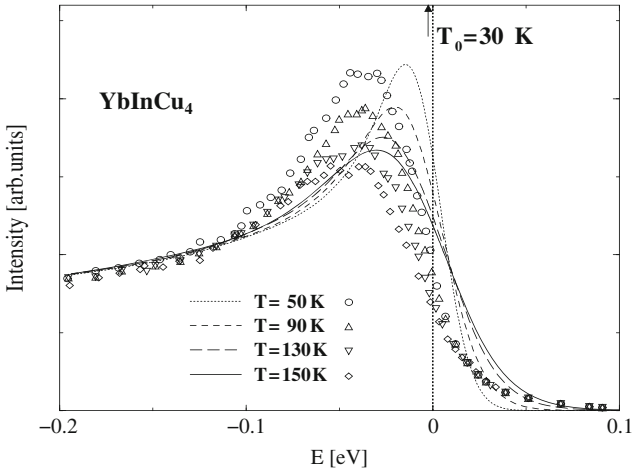

Fig. 5.15. Comparison of temperature dependence of calculated *PES* for Kondo lattice (*lines*) with experimental spectra (*symbols*) for $YbInCu_4$ [259]

this figure follows temperature dependence of $A_f(\omega)$ as shown in Fig. 5.13. Formulas (5.3.49) and (5.3.50) together with calculated values of $A_f(\omega)$ allow comparison with experimental spectroscopy data.

In Figs. 5.15 and 5.16 comparison of experimental and theoretical *PES* spectra for two compounds $YbInCu_4$ [259] and $YbAgCu_4$ [260] is presented. One can see that in both cases experimental curves form and their temperature dependence agree well with calculated spectra. Detail comparison of theory and experiment is done in [254, 255].

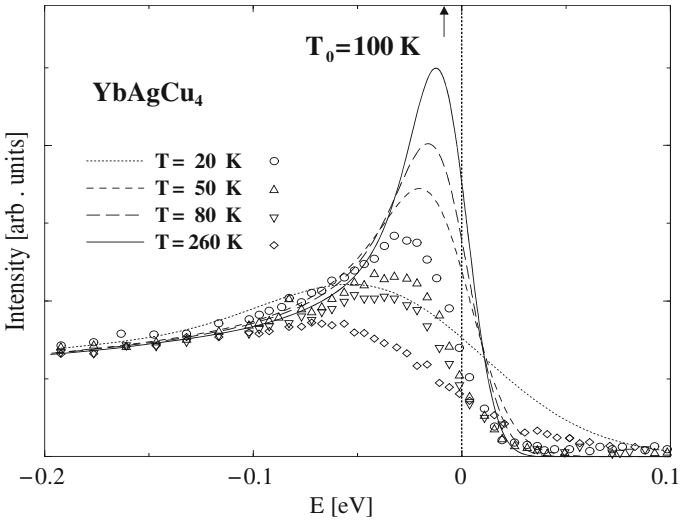

Fig. 5.16. Temperature dependence of *PES* for $YbAgCu_4$ [260] in comparison with calculations for Kondo lattice [254, 255]

5.3.5 Magnetic Ordering in Kondo Lattice Study by Continuous-Time *QMC* Method

Results of [254, 255] were obtained for rather weak exchange antiferromagnetic interaction $J/D = 0.3$. In work [145] detail study of Kondo lattice was performed for exchange interaction of both signs and broad range of values. That allowed to study phase transitions to magnetically ordered sates. Single impurity problem was solved by *CT-QMC* method with hybridization expansion (see Sect. 3.2.5). Exchange interaction of conduction electrons with localized spin has local character and was included in single-impurity problem. Zeroth order *GF* is a matrix whose eigenvalues can be easily found. Expansion in hybridization means that exchange interaction can be arbitrary large. *CT-QMC* method does not suffer from "sign problem" and can be effectively used for low temperatures.

We will present here few results from [145]. In Figs. 5.17 and 5.18 calculated values of electron *GF* as a function of thermodynamic time τ are presented for ferromagnetic (Fig. 5.17) and antiferromagnetic (Fig. 5.18) exchange interactions. Please note logarithmic scale on $G(\tau)$ axis that shows drastic decrease of *GF* with variation of exchange interaction $|J|$. Final (nonzero) values of $G(\tau)$ on whole τ interval evidence metallic ground state of the system.

In the ferromagnetic coupling case metal–insulator phase transition happens between values $J/t = -6$ and -8 while for antiferromagnetic coupling at lower J/t values. From Fig. 5.18 one can see that with T decrease $G(\tau)$ value falls fast and at $T \to 0$ a gap should open that means Kondo insulator state.

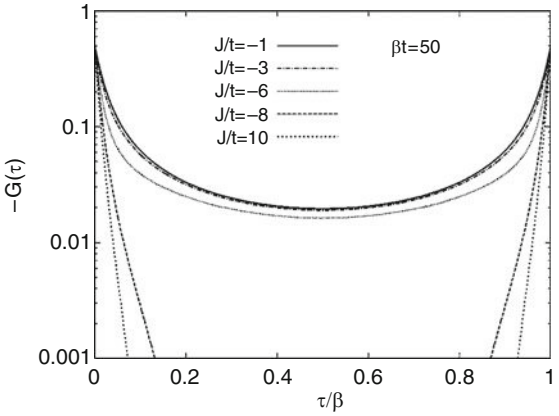

Fig. 5.17. Electron *GF* for Kondo lattice calculated by Continuous-time *QMC* method for ferromagnetic exchange interaction [145]

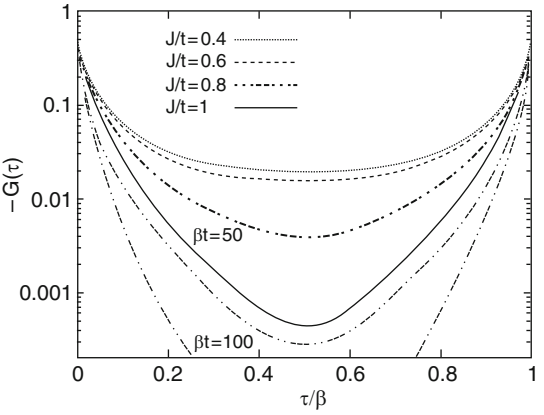

Fig. 5.18. Electron *GF* for Kondo lattice calculated by Continuous-time *QMC* method for antiferromagnetic exchange interaction [145]

In this state in spin and charge fluctuation spectra gaps Δ_S and Δ_C should open increasing with parameter $|J|/t$ increase (Fig. 5.19).

Similar behavior was found by Jarrell in *PAM* in Kondo regime in calculations by Hirsch-Fye *QMC* method [251].

In Fig. 5.20 we show sublattice magnetization on antiferromagnetic state as a function of J/t and T. In Fig. 5.20 one can see that for small $|J|$ values magnetic ordering vanishes for J/t values between 1.0 and 1.2 and quantum transition from antiferromagnetic to paramagnetic state happens. In classical case ($S = \infty$) Neel temperature is significantly lower than for quantum case ($S = 1/2$). In the same time quantity m^2 in quantum case is significantly smaller than in classical case due to suppression of antiferromagnetic order by

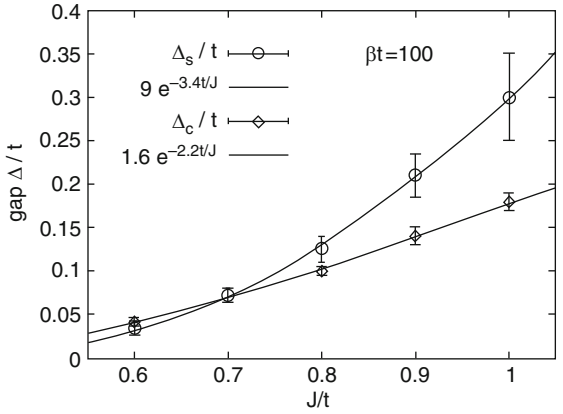

Fig. 5.19. Spin and charge gap as a function of antiferromagnetic exchange parameter J [145]

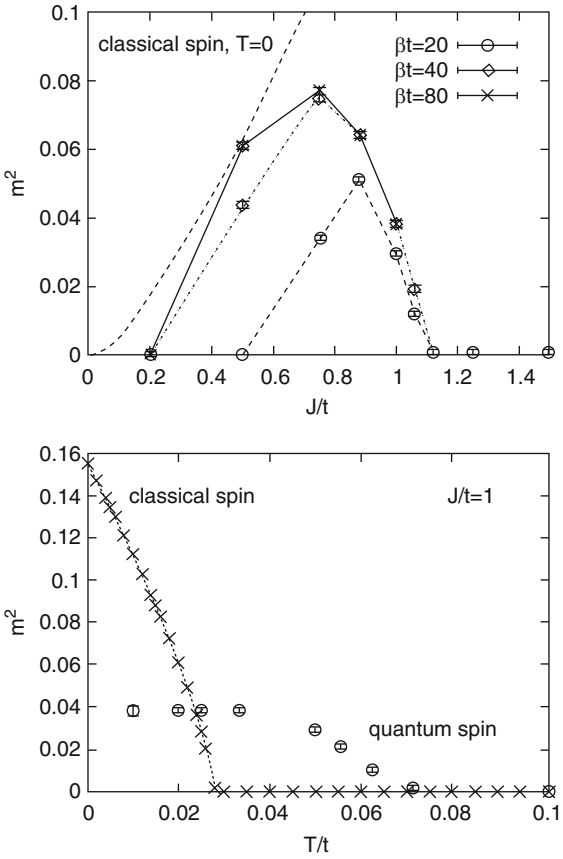

Fig. 5.20. Sublattice magnetization of antiferromagnetic Kondo model: (**a**) as a function of exchange interaction parameter and (**b**) as a function of temperature [145]

quantum fluctuations. From calculations in [145] it follows that for antiferromagnetic coupling antiferromagnetic state is connected with Kondo-insulator state.

5.4 Ferromagnetic Kondo Lattice

5.4.1 *DMFT* Equations for *sd*-Model with Classical Spin

In previous section we studied Kondo lattice model (or sf-exchange model) for antiferromagnetic coupling ($J < 0$). In this case Kondo effect reveal itself when localized spin is screened by conduction electrons. In this section we will consider ferromagnetic coupling ($J > 0$). sf-model for $J > 0$ and relatively small band width $J \gtrsim W$ is called "double exchange" model [36,37,261] and is considered as a working tool for manganites with colossal magnetoresistance effect. We will consider large spin case $S \gg 1$. In the limit $S \to \infty$ atomic spin can be considered as classical one and it is relevant for manganites as it is explained in Sect. 6.5.

sf-model Hamiltonian in the limit $S \to \infty$ can be written as:

$$H = \sum_{ij\sigma} t_{ij} \hat{c}^{\dagger}_{i\sigma} \hat{c}_{j\sigma} - J \sum_{i} \mathbf{m}_i \hat{c}^{\dagger}_{i\sigma} \boldsymbol{\sigma}_{\sigma\sigma'} \hat{c}_{i\sigma'}, \tag{5.4.51}$$

where $\mathbf{m}_i$ unit vector in localized spin direction on site i. We assume that $J_{sd}\mathbf{S}_i = (J_{sd}S)\mathbf{m}_i \equiv J\mathbf{m}_i$ and $J_{sd}S \equiv J$ is a final quantity in the limit $S \to \infty$.

According to the general *DMFT* idea lattice problem is reduced to effective single impurity problem. *DMFT* equations for Hamiltonian (5.4.51) were derived by Furukawa [262]. Later we follow works in [263, 264]. We define action for single impurity problem as:

$$\begin{aligned} S\left[\Psi^{\dagger}, \Psi; \mathbf{m}\right] = &- \int_0^{\beta} \int_0^{\beta} \mathrm{d}\tau_1 \mathrm{d}\tau_2 \Psi^{\dagger}(\tau_1) \mathcal{G}_0^{-1}(\tau_1 - \tau_2) \Psi(\tau_2) \\ &- J \int_0^{\beta} \mathrm{d}\tau \mathbf{m} \Psi^{\dagger}(\tau) \boldsymbol{\sigma} \Psi(\tau). \end{aligned} \tag{5.4.52}$$

Here $\Psi = (c^{\dagger}_{\uparrow}, c_{\downarrow})$ is two-component spinor composed of Grassmann variables. Electronic *GF* is a functional integral over fermionic variables and directions of vector $\mathbf{m}$:

$$G(\tau, \tau') = -\int D\left[\Psi^{\dagger}\right] D\left[\Psi\right] \mathrm{d}\mathbf{m} \mathrm{e}^{-S\left[\Psi^{\dagger}, \Psi; \mathbf{m}\right]} \Psi(\tau) \Psi^{\dagger}(\tau'). \tag{5.4.53}$$

This expression is a matrix 2×2 size in spin indexes. As action has quadratic form in Grassmann variables the functional integral can be calculated and we obtain expression for Fourier component of *GF* in variables $\tau - \tau'$:

$$G(i\omega_n) = \frac{1}{Z}\int \mathrm{d}\mathbf{m} P(\mathbf{m}) \left[\mathcal{G}_0^{-1}(i\omega_n) + J\mathbf{m}\boldsymbol{\sigma}\right]^{-1}, \tag{5.4.54}$$

where

$$P(\boldsymbol{m}) = \frac{1}{Z}\mathrm{e}^{-S_{\mathrm{eff}}(\boldsymbol{m})} \tag{5.4.55}$$

defines statistical probability for realization of localized spin direction $\mathbf{m}$ in the system.

Effective action $\tilde{S}_{\mathrm{eff}}(\mathbf{m})$ is defined by the following relation for partition function of the system:

$$Z = \int \mathrm{d}\mathbf{m} \int D\left[\Psi^\dagger\right] D\left[\Psi\right] \mathrm{e}^{-S\left[\Psi^\dagger,\Psi;\mathbf{m}\right]} \equiv \int \mathrm{d}\mathbf{m} \mathrm{e}^{-S_{\mathrm{eff}}(\mathbf{m})}, \tag{5.4.56}$$

and hence

$$S_{\mathrm{eff}}(\mathbf{m}) = -\ln \int D\left[\Psi^\dagger\right] D\left[\Psi\right] \mathrm{e}^{-S\left[\Psi^\dagger,\Psi;\mathbf{m}\right]}. \tag{5.4.57}$$

After functional integral is calculated we have from expression (5.4.57):

$$S_{\mathrm{eff}}(\mathbf{m}) = -\sum_n \ln \det \left[\frac{1}{i\omega_n}\left(\mathcal{G}_0^{-1}(i\omega_n) + J\mathbf{m}\boldsymbol{\sigma}\right)\right]. \tag{5.4.58}$$

According to $S_{\mathrm{eff}}(\mathbf{m})$ definition we have the following relations:

$$\int \mathrm{d}\mathbf{m} P(\mathbf{m}) = 1, \tag{5.4.59}$$

$$\langle \mathbf{m} \rangle = \int \mathrm{d}\mathbf{m} P(\mathbf{m}) \mathbf{m}; \tag{5.4.60}$$

The last relation defines magnetic moment in the system.

Now we can write *DMFT* equations for the model:

$$G(i\omega_n) = \sum_{\mathbf{k}} \frac{1}{i\omega_n + \mu - \varepsilon_{\mathbf{k}} - \Sigma(i\omega_n)}, \tag{5.4.61}$$

$$\mathcal{G}_0^{-1}(i\omega_n) = \Sigma(i\omega_n) - G^{-1}(i\omega_n). \tag{5.4.62}$$

All quantities in (5.4.61) and (5.4.62) namely $\mathcal{G}_0$, G, and Σ are 2×2 matrices. From these equations the following *DMFT* calculation scheme can be constructed:

1. For initial $\mathcal{G}_0^{-1}(i\omega_n)$ value $S_{\mathrm{eff}}(\mathbf{m})$ is calculated by formula (5.4.58) and single site *GF* by the formula (5.4.54).
2. Calculated $G(i\omega_n)$ value is substituted in left part of equation (5.4.61) and from it self-energy $\Sigma(i\omega_n)$ is calculated.
3. From Dyson equation (5.4.62) new value for $\mathcal{G}_0^{-1}(i\omega_n)$ is calculated and iteration process continues till self-consistency is achieved.

5.4.2 Analysis of *DMFT* Equations Solution

We will consider at the beginning few specific cases where analytical solution of *DMFT* equations can be found [263, 264]. For paramagnetic phase due to rotation invariance we have $G_0(i\omega_n) = g_0(i\omega_n)I$ where g_0 is a scalar and I unit matrix. Taking into account relations $\langle \mathbf{m} \rangle = 0$, $\langle \mathbf{m}^2 \rangle = 1$ we obtain from (5.4.54) expression for one-electron *GF* and self-energy:

$$G(i\omega_n) = \frac{1}{2}\left(\frac{1}{g_0^{-1}(i\omega_n) + J} + \frac{1}{g_0^{-1}(i\omega_n) - J},\right) I, \tag{5.4.63}$$

$$\Sigma(i\omega_n) = J^2 g_0(i\omega_n) I. \tag{5.4.64}$$

Spectral density

$$A(\omega) = -\frac{1}{\pi}\mathrm{Im}G(i\omega_n \to \omega + i\delta) \tag{5.4.65}$$

in this case has two peaks centered at $\omega = \pm J$ and having width $Ig_0^{-1}(\omega) \sim t$. Peaks intensity is the same for both spin projections.

For ferromagnetic state with spontaneous magnetization $M = \langle m_z \rangle$ spectral function intensity is redistributed between electrons with different spin projections. In order to obtain analytical estimation for electronic *GF* we consider a limit of large $J \gg W$ and take noninteracting *GF* as

$$g_0(\omega) = \frac{1}{\omega + \mu \mp J + iW}, \tag{5.4.66}$$

where W is a band width. Then from formula (5.4.54) we have for $G(\omega)$ with the accuracy of the order of W/J [263, 264]:

$$G_\sigma(\mathbf{k}, \omega) = \frac{P_\sigma^+}{\omega + J + \mu - P_\sigma^+ \varepsilon_{\mathbf{k}} + iP_\sigma^- W} + \frac{P_\sigma^-}{\omega - J + \mu - P_\sigma^- \varepsilon_{\mathbf{k}} + iP_\sigma^+ W}. \tag{5.4.67}$$

Here $P_\sigma^\pm$ is statistical weight of electronic states with different spin projections:

$$P_\sigma^\pm = \frac{1 \pm M\sigma}{2}. \tag{5.4.68}$$

So there are two one-electron bands centered at $\omega + \mu = \pm J$ with width W. For different spin projections intensities of lower and upper bands are interchanged. In ground state $M = 1$ electrons with spin $\sigma = \uparrow$ occupy lower band and electrons with spin $\sigma = \downarrow$ occupy upper band. Electronic system with such properties are usually called ferromagnetic half-metal. With temperature increase admixture of opposite spin appears in every band. In paramagnetic phase different spin intensities become equal that corresponds to expression (5.4.63) for single site (local) density of states. So model (5.4.51) describes in

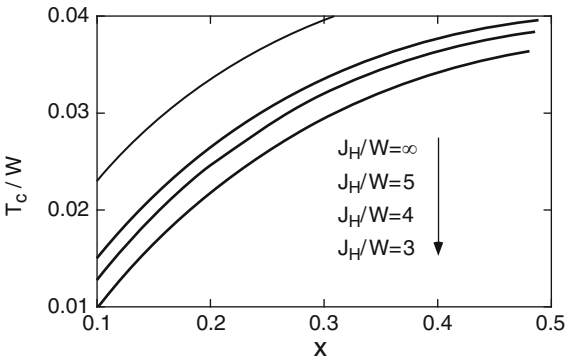

Fig. 5.21. Curie temperature T_c as a function of J/W and doping x for model (5.4.51) calculated by *DMFT* method [263, 264]

the limit $J \gg W$ half-metallic ground state where Fermi surface exists only for electrons with spin $\sigma = \uparrow$ and ferromagnetism is saturated.

We will consider later some results of numerical calculations based on (5.4.54), (5.4.61), and (5.4.62) [263, 264].

In Fig. 5.21 one can see that T_c increases with band width W increase that is a measure of kinetic energy. The relation $T_c \sim W$ reflects the mechanism of ferromagnetism in model (5.4.51) that is called kinetic exchange. This mechanism was proposed many years ago by Zener [261] to explain physical properties of manganites. In Fig. 5.21 it is shown that T_c increases with doping and at $J \gg W$ dependence of T_c on x is close to relation

$$T_c \sim Wx(1-x), \tag{5.4.69}$$

that reflects particle–hole symmetry of the model.

Please note that in Fig. 5.21 ferromagnetic state appears for some doping values depending on ratio J/W. At $x = 0$ in the system antiferromagnetic state is realized. *DMFT* equation solutions on Bethe lattice results in Neel temperature T_N dependence on J/W as shown in Fig. 5.22.

At $J \gg W$ T_N corresponds to Heisenberg model results with kinetic exchange $\sim \frac{t^2}{J} \sim \frac{W^2}{J}$. In other limit $J \ll W$ T_N corresponds to mean-field theory result for spin density wave state where $T_N \sim J$. Figure 5.22 combines both these limits so that at intermediate values of J/W curve for T_N comes through maximum, that reproduces result found in studies of other models for strongly correlated systems. In the interval $0 \ll x \ll 1$ at final values of J/W homogeneous ferromagnetic state is unstable and phase separation area exists where in antiferromagnetic matrix small islands of ferromagnetic phase appears or at high-temperature paramagnetic phase. In Fig. 5.23 we show phase diagram calculated for fixed value $\frac{J}{W} = 4$.

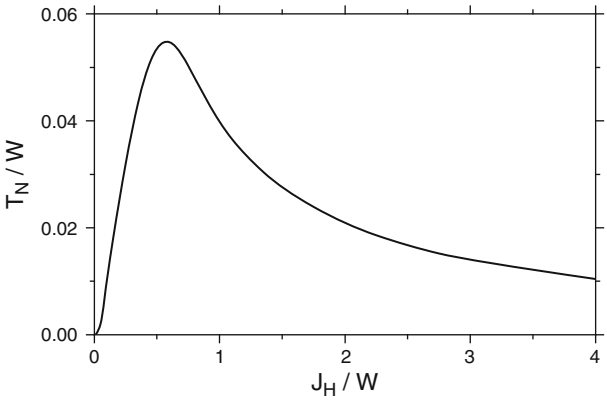

Fig. 5.22. Neel temperature at $x = 0$ calculated by *DMFT* method [263]

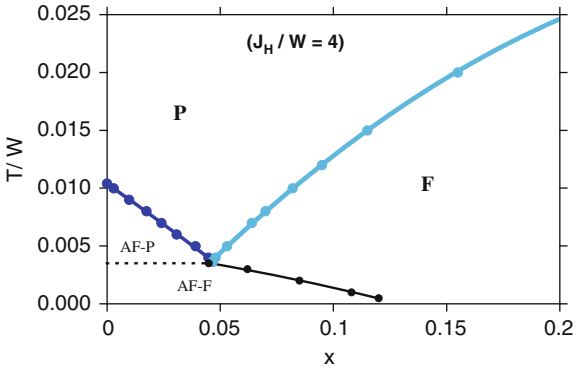

Fig. 5.23. Phase diagram of model (5.4.51) for $\frac{J}{W} = 4$ [263]. $AF - P$ and $AF - F$ mark inhomogeneous phases when in antiferromagnetic matrix small areas of paramagnetic phases appear

Furukawa calculated some other physical properties of the model (5.4.51) among them resistivity and magnetization temperature dependence, quasiparticle spectra for various T and x, spin wave spectra in ferromagnetic phase (see review in [263]). Calculation results agree rather well with experimental data for manganites where sf-model with ferromagnetic exchange coupling (it is also called double exchange model [36, 37, 261]) is considered as a relevant model. However, this agreement is more qualitative than quantitative one. For example dependence of T_c on x as shown in Fig. 5.21 resembles observed in manganites but the value of T_c is strongly overestimated.

Millis et al [265–268] proposed to extend model (5.4.51) with terms responsible for electron–lattice interaction that includes Jahn-Teller effect in crystal structure for real manganites. Results of calculation with this extended

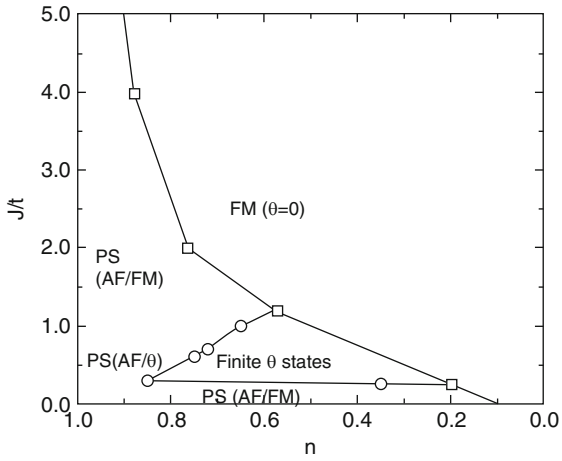

Fig. 5.24. Kondo lattice phase diagram with ferromagnetic exchange on the plane "exchange integral – electron concentration" [266]. θ is an angle between magnetic sublattice

model will be described in Sect. 6.5. As it was shown in [265–267] electron–lattice interaction allows to describe physical properties of manganites on quantitative level.

Phase diagram of the Kondo lattice with ferromagnetic exchange coupling was obtained in [266] using free energy calculations (see Fig. 5.24). This diagram agrees with the diagram shown in Fig. 5.23 where on y-coordinate not J but T was measured. For large J and not very small doping $x = 1-n$ ferromagnetic phase is present while for small $x \ll 1$ there is commensurate antiferromagnetic phase. Between them inhomogeneous phase (phase separation PS) is observed with incommensurate magnetic state. Phase transition between ferromagnetic and incommensurate phases is of the second order and between commensurate antiferromagnetic and incommensurate phase transition is of the first order.

6

Electronic Structure Calculations for Real Materials by *LDA + DMFT* Method

6.1 Combining Density Functional Theory and Dynamical Mean-Field Theory: *LDA + DMFT* method

6.1.1 Coulomb Interaction

In Chaps. 3–5 we have presented in details Dynamical Mean-Field Theory (*DMFT*) for Hubbard and Anderson models. The system under consideration was usually approximated by Bethe lattice or hypercubic lattice and often space dimension d was explicitly assumed to be infinite ($d \to \infty$ limit). Such models investigations were found to be very useful to study *DMFT* method abilities and gave fundamental new results in strongly correlated systems theory. The example is metal–insulator transition with gradual spectral weight transfer between Hubbard bands and quasiparticle band.

However, to study strongly correlated compounds of d- and f-elements it is necessary to go from model lattices (Bethe and hypercubic) to real crystal structures in finite space dimension ($d = 3$) and to take into account explicit atomic orbitals shape. The corresponding Hamiltonian construction and its parameters determining in Wannier functions basis were described in details in Sect. 2.2. In its full form Hamiltonian defined by formulas (2.2.24) and (2.2.47) is rather complicated and in real calculations various approximations are used.

When *DMFT* method is applied to the problem defined by such a Hamiltonian the calculation scheme can be considered as ab-initio method because all problem parameters were obtained from Density Functional Theory (*DFT*) calculations for full set of electronic states in realistic crystal structure without any adjustable or empirical quantities. Resulting method was given a name *LDA + DMFT* [122]

We consider at first Coulomb interaction part of the Hamiltonian (see Sect. 2.2.2). Full four-operators form of such a term (2.2.24) presents

very complicated for solution problem. It can be solved only with some approximations such as static mean-field method ($LDA + U$ method, see Sect. 2.3). In this approximation decoupling (2.3.63) of four-operators term in Hamiltonian (2.2.24) results in quadratic forms for creation–annihilation operators $\hat{c}^{+}_{ilm\sigma}, \hat{c}_{ilm\sigma}$ (see (2.3.65)). That leads to one-electron potential matrix $V^{\sigma}_{mm'}$ (2.3.66) depending on density matrix $n^{\sigma}_{mm'} \equiv \left\langle \hat{c}^{+}_{ilm\sigma}\hat{c}_{ilm'\sigma} \right\rangle$ in basis of orbitals $|ilm\sigma\rangle$.

In more complicated dynamical mean-filed approximation (Chap. 3) Coulomb interaction Hamiltonian in full four-operator form (2.2.24) practically was not used. From all developed in present time methods to solve effective impurity model appearing in $DMFT$ (see Sect. 3.1.5) only Continuous Time Quantum Monte Carlo ($CT - QMC$) method with expansion in Coulomb interaction [142] gives possibility to work with full four-operator form (2.2.24).

Popular standard Quantum Monte Carlo (QMC) method with Hirsch-Fye algorithm (see Sect. 3.2.1)) uses Hubbard-Stratonovich transformation (3.2.58) for Coulomb interaction Hamiltonian term as a product of particle number operators $\hat{n}_{m\sigma}\hat{n}_{m'\sigma'}$ (2.2.29). Due to that fact in nearly all $DMFT$ applications Coulomb interaction is assumed to be in the form of (2.2.29) or (2.2.30). Sometimes a term corresponding to pair spin flip (2.2.27) is added.

6.1.2 Computation of Lattice and Local Green Functions in General Case

Realistic systems are described by Hamiltonian in Wannier functions basis (2.2.47) obtained in calculation Hubbard–Stratonovich Sect. 2.2 and based on solution for Density Functional Theory equations (Sect. 2.1). In general case in the Hamiltonian not only localized d- and f-orbitals are included where interelectron Coulomb interaction is taken into account described by (2.2.30) but also the orbitals are present corresponding to itinerant states. Hybridization in the Hamiltonian (2.2.47) is defined not only between d and f orbital as in Hubbard model or between localized and itinerant states as in Anderson model but also among all states present in the Hamiltonian. In addition to that localized d and f state are degenerate and cannot be described by simple dispersion law $\varepsilon_{\mathbf{k}}$ and equation (3.1.38) for lattice GF used in Sect. 3.1.3 for basic $DMFT$ equation is not valid any more.

In most general case matrix of electronic lattice GF in the basis of orbitals $|ilm\rangle$ is defined by the following equation:

$$G_{ilm,i'l'm'}(i\omega_n) = \frac{1}{V_B}\int \mathrm{d}\mathbf{k}\left[(i\omega_n + \mu)\hat{I} - \hat{H}_0(\mathbf{k}) - \hat{\Sigma}(i\omega_n)\right]^{-1}_{ilm,i'l'm'}, \tag{6.1.1}$$

where $\hat{H}_0(\mathbf{k})$ is noninteracting Hamiltonian of the problem obtained from DFT Hamiltonian (2.2.47) by subtracting "double counting" correction $\hat{H}_{DC}$ (2.2.35). Wave vectors integration is performed over Brillouin zone volume

V_B and $\hat{I}$ is a unit matrix. As usual we consider paramagnetic case and spin indexes are omitted.

In this equation self-energy $\hat{\Sigma}(i\omega_n)$ is a matrix of the size equal to the size of the Hamiltonian $\hat{H}_0(\mathbf{k})$ matrix. However, its nonzero parts form matrix of smaller size N equal to a number of $d(f)$ orbitals in Coulomb interaction Hamiltonian (2.2.30). Correspondingly all *DMFT* equations defined in Sect. 3.1.3 also become matrix equation with dimensions $N \times N$.

We define GF of effective single impurity Anderson model $\hat{G}_{\text{imp}}$ as a matrix $G_{mm'}$ with dimensions $N \times N$ obtained from full matrix of lattice GF (6.1.1) preserving only terms where indexes $i = i' = i_d,\ l = l' = l_d$ ($i_d l_d$ corresponds to $d(f)$ atomic shells). Matrix "bath" GF $\hat{\mathcal{G}}_0(i\omega_n)$ is defined in the same way as in Chap. 3 where *DMFT* application to simple Hubbard model was considered:

$$\hat{\mathcal{G}}_0^{-1}(i\omega_n) = \hat{G}_{\text{imp}}^{-1}(i\omega_n) + \hat{\Sigma}(i\omega_n). \tag{6.1.2}$$

According to general *DMFT* calculation scheme we solve Anderson model with "bath" $\hat{\mathcal{G}}_0(i\omega_n)$ and calculate new impurity GF $\hat{G}_{\text{imp}}(i\omega_n)$. New approximation for self-energy $\hat{\Sigma}(i\omega_n)$ is calculated using equation (6.1.2):

$$\hat{\Sigma}(i\omega_n) = \hat{\mathcal{G}}_0^{-1}(i\omega_n) - \hat{G}_{\text{imp}}^{-1}(i\omega_n). \tag{6.1.3}$$

This new self-energy $\hat{\Sigma}(i\omega_n)$ is substituted in equation (6.1.1) to calculate new lattice GF and hence new approximation for "bath" GF $\hat{\mathcal{G}}_0(i\omega_n)$ from (6.1.2). This iteration loop continues till quantities $\hat{\Sigma}(i\omega_n)$ will stabilizes.

That defines matrix form of basic *DMFT* equations and formally their realization is straightforward. However additional problems appear. Using Coulomb interaction Hamiltonian as a product of particle number operators $\hat{n}_{m\sigma}\hat{n}_{m'\sigma'}$ (2.2.29) assumes that electrons occupy states corresponding to pure orbitals $|i_d l_d m\sigma\rangle$ and no mixing between those orbitals is allowed. However, if because of the problem symmetry off-diagonal in orbital index m matrix elements of matrices $\hat{G}_{\text{imp}}(i\omega_n)$ and $\hat{\Sigma}(i\omega_n)$ exist it correspond to possibility of mixing of orbitals with different m.

This contradiction can be lifted only if all three matrices $\hat{G}_{\text{imp}}(i\omega_n)$, $\hat{\mathcal{G}}_0(i\omega_n)$, and $\hat{\Sigma}(i\omega_n)$ are diagonal in index m. This approximation is used in practically all application of $LDA + DMFT$ method. For high-symmetry crystal structures this approximation is exact if a basis of orbitals $|i_d l_d m\sigma\rangle$ is chosen as basis of irreducible representations of point group symmetry operations corresponding to lattice site i_d.

There is a special case where relations (6.1.1–6.1.3) can be essentially simplified. If only d-orbitals are included in the Hamiltonian and those orbitals are degenerate by symmetry then matrix $\hat{\Sigma}(i\omega_n)$ is diagonal and equal in size to Hamiltonian matrix with diagonal matrix elements not depending on orbital index m ($\Sigma_{mm} \equiv \Sigma$). Then equation (6.1.1) can be written as:

$$G_{mm}(i\omega_n) = \frac{1}{V_B}\int \mathrm{d}\mathbf{k}\left[(i\omega_n + \mu - \Sigma(i\omega_n))\hat{I} - \hat{H}_0(\mathbf{k})\right]^{-1}_{mm}, \tag{6.1.4}$$

In integral (6.1.4) quantity $\Sigma(i\omega_n)$ enters as an addition to complex energy $i\omega_n + \mu$ so one can write:

$$G_{mm}(i\omega_n) = G^0_{mm}(i\omega_n - \Sigma(i\omega_n)), \tag{6.1.5}$$

where noninteraction GF is defined:

$$G^0_{mm}(i\omega_n) = \frac{1}{V_B}\int \mathrm{d}\mathbf{k}\left[(i\omega_n + \mu)\hat{I} - \hat{H}_0(\mathbf{k})\right]^{-1}_{mm}, \tag{6.1.6}$$

that can be expressed via density of states $\rho_0(\varepsilon) = -\frac{1}{\pi}\mathrm{Im}G^0_{mm}(\varepsilon)$ of noninteracting Hamiltonian with Hilbert transformation:

$$G^0(\zeta) = \int \mathrm{d}\varepsilon \frac{\rho_0(\varepsilon)}{\zeta - \varepsilon}. \tag{6.1.7}$$

Finally, interacting GF (6.1.4) can be expressed via integral of density of states:

$$G_{mm}(i\omega_n) = G^0_{mm}(i\omega_n - \Sigma(i\omega_n)) = \int \mathrm{d}\varepsilon \frac{\rho_0(\varepsilon)}{i\omega_n - \Sigma(i\omega_n) - \varepsilon}. \tag{6.1.8}$$

Equation (6.1.8) is widely used in $DMFT$ application but one should remember that it is fully justified only in a special case defined earlier. In all other cases when d-orbitals are not degenerate or other orbitals are included in the Hamiltonian one should use general expression (6.1.1).

6.1.3 Total Energy Calculation in *LDA + DMFT*

In $LDA + DMFT$ applications important part is calculation of total energy of the system as a function of external parameters (volume, crystal structure parameters, temperature, etc.). As $LDA + DMFT$ is a combination of LDA (see Sect. 2.1) and Dynamical Mean-Field Theory ($DMFT$) (see Chap. 3) then for total energy the following expression is used [269]:

$$E_{\mathrm{tot}} = E_{\mathrm{LDA}} + E_{\mathrm{DMFT}} - E_{\mathrm{MF}}, \tag{6.1.9}$$

where E_{LDA} is total energy obtained in LDA calculation, E_{DMFT} is an energy calculated in $DMFT$ and E_{MF} is an energy corresponding to static mean-field approximation (restricted Hartree-Fock) for the same Hamiltonian as used in $DMFT$ calculations. The last term is needed to avoid double counting for Coulomb interaction terms present in E_{LDA}. Then $E_{\mathrm{DMFT}} - E_{\mathrm{MF}}$ is pure correlation correction to E_{LDA}.

In its turn E_{DMFT} is a sum of two contributions: from noninteracting Hamiltonian $\hat{H}_0(\mathbf{k})$ and from Coulomb interaction Hamiltonian (2.2.29):

$$E_{\mathrm{DMFT}} = \frac{1}{\beta}\frac{1}{V_B}\int \mathrm{d}\mathbf{k}\sum_{\mathrm{n}} \mathrm{Tr}\hat{H}_0(\mathbf{k})\hat{G}_{\mathbf{k}}(i\omega_n)\mathrm{e}^{\mathrm{i}\omega_n 0^+}$$
$$+ \frac{1}{2}\sum_{i=i_d, l=l_d}\sum_{m,m',\sigma}\{U_{mm'}\langle\hat{n}_{ilm\sigma}\hat{n}_{ilm'\bar{\sigma}}\rangle + (U_{mm'} - J_{mm'})\langle\hat{n}_{ilm\sigma}\hat{n}_{ilm'\sigma}\rangle\}, \tag{6.1.10}$$

where $\hat{G}_{\mathbf{k}}(i\omega_n)$ is electronic GF corresponding to wave vector $\mathbf{k}$:

$$\hat{G}_{\mathbf{k}}(i\omega_n) = \left[(i\omega_n + \mu)\hat{I} - \hat{H}_0(\mathbf{k}) - \hat{\Sigma}(i\omega_n)\right]^{-1}, \tag{6.1.11}$$

The average values for particle number operators products $\langle \hat{n}_{ilm\sigma}\hat{n}_{ilm'\sigma}\rangle$ and $\langle \hat{n}_{ilm\sigma}\hat{n}_{ilm'\bar{\sigma}}\rangle$ can be calculated directly in QMC method (see Sect. 3.2).

Energy corresponding to static mean-filed approximation E_{MF} is calculated analogously to (6.1.10) with replacing interacting GF $\hat{G}_{\mathbf{k}}(i\omega_n)$ on $\hat{G}^{\mathrm{LDA}}_{\mathbf{k}}(i\omega_n)$ calculated with LDA Hamiltonian:

$$\hat{G}^{\mathrm{LDA}}_{\mathbf{k}}(i\omega_n) = \left[(i\omega_n + \mu)\hat{I} - \hat{H}^{\mathrm{LDA}}(\mathbf{k})\right]^{-1}, \tag{6.1.12}$$

and also with replacing second term in (6.1.10) on Coulomb interaction energy in the following form:

$$E_{\mathrm{Coulomb}} = \sum_{i=i_d, l=l_d} \frac{1}{2}\bar{U} n_d(n_d - 1), \tag{6.1.13}$$

where $n_d = \sum_{m\sigma}\langle \hat{n}_{i_d l_d m\sigma}\rangle$ is a total correlated electrons number on the site i_d and $\bar{U}$ is an average value of Coulomb interaction among different orbitals.

6.2 Early Transition Metal Oxides: Mott Insulators and Strongly Correlated Metals

$LDA + DMFT$ method described in Sect. 6.1 was last years widely used to study electron correlation effects in d and f elements compounds. In this chapter we will describe some typical results of this method application for various types of correlated systems.

At first we will consider a simplest example: $SrVO_3$ compound where there is only one electron in degenerate d-band. $LDA + DMFT$ method gave for this compound strongly correlated metal state with typical three peak structure of spectrum. Next example is classical Mott insulator V_2O_3 where in paramagnetic phase both metallic and insulating states could be realized. This system is more complicated than the first one because cubic degeneracy for d states is lifted by trigonal distortion and there are two electrons in d-band. In compound LiV_2O_4 formally there are 1.5 electrons per V atom and experimentally at low-temperatures strong enhancement for magnetic susceptibility and electron specific heat is observed that is typical for "heavy fermion" system with f-electrons but that was never previously found for d-systems.

All those compounds belong to Mott systems where strong correlation effects happens in partially filled d-band that is well separated in energy from occupied oxygen p band so that p-states could be projected out from the model and only d-states included in the Hamiltonian. There is another class of

strongly correlated materials called "charge transfer insulators" where energy separation between d and p states Δ is smaller than Coulomb interaction parameter U and oxygen p states should be explicitly included in the problem Hamiltonian. The lowest energy excitation in such materials happens between oxygen p and transition metal d states in contrast to $d-d$ transition in Mott insulators and hence the name "charge transfer insulators". We will consider typical "charge transfer insulators" NiO and also MnO where metal–insulator transition with pressure is observed.

Next we consider $LDA + DMFT$ results for f-system: metallic cerium where two different volume phases exist with drastically different degree of localization for $4f$ electrons. The effect of electron–lattice interaction taken into account in $LDA + DMFT$ will be demonstrated on the example of manganites $La_{1-x}Sr_xMnO_3$. In the end a problem of correlation effects influence on electronic structure of new superconductors based on pnictides materials will be considered.

6.2.1 $SrVO_3$: One Electron in Degenerate d-Band, Strongly Correlated Metal

$SrVO_3$ compound has cubic perovskite crystal structure where vanadium ions have as nearest neighbors six oxygen ions forming octahedron (Fig. 6.1). Point group symmetry for vanadium ion is cubic O_h and d states should transform according to irreducible representations of this group: triply degenerate t_{2g} and doubly degenerate e_g. In Fig. 6.2 results of LDA calculations for electronic structure of $SrVO_3$ are shown [270]. Fermi level is a zero and crosses partially

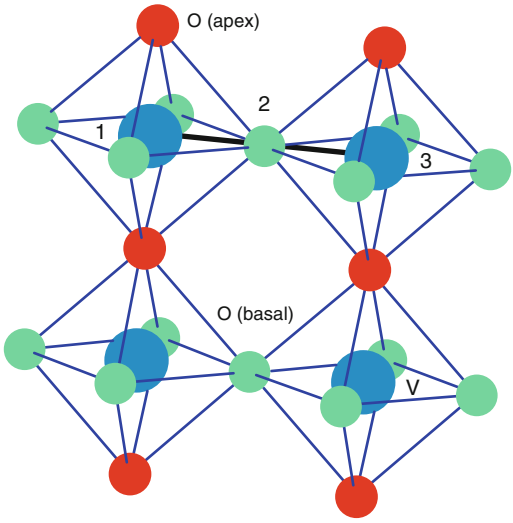

Fig. 6.1. Perovskite crystal structure for compound $SrVO_3$

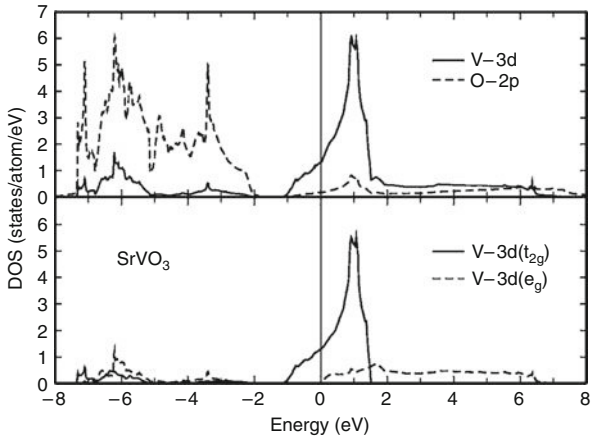

Fig. 6.2. Density of states from *LDA* calculation for $SrVO_3$ [270]

filled relatively narrow d-band of t_{2g} symmetry. Below it (from $-2\,\mathrm{eV}$ till $-7\,\mathrm{eV}$) there is occupied oxygen $2p$ band. Above from 0 to 6 eV one can see broad band formed by V3d states of e_g symmetry.

Well pronounced separation of those bands from each other allows to simplify the problem and consider only partially filled t_{2g} band. In Wannier function basis Hamiltonian construction procedure described in Sect. 2.2.4 this corresponds to the choice for projection in formula (2.2.39) only V3d t_{2g} atomic orbitals and Bloch functions corresponding to t_{2g} band.

In the result one has triply degenerate band with one electron (vanadium ion valence in this compound is equal to 4 that corresponds to configuration d^1). Please note that in this case it is possible to use Hilbert transformation for density of states to calculate electronic GF (formula (6.1.8)). Calculation of Coulomb interaction parameters by constrain DFT method (see Sect. 2.2.5) gave values $\bar{U} = 3.55\,\mathrm{eV}$ and $J = 1\,\mathrm{eV}$ [270]. Coulomb interaction Hamiltonian in a form (2.2.30) using Kanamori parameterization gave the following parameters: for electrons on the same orbital $U = 5.55\,\mathrm{eV}$ and on different orbitals $U' = U - 2J = 3.55\,\mathrm{eV}$ assuming that constrain DFT calculations result $\bar{U} = 3.55\,\mathrm{eV}$ corresponds to the average over all pairs of t_{2g} orbitals value.

$DMFT$ calculations for this Hamiltonian with effective impurity problem solved by Quantum Monte Carlo method in Hirsch-Fye algorithm (see Sect. 3.2) result in spectral functions presented in Fig. 6.3. Spectra have typical for $DMFT$ three peak structure described in details in Sect. 3.3: quasiparticle peak at Fermi level and two Hubbard bands corresponding to incoherent states: lower occupied band at $\approx -2\,\mathrm{eV}$ and upper empty band at $\approx 3\,\mathrm{eV}$. Essential difference with half-filled nondegenerate Hubbard model described in Sect. 3.3 is strong particle–hole asymmetry of spectral function in Fig. 6.3: lower Hubbard band has significantly lower intensity than upper Hubbard

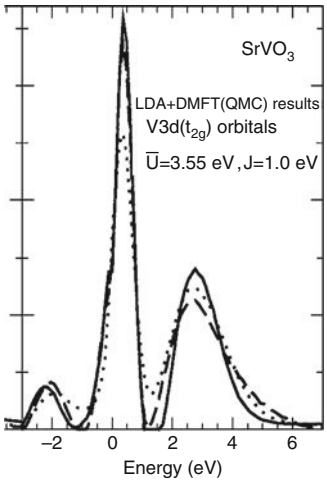

Fig. 6.3. Spectral function for d-states obtained in $LDA + DMFT$ calculations for $SrVO_3$ at $T = 300\,\mathrm{K}$ (*solid curve*) and $T = 700\,\mathrm{K}$ (*dashed line*) and $T = 1{,}100\,\mathrm{K}$ (*dotted line*) [270]

band. That is a consequence of d band degeneracy and occupancy value much less that corresponding to half filling.

In Fig. 6.3 calculation results are shown for three temperature values: $T = 300\,\mathrm{K}$ (solid line), $T = 700\,\mathrm{K}$ (dashed line) and $T = 1{,}100\,\mathrm{K}$ (dotted line). *QMC* calculations with Hirsch-Fye algorithm for such low-temperature value as $T = 300\,\mathrm{K}$ are very rare because for real compounds with degenerate d band they require huge computer resources and practically all calculation are usually done for $T = 1{,}100\,\mathrm{K}$ (that corresponds to $\beta = 10$). This result gave opportunity to analyze temperature dependence of spectral function. As one can see in Fig. 6.3 temperature lowering leads to intensity enhancement of quasiparticle peak on the Fermi level. That means that in order to describe susceptibility and electronic specific heat temperature lowering in *QMC* calculations can become crucial.

In Fig. 6.4 a comparison is presented between calculated and experimental spectra of $SrVO_3$. Calculated spectra were obtained by multiplying *DMFT* spectral function by Fermi distribution function $f_F(\varepsilon)$ (for comparison with photoemission spectra, left side of Fig. 6.4) or by $1 - f_F(\varepsilon)$ (for comparison with absorption spectra, right side of Fig. 6.4) and in addition some broadening was done to take into account experimental resolution.

As one can see from Fig. 6.4 agreement between calculated and experimental spectra is satisfactory. Main result is reproducing of experimental peak at $\approx -2\,\mathrm{eV}$ corresponding to lower Hubbard band in *DMFT* spectrum. A presence of such a peak in experimental spectrum is considered to be a direct evidence of strong correlation in $SrVO_3$ because in one-electron description based on *LDA* calculations (see Fig. 6.2) this peak cannot be reproduced.

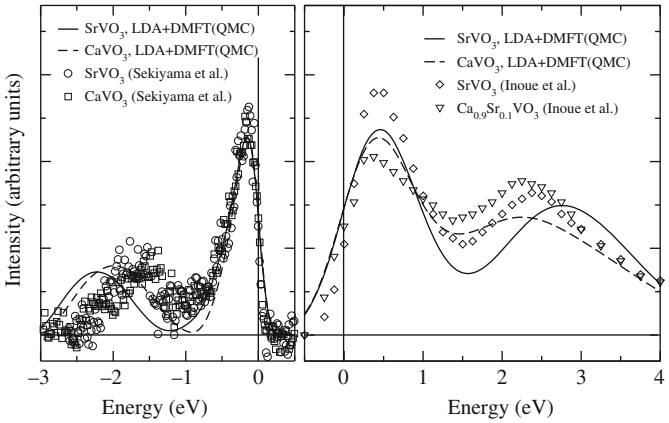

Fig. 6.4. Spectra obtained in $LDA + DMFT(QMC)$ calculations for $SrVO_3$ (*solid line*) in comparison with experimental spectra (*circles*) PES (*left*) and absorption spectra XAS (*right*) [271]

$SrVO_3$ example with high symmetry and small number of electrons allows to study correlation effects influence not only on total spectrum but also on wave vector $\mathbf{k}$ resolved spectral function $A(\mathbf{k}, \omega)$ and to obtain renormalized energy bands $\tilde{\varepsilon}(\mathbf{k})$.

For that one needs to calculate self-energy $\Sigma(\omega)$ for real energies ω. In $DMFT$ all calculations are performed for complex energy values corresponding to Matsubara frequencies $i\omega_n$ and it is necessary to analytically continue $\Sigma(i\omega_n)$ function on real energy axis. Maximum entropy method (Sect. 3.2.2) allows to calculate spectral function for real energies $A(\omega)$. Spectral function is defined by retarded GF $G^R(\omega)$: $A(\omega) = -\frac{1}{\pi}\mathrm{Im}G^R(\omega)$ and hence:

$$G^R(\omega) = \int \mathrm{d}\varepsilon \frac{A(\varepsilon)}{\omega + i\delta - \varepsilon}. \tag{6.2.14}$$

($i\delta$ is infinitesimal imaginary quantity).

Green function on real axis can be expressed using (6.1.8) via integral over density of states:

$$G^R(\omega) = \int \mathrm{d}\varepsilon \frac{\rho_0(\varepsilon)}{\omega + i\delta - \Sigma(\omega) - \varepsilon}. \tag{6.2.15}$$

Knowing $G^R(\omega)$ from (6.2.14) it is possible to find $\Sigma(\omega)$.

In Fig. 6.5 real and imaginary parts of $\Sigma(\omega)$ for $SrVO_3$ calculated in this way are presented. Spectral functions $A(\mathbf{k}, \omega)$ for wave vector values $\mathbf{k}$ were calculated with the following expression:

$$A(\mathbf{k}, \omega) = -\frac{1}{\pi}\mathrm{Im}\mathrm{Tr}\left[(\omega - \Sigma(\omega))\hat{I} - \hat{H}_0(\mathbf{k})\right]^{-1}. \tag{6.2.16}$$

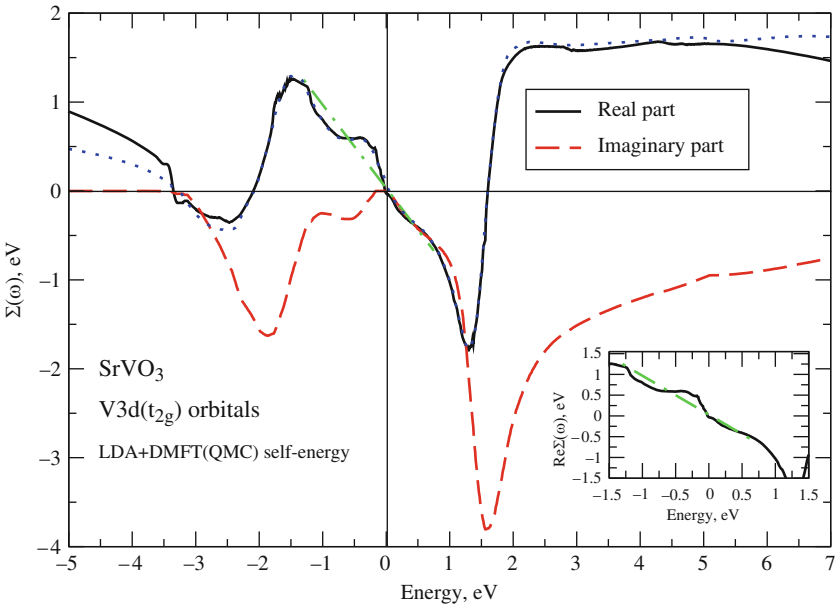

Fig. 6.5. Real (*solid line*) and imaginary (*dashed line*) parts of self-energy $\Sigma(\omega)$ obtained in $LDA + DMFT(QMC)$ calculation for $SrVO_3$ [272]. *Dotted line* shows slope of $\mathrm{Re}\Sigma(\omega)$ near Fermi level. In the inset behavior of $\mathrm{Re}\Sigma(\omega)$ is shown near Fermi level in magnification

Calculated spectral functions $A(\mathbf{k}, \omega)$ for wave vectors $\mathbf{k}$ along symmetric directions in cubic Brillouin zone are shown in Figs. 6.6 and 6.7. The curves $A(\omega, \mathbf{k})$ can be presented as a sum of Lorentzians with a width defined by the values of imaginary part of self-energy $\Sigma(\omega)$. As imaginary part of $\Sigma(\omega)$ tends to zero as ω^2 at $\omega \to 0$ then near Fermi level peaks $A(\mathbf{k}, \omega)$ become very narrow and it is possible to define new dispersion law $\tilde{\varepsilon}(\mathbf{k})$ as an energy value where function $A(\mathbf{k}, \omega)$ has a maximum.

In Fig. 6.8 calculation results for $\tilde{\varepsilon}(\mathbf{k})$ (points) are shown in comparison with $\varepsilon(\mathbf{k})$ calculated for noninteracting Hamiltonian $\hat{H}_0(\mathbf{k})$. $\tilde{\varepsilon}(\mathbf{k})$ bands looks like compressed in energy scale $\varepsilon(\mathbf{k})$ bands. Such renormalization due to Coulomb correlation effects can be explained in the following way.

Near Fermi level (see inset in Fig. 6.5) imaginary part of self-energy $\mathrm{Im}\Sigma(\omega)$ tends to zero and real part $\mathrm{Re}\Sigma(\omega)$ can be approximated by linear function:

$$\mathrm{Re}\Sigma(\omega) \approx \mathrm{Re}\Sigma(0) + \omega \frac{\mathrm{dRe}\Sigma(\omega)}{\mathrm{d}\omega}\Big|_{\omega=0}. \tag{6.2.17}$$

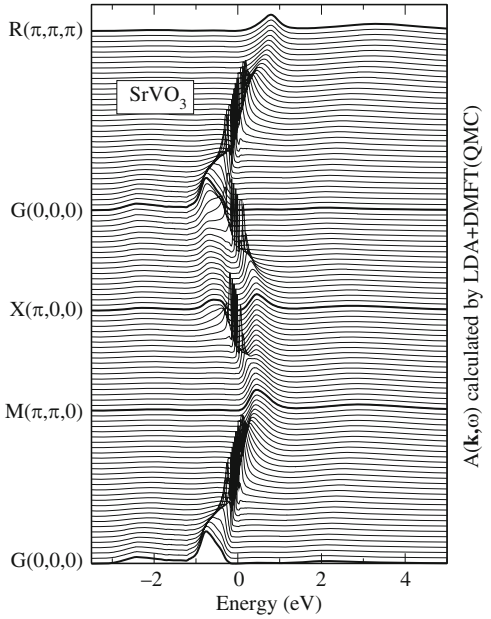

Fig. 6.6. Calculated by $LDA + DMFT(QMC)$ method spectral functions $A(\mathbf{k}, \omega)$ for V-3d (t_{2g}) bands of $SrVO_3$ compound [272]

Then expression (6.2.16) can be written as:

$$A(\mathbf{k},\omega) = -\frac{1}{\pi}\mathrm{Im}\mathrm{Tr}\left[(\omega(1-\frac{\mathrm{dRe}\Sigma(\omega)}{\mathrm{d}\omega}|_{\omega=0} - \mathrm{Re}\Sigma(0))\hat{I} - \hat{H}_0(\mathbf{k})\right]^{-1}$$
$$= -\frac{1}{\pi}\mathrm{Im}\mathrm{Tr}Z\left[(\omega - Z\mathrm{Re}\Sigma(0))\hat{I} - Z\hat{H}_0(\mathbf{k})\right]^{-1}. \tag{6.2.18}$$

$Z \equiv (1-\frac{\mathrm{dRe}\Sigma(\omega)}{\mathrm{d}\omega}|_{\omega=0})^{-1} = (m^*/m)^{-1}$ is quasiparticle spectral weight and m^* is quasiparticle effective mass. A term $Z\mathrm{Re}\Sigma(0)$ gives a shift of energy scale and in the result spectral functions $A(\mathbf{k}, \omega)$ calculated with (6.2.18) are delta functions for energies corresponding to eigenvalues of effective Hamiltonian $Z\hat{H}_0(\mathbf{k}) = (m^*/m)^{-1}\hat{H}_0(\mathbf{k})$. These eigenvalues give new dispersion law:

$$\tilde{\varepsilon}(\mathbf{k}) = (m^*/m)^{-1}\varepsilon(\mathbf{k}). \tag{6.2.19}$$

For $SrVO_3$ $m^*/m = Z^{-1} = 1.9$ and in Fig. 6.8 by dotted line $\tilde{\varepsilon}(\mathbf{k})$ are shown calculated from LDA bands by renormalization (6.2.19). As one can see agreement of $\tilde{\varepsilon}(\mathbf{k})$ calculated from (6.2.16) and the bands renormalized by (6.2.19) is very good. $LDA + DMFT$ calculation results obtained in [270] were later confirmed by works [273, 274].

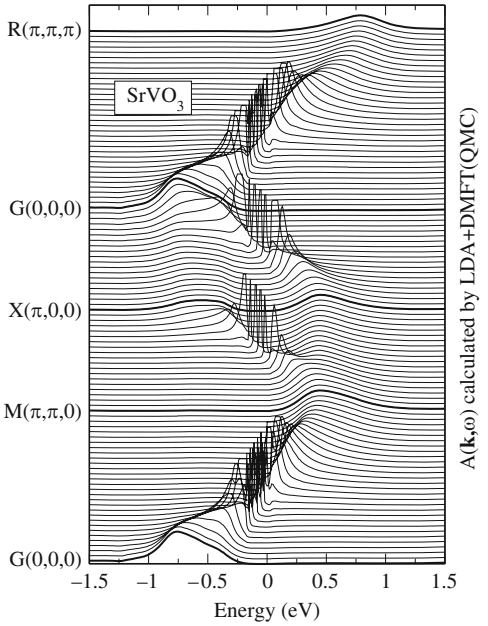

Fig. 6.7. Magnification of Fig. 6.6 near Fermi energy [272]

6.2.2 V_2O_3: Two Electrons in *d*-Band with Trigonal Crystal-Field Splitting

V_2O_3 is considered to be typical example of Mott insulator. This compound can be in metallic as well as in insulating phases and both of them are paramagnetic. Paramagnetic insulator state existence can be explained only in Mott-Hubbard theory.

V_2O_3 crytalizes in corundum structure where vanadium ions are surrounded by six oxygen ions forming octahedron with small trigonal distortion (Fig. 6.9). Vanadium d states transform according to irreducible representations of trigonal point symmetry group D_{3d}: a_{1g} (nondegenerate) and e_g (double degenerate). To representation e_g correspond two pairs of orbitals: e_g^π and e_g^σ. In Fig. 6.10 partial densities of states for V_2O_3 are shown calculated in *LDA* [275]. *d*-band consists of two well separated subbands: low-energy partially filled band formed by a_{1g} and e_g^π states (for undistorted octahedron with cubic symmetry those states correspond to t_{2g} orbitals), and high-energy empty band formed by e_g^σ (corresponding to cubic e_g orbitals). Vanadium valence in this compound is +3 that corresponds to configuration d^2.

Metallic and insulating phases of V_2O_3 are realized in the same corundum structure with different lattice parameters. Spectral functions for *d*-bands obtained in $LDA + DMFT(QMC)$ calculations for V_2O_3 [275] are presented in Fig. 6.11 (upper part corresponds to calculations with metallic phase lattice parameters and lower part is for insulating phase). As one can see calculations

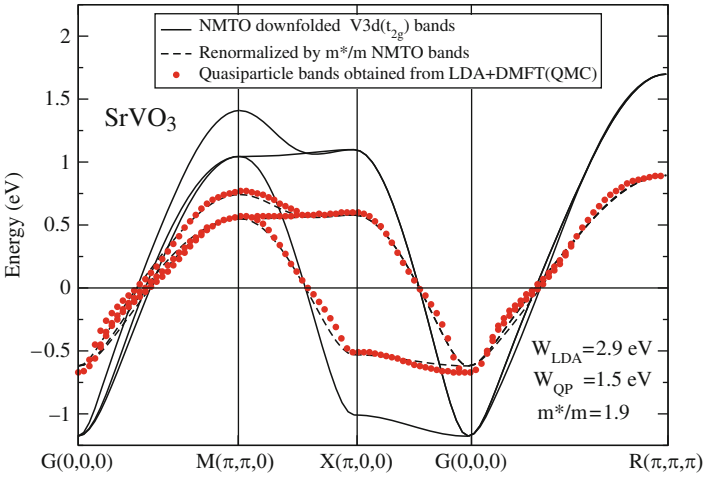

Fig. 6.8. Comparison of *LDA* band structure for $SrVO_3$ (*solid line*) with results of $LDA + DMFT(QMC)$ calculation (*dots*). $LDA + DMFT(QMC)$ bands are well described by *LDA* bands renormalized by effective mass ratio $m^*/m = Z^{-1} = 1.9$ (*dotted line*) [272])

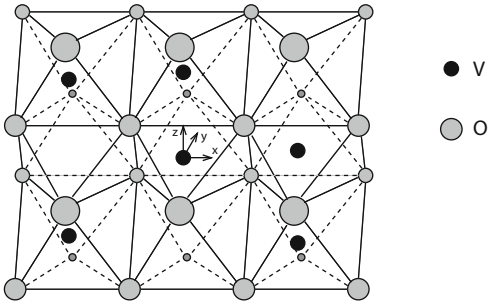

Fig. 6.9. Corundum crystal structure for compound V_2O_3

have allowed to reproduce metal–insulator transition with lattice parameters change. Temperature dependence of calculation results is even stronger than for $SrVO_3$ (Fig. 6.3). While for $T = 1160\,\mathrm{K}$ spectral function of metallic phase shows only weakly pronounce "bump" near Fermi level, room temperature $T = 300\,\mathrm{K}$ calculations gave high and sharp quasiparticle peak that is typical for strongly correlated systems on the edge of metal–insulator transition.

Spectral functions in Fig. 6.11 have much more complex character than simple three-peak structure obtained for $SrVO_3$ (Fig. 6.3). There are two reason for this fact. First of all d^2 configuration has more complicated multiplet atomic structure than simple d^1 configuration in $SrVO_3$. At the second trigonal crystal filed splitting of cubic t_{2g} states into a_{1g} and e_g^π states (Fig. 6.10) absent in $SrVO_3$ lifts degeneracy of partially filled d-band. While the strength

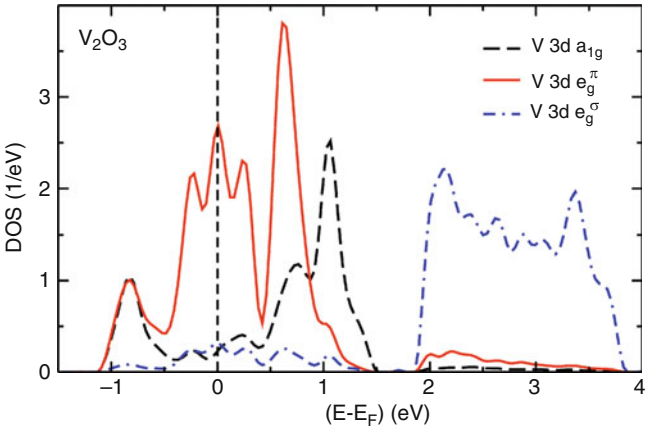

Fig. 6.10. Partial densities of states of d band for a_{1g} (*solid line*), e_g^{π} (*dashed line*) and e_g^{σ} (*dashed-dotted line*) obtained in *LDA* calculation for V_2O_3[275]

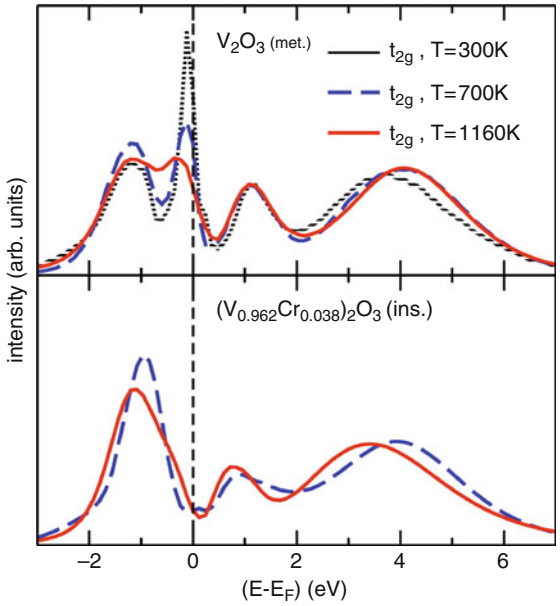

Fig. 6.11. Spectral functions for d-band obtained in $LDA+DMFT(QMC)$ calculation of V_2O_3 for crystal structure parameters corresponding to metallic (*upper part*) and insulating (*lower part*) phases for three temperature values $T = 1160\,\mathrm{K}$ (*solid line*), $700\,\mathrm{K}$ (*dashed line*), $300\,\mathrm{K}$ (*dotted line*) [275]

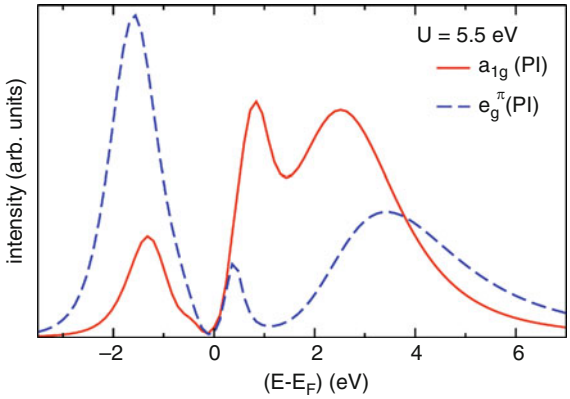

Fig. 6.12. Spectral functions corresponding to orbitals of a_{1g} (*solid line*) and e_g^π (*dashed line*) symmetry for paramagnetic insulator state V_2O_3 [275]

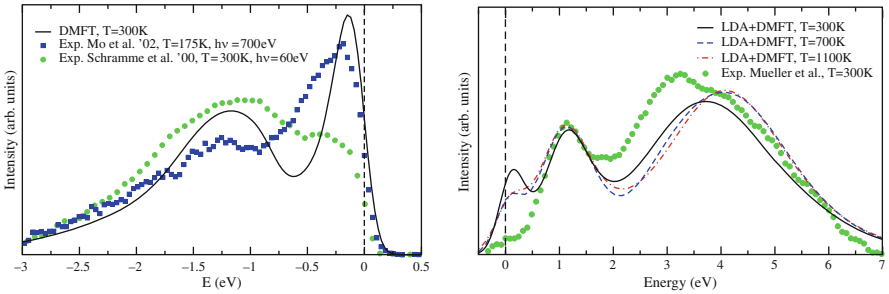

Fig. 6.13. Comparison of spectra obtained in $LDA + DMFT(QMC)$ calculations [275] for V_2O_3 in metallic phase with experimental spectra (*left side* – photoemission spectra [276, 277], *right side* X-ray absorption spectra [278])

of this trigonal splitting estimated as centers of gravity difference for partial densities of states for a_{1g} and e_g^π orbitals is relatively small (0.3 eV in comparison with band width 2.5 eV) it is enough to result in strong orbital polarization. In Fig. 6.12 spectral functions are shown corresponding to orbitals a_{1g} (solid line) and e_g^π (dashed line) obtained in $LDA + DMFT(QMC)$ calculations for V_2O_3 in insulating phase. One can see that occupied band below Fermi level is predominantly formed by e_g^π states while a_{1g} states form empty band above Fermi level. That results in occupancy 0.86 for every e_g^π orbital while occupancy for a_{1g} orbital is equal to 0.28.

Comparison of the spectra calculated in $LDA + DMFT(QMC)$ [275]) for V_2O_3 in metallic phase with experimental spectra (Fig. 6.13) shows a good agreement. Please note the presence in both calculated and experimental spectra of the peak at $\approx$1.5 eV corresponding to lower Hubbard band that is absent in *LDA* calculation results (Fig. 6.10).

6.2.3 LiV_2O_4: Heavy Fermion in *d*-Electron System

"Heavy fermion" phenomenon (drastic effective electron mass increase at low temperatures) is usually observed in f-electrons systems (rare-earth or actinides elements compounds). Recent discovery of such effect in d-system LiV_2O_4 with $m^*/m \approx 25$ was a great surprise because "heavy fermion" effect is explained by the presence of narrow Kondo peak at the Fermi level appearing from weak hybridization of localized f-electron with conduction band states. d-band width in transition metal compounds is of the order of few eV that excludes narrow Kondo peak presence.

In work [279] LiV_2O_4 was investigated by $LDA + DMFT$ method. The critical temperature where effective mass increase is observed is $T_K \approx 28\,\mathrm{K}$ and hence using QMC method with Hirsch-Fye algorithm as impurity solver (see Sect. 3.2.1) for this problem is impossible because it works for high temperatures only. For this case $PQMC$ method was applied (see Sect. 3.2.4) that was derived in the limit of $T \to 0$.

LiV_2O_4 has spinel crystal structure where vanadium ions are surrounded by six oxygen ions forming octahedron with small trigonal distortion (Fig. 6.14). In the same way as for V_2O_3 compound vanadium d-states in LiV_2O_4 transform according to irreducible representations of trigonal point symmetry group D_{3d}: a_{1g} (nondegenerate) and e_g (double degenerate). Formal valence of vanadium in LiV_2O_4 is +3.5 that corresponds to 1.5 electrons per vanadium atom. In Fig. 6.15 energy bands and partial densities of states are shown for partially filled d band obtained in LDA calculation for LiV_2O_4 [279].

From Fig. 6.14 one can see that width of a_{1g} is much smaller than the width of e_g^π band. Crystal field splitting estimated as difference of partial densities of states centers of gravity shows that energy of a_{1g} orbitals is 0.26 eV lower than energy of e_g^π orbitals. One can expect that with taking into account Coulomb correlations this fact will lead to electrons localization on a_{1g} orbitals.

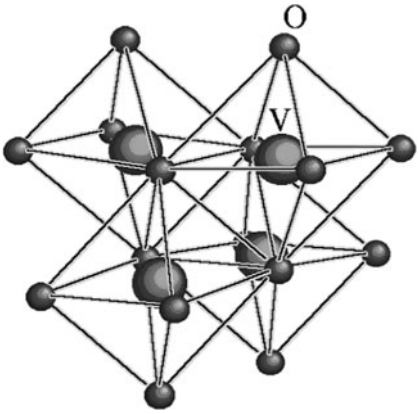

Fig. 6.14. Spinel crystal structure for compound LiV_2O_4

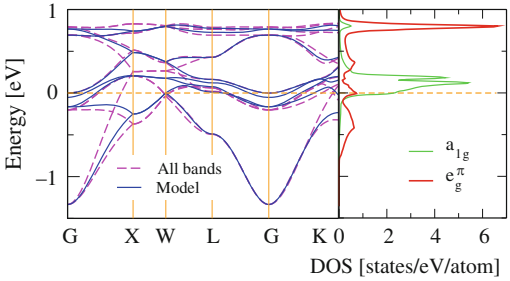

Fig. 6.15. Energy bands and partial densities of states for partially filled d-band for compound LiV_2O_4 obtained in *LDA* calculation [279]

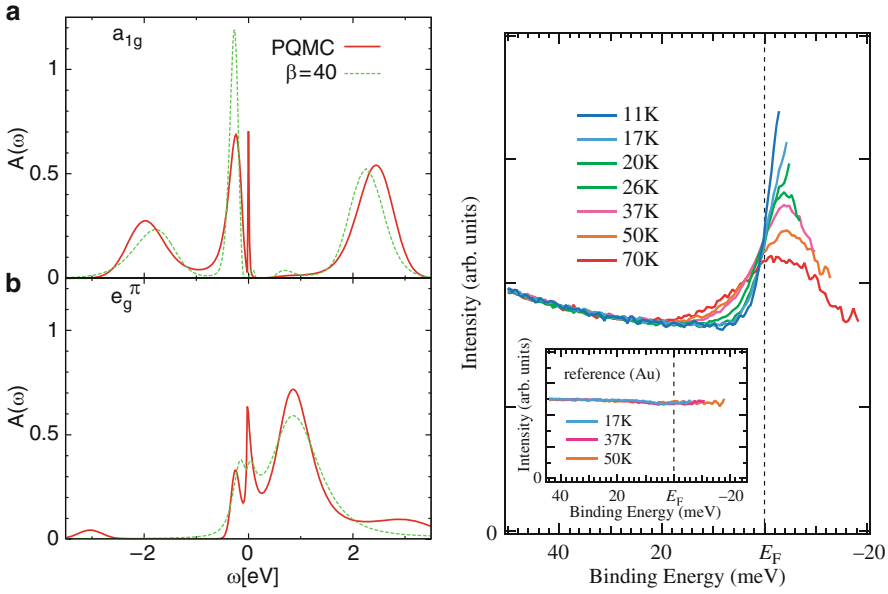

Fig. 6.16. *Left*: spectral functions from $LDA + DMFT$ calculations [279] of LiV_2O_4 for states of a_{1g} (*upper part*) and e_g^π (*lower part*) symmetry. *Solid line* corresponds to zero temperature (impurity problem solved by *PQMC*), *dashed line* is for final temperature $T = 1/\beta = 1/40$ eV. *Right*: corresponding experimental spectra divided on Fermi distribution function for various temperatures [280]

In Fig. 6.16 (left side) spectral functions for a_{1g} and e_g^π states obtained in $LDA+$ calculations [279] are shown. Indeed as it was expected a_{1g} orbitals show distribution characteristic for nearly insulating half-filled state. Number of a_{1g} electrons is equal to 0.98. As for e_g^π orbitals they are quarter filled (occupancy = 0.52) and their distribution is far from metal–insulator pattern.

Applying *PQMC* method with zero temperature as impurity solver was crucial for success of $LDA + DMFT$ calculations for LiV_2O_4 [279]. While

QMC-Hirsch-Fye calculations (dashed line in Fig. 6.16, left side) at T ≈ 300 K gave very weak feature on the Fermi level, *PQMC* curve (solid line) demonstrates very narrow (10 meV width) peak situating 4 meV above Fermi level.

Existence of such a peak was directly confirmed by high resolution photoemission spectroscopy. In Fig. 6.16 (right side) experimental photoemission spectra for LiV_2O_4 are shown divided by Fermi distribution function for various temperatures [280]. They demonstrate the presence of very narrow peak in density of states just above the Fermi level. Such narrow peak close to Fermi energy naturally explains high value of effective mass at low temperatures.

Physical reason for such a peak existence is very different from Kondo peak mechanism in f-elements compounds. In [279] an explanation was proposed based on lightly doped Mott insulator picture. In Fig. 3.18 in Chap. 3 spectral function evolution for doped Mott insulator is shown. At small doping values narrow peak on the Fermi level appears. In $LDA + DMFT$ calculations for LiV_2O_4 [279] occupancy of a_{1g} is equal to 0.98 corresponding to very small doping 0.02 that results in appearance of anomalously narrow peak in spectrum.

6.3 Late Transition Metal Oxides: Charge Transfer Insulators

6.3.1 NiO: Band Structure for Charge Transfer Insulator

All early transition metal compounds described earlier belong to Mott insulator class of materials where energy gap is opened between Hubbard bands formed by d-states. Filled oxygen p-bands are well below both Hubbard bands and can be projected out by constructing Hamiltonian with d-symmetry Wannier functions only. However for late transition metal oxides the picture is different: d-states energy is much lower than for early transition metal oxides and hence closer to oxygen p-bands so that Δ_{pd} (energy difference between ε_d and ε_p) becomes smaller than Coulomb parameter U. In the result lower Hubbard band falls below the top of oxygen band and then lowest excitation energy corresponds to transition from occupied oxygen band to unoccupied upper Hubbard band. In Zaanen-Sawatzky-Allen classification [281] such systems are called "charge transfer insulators" (meaning that lowest energy excitation corresponds to electron transfer from oxygen to metal ion). For proper description of such materials oxygen p states should be explicitly included in the Hamiltonian in addition to transition metal d-states [282].

Nickel oxide is a typical example of charge transfer insulators. This compound has cubic structure of NaCl type where every nickel atom is surrounded by six oxygen atoms forming an octahedron. Ni d-states transform according to two irreducible representations of cubic O_h symmetry group: triply degenerate t_{2g} and double degenerate e_g. Nickel valence in this compound is equal

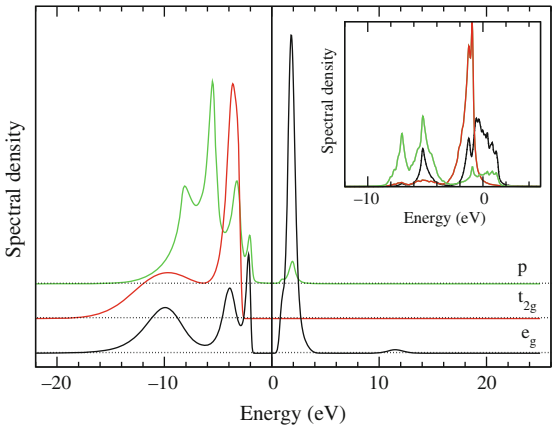

Fig. 6.17. Spectral functions for oxygen p states and nickel d-states of t_{2g} and e_g symmetry obtained in $LDA+DMFT$ calculation [283] for NiO. In inset corresponding partial densities of state from LDA calculations are presented

to +2 that corresponds to configuration d^8. Energy of t_{2g} states is lower than e_g orbitals that gives for eight d-electrons fully occupied t_{2g} electronic shell and half occupied e_g shell.

In work [283] NiO was studied by $LDA + DMFT(QMC)$ method with Wannier functions basis Hamiltonian including both nickel d-states and oxygen p states. In Fig. 6.17 spectral function are shown obtained in $LDA + DMFT(QMC)$ calculations. In inset in 6.17 noncorrelated partial densities of states are presented from LDA calculations. One can see that while noncorrelated curves show well separated bands formed by p and d states, $LDA + DMFT(QMC)$ spectral functions corresponds to complete overlap of occupied d states with oxygen band. Fully occupied t_{2g} orbitals gives contribution to lower Hubbard band while half-filled e_g states form both lower and upper Hubbard bands.

In Fig. 6.18 a comparison is presented of experimental photoemission and inverse photoemission spectra with $LDA + DMFT(QMC)$ spectral functions for Ni-d (solid line) and O-p (dashed area) states. Experimental spectrum for excitation energy 120 eV corresponds to predominantly Ni-d states while spectrum for 66 eV is determined by mainly O-p orbitals. One can see a good agreement between experimental and theoretical curves in energy separation among peaks for empty and occupied states as well as for Ni-d and O-p states distribution.

Spectral functions of Fig. 6.17 show that top of the valence band peak is formed by Ni-d states with a significant admixture of O-p states. That fact contradicts to "charge transfer insulator" classification for NiO where an energy gap should be between oxygen p states and upper Hubbard band d-states. The reason for this is strong $p-d$ hybridization. Pure Ni-d states of

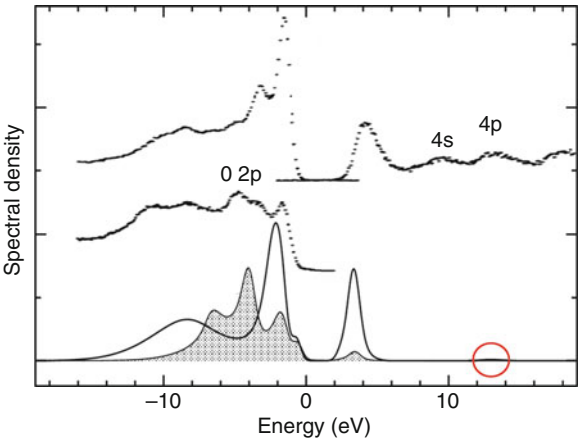

Fig. 6.18. Theoretical Ni-*d* and O-*p* (*dashed area*) spectra calculated in *LDA* + *DMFT* [283] for NiO in comparison with experimental photoemission and inverse photoemission spectra [284]. *Lower and upper curves* correspond to photoemission spectra obtained for excitation energies 120 eV and 66 eV and describing excitation of nickel and oxygen states, respectively

lower Hubbard band correspond to peak in *d* spectral function at −10 eV and are situated well below oxygen band.

In order to clarify the problem of orbital character for states at the top of valence band in [283] calculations were done for hole doped NiO. If NiO is indeed "charge transfer insulator" then additional holes should go into oxygen *p* band and then doping results in decreasing of oxygen orbitals occupancy while *d*-orbitals occupancy should not change. In Fig. 6.19 results of *LDA* + *DMFT*(*QMC*) calculations for NiO with hole concentration $n_h = 0.6$ are shown. Theoretical spectral functions correspond to strongly correlated metal with significant spectral weight transfer from Hubbard bands to quasiparticle peak on Fermi level. With doping increase this spectral weight transfer is enhanced as one can see from comparison of results for hole concentration $n_h = 0.6$ and 1.2 (see inset in Fig. 6.19).

There is a series of compounds $Li_xNi_{1-x}O$ that corresponds to hole doped nickel oxide. In Fig. 6.20 a comparison is presented of theoretical *LDA* + *DMFT*(*QMC*) spectral function for NiO with hole concentration $n_h = 0.6$ and experimental photoemission and inverse photoemission spectra for $Li_{0.4}Ni_{0.6}O$. Metallic character of both theoretical and experimental spectra is well pronounced with satellite peak at −8 eV corresponding to lower Hubbard band.

To analyze states appearing with hole doping in NiO calculated orbital occupancies are presented in Table 6.1. Comparing values for undoped ($n_h = 0$) and doped cases one can see that oxygen *p* states occupancies are significantly decreased when electrons are removed from NiO while occupancies for Ni-*d*

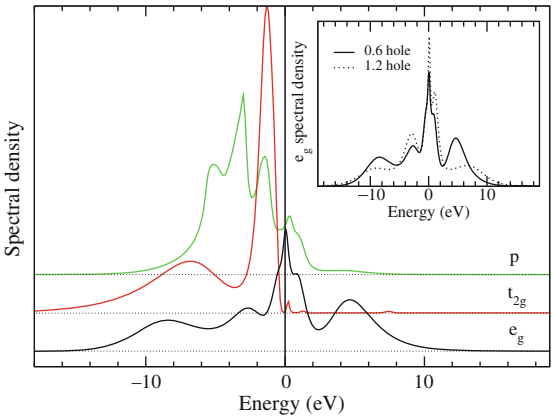

Fig. 6.19. Ni-d and O-p spectral functions in $LDA + DMFT$ for NiO with holes concentration $n_h = 0.6$ [283]. Inset shows e_g-states spectral function for holes concentrations $n_h = 0.6$ and 1.2

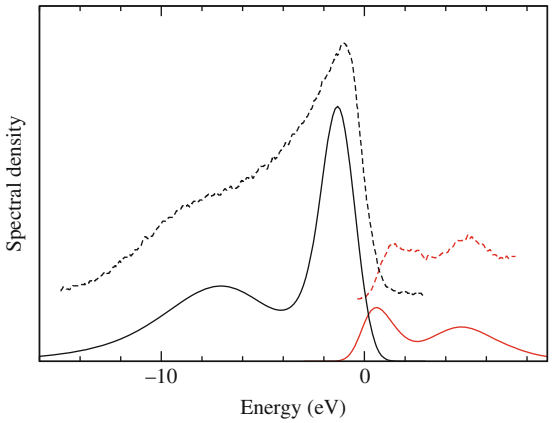

Fig. 6.20. Theoretical Ni-d spectra calculated in $LDA + DMFT$ [283] for NiO with holes concentration $n_h = 0.6$ in comparison with experimental photoemission spectra and inverse photoemission spectra [285] for $Li_{0.4}Ni_{0.6}O$

Table 6.1. Orbital occupancies and fluctuating magnetic moment m_d on Ni for various hole doping values obtained in $LDA + DMFT$ calculations [283] for NiO

n_h	n_{e_g}	$n_{t_{2g}}$	n_p	m_d
0	0.547	1.000	0.969	1.85
0.6	0.531	0.994	0.885	1.50
1.2	0.530	0.980	0.800	1.28

orbitals are much weaker influenced by doping. That confirm O-p character of hole states in NiO as it should be for "charge transfer insulator" in spite of Ni-d character of top of valence band peak for undoped NiO. Magnetic moment value m_d is strongly suppressed with hole doping. It is consequence of spectral weight transfer from Hubbard bands (that are responsible for localized states forming magnetic moment) to quasiparticle peak on Fermi level.

A presence in the same energy region of strongly correlated localized Ni-d states and delocalized O-p states results in unusual energy band structure in nickel oxide. It reveals itself in experimental data of Angle-Resolved Photoemission Spectroscopy ($ARPES$) for NiO [287]. In Fig. 6.21 by symbols energy bands $\varepsilon(\mathbf{k})$ measured by $ARPES$ are shown. One can see dispersive bands together with nearly flat bands. In [286] $LDA + DMFT(QMC)$ method was used to calculate spectral functions $A(\mathbf{k}, \omega)$ shown in Fig. 6.21 for wave vectors $\mathbf{k}$ along direction Γ-X. Darker regions of $(\mathbf{k}, \omega)$ plane correspond to larger values of $A(\mathbf{k}, \omega)$. Comparison with experimental data shows a good agreement of theoretical and experimental spectra. Analysis of orbital contributions to $A(\mathbf{k}, \omega)$ confirms that dispersive bands correspond to nearly pure O-p states while flat bands are formed by strongly correlated Ni-d states.

These results demonstrate that $LDA + DMFT$ method can be successfully applied to so complicated systems as late transition metal oxides belonging to "charge transfer insulator" class. A presence in these materials simultaneously correlated d states and delocalized oxygen p states hybridizing with each other makes more sophisticated problem than Hubbard or Anderson models. Good agreement of calculated and experimental spectra for NiO demonstrates great potential of $DMFT$ approach.

6.3.2 MnO: Metal–Insulator Transition with Pressure and *d*-ion Magnetic Moment Collapse

Manganese oxide (MnO) similar to NiO crystallizes in cubic structure of NaCl type and belongs to "charge transfer insulator" class of materials. However, d shell of transition metal ion in this material is half-filled (configuration d^5) that results in high-spin ground state of Mn^{+2} with $S = 5/2$. With pressure metal–insulator transition of the first order is experimentally observed in MnO with a volume jump $V/V_0 = 0.68 \rightarrow 0.63$ and magnetic moment collapse from $5\mu_B$ to $< 1\mu_B$ (see review of experimental data in [288]).

In [288] electronic structure and magnetic properties of this compound in paramagnetic state as a function of volume and pressure was studied by $LDA + DMFT(QMC)$ method. As for NiO calculations were done with full set of Wannier functions having symmetry of oxygen p and nickel d states. In Fig. 6.22 occupancy of t_{2g} and e_g orbitals are shown as a function of volume together with local magnetic moment values defined as a square root of average value of magnetic moment on site operator square $M_s = \sqrt{\langle \hat{m}_z^2 \rangle}$. At ambient pressure ($V/V_0 = 1$) manganese ion is in well defined high-spin state $M_s = 5\mu_B$ with the same half filling for both t_{2g} and e_g orbitals. With

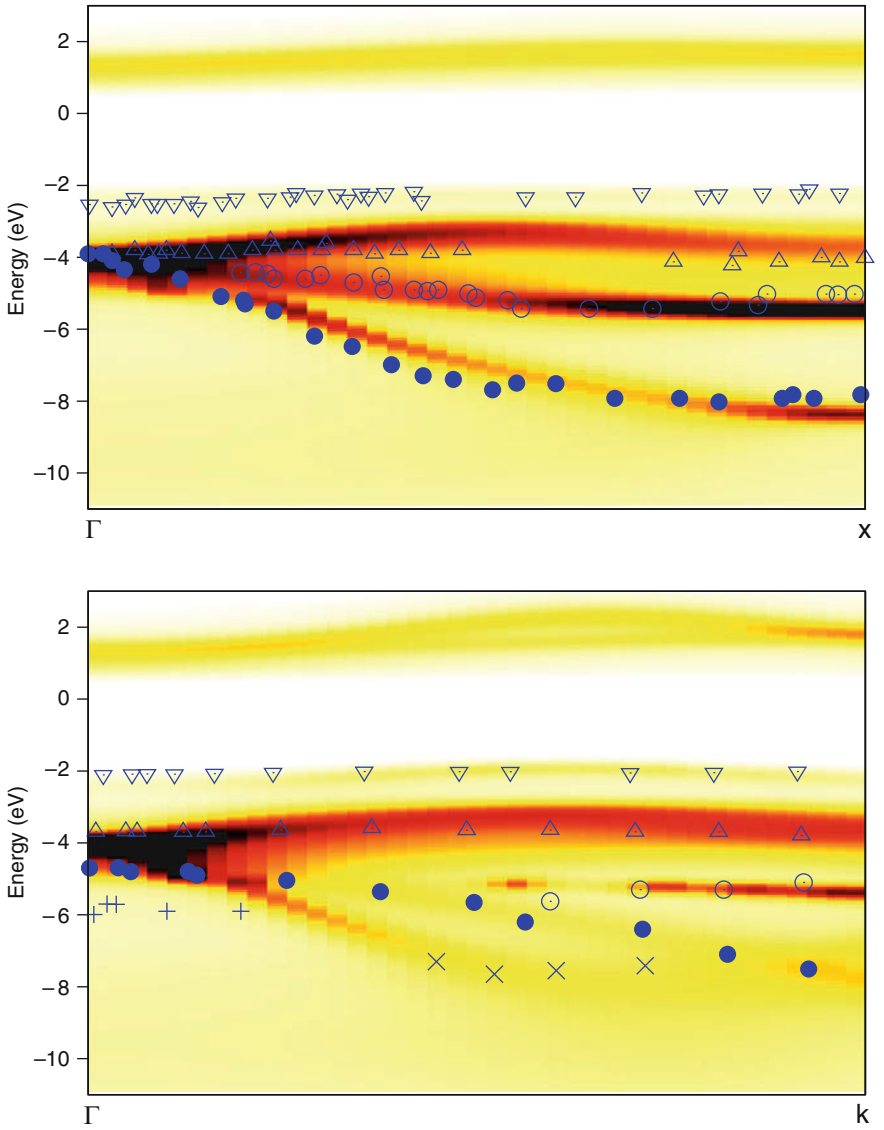

Fig. 6.21. Spectral function $A(\mathbf{k},\omega)$ (*darker areas* corresponds to larger values of $A(\mathbf{k},\omega)$) for wave vectors $\mathbf{k}$ along direction Γ-X calculated in $LDA + DMFT$ [286] for NiO. Symbols show the bands measured in [287]

volume decrease below $V/V_0 = 0.7$ magnetic moment value sharply decreases with simultaneous decreasing of e_g orbitals occupancy and increasing of t_{2g} occupancy. For volume less than $V/V_0 = 0.6$ system is in low-spin state with $M_s \approx 1\mu_B$ nearly empty e_g orbitals and nearly occupied t_{2g} orbitals $n_{t_{2g}} \approx 0.8$.

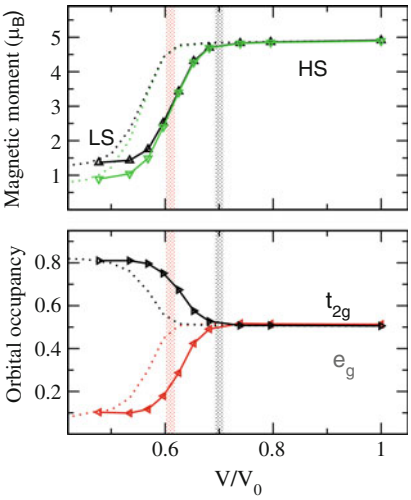

Fig. 6.22. Dependence on volume of local magnetic moment M_s (*upper panel*) and occupancies of e_g and t_2g orbitals (*lower panel*) calculated in $LDA + DMFT$ [288] for MnO. *Solid lines* correspond to calculations with parameters $U = 6.9\,\text{eV}$, $J = 0.86\,\text{eV}$, *dashed lines* to calculation with enhanced exchange parameter $J = 1\,\text{eV}$. *Vertical lines* show the volume value where gaps are closed for t_{2g} and e_g spectral functions

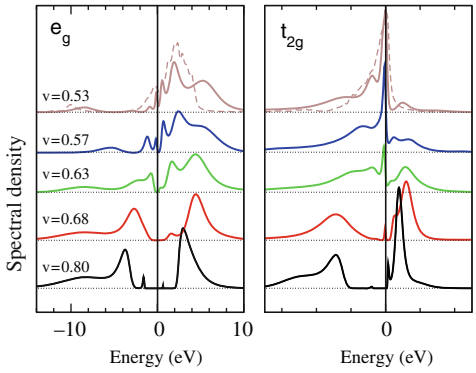

Fig. 6.23. Evolution with volume of Mn $3d$ spectral functions (e_g – left and t_{2g} – right) calculated in $LDA + DMFT$ [288] for MnO. *Dashed line* corresponds to noncorrelated (LDA) partial densities of states

Spectral functions evolution with volume obtained in $LDA+DMFT(QMC)$ calculation is shown in Fig. 6.23. For $V/V_0 = 0.8$ typical insulating ground state is observed with half-filled t_{2g} and e_g orbitals corresponding to high-spin state of Mn ion. With volume decrease transition to metallic state happens with well pronounced quasiparticle peak for t_{2g} spectral function and nearly empty e_g band ($V/V_0 = 0.53$). In Fig. 6.23 by dashed line noncorrelated partial densities of states are shown obtained in LDA calculation. As one can see they

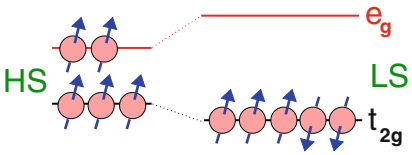

Fig. 6.24. Schematic diagram of Mn $3d$ energy levels corresponding to high-spin (HS) and low-spin (LS) states realizing at normal conditions (HS) and for pressure higher then critical one (LS). In high-spin case two electrons with spin-up occupy e_g levels increasing total energy on $2\Delta_{cf}$ due to crystal field splitting but winning exchange energy $-10J$. In low-spin state crystal field splitting Δ_{cf} becomes too large and only t_{2g} become occupied [288]

are very close to $LDA + DMFT(QMC)$ spectral function for $V/V_0 = 0.53$. It means that in low-spin state with empty e_g band and partially filled t_{2g} band the system is in weakly correlated regime in contrast to high-spin state for $V/V_0 = 0.8$ where t_{2g} and e_g spectral functions show Mott insulator state with large energy separation among Hubbard bands.

In order to clarify the physical origin of metal–insulator transition with pressure in MnO let us consider a problem of d^5 configuration ion in cubic crystal field. In Fig. 6.24 energy level scheme for this problem is presented. Cubic crystal field splits five-degenerate d level on triply degenerate t_{2g} level and doubly degenerate e_g level with energy separation among them equal to Δ_{cf}. In high-spin state (left side) five states with the same spin projection are occupied so that t_{2g} and e_g levels are half filled. That gives a loss of energy $2\Delta_{cf}$ due to two electrons in high-energy e_g states that is compensated by a gain in exchange energy $-10J$. In low-spin state all five electrons are on low-energy t_{2g} level (right side) and there is no loss of energy due to crystal field splitting but exchange energy decreases to $-4J$. Hence there is a competition between crystal field splitting and exchange interaction with equal energies for high-spin and low-spin states when $\Delta_{cf} = 3J$.

With lattice compression under pressure exchange energy parameter J is practically unchanged because it is determined by intraion interactions. However, crystal field splitting parameter Δ_{cf} significantly increases due to increased orbitals overlap with contraction of interatomic distances. In inset of Fig. 6.25 volume dependence of Hamiltonian parameters is shown: crystal field splitting parameter Δ_{cf} increases 2.5 times with volume compression from $\Delta_{cf} \approx 1\,\text{eV}$ at ambient pressure to $\Delta_{cf} \approx 2.5\,\text{eV}$ at volume value corresponding to metal–insulator transition $V/V_0 = 0.6$. This agrees well with the relation $\Delta_{cf} = 3J$ for critical value of crystal field splitting parameter because exchange interaction parameter used in calculation was equal to $J = 0.86$.

In [288] total energy as a function of volume for MnO was calculated (see Sect. 6.1.3). In Fig. 6.25 (left side) the corresponding curve is shown. At volume value corresponding to the transition a bend on the curve is observed. Spline interpolation for $E(V)$ is shown by dashed line. Differentiation of

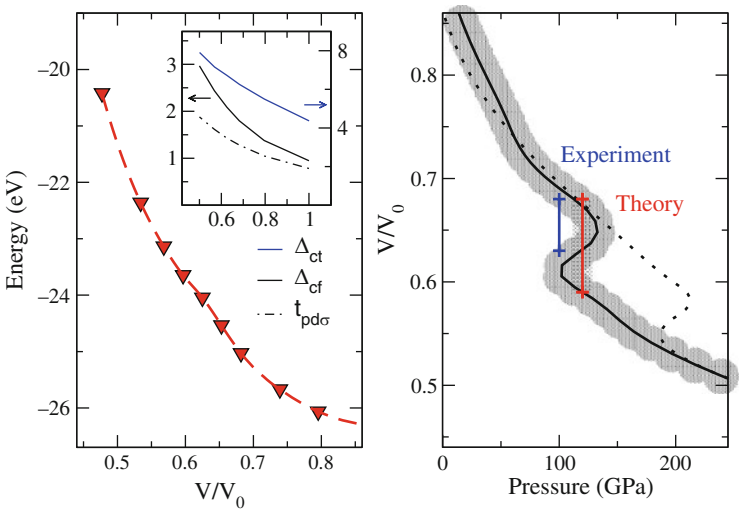

Fig. 6.25. Equation of state calculated in *LDA + DMFT* [288] for MnO. On the *left side* energy as a function of volume is shown (*dashed line* is spline interpolation) and on the *right side* volume as a function of pressure (hatch marks calculation accuracy). *Vertical lines* on $V(P)$ curve show critical pressure for transition $P_c^{\text{th}} = 120 \pm 15$ GPa determining volume collapse $V/V_0 = 0.68 \rightarrow 0.59$. *Dashed line* gives curve $V(P)$ calculated for enhanced exchange parameter $J = 1$ eV. Inset on the left panel shows dependence of the Hamiltonian parameters on the volume: crystal field splitting parameter Δ_{cf} increases 2.5 times in going from normal to critical pressure

$E(V)$ function gave pressure $P = \mathrm{d}E/\mathrm{d}V$ and allows to calculate volume as a function pressure $V(P)$ (right side of Fig. 6.25). This curve shows that at critical pressure value $P_c^{\text{th}} = 120 \pm 15$ GPa volume collapse happens $V/V_0 = 0.68 \rightarrow 0.59$. This agrees well with experimental values of critical pressure $P_c^{\text{exp}} \approx 100$ GPa and volume collapse $V/V_0 = 0.68 \rightarrow 0.63$.

LDA + DMFT calculation [288] show that a reason for metal–insulator transition with pressure in MnO is not simple band width increase and competition between kinetic and Coulomb energy as in standard Mott transition but magnetic transition from high-spin to low-spin state in manganese ion *d*-shell. To check this conclusion *LDA + DMFT* calculation with increased exchange parameter value $J = 1.0$ eV was performed [288] instead of $J = 0.86$ eV value obtained in constrain *DFT* calculations (Sect. 2.2.5). The corresponding curve is shown by dashed line in right side of Fig. 6.25 and in Fig. 6.22. As one can see from comparison of curves for $J = 1.0$ eV and $J = 0.86$ eV exchange parameter increase results in critical pressure value increase and hence to decrease of volume value where the transition happens. That agrees well with relation $\Delta_{cf} = 3J$ for critical value of crystal filed splitting: larger J value requires larger Δ_{cf} that means smaller volume.

6.4 f-Electron Systems: $\alpha - \gamma$ Transition in Ce

f-electron systems comparing with d-electron materials considered earlier have some special features. f-electrons are much more localized than d-electrons and for rare-earth elements $4f$-electrons are often considered as free ion electron shell not interacting with crystal. In addition to that "heavy fermion" materials where experimentally strong increase of carriers effective mass is observed are intermetallic compounds where narrow band of nearly localized f-electrons is embedded into wide metallic bands of delocalized *spd* electrons.

Metallic cerium in spite of its simple chemical composition and cubic face centered crystal (FCC) structure demonstrates very unusual physical properties. Low-temperature α-phase and high-temperature γ-phase of cerium have the same FCC crystal structure but their volume values have 15% difference. Temperature dependence of magnetic susceptibility shows Curie-Weiss law for γ-phase that means local magnetic moment existence. At the same time α-phase is Pauli paramagnet that gives local magnetic moments absence in this phase.

Earlier various approaches were proposed to explain those effects. In [289, 290] it was assumed that while in γ-phase f-electrons are localized and so form local moment and do not participate in chemical bond, in α-phase volume decrease leads to hybridization enhancement and hence their complete delocalization. Alternative explanation [291, 292] was based on Kondo model. Stronger hybridization of f-electrons in α-phase gives larger Kondo temperature parameter value comparing with γ-phase. In the result in α-phase local moments are completely screened by Kondo exchange and do not reveal themselves in magnetic experiments while in γ-phase the screening is absent.

In all those theories uncontrolled assumptions were done for parameters values and only direct solution of the problem where correlated f-electrons hybridize with *spd*-states and each other can clarify this issue. In [293] $LDA+DMFT(QMC)$ method was used to study $\alpha - \gamma$ transition in Ce. In problem Hamiltonian complete set of orbitals including f as well as *spd* states was included.

In Fig. 6.26 densities of state are shown obtained in LDA calculation for cerium in γ-phase. Fermi level crosses lower edge of partially filled narrow (width $\approx$1 eV) f-band. Coulomb parameter U value from constrain DFT calculations (Sect. 2.2.5) is equal to 6 eV. So large value of Coulomb interaction to band width ratio $U/W \approx 6$ means that cerium f states are in strongly correlated regime.

In Fig. 6.27 (left side) $LDA + DMFT(QMC)$ spectral functions $A(\omega)$ are presented for various volume values. For $V = 45\text{Å}^3$ in $A(\omega)$ only Hubbard bands are observed so that f-electrons are fully localized. At $V = 34\text{Å}^3$ that corresponds to γ-phase quasiparticle states appear at Fermi level but their spectral weight (the strength of Kondo peak) is very weak. At volume value

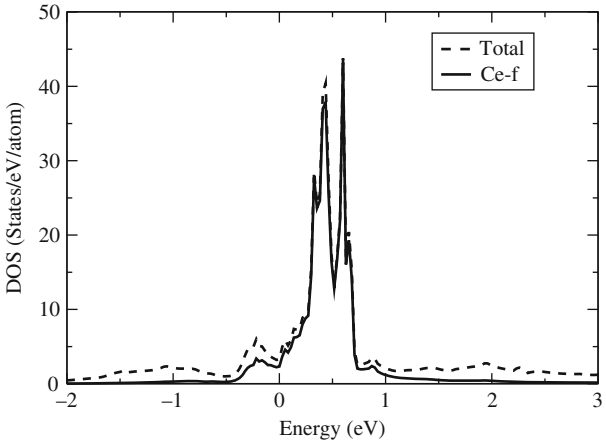

Fig. 6.26. Total (*solid line*) and $4f$-partial (*dashed line*) densities of states for cerium in γ-phase from *LDA* calculations

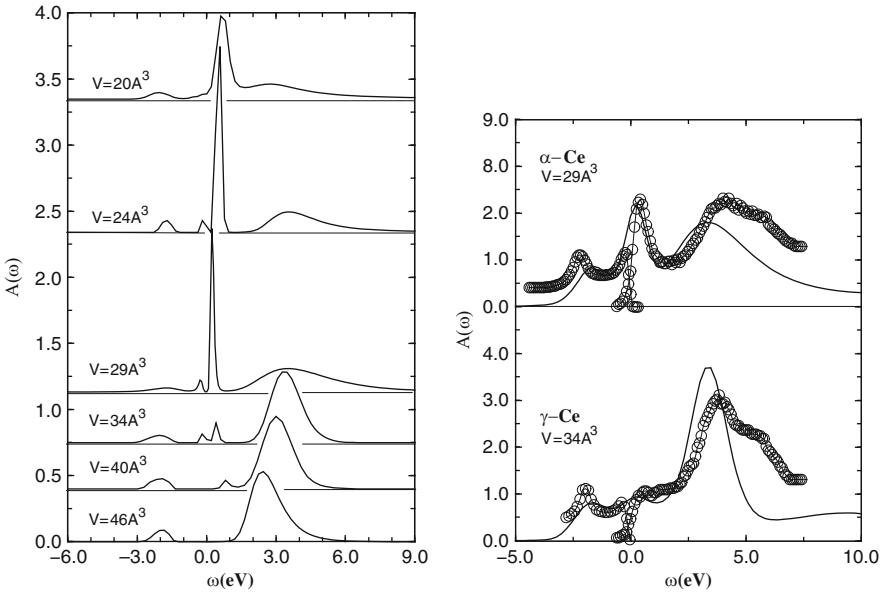

Fig. 6.27. *Left*: evolution with volume of spectral function $A(\omega)$ calculated in $LDA+DMFT(QMC)$ for Ce [293] at $T = 632$ K. Central quasiparticle peak spectral weight drastically decreases with volume increase from $V = 29$ to 34Å^3 corresponding to α-γ transition. *Right*: comparison of spectral calculated in $LDA + DMFT(QMC)$ with experimental photoemission and inverse photoemission spectra for α (*upper part*) and γ (*lower part*) phases [294]

$V = 29\text{Å}^3$ corresponding to α-phase intensity of the peak on Fermi level is strongly enhanced due to spectral weight transfer from Hubbard bands. With further compression till $V = 20\text{Å}^3$ nearly all spectral weight is in quasiparticle band with weak shoulders at Hubbard bands positions.

In right side of Fig. 6.27 comparison is shown of experimental and theoretical spectra obtained from $A(\omega)$ by multiplying on Fermi distribution function $f_F(\omega)$ for photoemission spectra and on $1 - f_F(\omega)$ for inverse photoemission spectra for α (upper part) and γ (lower part) phases [294]. In going from γ to α phase a strong increase of intensity for peak on Fermi level is observed in both theoretical and experimental spectra.

A total energy as a function of volume calculations for various temperatures was also calculated in [293]. In Fig. 6.28 corresponding $LDA + DMFT(QMC)$ curves for $E(V)$ are shown (solid lines) together with $E(V)$ curves obtained in polarized unrestricted Hartree-Fock calculations for the same Hamiltonian (dashed line). A difference between $DMFT$ and Hartree-Fock results can be considered as pure correlation effect. One can see that all Hartree-Fock curves have only one minimum at volume values higher than γ phase volume. $LDA + DMFT(QMC)$ curves for $E(V)$ at higher temperatures also have minimum at γ phase volume value. With temperature lowering at first a bend in the curve appears near α volume value and at lowest calculations temperature this bend transforms into minimum.

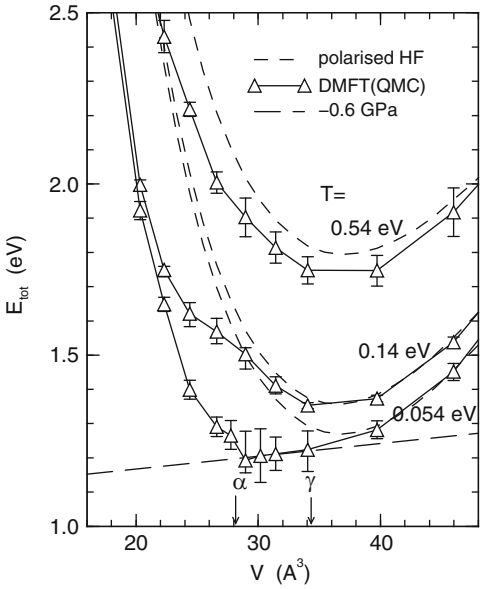

Fig. 6.28. Total energy for Ce calculated in $LDA + DMFT(QMC)$ (*solid line*) and in polarized Hartree-Fock approximation (*dashed line*) [293] for three temperature values. *Long dashed line* corresponds to pressure for α-γ transition: $E = -P_{\text{exp}}V$

Such minimal temperature $T = 0.054\,eV \approx 600\,\mathrm{K}$ is significantly higher than experimental transition temperature but qualitatively $LDA + DMFT(QMC)$ method describes successfully α-γ transition in cerium metal.

6.5 Manganites

6.5.1 Manganites Physical Properties

Manganites with perovskite crystal structure attract great interest due to colossal magnetoresistance effect (see [295–297]). General chemical formula for these materials is $\mathrm{T}_{1-x}\mathrm{D}_x\mathrm{MnO}_3$ where T is three-valence rare-earth ion ($\mathrm{T} = \mathrm{La}, \mathrm{Pr}, \mathrm{Nd}, \ldots$) and D is two-valence alkaline-earth ion ($\mathrm{D} = \mathrm{Ca}, \mathrm{Sr}, \ldots$). In Fig. 6.29 perovskite crystal structure is shown with six oxygen atoms octahedron surrounding Mn ion.

Manganites have complex phase diagram. Typical example is shown in Fig. 6.30. While ending members of $\mathrm{T}_{1-x}\mathrm{D}_x\mathrm{MnO}_3$ series for $x = 0$ and $x = 1$ are insulators there is a broad range of doping values where ferromagnetic metallic (FM) state is realized. Long ago there was proposed [261] that the source of ferromagnetism in these materials is not standard superexchange between Mn ions that should be antiferromagnetic but so called "double exchange" that has kinetic energy nature and is formed by itinerant electrons interacting via Hund exchange with local magnetic moments on Mn ions.

Colossal magnetoresistance effect with its great application potential for electronics consists in strong suppression of electrical resistivity $R(H)$ with applying magnetic field for materials in FM area of phase diagram. The effect measure is quantity $\eta = \frac{R(0)-R(H)}{R(H)}$ that can have value of tens percents or even hundreds percents (Fig. 6.31). $R(T)$ curve strongly depends on doping value. As one can see from Fig. 6.31a at small doping values $\mathrm{La}_{1-x}\mathrm{Sr}_x\mathrm{MnO}_3$ is insulator and for $x > 0.15$ it is metal. For all x values $R(T)$ maximum is near Curie temperature T_c. Magnetoresistivity effect is illustrated in Fig. 6.31b: in field $B = 15T$ resistivity near T_c falls two times. In general magnetoresistivity effect is due to magnetic moments ordering in the system with external magnetic field that results in decreasing electrons scattering on magnetic fluctuations. The closer temperature T is to T_c the stronger effect should be.

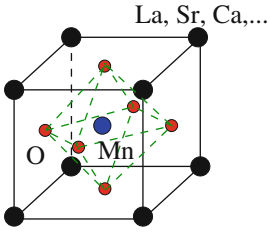

Fig. 6.29. Perovskite crystal structure for manganites

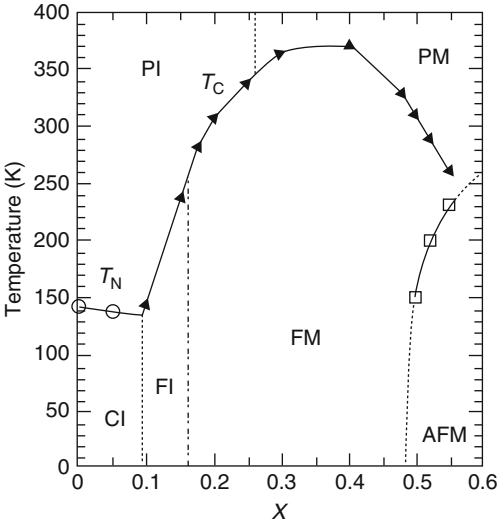

Fig. 6.30. Phase diagram for $La_{1-x}Sr_xMnO_3$ on plane temperature-doping. PI is paramagnetic insulator, PM – paramagnetic metal, CI – canted magnetic structure, FM – ferromagnetic metal, AFM – antiferromagnetic metal, T_c – Curie temperature; T_N – Neel temperature [296]

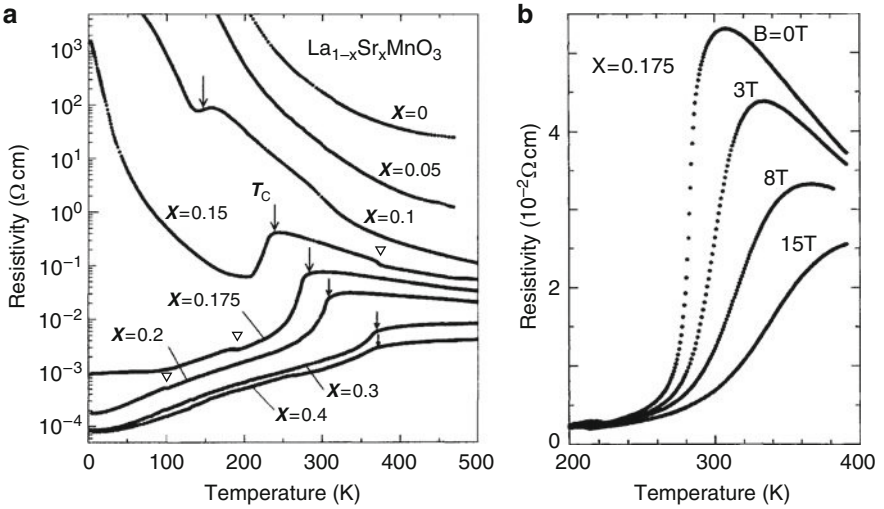

Fig. 6.31. Resistivity of $La_{1-x}Sr_xMnO_3$ as a function of temperature (**a**) at various doping values and (**b**) for various magnetic field values and fixed doping [298]

However, decreasing of $R(T)$ for $T > T_c$ is a results of electronic structure peculiarities and requires detailed theoretical study.

Manganites properties were considered in Furukawa works [262–264] and described in Sect. 5.4 on the basis of *sd*-model with ferromagnetic coupling (double exchange model). *DMFT* calculations gave correct behavior of electrical resistivity, magnetization, and optical conductivity but only qualitative agreement was found with experimental data. For example it was shown that Curie temperature depends on doping as $T_c \sim x(1-x)$ but T_c value was strongly overestimated, nearly an order of magnitude larger than experimental value. Millis et al. [295] have shown that to get quantitative agreement with experiment double exchange model should be extended to take into account electron–lattice interaction, especially Jahn-Teller effect and peculiarities of manganites electronic structure.

6.5.2 Electronic Model for Manganites

Mn ions with local magnetic moments are in cubic crystal field due to octahedral surrounding and hence 5-degenerate $3d$ level is split in two multiplets: three t_{2g} orbitals (d_{xy}, d_{yz}, d_{zx}) and two e_g orbitals $(d_{x^2-y^2}, d_{3z^2-r^2})$. t_{2g} level is lower in energy and is occupied by three electrons that have parallel spins due to Hund exchange interaction thus forming localized Mn ion spin $S = 3/2$. Two e_g orbitals have $1 - x$ electrons per Mn ion.

Jahn and Teller have shown that cubic symmetry with two degenerate e_g orbitals is unstable and lattice distortion should happen that lowers system energy. Hence in $LaMnO_3$ cubic perovskite structure is distorted and e_g level is split. In addition to that one should take into account electrons interaction with dynamic phonons of oxygen ions surrounding Mn because such phonons can lead to dynamical transition among e_g states. Corresponding local modes are shown in Fig. 6.32.

That results in the following model for manganites characterized by Hamiltonian [300]:

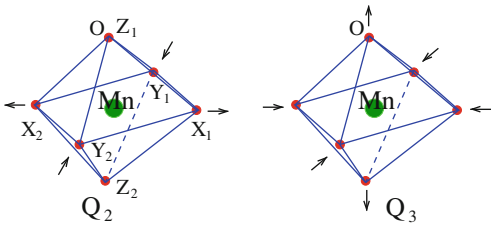

Fig. 6.32. Oxygen atoms vibrations for two Jahn-Teller modes Q_2 and Q_3 [299]

$$H = \sum_{ij\sigma}\sum_{lm} t_{ij}^{lm}\hat{c}_{il\sigma}^{+}\hat{c}_{jm\sigma} - J\sum_{im\sigma\sigma'}\mathbf{S}_i\hat{c}_{im\sigma}^{+}\sigma_{\sigma\sigma'}\hat{c}_{im\sigma'}$$
$$+ U\sum_{im}\hat{n}_{im\uparrow}\hat{n}_{im\downarrow} + \sum_{i\sigma\sigma'}(U' - \delta_{\sigma\sigma'}J)\hat{n}_{i1\sigma}\hat{n}_{i2\sigma'}$$
$$+ g\sum_{i\sigma}\sum_{m_1m_2}\hat{c}_{im_1\sigma}^{+}(Q_2\tau^z + Q_3\tau^x)_{m_1m_2}\hat{c}_{im_2\sigma} + \sum_a(\frac{1}{2}P_a^2 + \frac{1}{2}\Omega^2Q_a^2). \tag{6.5.20}$$

Here first line is double exchange Hamiltonian with degenerate e_g orbitals (indexes l and m mark orbitals $d_{3z^2-r^2}$ and $d_{x^2-y^2}$). The second line describes Coulomb and exchange interaction of electrons on Mn ion and third line corresponds to electrons interaction with Jahn-Teller modes Q_2 and Q_3 and these modes energy. In the last term index a marks these modes; Ω is frequency of localized mode that are supposed to be degenerate, Q_a (i.e., Q_2 and Q_3) are normal vibrations and P_a is corresponding momentum. Pauli matrices τ^x and τ^z describe transitions between e_g orbitals and their splitting due to oxygen ions vibrations. Electron–phonon interaction structure in H was proposed by Kanamori [301].

6.5.3 *QMC* for Systems with Electron–Lattice Coupling

To solve auxiliary single impurity problem corresponding to Hamiltonian (6.5.20) Quantum Monte Carlo method can be used generalized for lattice degrees of freedom and electron–lattice interaction [299]. For nondegenerate Hubbard model *QMC* method in Hirsch-Fye algorithm was described in Sect. 3.2. Before going to *QMC* for complicated Hamiltonian (6.5.20) we consider at first simple model for noninteracting nondegenerate electrons coupled to local phonons. Later we follow [299].

We consider Hamiltonian

$$H = \sum_{ij\sigma} t_{ij}\hat{c}_{i\sigma}^{+}\hat{c}_{j\sigma} - g\sum_i \hat{n}_i\Phi_i + \frac{1}{2}\sum_i(\pi_i^2 + \Omega^2\Phi_i^2). \tag{6.5.21}$$

Here Φ_i and π_i are normal coordinates and momenta for atomic displacements. Second term in H describes electrons interaction with vibration modes and the third term presents Hamiltonian for harmonic local lattice vibrations.

In *DMFT* effective action for auxiliary single impurity problem should be defined and we choose it as:

$$S = -\int_0^\beta d\tau d\tau' \sum_\sigma \hat{c}_\sigma^{+}(\tau)\mathcal{G}_0^{\sigma^{-1}}(\tau - \tau')\hat{c}_\sigma(\tau')$$
$$-g\int_0^\beta d\tau\hat{n}(\tau)\Phi_\tau + \frac{1}{2}\int_0^\beta d\tau\left[(\Phi')^2 + \Omega^2\Phi_\tau^2\right], \tag{6.5.22}$$

where $\Phi_\tau \equiv \Phi(\tau)$, $\Phi_\tau^{'} \equiv d\Phi(\tau)/d\tau$. Partition function and Green function are written as functional integrals over Grassmann variables $c_\sigma(\tau)$ and $c_\sigma^{+}(\tau)$ for

electrons and Φ_τ for phonons:

$$Z = \int \mathcal{D}[c^+]\mathcal{D}[c]\mathcal{D}\Phi \mathrm{e}^{-S}, \tag{6.5.23}$$

$$G(\tau) = -\frac{1}{Z}\int \mathcal{D}[c^+]\mathcal{D}[c]\mathcal{D}\Phi c_\sigma(\tau)c_\sigma^+(0)\mathrm{e}^{-S}. \tag{6.5.24}$$

As it was described in Sect. 3.2.1 we divide time interval $0 \le \tau \le \beta$ on L slices with discrete time values $\tau_l = (l-1)\Delta\tau$ where $\Delta\tau = \beta/L$. Then instead of formulas (6.5.23) and (6.5.24) the corresponding quantities can be introduced with fixed set of phonon fields $\{\Phi_l\}$:

$$Z_{\{\Phi_l\}} = \int \mathcal{D}[c^+]\mathcal{D}[c]\mathrm{e}^{-S_{\{\Phi_l\}}}, \tag{6.5.25}$$

$$G^\sigma_{mn}(\{\Phi_l\}) = -\frac{1}{Z_{\{\Phi_l\}}}\int \mathcal{D}[c^+]\mathcal{D}[c]c_{m\sigma}c^+_{n\sigma}\mathrm{e}^{-S_{\{\Phi_l\}}}, \tag{6.5.26}$$

where $c_{m\sigma} \equiv c_\sigma(\tau_m)$

$$S_{\{\Phi_l\}} = -\sum_{lm}^{L}\sum_{\sigma} c^+_{l\sigma}\left(\mathcal{G}^\sigma_0\right)^{-1}_{lm} c_{m\sigma} - g\Delta\tau\sum_{l}^{L} n_l\Phi_l + K(\{\Phi_l\}), \tag{6.5.27}$$

$$K(\{\Phi_l\}) = \frac{\Delta\tau}{2}\sum_{l}^{L}\left[\left(\frac{\Phi_{l+1}-\Phi_l}{\Delta\tau}\right)^2 + \Omega^2\Phi_l^2\right]. \tag{6.5.28}$$

Impurity GF G^σ_{mn} is given by expression

$$G^\sigma_{mn} = \sum_{\{\Phi_l\}}\frac{Z_{\{\Phi_l\}}}{Z}G^\sigma_{mn}(\{\Phi_l\}). \tag{6.5.29}$$

Quantity $Z_{\{\Phi\}}/Z$ is a measure of probability for configuration $\{\Phi_l\}$. Functional integrals over $\Phi(\tau)$ in expressions (6.5.23) and (6.5.24) come then to sums over discretized configurations $\{\Phi_l\}$ that could be calculated numerically with *QMC*. In these terms single-site GF is written as:

$$G^\sigma_{mn} = \frac{\sum_{\{\Phi_l\}} G^\sigma_{mn}(\{\Phi_l\})}{\sum_{\{\Phi_l\}} 1}. \tag{6.5.30}$$

Now we consider full model with Hamiltonian (6.5.20). Partition function and single-site electronic GF can be expressed as functional integrals over all fields:

$$Z = \int \mathcal{D}[\mathbf{S}]\mathcal{D}[c^+]\mathcal{D}[c]\mathcal{D}[Q_2]\mathcal{D}[Q_3]\mathrm{e}^{-S}, \tag{6.5.31}$$

$$G^{\mu\nu\sigma}_{mn} = -\frac{1}{Z}\int \mathcal{D}[\mathbf{S}]\mathcal{D}[c^+]\mathcal{D}[c]\mathcal{D}[Q_2]\mathcal{D}[Q_3]c_{m\mu\sigma}c^+_{n\nu\sigma}\mathrm{e}^{-S}. \tag{6.5.32}$$

Here indexes μ and ν note two e_g orbitals and have two values: 1 and 2. Due to rotational invariance of Hamiltonian integral over vector $\mathbf{S}$ orientations can be replaced by sum over two opposite directions $S^z = \pm[\mathbf{S}]$.

In integration over Grassmann variables we can use Hubbard–Stratonovich-Hirsch transformation (3.2.58) to linearize Coulomb term in Hamiltonian. For all inter and intra orbital interactions that gives six auxiliary Ising fields (see Sect. 3.2). These discrete fields can be combined with fields corresponding to Jahn-Teller modes. In the result partition function and single-site GF are presented in the form:

$$Z = \sum_{\{S^l,Q^l\}} Z_{\{S^l,Q^l\}}, \tag{6.5.33}$$

$$G^{\mu\nu\sigma}_{mn} = \sum_{\{S^l,Q^l\}} \frac{Z_{\{S^l,Q^l\}}}{Z} G^{\mu\nu\sigma}_{mn}(\{S^l,Q^l\}), \tag{6.5.34}$$

$$Z_{\{S^l,Q^l\}} = \int \mathcal{D}[c^+]\mathcal{D}[c]\mathrm{e}^{-S_{\{S^l,Q^l\}}}, \tag{6.5.35}$$

$$G^{\mu\nu\sigma}_{mn}(\{S^l,Q^l\}) = -\frac{1}{Z_{\{S^l,Q^l\}}}\int \mathcal{D}[c^+]\mathcal{D}[c]c_{m\sigma}c^+_{n\sigma}\mathrm{e}^{-S_{\{S^l,Q^l\}}}. \tag{6.5.36}$$

Integration over $\mathbf{S}$ directions is omitted because we assume ferromagnetic state with saturated magnetic moment.

Effective action in (6.5.35) and (6.5.36) is a sum of terms:

$$S(\{S^l,Q^l\}) = S_0 + K_Q + S_J + S_Q + S_U, \tag{6.5.37}$$

where

$$\begin{aligned}
S_0 &= -\sum_{lm,\mu\nu\sigma} c^+_{l\mu\sigma}(\mathcal{G}^\sigma_0)^{-1}_{lm,\mu\nu}c_{m\nu\sigma},\\
K_Q &= \frac{\Delta\tau}{2}\sum_{la}\left[\left(\frac{Q^{l+1}_a - Q^l_a}{\Delta\tau}\right)^2 + \Omega^2(\Omega^l_a)^2\right],\\
S_J &= -J|\mathbf{S}|\Delta\tau\sum_{l\mu}(n_{l\mu\uparrow} - n_{l\mu\downarrow}),\\
S_Q &= -g\Delta\tau\sum_{l\mu\nu\sigma} c^+_{l\mu\sigma}(Q^l_2\tau^x + Q^l_3\tau^z)c_{l\nu\sigma},\\
S_U &= -\sum_l\left[\lambda_U S^l_U(n_{l1\uparrow} - n_{l1\downarrow}) + \lambda_U\tilde{S}^l_U(n_{l2\uparrow} - n_{l2\downarrow})\right]\\
&\quad -\sum_{l\sigma}\left[\lambda_V S^{l\sigma}_V(n_{l1\sigma} - n_{l2\bar{\sigma}}) + \lambda_{V-F}S^{l\sigma}_{V-F}(n_{l1\sigma} - n_{l2\sigma})\right].
\end{aligned} \tag{6.5.38}$$

Here $\lambda_x = arccosh(\mathrm{e}^{x\Delta\tau/2})$; $\{S_U^l, \tilde{S}_U^l, S_V^{l\sigma}, S_{V-F}^{l\sigma}\}$ are Ising auxiliary fields for $\{Un_{m\uparrow}n_{m\downarrow}, Vn_{1\sigma}n_{2\bar{\sigma}}, (V-F)n_{1\sigma}n_{2\sigma}\}$ correspondingly. We remind that $Q_a^l \equiv Q_a(\tau_a)$ and $c_{m\nu\sigma} \equiv c_{\nu\sigma}(\tau_m)$.

Effective action S is diagonal in spin but has off-diagonal matrix elements between e_g orbitals and hence 2×2 matrix should be introduced for every time τ_l:

$$V^{l\sigma} = V_Q^{l\sigma} + V_S^{l\sigma}, \tag{6.5.39}$$

where

$$V_Q^{l\sigma} = -\begin{pmatrix} g\Delta\tau Q_3^l & g\Delta\tau Q_2^l \\ g\Delta\tau Q_2^l & -g\Delta\tau Q_l^3 \end{pmatrix} \tag{6.5.40}$$

from phonon contribution S_Q and

$$V_S^{l\sigma} = -\begin{pmatrix} \lambda_U S_U^l\sigma + \lambda_V S_V^{l\sigma} + \lambda_{V-F} S_{V-F}^{l\sigma} & 0 \\ 0 & \lambda_U \tilde{S}_U^l\sigma - \lambda_V S_V^{l\bar{\sigma}} - \lambda_{V-F} S_{V-F}^{l\sigma} \end{pmatrix} \tag{6.5.41}$$

from Coulomb contribution S_U.

The further *QMC* calculation scheme is the same as described in Sect. 3.2 for nondegenerate Hubbard model. The same equations are valid connecting *GF* for some Ising fields configuration $\{S^l, Q^l\}$ with configuration $\{\bar{S}^l, \bar{Q}^l\}$ that differs from previous one by sign change of only one Ising field. If we denote

$$g_{mn}^{\mu\nu\sigma} = -G_{mn}^{\mu\nu\sigma}(\{S^l, Q^l\})$$
$$\bar{g}_{mn}^{\mu\nu\sigma} = -G_{mn}^{\mu\nu\sigma}(\{\bar{S}^l, \bar{Q}^l\}).$$

Then quantities g and $\bar{g}$ are connected by equation

$$\bar{g}_{mn}^{\sigma} = g_{mn}^{\sigma} + (g_{ml}^{\sigma} - \delta_{ml})\Delta_0 \left[1 + (1 - g_{ll}^{\sigma})\Delta_0\right]^{-1} g_{\mathrm{ln}}^{\sigma}. \tag{6.5.42}$$

where

$$\Delta_0^{\sigma} = \mathrm{e}^{\tilde{V}^{\sigma}} \mathrm{e}^{-V^{\sigma}} - 1. \tag{6.5.43}$$

This equation leads to the probability ratio of new configuration realization with respect to previous one:

$$R = \mathrm{e}^{-K_{\bar{Q}} - K_Q} \prod_{\sigma} det(1 + (1 - g_{ll}^{\sigma})\Delta_0). \tag{6.5.44}$$

Here determinant is calculated over orbital indexes only. In *QMC* calculations every configuration change denoted by line above includes shift of all bosonic fields and spin flip of one of arbitrary chosen Ising fields for time index l. Relations (6.5.42)–(6.5.44) are generalization of corresponding relation of Sect. 3.2.

6.5.4 $LDA + DMFT(QMC)$ Results for $La_{1-x}Sr_xMnO_3$

For $LaMnO_3$ compound the following Coulomb interaction parameters values were chosen: $U' = 3.5\,eV$ from [302], $J = 0.75\,eV$ calculated from energy splitting between spin states $\uparrow$ and $\downarrow$ from $LSDA$ calculations. Localised spin of t_{2g} states $S = 3/2$ was considered as classical spin.

Calculated spectra for e_g orbitals are presented in Fig. 6.33. On upper panels dispersion curves are shown for symmetrric directions in cubic and orthorhombic lattices calculated in LDA. Fermi level for nonmagnetic LDA calculations is below all e_g bands and crosses t_{2g} band (not shown on the figure) giving metallic ground state. x is dimensionless parameter equal to ratio of crystal field splitting of e_g states to hopping parameter $t \approx W/6$ where W is band width for e_g states. On middle panels $LDA+U$ calculation results are shown with Fermi level in the gap between e_g states split by Coulomb interaction. That gives insulating ground state but it is known that $LDA+U$ method overestimates correlation effects. On lower panels $LDA + DMFT$ calculation

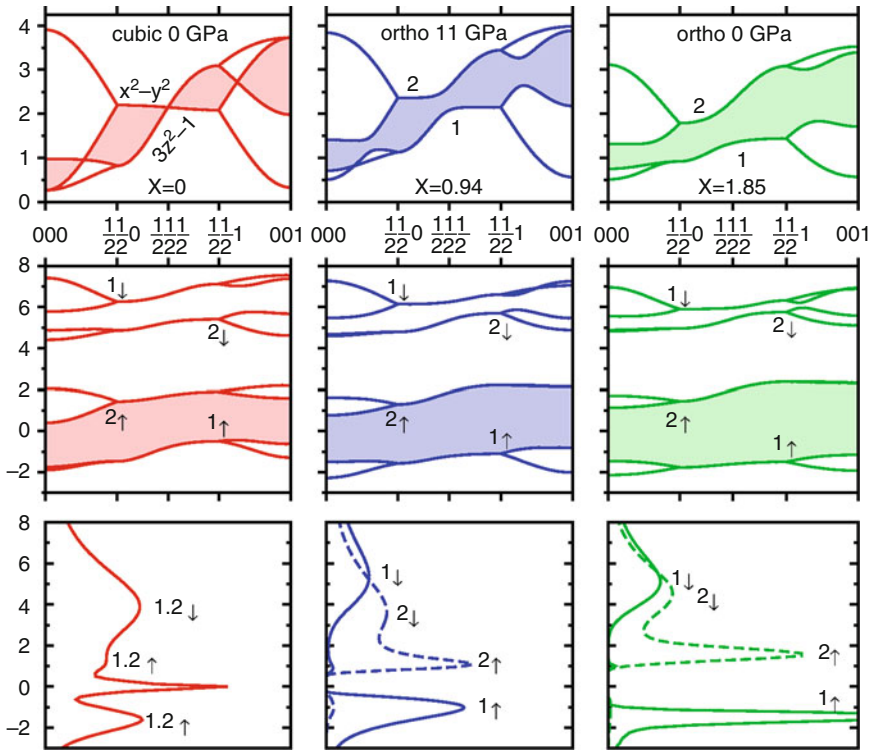

Fig. 6.33. Band structure of $LaMnO_3$ for cubic (*left panel*) and orthorhombic (*right panel*) crystal structures by LDA (*upper part*), $LDA+U$ (*center*) and $LDA+DMFT$ (*lower part*) [302, 303]. Energies are in eV, wave vectors in π/a units. Fermi level is in $\omega = 0$

results are presented. They show that in cubic phase $LaMnO_3$ should be a metal while in orthorhombic phase it is an insulator with a gap $\approx 2\,\mathrm{eV}$ in agreement with experimental data. Hence a correct description of manganite $LaMnO_3$ in $LDA + DMFT$ calculation can be achieved with simultaneous inclusion of Coulomb correlations and electron–lattice interaction.

Please note arrows and numbers near dispersive curves and densities of state in Fig. 6.33. Arrows mark spin direction and numbers are for orbitals $d_{3z^2-r^2}$ and $d_{x^2-y^2}$. In $LDA + DMFT$ t_{2g} states are not included explicitly but only as localized spins interacting with e_g-electrons. Due to this exchange interaction e_g-electrons are spin polarized as one can see in central lower panel in Fig. 6.33. In right lower panel dashed line is density of states for $d_{x^2-y^2}$ orbitals and solid line is for $d_{3z^2-r^2}$ orbitals. On the left panel $d_{x^2-y^2}$ and $d_{3z^2-r^2}$ density of states are degenerate.

In Figs. 6.34–6.36 calculation results are presented for local density of states with electron–lattice interaction taken into account (lattice model Hamiltonian (6.5.20)). Model parameter values were:

$$U = 5\,\mathrm{eV},\ F = 0.75\,\mathrm{eV},\ V = U - 2F = 3.5\,\mathrm{eV},\ 2JS = 2.7\,\mathrm{eV},\ W = 3.6\,\mathrm{eV}.$$

From Raman spectroscopy phonon frequency $\Omega = 0.07\,\mathrm{eV}$ was obtained in [304]. Coupling constant g in calculations was free parameter. In contrast to LDA calculations where static Jahn-Teller effect was taken into account inclusion of phonon in Hamiltonian (6.5.20) allowed to consider effect of dynamic Jahn-Teller distortions.

Spectral function in Fig. 6.34 has three-peak structure analogous to those shown in lower panel of Fig. 6.33 for orthorhombic phase. Energy gap value

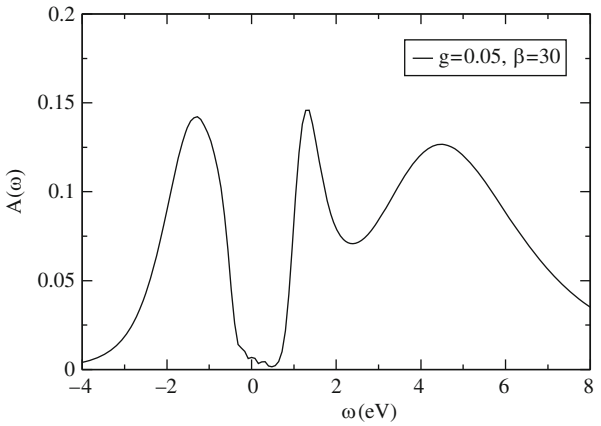

Fig. 6.34. Local spectral density in paramagnetic phase of $LaMnO_3$ for model including electron–phonon interaction with parameter values: $g = 0.05\ (\mathrm{eV})^{-3/2}$, $W = 3.6\,\mathrm{eV}$ and $\beta = 30$. In QMC calculation time slice value is $\Delta\tau = 0.35$ so that number of time slices for interval $0 < \tau < \beta$ was $L = 120$ [299]

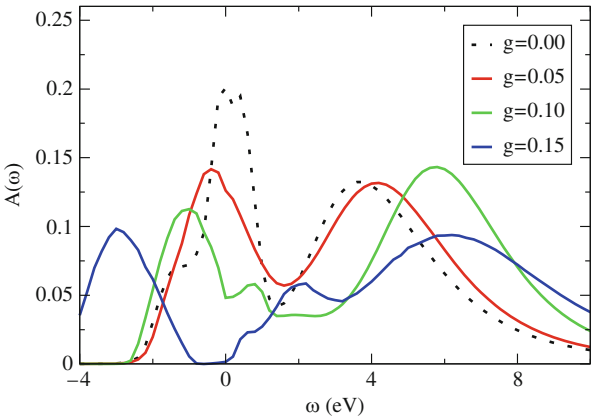

Fig. 6.35. Local spectral density in paramagnetic phase for various values of electron–phonon constant g and model parameters: $\beta = 16$, $n = 0.8$ [299]

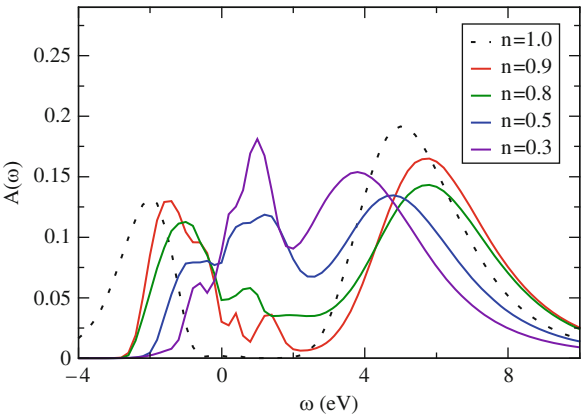

Fig. 6.36. Local spectral density for various values of electron concentration n and parameters: $\beta = 16$, $g = 0.10$ [299]

agrees with experiment that gives $LaMnO_3$ as insulator but in Fig. 6.34 there is small final density of states near $\omega = 0$.

Special interest present calculation results for doped manganites in concentration x interval where ferromagnetic metallic state is formed. In Fig. 6.35 results for electronic concentration $n = 0.8$ (corresponding to $x = 1 - n = 0.2$) are shown for various values of Jahn-Teller coupling constant value. Without Jahn-Teller coupling spectrum has broad quasiparticle peak on Fermi level and the system is metallic. With g increasing quasiparticle peak is gradually suppressed and spectral weight on Fermi level decreases with a dip in $A(\omega)$ near $\omega = 0$ and for large g values a gap appears. Lower Hubbard band is shifted to lower energies while upper Hubbard band shifts higher in energy.

Fig. 6.36 shows evolution of spectral function with doping increase. Stoichiometric compound ($n = 1$) is a good insulator. For small doping $x = 0.1$ states in the gap appear so that pseudogap is formed that becomes completely filled at $n = 0.3$ ($x = 0.7$).

Analogous behavior of spectra is observed in optical conductivity $\sigma(\omega)$. Fig. 6.37 shows optical conductivity calculated for paramagnetic phase at various electron concentrations. Spectra have two peaks at $1 - 2\,\text{eV}$ and $6\,\text{eV}$ and with doping increase low-energy peak shifts down in agreement with experimental data (Fig. 6.38).

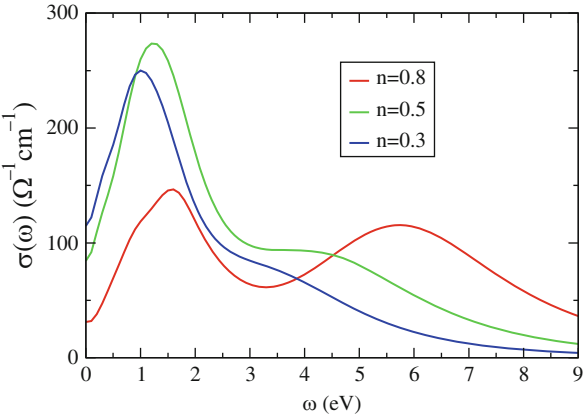

Fig. 6.37. Optical conductivity in paramagnetic phase at various values of electron concentration n; $\beta = 30$, $g = 0.10$ [299]

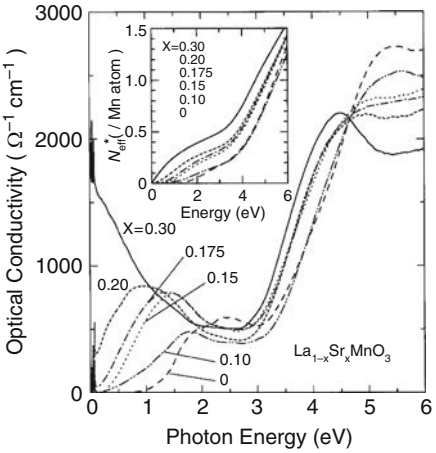

Fig. 6.38. Optical conductivity of $La_{1-x}Sr_xMnO_3$ at room temperature and dopings: ($x = 0$; 0.10; 0.15; 0.175; 0.20; 0.30 [305])

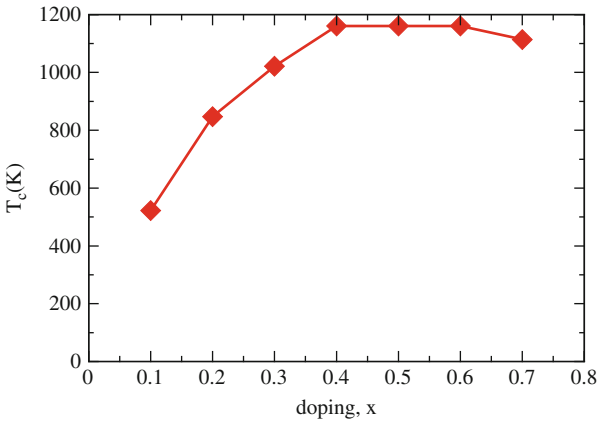

Fig. 6.39. Curie temperature T_c as a function of doping for $g = 0.10$ [299]

From Fig. 6.38 one can see that phase transition from insulator to metal happens for doping values between $x = 0.175$ and 0.20. Doped compounds are insulating for $(0 \leq x < 0.175)$ and metallic for $x = 0.3$. Low-energy part of optical conductivity is strongly suppressed in insulating phase and Drude peak appears in metallic phase at $x > 0.3$. In insulating phase optical conductivity has two peaks: low-energy peak at $\omega \approx 1 - 2\,\text{eV}$ and high-energy peak at $\omega \approx 6\,\text{eV}$. That agrees with calculated $\sigma(\omega)$ curve shown in Fig. 6.37.

Let us consider now calculation results for Curie temperature T_c obtained from magnetic susceptibility temperature dependence $\chi(T)$. In Fig. 6.39 T_c as a function of doping is shown. Theoretical prediction for T_c at fixed coupling constant value agrees in form with phase diagram in Fig. 6.30 but the values are 2–3 times larger than experimental values. As one can see from Fig. 6.40 T_c depends strongly on electron–lattice coupling constant value. g variation from $g = 0.10$ (Fig. 6.39) to $g = 0.12$ corresponding to $\lambda = 2.0/2.2$ (Fig. 6.40) decreases T_c nearly two times. Results presented in Fig. 6.40 are close to earlier obtained by Millis et al. [265] and Edwards [306].

Comparison of calculated and experimental results gives a set of parameter values giving the best agreement for all observed properties in $La_{1-x}Sr_xMnO_3$ [299]:

$$W = 3.6\,\text{eV};\ U = 3.3\,\text{eV};\ 2JS = 2.7\,\text{eV};\ F = 0.75\,\text{eV};$$

$$\Omega = 0.07\,\text{eV};\ g = 0.077\ (\text{eV})^{3/2}.$$

Main conclusion from $LDA + DMFT(QMC)$ calculations for $La_{1-x}Sr_xMnO_3$ is the following: Jahn-Teller distortions of oxygen ions surrounding Mn are essential to understand manganites physics. However, these distortions alone are not enough to reproduce energy gap appearance in electronic spectrum. Only simultaneous effect of Coulomb correlations and Jahn-Teller distortions allows to understand stoichiometric and doped compounds. Microscopic model defined by Hamiltonian (6.5.20) is complete enough for perovskite manganites.

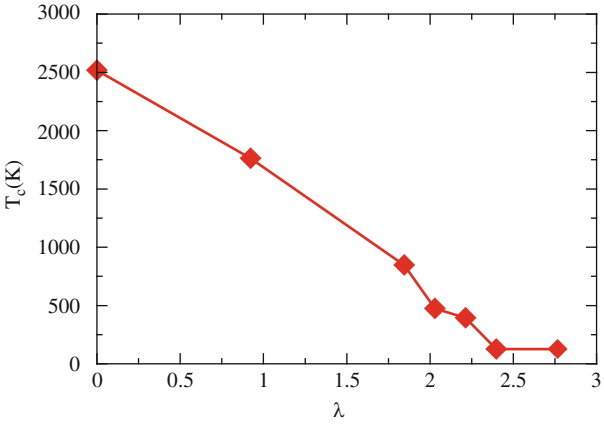

Fig. 6.40. Curie temperature as a function of dimensionless coupling parameter $\lambda = 9/\Omega\sqrt{t_0}$ at $n = 0.8$ and parameter values: $t_0 = 0.6\,\text{eV}$ and $\Omega = 0.07\,\text{eV}$ [299]

6.6 High-T_c Superconductors Based on Pnictides Compounds

Recently, high-temperature superconductivity ($T_c = 28{-}56\,\text{K}$) was discovered in a new class of materials: pnictides compounds with typical example LaOFeAs [307]. At stoichiometry LaOFeAs is not superconducting but below $T = 135\,\text{K}$ spin density wave state is observed. With substitution of part of oxygen by fluorine spin density wave formation is suppressed and $LaFeAsO_{1-x}F_x$ becomes superconducting.

LaOFeAs crystal structure consists from alternating layers of LaO and FeAs (see Fig. 6.41). Every iron ion is surrounded by four arsenic atoms forming tetrahedron that is slightly distorted by squeezing along c axis. Lanthanum and oxygen atoms are situated far enough in space from iron ions and it is reasonable to expect that their electronic states will be weakly hybridizing with d orbitals of Fe ions. Formal valence of Fe in LaOFeAs is $+2$ that corresponds to configuration d^6.

Density Functional (DFT) calculations for LaOFeAs [308] gave energy band structure in a good agreement with the earlier analysis. In Fig. 6.42 one can see partially filled band from $-2\,\text{eV}$ till $+2\,\text{eV}$ (Fermi level is at zero) formed by Fe-3d states. This band is separated from occupied band formed by oxygen and arsenic p states that is situated at $[-5.5\,\text{eV}/-2\,\text{eV}]$ interval. Fe-3d band filling corresponds to 6 electrons per Fe atom and the band has a width of $\approx 4\,\text{eV}$. It consists of two sub-bands separated by a deep depression with Fermi level situated on the upper slope of the lower sub-band. These sub-bands corresponds to bonding and antibonding combination of Fe-3d orbitals due to strong hybridization among Fe-3d state in FeAs layer.

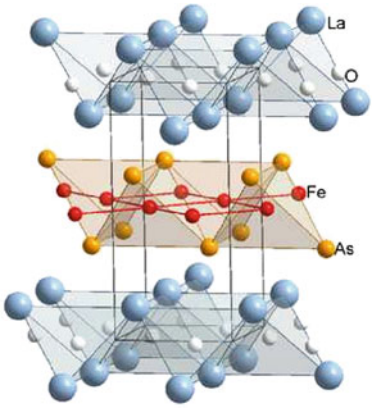

Fig. 6.41. Crystal structure of LaOFeAs

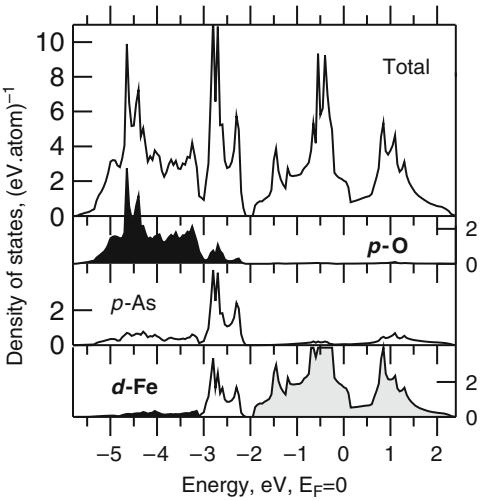

Fig. 6.42. Total and partial densities of states for LaOFeAs obtained in *DFT* calculations [308]

Tetrahedral surrounding of iron ion by As atoms leads to crystal field splitting of d-states on low-energy double degenerate set corresponding to representation e_g (orbitals $3z^2 - r^2$, xy) and high-energy triply degenerate t_{2g} representation set (orbitals $x^2 - y^2$, xz, yz). However, the actual value of crystal field splitting parameter is rather small $\Delta_{cf} \approx 0.25\,\text{eV}$. Slight tetragonal distortion results in additional small splitting and finally orbitals energies are: $\varepsilon_{3z^2-r^2} = 0.00$ eV, $\varepsilon_{xy} = 0.03$ eV, $\varepsilon_{xz,yz} = 0.26$ eV, $\varepsilon_{x^2-y^2} = 0.41$ eV. Those quantities are much smaller than the d-band width and all five d-orbitals form common band.

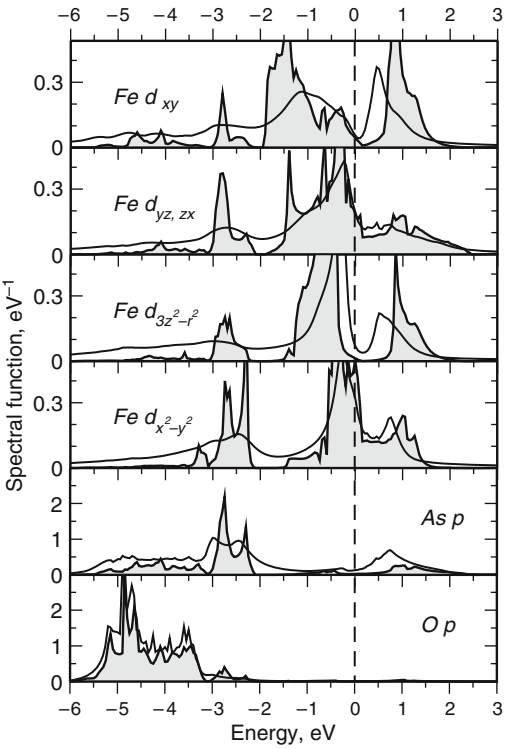

Fig. 6.43. Partial densities of states for Fe-3d, As-4p and O-2p states obtained within the *DFT* (filled areas) and *LDA* + *DMFT* orbitally resolved spectral functions [308]

The problem of Coulomb correlation influence of LaOFeAs electronic structure was investigated by $LDA + DMFT$ method in [308–310]. Constrain *DFT* calculations in [308] gave Coulomb interaction parameter values $U = 3.5\,\text{eV}$ and $J = 0.8\,\text{eV}$. We will present later results of $LDA + DMFT$ calculations for LaOFeAs [308] with these parameter values. In Fig. 6.43 spectral functions from $LDA + DMFT$ calculations are shown in comparison with noninteracting partial densities of states from *DFT* calculations.

Analysis of the curves in Fig. 6.43 leads to conclusion that LaOFeAs is not strongly correlated material. The general shape of spectra does not show either Kondo resonance at the Fermi level or Hubbard bands; the features in Fe-d spectral functions below $-2\,\text{eV}$ correspond to hybridization with As-p and O-p bands. The reason for such weak correlation effects in spite of the relatively large Coulomb interaction parameter value is a strong hybridization of the Fe-d orbitals with As-p states (see the peaks in the Fe-d spectral function in the $-2/-3\,\text{eV}$ range corresponding to mixing with As-p bands).

This hybridization provides an additional very efficient channel for screening of the Coulomb interaction among Fe-d electrons.

However, this material cannot be called "weakly correlated" either because quasiparticle states near Fermi level show significant renormalization comparing with noninteracting bands. The calculated values of the quasiparticle renormalization factor $Z = (1 - \frac{\partial \Sigma(\omega)}{\partial \omega}|_{\omega=0})^{-1}$ are found to be 0.56, 0.54, 0.45, 0.56 for d_{xy}, d_{yz} (or d_{zx}), $d_{3z^2-r^2}$, $d_{x^2-y^2}$ orbitals, respectively. These values agree well with the effective narrowing of the LDA+DMFT spectral functions comparing with *LDA DOS* (Fig. 6.43).

The effective mass enhancement values $m^* = Z^{-1}$ are 1.8, 1.59, 1.41, 2.17 for d_{xy}, d_{yz} (or d_{zx}), $d_{3z^2-r^2}$, $d_{x^2-y^2}$ orbitals, respectively, agree well with the mass enhancement factor between 1.7 and 2.1 reported in the dHvA study [311]. The $d_{x^2-y^2}$ orbital has the largest effective mass and exhibits the most evident narrowing of LDA spectrum (see Fig. 6.43). This orbital has its lobes directed into the empty space among nearest iron neighbors in the Fe plane. Hence, it has the weakest overlap, the smallest band width, and the largest U/W ratio.

In Fig. 6.44 the total LDA+DMFT spectral function calculated in *LDA + DMFT* [308] is shown together with the experimental photoemission data of [312]. One can see a good agreement between the theory and experiment. The sharp peak at the Fermi energy corresponds to a partially filled Fe-d band

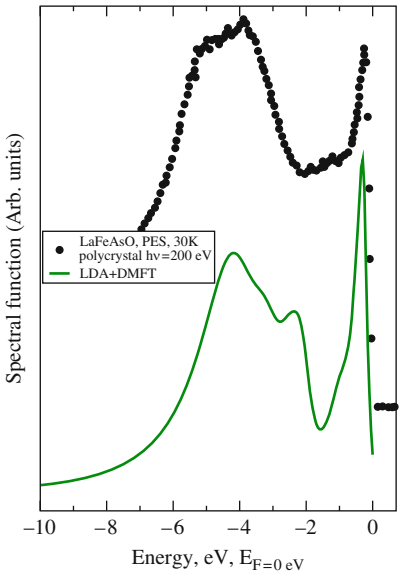

Fig. 6.44. Calculated total *LDA + DMFT* [308] spectral function (*solid line*) and experimental LaFeAsO photoemission *PES* spectrum (*circles*) from [312]

while the broad feature between −2 and 6 eV corresponds to the oxygen and arsenic p bands.

Quasiparticle band narrowing by a factor of $m^* \approx 2$ obtained in $LDA + DMFT$ [308] can be compared with Angle Resolved Photoemission Spectroscopy ($ARPES$) experiments. Good quality $ARPES$ data are available for $BaFe_2As_2$ compound [313] that has physical properties analogous to LaFeAsO. $LDA + DMFT$ calculations for this material were done in [314] and have shown results close to those for LaFeAsO in [308] with effective mass values $m^* = 2.05, 2.05, 2.05, 1.85$ for d_{xy}, d_{yz} (or d_{zx}), $d_{3z^2-r^2}$, $d_{x^2-y^2}$ orbitals.

In Fig. 6.45 the theoretical $\mathbf{k}$-dependent spectral function $A(\mathbf{k}, \omega)$ is compared with ARPES data of Liu et al. [313]. Both theory and experiment show dispersive bands crossing the Fermi level near the Γ and X points. Near Γ point in addition to that two weakly pronounced relatively flat bands can be seen in the region of −0.2/−0.3 eV and at −0.5/−0.6 eV. The shape and

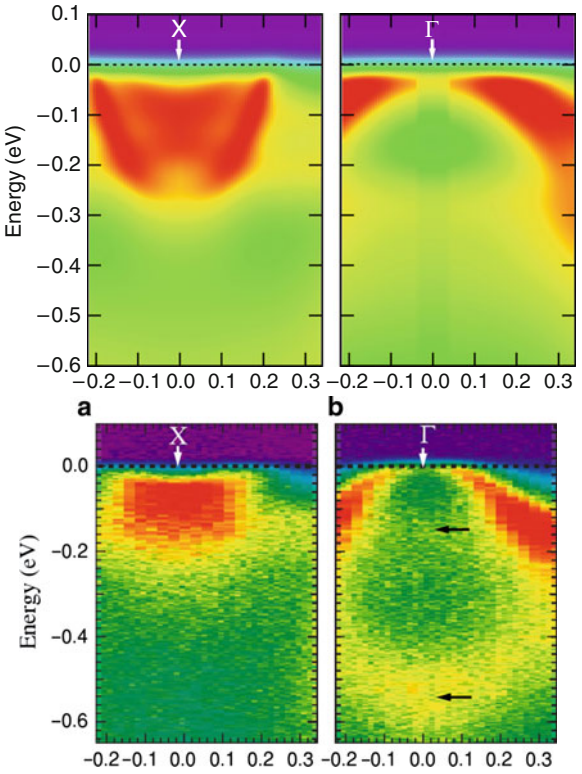

Fig. 6.45. The $\mathbf{k}$-resolved total spectral function A($\mathbf{k}$, ω) for $BaFe_2As_2$ calculated in $LDA + DMFT$ [314] along the Γ-X line in the Brillouin zone(*upper panels*). The left and right upper panels correspond to X and Γ point regions. The two lower panels represent the experimental ARPES intensity map of Liu et al. [313]

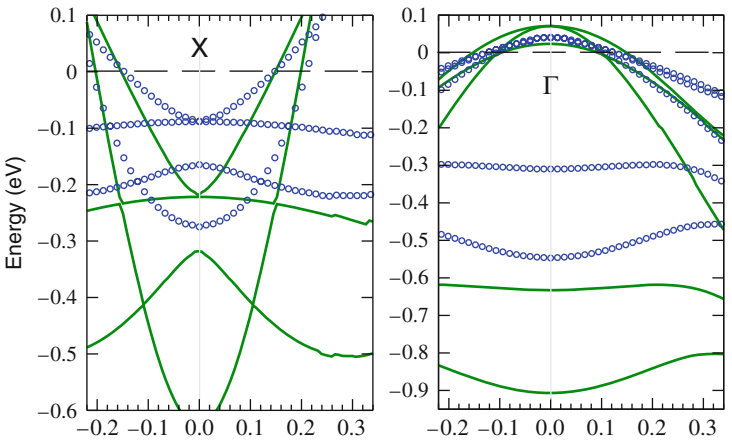

Fig. 6.46. Energy bands of $BaFe_2As_2$ along the Γ-X line in the Brillouin zone calculated in LDA+DMFT (*open circles*) and LDA (*solid lines*) [314]. The same regions of Γ-X direction as in Fig. 6.45 are used

size of electron and hole pockets centered, respectively, at X and Γ points in calculated spectral function are also in good agreement with ARPES data.

For more detailed analysis of the DMFT calculations results presented in Fig. 6.45 peaks position were calculated for the spectral function $A(\mathbf{k}, \omega)$. A set of these peaks positions as a function of wave vector $\mathbf{k}$ gives energy bands renormalized by correlation effects. In Fig. 6.46 the DMFT band structure is compared with noncorrelated bands obtained in LDA. Comparison of DMFT and LDA bands shows that the former can be with a good accuracy obtained from the latter by compressing approximately by factor of 2. This bands renormalization agrees well with a number of experimental studies for $BaFe_2As_2$ [315, 316].

6.7 The List of Strongly Correlated Materials Investigated by *DMFT* Method

In Chap. 6 we described *LDA + DMFT* calculation results for some typical examples of strongly correlated materials that illustrate the method and its ability to study physical properties influenced by Coulomb correlations. The choice of these examples naturally is defined by the authors preferences but we consider those materials as a representative set. Many other materials investigated by *LDA + DMFT* method are listed in Table 6.2. A reader can learn about these calculation results from the references in the table. In a third column basic physical properties studied in the corresponding work are mentioned. Example are density of states (spectral function) $\rho(\omega)$, optical conductivity $\sigma(\omega)$, static magnetic susceptibility $\chi(T)$, magnetization as a

Table 6.2. Materials studied by $LDA + DMFT$ method

Material	Physical problems	Calculated properties	References
d-systems			
V_2O_3	MI transition	See Sect. 6.2.2	[275, 317, 318]
VO_2	Peierls insulator at $T < T_c$	$\rho(\omega)$ for $T > T_c$ and $T < T_c$	[319, 320]
$SrVO_3$, $CaVO_3$	MI transition		[270, 272, 321–323]
$LaTiO_3$, $YTiO_3$	Orbital ordering	See Sect. 6.2.1	[324–328]
$SrTiO_3/LaTiO_3$	Kinks		
LiV_2O_4	Heavy fermions	See Sect. 6.2.3	[329–331]
$La_{1-x}Ca_xMnO_3$, $LaCoO_3$	Colossal magnetoresistance	$M(x)$, $M(T)$, $\rho(\omega)$, $\sigma(\omega)$ see Sect. 6.5	[262, 300, 302, 332, 333]
$Ca_{2-x}Sr_xRuO_4$	Unconventional superconductivity, orbital selective Mott transition	Normal phase: $\rho(\omega)$, $E(\mathbf{k})$	[187, 334–337]
Na_xCoO_2	Unconventional superconductivity, hole pockets in Fermi surface	Normal phase: $\rho(\omega)$, $E(\mathbf{k})$	[119, 338–342]
NiO, NiS , TaS_2	Charge transfer insulators	See Sect. 6.3.1	[283, 286, 343–348]
$KCuF_3$	Jahn-Teller effect	Lattice distortions	[349, 350]
FeSi	Correlated band insulator	$R(T)$, $\chi(T)$	[351]
MnO, FeO, CoO, Fe_2O_3	MI transition with a change of spin state	See Sect. 6.3.2	[288, 345, 352]
Fe_3O_4	Verwey transition	$\rho(\omega)$ with Jahn-Teller distortions	[353]
$Tl_2Mn_2O_7$	Insulator in contradiction with LDA results	$\rho(\omega)$, $\sigma(\omega)$	[354]
TiOCl	Insulator in contradiction with LDA results	$\rho(\omega)$	[355, 356]
NiMnSb, FeMnSb, VAs, CrAs, CrO_2, $Co_2Mn_{1-x}Fe_xSi$, $YbRh_2Si_2$	Half-metallic ferromagnets, nonquasiparticle states	$\rho_\uparrow(\omega)$, $\rho_\downarrow(\omega)$, $\sigma(\omega)$	[357–364]
Fe, Ni, CoPt	Ferromagnetic metals	$\rho(\omega)$, $M(T)$, $\chi(T)$	[365–369]
$Ga_{1-x}Mn_xAs$	Ferromagnetic semiconductors	$M(T)$, $M(x)$	[370]
$LiRh_2O_4$	Thermopower	$R(T)$,	[371]
f-			
Ce	Isostructural phase transition	See Sect. 6.4	[293, 372–376]

(*Continued*)

Table 6.2. (Continued)

Material	Physical problems	Calculated properties	References
Pu		See review G. Kotliar et al., Rev. Mod. Phys. **78**, 866 (2006).	[9, 377–381]
Am			[382, 383]
Ce, Nd, Pr	Structural transitions under pressure	$\rho(\omega)$, $E(V)$, $P(V)$, $n_f(V)$	[374]
$CeCu_2Si_2$	Heavy fermions	$\rho(\omega)$, $n_f(V)$	[384]
AmN, AmSb, PuTe, PuSe		$\rho(\omega)$	[385]
USe, PuSe, UTe	Ferro and antiferromagnetics with strong spin-orbit coupling	$\rho(\omega)$ comparison with PES	[386]
$PuCoGa_5$	superconductor with $T_c = 18.5\,K$ and d-symmetry order parameter	$\rho(\omega)$ quasiparticle peak	[387]

function of temperature $M(T)$, and doping $M(x)$ and also quasiparticle dispersion $E(\mathbf{k})$. This list reflect the present state of the field and undoubtedly will soon be come obsolete as a flow of new $LDA+DMFT$ studies is increasing now.

7

Conclusion

Two decades have passed since first ideas appeared leading to development of Dynamical Mean-Field Theory (*DMFT*) that becomes now a basic method to study strongly correlated systems (*SCS*). During this time hundreds of theoretical works were done using *DMFT* to study as basic models as well as real materials where physics is determined by correlation effects. A basic approximation of *DMFT* is neglect of spatial correlations with full description of local dynamical fluctuations. That is equivalent to approximation where self-energy is local depending only on frequency but not on wave vector. In *DMFT* method lattice problem is mapped on single-site impurity problem where atom with Coulomb interaction among electrons in d or f shell is embedded in energy (or time) dependent Weiss field (hence the name of the method: *dynamical* mean field). Spatial correlations neglect is justified when the system is not close to transition in long-range ordering state so that long coherent length fluctuations do not develops. With very few exceptions like high-T_c cuprates such conditions are realized in real materials and *DMFT* method was very successful in vast majority of applications.

Auxiliary single-site impurity problem in *DMFT* is much simpler for solution than initial lattice problem and can be solved with a high accuracy without severe approximations. The most widely used last years was Quantum Monte Carlo (*QMC*) method in Hirsch-Fye algorithm that is exact if statistic of stochastic sampling is good enough but it is applicable only for high temperature values because needed computer time resources grow exponentially with T lowering. Recently new versions of *QMC* method were developed like Continuous Time *QMC* and Projective *QMC* that allow to study low-temperature physics.

Initially, *DMFT* was applied to basic *SCS* models like nondegenerate Hubbard model, periodic Anderson model and *sd*-model (Kondo lattice model). In these studies the structure of quasiparticle spectra was investigated and its evolution with variation of Coulomb interaction parameter U to band width W ratio value. In half-filled Hubbard model spectral function evolves with U increase from metal to insulator with Mott-Hubbard transition at $U \approx W$.

Near transition three-peak structure appears with quasiparticle peak on Fermi level and two Hubbard bands corresponding to incoherent states. With varying U and T values intensity and width of quasiparticle peak changes showing strong renormalization of effective carriers mass value responsible for transport properties. *DMFT* also allowed to investigate three-peak spectra evolution with deviation from half-filling with doping δ thus producing full phase diagrams on planes (T, U) and (T, δ).

In periodic Anderson model strong Coulomb interaction also lead to sharp quasiparticle peak on Fermi level thus explaining "heavy fermion" phenomenon. *DMFT* calculations show appearing of universal energy scale T_0 separating high-temperature area ($T \gtrsim T_0$) where f-electrons form local magnetic moments and low-temperature region $T < T_0$ where Kondo singlets are formed and local moments are screened.

DMFT method gave many spectacular examples of successful description for physical properties of *SCS*. For example not only paramagnetic state can be treated by this approach also but long-range ordering: antiferromagnetic and superconducting. For that *DMFT* scheme should be extended by replacing effective single-impurity model on cluster model with few atoms in cluster instead of only one. For antiferromagnetism with two sublattices two-atom cluster is enough while for superconductivity with d-symmetry order parameter minimal cluster is four-atomic plaquet. Special calculation scheme was developed: Dynamical Cluster *DMFT* to treat short-range fluctuations in the system.

Going beyond local approximation for self-energy that is a basis of *DMFT* approach is needed when spatial fluctuations are important as it is for pseudogap effect in cuprates. This effect appears for normal metal phase with partial destruction of Fermi surface on certain areas. It can be treated by *DMFT* if short-wave fluctuations are included in microscopic theory or long wave fluctuations in phenomenological theory. There were attempts to extend *DMFT* by adding corrections of the order of $1/d$ (*DMFT* itself is exact in the limit of infinite dimensions $d = \infty$). The theories were also developed where instead of static Coulomb interaction U frequency dependent interaction $U(\omega)$ is defined (in diagrammatic technique that corresponds to taking into account dynamical local vertexes).

DMFT can be applied not only to one of the basic models of *SCS* but also to real materials. Density functional theory (*DFT*) in local density approximation (*LDA*) was successful in calculation of densities of states and dispersion laws for any materials knowing only its crystal structure and elements numbers in periodic table. Combining *LDA* and *DMFT* lead to development *LDA* + *DMFT* method that was very effective in strongly correlated materials studies.

In contrast to model approach in *LDA* + *DMFT* full set of degenerate d or f orbitals characteristic for material is included in problem Hamiltonian. This approach can be called "first principles" one but there are some approximations used in calculation scheme. At first certain orbitals are considered

as interacting ones while all others are left as they were given by *LDA*. At second Coulomb interaction is considered to be local on site. The most important approximation is a choice of method to solve effective impurity problem: *IPT*, *NRG*, *QMC*. *QMC* is a rigorous method but is requires large computer resources.

In spite of many approximations used in calculation scheme $LDA+DMFT$ results are sufficiently reliable as can be checked by comparison with experimental data. Many different classes of materials were treated in this approach: transition metal oxides, high-T_c cuprates, f-electron compounds with heavy fermions, ferromagnetic metals and half-metallic ferromagnets, rare-earth and actinide materials. The list of materials presented in Table 6.2 is fast extending with time. It is safe to say that now *DMFT* is an universal tool to study strongly correlated materials.

It is worth to note that many $LDA + DMFT$ calculations cannot be called fully ab initio because Coulomb interaction parameters were not calculated from "first principles" but taken as calculation parameter. "First principles" calculations for U were done in few cases but they are in general rare. Another important direction to extend calculation scheme is to calculate lattice properties such as compressibility, phonon spectra and lattice structure parameters.

A

Functional Integral and Partition Function

Partition function of the system with Hamiltonian $\hat{H}$ is defined as a trace of operator $\mathrm{e}^{-\beta\hat{H}}$:

$$Z = \mathrm{Tr}\ \mathrm{e}^{-\beta\hat{H}} = \sum_{\alpha} \left\langle \alpha | \mathrm{e}^{-\beta\hat{H}} | \alpha \right\rangle . \tag{A.1}$$

Here $|\alpha\rangle$ form full orthogonal basis for expansion of Hamiltonian $\hat{H}$ eigenfunctions. For Z calculation any basis can be used, however, for numerical calculations so called coherent states basis is most convenient. Such choice leads to presentation of Z as functional integral over some fields with structure different for Bose and Fermi systems. While for Bose systems such fields can be determined by ordinary complex numbers, for Fermi systems they are defined by some anticommutating quantities called *Grassmann* variables. In both cases coherent states are defined via creation–annihilation operators in second quantization representation and difference among fields generated by these coherent states is connected with commutation rules for these operators. Anticommutation of Fermi operators results in need for Grassmann variables in Fermi systems. Ideology of coherent states method is the same for Bose and Fermi systems but its realization depends on commutation rules for second quantization operators. Later we at first present the method for Bose systems and then for Fermi systems. Functional integral method was initially developed by Feynman [388, 389] and full details of mathematical derivations can be found in monographs and reviews [390–393].

Bose Systems

Let us consider systems of bosons described by creation and annihilation operators $\hat{a}_i^+, \hat{a}_i$ where i are quantum numbers defining particle state (site number, band number, polarization, etc.). The system Hamiltonian

$$\hat{H} \equiv \hat{\mathcal{H}}[\hat{a}_i^+, \hat{a}_i]. \tag{A.2}$$

is a polynomial of operators $\hat{a}_i^+, \hat{a}_i$ in normal form (creation operators are left of annihilation operators).

At first for simplicity we consider the case where only one state of Bose system exists so that index i of operators $\hat{a}_i^+, \hat{a}_i$ can be omitted. This state with n bosons can be defined as:

$$|n\rangle = \frac{(\hat{a}^+)^n}{n!}|0\rangle,\ \hat{a}|0\rangle = 0, \tag{A.3}$$

where $|0\rangle$ is vacuum state. It is easy to check that set of states $|n\rangle$ form orthonormal basis:

$$\langle n|m\rangle = \delta_{nm}. \tag{A.4}$$

From states $|n\rangle$ new basis can be defined as linear combinations $|\alpha\rangle$ that could be more convenient for our task: partition function calculation. For that we introduce operator:

$$\hat{\mathcal{D}}(\alpha) = \exp\,(\alpha\hat{a}^+ - \alpha^*\hat{a}), \tag{A.5}$$

depending on two complex numbers α and α^*. Using Becker-Hausdorf identity expression (A.5) can be rewritten as:

$$\hat{\mathcal{D}}(\alpha) = \mathrm{e}^{-\frac{|\alpha|^2}{2}}\mathrm{e}^{\alpha\hat{a}^+}\mathrm{e}^{-\alpha^*\hat{a}}, \tag{A.6}$$

This identity for two operators $\hat{A}$ and $\hat{B}$ satisfying condition

$$[\hat{A},[\hat{A},\hat{B}]] = [\hat{B},[\hat{A},\hat{B}]] = 0,$$

corresponds to relation

$$\mathrm{e}^{\hat{A}+\hat{B}} = \mathrm{e}^{-\frac{1}{2}[\hat{A},\hat{B}]}\mathrm{e}^{\hat{A}}\mathrm{e}^{\hat{B}}. \tag{A.7}$$

Let us introduce a set of states $|\alpha\rangle$ characterized by α number:

$$|\alpha\rangle = \hat{\mathcal{D}}(\alpha)|0\rangle = \mathrm{e}^{-\frac{|\alpha|^2}{2}}\mathrm{e}^{\alpha\hat{a}^+}|0\rangle, \tag{A.8}$$

Expending the exponent in Tailor series it is easy to show that $|\alpha\rangle$ is a linear combination of states $|n\rangle$:

$$|\alpha\rangle = \mathrm{e}^{-\frac{|\alpha|^2}{2}}\sum_{n=0}^{\infty}\frac{\alpha^n}{\sqrt{n!}}|n\rangle, \tag{A.9}$$

So coherent states are superposition of states with different particles number values.

We will now show that $|\alpha\rangle$ is eigenfunction of annihilation operator $\hat{a}$. For that we will act by operator $\hat{a}$ on relation (A.9) and use standard relation from second quantization method:

$$\hat{a}|n\rangle = \sqrt{n}|n-1\rangle,\ (n \geq 1), \hat{a}|0\rangle = 0. \tag{A.10}$$

That results in equation

$$\hat{a}|\alpha\rangle = \alpha|\alpha\rangle, \tag{A.11}$$

proving that $|\alpha\rangle$ is eigenfunction of annihilation operator. This remarkable property makes coherent states a convenient basis to calculate Z.

Normalization condition $\langle\alpha|\alpha\rangle = 1$ is satisfied if one takes into account relation $\langle\alpha|\hat{a}^+ = \langle\alpha|\alpha^*$. States $|n\rangle$ defined by expression (A.3) form full basis because the following relation is valid:

$$\sum_{n=0}^{\infty} |n\rangle\langle n| = 1, \tag{A.12}$$

Coherent functions $|\alpha\rangle$ also form complete basis that corresponds to relation

$$\int \frac{\mathrm{d}^2\alpha}{\pi} |\alpha\rangle\langle\alpha| = 1, \tag{A.13}$$

where $\mathrm{d}^2\alpha = \mathrm{d}(\mathrm{Re}\ \alpha)\mathrm{d}(\mathrm{Im}\ \alpha)$ and integration is performed over full complex variables plane.

To prove last relation we substitute expression (A.9) (and its conjugated counterpart) to left side of equation (A.13) and transform to polar coordinates $\alpha = \rho \mathrm{e}^{\mathrm{i}\phi}$. Then

$$\int \frac{\mathrm{d}^2\alpha}{\pi} |\alpha\rangle\langle\alpha| = \frac{1}{\pi} \int_0^{\infty} \mathrm{d}\rho\rho \mathrm{e}^{-\rho^2} \sum_{n,m} \frac{\rho^{m+n}}{\sqrt{m!n!}} \int_0^{2\pi} \mathrm{d}\phi \mathrm{e}^{\mathrm{i}(n-m)\phi},$$

and keeping in mind that integral over $\mathrm{d}\phi$ is proportional to δ_{nm} we arrive to relation (A.13).

Relation (A.13) can be considered as operator expansion of unit and one can use it to represent arbitrary operator $\hat{L}$ via its matrix elements in coherent states basis:

$$\hat{L} = \hat{1}\hat{L}\hat{1} = \int \frac{\mathrm{d}^2\alpha}{\pi} \int \frac{\mathrm{d}^2\beta}{\pi} \langle\alpha|\hat{L}|\beta\rangle |\alpha\rangle\langle\beta|, \tag{A.14}$$

We apply this relation to Hamiltonian $\hat{H}$ presented as normal expansion in second quantization operators:

$$\hat{H} \equiv \hat{\mathcal{H}}(\hat{a}_i^+, \hat{a}_i) = \sum_{n,m} \frac{\mathcal{L}_{mn}}{\sqrt{m!n!}} (\hat{a}^+)^n (\hat{a})^m.$$

Because of relation (A.11) we have

$$\langle\alpha|\hat{H}|\beta\rangle = \sum_{n,m} \frac{\mathcal{L}_{mn}}{\sqrt{m!n!}} (\alpha^*)^n (\beta)^m = \mathcal{H}(\alpha^*, \beta). \tag{A.15}$$

So Hamiltonian matrix element among coherent states written in normal form can be obtained by simple substitution of operators $\hat{a}^+$ and $\hat{a}$ by complex

numbers. This can be done not only for Hamiltonian but also for any operator in normal form.

It is easy to produce inverse expansion of $|n\rangle$ function via coherent states:

$$|n\rangle = \int \frac{\mathrm{d}^2\alpha}{\pi} \frac{(\alpha^*)^n}{\sqrt{n!}} \mathrm{e}^{-\frac{|\alpha|^2}{2}} |\alpha\rangle, \tag{A.16}$$

and also to prove two useful relations

$$\langle\alpha|\beta\rangle = \exp\left(-\frac{|\alpha|^2}{2} - \frac{|\beta|^2}{2} + \alpha^*\beta\right), \tag{A.17}$$

$$\mathrm{Tr}\ \hat{L} = \sum_{n=0}^{\infty} \langle n|\hat{L}|n\rangle = \int \frac{\mathrm{d}^2\alpha}{\pi} \langle\alpha|\hat{L}|\alpha\rangle. \tag{A.18}$$

Now we generalize obtained results on general case where Bose particle is characterized by combined index $i = \{i_1, i_2, \ldots, i_N\}$ with N possible values. In this case for coherent states definition a set of complex numbers $\{\alpha_1, \alpha_2, \ldots, \alpha_N\}$ is needed and then

$$|\alpha\rangle = \prod_i \mathrm{e}^{\alpha_i \hat{a}_i^+ - \alpha_i^* \hat{a}_i} |0\rangle = \mathrm{e}^{\sum_i (\alpha_i \hat{a}_i^+ - \alpha_i^* \hat{a}_i)} |0\rangle, \tag{A.19}$$

Instead of relation (A.17) we have now

$$\langle\alpha|\beta\rangle = \exp\left(-\sum_i \left(\frac{|\alpha_i|^2}{2} + \frac{|\beta_i|^2}{2} - \alpha_i^*\beta_i\right)\right) \tag{A.20}$$

Equations (A.13) and (A.18) are still valid but one should keep in mind that

$$\frac{\mathrm{d}^2\alpha}{\pi} \to \prod_i \frac{\mathrm{d}^2\alpha_i}{\pi}. \tag{A.21}$$

Now everything is ready to calculate partition function. According to general relation (A.18) we write Z as:

$$Z = \int \frac{\mathrm{d}^2\alpha}{\pi} \langle\alpha|\mathrm{e}^{-\beta\hat{H}}|\alpha\rangle. \tag{A.22}$$

We use a known limit

$$\mathrm{e}^{-\beta\hat{H}} = \lim_{L\to\infty} \mathrm{Tr} \left(1 - \frac{\beta\hat{H}}{L}\right)^L \tag{A.23}$$

and consider expression with final L value:

$$\mathrm{Tr}\left(1-\frac{\beta\hat{H}}{L}\right)^{L}=\int\mathcal{D}^{L}\alpha\mathcal{D}^{L}\alpha^{*}$$
$$\langle\alpha_0|1-\frac{\beta\hat{H}}{L}|\alpha_1\rangle\langle\alpha_1|1-\frac{\beta\hat{H}}{L}|\alpha_2\rangle\cdots\langle\alpha_L|1-\frac{\beta\hat{H}}{L}|\alpha_0\rangle. \tag{A.24}$$

We define here matrix element for power of operator $(1-\frac{\beta\hat{H}}{L})$ via matrix elements product. The variables $\alpha_l(l=1,2,\ldots,L)$ are sets of complex numbers $\alpha_l=\{\alpha_{1l},\alpha_{2l},\ldots,\alpha_{Nl}\}$ and also

$$\mathcal{D}^{L}\alpha\mathcal{D}^{L}\alpha^{*}=\prod_{i}\prod_{l=0}^{L}\frac{\mathrm{d}^2\alpha_{il}}{\pi}. \tag{A.25}$$

According to relations (A.20) and (A.15) we transform every multiplier in (A.24) in the following way:

$$\langle\alpha_{l-1}|1-\frac{\beta\hat{H}}{L}|\alpha_l\rangle=\exp\left(-\sum_i[\left(\frac{|\alpha_{i,l-1}|^2}{2}+\frac{|\alpha_{il}|^2}{2}-\alpha^{*}_{i,l-1}\alpha_{il}\right)\right.$$
$$\left.-\frac{\beta}{L}\mathcal{H}(\alpha^{*}_{i,l-1},\alpha_{il})]\right). \tag{A.26}$$

Using the fact that for large L quantity $\frac{\beta\hat{H}}{L}$ is small we transform expansion in $1/L$ in exponent. Multiplying all terms in (A.24) we present this expression as:

$$\mathrm{Tr}\left(1-\frac{\beta\hat{H}}{L}\right)^{L}=\int\mathcal{D}^{L}\alpha\mathcal{D}^{L}\alpha^{*}\exp\left(-\sum_i[\alpha^{*}_{iL}(\alpha_{iL}-\alpha_{i,L-1})\right.$$
$$+\alpha^{*}_{i,L-1}(\alpha_{i,L-1}-\alpha_{i,L-2})+\ldots+\alpha^{*}_{i1}(\alpha_{i1}-\alpha_{i,0})$$
$$\left.\left.-\frac{\beta}{L}\sum_l\mathcal{H}(\alpha^{*}_{i,l-1},\alpha_{il})\right]\right). \tag{A.27}$$

For Z calculations a limit of $L\to\infty$ is needed and then sum over l in expression (A.27) will become an integral and differences α_{il} for nearest values of l can be written via derivatives:

$$\alpha_{i,l}-\alpha_{i,l-1}\approx\frac{\partial\alpha_i}{\partial\tau_l}\cdot\frac{\beta}{L}. \tag{A.28}$$

In the result we arrive to presentation Z as a functional integral

$$Z=\int\mathcal{D}\alpha(\tau)\mathcal{D}\alpha^{*}(\tau)\exp\left(\int_0^{\beta}\mathrm{d}\tau\mathcal{L}(\alpha^{*}(\tau),\alpha(\tau))\right). \tag{A.29}$$

where

$$\mathcal{L} = -\sum_i \alpha_i^*(\tau)\frac{\partial}{\partial\tau}\alpha_i(\tau) - \mathcal{H}(\alpha_i^*(\tau), \alpha_i(\tau)). \tag{A.30}$$

In this functional integral integration is done over all complex functions $\alpha_i^*(\tau)$ and $\alpha_i(\tau)$ with boundary conditions:

$$\alpha_i^*(\beta) = \alpha_i^*(0),\ \alpha_i(\beta) = \alpha_i(0). \tag{A.31}$$

If $\mathcal{H}$ has quadratic form in Bose operators (free particles) then functional integral can be calculated explicitly. For that one should use the following expression for finite-dimensional Gaussian integral

$$\int \prod_i \frac{\mathrm{d}^2\alpha_i}{\pi}\exp(-\sum_{ij}\alpha_i^* L_{ij}\alpha_j) = (\det\hat{L})^{-1}, \tag{A.32}$$

where L_{ij} is hermitian matrix. This equality is easy to prove if matrix is diagonalized by unitary transformation of variables. In the result of standard Gaussian integral calculation we have result as a product of eigenvalues of matrix L_{ij} and that is equal to matrix determinant.

Let Hamiltonian be a quadratic form of creation–annihilation operators for bosons:

$$\hat{H} = \sum_{ij}\hat{a}_i^+ h_{ij}\hat{a}_j, \tag{A.33}$$

where h_{ij} in general can depend on time τ. Then expression (A.30) is also a quadratic form of variables α_i^* and α_i depending on τ. Gaussian integral calculation corresponding to functional integral (A.29) gives the same result (A.32) and partition function is given by expression

$$Z = \left[\det\left(-\frac{\partial}{\partial\tau} - \hat{h}\right)\right]^{-1}. \tag{A.34}$$

This expression can be connected with one-particle Green function. We introduce GF corresponding to operator $(-\frac{\partial}{\partial\tau} - \hat{h})$ satisfying to equation

$$-\frac{\partial}{\partial\tau}G_{ij}(\tau,\tau') - \sum_k h_{ik}G_{kj}(\tau,\tau') = \delta_{ij}\delta(\tau-\tau'), \tag{A.35}$$

or in operator form

$$\hat{G} = \left(-\frac{\partial}{\partial\tau} - \hat{h}\right)^{-1}, \tag{A.36}$$

Then expression (A.34) for partition function can be written as

$$Z = \det\hat{G}, \tag{A.37}$$

For interacting bosons ($\hat{H} = \hat{H}_0 + \hat{H}_{\mathrm{int}}$) functional integral (A.29) can be calculated in perturbation theory via exponent expansion in powers of $\hat{H}_{\mathrm{int}}$ with integration of every term of the series. That gives diagrammatic techinque for Bose systems.

Fermi Systems

The system Hamiltonian is expressed via fermion operators $\hat{c}_i^+, \hat{c}_i$ as polynomial with normal ordering of creation–annihilation operators:

$$\hat{H} = \mathcal{H}(\hat{c}_i^+, \hat{c}_i), \tag{A.38}$$

Fermionic operators satisfy anticommutation relations

$$[\hat{c}_i^+, \hat{c}_j)]_+ = \delta_{ij},\ [\hat{c}_i^+, \hat{c}_j^+)]_+ = [\hat{c}_i, \hat{c}_j)]_+ = 0\ , \tag{A.39}$$

Our task is to present partition function as functional integral over variables β_i and β_i^* that are not ordinary complex numbers but so called Grassmann variables with anticommutation rules for multiplication operation:

$$\beta_i \beta_j = -\beta_j \beta_i, \tag{A.40}$$

and standard other multiplication operation rules:

$$\beta_i(\beta_j \beta_k) = (\beta_i \beta_j)\beta_k;\ (\beta_i + \beta_j)\beta_k = \beta_i \beta_k + \beta_j \beta_k,$$

In analogy with Bose systems we introduce coherent states:

$$|\beta_i\rangle = \mathrm{e}^{\beta_i \hat{c}_i^+}|0\rangle, \tag{A.41}$$

where $|0\rangle$ is vacuum state ($c_i|0\rangle = 0$). Taking into account properties of Grassmann variables and fermionic operators

$$\beta_i^2 = 0,\ (\hat{c}_i^+)^2 = 0, \tag{A.42}$$

we have $\mathrm{e}^{\beta_i \hat{c}_i^+} = 1 + \beta_i \hat{c}_i^+$ and then following relations are valid:

$$\beta_i|\beta_i\rangle = \beta_i(1 + \beta_i \hat{c}_i^+)|0\rangle = \beta_i|0\rangle,$$
$$\hat{c}_i|\beta_i\rangle = \hat{c}_i(1 + \beta_i \hat{c}_i^+)|0\rangle = \beta_i|0\rangle.$$

That gives equation

$$\hat{c}_i|\beta_i\rangle = \beta_i|\beta_i\rangle, \tag{A.43}$$

showing that $|\beta_i\rangle$ is eigenfunction for annihilation operator. Analogously to Bose systems case we introduce two sets of Grassmann variables β_i^* and β_i with properties:

$$\beta_i^* \beta_j = -\beta_j \beta_i^*. \tag{A.44}$$

The asterisk sign does not mean complex conjugation. It is used here to define a pair of "numbers" β_i^* and β_i.

If we have only one degree of freedom (to omit index i for operators $\hat{c}_i^+$ and $\hat{c}_i$) then any function of β_i^* and β_i can be presented as

$$f(\beta^*, \beta) = f_{00} + f_{01}\beta + f_{10}\beta^* + f_{11}\beta\beta^*. \tag{A.45}$$

where f_{ik} are standard complex numbers.

Let us define integration over Grassmann variables via following formulas:

$$\int \mathrm{d}\beta = 0, \ \int \mathrm{d}\beta^* = 0, \ \int \mathrm{d}\beta\beta = 1, \ \int \mathrm{d}\beta^*\beta^* = 1, \tag{A.46}$$

assuming that $\mathrm{d}\beta^*$, $\mathrm{d}\beta$ are Grassmann variables anticommutating with each other and with β, β^*. Then integrating expression (A.45) over both variables we obtain:

$$\int \mathrm{d}\beta^*\mathrm{d}\beta f(\beta^*, \beta) = \int \mathrm{d}\beta^* \left[\int \mathrm{d}\beta f(\beta^*, \beta)\right] = \int \mathrm{d}\beta^*[f_{01} + f_{11}\beta^*] = f_{11}.$$

Now we clarify the problem of completeness of $|\beta\rangle$ states set. For fermions with one degree of freedom states space basis consists of two vectors: vacuum state $|0\rangle$ and occupied state $|1\rangle = \hat{c}^+|0\rangle$ so that completeness condition can be written as:

$$|0\rangle\langle 0| + |1\rangle\langle 1| = 1, \tag{A.47}$$

meaning that the state is either occupied or empty. For coherent states $|\beta\rangle$ corresponding condition is given by equality:

$$\int \mathrm{d}\beta^*\mathrm{d}\beta \mathrm{e}^{-\beta^*\beta}|\beta\rangle\langle\beta| = 1. \tag{A.48}$$

This relation can be proved presenting integral as:

$$\int \mathrm{d}\beta^*\mathrm{d}\beta(1 - \beta^*\beta)(|0\rangle + \beta|1\rangle)(\langle 0| + \langle 1|\beta^*).$$

Term by term integration gives expression $|0\rangle\langle 0| + |1\rangle\langle 1|$ that due to equality (A.47) is equal 1 that finalize the prove.

There are two additional relations. The first one gives matrix element of operator $\hat{H}$ if it is written in normal form

$$\langle\alpha|\hat{H}|\beta\rangle = \mathcal{H}(\alpha^*, \beta), \tag{A.49}$$

in the same way as it is for Bose systems. Second relation defines overlapping for coherent states:

$$\langle\gamma|\beta\rangle = (\langle 0| + \langle 1|\gamma^*)(|0\rangle + \beta|1\rangle) = 1 + \gamma^*\beta = \mathrm{e}^{\gamma^*\beta},$$

Now we write expression for coherent states and overlapping in general case where fermion has many degrees of freedom marked by index i:

$$|\beta\rangle = \exp(\sum_i \beta_i \hat{c}_i^+)|0\rangle, \tag{A.50}$$

$$\langle\gamma|\beta\rangle = \exp(\sum_i \gamma_i^* \beta_i), \tag{A.51}$$

These formulas help us to represent partition function as a functional integral.

In the same way as for Bose systems we write using expansion (A.48) for unit:

$$Z = \lim_{L\to\infty} \int \prod_i \prod_l \mathrm{d}\beta_{il}^* \mathrm{d}\beta_{il} \exp\{-\sum_i [\beta_{iL}^*(\beta_{iL} - \beta_{i,L-1}) + \beta_{i,L-1}^*(\beta_{i,L-2} - \beta_{i,L-2}) + \ldots + \beta_{i1}^*(\beta_{i1} - \beta_{i0}) - \frac{\beta}{L}\sum_l \mathcal{H}(\beta_{i,l-1}^*, \beta_{il})]\}. \tag{A.52}$$

Replacing differences $(\beta_{il} - \beta_{i,l-1})$ by derivatives over $\tau_l = l\frac{\beta}{L}$ we present (A.52) in a final form:

$$Z = \int \mathcal{D}\beta^*(\tau)\mathcal{D}\beta(\tau) \exp\left(\int_0^\beta \mathrm{d}\tau \mathcal{L}(\beta^*(\tau), \beta(\tau))\right), \tag{A.53}$$

where

$$\mathcal{L} = -\sum_i \beta_i^*(\tau)\frac{\partial}{\partial\tau}\beta_i(\tau) - \mathcal{H}(\beta_i^*(\tau), \beta_i(\tau)), \tag{A.54}$$

$$\mathcal{D}\beta^*(\tau)\mathcal{D}\beta(\tau) = \lim_{L\to\infty} \prod_i \prod_{l=0}^{L} \mathrm{d}\beta_{il}^* \mathrm{d}\beta_{il}. \tag{A.55}$$

Formally partition function expression is the same for Bose and Fermi systems but while for Bose systems integration is on the field of complex numbers for Fermi systems it is done on the field of Grassmann variables. Border conditions in contrast to (A.31) are antiperiodic ($\beta = 1/T$):

$$\beta_i^*(\beta) = -\beta_i^*(0),\ \beta_i(\beta) = -\beta_i(0). \tag{A.56}$$

For noninteracting Fermions Hamiltonian $\mathcal{H}$ is bilinear in variables β^* and β and functional integral comes to Gaussian integral. It can be calculated using (A.46). In its simplest form such integral is:

$$\int \mathrm{d}\beta^* \mathrm{d}\beta \mathrm{e}^{-\lambda\beta^*\beta} = \int \mathrm{d}\beta^* \mathrm{d}\beta(1 - \lambda\beta^*\beta) = \int \mathrm{d}\beta^* \mathrm{d}\beta(1 + \lambda\beta\beta^*) = \lambda. \tag{A.57}$$

General form Gaussian integral over Grassmann variables with arbitrary quadratic form in exponent is calculated bytransforming it in diagonal form

and we have:

$$\int \prod_i \mathrm{d}\beta^* \mathrm{d}\beta \exp\left(-\sum_{ij} \beta_i^* A_{ij} \beta_j\right) = \det \hat{A}. \tag{A.58}$$

It is interesting that determinant appears here in numerator and not in denominator as in corresponding expression (A.32) for Bose systems.

If Hamiltonian for fermions has the form:

$$\hat{H} = \sum_{ij} \hat{c}_i^+ h_{ij} \hat{c}_j, \tag{A.59}$$

then in contrast to (A.34) we have the following expression for partition function:

$$Z = \det\left(-\frac{\partial}{\partial\tau} - \hat{h}\right), \tag{A.60}$$

or

$$Z = [\det \hat{G}]^{-1}, \tag{A.61}$$

where $\hat{G}$ is Green function for operator $(-\frac{\partial}{\partial\tau} - \hat{h})$ satisfying equation

$$-\frac{\partial}{\partial\tau} G_{ij}(\tau, \tau') - \sum_k h_{ik} G_{kj}(\tau, \tau') = \delta_{ij}\delta(\tau - \tau'), \tag{A.62}$$

with antiperiodic boundary condition

$$\hat{G}(\tau + \beta, \tau') = \hat{G}(\tau, \tau' + \beta) = -\hat{G}(\tau, \tau'). \tag{A.63}$$

To calculate many-particle GF it is convenient to introduce generating functional $Z_B[V^\dagger, V]$ that is generalization of partition function Z:

$$Z_B[V^\dagger, V] = \mathrm{Tr}\{\mathrm{e}^{-\beta H} T_\tau \mathrm{e}^{V^\dagger \hat{a} + \hat{a}^\dagger V}\}. \tag{A.64}$$

Here

$$V^\dagger \hat{a} + \hat{a}^\dagger V = \sum_i (V_i^\dagger \hat{a}_i + \hat{a}_i^\dagger V_i) \tag{A.65}$$

is a linear combination of creation–annihilation operators in state i and $V_i^\dagger$, V_i are corresponding to them fluctuating fields. Those fields are ordinary complex numbers for Bose systems and Grassmann variables for fermions.

We consider at first Bose systems. One-particle GF is expressed as a second derivative over fields $V^\dagger$ and V from generating functional

$$\begin{aligned} G(1,2) &= -<T_\tau \hat{a}_{i_1}(\tau_1)\hat{a}_{i_2}(\tau_2)> \\ &= -\frac{\delta^2}{\delta V_1 \delta V_2} Z_B[V^\dagger, V]\big|_{V=0}, \end{aligned} \tag{A.66}$$

and two-particle GF can be defined as a fourth order derivative

$$G(12;34) = (-1)^2 < T_\tau \hat{a}_{i_1}(\tau_1)\hat{a}_{i_2}(\tau_2)\hat{a}_{i_3}(\tau_3)\hat{a}_{i_4}(\tau_4) > \qquad (A.67)$$
$$(-1)^2 \frac{\delta^4}{\delta V_1 \delta V_2 \delta V_3 \delta V_4} Z_B[V^\dagger, V]\big|_{V=0}.$$

Numbers $1, 2 \ldots$ are used as combined indexes (e.g., $1 = (i_1\tau_1)$).

Generating functional can be represented as a functional integral over complex fields α and α^* analogously with partition function representation (A.29):

$$Z_B[v^\dagger, v] = \int D\alpha(\tau) D\alpha^*(\tau) \exp\left(\int_0^\beta \mathrm{d}\tau \left\{ -\sum_i \alpha_i^*(\tau) \frac{\partial}{\partial \tau} \alpha_i(\tau) \right.\right.$$
$$\left.\left. -\mathcal{H}(\alpha_i^*(\tau), \alpha_i(\tau)) + \alpha_i^*(\tau) v_i(\tau) + \alpha_i(\tau) v_i^\dagger(\tau) \right\} \right). \qquad (A.68)$$

If interaction term in Hamiltonian is neglected leaving only quadratic form in α_i then Gaussian integral appears that can be calculated and the results is:

$$\int D\alpha D\alpha^* \mathrm{e}^{-\alpha^* K \alpha + \alpha^* v + \alpha v^\dagger} = (\det K)^{-1} \mathrm{e}^{-v^\dagger K^{-1} v}. \qquad (A.69)$$

To prove this relation we consider final-dimension integral over $\prod_i d\alpha_i d\alpha_i^*$ and do transformation of variables $\alpha = \alpha' + K^{-1}v$. Then integral (A.69) will be:

$$\mathrm{e}^{-v^\dagger K^{-1} v} \int D\alpha' D\alpha^{*\prime} \mathrm{e}^{-\alpha^{*\prime} K \alpha'}. \qquad (A.70)$$

Instead of variables α' and $\alpha^{*\prime}$ we introduce $\alpha' = x + iy$ and $\alpha^{*\prime} = x - iy$ and from variables x and y come to x' and y' using following formulas:

$$x = K^{-1/2} x', \quad y = K^{-1/2} y'.$$

Transformation Jacobian is

$$\det \begin{vmatrix} \frac{\partial x}{\partial x'} & \frac{\partial x}{\partial y'} \\ \frac{\partial y}{\partial x'} & \frac{\partial y}{\partial y'} \end{vmatrix} = \det \begin{vmatrix} K^{-1/2} & 0 \\ 0 & K^{-1/2} \end{vmatrix} = \det K^{-1} = (\det K)^{-1},$$

and after standard Gaussian integrals calculations over x_i and y_i we arrive to relation (A.69). Comparing expressions (A.65) and (A.66) we come to $K = G_0^{-1}$. Assuming $v = v^* = 0$ in (A.69) we obtain expression (A.34) for partition function of noninteracting bosons. Now we perform the same calculations for fermions. We introduce generating functional

$$Z_F[v^\dagger, v] = \mathrm{Tr}\{\mathrm{e}^{-\beta H} T_\tau \mathrm{e}^{v^\dagger \hat{b} + \hat{b}^\dagger v}\}, \tag{A.71}$$

where

$$v^\dagger \hat{b} + \hat{b}^\dagger v = \sum_i (v_i^\dagger \hat{b}_i + \hat{b}_i^\dagger v_i), \tag{A.72}$$

$v_i^\dagger$ and v_i are Grassmann variables.

One-particle fermionic GF in the same way as bosonic GF can be calculated as second derivative of generating functional and two-particle as a fourth order derivative. The only difference is that for fermions one should distinguish "left" and "right" derivatives over Grassmann fields. So we have:

$$G(1,2) = - < T_\tau b_{i_1}(\tau_1) b_{i_2}^\dagger(\tau_2) > \tag{A.73}$$

$$= -\frac{\overrightarrow{\delta}}{\delta v_2} \frac{\overleftarrow{\delta}}{\delta v_1^\dagger} Z_F[v^\dagger, v]\big|_{v=0},$$

$$G(12;34) = - < T b_{i_1}(\tau_1) b_{i_2}(\tau_2) b_{i_3}^\dagger(\tau_3) b_{i_4}^\dagger(\tau_4) > \tag{A.74}$$

$$= -\frac{\overrightarrow{\delta}}{\delta v_4} \frac{\overrightarrow{\delta}}{\delta v_3} \frac{\overleftarrow{\delta}}{\delta v_2^\dagger} \frac{\overleftarrow{\delta}}{\delta v_1^\dagger} Z_F(v^\dagger, v)\big|_{v=0}.$$

Distinguishing "left" and "right" derivatives is needed only to take into account sign change in transposition of Grassmann variables when derivative is calculated of some product. For "left" derivative it is needed to put the corresponding variable (the derivative is taken with respect to) to leftmost position and for "right" derivative to rightmost position.

For Fermi systems the formula analogous to (A.69) for functional integral can be derived if interaction H_{int} is ignored:

$$\int D\beta^* D\beta \mathrm{e}^{-\beta^* K \beta + \beta^* V + \beta V^\dagger} = (\det K) \mathrm{e}^{-V^\dagger K^{-1} V}. \tag{A.75}$$

It is interesting to note that in this formula the factor $\det K$ is present while for Bose systems the corresponding factor is $(\det K)^{-1}$. This fact is due to antisymmetry of matrix K in expression (A.75):

$$K^{\mathrm{T}} = -K, \tag{A.76}$$

here K^{T} is transposed K matrix.

After linear transformation $\beta = \beta' - K^{-1}V$ integral in the left part of equation (A.75) comes to

$$\mathrm{e}^{-V^\dagger K^{-1} V} \int D\beta^* D\beta \mathrm{e}^{-\beta^* K \beta}. \tag{A.77}$$

In the last integral we do transformation of variables $\beta = L\beta'$ and then quadratic form in exponent becomes

$$\beta^* K\beta = \beta'^* K'\beta', \quad K' = L^{\mathrm{T}} KL. \tag{A.78}$$

It is known that for any antisymmetric matrix K of even dimensionality there is unimodal ($\det L = 1$) matrix L such that $K' = L^{\mathrm{T}} KL$ is quasidiagonal matrix consisting of n two-dimensional blocks:

$$K^{-1} = \begin{pmatrix} 0 & \dots & 0 & \lambda_1 \\ 0 & \dots & -\lambda_1 & 0 \\ \vdots & & & \\ 0 & -\lambda_{\mathrm{n}} & \dots & 0 \\ -\lambda_{\mathrm{n}} & 0 & \dots & 0 \end{pmatrix}, \tag{A.79}$$

and

$$\prod_{i=1}^{n} \lambda_i = \varepsilon(\det K)^{1/2}, \tag{A.80}$$

where ε can have values 1 and -1.

Now we can calculate integrals in expression (A.77).

$$\begin{aligned} \int D\beta D\beta^* \mathrm{e}^{-\beta^* K\beta} &= \int D\beta' D\beta'^* \exp\left\{ \sum_{i=1}^{n} (\beta'^*_{2i-1}, \beta'^*_{2i}) \begin{pmatrix} 0 & \lambda_i \\ -\lambda_i & 0 \end{pmatrix} \begin{pmatrix} \beta'_{2i-1} \\ \beta'_{2i} \end{pmatrix} \right\} \\ &= \int D\beta' D\beta'^* \prod_{i=1}^{n} (1 - \lambda_i \beta'^*_{2i-1} \beta'_{2i}) \prod_{j=1}^{n} (1 - \lambda_j \beta'^*_{2j} \beta'_{2j-1}) \\ &\quad - \left(\prod_{i=1}^{n} \lambda_i \right) \left(\prod_{j=1}^{n} \lambda_j \right) = \det K \end{aligned} \tag{A.81}$$

Substituting this result in expression (A.77) we arrive to relation (A.75) with sign ambiguity. We assume for certainty positive sign here. Relation (A.75) for fermions differs from corresponding relation (A.69) for bosons due to different symmetry of K matrix in these relations.

In conclusion we give expressions for one-particle GF of Bose and Fermi systems as functional integrals over complex fields $\alpha(\tau)$, $\alpha^*(\tau)$ in the first case and Grassmann variables $\beta(\tau)$, $\beta^*(\tau)$ in the second case.

$$\begin{aligned} G(i_1\tau_1, i_2\tau_2) = -\frac{1}{Z_B} \int D\alpha(\tau) D\alpha^*(\tau) \\ \exp\left(\int_0^\beta d\tau \mathcal{L}(\alpha^*(\tau), \alpha(\tau)) \right) \alpha_{i_1}(\tau_1) \alpha^*_{i_2}(\tau_2), \end{aligned} \tag{A.82}$$

$$G(i_1\tau_1, i_2\tau_2) = -\frac{1}{Z_F}\int D\beta(\tau)D\beta^*(\tau) \exp\left(\int_0^\beta d\tau \mathcal{L}(\beta^*(\tau), \beta(\tau))\right)\beta_{i_1}(\tau_1)\beta^*_{i_2}(\tau_2), \quad \text{(A.83)}$$

Here Z is partition function determined by integral (A.29) for Bose systems and by integral (A.53) for Fermi systems. Both relations can be obtained from expressions (A.66) and (A.73) presenting GFs as variational derivatives of generating functional over fields.

B

Green Functions Formalism

Mathematical basis of Dynamical Mean-Field Theory ($DMFT$) is temperature (Matsubara) Green functions formalism [115]. For fermions one-particle GF is defined by expression

$$G_\sigma(i_1\tau_1; i_2\tau_2) = - < T_\tau \hat{\tilde{c}}_{i_1\sigma}(\tau_1)\hat{\tilde{c}}^\dagger_{i_2\sigma}(\tau_2) >, \tag{B.1}$$

where $\hat{c}_{i\sigma}$ and $\hat{c}^\dagger_{i\sigma}$ are creation–annihilation operators for electron in Heisenberg representation with full Hamiltonian $\mathcal{H}$:

$$\hat{\tilde{c}}_{i\sigma}(\tau) = \mathrm{e}^{\mathcal{H}\tau} c_{i\sigma} \mathrm{e}^{-\mathcal{H}\tau}, \quad \hat{\tilde{c}}^\dagger_{i\sigma}(\tau) = \mathrm{e}^{\mathcal{H}\tau} c^\dagger_{i\sigma} \mathrm{e}^{-\mathcal{H}\tau}. \tag{B.2}$$

Here $< \ldots >$ is statistical averaging, T_τ is chronological time ordering operator putting operators in order of increasing thermodynamical time τ that varies in interval $0 \le \tau \le 1/T$, T is temperature [394]. We emphasize that $\hat{c}^\dagger_{i\sigma}(\tau)$ is not hermitian conjugated to $\hat{c}^\dagger_{i\sigma}$ quantity because τ is imaginary time. In standard textbook [115] this quantity is marked as $\hat{\tilde{c}}_{i\sigma}(\tau)$. We will use definition of (B.1).

If Hamiltonian is divided in two parts $\mathcal{H} = \mathcal{H}_0 + \mathcal{H}_{\mathrm{int}}$ then GF [115] can be written in interaction representation where:

$$< T_\tau \hat{\tilde{c}}_{i_1\sigma_1}(\tau_1)\hat{\tilde{c}}^\dagger_{i_2\sigma_2}(\tau_2) >= \frac{< T_\tau \hat{c}_{i_1\sigma_1}(\tau_1)\hat{c}^\dagger_{i_2\sigma_2}(\tau_2)\sigma(\beta) >_0}{< \sigma(\beta) >_0}. \tag{B.3}$$

Here symbol $< \ldots >_0$ in contrast to $< \ldots >$ means statistical averaging with Hamiltonian H_0 and $c_{i\sigma}(\tau)$ and $c^\dagger_{i\sigma}(\tau)$ are operators in interaction representation, they are given by formulas (B.2) where H is replaced by H_0.

$\sigma(\beta)$ is temperature scattering matrix:

$$\begin{aligned} \sigma(\beta) &= T_\tau \mathrm{e}^{-\int_0^\beta H_{\mathrm{int}}(\tau)\mathrm{d}\tau} \\ &= \sum_{n=0}^{\infty} \frac{(-1)^n}{n!} \int_0^\beta \ldots \int_0^\beta \mathrm{d}\tau_1 \ldots \mathrm{d}\tau_n T_\tau \{H_{\mathrm{int}}(\tau_1) \ldots H_{\mathrm{int}}(\tau_n)\}, \end{aligned} \tag{B.4}$$

where

$$H_{\rm int}(\tau) = {\rm e}^{H_0\tau} H_{\rm int} {\rm e}^{-H_0\tau}. \tag{B.5}$$

GF (B.1) depends on time difference $\tau_1 - \tau_2$ and can be expanded in Fourier series with discrete frequencies:

$$G_\sigma(i_1\tau_1; i_2\tau_2) = T\sum_{\rm n} G_\sigma(i_1 i_2; i\omega_{\rm n}){\rm e}^{-i\omega_{\rm n}(\tau_1-\tau_2)}. \tag{B.6}$$

For Fermi systems (Matsubara) frequencies $\omega_{\rm n}$ are odd:

$$\omega_{\rm n} = (2n+1)\pi T, \tag{B.7}$$

and for Bose systems they are even.

Expression (B.4) for scattering matrix reduces electronic *GF* calculation to perturbation series in powers of $H_{\rm int}$. Averaging $< T_\tau \ldots >_0$ of corresponding Fermi-operators products can be performed using Wick theorem:

$$\begin{aligned} &< T_\tau c_1^\dagger(\tau_1) c_2^\dagger(\tau_2) \ldots c_l(\tau_l) \ldots c_m^\dagger(\tau_m) >_0 \\ \pm G^0_{l1}(\tau_l - \tau_1) &< T_\tau [c_1^\dagger, c_l]_{\tau_1} c_2^\dagger(\tau_2) \ldots c_m^\dagger(\tau_m) >_0 \\ \pm G^0_{l2}(\tau_l - \tau_2) &< T_\tau c_1^\dagger(\tau_1) [c_2^\dagger, c_l]_{\tau_2} \ldots c_m^\dagger(\tau_m) >_0 \pm \ldots \\ \pm G^0_{lm}(\tau_l - \tau_m) &< T_\tau c_1^\dagger(\tau_1) c_2^\dagger(\tau_2) \ldots [c_m^\dagger, c_l]_{\tau_m} >_0 . \end{aligned} \tag{B.8}$$

In the left part there is an average of T-product of m operators c and $c^\dagger$. The number of c and $c^\dagger$ should be equal to each other, if not then average is equal to zero. Let c_l is operator for electron in state l. In right part of (B.8) expression $[c_p^\dagger, c_l]_{\tau_p}$ is a commutator $[c_p^\dagger, c_l]_+$ in interaction representation for coinciding time values τ_p. Quantities $G^0_{lp}(\tau)$ are one-electron *GF* of zeroth approximation.

$$G^0_{lp}(\tau) = -\delta_{lp} < T_\tau c_l(\tau) c_p^\dagger(0) >_0 . \tag{B.9}$$

Sign in front of summand in right part of (B.8) is defined by parity of operator c_l transposition from original position to the given one.

Anticommutator of c and $c^\dagger$ operators is a c-number

$$[c_p^\dagger, c_l]_{\tau_p} = \delta_{lp}, \tag{B.10}$$

and in every summand in right part of (B.8) there are two operators less than in original average in left part. Repeating algorithm (B.8) it is possible to reduce original average to a set of summands consisting of products of $G^0(\tau)$. That is an idea of Wick theorem. Expansion (B.4) for scattering matrix and algorithm defined by (B.8) is a basis of diagrammatic technique (graphic representation of perturbation series) for *GF* calculations. Diagrammatic technique for Fermi systems was described in many textbooks such as, e.g., [115]. Algorithms of the (B.8) type can be developed for other more complicated operators, such as spin operators and X Hubbard operators [44, 395].

Temperature *GF*s have no direct physical meaning but they are connected with other functions such as retarded and advanced *GF*s [396,397] that defines observable properties and response functions. Retarded electron *GF* is defined as

$$G^R_\sigma(i_i t_1; i_2 t_2) = -i\Theta(t_1 - t_2) < [c_{i_1\sigma}(t_1), c^\dagger_{i_2\sigma}(t_2)]_+ > . \tag{B.11}$$

Here $< \ldots >$ is symbol of statistical averaging, $c_{i\sigma}(t)$ and $c^\dagger_{i\sigma}(t)$ are Fermi operators in Heisenberg representation in real time:

$$c_{i\sigma}(t) = \mathrm{e}^{\mathrm{i}\mathcal{H}t} c_{i\sigma} \mathrm{e}^{-\mathrm{i}\mathcal{H}t}, \quad c^\dagger_{i\sigma}(t) = \mathrm{e}^{\mathrm{i}\mathcal{H}t} c^\dagger_{i\sigma} \mathrm{e}^{-i\mathcal{H}t}, \tag{B.12}$$

$c^\dagger_{i\sigma}(t)$ is hermitian conjugated to $c_{i\sigma}(t)$. In addition to retarded *GF* it is possible to define advanced *GF*:

$$G^A_\sigma(i_i t_1; i_2 t_2) = i\Theta(t_2 - t_1) < [c_{i_1\sigma}(t_1), c^\dagger_{i_2\sigma}(t_2)]_+ > . \tag{B.13}$$

G^R and G^A depends on time difference $t_1 - t_2$ and can be expanded in Fourier integral:

$$G^{R,A}_\sigma(i_i t_1; i_2 t_2) = \frac{1}{2\pi} \int_{-\infty}^{\infty} \mathrm{d}\omega \mathrm{e}^{-i\omega(t_1 - t_2)} G^{R,A}_\sigma(i_1 i_2; \omega). \tag{B.14}$$

Temperature, retarded and advanced *GF* are connected with each other as is seen in their spectral representations [115]:

$$G_\sigma(i_1 i_2; i\omega_\mathrm{n}) = \int_{-\infty}^{\infty} \mathrm{d}\omega' \frac{\rho_\sigma(i_1 i_2; \omega')}{i\omega_\mathrm{n} - \omega'}, \tag{B.15}$$

$$G^{R,A}_\sigma(i_1 i_2; \omega) = \int_{-\infty}^{\infty} \mathrm{d}\omega' \frac{\rho_\sigma(i_1 i_2; \omega')}{\omega \pm i\delta - \omega'}. \tag{B.16}$$

Here $\rho_\sigma(i_1 i_2; \omega)$ is (real) spectral density of *GF*. From relation (B.16) follows that retarded *GF* is analytical in upper complex half-plane. On real axis imaginary part of *GF* has a jump that is defined by spectral density of corresponding correlators:

$$< c_{i_1\sigma}(t) c^\dagger_{i_2\sigma}(0) > = \frac{1}{2\pi} \int_{-\infty}^{\infty} \mathrm{d}\omega J_\sigma(i_1 i_2; \omega) \mathrm{e}^{-i\omega t}, \tag{B.17}$$

$$< c^\dagger_{i_2\sigma}(0) c_{i_1\sigma}(t) > = \frac{1}{2\pi} \int_{-\infty}^{\infty} \mathrm{d}\omega J_\sigma(i_1 i_2; \omega) \mathrm{e}^{-\beta\omega} \mathrm{e}^{-i\omega t}, \tag{B.18}$$

here

$$J_\sigma(i_1 i_2; \omega) = -i \frac{G^R_\sigma(i_1 i_2; \omega) - G^A_\sigma(i_1 i_2; \omega)}{1 - \mathrm{e}^{-\beta\omega}}. \tag{B.19}$$

Remarkable result from comparison of spectral relations (B.15) and (B.16) is a statement: causal (thermodynamic) *GF* after analytical continuation from discrete points on imaginary axis to real axis gives retarded *GF* [115]. That

defines a way to calculate various observable properties of the system. For that one can calculate corresponding thermodynamic *GF* using diagrammatic technique based on Wick theorem and then perform analytical continuation to real axis to obtain retarded *GF*.

There is another method: to use from the beginning retarded *GF* formalism where there is no diagrammatic technique but it is possible to write equations of motion and to solve them with some approximations, for example equations decoupling [397].

For retarded *GF* it is convenient to use special symbols. Let us define *GF* determined by (B.11) as $<< c_{i\sigma}(t)|c^{\dagger}_{j\sigma}(t') >>$. Differentiating this quantity with respect to t variable we obtain the following equation:

$$i\frac{\mathrm{d}}{\mathrm{d}t} << c_{i\sigma}(t)|c^{\dagger}_{j\sigma}(t') >> = < [c_{i\sigma}, c^{\dagger}_{j\sigma}]_{+} > \delta(t-t') + << [c_{i\sigma}, H]_{t}|c^{\dagger}_{j\sigma}(t') >>. \tag{B.20}$$

In the last term of this equation we take into account equation of motion for operator:

$$i\frac{d}{dt}c_{i\sigma}(t) = [c_{i\sigma}(t), H]. \tag{B.21}$$

Equation of motion (B.20) connects original one-electron *GF* with more complicated *GF* in the last term of (B.20). For them special equation should be written by calculating derivatives over t or t'. In such a way a chain of equations can be obtained that can be cut off with some approximation.

References

1. P. Fulde, *Electron correlations in Molecules and Solids* (Springer, Berlin, 1995)
2. J. Hubbard, Proc. R. Soc. London A **276**, 238 (1963)
3. J. Hubbard, Proc. R. Soc. London A **281**, 401 (1964)
4. W. Metzner, D. Vollhardt, Phys. Rev. Lett. **62**, 324 (1989)
5. A. Georges, G. Kotliar, Phys. Rev. B **45**, 6479 (1992)
6. M. Jarrell, Phys. Rev. Lett. **69**, 168 (1992)
7. X.Y. Zhang, M.J. Rozenberg, G. Kotliar, Phys. Rev. Lett. **70**, 1666 (1993)
8. A. Georges, G. Kotliar, W. Krauth, M. Rozenberg, Rev. Mod. Phys. **68**(1), 13 (1996)
9. G. Kotliar, S. Savrasov, V. Oudovenko, O. Parcolet, C. Marianetti, Rev. Mod. Phys. **78**, 865 (2006)
10. K. Held, Adv. Phys. **56**, 829 (2007)
11. Y.A. Izyumov, E.Z. Kurmaev, Physics-Uspekhi **51**, 25 (2008)
12. http://www.agilent.com/about/newsroom/presrel/2006/08 mara106001.html (2006)
13. J. Hubbard, Phys. Rev. B **20**, 4584 (1979)
14. J. Hubbard, Phys. Rev. B **23**, 5974 (1981)
15. J. Hubbard, Phys. Rev. B **19**, 2626 (1979)
16. H. Hasegawa, J. Phys. Soc. Jpn. **46**, 1504 (1979)
17. H. Hasegawa, J. Phys. Soc. Jpn. **49**, 178 (1980)
18. Y. Kakehashi, P. Fulde, Phys. Rev. B **32**, 1995 (1985)
19. Y. Kakehashi, Phys. Rev. B **45**, 7196 (1992)
20. Y. Kakehashi, Phys. Rev. B **65**, 184420 (2002)
21. Y. Kakehashi, Phys. Rev. B **66**, 104428 (2002)
22. Y. Kakehashi, P. Fulde, Phys. Rev. B **69**, 045101 (2004)
23. Y. Kakehashi, P. Fulde, Phys. Rev. B **70**, 155112 (2004)
24. Y. Kakehashi, P. Fulde, Phys. Rev. B **70**, 195102 (2004)
25. Y. Kakehashi, P. Fulde, Phys. Rev. Lett. **94**, 156401 (2005)
26. S. Hirooka, M. Shimizu, J. Phys. Soc. Jpn. **43**, 70 (1977)
27. Y. Kakehashi, Adv. Phys., **53**, 497 (2004)
28. S.V. Vonsovskii, JETP **16**, 981 (1946)
29. C. Zener, Phys. Rev **82**(3), 403 (1951)
30. P. Anderson, Phys. Rev **124**(1), 41 (1961)
31. K.A. Chao, J. Spalek, A.M. Oles, J. Phys. C **10** (1977)

32. T. Moria, *Spin fluctuations in itinerant electron magnetism* (Springer Verlag, Berlin, Heidelberg, New York, Tokyo, 1985)
33. P. Anderson, Phys. Rev **115**(1), 2 (1959)
34. A.A. Abrikosov, Physics **2**, 21 (1965)
35. C. Zener, Phys. Rev **81**(4), 440 (1951)
36. P.W. Anderson, H. Hasegawa, Phys. Rev. **100**, 675 (1955)
37. P.G. deGennes, Phys. Rev. **118**, 141 (1960)
38. F. Mancini, A. Avella, Adv. Phys. **53**, 537 (2004)
39. M.C. Gutzwiller, Phys. Rev. Lett. **10**, 159 (1963)
40. Y.A. Izyumov, Physics-Uspekhi **38**, 389 (1995)
41. Y.A. Izyumov, Physics-Uspekhi **40**, 445 (1997)
42. Y.A. Izyumov, Physics-Uspekhi **42**, 215 (1999)
43. Y.A. Izyumov, Y.N. Skryabin, Physics-Uspekhi **44**, 109 (2001)
44. Yu. A. Izymov, N.N. Chashin, D.S. Alekseev, *Teoriya silno korrelirovannyh sistem: metod proizvodjashego funkcionala (Theory for strongly correlated systems: producing functional method)* (Regular and chaotic mechanics, Moscow-Izhevsk, 2006)
45. P. Hohenberg, W. Kohn, Phys. Rev. **136**(3), B864 (1964)
46. W. Kohn, L. Sham, Phys. Rev. **140**(4), A1133 (1965)
47. L. Sham, W. Kohn, Phys. Rev. **145**(2), 561 (1966)
48. L. Hedin, B. Lundqvist, J. Phys. C **4**, 2064 (1971)
49. R. Jones, O. Gunnarson, Rev. Mod. Phys. **61**(3), 689 (1989)
50. W. Kohn, Rev. Mod. Phys. **71**(5), 1253 (1999)
51. O. Andersen, Phys. Rev. B **12**(8), 3060 (1975)
52. E. Wimmer, H. Krakauer, M.Weinert, A.J. Freeman, Phys. Rev. B **24**, 864 (1981)
53. V. Heine, in *Solid State Physics, Advances in Research and Applications*, vol. 24, ed. by H. Ehrenreich, F. Seitz, D. Turnbul (Academic Press, New York – London, 1970)
54. J. de Boer, E. Verway, Proc. Phys. Soc. Lond, Ser. A **49**, 59 (1937)
55. N. Mott, Proc. Phys. Soc. London, Ser. A **49**, 72 (1937)
56. S.V. Vonsovskii, M.I. Katsnelson, A.V. Trefilov, Phys Metals Metallography **76**(3), 3 (1993)
57. S.V. Vonsovskii, M.I. Katsnelson, A.V. Trefilov, Physics of Metals and Metallography **76**(4), 3 (1993)
58. P. Anderson, in *50 years of the Mott phenomenon, in frontiers and borderlines in many particle physics*, ed. by J. Schrieffer, R. Broglia (North-Holland, Amsterdam, 1988)
59. N. Hamada, H. Sawada, K. Terakura, in *Spectroscopy of Mott insulators and correlation metals*, ed. by A. Fujimori, Y. Tokura (Springer-Verlag, Berlin, 1995)
60. D. Sarma, N. Shanthi, S. Barman, N. Hamada, H. Sawada, K. Terakura, Phys. Rev. Lett. **75**(6), 1126 (1995)
61. V. Anisimov, J. Zaanen, O. Andersen, Phys. Rev. B **44**(3), 943 (1991)
62. K. Terakura, T. Oguchi, A. Williams, J. Kübler, Phys. Rev. B **30**(8), 4734 (1984)
63. W. Pickett, Rev. Mod. Phys. **61**(2), 433 (1989)
64. A. Yanase, K. Siratori, J. Phys. Soc. Jpn. **53**(3), 312 (1984)
65. Z. Zhang, S. Satpathy, Phys. Rev. B **44**(24), 13319 (1991)

66. V. Anisimov, I. Elfimov, N. Hamada, K. Terakura, Phys. Rev. B **54**(7), 4387 (1996)
67. D. Langreth, M. Mehl, Phys. Rev. B **28**(4), 1809 (1983)
68. A. Becke, Phys. Rev. A **38**(6), 3098 (1988)
69. J. Perdew, J. Chevary, S. Vosko, K. Jackson, M. Pederson, D. Singh, C. Fiolhais, Phys. Rev. B **46**(11), 6671 (1992)
70. P. Dufek, P. Blaha, V. Sliwko, K. Schwarz, Phys. Rev. B **49**(15), 10170 (1994)
71. S. Massidda, M. Posternak, A. Baldereschi, Phys. Rev. B **48**(8), 5058 (1993)
72. O. Gunnarsson, O. Andersen, O. Jepsen, J. Zaanen, Phys. Rev. B **39**(3), 1708 (1989)
73. A. Svane, O. Gunnarsson, Phys. Rev. Lett **65**(9), 1148 (1990)
74. R. Cowan, Phys. Rev **163**(1), 54 (1967)
75. J. Perdew, A. Zunger, Phys. Rev. B **23**(10), 5048 (1981)
76. T. Fujiwara, M. Arai, Y. Ishii, in *Strong Coulomb correlations in electronic structure calculations: Beyond the local density approximation*, vol. 1, ed. by V. Anisimov (Gordon and Breach Science Publishers, Singapore, 2000), chap. 3, pp. 167–202
77. L. Hedin, Phys. Rev. **139**(3), A796 (1965)
78. J. Quinn, R. Ferrell, Phys. Rev. **112**(3), 812 (1958)
79. F. Aryasetiawan, O. Gunnarsson, Rep. Prog. Phys. **61**(2), 237 (1998)
80. R. Godby, M. Schlüter, L. Sham, Phys. Rev. Lett. **56**(22), 2415 (1986)
81. G. Strinati, H. Mattausch, W. Hanke, Phys. Rev. B **25**(4), 2867 (1982)
82. M. Hybertsen, S. Louie, Phys. Rev. Lett. **55**(13), 1418 (1985)
83. A. Lichtenstein, M. Katsnelson, Phys. Rev. B **57**(12), 6884 (1998)
84. M. Katsnelson, A. Lichtenstein, J. Phys.: Condens. Matter **11**(4), 1037 (1999)
85. M. Katsnel'son, A. Lichtenstein, A. Trefilov, Phys. Met. Metallography, Suppl. 1 **89**, S30 (2000)
86. A. Lichtenstein, M. Katsnelson, G. Kotliar, Phys. Rev. Lett **87**(067205) (2001)
87. V.I. Anisimov, A.V. Kozhevnikov, Phys. Rev. B **72**, 075125 (2005)
88. J. Slater, in *Self-consistent field methods for molecules and solids* (McGraw-Hill, New York, 1974)
89. G.H. Wannier, Phys. Rev. **52**, 191 (1937)
90. V.I. Anisimov, A.V. Kozhevnikov, M.A. Korotin, A.V. Lukoyanov, D.A. Khafizullin, J. Phys.: Condens. Matter **19**, 106206 (2007)
91. B. Judd, in *Operator techniques in atomic spectroscopy* (McGraw-Hill, New York, 1963)
92. N. Marzari, D. Vanderbilt, Phys. Rev. B **56**, 12847 (1997)
93. W. Ku, H. Rosner, W.E. Pickett, R.T. Scalettar, Phys. Rev. Lett. **89**, 167204 (2002)
94. D. Korotin, A.V. Kozhevnikov, S.L. Skornyakov, I. Leonov, N. Binggeli, V.I. Anisimov, G. Trimarchi, Eur. Phys. J. B **65**, 91 (2008)
95. S. Baroni, A.D. Corso, S. de Gironcoli, P. Giannozzi, C. Cavazzoni, G. Ballabio, S. Scandolo, P.F. G. Chiarotti, A. Pasquarello, K. Laasonen, A. Trave, R. Car, N. Marzari, A. Kokalj, http://www.pwscf.org/
96. V. Anisimov, O. Gunnarsson, Phys. Rev. B **43**(10), 7570 (1991)
97. F. de Groot, J. Fuggle, B. Thole, G. Sawatzky, Phys. Rev. B **42**(9), 5459 (1990)
98. T. Fujiwara, M. Korotin, Phys. Rev. B **59**(15), 9903 (1999)
99. I.V. Solovyev, M. Imada, Phys. Rev. B **71**, 045103 (2005)
100. F. Aryasetiawan, K. Karlsson, O. Jepsen, U. Schonberger, Phys. Rev. B. **74**, 125106 (2006)

101. M. Cococcioni, S. de Gironcoli, Phys. Rev. B **71**, 035105 (2005)
102. W.E. Pickett, S.C. Erwin, E.C. Ethridge, Phys. Rev. B **58**, 1201 (1998)
103. K. Nakamura, R. Arita, Y. Yoshimoto, S. Tsuneyuki, Phys. Rev. B **74**, 235113 (2006)
104. A. Liechtenstein, V. Anisimov, J. Zaanen, Phys. Rev. B **52**(8), R5467 (1995)
105. A. Liechtenstein, M. Katsnelson, V. Antropov, A. Gubanov, J. Magn. Magn. Mater **67**(1), 65 (1987)
106. H. Wu, Q. Zheng, X. Gong, H.Q. Lin, J. Phys.: Condens. Matter **11**, 4637 (1999)
107. E.J.W. Verwey, P.W. Haayman, Physica **8**, 979 (1941)
108. J. Verwey, P.W. Haayman, F.C. Romeijn, J. Chem. Phys. **15**, 181 (1947)
109. I. Leonov, A.N. Yaresko, V.N. Antonov, M.A. Korotin, V.I. Anisimov, Phys. Rev. Lett. **93**, 146404 (2004)
110. K.I. Kugel, D.I. Khomskii, JETP **64**(4), 1429 (1973)
111. K.I. Kugel, D.I. Khomskii, Soviet Physics-Uspekhi **25**, 231 (1982)
112. V. Anisimov, I. Elfimov, M. Korotin, K. Terakura, Phys. Rev. B **55**(23), 15494 (1997)
113. Z. Jirák, S. Krupička, Z. Šimša, M. Dlouhá, S. Vratislav, J. Magn. Magn. Mater **53**(1-2), 153 (1985)
114. M. Korotin, I. Elfimov, V. Anisimov, M. Troyer, D. Khomskii, Phys. Rev. Lett. **83**(7), 1387 (1999)
115. A.A. Abrikosov, L.P. Gor'kov, I.E. Dzyaloshinskii, *Methods of quantum field theory in statistical physics* (Dover, New York, 1975)
116. K.G. Wilson, Rev. Mod. Phys. **47**, 773 (1975)
117. R. Bulla, T.A. Costi, D. Vollhardt, Phys. Rev. B **64**, 045103 (2001)
118. M. Caffarel, W. Krauth, Phys. Rev. Lett. **72**, 1545 (1994)
119. C.A. Perroni, H. Ishida, A. Liebsch, Phys. Rev. B **75**, 045125 (2007)
120. M.J. Rozenberg, G. Kotliar, X.Y. Zhang, Phys. Rev. B **49**, 10181 (1994)
121. H. Kajuter, G. Kotliar, G. Moeller, Phys. Rev. B **53**, 16214 (1996)
122. V.I. Anisimov, A.I. Poteryaev, M.A. Korotin, A.O. Anokhin, G. Kotliar, J. Phys: Condens Matter **9**, 7359 (2097)
123. T. Pruschke, D.L. Cox, M. Jarrell, Phys. Rev. B **47**, 3553 (1993)
124. N.E. Bickers, Rev. Mod. Phys. **59**, 845 (1987)
125. H.O. Jeschke, G. Kotliar, Phys. Rev. B **71**, 085103 (2005)
126. I.V. Stasyuk, O.B. Hera, Phys. Rev. B **72**, 045134 (2005)
127. J.E. Hirsch, Phys. Rev. B **28**, 4059 (1983)
128. J.E. Hirsch, R.M. Fye, Phys. Rev. Lett. **56**, 2521 (1986)
129. R.M. Fye, J.E. Hirsch, Phys. Rev. B **38**, 433 (1988)
130. K. Haule, http://www.physics.rutgers.edu/grad/509/
131. R. Blankenbecler, D.J. Scalapino, R.L. Sugar, Phys. Rev. D **24**, 2278 (1981)
132. R.N. Silver, D.S. Sivia, J.E. Gubernatis, Phys. Rev. B **41**, 2380 (1990)
133. R.N. Silver, D.S. Sivia, J.E. Gubernatis, M. Jarrell, Phys. Rev. Lett. **65**, 496 (1990)
134. J.E. Gubernatis, M. Jarrell, R.N. Silver, D. Sivia, Phys. Rev. B **44**, 6011 (1991)
135. M. Jarrell, J.E. Gubernatis, Phys. Rep. **269**, 133 (1996)
136. M. Jarrell, private communication
137. M. Feldbacher, K. Held, F.F. Assaad, Phys. Rev. Lett. **93**, 136405 (2004)
138. R. Arita, K. Held, Phys. Rev. B **72**, 201102 (2005)
139. R. Arita, K. Held, Phys. Rev. B **73**, 064515 (2006)

140. S.R. White, D.J. Scalapino, R.L. Sugar, E.Y. Loh, J.E. Gubernatis, R.T. Scalettar, Phys. Rev. B **40**, 506 (1989)
141. N.V. Prokof'ev, B.V. Svistuniv, I.S. Tupicin, JETP Lett. **64**, 853 (1996)
142. A.N. Rubtsov, V.V. Savkin, A.I. Lichtenstein, Phys. Rev. B **72**, 035122 (2005)
143. P. Werner, A. Comanac, L. Medici, M. Troyer, A.J. Millis, Phys. Rev. Lett. **97**, 076405 (2006)
144. K. Haule, Phys. Rev. B **75**, 155113 (2007)
145. P. Werner, A.J. Millis, Phys. Rev. B **74**, 155107 (2006)
146. P. Werner, A.J. Millis, Phys. Rev. B **75**, 085108 (2007)
147. A. Georges, W. Krauth, Phys. Rev. Lett. **69**, 1240 (1992)
148. R. Bulla, Phys. Rev. Lett. **83**, 136 (1999)
149. A. Georges, cond-mat/0403123
150. D.S. Fischer, G. Kotliar, G. Moeller, Phys. Rev. B **52**, 17112 (1995)
151. G. Kotliar, S. Murthy, M.J. Rozenberg, Phys. Rev. Lett. **89**, 046401 (2002)
152. D.J. Garcia, E. Miranda, K. Hallberg, M.J. Rozenberg, Phys. Rev. B **75**, 121102 (2007)
153. D.J. Garcia, K. Hallberg, M.J. Rozenberg, Phys. Rev. Lett. **93**, 246403 (2004)
154. U. Schollwock, Rev. Mod. Phys. **77**, 259 (2005)
155. K. Hallberg, Adv. Phys. **55**, 477 (2006)
156. M. Potthoff, Eur. Phys. J. B **32**, 429 (2003)
157. M. Eckstein, M. Koller, M. Potthoff, D. Vollhardt, Phys. Rev. B **75**, 125103 (2007)
158. J. Bauer, A.C. Hewson, Eur. Phys. J. B **57**, 235 (2007)
159. H. Park, K. Haule, C.A. Marianetti, G. Kotliar, Phys. Rev. Lett. **77**, 035107 (2008)
160. Y. Nagaoka, Phys. Rev. **147**, 392 (1966)
161. R. Zitzler, T. Pruschke, R. Bulla, Eur. Phys. J. B **27**, 473 (2002)
162. E. Demler, W. Hanke, S.C. Zhang, Rev. Mod. Phys. **76**, 909 (2004)
163. A.M.S. Tremblay, B. Kyung, D. Senechal, Low Temp. Phys. **32**, 424 (2006)
164. D. Senechal, P.L. Lavertu, M.A. Marois, A.M.S. Tremblay, Phys. Rev. Lett. **94**, 156404 (2005)
165. M. Aichhorn, E. Arrigoni, Europhys. Lett. **72**, 117 (2005)
166. M. Capone, G. Kotliar, Phys. Rev. B **74**, 054513 (2006)
167. A.I. Lichtenstein, M.I. Katsnelson, Phys. Rev. B **62** (2000)
168. M.H. Hettler, A.N. Tahvildar-Zadeh, M. Jarrell, H.R. Krishnamurthy, Phys. Rev. B **58**, 7475 (1998)
169. L.N. Bulaevskii, A.I. Buzdin, M.L. Kuli, S.V. Panjukov, Adv. Phys. **34**, 175 (1985)
170. Y.A. Izyumov, V.M. Laptev, Int. J. Mod. Phys. B **4**, 447 (1990)
171. E. Muller-Hartman, Z. Phys. B **74**, 507 (1989)
172. V. Zlatic, B. Horvatic, Solid State Commun. **75**, 263 (1990)
173. M. Jarrell, T. Pruschke, Z. Phys. B **90**, 187 (1993)
174. M. Jarrell, J.K. Freericks, T. Pruschke, Phys. Rev. B **51**, 11704 (1995)
175. M. Jarrell, T. Pruschke, Phys. Rev. B **49**, 1458 (1994)
176. K. Haule, A. Rosh, J. Kroha, Phys. Rev. Lett. **89**, 236402 (2002)
177. K. Haule, A. Rosh, J. Kroha, Phys. Rev. B **68**, 155119 (2003)
178. Y.A. Izyumov, F.A. Kasan-Ogli, Y.N. Skryabin, *Polevye metody v teorii ferromagnetisma (Field theory methods in ferromagnetism theory)* (Nauka, Moscow, 1974)

179. J.L. Smith, Q. Si, Phys. Rev. B **61**, 5184 (2000)
180. R. Chitra, G. Kotliar, Phys. Rev. Lett. **84**, 3678 (2000)
181. Y. Motome, G. Kotliar, Phys. Rev. B **62**, 12800 (2000)
182. S. Pankov, G. Kotliar, Y. Motome, Phys. Rev. B **66**, 045117 (2002)
183. P. Sun, G. Kotliar, Phys. Rev. B **66**, 085120 (2002)
184. S. Sakai, K. Arita, H. Aoki, Phys Rev. B **70**, 172504 (2004)
185. Y. Motome, M. Imada, J. Phys. Soc. Jpn. **66**, 1872 (1997)
186. J.E. Han, Phys. Rev. B **70**, 054513 (2004)
187. V.I. Anisimov, I.A. Nekrasov, D.E. Kondakov, T.M. Rice, M. Sigrist, Eur. Phys. J. B **25**, 191 (2002)
188. A. Koga, N. Kawakami, T.M. Rice, M. Sigrist, Phys. Rev. Lett. **92**, 216402 (2004)
189. Y. Motome, M. Imada, J. Phys. Soc. Jpn. **67**, 3199 (1998)
190. A. Liebsch, Phys. Rev. Lett. **91**, 226401 (2003)
191. A. Liebsch, Phys. Rev. Lett. **95**, 116402 (2005)
192. H. Kusunose, J. Phys. Soc. Jpn. **75**, 054713 (2006)
193. A. Toschi, A.A. Katanin, K. Held, Phys. Rev. B **75**, 045118 (2007)
194. M.V. Sadovskii, Physics-Uspekhi **44**, 515 (2001)
195. M.V. Sadovskii, cond-mat/0408489
196. T. Yoshida, X.J. Zhou, D.H. Lu, Y. Ando, H. Eisaki, T. Kakeshita, S. Uchida, Z. Hussain, Z.X. Shen, A. Fujimori, J. Phys.: Condens. Matter **19**, 125209 (2007)
197. E.Z. Kuchinskii, I.A. Nekrasov, Z.V. Pchelkina, M.V. Sadovskii, JETP **131**, 908 (2007)
198. A.J. Millis, H. Momen, D. Pines, Phys. Rev. B **42**, 167 (1990)
199. M.V. Sadovskii, JETP **77**, 2070 (1979)
200. Y.M. Vilk, A.M.S. Tremblay, J. Phys. I France **7**, 1309 (1997)
201. M.V. Sadovskii, I.A. Nekrasov, E.Z. Kuchinskii, T. Pruschke, V.I. Anisimov, Phys. Rev. B **72**, 155105 (2005)
202. E.Z. Kuchinskii, I.A. Nekrasov, M.V. Sadovskii, Low Temp Phys **32**, 398 (2006)
203. E.Z. Kuchinskii, I.A. Nekrasov, M.V. Sadovskii, Phys. Rev. B **75**, 115102 (2007)
204. E.Z. Kuchinskii, I.A. Nekrasov, M.V. Sadovskii, JETP Lett. **82**, 217 (2005)
205. T. Maier, M. Jarrell, T. Pruschke, M.H. Hettler, Rev. Mod. Phys. **77**, 1027 (2005)
206. M. Jarrell, T. Maier, C. Huscroft, S. Moukouri, Phys. Rev. B **64**, 195130 (2001)
207. J.P. Hague, M. Jarrell, T.C. Schultess, Phys. Rev. B **69**, 165113 (2004)
208. S. Moukouri, S. Allen, F. Lemay, B. Kyung, D. Poulin, Y.M. Vilk, A.M.S. Tremblay, Phys. Rev. B **69**, 165113 (2004)
209. B. Kyung, S.S. Karcharla, D. Senechal, A.M.S. Tremblay, Civelli, G. Kotliar, Phys. Rev. B **73**, 165114 (2006)
210. A.H. Nevidomskyy, D. Senechal, A.M.S. Tremblay, Phys. Rev. B **77**, 075105 (2008)
211. T.D. Stanescu, G. Kotliar, Phys. Rev. B **74**, 125110 (2006)
212. N.M. Plakida, V.S. Oudovenko, JETP **131**, 259 (2007)
213. A. Sherman, Phys. Rev. B **73**, 155105 (2006)
214. A. Sherman, Phys. Rev. B **74**, 035104 (2006)
215. A. Sherman, M. Schreiber, Phys. Rev. B **76**, 245112 (2007)
216. M.I. Vladimir, V.A. Moskalenko, Teoreticheskaya i Matematicheskaya Fizika (Theoretical and Mathematical Physics) **82**, 428 (1990)

217. W. Metzner, Phys. Rev. B **43**, 8549 (1991)
218. J.E. Hirsch, Phys. Rev. B **31**, 4403 (1985)
219. H. Park, K. Haule, G. Kotliar, cond-mat/0803.1324
220. K. Haule, G. Kotliar, Phys. Rev. B **76**, 104509 (2007)
221. O. Parcollet, G. Biroli, G. Kotliar, Phys. Rev. Lett. **92**, 226402 (2004)
222. M. Civelli, M. Capone, S.S. Kancharla, O. Parcollet, G. Kotliar, Phys. Rev. Lett. **95**, 106402 (2005)
223. G. Baym, L.P. Kadanoff, Phys. Rev. **124**, 287 (1961)
224. G. Kotliar, Eur. Phys. J. B **11**, 27 (1999)
225. R. Chitra, G. Kotliar, Phys. Rev. B **62**, 12715 (2000)
226. G.K. R. Chitra, Phys. Rev. Lett. **63**, 115110 (2001)
227. S.Y. Savrasov, G. Kotliar, cond-mat/0308053
228. P.W. Anderson, Phys. Rev. **109**, 1492 (1958)
229. A.M. Finkelshtein, Sov. Phys. JETP **75**, 97 (1983)
230. C. Castellani, C. diCastro, Phys. Rev. B **34**, 5935 (1986)
231. C. Castellani, C. diCastro, G. Kotliar, P.A. Lee, Phys. Rev. Lett. **56**, 1179 (1986)
232. R. Vlaming, D. Vollhardt, Phys. Rev. B **45**, 4637 (1992)
233. V. Dobrosavljevic, G. Kotliar, Phys. Rev. Lett. **78**, 3943 (1997)
234. K. Byczuk, W. Hofstetter, D. Vollhardt, Phys. Rev. Lett. **94**, 056404 (2005)
235. V. Dobrosavljevic, A.A. Pastor, B.K. Nikolic, Europhys. Lett. **62**, 76 (2003)
236. E.Z. Kuchinskii, I.A. Nekrasov, M.V. Sadovskii, JETP **106**, 581 (2008)
237. M.V. Sadovskii, in *Soviet Scientific Reviews—Physics Reviews*, ed. by I. Khalatnikov (Harwood Academic Publisher, NY, 1986)
238. U. Yu, K. Byczuk, D. Vollhardt, Phys. Rev. Lett. **100**, 246401 (2008)
239. M.C.O. Aguiar, E. Miranda, V. Dobrosavljevic, Phys. Rev. B **68**, 125104 (2003)
240. C. Grenzebach, F.B. Anders, G. Czycholl, T. Pruschke, Phys. Rev. B **77**, 115125 (2008)
241. J.R. Schrieffer, P.A. Wolff, Phys. Rev. **149**, 491 (1966)
242. J. Kondo, Progr. Theor. Phys. **32**, 37 (1964)
243. A.C. Hewson, *The Kondo problem to heavy fermions* (Cambridge University Press, Cambridge, 1993)
244. H. Suhl, Phys. Rev. **138** (1965)
245. T.M. Rice, K. Ueda, Phys. Rev. Lett. **55**, 995 (1985)
246. T.M. Rice, K. Ueda, Phys. Rev. B **34**, 6420 (1986)
247. M.C. Gutzwiller, Phys. Rev. **137** (1965)
248. N. Read, D.M. Newns, S. Doniack, Phys. Rev. B **30**, 3841 (1984)
249. P. Coleman, Phys. Rev. B **29**, 3035 (1984)
250. B.H. Brandow, Phys. Rev. B **33**, 215 (1986)
251. M. Jarrell, Phys. Rev. B **51**, 7429 (1995)
252. T. Pruschke, R. Bulla, M. Jarrell, Phys. Rev. B **61**, 12799 (2000)
253. P. Nozieres, Eur. Phys. J. B **6**, 447 (1998)
254. T.A. Costi, N. Manini, J.Low Temp. Phys. **126**, 835 (2002)
255. T.A. Costi, Phys. Rev. Lett. **85**, 1504 (2000)
256. H.R. Krishnamurthy, J.W. Wilkins, K.G. Wilson, Phys. Rev. B **21**, 1003 (1980)
257. R. Bulla, T. Pruschke, A.C. Hewson, J. Phys.: Condens. Matter **9**, 10463 (1997)
258. S. Burdin, A. Georges, D.R. Grempel, Phys. Rev. Lett. **85**, 1048 (2000)
259. D.P. Moore, J.J. Joyce, A.J. Arko, J.L. Sarrao, L. Morales, Y. Hochst, D. Chuang, Phys. Rev. B **62**, 16492 (2000)

260. P. Weibel, M. Grioni, D. Malterve, B. Dardel, Y. Baer, M.J. Besnus, Z. Phys. B **91**, 337 (1993)
261. C. Zener, Phys. Rev. **82**, 403 (1951)
262. N.J. Furukawa, J. Phys. Soc. Jpn. **63**, 3214 (1994)
263. N. Furukawa, cond-mat/9812066
264. N. Furukawa, in *Physics of manganites*, ed. by A. Kaplan, S.D. Mahanti (Kluwer Academic, New York, 1999)
265. A.J. Millis, R. Mueller, B.I. Shraiman, Phys. Rev. B **54**, 5405 (1996)
266. A. Chattopadhyay, A.J. Millis, S. Das-Sarma, Phys. Rev. B **64**, 012416 (2001)
267. A. Chattopadhyay, A.J. Millis, S. Das-Sarma, Phys. Rev. B **61**, 10738 (2000)
268. C. Lin, A.J. Millis, Phys. Rev. B **72**, 245112 (2005)
269. A.K. McMahan, K. Held, R.T. Scalettar, Phys. Rev. B **67**, 075108 (2003)
270. I.A. Nekrasov, G. Keller, D.E. Kondakov, A.V. Kozhevnikov, T. Pruschke, K. Held, D. Vollhardt, V.I. Anisimov, Phys. Rev. B **72**, 155106 (2005)
271. A. Sekiyama, H. Fujiwara, S. Imada, S. Suga, H. Eisaki, S.I. Uchida, K. Takegahara, H. Harima, Y. Saitoh, I.A. Nekrasov, G. Keller, D.E. Kondakov, A.V. Kozhevnikov, T. Pruschke, K. Held, D. Vollhardt, V.I. Anisimov, Phys. Rev. Lett. **93**, 156402 (2004)
272. I.A. Nekrasov, K. Held, G. Keller, D.E. Kondakov, T. Pruschke, M. Kollar, O.K. Andersen, V.I. Anisimov, D. Vollhardt, Phys. Rev. B **73**, 155112 (2006)
273. F. Lechermann, A. Georges, A. Poteryaev, S. Biermann, M. Posternak, A. Yamasaki, O.K. Andersen, Phys. Rev. B **74**, 125120 (2006)
274. B. Amadon, F. Lechermann, A. Georges, F. Jollet, T.O. Wehling, A.I. Lichtenstein, Phys. Rev. B **77**, 205112 (2008)
275. G. Keller, V.E. K. Held, D. Vollhardt, V.I. Anisimov, Phys. Rev. B **70**, 205116 (2004)
276. M. Schramme. Ph.D Thesis, Universität Augsburg, 2000
277. S.K. Mo, J.D. Denlinger, H.D. Kim, J.H. Park, J.W. Allen, A. Sekiyama, A. Yamasaki, K. Kadono, S. Suga, Y. Saitoh, T. Muro, P. Metcalf, G. Keller, K. Held, V. Eyert, V.I. Anisimov, D. Vollhardt, Phys. Rev. Lett. **90**, 186403 (2003)
278. O. Müller, J.P. Urbach, E. Goering, T. Weber, R. Barth, H. Schuler, M. Klemm, S. Horn, Phys. Rev. B **56**, 15056 (1997)
279. R. Arita, K. Held, A.V. Lukoyanov, V.I. Anisimov, Phys. Rev. Lett. **98**, 166402 (2007)
280. A. Shimoyamada, S. Tsuda, K. Ishizaka, T. Kiss, T. Shimojima, T. Togashi, S. Watanabe, C.Q. Zhang, C.T. Chen, Y. Matsushita, H. Ueda, Y. Ueda, S. Shin, Phys. Rev. Lett. **96**, 026403 (2006)
281. J. Zaanen, G. Sawatzky, J. Allen, Phys. Rev. Lett. **55**(4), 418 (1985)
282. A. Fujimori, F. Minami, S. Sugano, Phys. Rev. B **29**, 5225 (1984)
283. J. Kunes, V.I. Anisimov, A.V. Lukoyanov, D. Vollhardt, Phys. Rev. B **75**, 165115 (2007)
284. G. Sawatzky, J.W.Allen, Phys. Rev. Lett. **53**, 2339 (1984)
285. J. van Elp, H. Eskes, P. Kuiper, G.A. Sawatzky, Phys. Rev. B **45**, 1612 (1992)
286. J. Kunes, V.I. Anisimov, S.L. Skornyakov, A.V. Lukoyanov, D. Vollhardt, Phys. Rev. Lett. **99**, 156404 (2007)
287. Z.X. Shen, R.S. List, D.S. Dessau, B.O. Wells, O. Jepsen, A.J. Arko, R. Barttlet, C.K. Shih, F. Parmigiani, J.C. Huang, P.A.P. Lindberg, Phys. Rev. B **44**, 3604 (1991)

288. J. Kunes, A.V. Lukoyanov, V.I. Anisimov, R.T. Scalettar, W.E. Pickett, Nature Materials **7**, 198 (2008)
289. B. Johansson, Philos. Mag. **30**, 469 (1974)
290. B. Johansson, I.A. Abrikosov, M. Aldén, A.V. Ruban, H.L. Skriver, Phys. Rev. Lett. **74**, 2335 (1995)
291. J.W. Allen, R.M. Martin, Phys. Rev. Lett. **49**, 1106 (1982)
292. M. Lavagna, C. Lacroix, M. Cyrot, Phys. Lett. **90A**, 210 (1982)
293. A.K. McMahan, K. Held, R.T. Scalettar, Phys. Rev. B **67**, 075108 (2003)
294. L.Z. Liu, J.W. Allen, O. Gunnarson, N.E. Christensen, O.K. Andersen, Phys. Rev. B **45**, 8934 (1992)
295. A.J. Millis, Nature **392**, 147 (1998)
296. E. Dagotto, T. Hotta, A. Moreo, Phys. Rep. **344**, 1 (2001)
297. M.B. Salamon, M. Jaime, Rev. Mod. Phys. **73**, 583 (2001)
298. Y. Tokura, A. Uruskibara, Y. Moritomo, T. Arima, A. Asamitsu, G. Kido, N. Fuvukawa, J. Phys. Soc. Jpn. **63**, 3931 (1994)
299. Y.F. Yang. Dynamical mean field theory for manganite. Ph.D Thesis, Max-Plank-Institute für festkörperforschung, Stuttgart, 2007
300. Y.F. Yang, K. Held, Phys. Rev. B **76**, 212401 (2007)
301. J. Kanamori, J. Appl. Phys. **31**, S14 (1960)
302. A. Yamasaki, M. Feldbacher, Y.F. Yang, O.K. Andersen, K. Held, Phys. Rev. Lett. **96**, 166401 (2006)
303. K. Held, O.K. Andersen, M. Feldbacker, A. Yamasaki, Y.F. Yang, J. Phys: Condens. Matter **20**, 064202 (2008)
304. M.N. Iliev, M.V. Abrashev, H.G. Lee, V.N. Popov, Y.Y. Sun, C. Thomsen, R.L. Meng, C.W. Chu, Phys. Rev. B **57**, 2872 (1998)
305. K. Takenaka, K. Iida, Y. Sawaki, S. Sugai, Y. Moritomo, A. Nakamuro, J. Phys. Soc. Jpn. **68**, 1828 (1999)
306. D.M. Edwards, cond-mat/0201558
307. Y. Kamihara, T. Watanabe, M. Hirano, H. Hosono, J. Am. Chem. Soc. **130**, 3296 (2008)
308. V.I. Anisimov, D.M. Korotin, M. Korotin, A.V. Kozhevnikov, J. Kunes, A.O. Shorikov, S.L. Skornyakov, S.V. Streltsov, J. Phys.: Condens. Matter **21**, 075602 (2009)
309. K. Haule, J.H. Shim, G. Kotliar, Phys. Rev. Lett. **100**, 226402 (2008)
310. A.O. Shorikov, M.A. Korotin, S.V. Streltsov, D.M. Korotin, V.I. Anisimov, S.L. Skornyakov, J. Exp. Theoret. Phys. **108**, 121 (2009)
311. A.I. Coldea, J.D. Fletcher, A. Carrington, et al., Phys. Rev. Lett. **101**, 216402 (2008)
312. A. Koitzsch, D. Inosov, J. Fink, et al., Phys. Rev. B **78**, 180506 (2008)
313. C. Liu, G.D. Samolyuk, Y. Lee, N. Ni, T. Kondo, A.F. Santander-Syro, S.L. Bud'ko, J.L. McChesney, E. Rotenberg, T. Valla, A.V. Fedorov, P.C. Canfield, B.N. Harmon, A. Kaminski, Phys. Rev. Lett. **100**, 177005 (2008)
314. S. Skornyakov, A. Efremov, N. Skorikov, M. Korotin, Y. Izyumov, V. Anisimov, A. Kozhevnikov, D. Vollhardt, cond-mat/0906.3218
315. H. Ding, K. Nakayama, P. Richard, S. Souma, T. Sato, T. Takahashi, M. Neupane, Y.M. Xu, Z.H. Pan, A.V. Federov, Z. Wang, X. Dai, Z. Fang, G.F. Chen, J.L. Luo, N.L. Wang, cond-mat/0812.0534
316. M. Yi, D.H. Lu, J.G. Analytis, J.H. Chu, S.K. Mo, R.H. He, X.J. Zhou, G.F. Chen, J.L. Luo, N.L. Wang, Z. Hussain, D.J. Singh, I.R. Fisher, Z.X. Shen, cond-mat/0902.2628

317. K. Held, G. Keller, V. Eyert, V.I. Anisimov, D. Vollhardt, Phys. Rev. Lett. **86**, 5345 (2001)
318. A.I. Poteryaev, J.M. Tomczak, S. Biermann, A. Georges, A.I. Lichtenstein, A.N. Rubtsov, T. Saha-Dasgupta, O.K. Andersen, Phys. Rev. B **76**, 085127 (2007)
319. M.S. Laad, L. Craco, E. Müller-Hartmann, Phys. Rev. B **73**, 195120 (2006)
320. S. Biermann, A. Poteryaev, A.I. Lichtenstein, A. Georges, Phys. Rev. Lett. **94**, 026404 (2005)
321. E. Pavarini, S. Biermann, A. Poteryaev, A.I. Lichtenstein, A. Georges, O.K. Andersen, Phys. Rev. Lett. **92**, 176403 (2004)
322. K. Byczuk, M. Kollar, K. Held, Y.F. Yang, I.A. Nekrasov, T. Pruschke, D. Vollhardt, Nature Physics **3**, 168 (2007)
323. L. Craco, S. Leoni, E. Müller-Hartmann, Phys. Rev. B **74**, 155128 (2006)
324. M. Takizawa, H. Wadati, K. Tanaka, et al., Phys. Rev. Lett. **97**, 057601 (2006)
325. V.S. Oudovenko, K. Haule, S.Y. Savrasov, D. Villani, G. Kotliar, cond-mat/0401539
326. V.S. Oudovenko, G. Palsson, S.Y. Savrasov, K. Haule, G. Kotliar, Phys. Rev. B **70**, 125112 (2004)
327. A. Liebsch, Phys. Rev. B **77**, 115115 (2008)
328. L. Craco, S. Leoni, M.S. Laad, H. Rosner, Phys. Rev. B **76**, 115128 (2007)
329. I.A. Nekrasov, Z.V. Pchelkina, G. Keller, T. Pruschke, K. Held, A. Krimmel, D. Vollhardt, V.I. Anisimov, Phys. Rev. B **67**, 085111 (2003)
330. M.S. Laad, L. Craco, E. Müller-Hartmann, Phys. Rev. B **67**, 033105 (2003)
331. R. Arita, K. Held, A.V. Lukoyanov, V.I. Anisimov, Phys. Rev. Lett. **98**, 166402 (2007)
332. B. Michaelis, A.J. Millis, Phys. Rev. B **68**, 115111 (2003)
333. L. Craco, E. Müller-Hartmann, Phys. Rev. B **77**, 045130 (2008)
334. A. Liebsch, A. Lichtenstein, Phys. Rev. Lett. **84**, 1591 (2000)
335. Z.V. Pchelkina, I.A. Nekrasov, T. Pruschke, A. Sekiyama, S. Suga, V.I. Anisimov, D. Vollhardt, Phys. Rev. B **75**, 035122 (2007)
336. S. Okamoto, A.J. Millis, Phys. Rev. B **70**, 195120 (2004)
337. F. Lechermann, S. Biermann, A. Georges, cond-mat/0505241
338. H. Ishida, M.D. Johannes, A. Liebsch, Phys. Rev. Lett. **94**, 196401 (2005)
339. C.A. Marianetti, K. Haule, D. Parcollet, Phys. Rev. Lett. **99**, 246404 (2007)
340. S. Zhou, M. Cao, H. Ding, P.A. Lee, Z. Wang, Phys. Rev. Lett. **94**, 206401 (2005)
341. D. Pillay, M.D. Johannes, I.I. Mazin, O.K. Andersen, Phys. Rev. B **78**, 012501 (2008)
342. A. Bourgeois, A. Aligia, M. Rozenberg, Phys. Rev. Lett. **102**, 066402 (2009)
343. S.Y. Savrasov, G. Kotliar, Phys. Rev. Lett. **90**, 056401 (2003)
344. X. Ren, I. Leonov, G. Keller, M. Kollar, I.A. Nekrasov, D. Vollhardt, Phys. Rev. B **74**, 195114 (2006)
345. X. Wan, Q. Yin, S.Y. Savrasov, Phys. Rev. Lett. **97**, 266403 (2006)
346. O. Miura, T. Fujiwara, Phys. Rev. B **77**, 195124 (2008)
347. B. Amadon, F. Lechermann, A. Georges, F. Jollet, T.O. Wehling, A.I. Lichtenstein, Phys. Rev. B **77**, 205112 (2008)
348. J.K. Freericks, H.R. Krishnamurthy, Y. Ge, A.Y. Liu, T. Pruschke, Phys. Stat. Sol. B **246**, 948 (2009)
349. E. Pavarini, E. Koch, A.I. Lichtenstein, Phys. Rev. Lett. **101**, 266405 (2008)

350. I. Leonov, N. Binggeli, D. Korotin, V.I. Anisimov, N. Stojic, D. Vollhardt, Phys. Rev. Lett. **101**, 096405 (2008)
351. J. Kunes, V.I. Anisimov, Phys. Rev. B **78**, 033109 (2008)
352. J. Kunes, D.M. Korotin, M.A. Korotin, V.I. Anisimov, P. Werner, Phys. Rev. Lett. **102**, 146402 (2009)
353. L. Craco, M. S.Laad, E. Müller-Hartmann, Phys. Rev. B **74**, 064425 (2006)
354. L. Craco, C.I. Ventura, A.N. Yaresko, E. Müller-Hartmann, Phys. Rev. B **73**, 094432 (2006)
355. T. Saha-Dasgupta, A.I. Lichtenstein, R. Valenti, Phys. Rev. B **71**, 153108 (2005)
356. L. Craco, M.S. Laad, E. Müller-Hartmann, cond-mat/0410472
357. L. Chioncel, M.I. Katsnelson, R.A. de Groot, A.I. Lichtenstein, Phys. Rev. B **68**, 144425 (2003)
358. S. Chadov, J. Minar, H. Ebert, A. Perlov, L. Chioncel, M.I. Katsnelson, A.I. Lichtenstein, Phys. Rev. B **74**, 140411 (2006)
359. L. Chioncel, E. Arrigoni, M.I. Katsnelson, A.I. Lichtenstein, Phys. Rev. Lett. **96**, 137203 (2006)
360. L. Craco, M.S. Laad, E. Müller-Hartmann, Phys. Rev. B **68**, 233310 (2003)
361. L. Chioncel, P. Mavropoulos, M. Lezaic, S. Blügel, E. Arrigoni, M.I. Katsnelson, A.I. Lichtenstein, Phys. Rev. Lett. **96**, 197203 (2006)
362. L. Chioncel, M.I. Katsnelson, G.A. de Wijs, R.A. de Groot, A.I. Lichtenstein, Phys. Rev. B **71**, 085111 (2005)
363. S. Chadov, G. Fecher, C. Felser, J. Minar, J. Braun, H. Ebert, arXiv:0811.4625v1 [cond-mat.str-el] (2008)
364. M.S. Laad, arXiv:0811.3767v1 [cond-mat.str-el] (2008)
365. X. Dai, K. Haule, G. Kotliar, J. Phys: Condens Matter **17**, 61 (2005)
366. A.I. Lichtenstein, M.I. Katsnelson, G. Kotliar, Phys. Rev. Lett. **87**, 067205 (2001)
367. S. Biermann, F. Aryasetiawan, A. Georges, Phys. Rev. Lett. **90**, 086402 (2003)
368. O. Šipr, J. Minár, S. Mankovsky, H. Ebert, Phys. Rev. B **78**(14), 144403 (2008)
369. A. Grechnev, I.D. Marco, M.I. Katsnelson, A.I. Lichtenstein, J. Wills, O. Eriksson, Phys. Rev. B **76**, 035107 (2007)
370. K. Aryanpour, J. Moreno, M. Jarrell, R.S. Fishman, Phys. Rev. B **72**, 045343 (2005)
371. R. Arita, K. Kuroki, K. Held, A.V. Lukoyanov, S. Skornyakov, V.I. Anisimov, Phys. Rev. B **78**, 115121 (2008)
372. M.B. Zoelfl, I.A. Nekrasov, T. Pruschke, V.I. Anisimov, J. Keller, Phys. Rev. Lett. **87**, 276403 (2001)
373. K. Held, A.K. McMahan, R.T. Scalettar, Phys. Rev. Lett. **87**, 276404 (2001)
374. A.K. McMahan, Phys. Rev. B **72**, 115125 (2005)
375. K. Haule, V.S. Oudovenko, S.Y. Savrasov, G. Kotliar, Phys. Rev. Lett. **94**, 036401 (2005)
376. B. Amadon, S. Biermann, A. Georges, F. Aryasetiawan, Phys. Rev. Lett. **96**, 066402 (2006)
377. S.Y. Savrasov, G. Kotliar, E. Abrahams, Nature **410**, 793 (2001)
378. L.V. Pourovskii, M.I. Katsnelson, A.I. Lichtenstein, L. Havela, T. Gouder, F. Wastin, A.B. Shick, V. Drchal, G.H. Lander, Europhys. Lett. **74**, 479 (2006)
379. X. Dai, S.Y. Savrasov, G. Kotliar, A. Migliori, H. Ledbetter, E. Abrahams, Science **300**, 953 (2003)

380. C.A. Marianetti, K. Haule, G. Kotliar, M.J. Fluss, Phys. Rev. Lett. **101**, 056403 (2008)
381. J.X. Zhu, A.K. McMahan, M.D. Jones, T. Durakiewicz, J.J. Joyce, J.M. Wills, R.C. Albers, Phys. Rev. B **76**, 245118 (2007)
382. S.Y. Savrasov, K. Haule, G. Kotliar, Phys. Rev. Lett. **96**, 036404 (2006)
383. J.H. Shim, K. Haule, S. Savrasov, G. Kotliar, Phys. Rev. Lett. **101**, 126403 (2008)
384. M.S. Laad, arXiv:0805.2115 [cond-mat.str-el] (2008)
385. A. Shick, J. Kolorenc, L. Havela, V. Drchal, T. Gouder, Europhys. Lett. **77**, 17003 (2007)
386. L.V. Pourovskii, M.I. Katsnelson, A.I. Lichtenstein, Phys. Rev. B **72**, 115106 (2005)
387. L.V. Pourovskii, M.I. Katsnelson, A.I. Lichtenstein, Phys. Rev. B **73**, 060506 (2006)
388. R.P. Feynman, Rev. Mod. Phys. **20**, 367 (1948)
389. R.P. Feynman, A.R. Hibbs, *Quantum mechanics and path integrals* (McGrow Hills, New York, 1965)
390. L.D. Faddeev, A.A. Slavnov, *Gauge fields: Introduction to quantum theory* (Benjamin, Reading, Mass., 1980)
391. F.A. Berezin, *The Methods of Second Quantization* (Acadamic Press, New York, 1966)
392. W.M. Zhang, D.H. Feng, R. Gilmore, Rev.Mod.Phys. **62**, 867 (1990)
393. A. Auerbach, *Interacting Electrons and Quantum Magnetism* (Springer, Berlin, 1994)
394. T. Matsubara, Progr. Theor. Phys. **14**, 351 (1955)
395. Y.A. Izyumov, Y.N. Skryabin, *Bazovye modeli v kvantovoj teorii magnetizma (Basic models in quantum theory of magnetism)* (Russian Academy of Scince-Ural division, Yekaterinburg, 2002)
396. N.N. Bogolubov, S.V. Tyablikov, Sovet Physics – Doklady **4**, 589 (1959)
397. D.N. Zubarev, Soviet Physics-Uspekhi **3**, 320 (1960)

Index